

POLISH SOCIETY OF THEORETICAL AND APPLIED MECHANICS

**JOURNAL OF THEORETICAL
AND APPLIED MECHANICS**

No. 1 • Vol 55

Quarterly

WARSAW, JANUARY 2017

JOURNAL OF THEORETICAL AND APPLIED MECHANICS

(until 1997 Mechanika Teoretyczna i Stosowana, ISSN 0079-3701)

Beginning with Vol 45, No. 1, 2007, *Journal of Theoretical and Applied Mechanics* (JTAM) has been selected for coverage in Thomson Reuters products and custom information services. Now it is indexed and abstracted in the following:

- Science Citation Index Expanded (also known as SciSearch®)
- Journal Citation Reports/Science Edition

Advisory Board

MICHAŁ KLEIBER (Poland) – Chairman

JORGE A.C. AMBROSÍO (Portugal) * ANGEL BALTOV (Bulgaria) * ROMESH C. BATRA (USA) *
ALAIN COMBESCURE (France) * JÜRI ENGELBRECHT (Estonia) * WITOLD GUTKOWSKI (Poland) *
JÓZEF KUBIK (Poland) * GERARD A. MAUGIN (France) * ZENON MRÓZ (Poland) *
RYSZARD PARKITNY (Poland) * EUGENIUSZ ŚWITOŃSKI (Poland) * HISAAKI TOBUSHI (Japan) *
DIETER WEICHERT (Germany) * JOSE E. WESFREID (France) * JÓZEF WOJNAROWSKI (Poland) *
JOSEPH ZARKA (France) * VLADIMIR ZEMAN (Czech Republic)

Editorial Board

WŁODZIMIERZ KURNIK – Editor-in-Chief,

PIOTR CUPIAŁ, KRZYSZTOF DEMS, KURT FRISCHMUTH (Germany), PIOTR KOWALCZYK,
ZBIGNIEW KOWALEWSKI, TOMASZ KRZYŻYŃSKI, STANISŁAW KUKLA, TOMASZ ŁODYGOWSKI,
EWA MAJCHRZAK, WIESŁAW NAGÓRKO, JANUSZ NARKIEWICZ, BŁAŻEJ SKOCZEŃ,
ANDRZEJ STYCZEK, ANDRZEJ TYLIKOWSKI, UTZ VON WAGNER (Germany), JERZY WARMIŃSKI,
ELŻBIETA WILANOWSKA – Secretary, PIOTR PRZYBYŁOWICZ – Language Editor,
EWA KOISAR – Technical Editor



Articles in JTAM are published under Creative Commons Attribution – Non-commercial 3.0. Unported License <http://creativecommons.org/licenses/by-nc/3.0/legalcode>. By submitting an article for publication, the authors consent to the grant of the said license.



The journal content is indexed in Similarity Check, the Crossref initiative to prevent plagiarism.

* * * * *

Editorial Office

Al. Armii Ludowej 16, room 650

00-637 Warszawa, Poland

phone (+48 22) 825 7180, (+48) 664 099 345, e-mail: biuro@ptmts.org.pl

www.ptmts.org.pl/jtam.html

* * * * *



Publication supported by Ministry of Science and Higher Education of Poland

(Journal of Theoretical and Applied Mechanics: 1) digitalizacja publikacji i monografii naukowych w celu zapewnienia i utrzymania otwartego dostępu do nich przez sieć Internet, 2) stworzenie anglojęzycznych wersji wydawanych publikacji, 3) wdrożenie procedur zabezpieczających oryginalność publikacji naukowych oraz zastosowane techniki zabezpieczeń – są finansowane ze środków Ministra Nauki i Szkolnictwa Wyższego przeznaczonych na działalność upowszechniającą naukę)

DETERMINATION OF THE POSITION OF THE CONTACT POINT OF A TIRE MODEL WITH AN UNEVEN ROAD SURFACE FOR PURPOSES OF VEHICLE DYNAMICAL ANALYSIS

SZYMON TENGLER, ANDRZEJ HARLECKI

University of Bielsko-Biala, Department of Mechanics, Bielsko-Biala, Poland

e-mail: stengler@ath.bielsko.pl

Two algorithms which allow one to take an uneven road surface into account in the vehicle dynamics analysis are presented in the article. Their essence is to determine the position of the contact point of the tire model with the uneven road surface. According to the concept of the authors, the names of the algorithms are to refer to the essence of the matter of the procedures assumed. The first of them – named Plane – can be used while considering the continuous model of the surface obtained by use of “the bicubic interpolation” taken from computer graphics, and the second one – named 4Points – in the case of the discrete model of this surface, developed especially for needs of the methods presented. In the work, it is assumed that only continuous changes of the road profile, without its possible abrupt changes, e.g. in form of a transversely placed threshold of sharp edges, can be considered. Therefore, the mapping of the road surface, obtained in the case of including its both models, is smooth. The developed algorithms are used to analyze dynamics of a technical rescue vehicle which can drive in terrain conditions.

Keywords: dynamical analysis, uneven road surface, contact point

1. Introduction

While analyzing vehicle dynamics, forces and reaction torques acting on models of their tires from the road surface must be considered appropriately. In real conditions, tire contact with an uneven surface takes place within the definite area. When the tire is modeled, the contact surface is usually limited to a point (Hirschberg *et al.*, 2002, 2007; Rill, 2013). The authors of this work followed also that procedure, assuming that the modeled tire – considered in form of a deformable rim – contacts with the mapping surface of the road surface in a definite point.

The proposed method is based on the use of homogenous transformation matrices taken from robotics with dimensions 4×4 , which enable one to make transformations between the assumed coordinate systems (Craig, 1989).

If the position of any point A in the given coordinate system $\{j\}$, expressed by position vector ${}^{\{j\}}\mathbf{r}_A$ of dimensions 3×1 is known, then the position of this point in the coordinate system $\{i\}$ can be determined by the position vector ${}^{\{i\}}\mathbf{r}_A$ of dimensions 3×1 (Fig. 1) using only one arithmetic operation, namely multiplication

$${}^{\{i\}}\mathbf{r}_A^* = {}^{\{i\}}_{\{j\}}\mathbf{T} {}^{\{j\}}\mathbf{r}_A^* \quad (1.1)$$

where: ${}^{\{i\}}\mathbf{r}_A^*$ are position vectors of dimensions 4×1 , named vectors of homogenous coordinates, determining the position of point A in the system $\{i\}$ and $\{j\}$, respectively; ${}^{\{i\}}_{\{j\}}\mathbf{T}$ – transformation matrix of dimensions 4×4 from the coordinate system $\{j\}$ to the system $\{i\}$; ${}^{\{i\}}_{\{j\}}\mathbf{R}$ – rotation

matrix of dimensions 3×3 from the coordinate system $\{j\}$ to the system $\{i\}$ (elements of this matrix are dot products of the versors)

$$\begin{aligned} \{i\}\mathbf{r}_A^* &= \begin{bmatrix} \{i\}\mathbf{r}_A \\ 1 \end{bmatrix} & \{j\}\mathbf{r}_A^* &= \begin{bmatrix} \{j\}\mathbf{r}_A \\ 1 \end{bmatrix} \\ \{i\}\mathbf{T} &= \begin{bmatrix} \{i\}\mathbf{R} & \{i\}\mathbf{r}_j \\ \{j\} & 0 & 0 & 1 \end{bmatrix} & \{i\}\mathbf{R} &= \begin{bmatrix} \hat{X}_j \cdot \hat{X}_i & \hat{Y}_j \cdot \hat{X}_i & \hat{Z}_j \cdot \hat{X}_i \\ \hat{X}_j \cdot \hat{Y}_i & \hat{Y}_j \cdot \hat{Y}_i & \hat{Z}_j \cdot \hat{Y}_i \\ \hat{X}_j \cdot \hat{Z}_i & \hat{Y}_j \cdot \hat{Z}_i & \hat{Z}_j \cdot \hat{Z}_i \end{bmatrix} \end{aligned}$$

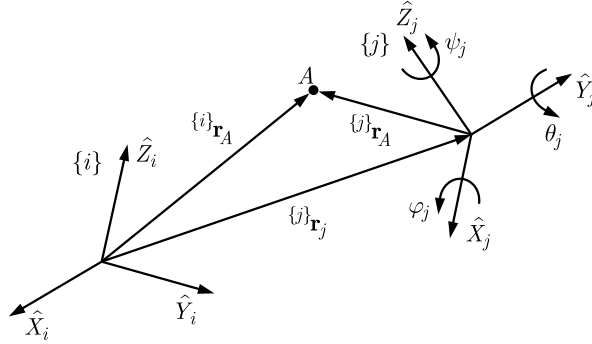


Fig. 1. Determination of the A point position in the coordinate system $\{i\}$ and $\{j\}$

2. Modeling of an uneven road surface

In order to map the real profile of an uneven road surface, the authors assumed its two models – continuous and discrete. In the case of each of them, the mapping surface of the road surface is smooth. Therefore, the abrupt changes of its profile, e.g. in form of a transversely placed threshold with sharp edges, cannot be taken into account. In the continuous model, the mapping surface is obtained by the use of “the bicubic interpolation” (Keys, 1981). In the discrete model, developed especially for the needs of the method presented, the uneven road surface is modeled in form of the mapping surface made of triangles or rectangles. The detailed description of both models assumed is presented in (Tengler, 2012; Tengler and Harlecki, 2015).

Each of the road surface model can be characterized by an equation of the assumed mapping surface in the form of

$$z = z(x, y) \quad (2.1)$$

In further considerations, it is assumed that in any point P of this surface of coordinates x_P, y_P, z_P determined in any immovable coordinate system $\{0\}$ assumed, being a reference system (Fig. 2a), the normal versor $\hat{\mathbf{e}}$ to this surface is known.

According to the suggestions presented in work by Hirsching *et al.* (2007), in the case of the continuous model of the road surface in the neighborhood of point P (Fig. 2b), it is assumed that there are four auxiliary points of the coordinates determined in the reference system $\{0\}$ as

$$\begin{aligned} P^{(x^+)}(x_P + \Delta, y_P, z(x_P + \Delta, y_P)) & \quad P^{(x^-)}(x_P - \Delta, y_P, z(x_P - \Delta, y_P)) \\ P^{(y^+)}(x_P, y_P + \Delta, z(x_P, y_P + \Delta)) & \quad P^{(y^-)}(x_P, y_P - \Delta, z(x_P, y_P - \Delta)) \end{aligned} \quad (2.2)$$

Then, the normal versor can be determined according to the following formula

$$\hat{\mathbf{e}} = \frac{\mathbf{r}^{(x)} \times \mathbf{r}^{(y)}}{|\mathbf{r}^{(x)} \times \mathbf{r}^{(y)}|} \quad (2.3)$$

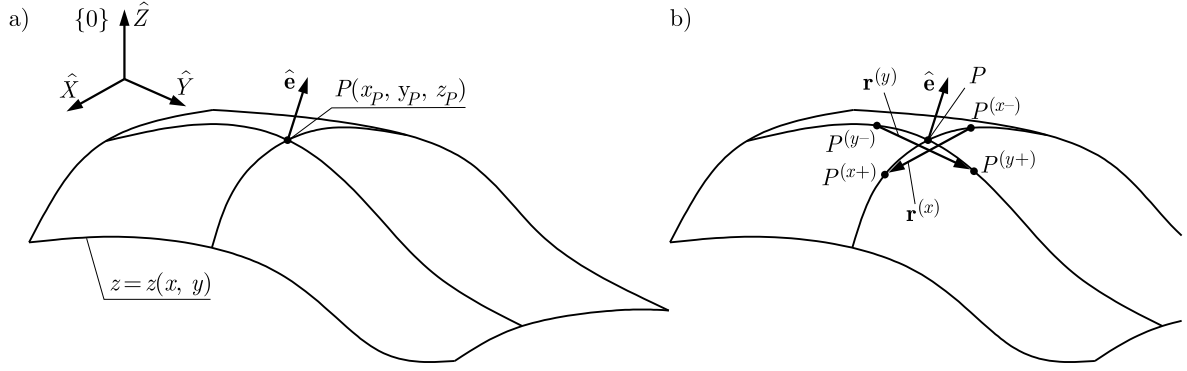


Fig. 2. Normal vector $\hat{\mathbf{e}}$ to the mapping surface in point $P(x_P, y_P, z_P)$

where: $\mathbf{r}^{(x)}$ is the vector with the origin in point $P^{(x^-)}$ and the end in point $P^{(x^+)}$, $\mathbf{r}^{(y)}$ – vector with the origin in point $P^{(y^-)}$ and the end in point $P^{(y^+)}$, Δ [m] – short distance (in the work it was assumed $\Delta = 0.01$ m).

In the case of the discrete model of the road surface based on the triangles or rectangles implemented, the normal vector $\hat{\mathbf{e}}$ can be determined on the basis of the known basic geometrical relationships.

3. Algorithms of iterative determination of the contact point position

As it is known, in any point of the mapping surface, a plane tangent to it can be placed. In this method, as it was done by Hirschberg *et al.* (2002, 2007), Rill (2013), Unrau and Zamov (1997), it is assumed that the tire is modeled in form of a deformable rim obtained as a result of longitudinal cut of this tire in its symmetry plane. This rim in the deformable part adheres to the mapping surface – even so for the needs of the model it is assumed that its contact with this surface takes place in the definite point (it is the contact point C). In a non-deformable form, this rim is a circle with the symmetry center O , overlapping with the symmetry center of the non-deformed tire. In the contact point C , there is also plane Π – tangent to the mapping surface (Fig. 3). On the basis of the suggestions by Unrau and Zamov (1997), in addition to the reference system $\{0\}$ mentioned already, two local coordinate systems – $\{w\}$ and $\{r\}$ are assumed. The movable system $\{w\}$ is connected with the rim. Its origin is placed in the O symmetry center of the non-deformed rim, the versor $\hat{\mathbf{Y}}_w$ overlaps with its axis of rotation (and therefore, also with the axis of rotation of the modeled tire), and the versor $\hat{\mathbf{X}}_w$ remains parallel to the plane Π during the whole time of vehicle motion. The origin of the immovable system $\{r\}$ overlaps with the contact point C , its versor $\hat{\mathbf{Z}}_w$ is normal to plane Π – and also to the mapping surface (angle γ between it and versor $\hat{\mathbf{Z}}_w$ is an inclination angle of the tire), whereas the versor $\hat{\mathbf{X}}_r$ lying in this plane remains parallel to the versor $\hat{\mathbf{X}}_w$ of the $\{w\}$ system during the vehicle motion. While modeling the interaction of the road surface on the tire, it is assumed that in the contact point C the following forces and reaction torques are applied: \mathbf{F}_x – longitudinal reaction force, \mathbf{F}_y – lateral reaction force, \mathbf{F}_z – the reaction force normal to the mapping surface (plane Π), \mathbf{M}_x – the overturning torque, \mathbf{M}_y – rolling resistance torque, \mathbf{M}_z – aligning torque. Their directions are consistent with the directions of versors of the $\{r\}$ system. Values of these forces and torques are calculated by the use of formulas offered by the so called Pacejka tire model (Pacejka *et al.*, 1989; Pacejka and Bakker, 1993; Pacejka, 2005) taken into account in the method proposed. In this work, a version of the Magic Formula – Pacejka 89 tire model is used due to a lower number of coefficients needed to identify the tire than in other versions of the Pacejka tire model. A precise way of determining the values of forces and reaction moments

acting on the tire with the information on the assumed coefficients characterizing the tire model was presented in the doctoral dissertation by Rill (2013).

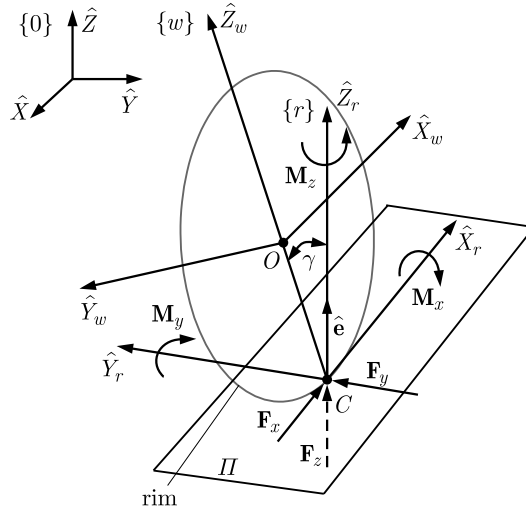


Fig. 3. Location of the local systems $\{w\}$ and $\{r\}$

While performing analysis of the vehicle dynamics, it is assumed that the position of the $\{w\}$ system origin is known at any time of its motion (as known, identical with the O symmetry center of the non-deformed rim) and orientation of its versor \hat{Y}_w in the $\{0\}$ reference system. The authors of the article also made the same assumption in (Hirschberg *et al.*, 2002). Additionally, the position of the contact point C being the beginning of the $\{r\}$ system and orientation of versors in the $\{0\}$ reference system must be known. Iterative determination of this position and orientation is a subject of the algorithms presented in this work. When a distance of origins of the systems $\{w\}$ and $\{r\}$ is known, values of forces and reaction torques acting on the tire from the road surface can be determined by the use of the Pacejka tire model. Knowledge about orientation of versors of the $\{r\}$ system in the $\{0\}$ reference system will allow one to find directions of action of these forces and torques – this information is needed to make analysis of the dynamics of the vehicle in question while using the Pacejka tire model mentioned or other tire models, relying on the similar assumptions regarding the way of applying forces and torques.

Two algorithms intended for determination of the position of the contact point C and orientation of the vectors of the $\{r\}$ coordinate system are proposed. In accordance with intention of the authors, the names of the algorithms are to refer to the essence of the procedure assumed in each case. The Plane algorithm is designed for the continuous model of the road surface, whereas the 4Points algorithm for the discrete model of this surface.

3.1. Algorithm Plane

Determination of the position of the contact point C by the algorithm Plane refers to performing a definite number of iterations. Execution of the first of them is presented in Fig. 4.

In the neighborhood of the O symmetry center of the non-deformed rim (Fig. 4a) the point of origin P_S of coordinates x_S, y_S, z_S defined in the $\{0\}$ reference system is selected. In this work, it has been assumed that it is point O . Then, coordinates of the C_0 point, being an orthogonal projection to the mapping surface, are determined in this system

$$C_0 = (x_{C_0}, y_{C_0}, z_{C_0}) = (x_O, y_O, z(x_O, y_O)) \quad (3.1)$$

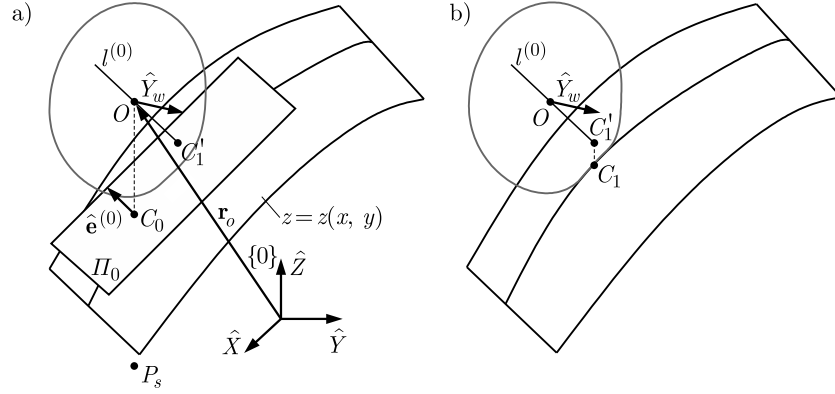


Fig. 4. Algorithm Plane – the first approximation of the position of the contact point C

The next step is to determine the plane Π_0 tangent to the mapping surface in the point C_0 . A point-normal equation of this plane can be presented in the following form

$$e_x^{(0)}x + e_y^{(0)}y + e_z^{(0)}z + \delta^{(0)} = 0 \quad (3.2)$$

where: $e_x^{(0)}, e_y^{(0)}, e_z^{(0)}$ are components of the $\hat{\mathbf{e}}^{(0)}$ versor normal to the mapping surface in the C_0 point determined in the $\{0\}$ reference system, and

$$\delta^{(0)} = -\left(e_x^{(0)}x_{C_0} + e_y^{(0)}y_{C_0} + e_z^{(0)}z_{C_0}\right)$$

The point $C'_1(x_{C'_1}, y_{C'_1}, z_{C'_1})$ in which the straight line $l^{(0)}$ going through the O points pierces the plane Π_0 perpendicularly is determined next. Its coordinates in the $\{0\}$ reference system can be determined by the position vector (Fig. 4b) as

$$\mathbf{r}_{C'_1} = \mathbf{r}_O - d_0 \hat{\mathbf{e}}^{(0)} \quad (3.3)$$

where: $d_0 = |e_x^{(0)}x_O + e_y^{(0)}y_O + e_z^{(0)}z_O + \delta^{(0)}|$ is the distance between points O and C'_1 .

As a result, these coordinates can be presented as

$$C'_1(x_{C'_1}, y_{C'_1}, z_{C'_1}) = C'_1(x_O - e_x^{(0)}d_0, y_O - e_y^{(0)}d_0, z_O - e_z^{(0)}d_0) \quad (3.4)$$

Then, the coordinates of point C_1 , being the first approximation of the contact point C , are determined

$$C_1(x_{C_1}, y_{C_1}, z_{C_1}) = C_1(x_{C'_1}, y_{C'_1}, z(x_{C'_1}, y_{C'_1})) \quad (3.5)$$

To determine the n -th approximation of the position of the contact point C , the algorithm can be generalized to $i = 1, \dots, n$ iterations writing formulas (3.4) and (3.5) as

$$\begin{aligned} C'_i(x_{C'_i}, y_{C'_i}, z_{C'_i}) &= C'_i(x_O - e_x^{(i-1)}d_{i-1}, y_O - e_y^{(i-1)}d_{i-1}, z_O - e_z^{(i-1)}d_{i-1}) \\ C_i(x_{C_i}, y_{C_i}, z_{C_i}) &= C_i(x_{C'_i}, y_{C'_i}, z(x_{C'_i}, y_{C'_i})) \end{aligned} \quad (3.6)$$

The n -th value is determined by the criterion

$$\sqrt{(x_{C_{n-1}} - x_{C'_n})^2 + (y_{C_{n-1}} - y_{C'_n})^2 + (z_{C_{n-1}} - z_{C'_n})^2} \leq \varepsilon \quad (3.7)$$

where ε is the assumed acceptable absolute error of calculations.

The versor $\hat{X}_r^{(n)}$ of the $\{r\}$ system in the reference system $\{0\}$ can be determined by the formula (Fig. 3)

$$\hat{X}_r^{(n)} = \frac{\hat{Y}_w \times \hat{\mathbf{e}}^{(n)}}{|\hat{Y}_w \times \hat{\mathbf{e}}^{(n)}|} \quad (3.8)$$

and then other versors as

$$\hat{Y}_r^{(n)} = \hat{X}_r \times \hat{\mathbf{e}}^{(n)} \quad \hat{Z}_r^{(n)} = \hat{\mathbf{e}}^{(n)} \quad (3.9)$$

3.2. Algorithm 4Points

As it has been found out, algorithm Plane is used in the case of the continuous model of the road surface. However, in the case of the discrete model when some fragments of the surface are flat, determination of the position of the contact point C by its use may not be accurate enough. Such a situation is presented in Fig. 5.

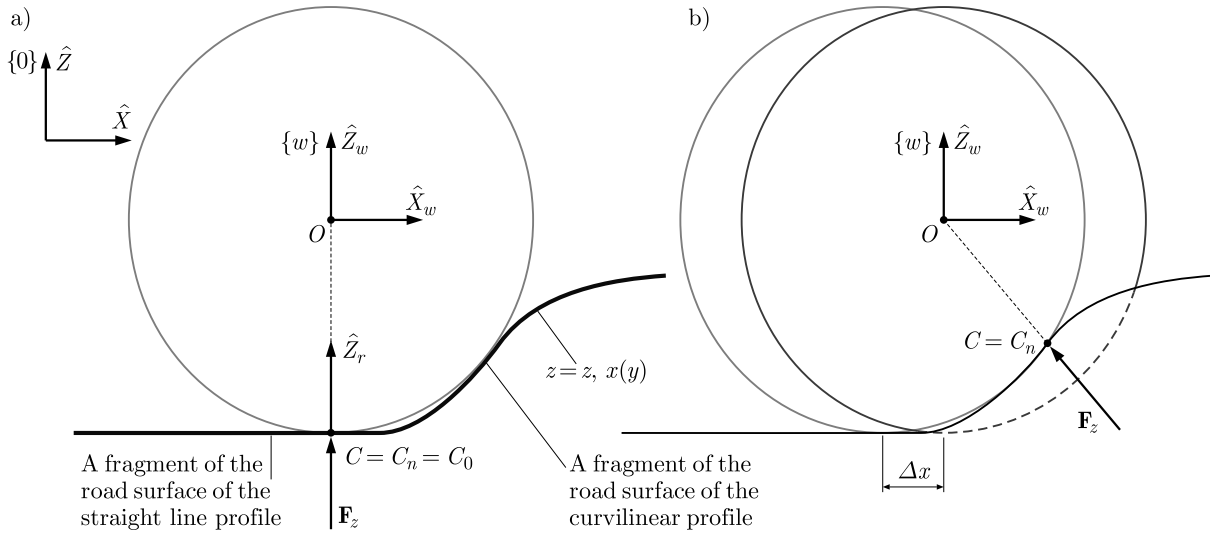


Fig. 5. Algorithm Plane – the determined positions of the contact point C : (a) at the beginning of running of the modeled tire over unevenness, (b) after covering a distance Δx

While considering the position of the modeled tire presented in Fig. 5a, it can be noticed that the contact point C is orthogonal projection of the symmetry center O of the non-deformed rim on a flat fragment of the road surface. It can be stated that condition (3.7), determining completion of calculations, is met after the first iteration because already then the following holds

$$\sqrt{(x_{C_{n-1}} - x_{C'_n})^2 + (y_{C_{n-1}} - y_{C'_n})^2 + (z_{C_{n-1}} - z_{C'_n})^2} = 0 < \varepsilon$$

Here, an undesirable effect is too late reaction of the rim to the changeable surface profile. Since algorithm Plane does not allow one to take the rim contact with the road fragment of the curvilinear profile (marked in the figure) into account early enough, so the direction of the normal reaction force \mathbf{F}_z (acting on the rim in accordance with the \hat{Z}_w versor direction) turns out to be incorrect. It can be stated that this direction “does not keep up with the new situation on the road”. The normal reaction force changes its direction after the modeled tire has covered the Δx distance (Fig. 5b) – so too late – and this change is rather rapid. Therefore, it has been required to develop an algorithm which would enable one to determine an appropriate position of the contact point C ensuring that the shape changes of the mapping surface are considered

early enough, what would provide a more accurate direction of the \mathbf{F}_z normal reaction force, because closer to the real one.

At the beginning of realization of the new algorithm named 4Points in the planes $\widehat{X}_w \widehat{Z}_w$ and $\widehat{Y}_w \widehat{Z}_w$ of the $\{w\}$ system, there are four auxiliary points $O^{(x^+)}$, $O^{(x^-)}$, $O^{(y^+)}$, $O^{(y^-)}$ assumed, respectively (Fig. 6).

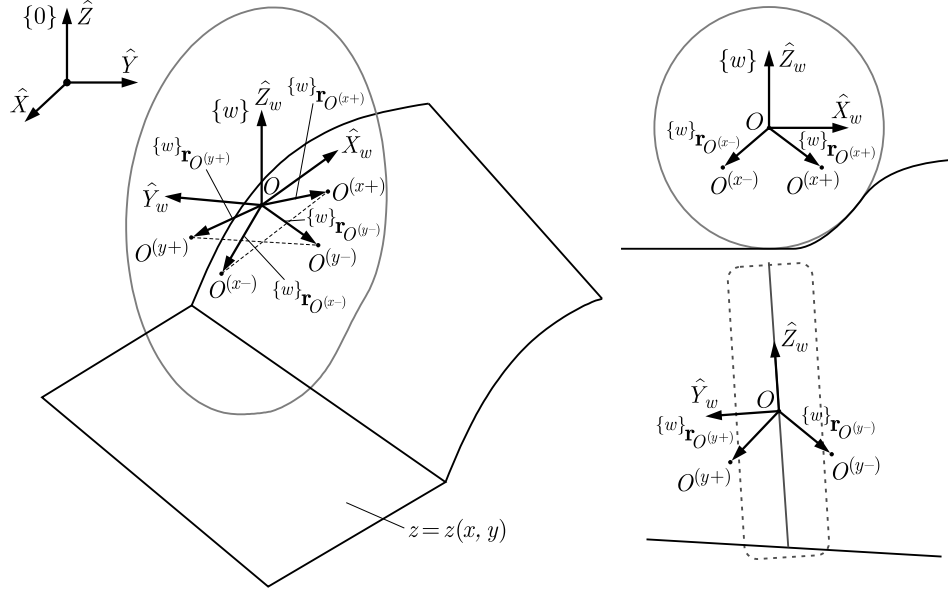


Fig. 6. Algorithm 4Points – positions of the auxiliary points

The coordinates of them in the $\{w\}$ system can be determined by the position vectors of the homogenous coordinates

$$\begin{aligned}
 w \mathbf{r}_{O^{(x^+)}}^* &= \begin{bmatrix} w \mathbf{r}_{O^{(x^+)}} \\ 1 \end{bmatrix} & w \mathbf{r}_{O^{(x^+)}} &= \begin{bmatrix} \Delta x \\ 0 \\ -\Delta z \end{bmatrix} \\
 w \mathbf{r}_{O^{(x^-)}}^* &= \begin{bmatrix} w \mathbf{r}_{O^{(x^-)}} \\ 1 \end{bmatrix} & w \mathbf{r}_{O^{(x^-)}} &= \begin{bmatrix} -\Delta x \\ 0 \\ -\Delta z \end{bmatrix} \\
 w \mathbf{r}_{O^{(y^+)}}^* &= \begin{bmatrix} w \mathbf{r}_{O^{(y^+)}} \\ 1 \end{bmatrix} & w \mathbf{r}_{O^{(y^+)}} &= \begin{bmatrix} 0 \\ \Delta y \\ -\Delta z \end{bmatrix} \\
 w \mathbf{r}_{O^{(y^-)}}^* &= \begin{bmatrix} w \mathbf{r}_{O^{(y^-)}} \\ 1 \end{bmatrix} & w \mathbf{r}_{O^{(y^-)}} &= \begin{bmatrix} 0 \\ -\Delta y \\ -\Delta z \end{bmatrix}
 \end{aligned} \tag{3.10}$$

where Δx , Δy , Δz [m] – distances resulting from tire size (in the work the following values were assumed: $\Delta x = 0.17$, $\Delta y = 0.07$, $\Delta z = 0.1$).

Then, the vectors of the homogenous coordinates determining the position of the auxiliary points in the $\{0\}$ reference system can be determined as

$$\begin{aligned}
\mathbf{r}_{O(x^+)}^* &= \mathbf{T}_w {}^w \mathbf{r}_{O(x^+)}^* & \mathbf{r}_{O(x^+)}^* &= \begin{bmatrix} \mathbf{r}_{O(x^+)} \\ 1 \end{bmatrix} & \mathbf{r}_{O(x^+)} &= \begin{bmatrix} x_{O(x^+)} \\ y_{O(x^+)} \\ z_{O(x^+)} \end{bmatrix} \\
\mathbf{r}_{O(x^-)}^* &= \mathbf{T}_w {}^w \mathbf{r}_{O(x^-)}^* & \mathbf{r}_{O(x^-)}^* &= \begin{bmatrix} \mathbf{r}_{O(x^-)} \\ 1 \end{bmatrix} & \mathbf{r}_{O(x^-)} &= \begin{bmatrix} x_{O(x^-)} \\ y_{O(x^-)} \\ z_{O(x^-)} \end{bmatrix} \\
\mathbf{r}_{O(y^+)}^* &= \mathbf{T}_w {}^w \mathbf{r}_{O(y^+)}^* & \mathbf{r}_{O(y^+)}^* &= \begin{bmatrix} \mathbf{r}_{O(y^+)} \\ 1 \end{bmatrix} & \mathbf{r}_{O(y^+)} &= \begin{bmatrix} x_{O(y^+)} \\ y_{O(y^+)} \\ z_{O(y^+)} \end{bmatrix} \\
\mathbf{r}_{O(y^-)}^* &= \mathbf{T}_w {}^w \mathbf{r}_{O(y^-)}^* & \mathbf{r}_{O(y^-)}^* &= \begin{bmatrix} \mathbf{r}_{O(y^-)} \\ 1 \end{bmatrix} & \mathbf{r}_{O(y^-)} &= \begin{bmatrix} x_{O(y^-)} \\ y_{O(y^-)} \\ z_{O(y^-)} \end{bmatrix}
\end{aligned} \tag{3.11}$$

where \mathbf{T}_w is the known transformation matrix from the system $\{w\}$ to the reference system $\{0\}$.

In the further procedure, the auxiliary points $O^{(x^+)}$, $O^{(x^-)}$, $O^{(y^+)}$, $O^{(y^-)}$ are projected onto the mapping surface (Fig. 7a), and next the homogenous vectors determining the coordinates of their projections $O'^{(x^+)}$, $O'^{(x^-)}$, $O'^{(y^+)}$, $O'^{(y^-)}$ in the $\{0\}$ reference system are determined as

$$\begin{aligned}
\mathbf{r}_{O'^{(x^+)}}^* &= \begin{bmatrix} \mathbf{r}_{O'^{(x^+)}} \\ 1 \end{bmatrix} & \mathbf{r}_{O^{(x^+)}} &= \begin{bmatrix} x_{O'^{(x^+)}} \\ y_{O'^{(x^+)}} \\ z_{O'^{(x^+)}} \end{bmatrix} = \begin{bmatrix} x_{O(x^+)} \\ y_{O(x^+)} \\ z(x_{O(x^+)}, y_{O(x^+)}) \end{bmatrix} \\
\mathbf{r}_{O'^{(x^-)}}^* &= \begin{bmatrix} \mathbf{r}_{O'^{(x^-)}} \\ 1 \end{bmatrix} & \mathbf{r}_{O^{(x^-)}} &= \begin{bmatrix} x_{O'^{(x^-)}} \\ y_{O'^{(x^-)}} \\ z_{O'^{(x^-)}} \end{bmatrix} = \begin{bmatrix} x_{O(x^-)} \\ y_{O(x^-)} \\ z(x_{O(x^-)}, y_{O(x^-)}) \end{bmatrix} \\
\mathbf{r}_{O'^{(y^+)}}^* &= \begin{bmatrix} \mathbf{r}_{O'^{(y^+)}} \\ 1 \end{bmatrix} & \mathbf{r}_{O^{(y^+)}} &= \begin{bmatrix} x_{O'^{(y^+)}} \\ y_{O'^{(y^+)}} \\ z_{O'^{(y^+)}} \end{bmatrix} = \begin{bmatrix} x_{O(y^+)} \\ y_{O(y^+)} \\ z(x_{O(y^+)}, y_{O(y^+)}) \end{bmatrix} \\
\mathbf{r}_{O'^{(y^-)}}^* &= \begin{bmatrix} \mathbf{r}_{O'^{(y^-)}} \\ 1 \end{bmatrix} & \mathbf{r}_{O^{(y^-)}} &= \begin{bmatrix} x_{O'^{(y^-)}} \\ y_{O'^{(y^-)}} \\ z_{O'^{(y^-)}} \end{bmatrix} = \begin{bmatrix} x_{O(y^-)} \\ y_{O(y^-)} \\ z(x_{O(y^-)}, y_{O(y^-)}) \end{bmatrix}
\end{aligned} \tag{3.12}$$

On the basis of formula (2.3), the versor normal to the plane Π , including the projections of the auxiliary points, can be determined as

$$\hat{\mathbf{e}} = \frac{\mathbf{r}_{O'}^{(x)} \times \mathbf{r}_{O'}^{(y)}}{|\mathbf{r}_{O'}^{(x)} \times \mathbf{r}_{O'}^{(y)}|} \tag{3.13}$$

where: $\mathbf{r}_{O'}^{(x)} = \mathbf{r}_{O'^{(x^+)}} - \mathbf{r}_{O'^{(x^-)}}$ is the vector of origin in point $O'^{(x^+)}$ and the end in point $O'^{(x^-)}$, $\mathbf{r}_{O'}^{(y)} = \mathbf{r}_{O'^{(y^+)}} - \mathbf{r}_{O'^{(y^-)}}$ is the vector of origin in point $O'^{(y^+)}$ and end in point $O'^{(y^-)}$.

On the basis of the determined normal versor $\hat{\mathbf{e}}$ and one of any selected auxiliary points $O'^{(x^+)}$, $O'^{(x^-)}$, $O'^{(y^+)}$, $O'^{(y^-)}$, the plane Π mentioned is sought for, the point-normal equation of which has form

$$e_x x + e_y y + e_z z + \delta = 0 \tag{3.14}$$

where: e_x, e_y, e_z are the components of the versor $\hat{\mathbf{e}}$ normal to the plane Π determined in the $\{0\}$ reference system, $\delta = -(e_x x_{O'^{(x^+)}} + e_y y_{O'^{(x^+)}} + e_z z_{O'^{(x^+)}})$ if the selected point is $O'^{(x^+)}$.

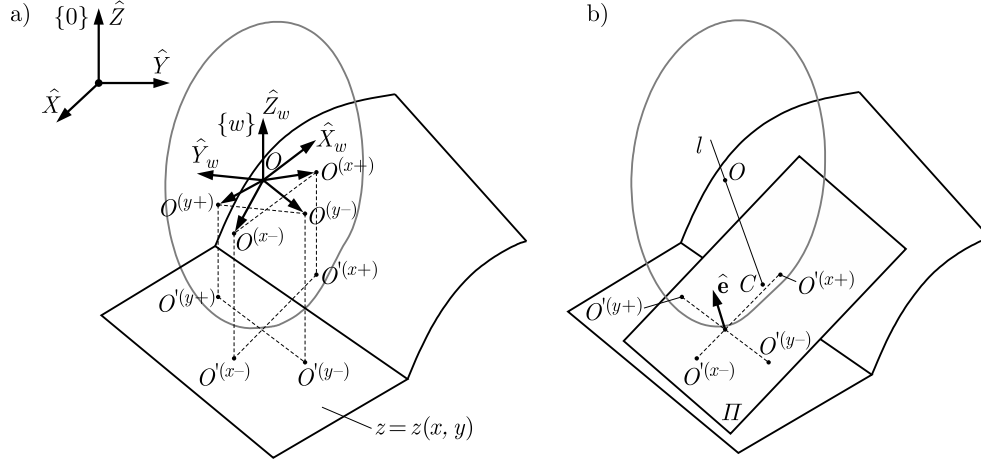


Fig. 7. Algorithm 4Points – determination of the orthogonal projections of the auxiliary points on the mapping surface

The sought contact point C is determined as a point in which the straight line l going through the point O pierces the plane Π perpendicularly (Fig. 7b). Its coordinates in the $\{0\}$ reference system are determined as the components of the position vector

$$\mathbf{r}_C = \mathbf{r}_O - d_0 \hat{\mathbf{e}} \quad (3.15)$$

where $d_0 = |e_x x_O + e_y y_O + e_z z_O + \delta|$ is the distance between points O and C .

As a result, the coordinates of the contact point C can be determined as

$$C(x_C, y_C, z_C) = C(x_O - e_x d_0, y_O - e_y d_0, z_O - e_z d_0) \quad (3.16)$$

Using this algorithm for the case illustrated in Fig. 5a, the position of the contact point C can be determined as presented in Fig. 8. The corrected direction of the reaction force \mathbf{F}_z is presented in this figure.

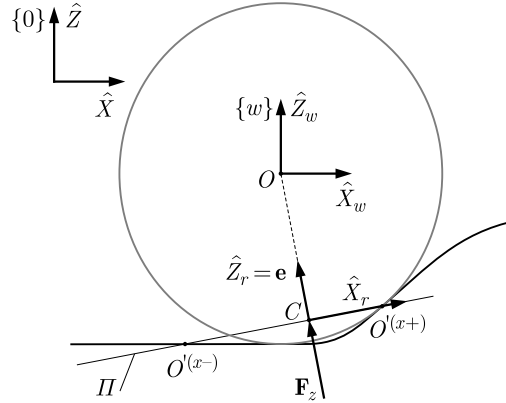


Fig. 8. Algorithm 4Points – determination of the position of the contact point C and the corrected direction of the normal reaction force \mathbf{F}_z

The versor directions of the $\{r\}$ system are determined in a similar way as in the case of algorithm Plane, that is according to relationships (3.8) and (3.9).

4. Computer simulations

A technical rescue vehicle which can drive in terrain conditions has been used in analysis. Its physical model in form of a multibody system of an open structure built by the use of

joint coordinates defining the relative position of the modeled components and a mathematical model corresponding to it developed on the basis of Lagrange equations formalism by the use of homogenous transformation matrices (Grzegożek *et al.*, 2003), was presented in the doctoral dissertation (Tengler, 2012). Program Blender (www.blender.org) has been used to model the uneven road surface and to develop a model of the vehicle used in computer animations. The models obtained in such a way have been imported to the author's own program to perform computer animations. The import procedure was described in details in (Tengler and Harlecki, 2015).

In each considered case the modeled vehicle moves in the direction consistent with the versor \hat{X} of the $\{0\}$ reference system. The vehicle initial speed is 5 km/h, and simulation duration time 6 s.

Example I

The assumed continuous model of the road surface in form of a grid of control points is presented in Fig. 9. The boundary values of the coordinates of those points in the $\{0\}$ reference system are following: $x_{min} = -2$, $x_{max} = 49$, $y_{min} = -8$, $y_{max} = 8$, $z_{min} = -0.8$, $z_{max} = 1.2$.

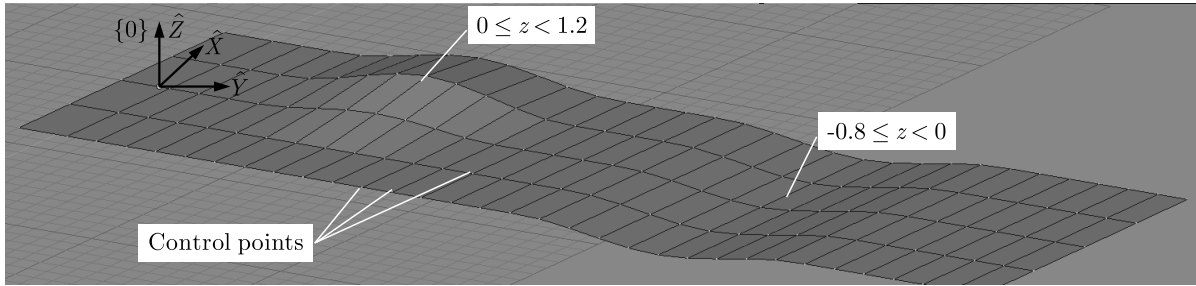


Fig. 9. The control point grid in the case of the continuous model of the road surface

Some examples of the calculation results which concern determination of the vertical course of the gravity center displacement of the vehicle model (towards the versor \hat{Z} of the $\{0\}$ references system) – taking algorithm Plane into account – are presented in Fig. 10

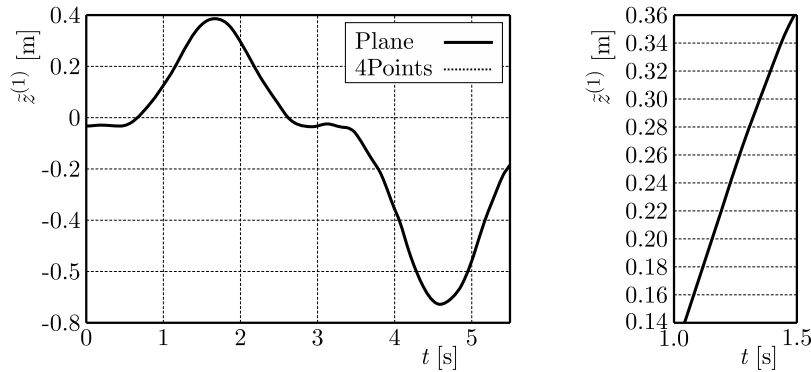


Fig. 10. The course of the vertical displacement of the vehicle gravity center in the case of considering the continuous model of the road surface

This diagram is compared with the vertical course of this center determined by algorithm 4Points. The results obtained are almost identical. Therefore, it may be concluded that in the case of a smooth unevenness, the selection of the algorithm has a slight influence on the computer simulation results.

Example II

The assumed discrete model of the road surface in form of the grid of the control points is presented in Fig. 11. It consists of two flat fragments adjacent to a bump. Since there are no inclination of the surface in the direction consistent with versor \hat{Y} of the $\{0\}$ reference system, its model was made by use of rectangles placed as shown in the figure. The assumed boundary values of the grid points coordinates are following: $x_{min} = -2$, $x_{max} = 11.5$, $y_{min} = -2$, $y_{max} = 2$, $z_{min} = 0$, $z_{max} = 0.2$.

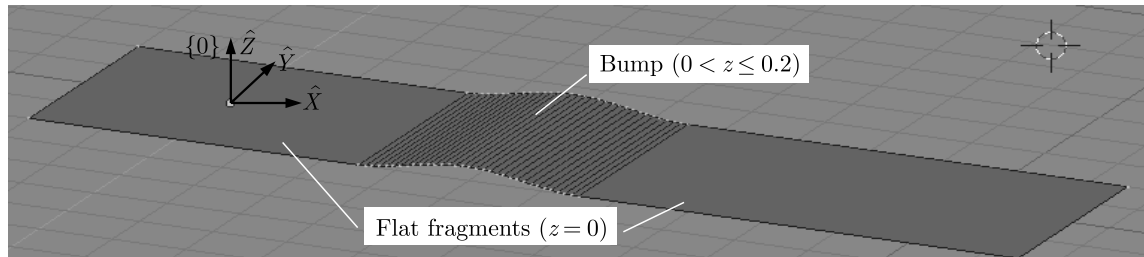


Fig. 11. The discrete model of the road surface made by the use of rectangles

Within the computer animation performed, passing of the vehicle over the unevenness has been simulated (Fig. 12).

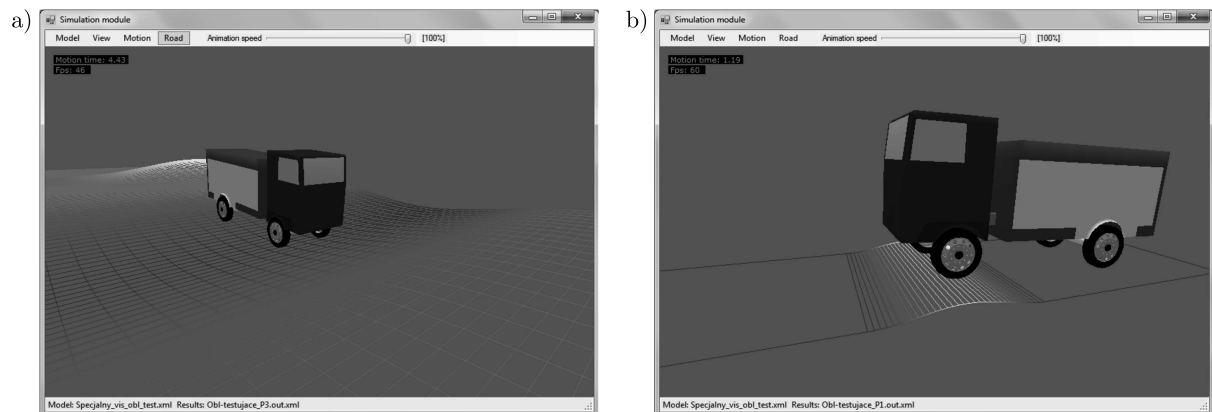


Fig. 12. Some screen shots made during computer animation: (a) unevenness presented in example I, (b) unevenness presented in example II

Some examples of the calculations results which concern determination of the vertical displacement course of the gravity center of the vehicle model considering algorithm 4Points are presented in Fig. 13a.

Two phases of motion can be differentiated here when the first front wheels and then rear wheels of the vehicle drive over the bump. By analyzing the results in Fig. 13a, it can be noticed that when algorithm 4Points is used, the displacement of the gravity center of the vehicle while its going up to the bump takes place earlier than in the case of using algorithm Plane, see the dashed line visible before the solid line (Fig. 13b). An analogous situation can be observed during going down from the bump. In this case algorithm 4Points is more “sensitive” to the unevenness profile change behind the wheels – the dashed line is visible behind the solid line (Fig. 13c). Therefore, the thesis is confirmed that in the case of overcoming the unevenness where the road fragments are flat, better results are obtained when by making use of algorithm 4Points.

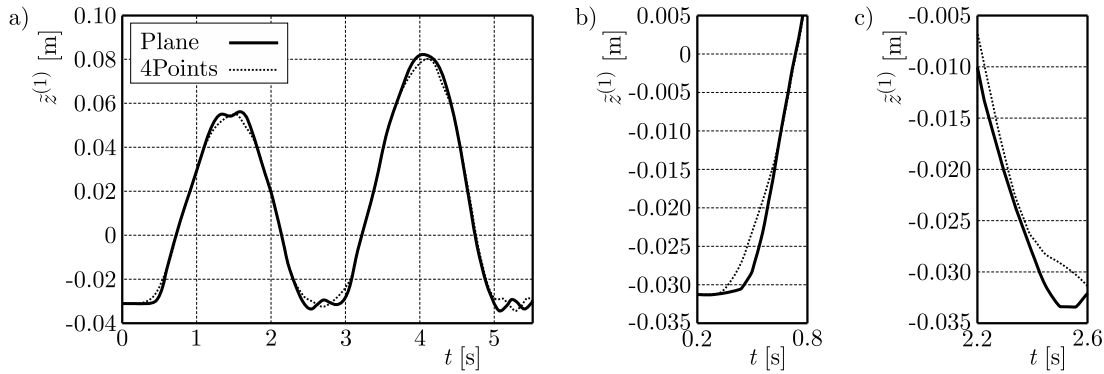


Fig. 13. The course of the vertical displacement of the vehicle gravity center when the discrete model of the road surface made by the use of rectangles is considered

5. Summary

The presented algorithms are of general significance and that is why they can be used in the case of considering more advanced tire models. In order to sum up this article, it should be emphasized that the development of the presented algorithms has only been a part of the task undertaken by the authors. These algorithms with tire models are included into an advanced mathematical model of the selected terrain vehicle, developed with a view to performing analysis of its dynamics. This model with the prepared models of the road surface and the developed computer programs constitute a prototype of a technical rescue vehicle. According to the authors, the observations made during computer simulations of its motion can aid the process of designing of this type of vehicles in the future. In addition to the statements presented, the authors would like to point out – in the case of the proposed method – a variety of possibilities of the Blender program, especially while developing road surface models and also vehicle models used in computer animations.

References

1. CRAIG J.J., 1989, *Introduction to Robotics. Mechanics and Control*, Addison-Wesley Publishing Company, Inc.
2. GRZEGOŹEK W., ADAMIEC-WÓJCIK I., WOJCIECH S., 2003, *Computer Modelling of Dynamics of Motor Vehicles* (in Polish), Publisher of Technical University of Cracow, Cracow
3. HIRSCHBERG W., RILL G., WEINFURTER H., 2002, User-appropriate tyre-modeling for vehicle dynamics in standard and limit situation, *Vehicle System Dynamics*, **38**, 2
4. HIRSCHBERG W., RILL G., WEINFURTER H., 2007, Tire model TMeasy, *Vehicle System Dynamics*, **45**, 101-119
5. KEYS R., 1981, Cubic convolution interpolation for digital image processing, *Acoustics, Speech and Signal Processing*, **29**, 1153-1160
6. PACEJKA H.B., 2005, Spin: camber and turning, *Vehicle System Dynamics*, **43**, 3-17
7. PACEJKA H.B., BAKKER E., 1993, The magic formula tyre model, *Vehicle System Dynamics*, **21**, 1-18
8. PACEJKA H.B., BAKKER E., LIDNER L., 1989, New tire model with an application in vehicle dynamics studies, *SAE Technical Paper 890087*
9. RILL G., TMeasy – the handling tire model for all driving situations, [In:] Savi M.A. (Ed.), *Proceedings of the XV International Symposium on Dynamic Problems of Mechanics DINAME 2013*, Buzios, Brazil

10. TENGLER S., 2012, *Analysis of Dynamics of Special Vehicles with High Gravity Center* (in Polish), PhD Thesis, Faculty of Mechanical Engineering and Computer Science, University of Bielsko-Biala, Poland
11. TENGLER S., HARLECKI A., 2012, Ways of uneven road surface modeling used in the vehicle dynamics analysis, *Journal of KONES Powertrain and Transport*, **19**, 1
12. TENGLER S., HARLECKI A., 2015, Computer program for dynamic analysis of special vehicles with high gravity centre, *Technical Transactions*, **2-M/2015**
13. UNRAU H.-J., ZAMOW J., 1997, *TYDEX-Format. Description and Reference Manual. Release 1.3*
14. www.blender.org – Blender, free and open source software for 3D graphics available

Manuscript received November 14, 2015; accepted for print February 15, 2016

MECHANICAL ANALYSIS OF AUTOFRETTAGED HIGH PRESSURE APPARATUS

RUILIN ZHU

College of Engineering and Design, Hunan Normal University, Changsha, China
e-mail: zrl200701@sina.com

GUOLIN ZHU

Basic Courses Department, Jiangxi Police College, Nanchang, China

AIFENG MAO

Moshanjie School, Nanchang, China

High pressure apparatus is widely used in industries, the design of them depends on stress distributions in their walls. Most of high pressure apparatuses are made in form of cylinders. To raise load-bearing capacity and extend operation life for high pressure apparatus, the autofrettage technology is often used. To design autofrettaged high pressure apparatus, it is necessary to study characteristics of stresses in the wall of thick-wall cylinders, including residual stresses and total stresses, etc. In this study, through investigating the characteristics of stresses of cylinders subjected to internal pressure according to the maximum distortion strain energy theory, a set of simplified equations for residual stresses and total stresses are obtained, the safe and optimum load-bearing conditions for autofrettaged cylinders are found out, which are the basis for design of autofrettaged high pressure apparatus.

Keywords: thick-wall cylinder, autofrettage, total stress, residual stress, load-bearing capacity

Nomenclature

r_i, r_j, r_o	–	inside radius, radius of elastic-plastic juncture, outside radius, respectively
k	–	ratio of outside to inside radius, $k = r_o/r_i$
k_j	–	depth of plastic zone or plastic depth, $k_j = r_j/r_i$
k_{j^*}	–	optimum k_j
k_c	–	critical radius ratio, $k_c = 2.2184574899167\dots$
x	–	relative location, $x = r/r_i$
p, p_y	–	internal and entire yield pressure
p_a	–	autofrettage pressure
p_e	–	maximum elastic load-bearing capability of unautofrettaged cylinder or initial yield pressure;
σ_y	–	yield strength
σ_e	–	equivalent stress

Superscripts

p, t, l – quantity related with internal pressure, total and residual stress, respectively.

Subscripts

z, r, θ – axial, radial and circumferential direction, respectively.

1. Introduction

Cylinders are widely used in manufacturing high and ultra-pressure vessels, high-pressure pumps, battleship and tank cannon barrels as well as fuel injection systems for diesel engines, etc. The autofrettage technique is an effective method to raise load-bearing capacity and extend operation life of cylinders. Usually, in the most commonly employed autofrettage process, a cylinder is pressurized to a quite high internal hydraulic pressure, as a result, the portion of the cylinder from inner radius to some intermediate radius becomes plastic while the remaining portion remains elastic. After releasing the pressure, the residual stresses are set up in the wall of the cylinder.

Studies on autofrettage about specific engineering problems have been done widely. Finite element simulations and experiments, the interaction between manufacturing processes with respect to residual stresses and deformations was studied by Br unnet and B ahre (2014). Farrahi *et al.* (2012) investigated the residual stress distribution at the wall of a thick-walled tube affected by the re-autofrettage process. The effects of thermal autofrettage on the residual stresses in a titanium-copper brazed joint were studied by Hamilton *et al.* (2015). Lin *et al.* (2009) built the autofrettage damage mechanics model from an ultra-high pressure vessel autofrettage damage mechanism. By using continuum damage mechanics approach, Lvov and Kostromitskaya (2014) analyzed the autofrettage process and derived general set of government equations of elastic-plastic bodies by using the effective stress concept. A finite element model of the swaging process was developed in ANSYS and systematically refined to investigate the mechanism of deformation and subsequent development of residual stresses by Gibson *et al.* (2014). Noraziah *et al.* (2011a,b) set an analytical autofrettage procedure to predict the required autofrettage pressure for various levels of allowable pressure and to achieve maximum fatigue life. By using Huang's model for modeling reverse yielding due to Bauschinger effect, Bhatnagar (2013) presented an original concept of an autofrettage compounded tube which was modeled for the autofrettage process. By using the Kendall model, which was adopted by ASME Code, Shim *et al.* (2010) predicted the accurate residual stress of SNCM 8 high strength steel. Zheng and Xuan (2010, 2011) analyzed the optimum autofrettage pressure of a thick wall cylinder under thermo-mechanical loadings and investigated theoretically and validated by the finite element method (FEM) the closed form solution of the limit thermal load of autofrettage and the optimum autofrettage pressure under plane strain and open-ended conditions. Zhu (2008) investigated the optimum plastic depth and load-bearing capacity of an autofrettaged cylinder in terms of the point of view of avoiding compressive yield after removing autofrettage pressure and raising load-bearing capacity as far as possible simultaneously. Zhu and Zhu (2013) studied autofrettage of cylinders by limiting circumferential residual stress and according to Mises Yield criterion. Zhu and Li (2014) presented equations of optimum overstrain (ε_λ) and depth of the plastic zone ($k_{j\lambda}$) for a certain load-bearing capacity and radius ratio (k).

This paper is intended to investigate the varying tendency and distribution laws of stresses in autofrettaged cylinders so as to provide the theoretic basis for the design of high pressure apparatus. Engineering conditions are in endless variety. This paper is based on ideal conditions including (1) the material of a cylinder is perfectly elastic-plastic and the Bauschinger effect is neglected, the compressive yield limit is equal to the tensile one; (2) strain hardening is ignored; (3) there is not any defect in the material.

2. General residual stresses

After removing autofrettage pressure, residual stresses remain in the wall of a cylinder. Yu (1980) put forward the residual stresses at a general radius location which has been re-arranged as follows:

— in the plastic zone

$$\begin{aligned}\frac{\sigma'_z}{\sigma_y} &= \frac{1}{\sqrt{3}} \left[\frac{k_j^2}{k^2} + \ln \frac{x^2}{k_j^2} - \left(1 - \frac{k_j^2}{k^2} + \ln k_j^2 \right) \frac{1}{k^2 - 1} \right] \\ \frac{\sigma'_r}{\sigma_y} &= \frac{1}{\sqrt{3}} \left[\frac{k_j^2}{k^2} - 1 + \ln \frac{x^2}{k_j^2} - \left(1 - \frac{k_j^2}{k^2} + \ln k_j^2 \right) \frac{1}{k^2 - 1} \left(1 - \frac{k^2}{x^2} \right) \right] \\ \frac{\sigma'_\theta}{\sigma_y} &= \frac{1}{\sqrt{3}} \left[\frac{k_j^2}{k^2} + 1 + \ln \frac{x^2}{k_j^2} - \left(1 - \frac{k_j^2}{k^2} + \ln k_j^2 \right) \frac{1}{k^2 - 1} \left(1 + \frac{k^2}{x^2} \right) \right]\end{aligned}\quad (2.1)$$

According to the Mises criterion, the equivalent residual stress is

$$\frac{\sigma'_e}{\sigma_y} = \frac{\sqrt{3}}{2} \left(\frac{\sigma'_\theta}{\sigma_y} - \frac{\sigma'_r}{\sigma_y} \right) = 1 - \frac{k^2 - k_j^2 + k^2 \ln k_j^2}{(k^2 - 1)x^2} \quad (2.2)$$

— in the elastic zone

$$\begin{aligned}\frac{\sigma'_z}{\sigma_y} &= \frac{1}{\sqrt{3}} \left[\frac{k_j^2}{k^2} - \left(1 - \frac{k_j^2}{k^2} + \ln k_j^2 \right) \frac{1}{k^2 - 1} \right] \\ \frac{\sigma'_r}{\sigma_y} &= \frac{1}{\sqrt{3}} \left(1 - \frac{k^2}{x^2} \right) \left[\frac{k_j^2}{k^2} - \left(1 - \frac{k_j^2}{k^2} + \ln k_j^2 \right) \frac{1}{k^2 - 1} \right] = \left(1 - \frac{k^2}{x^2} \right) \frac{\sigma'_z}{\sigma_y} \\ \frac{\sigma'_\theta}{\sigma_y} &= \frac{1}{\sqrt{3}} \left(1 + \frac{k^2}{x^2} \right) \left[\frac{k_j^2}{k^2} - \left(1 - \frac{k_j^2}{k^2} + \ln k_j^2 \right) \frac{1}{k^2 - 1} \right] = \left(1 + \frac{k^2}{x^2} \right) \frac{\sigma'_z}{\sigma_y}\end{aligned}\quad (2.3)$$

The equivalent residual stress at a general radius location based on the Mises criterion is

$$\frac{\sigma'_e}{\sigma_y} = \frac{\sqrt{3}}{2} \left(\frac{\sigma'_\theta}{\sigma_y} - \frac{\sigma'_r}{\sigma_y} \right) = \frac{k^2(k_j^2 - 1 - \ln k_j^2)}{(k^2 - 1)x^2} \quad (2.4)$$

Since $\sigma'_e = \sigma'_\theta - \sigma'_r$ based on the maximum shear stress theory (Tresca criterion) and $\sigma'_e = (\sqrt{3}/2)(\sigma'_\theta - \sigma'_r)$ based on the Mises criterion, while the components of the residual stress based on Mises criterion are $2/\sqrt{3}$ times those based on Tresca criterion, the equivalent residual stresses based on both criterions must be the same.

At the inner surface, $x = 1$. For Eq. (2.2), letting $x = 1$ and $\sigma'_e = -\sigma_y$ obtains an equation for k_{j^*} , the maximum and optimum plastic depth (k_j) for a certain k to avoid compressive yield after removing p_a

$$k^2 \ln k_{j^*}^2 - k^2 - k_{j^*}^2 + 2 = 0 \quad k_{j^*} \geq \sqrt{e} \quad (2.5)$$

where $\sqrt{e} \leq k_{j^*} \leq k_c$ and $k \geq k_c$. When $k \leq k_c$, $|\sigma'_e/\sigma_y| < 1$, irrespective of k_j , Eq. (2.5) is just the equation proposed by Zhu (2008) in another method.

3. Residual stresses and total stresses when $p = p_a$

The total stresses σ^t include the residual stresses plus the stresses caused by p , or $\sigma^t = \sigma' + \sigma^p$.

To produce plastic depth k_j , the pressure subjected to a cylinder is the autofrettage pressure p_a

$$\frac{p}{\sigma_y} = \frac{2}{\sqrt{3}} \ln k_j + \frac{k^2 - k_j^2}{\sqrt{3}k^2} = \frac{p_a}{\sigma_y} \quad (3.1)$$

Letting $k = \infty$ in Eq. (3.1), one obtains

$$\frac{p_\infty}{\sigma_y} = \frac{2}{\sqrt{3}} \ln k_j + \frac{1}{\sqrt{3}} \quad (3.2)$$

Inappropriate k_j causes compressive yield or reduces load-bearing capacity. To avoid compressive yield, the plastic depth k_j for a certain k must be smaller than or equal to the magnitude calculated by Eq. (2.5). Then, to raise load-bearing capacity fully, combining Eqs. (2.5) and (3.1), one obtains

$$\frac{p}{\sigma_y} = \frac{2(k^2 - 1)}{\sqrt{3}k^2} = \frac{2p_e}{\sigma_y} \quad (3.3)$$

Equation (3.3) is the optimum load-bearing capacity of an autofrettaged cylinder, it is just two times the initial yield load. The limit of Eq. (3.3) with $k \rightarrow \infty$ is $p/\sigma_y = 2/\sqrt{3}$, which can be obtained by letting $k_j = \sqrt{e}$ in Eq. (3.2) as well.

The stresses caused by p at a general radius location are

$$\frac{\sigma_z^p}{\sigma_y} = \frac{1}{k^2 - 1} \frac{p}{\sigma_y} \quad \frac{\sigma_r^p}{\sigma_y} = \left(1 - \frac{k^2}{x^2}\right) \frac{\sigma_z^p}{\sigma_y} \quad \frac{\sigma_\theta^p}{\sigma_y} = \left(1 + \frac{k^2}{x^2}\right) \frac{\sigma_z^p}{\sigma_y} \quad (3.4)$$

The equivalent stress of Eq. (3.4) based on the Mises criterion is

$$\frac{\sigma_e^p}{\sigma_y} = \frac{\sqrt{3}}{2} \left(\frac{\sigma_\theta^p}{\sigma_y} - \frac{\sigma_r^p}{\sigma_y} \right) = \frac{\sqrt{3}k^2}{k^2 - 1} \frac{p}{\sigma_y} \frac{1}{x^2} \quad (3.5)$$

When $p = p_a$, Eq. (3.5) becomes

$$\frac{\sigma_e^p}{\sigma_y} = \frac{2k^2}{k^2 - 1} \frac{p}{\sigma_y} \frac{1}{x^2} = \frac{k^2 - k_j^2 + k^2 \ln k_j^2}{(k^2 - 1)x^2} \quad (3.6)$$

The equivalent total stress σ_e^t is

$$\sigma_e^t = \frac{\sqrt{3}}{2} (\sigma_\theta^t - \sigma_r^t) = \frac{\sqrt{3}}{2} [(\sigma_\theta' + \sigma_\theta^p) - (\sigma_r' + \sigma_r^p)] = \frac{\sqrt{3}}{2} [(\sigma_\theta' - \sigma_r') + (\sigma_\theta^p - \sigma_r^p)] = \sigma_e' + \sigma_e^p \quad (3.7)$$

Then, generally, in the plastic zone

$$\frac{\sigma_e^t}{\sigma_y} = 1 - \frac{k^2 - k_j^2 + k^2 \ln k_j^2}{(k^2 - 1)x^2} + \frac{\sqrt{3}k^2}{k^2 - 1} \frac{p}{\sigma_y} \frac{1}{x^2} \quad (3.8)$$

in the elastic zone

$$\frac{\sigma_e^t}{\sigma_y} = \frac{k^2(k_j^2 - 1 - \ln k_j^2)}{(k^2 - 1)x^2} + \frac{\sqrt{3}k^2}{k^2 - 1} \frac{p}{\sigma_y} \frac{1}{x^2} \quad (3.9)$$

At the elastic-plastic juncture ($x = k_j$), Eqs (3.8) and (3.9) both become

$$\frac{\sigma_e^t}{\sigma_y} = \frac{k^2(k_j^2 - 1 - \ln k_j^2)}{(k^2 - 1)k_j^2} + \frac{\sqrt{3}k^2 p}{\sigma_y (k^2 - 1)k_j^2} \quad (3.10)$$

When $p = p_a$, the first one of Eq. (3.4) becomes

$$\frac{\sigma_z^p}{\sigma_y} = \frac{k^2 \ln k_j^2 + k^2 - k_j^2}{\sqrt{3}k^2(k^2 - 1)} \quad (3.11)$$

Using Eqs. (3.11) and (3.4), the general residual stress, Eqs. (2.1)-(2.4), can be rewritten as follows:

— in the plastic zone

$$\begin{aligned}\frac{\sigma'_z}{\sigma_y} &= \frac{1}{\sqrt{3}} \left(\frac{k_j^2}{k^2} + \ln x^2 - \ln k_j^2 \right) - \frac{\sigma_z^p}{\sigma_y} & \frac{\sigma'_r}{\sigma_y} &= \frac{1}{\sqrt{3}} \left(\frac{k_j^2}{k^2} - 1 + \ln x^2 - \ln k_j^2 \right) - \frac{\sigma_r^p}{\sigma_y} \\ \frac{\sigma'_\theta}{\sigma_y} &= \frac{1}{\sqrt{3}} \left(\frac{k_j^2}{k^2} + 1 + \ln x^2 - \ln k_j^2 \right) - \frac{\sigma_\theta^p}{\sigma_y} & & \\ \frac{\sigma'_e}{\sigma_y} &= \frac{\sqrt{3}}{2} \left(\frac{\sigma'_\theta}{\sigma_y} - \frac{\sigma'_r}{\sigma_y} \right) = 1 - \left(\frac{\sigma_\theta^p}{\sigma_y} - \frac{\sigma_r^p}{\sigma_y} \right) = 1 - \frac{\sigma_e^p}{\sigma_y}\end{aligned}\quad (3.12)$$

— in the elastic zone

$$\begin{aligned}\frac{\sigma'_z}{\sigma_y} &= \frac{1}{\sqrt{3}} \frac{k_j^2}{k^2} - \frac{\sigma_z^p}{\sigma_y} & \frac{\sigma'_r}{\sigma_y} &= \frac{1}{\sqrt{3}} \left(\frac{k_j^2}{k^2} - \frac{k_j^2}{x^2} \right) - \frac{\sigma_r^p}{\sigma_y} \\ \frac{\sigma'_\theta}{\sigma_y} &= \frac{1}{\sqrt{3}} \left(\frac{k_j^2}{k^2} + \frac{k_j^2}{x^2} \right) - \frac{\sigma_\theta^p}{\sigma_y} & \frac{\sigma'_e}{\sigma_y} &= \frac{\sqrt{3}}{2} \frac{\sigma'_\theta}{\sigma_y} - \frac{\sigma'_r}{\sigma_y} = \frac{k_j^2}{x^2} - \frac{\sqrt{3}}{2} \left(\frac{\sigma_\theta^p}{\sigma_y} - \frac{\sigma_r^p}{\sigma_y} \right) = \frac{k_j^2}{x^2} - \frac{\sigma_e^p}{\sigma_y}\end{aligned}\quad (3.13)$$

Therefore, when $p = p_a$, irrespective of k_j , the total stresses are:

— in the plastic zone

$$\begin{aligned}\frac{\sigma_z^t}{\sigma_y} &= \frac{\sigma'_z}{\sigma_y} + \frac{\sigma_z^p}{\sigma_y} = \frac{1}{\sqrt{3}} \left(\frac{k_j^2}{k^2} + \ln x^2 - \ln k_j^2 \right) \\ \frac{\sigma_r^t}{\sigma_y} &= \frac{\sigma'_r}{\sigma_y} + \frac{\sigma_r^p}{\sigma_y} = \frac{1}{\sqrt{3}} \left(\frac{k_j^2}{k^2} - 1 + \ln x^2 - \ln k_j^2 \right) \\ \frac{\sigma_\theta^t}{\sigma_y} &= \frac{\sigma'_\theta}{\sigma_y} + \frac{\sigma_\theta^p}{\sigma_y} = \frac{1}{\sqrt{3}} \left(\frac{k_j^2}{k^2} + 1 + \ln x^2 - \ln k_j^2 \right) & \frac{\sigma_e^t}{\sigma_y} &\equiv 1\end{aligned}\quad (3.14)$$

— in the elastic zone

$$\begin{aligned}\frac{\sigma_z^t}{\sigma_y} &= \frac{\sigma'_z}{\sigma_y} + \frac{\sigma_z^p}{\sigma_y} = \frac{1}{\sqrt{3}} \frac{k_j^2}{k^2} & \frac{\sigma_r^t}{\sigma_y} &= \frac{\sigma'_r}{\sigma_y} + \frac{\sigma_r^p}{\sigma_y} = \frac{1}{\sqrt{3}} \left(\frac{k_j^2}{k^2} - \frac{k_j^2}{x^2} \right) \\ \frac{\sigma_\theta^t}{\sigma_y} &= \frac{\sigma'_\theta}{\sigma_y} + \frac{\sigma_\theta^p}{\sigma_y} = \frac{1}{\sqrt{3}} \left(\frac{k_j^2}{k^2} + \frac{k_j^2}{x^2} \right) & \frac{\sigma_e^t}{\sigma_y} &= \frac{k_j^2}{x^2}\end{aligned}\quad (3.15)$$

The components of total stresses based on the Mises criterion are $2/\sqrt{3}$ times those based on the Tresca criterion, but the equivalent total stresses based on both theories in the plastic and elastic zone are the same, respectively. The reason is that the equivalent total stress based on the Tresca criterion is $2/\sqrt{3}$ times that based on the Mises criterion since $\sigma_z = (\sigma_r + \sigma_\theta)/2$ for cylinders.

4. Residual stresses and total stresses when $k_j = k_{j^*}$ and $p = p_a$

If k_j is determined by Eq. (2.5), or $k_j = k_{j^*}$, Eqs. (3.8) and (3.9) become respectively

$$\frac{\sigma_e^t}{\sigma_y} = 1 - \frac{2}{x^2} + \frac{\sqrt{3}k^2}{k^2 - 1} \frac{p/\sigma_y}{x^2} \quad \frac{\sigma_e^t}{\sigma_y} = \frac{k_j^2 - 2}{x^2} + \frac{\sqrt{3}k^2}{k^2 - 1} \frac{p/\sigma_y}{x^2}\quad (4.1)$$

From Eq. (4.1)₁, it is seen that:

- (1) provided $p/\sigma_y > -2(k^2 - 1)(x^2 - 1)/\sqrt{3}k^2$ (negative), $\sigma_e^t > -\sigma_y$, this is definitely feasible for $p > 0$ in engineering;

- (2) as long as $p/\sigma_y > (k^2 - 1)(2 - x^2)/\sqrt{3}k^2$, $\sigma_e^t > 0$, while $(k^2 - 1)(2 - x^2)/\sqrt{3}k^2 < p_e/\sigma_y$, so when $p > p_e$, $\sigma_e^t > 0$;
- (3) so long as $p < 2p_e$, $\sigma_e^t < \sigma_y$. Thus, when $p_e < p < 2p_e$, $0 < \sigma_e^t < \sigma_y$.

From Eq. (4.1)₂, it is known that:

- (1) provided $p/\sigma_y > -(k^2 - 1)(k_j^2 - 2)/\sqrt{3}k^2$ (negative), $\sigma_e^t > 0$, this is certain for $p > 0$ in engineering, so the equivalent residual stress in the elastic zone is always tensile;
- (2) so long as $p/\sigma_y < (k^2 - 1)(x^2 - k_j^2 + 2)/\sqrt{3}k^2$, $\sigma_e^t < \sigma_y$, so when $p < 2p_e$, $\sigma_e^t < \sigma_y$.

At the inside surface, $x = 1$, then, from Eq. (4.1)₁

$$\frac{\sigma_e^t}{\sigma_y} = \frac{\sqrt{3}k^2}{k^2 - 1} \frac{p}{\sigma_y} - 1 \quad (4.2)$$

Unless $p < 0$, σ_e^t can not be lower than $-\sigma_y$. Unless $p > 2p_e$, σ_e^t can not be higher than σ_y . So, when $0 < p < 2p_e$, $-1 < \sigma_e^t/\sigma_y < 1$. Especially, when $p = 2p_e$, $\sigma_e^t \equiv \sigma_y$ in the whole plastic zone.

At the elastic-plastic juncture, $x = k_j$, from (4.1)₁ or (4.1)₂

$$\frac{\sigma_e^t}{\sigma_y} = \frac{k_j^2 - 2}{k_j^2} + \frac{\sqrt{3}k^2}{k^2 - 1} \frac{p/\sigma_y}{k_j^2} \quad (4.3)$$

Clearly, $\sigma_e^t > 0$ in the elastic zone. If $p < 2p_e$, σ_e^t can not be higher than σ_y . So, when $0 < p < 2p_e$, $0 < \sigma_e^t/\sigma_y < 1$. Especially, when $p = 2p_e$, $\sigma_e^t = \sigma_y$ at the elastic-plastic juncture and $\sigma_e^t/\sigma_y = k_j^2/x^2$ at a general radius location in the elastic zone.

When $k_j = k_{j^*}$, by the aid of Eq. (2.5), Eqs (2.1)-(2.4) can be simplified as follows:

— in the plastic zone

$$\begin{aligned} \frac{\sigma'_z}{\sigma_y} &= \frac{\ln x^2}{\sqrt{3}} - \frac{1}{\sqrt{3}} & \frac{\sigma'_r}{\sigma_y} &= \frac{\ln x^2}{\sqrt{3}} + \frac{2}{\sqrt{3}x^2} - \frac{2}{\sqrt{3}} \\ \frac{\sigma'_\theta}{\sigma_y} &= \frac{\ln x^2}{\sqrt{3}} - \frac{2}{\sqrt{3}x^2} & \frac{\sigma'_e}{\sigma_y} &= 1 - \frac{2}{x^2} \end{aligned} \quad (4.4)$$

— in the elastic zone

$$\begin{aligned} \frac{\sigma'_z}{\sigma_y} &= \frac{k_j^2 - 2}{\sqrt{3}k^2} & \frac{\sigma'_r}{\sigma_y} &= \left(1 - \frac{k^2}{(r/r_i)^2}\right) \frac{\sigma'_z}{\sigma_y} = \left(1 - \frac{k^2}{x^2}\right) \frac{\sigma'_z}{\sigma_y} \\ \frac{\sigma'_\theta}{\sigma_y} &= \left(1 + \frac{k^2}{x^2}\right) \frac{\sigma'_z}{\sigma_y} & \frac{\sigma'_e}{\sigma_y} &= \frac{k_j^2 - 2}{x^2} \end{aligned} \quad (4.5)$$

The equations of residual stresses are greatly simplified, and cylinders are safe after removing p_a .

When $k = \infty$, $k_j = \sqrt{e}$, from Eq. (4.5)₄, the equivalent residual stress at a general radius location in the elastic zone is

$$\frac{\sigma'_e}{\sigma_y} = \frac{e - 2}{x^2} \quad \frac{\sigma'_e}{\sigma_y} = 1 - \frac{2}{e} \rightarrow 0 \quad \text{when } x = \sqrt{e} \rightarrow \infty \quad (4.6)$$

When $k_j = k_{j^*}$, the distributions of equivalent residual stresses in the plastic and elastic zones – which are the same as those based on Tresca criterion – are illustrated in Fig. 1. In Fig. 1:

- (1) Curve *BAA*: $k = k_j = k_c$, x varies from 1 to k_j in the plastic zone (from point *B* to *A*), and from $2.2184574899167\dots(k_j)$ to $2.2184574899167\dots(k)$ (from point *A* to *A*) in the elastic zone (no elastic zone).

- (2) Curve BCD : $k = 2.25$, $k_j = 2.046308\dots$, x varies from 1 to 2.046308... in the plastic zone (from point B to C), and from 2.046308... to 2.25 (from point C to D) in the elastic zone.
- (3) Curve BEF : $k = 3$, $k_j = 1.748442\dots$, x varies from 1 to 1.748442... in the plastic zone (from point B to E), and from 1.748442... to 3 (from point E to F) in elastic zone.
- (4) Curve BMN : $k = \infty$, $k_j = \sqrt{e}$, x varies from 1 to $\sqrt{e} = 1.648721\dots$ in the plastic zone (from point B to M), and from \sqrt{e} to $k = \infty$ (from point M to N) in the elastic zone.

The above results and Fig. 1 are fit for both the Tresca and Mises criterion.

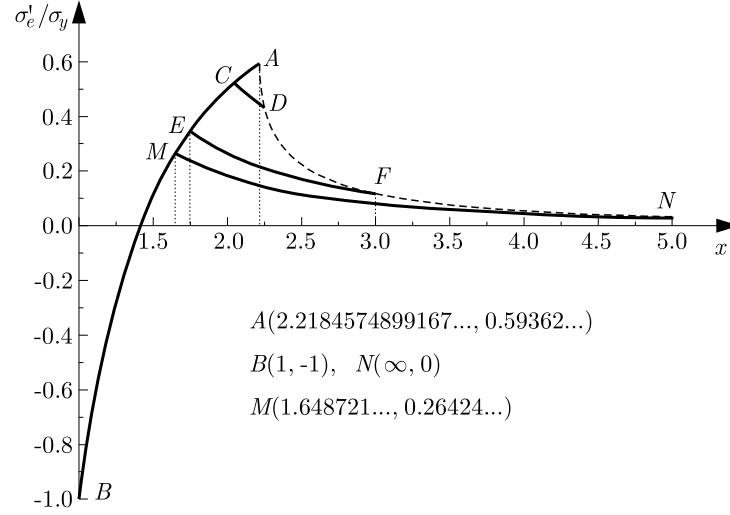


Fig. 1. The distributions of equivalent residual stresses in the whole wall

Figure 1 and Eq. (4.4)₄ show that all curves of equivalent residual stresses for any k and k_j in the plastic zone are located on the identical curve AB and pass through the same point $(\sqrt{2}, 0)$, except that a different curve for different k and k_j is located in a different section of the curve AB , i.e. curves BA , BC , BE and BM are all on the curve BA or they coincide with each other. However, if $k_j \neq k_{j^*}$ or the relation between k_j and k does not satisfy Eq. (2.5), the above argument is untenable, or even $|\sigma'_e| > \sigma_y$. This case is illustrated in Fig. 2, where the curves BEF and BKL coincide with each other in the plastic zone and both pass through point $(\sqrt{2}, 0)$ because $k_j = k_{j^*}$, but curves HSI and GQJ neither coincide with each other in the plastic zone nor pass through the point $(\sqrt{2}, 0)$, and they do not coincide with the curves BEF and BKL in the plastic zone for $k_j \neq k_{j^*}$.

When $p = 2p_e$, Eq. (3.4) and (3.5) become Eq. (4.7) and Eq. (4.8), respectively

$$\frac{\sigma_z^p}{\sigma_y} = \frac{2}{\sqrt{3}k^2} \quad \frac{\sigma_r^p}{\sigma_y} = \frac{2}{\sqrt{3}k^2} - \frac{2}{\sqrt{3}x^2} \quad \frac{\sigma_\theta^p}{\sigma_y} = \frac{2}{\sqrt{3}k^2} + \frac{2}{\sqrt{3}x^2} \quad (4.7)$$

and

$$\frac{\sigma_e^p}{\sigma_y} = \frac{2}{x^2} \quad (4.8)$$

When $k_j = k_{j^*}$, $p = p_a = 2p_e$, thus, when $p = p_a = 2p_e$, Eqs. (3.14) and (3.15) for the total stresses become:

— in the plastic zone

$$\begin{aligned} \frac{\sigma_z^t}{\sigma_y} &= \frac{\ln x^2}{\sqrt{3}} - \frac{1}{\sqrt{3}} + \frac{2}{\sqrt{3}k^2} & \frac{\sigma_r^t}{\sigma_y} &= \frac{\ln x^2}{\sqrt{3}} - \frac{2}{\sqrt{3}} + \frac{2}{\sqrt{3}k^2} \\ \frac{\sigma_\theta^t}{\sigma_y} &= \frac{\ln x^2}{\sqrt{3}} + \frac{2}{\sqrt{3}k^2} & \frac{\sigma_e^t}{\sigma_y} &= \frac{\sqrt{3}}{2} \left(\frac{\sigma_\theta^t}{\sigma_y} - \frac{\sigma_r^t}{\sigma_y} \right) \equiv 1 \end{aligned} \quad (4.9)$$

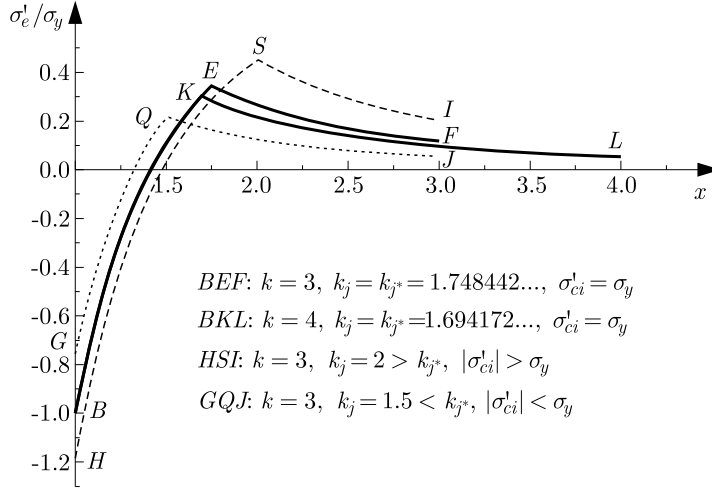


Fig. 2. Comparison between equivalent residual stresses for different k and k_j

— in the elastic zone

$$\begin{aligned}
 \frac{\sigma_z^t}{\sigma_y} &= \frac{\sigma_z'}{\sigma_y} + \frac{\sigma_z^p}{\sigma_y} = \frac{k_j^2}{\sqrt{3}k^2} & \frac{\sigma_r^t}{\sigma_y} &= \frac{\sigma_r'}{\sigma_y} + \frac{\sigma_r^p}{\sigma_y} = \frac{k_j^2}{\sqrt{3}} \left(\frac{1}{k^2} - \frac{1}{x^2} \right) \\
 \frac{\sigma_\theta^t}{\sigma_y} &= \frac{\sigma_\theta'}{\sigma_y} + \frac{\sigma_\theta^p}{\sigma_y} = \frac{k_j^2}{\sqrt{3}} \left(\frac{1}{k^2} + \frac{1}{x^2} \right) & \frac{\sigma_e^t}{\sigma_y} &= \frac{k_j^2}{x^2} & \frac{\sigma_e^t}{\sigma_y} &= \frac{e}{x^2}
 \end{aligned} \tag{4.10}$$

where $k = \infty, x \in (\sqrt{e}, \infty)$.

The equations of total stresses are greatly simplified, and cylinders are safe after removing p_a and in operation. Figure 3 shows the distribution of equivalent stress of the total stress when $p = 2p_e$ and $k_j = k_{j^*}$. In Fig. 3:

- (1) Horizontal line baa : $k = k_j = k_c$. In the plastic zone, σ_e^t/σ_y is a horizontal line: $\sigma_e^t/\sigma_y = 1$, x varies from 1 to k_j (from point b to a) and from k_j to k (from point a to a) in the plastic zone (no elastic zone).
- (2) Curve bcd : $k = 2.25, k_j = 2.046308\dots$. In the plastic zone, σ_e^t/σ_y is a horizontal line, bc : $\sigma_e^t/\sigma_y = 1$, x varies from 1 to k_j (from point b to c) and from k_j to k (from point c to d) in the elastic zone.
- (3) Curve bef : $k = 3, k_j = 1.748442\dots$. In the plastic zone, σ_e^t/σ_y is a horizontal line, be : $\sigma_e^t/\sigma_y = 1$, x varies from 1 to k_j (from point b to e) and from k_j to k (from point e to f) in the elastic zone.
- (4) Curve $bm n$: $k = \infty, k_j = \sqrt{e}$. In the plastic zone, σ_e^t/σ_y is a horizontal line: $\sigma_e^t/\sigma_y = 1$, bm : x varies from 1 to k_j (from point b to m) and from k_j to $k(\infty)$ (from point m to n) in the elastic zone.

If $k_j \neq k_{j^*}$ or $p \neq 2p_e$, the above traits can not arise. Figure 4 is comparison between the equivalent total stresses under different internal pressure and $k_j = k_{j^*}$ from which it is known that only when $p = 2p_e$ and $k_j = k_{j^*}$, the operation state is optimum, otherwise, or $p \neq 2p_e$ and/or $k_j \neq k_{j^*}$, either $\sigma_e^t > \sigma_y$ or load-bearing capacity is lowered or compressive yield occurs. In Fig. 4, curve 1 is just curve bef in Fig. 3.

Besides, for a certain k , when $k_j < k_{j^*}$, though residual stresses are lower than those when $k_j = k_{j^*}$, the load-bearing capacity is dropped. For example, for $k = 3$, if $k_j = k_{j^*} (= 1.748442)$, from Eq. (3.3), $p/\sigma_y = 1.0264\dots$; while if $k_j = 1.5$, from Eq. (3.1), $p/\sigma_y = 0.901203\dots < 1.0264$.

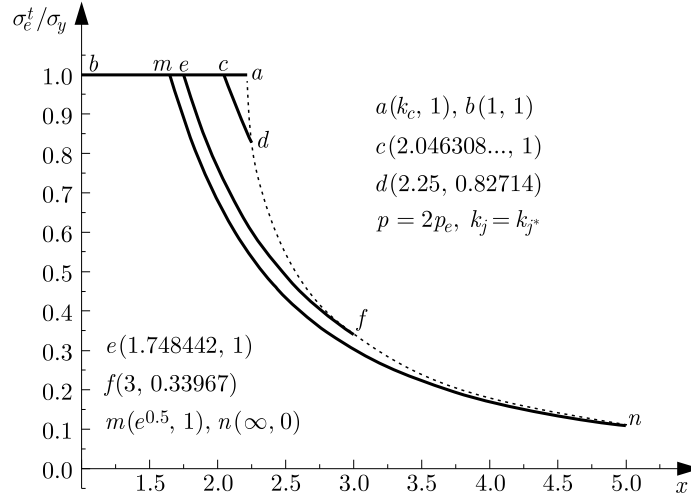


Fig. 3. The distribution of equivalent total stress when $p = 2p_e$ and $k_j = k_{j^*}$

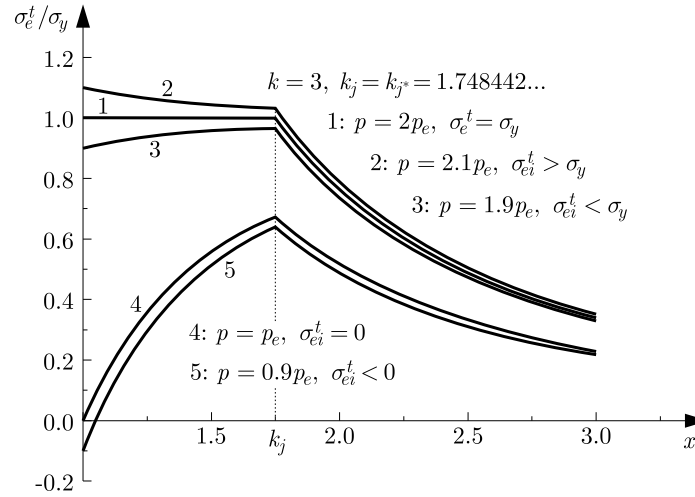


Fig. 4. Comparison between the equivalent total stresses for different internal pressure and $k_j = k_{j^*}$

5. Conclusions

It is the combination of $k^2 \ln k_{j^*}^2 - k^2 - k_{j^*}^2 + 2 = 0$ and $p = 2p_e$ that results in optimum results of an autofrettaged cylinder – the load-bearing capacity is the highest and no compressive yield occurs after removing p_a . Under these two conditions, neither compressive yield occurs nor do the equivalent total stresses exceed σ_y , and the equivalent total stress in the whole plastic zone is even, identically equal to σ_y , while the equivalent total stress in the elastic zone is lower than σ_y .

The equations concerned with autofrettage are simplified greatly because of the conditions $k^2 \ln k_{j^*}^2 - k^2 - k_{j^*}^2 + 2 = 0$ and $p = 2p_e$.

When $k_j = k_{j^*}$, in the plastic zone, the equivalent residual stress σ_e' / σ_y shares the same curve and pass through the point $(\sqrt{2}, 0)$. When $x \leq \sqrt{2}$, $\sigma_e' \leq 0$; when $x \geq \sqrt{2}$, $\sigma_e' \geq 0$. The equivalent residual stress at the inside surface $\sigma_{ei}' = -\sigma_y$; in the whole wall, $|\sigma_e'| \leq \sigma_y$. So when $k_j = k_{j^*}$, cylinders are safe.

When $p > 2p_e$ and $k_j = k_{j^*}$, the equivalent total stress is greater than σ_y and uneven. When $p < 2p_e$ and $k_j = k_{j^*}$, the equivalent total stress is lower than σ_y but load-bearing capacity is reduced, and equivalent total stress is uneven. When $p < p_e$, σ_e^t at the inside surface is lower

than 0, σ_e^t can not be lower than $-\sigma_y$ in the whole plastic zone, the load-bearing capacity is reduced greatly and the equivalent total stress is uneven.

As long as an autofrettaged cylinder contains the autofrettage pressure p_a , there must be an inexorable law irrespective of k_j and k : $\sigma_e/\sigma_y \equiv 1$ in the plastic zone and $0 < \sigma_e/\sigma_y = k_j^2/x^2 < 1$ in the elastic zone. Nevertheless, too great k_j causes compressive yield after removing p_a , too small k_j reduces the load-bearing capacity of a cylinder. The optimum plastic depth is $k_j = k_{j^*}$, and when $k_j = k_{j^*}$, $p = p_a = 2p_e$.

On the basis of the results in this study, when an autofrettaged cylinder is subjected to the load $p = 2p_e = (2/\sqrt{3})[(k^2 - 1)/k^2]\sigma_y$, its optimum design thickness is

$$t = r_i(k - 1) = r_i \left(\sqrt{\frac{2\sigma_y}{\sigma_y - \sqrt{3}p}} - 1 \right)$$

its optimum plastic depth k_{j^*} is calculated by

$$\frac{2\sigma_y}{\sigma_y - \sqrt{3}p} \ln k_{j^*}^2 - \frac{2\sigma_y}{\sigma_y - \sqrt{3}p} - k_{j^*}^2 + 2 = 0$$

Acknowledgments

This project has been supported by Scientific Research Fund of Hunan Provincial Education Department (Grant No. 12A087)

References

1. BHATNAGAR R.M., 2013, Modelling, validation and design of autofrettage and compound cylinder, *European Journal of Mechanics-A Solids*, **39**, 17-25
2. BRÜNNET H., BÄHRE D., 2014, Full exploitation of lightweight design potentials by generating pronounced compressive residual stress fields with hydraulic autofrettage, *Advanced Materials Research*, **907**, 17-27
3. FARRAHI G.H., VOYIADJIS G.Z., HOSEINI S.H., HOSSEINIAN E., 2012, Residual stress analyses of re-autofrettaged thick-walled tubes, *International Journal of Pressure Vessels and Piping*, **98**, 57-64
4. GIBSON M.C., HAMEED A., HETHERINGTON J.G., 2014, Investigation of residual stress development during swage autofrettage, using finite element analysis, *Journal of Pressure Vessel Technology*, **136**, 2, 45-51
5. HAMILTON N.R., WOOD J., EASTON D., ROBBIE M.B.O., ZHANG Y., GALLOWAY A., 2015, Thermal autofrettage of dissimilar material brazed joints, *Materials and Design*, **67**, 405-412
6. LIN Y., DONG Q., JIA J., 2009, Autofrettage damage residual stress of thick-walled cylinder (in Chinese), *Science Technology and Engineering*, **9**, 24, 7306-7309
7. LVOV G., KOSTROMITSKAYA O., 2014, Effect of material damage on autofrettage of thick-walled cylinder, *Universal Journal of Mechanical Engineering*, **2**, 2, 44-48
8. NORAZIAH W., AMRAN A., ELBASHEER M.K., 2011a, Effect of autofrettage on allowable pressure of thick-walled cylinders, *Proceedings of International Conference on Environmental and Agriculture Engineering (ICEAE 2011)*, Singapore
9. NORAZIAH W., AMRAN A., ELBASHEER M.K., 2011b, Effect of optimum autofrettage on pressure limits of thick-walled cylinder, *International Journal of Environmental Science and Development*, **2**, 4, 329-333
10. SHIM W.S., KIM J.H., LEE Y.S., CHA K.U., HONG K.S., 2010, A Study on hydraulic autofrettage of thick-walled cylinders incorporating Bauschinger effect, *Experimental Mechanics*, **50**, 5, 621-626

11. YU G., 1980, *Chemical Pressure Vessels and Equipment* (in Chinese), Beijing: Chemical Industrial Press
12. ZHENG X.T., XUAN F.Z., 2010, Investigation on autofrettage and safety of the thick-walled cylinder under thermo-mechanical loadings (in Chinese), *Journal of Mechanical Engineering*, **46**, 16, 156-161
13. ZHENG X.T., XUAN F.Z., 2011, Autofrettage and shakedown analysis of strain-hardening cylinders under thermo-mechanical loadings, *Journal of Strain Analysis Engineering and Design*, **46**, 1, 45-55
14. ZHU R., 2008, Ultimate load-bearing capacity of cylinder derived from autofrettage under ideal condition, *Chinese Journal of Mechanical Engineering*, **21**, 5, 80-87
15. ZHU R., LI Q., 2014, Inquire into the marvellousness of autofrettage for mono-layered cylinders, *Journal of Theoretical and Applied Mechanics*, **52**, 2, 359-372
16. ZHU R., ZHU G., 2013, On autofrettage of cylinders by limiting circumferential residual stress based on Mises yield criterion, *Journal of Theoretical and Applied Mechanics*, **51**, 3, 697-710

Manuscript received November 4, 2015; accepted for print April 5, 2016

THE APPLICATION OF SELF-OSCILLATION IN WIRE GAUGES

GRZEGORZ CIEPŁOK, ŁUKASZ KOPIJ

AGH University of Science and Technology, Kraków, Poland

e-mail: cieplik@agh.edu.pl; lkopij@agh.edu.pl

In the presented paper, an original solution to the system maintaining vibrations of a wire transducer, which has been based upon the phenomenon of self-oscillation, is described. The vibrations generated in this manner do not fade in time, are resistant to disturbances and allow measurement of the signal rapidly changing in time. The dynamic equations and numerical simulations of motion of the wire interconnected with the van der Pol oscillator are presented. Based on the conceptual model, a laboratory stand has been built, which served to verify properties of the presented solution and possibilities of useful applications.

Keywords: self-oscillation, wire transducer

1. Introduction

The measurement technique using wire transducers has been known since 1931, when French engineer André Coyne became the first scientist to patent a sensor working on the principle of vibrating wires (Bordes, 2011). In the 1930s, wire sensors became very popular in the technical health monitoring of water dams. The first measurement system was applied to the dam across the Truyere River in Bomme, France (Bordes, 2011). This method was also applied to control technical health of bridges (Bar *et al.*, 2012; Gastineau *et al.*, 2009; Wenzel, 2009), tunnels, large-scale halls, and is currently also being applied in stadiums and transport infrastructure.

Wire measurement is currently an important branch of surveying, being applied in the measurement of displacement of elements, deformation, changes in characteristics, changes in the leaning angle of buildings, subsidence of supports, ground support for construction elements, and determination of force in earth anchors, etc. (Benmokrane *et al.*, 1995; Hayes and Simmonds, 2002; Neild *et al.*, 2005; Sharma *et al.*, 1999).

Wire sensors have a range of benefits. The output signal from a transducer has a frequency character which makes it resistant to external disturbances and the influence of cables transferring data between the transducer and the recording device. This makes it possible to install the transducer in a significant distance away from the location of data acquisition point (Simonetti, 2012). Its simple and solid construction ensures high resistance to mechanical damage and insensitivity to atmospheric conditions. It is also possible to use wireless communication between the transducer and the measuring system (Park *et al.*, 2013).

The most important feature of wire sensors is their high metrological stability, which – according to the research conducted by Norwegian Geotechnical Institute – can last for 27 years (DiBiagio, 2003). The features of wire transducers mean that they are still often applied in SHM systems of constructions.

One example of the use of wire measurement techniques on a large scale is the monitoring system of A1 motorway embankment in Poland. This covers an area of approximately 100 thousands m². Around 15 thousands wire transducers are used there.

During the last 80 years, the construction and working principle of wire sensors have not changed. They consist of steel wires excited into transverse vibration with the help of an electro-magnet (Simonetti, 2012). A change in the force of the wire influences its transverse vibration frequency – and that is the basis for finding the relative extension of the wire, and then defining the deformation of the object to which the sensor has been mounted. The electro-magnet also performs function of a vibration detector.

Wire transducers are designed in principle for measurement of slow-changing or static loads. This limitation results from its working principle, in which successive vibration excitement of the wire is only possible after the previous vibration has subsided. Excessively early excitation may cause mutual interference between vibrations and lead to disturbances and impracticality of the metrological signal. As a result, the maximum excitation frequency of the wire for a typical solution is defined at the level of 1 Hz. As can be seen, the method has limited application in the case of constant measurement with the aim of registering the course of fast-changing changes, e.g. in high objects affected by the wind (Qing *et al.*, 2008), such as chimneys, masts and towers, or machine supports, for example, foundations under turbo-generators, railway and road bridges in the event of para-seismic and seismic disturbance.

In the literature, it is possible to find solutions that allow measurement of quasi-constant fast-changing deformation. In this case, the most important element of the method is the maintenance of natural non-decreasing vibrations of wires by cyclical, in accordance with the phase of wire vibration, excitation with electro-magnetic impulses. This method does not, however, guarantee the continuity of measurement. Some of signals are lost due to the presence of transition states caused by the exciting impulses. There is a high probability that, as a result of violent changes in the measured deformation, the impulse phase will not correlate with the wire vibration phase, which most frequently leads to formation of undesired transition states, and even to suppression of wire vibration.

2. Maintenance of non-decreasing natural vibration of wires

One way to excite and maintain non-decreasing natural vibration of wires, according to the authors, is to introduce self-oscillation in wires. Vibrations of this type are well-known in mechanical engineering (Den Hartog, 1956). They appear in non-conservative systems and are capable of independently replenishing lost energy. Their amplitude and frequency are defined by physical parameters of the system. Due to this, they are different from damped vibrations in that they do not fade out in time, and that the frequency of vibrations in the steady state is not dependent on the frequency of external forces.

An example of an equation that describes self-oscillation comes from van der Pol (Atay, 1998)

$$\frac{d^2y}{dt^2} - \varepsilon(1 - y^2)\frac{dy}{dt} + y = 0 \quad (2.1)$$

This contains a non-linear component $-\varepsilon(1 - y^2)(dy/dt)$ responsible for the maintenance of vibrations, which will further be named in this work as the van der Pol component. An example of the solution to (2.1) is presented in Fig. 1. It can be seen that for various initial conditions, the trajectory of the solution winds on a fixed limit cycle. By modifying equation (2.1) to form (2.2), it is possible to provide it with a physical interpretation. This then describes motion of mass m located on a viscoelastic suspension under the force in accordance with the formula of the van der Pol component, see Fig. 2.

$$m\frac{d^2y}{dt^2} + b\frac{dy}{dt} + ky = \varepsilon(a^2 - y^2)\frac{dy}{dt} \quad (2.2)$$

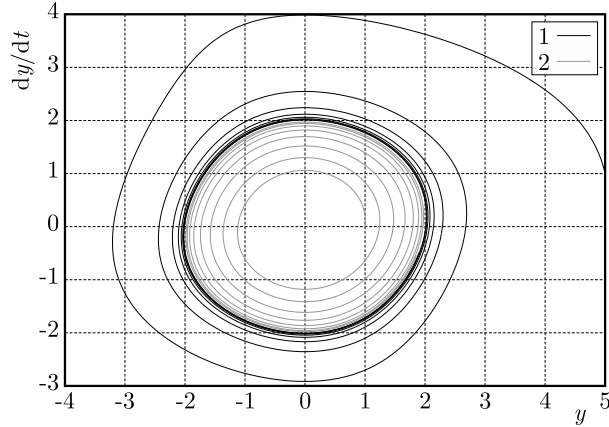


Fig. 1. Phase portrait of Eq. (2.1) for two various initial conditions. Trajectory 1 has a direction field from the external side of the limit cycle contour, while trajectory 2 comes from the internal side

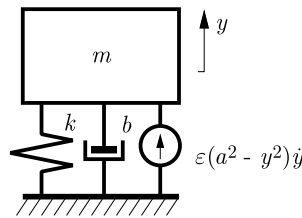


Fig. 2. Model of the mechanical structure representing equation (2.2)

If the absolute value of the coordinate y falls below the value of the parameter a , the van der Pol component supplies energy to the system, otherwise it dissipates it. One characteristic feature that the authors of the work have noticed is the lack of turbulent transition states appearing in the event of violent changes in the elasticity coefficient k , see Figs. 3a and 3b. Of course, the coordinate y changes its course because it sets a new cycle with a different frequency, however, this process takes place without any significant disturbance to motion. The new vibration frequency of the mass m is set almost immediately.

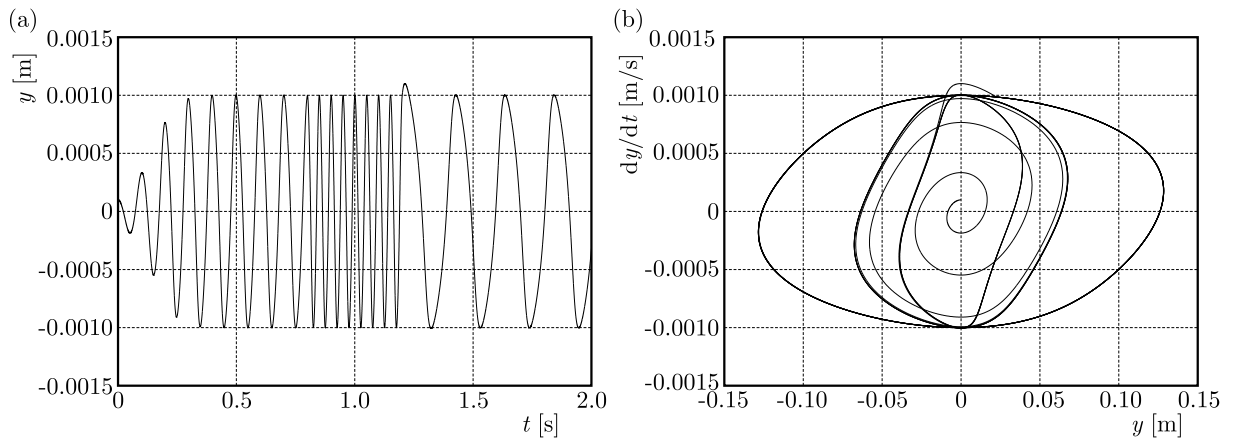


Fig. 3. (a) Course of the coordinate y for stepwise changes of the coefficient k (changes of the coefficient took place at 0.8s and 1.2s), (b) trajectory with three limit cycles

This feature of the system has become a basic principle of the application of self-oscillation in wire sensors. In this case, the van der Pol component ensures the maintenance of non-decreasing transverse vibration of the wire, and violent changes in its load (in the longitudinal direction) do not cause any disturbance in its transverse motion. The new vibration frequency is set almost immediately and is ready to be read by a signal processing system.

3. Mathematical model of a wire

Let us analyse a wire simultaneously performing transverse vibration and longitudinal motion, see Fig. 4. Designating by A the field of the wire transverse cross-section, ρ – material density, and dx – the elementary section of the wire, we can write

$$dm = \rho A dx \quad (3.1)$$

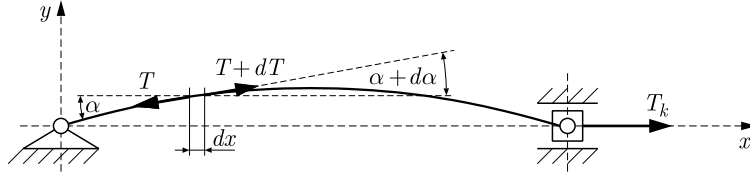


Fig. 4. Model of a wire subjected to longitudinal load

Treating the elementary mass dm as a material point in planar motion, we can, based on Newton's second law, formulate a dynamic equation of its motion. Designating the location of the mass dm with the coordinates x and y , we obtain the equation for transverse motion

$$dm \frac{\partial^2 y}{\partial t^2} = (T + dT) \sin(\alpha + d\alpha) - T \sin \alpha - b_y \frac{\partial y}{\partial t} dx + q(x, t) dx \quad (3.2)$$

in which T designates the force in the wire, b_y – coefficient of viscous friction calculated as a unit of distance and q – linear density of the external transverse force. Assuming a small value of the angle α , equation (3.2) can be simplified to

$$dm \frac{\partial^2 y}{\partial t^2} = T d\alpha + \alpha dT - b_y \frac{\partial y}{\partial t} dx + q(x, t) dx \quad (3.3)$$

Expressing α by $\partial y(x, t)/\partial x$ and using dependency (3.1), we can write the equation of the wire transverse motion in form

$$\rho A \frac{\partial^2 y(x, t)}{\partial t^2} - T(x, t) \frac{\partial^2 y(x, t)}{\partial x^2} + b_y \frac{\partial y(x, t)}{\partial t} = \frac{\partial y(x, t)}{\partial x} \frac{\partial T(x, t)}{\partial x} + q(x, t) \quad (3.4)$$

In the last equation, the force T is not constant. Its temporary value can be determined based on the equation of motion of the longitudinal mass dm , where u designates the displacement of the elementary section of the wire along its axis

$$dm \frac{\partial^2 u}{\partial t^2} = -T \cos \alpha + (T + dT) \cos(\alpha + d\alpha) - b_x \frac{\partial u}{\partial t} dx \quad (3.5)$$

By using a small-angle approximation as well as assuming uniformity of the material, we obtain the equation of wire longitudinal motion

$$\frac{\partial^2 u(x, t)}{\partial t^2} + \frac{b_x}{A\rho} \frac{\partial u(x, t)}{\partial t} - \frac{E}{\rho} \frac{\partial^2 u(x, t)}{\partial x^2} = 0 \quad (3.6)$$

where E is Young's modulus, b_x – coefficient of viscous friction calculated as a unit of distance.

Based on Hook's law, we can express the force in the wire by its local deformation, that is

$$T = A\sigma = AE\varepsilon = AE \frac{\partial u}{\partial x} \quad (3.7)$$

or

$$\frac{\partial T}{\partial x} = EA \frac{\partial^2 u}{\partial x^2} \quad (3.8)$$

By placing dependency (3.8) into equation (3.4), we obtain

$$\rho A \frac{\partial^2 y(x, t)}{\partial t^2} + b_y \frac{\partial y(x, t)}{\partial t} - AE \frac{\partial u(x, t)}{\partial x} \frac{\partial^2 y(x, t)}{\partial x^2} = EA \frac{\partial y(x, t)}{\partial x} \frac{\partial^2 u(x, t)}{\partial x^2} + q(x, t) \quad (3.9)$$

The set of equations (3.6) and (3.9) represent the basis for a mathematical description of wire motion, whose points perform transverse and longitudinal movement coupled with each other.

The method for fixing the wire is defined by the boundary conditions. In the considered cases, the wire is mounted unilaterally. The second end is conducted linearly and is affected by the external force T_k . On this basis, it is possible to write the following conditions

$$y(0, t) = 0 \quad y(l, t) = 0 \quad (3.10)$$

and

$$u(0, t) = 0 \quad \frac{\partial u(l, t)}{\partial x} = \frac{1}{EA} T_k \quad (3.11)$$

4. Adaptation of van der Pol's equation to maintain non-decreasing natural vibrations of a wire

Transferring the idea of applying self-oscillation to wire gauges is presented in Fig. 5. Untied between two points, it is propelled to move transversely using the Lorentz force created as a result of the interference of current i flowing through the wire as well as the magnetic field created by fixed magnets. The intensity of current i is shaped by the electric system working in a feedback loop, in which the input signal is the voltage induced in the magneto-electric transducer. In order to adapt the input voltage to an electronic system, it is first amplified, and then undergoes integration in time so that the wire displacement signal is obtained from the amplitude transducer. After transformation of the signal by the multiplier-summing systems realizing the van der Pol component, it is amplified to a value that allows creation of a force ensuring vibrations at a level which enable their recording.

5. Results of computer simulations

Based on the equations from the previous Section, computer simulations of motion of the wire subjected to a stepwise load have been performed. In order to solve the differential equation of motion, the finite difference method with the "time step" variant has been applied. After replacing the partial derivatives in equations (3.6) and (3.9) with the following finite differences

$$\begin{aligned} \frac{\partial y}{\partial x} &= \frac{y(i+1, j) - y(i, j)}{\Delta x} & \frac{\partial^2 y}{\partial x^2} &= \frac{y(i+1, j) - 2y(i, j) + y(i-1, j)}{(\Delta x)^2} \\ \frac{\partial y}{\partial t} &= \frac{y(i, j+1) - y(i, j)}{\Delta t} & \frac{\partial^2 y}{\partial t^2} &= \frac{y(i, j+1) - 2y(i, j) + y(i, j-1)}{(\Delta t)^2} \end{aligned} \quad (5.1)$$

and

$$\begin{aligned} \frac{\partial u}{\partial x} &= \frac{u(i+1, j) - u(i, j)}{\Delta x} & \frac{\partial^2 u}{\partial x^2} &= \frac{u(i+1, j) - 2u(i, j) + u(i-1, j)}{(\Delta x)^2} \\ \frac{\partial u}{\partial t} &= \frac{u(i, j+1) - u(i, j)}{\Delta t} & \frac{\partial^2 u}{\partial t^2} &= \frac{u(i, j+1) - 2u(i, j) + u(i, j-1)}{(\Delta t)^2} \end{aligned} \quad (5.2)$$

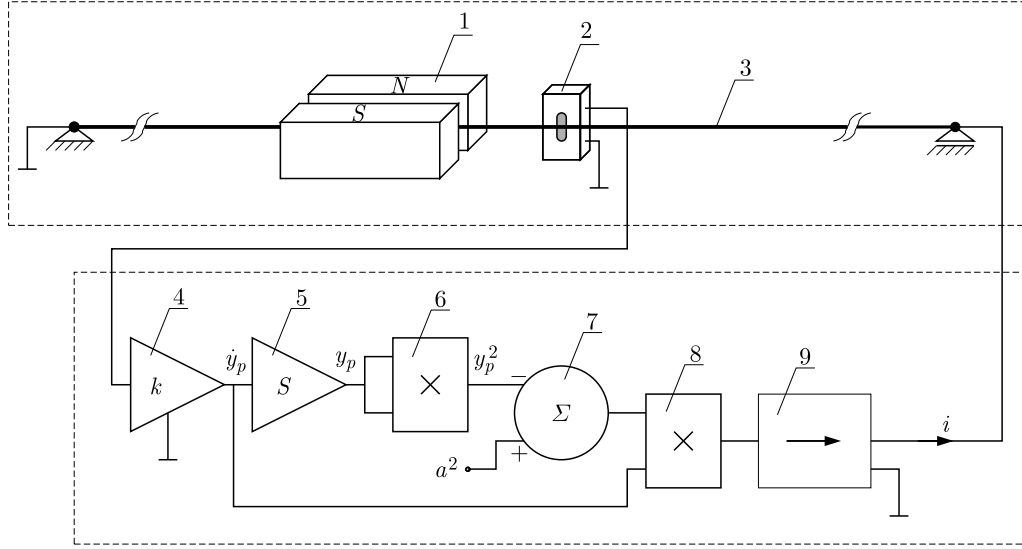


Fig. 5. Sketch of the control system of the wire gauge based on the van der Pol equation. 1 – fixed magnet, 2 – magneto-electric transducer, 3 – wire, 4 – voltage amplifier, 5 – integrating system, 6,8 – multiplying system, 7 – summing system, 9 – current amplifier

we obtain relationships for the transverse displacement $y(i, j + 1)$ and longitudinal displacement $u(i, j + 1)$ at points of the wire with reference to the displacement from the previous time moment, that is, $y(i, j)$, $u(i, j)$

$$\begin{aligned}
 y(i, j + 1) = & \left\{ \frac{q(i, j)}{\rho A} - \frac{1}{(\Delta t)^2} [y(i, j - 1) - 2y(i, j)] \right. \\
 & + \frac{u(i + 1, j) - u(i, j)}{(\Delta x)^3} \frac{E}{\rho} [y(i + 1, j) - 2y(i, j) + y(i - 1, j)] + \frac{b_y}{\rho A} \frac{1}{\Delta t y(i, j)} \left. \right\} \\
 & \cdot \left[\frac{1}{(\Delta t)^2} + \frac{b_y}{\rho A (\Delta t)} \right]^{-1}
 \end{aligned} \tag{5.3}$$

$$\begin{aligned}
 u(i, j + 1) = & \left\{ - \frac{1}{(\Delta t)^2} [u(i, j - 1) - 2u(i, j)] + \frac{E}{\rho} \frac{1}{(\Delta x)^2} [u(i + 1, j) - 2u(i, j) + u(i - 1, j)] \right. \\
 & \left. + \frac{b_x}{\rho A (\Delta t)} u(i, j) \right\} \left[\frac{1}{(\Delta t)^2} + \frac{b_x}{\rho A (\Delta t)} \right]^{-1}
 \end{aligned}$$

where

$$q(i, j) = \varepsilon [a^2 - y(i, j)^2] \frac{y(i, j + 1) - y(i, j)}{\Delta t} \tag{5.4}$$

describes the action of the van der Pol component.

For simulation purposes, the following parameters have been adopted:

$l = 0.15$ m	– length of the wire,
$D = 0.0002$ m	– diameter of the wire,
$\rho = 7800$ kg/m ³	– density of the wire,
$T_k = 14.115$ N	– tension at the end of the wire,
$\tau = 24.5E-05$ kg/m	– linear density of the wire,
$E = 220$ GPa	– Young's modulus,
$a = 0.0001$ m	– parameter of the van der Pol component.

Figure 6a presents the longitudinal displacement u of the point lying in the middle of the wire, when the changes in the load took place at the moments $t_1 = 0.009$ s with the value

$T_k = 14.12$ N at $T_k = 7.06$ N as well as $t_2 = 0.0175$ s with the value $T_k = 7.06$ N at $T_k = 28.23$ N. Figure 6b presents the respective changes of transverse vibration of the same point starting from the initial state representing the equilibrium position until the development of set vibrations. The vibration amplitude, in accordance with theoretical knowledge, obtains a value twice as high as the value of the parameter a , in other words, 0.2 mm. The vibration frequency of the first form in this section equals 800 Hz, and in the next two time sections it equals 562 Hz and 1135 Hz, respectively.

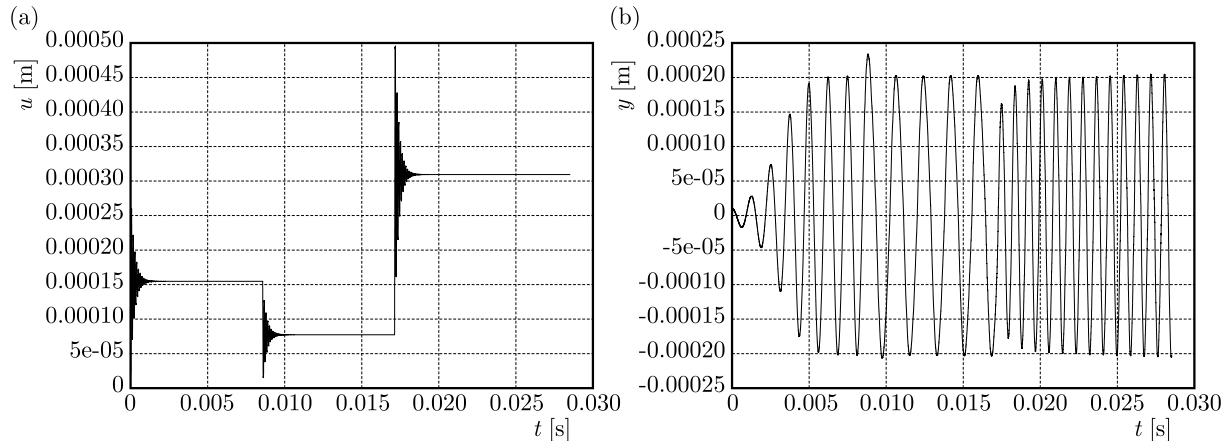


Fig. 6. (a) Course of the longitudinal displacement u at the point lying in the middle of the wire ($x = l/2$); (b) course of the transverse displacement of the point lying in the middle of the wire ($x = l/2$)

The frequency values differ from the values obtained based on the below given theoretical formula (5.5) for free wires by about 8 Hz (1%), which is reflected in the scientific literature

$$f_0 = \frac{1}{2l} \sqrt{\frac{T_k}{\tau}} \quad (5.5)$$

where f_0 is the natural vibration frequency of the wire.

As in the case of a discrete system, transfer between new work states takes place without causing turbulent transition states in the transverse direction, and the new frequencies are set almost immediately. There is a noticeable lack of any significant influence of the transition states appearing along the wire.

6. Modification of the van der Pol component

The regulator shaping the van der Pol force component requires the use of a displacement signal of the vibrating mass. From the magneto-electric transducer registering wire motion, we obtain, however, a signal proportional to velocity of the mass motion. Although transforming the velocity signal to a displacement signal is theoretically easy, in practice we encounter the problem of constant value, trend and filtering process leading to phase shift. There is, however, a simpler solution proposed by J. Michalczyk¹. Namely, instead of using the displacement signal in the van der Pol component, it is possible to use a vibration velocity signal provided directly by the magneto-electric transducer. Equation (2.2) then takes form of the following equation

$$m \frac{d^2 y}{dt^2} + b \frac{dy}{dt} + ky = \varepsilon \left[a^2 - \left(\frac{dy}{dt} \right)^2 \right] \frac{dy}{dt} \quad (6.1)$$

¹Faculty seminar. Faculty of Mechanics and Vibroacoustics AGH.

The solution to equation (6.1) for $a = 0.04$ is presented in Figs. 7a and 7b in form of time and phase portraits, respectively. As can be seen, the equation shows all the features of the equation describing self-oscillation, including the existence of a limit cycle on which trajectories of the phase solution have a direction field from the inside or the outside. And just as in the case of the initial equation, stepwise changes in the coefficient of elasticity k do not lead to undesired transition states in the solution of the equation. This fact becomes a basis for removal of integrating system “5” from the scheme presented in Fig. 5.

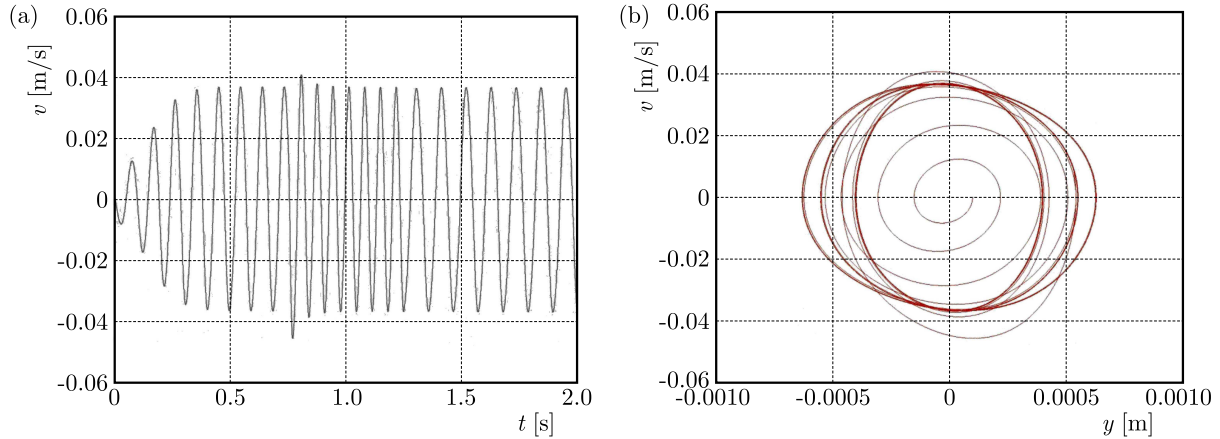


Fig. 7. Courses of the solution to equation (6.1) for three stepwise variables of the parameter k : (a) time form, (b) phase portrait

7. Construction of the test stand

Based on the scheme in Fig. 5, a physical model of the system has been constructed. It consists of a mechanical part, including the wire system together with transducers, as well as an electrical part which performs the task of maintaining self-excited wire vibrations.

The electrical part is presented in Fig. 8. The signal from the magneto-electric transducer after initial amplification in the U1 voltage amplifier (Fig. 8b) is conducted to the pins of two integrated systems, U2 and U3 (Fig. 8a). These are AD633JN/A summing-multiplying systems, using which the feedback loop signal is obtained. System U2 formulates the signal $a^2 - (dy/dt)^2$ in which the value of the parameter a is set with the help of potentiometer Pt1. In turn, system U3 formulates the signal of the sum of the output signals of system U2 (end 7) and the signal of vibration velocity dy/dt – input 3 of U3 system. Such an obtained signal is then amplified with an current amplifier. In the photograph presented in Fig. 9, the elements of the mechanical part of the system are shown. A uniform guitar string fastened between two pegs (Fig. 9a) is used as a wire. The pegs are mounted through the bars to a steel base, which simultaneously performs function of the deformed element. In the central part of the wire, two flat neodymium magnets (Fig. 9c), separated from each other with isolation pads, are mounted. The pads have the task of setting the suitable depth of the air passage, which should ensure free vibration of the wire and guarantee interaction between the magnets and the wire at a level sufficient to develop vibration at the measurement amplitude. A guitar magneto-electric transducer is located in the neighbourhood of the magnets at a distance ensuring the lack of significant interference of the magnetic field (Fig. 9b).

Such a workstation enables research to be carried out into wire vibration formed as a result of changes in its tension and interference of the Lorentz forces formulated in the non-linear van der Pol component designated for generation of self-oscillation.

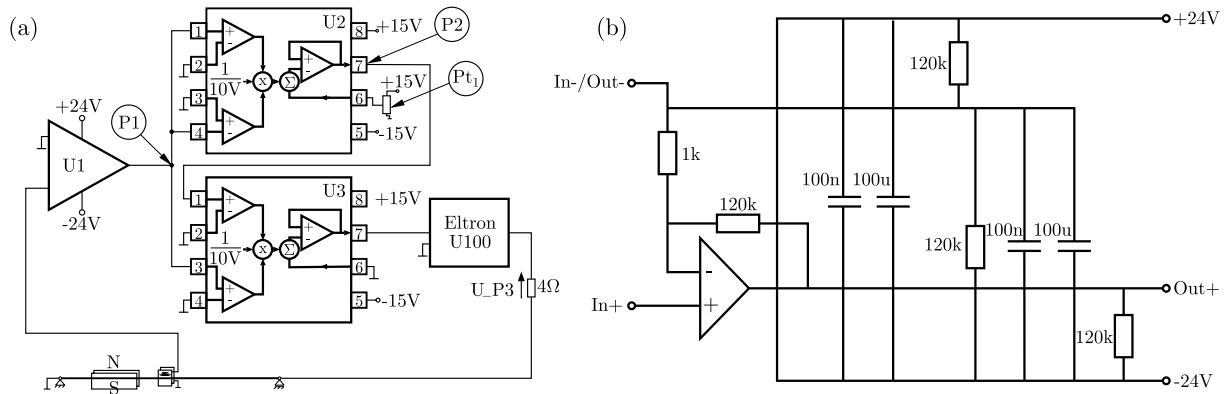


Fig. 8. (a) U2, U3: AD633JN/A multiplying systems, (b) input amplifier U1

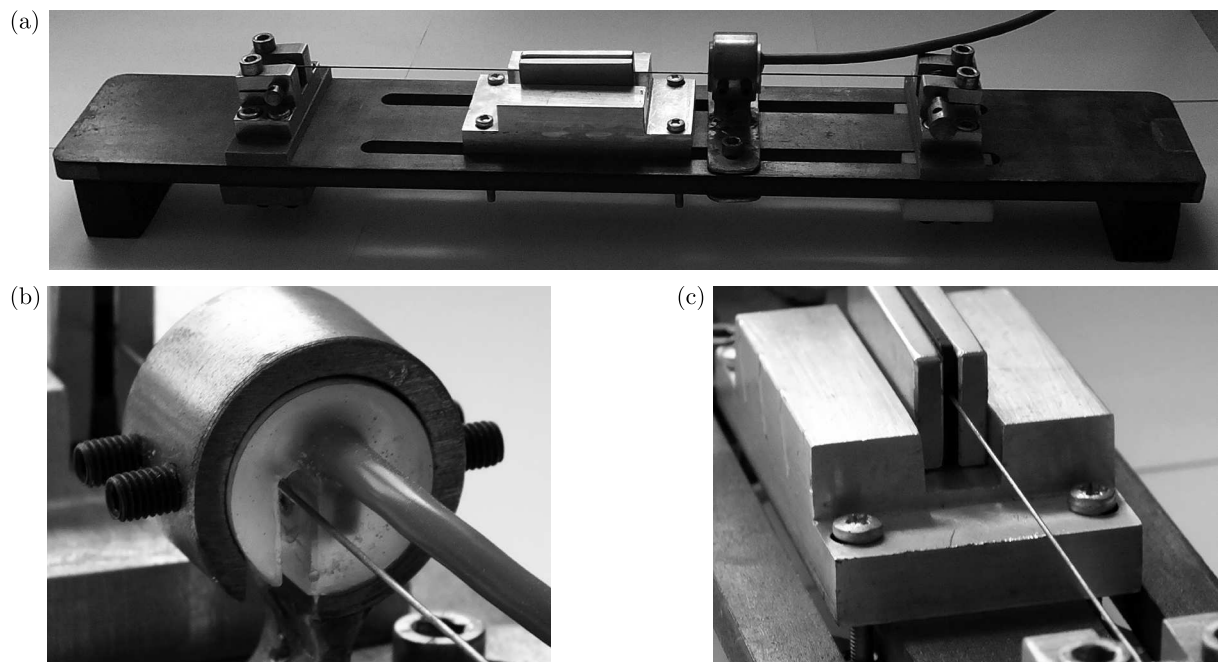


Fig. 9. Photographs of the wire transducer: (a) wire mounted to the deformed base, (b) magneto-electric transducer, (c) neodymium fixed magnets

8. Results of laboratory tests

Measurements have been carried out with a two-channel Hewlett Packard HP3560A recorder. This device allows recording of short signals, tens of milliseconds long, at a sampling frequency equalling 2.5 kHz. Therefore, in the measurements presented below, only set states have been captured (transient states on the base of observation did not develop noticeably). Figure 10a presents trajectories recorded at two points of the system, that is, the output of U1 input amplifier (course designated as P1) as well as the output of U2 multiplier system (course designated as P2). Figure 10b presents the course recorded at P1 as well as the course of voltage in the output resistor U_P3 of the current amplifier system. Both figures present vibration for an initially tensioned wire, which in the second case slightly changes the parameter a .

The courses presented in Fig. 11a refer to the case in which the wire is significantly tensioned. As in the previous cases, it presents courses of the output from the input amplifier and the multiplying system. The vibration frequency of the wire increased from 800 Hz to 2200 Hz.

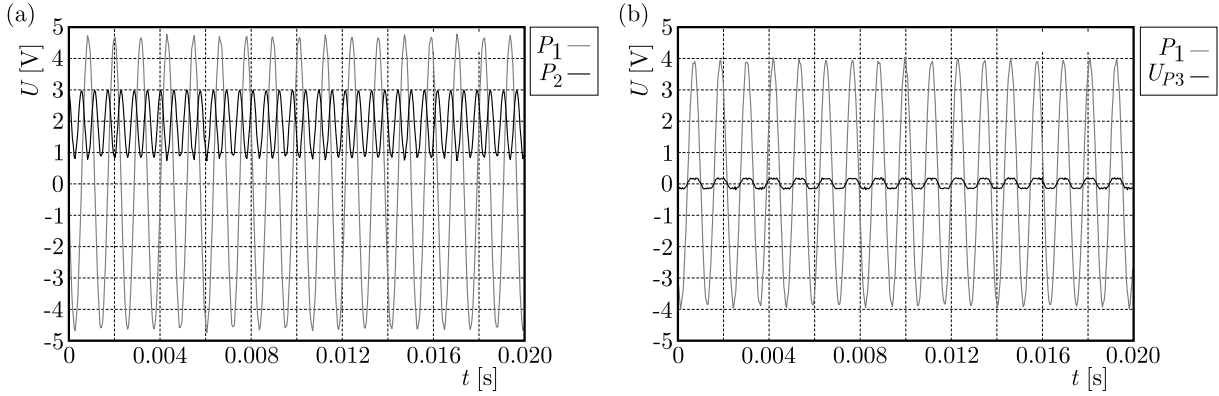


Fig. 10. Wire under initial load: (a) course of voltage signals at points P1 and P2 of the system presented in Fig. 8, (b) voltage in the output of U1 amplifier (P1) and in output resistor of the current amplifier (U_P3)

The final figure, Fig. 11b, presents the course after removing the load and after significantly reducing the value of the parameter a .

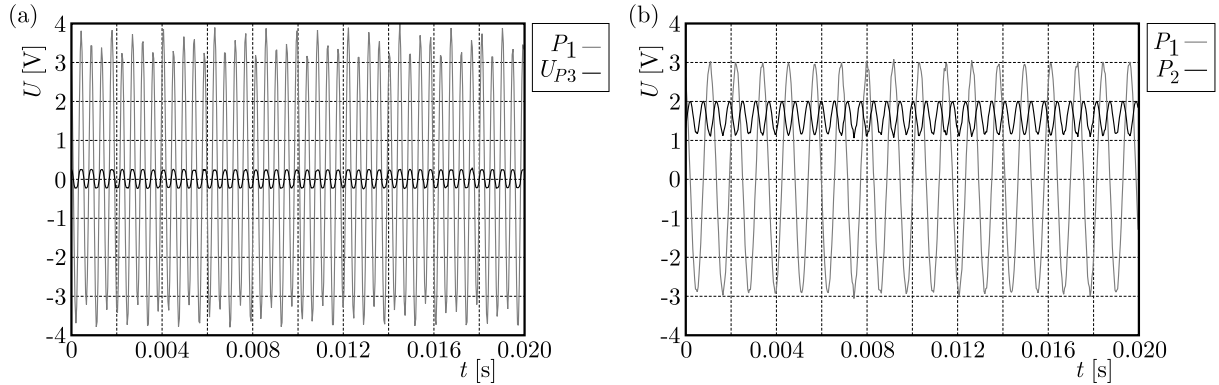


Fig. 11. (a) Wire under load: (a) voltage course in the output of U1 amplifier (P1) and in output resistor of the current amplifier (U_P3), (b) wire after removal of the load. Courses of voltage signals at points P1 and P2

While comparing the figures, it is possible to state that the task of maintaining non-decreasing self-oscillation in the wire, regardless of the wire tension, has been achieved, and the vibration velocity amplitude can be set by changing the value of one of the regulator parameters. Based on the observations of the wire behaviour under violent changes of the load, the formation of transition states which would lead to motion of the wire with chaotic vibrations and the loss of measurement ability, has not been observed.

9. Summary

The aim of the presented research is to show the possibility of using self-oscillation to maintain non-decreasing natural vibrations in a wire resistant to violent changes in the tension.

On the basis of the presented results, it can be stated that this idea has been confirmed in simulation tests and then in real conditions on the laboratory stand. Self-oscillation does not show a clear tendency to develop turbulent transition states during violent changes in the load. In fact, the opposite case has been observed, the transition from one load state to the second one took place very smoothly, without the loss of any period.

The presented solution may be used to construct wire sensors with special purposes, resistant to impact or fast-changing loads. The construction of the system significantly differs from the one universally used in measurement techniques with single-coil wire sensors, in which the coil itself performs function of both input sensor tracing motion of the wire and vibration exciter. This solution is more expensive and energy-consuming. However, as opposed to conventional solutions, it does not bring the risk of losing synchronization between the system stimulating and recording the vibrations.

Acknowledgements

The study described in this paper has been executed within the project No. 11.11.130.955

References

1. ATAY F.M., 1998, Van der Pol's oscillator under delayed feedback, *Journal of Sound and Vibration*, **218**, 2, 333-339
2. BARR P.J., PETROFF S.M., HODSON D.J., THURGOOD T.P., HALLING M.W., 2012, Baseline testing and long-term monitoring of the Lambert Road Bridge for the long-term bridge performance program, *Journal of Civil Structural Health Monitoring*, **2**, 2
3. BENMOKRANE B., CHEKIRED M., XU, H., 1995, Monitoring behavior of grouted anchors using vibrating-wire gauges, *Journal of Geotechnical Engineering*, **121**, 6, 466-475
4. BORDES J.-L., 2011, Dams and large scale experiments: monitoring and control. Documents pour l'histoire des techniques, no. 20, semestre 2011
5. DEN HARTOG J.P., 1956, *Mechanical Vibrations*, 4th Edition, McGraw-Hill Book Company, New York
6. DIBIAGIO E., 2003, A case study of vibrating-wire sensors that have vibrated continuously for 27 years, *6th International Symposium on Field Measurements in Geomechanics (FMGM)*, Oslo, Norway
7. GASTINEAU A., JOHNSON T., SCHULTZ A., 2009, *Bridge Health Monitoring and Inspections – A Survey of Methods* Department of Civil Engineering University of Minnesota. Final Report No. MN/RC 2009-29
8. HAYES J., SIMMONDS T., 2002, Interpreting strain measurements from load tests in bored piles, *Ninth International Conference On Piling And Deep Foundations*, Nice, 663-669
9. NEILD S.A., WILLIAMS M.S., MCFADDEN P.D., 2005, Development of a vibrating wire strain gauge for measuring small strains in concrete beams, *Strain*, **41**, 1, 3-9
10. PARK H.S., LEE H.Y., CHOI S.W., KIM Y., 2013, A practical monitoring system for the structural safety of mega-trusses using wireless vibrating wire strain gauges, *Multidisciplinary Digital Publishing Institute, Sensors*, ISSN:1424-8220
11. QING N.Y., YONG X., YANG L.W., PENG Z., 2008, Development of a structural health monitoring system for guangzhou new TV tower, *Advances in Science and Technology*, **56**, 414-419
12. SHARMA V.M., NAIR M.D., MELLER S., 1999, The use of vibrating wire strain gauges in geotechnics, *International Conference on Offshore and Nearshore Geotechnical Engineering, GEOShore*
13. SIMONETTI A., 2012, *A Measurement Technique for the Vibrating Wire Sensors*, NORCHIP, Copenhagen, Denmark
14. WENZEL H., 2009, *Health Monitoring of Bridges*, John Wiley & Sons, Ltd.

BENDING AND BUCKLING OF A METAL SEVEN-LAYER BEAM WITH A LENGTHWISE CORRUGATED MAIN CORE – COMPARATIVE ANALYSIS WITH THE SANDWICH BEAM

EWA MAGNUCKA-BLANDZI

Poznan University of Technology, Institute of Mathematics, Poznań, Poland
e-mail: ewa.magnucka-blandzi@put.poznan.pl

MARCIN RODAK

Poznan University of Technology, Institute of Applied Mechanics, Poznań, Poland
e-mail: marcin.rodak@put.poznan.pl

The subject of analytical investigations is a metal seven-layer beam, a plate band with a lengthwise trapezoidal corrugated main core and two crosswise trapezoidal corrugated cores of faces. The hypothesis of deformation of normal to the middle surface of the beam after bending is formulated. Equations of equilibrium are derived based on the theorem of minimum total potential energy. The equations are analytically solved. Three point bending and buckling for axially compression of the simply supported beam are theoretically studied. The deflection and the critical axial force are determined for different values of the trapezoidal corrugation pitch of the main core. Moreover, an adequate model of the sandwich beam with steel foam core is formulated. The deflection and the critical axial force are determined for this sandwich beam. The results studied of the seven layer beam and the adequate sandwich beam are compared and presented in tables and figures.

Keywords: layered plate-band, trapezoidal corrugated cores, deflection, critical load

1. Introduction

The primary scientific description referring to the analysis and design of sandwich structures is the monograph by Allen (1969). A review of problems related to modelling and calculations of sandwich structures was presented by Noor *et al.* (1996), Vinson (2001) and Carrera and Brischetto (2009). A developed and analytical model of corrugated composite cores was described by Kazemahvazi and Zenkert (2009). The quasi-isotropic bending response of sandwich plates with bi-directionally corrugated cores was presented by Seong *et al.* (2010). The mathematical modelling of a rectangular sandwich plate under in plane compression is described by Magnucka-Blandzi (2011). The theoretical study of transverse shear modulus of elasticity for thin-walled corrugated cores of sandwich beams was presented by Magnucka-Blandzi and Magnucki (2014) and Lewinski *et al.* (2015). The problem of an equivalent plate model for corrugated-core sandwich panels was presented by Cheon and Kim (2015).

The subject of the paper is the metal seven-layer beam – a plate band. The beam is composed of a lengthwise trapezoidal corrugated main core, two inner flat sheets, two crosswise trapezoidal corrugated cores of the faces and two outer flat sheets.

2. Theoretical model of the seven-layer beam with the lengthwise corrugated main core

The seven-layer simply supported beam of length L , width b , thicknesses of the main core t_{c1} , facing cores t_{c2} and flat sheets t_s is shown in Fig. 1.

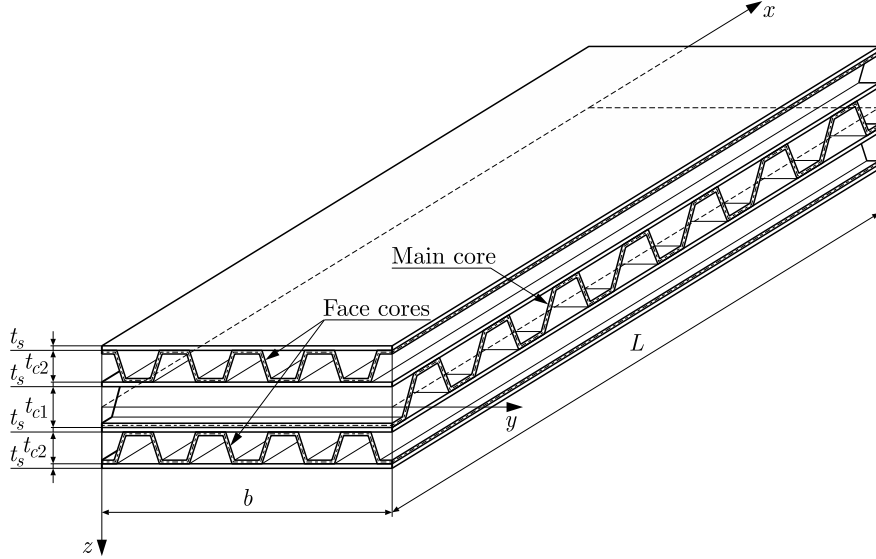


Fig. 1. Scheme of the seven-layer beam with the lengthwise corrugated main core

The directions of corrugations of the main core and the face cores are orthogonal. Trapezoidal corrugations of the main core and facing cores are shown in Fig. 2. The index $i = 1$ refers to the main core, while the index $i = 2$ refers to the face cores. Total depth of the cores is t_{ci} and length of one pitch of the corrugation is b_{0i} .

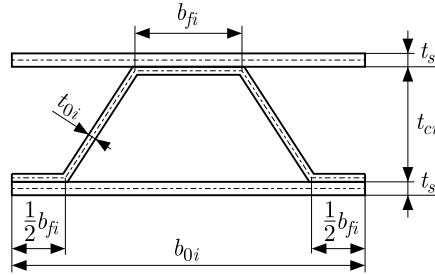


Fig. 2. Scheme of trapezoidal corrugations of the main core ($i = 1$) or face cores ($i = 2$)

Taking into account the layered structures of the beam, the hypothesis of the broken line (Fig. 3) is assumed. The plane cross-section before bending does not remain plane and normal after bending. The hypothesis for multi-layer structures was described in details by Carrera (2003), Magnucka-Blandzi (2012) and Magnucki *et al.* (2016).

The displacements with consideration of this hypothesis are as follows:

— the upper sandwich facing for $-(0.5 + 2x_1 + x_2) \leq \zeta \leq -0.5$

$$u(x, y, z) = -t_{c1} \left[\zeta \frac{dw}{dx} + \psi(x) \right] \quad (2.1)$$

— the main corrugated core for $-0.5 \leq \zeta \leq 0.5$

$$u(x, z) = -t_{c1} \zeta \left[\frac{dw}{dx} - 2\psi(x) \right] \quad (2.2)$$

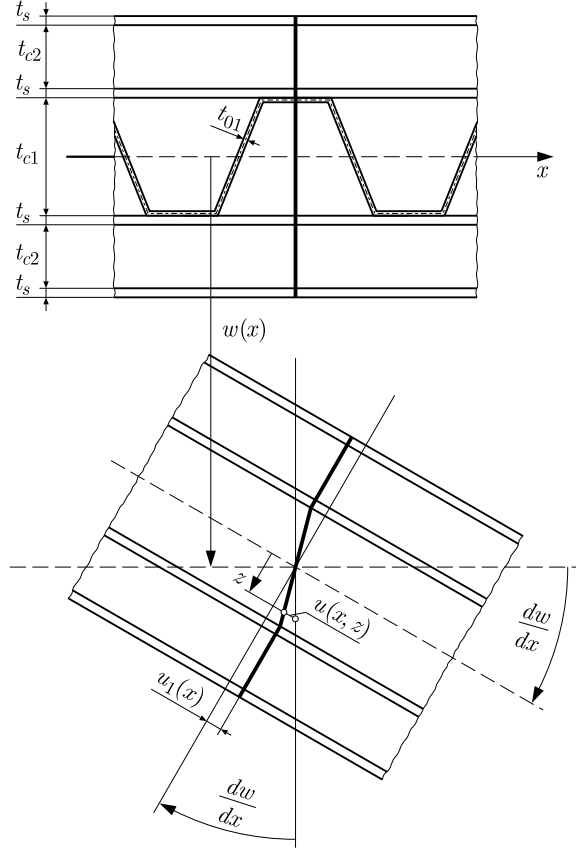


Fig. 3. Scheme of the hypothesis of the seven-layer beam

— the lower sandwich facing for $0.5 \leq \zeta \leq 0.5 + 2x_1 + x_2$

$$u(x, y, z) = -t_{c1} \left[\zeta \frac{dw}{dx} - \psi(x) \right] \quad (2.3)$$

where $x_1 = t_s/t_{c1}$, $x_2 = t_{c2}/t_{c1}$ are dimensionless parameters, $\zeta = z/t_{c1}$ – dimensionless coordinate, $\psi(x) = u_1(x)/t_{c1}$ – dimensionless functions of displacements, $u_1(x)$ – displacement in the x direction and $w(x)$ – deflection (Fig. 3).

Thus, linear relations for the strains are as follows:

— the main corrugated core

$$\varepsilon_x = -t_{c1} \zeta \left(\frac{d^2 w}{dx^2} - 2 \frac{d\psi}{dx} \right) \quad \gamma_{xz} = 2\psi(x) \quad (2.4)$$

— the upper/lower sandwich facings

$$\varepsilon_x = -t_{c1} \left(\zeta \frac{d^2 w}{dx^2} \pm \frac{d\psi}{dx} \right) \quad \gamma_{xz} = 0 \quad (2.5)$$

The sign “+” refers to the upper facing (u), and the sign “–” refers to the lower facing (l).

Strains (2.4) and (2.5) and Hook’s law make a basis for the formulation of elastic strain energy of the seven-layer beam.

3. The equations of equilibrium of the seven-layer beam

The elastic strain energy of the beam is a sum of the energy of particular layers

$$U_\varepsilon^{(beam)} = U_\varepsilon^{(c-1)} + U_\varepsilon^{(s-i)} + U_\varepsilon^{(c-2)} + U_\varepsilon^{(s-o)} \quad (3.1)$$

The addends are as follows:

➤ energy of the main corrugated core

$$U_{\varepsilon}^{(c-1)} = \frac{1}{2} E_s b t_{c1} \int_0^L \int_{-\frac{1}{2}}^{\frac{1}{2}} [\tilde{E}_x^{(c-1)} \varepsilon_x^2 + \tilde{G}_{xz}^{(c-1)} \gamma_{xz}^2] d\zeta dx \quad (3.2)$$

where E_s is Young's modulus, dimensionless longitudinal elastic modulus of the main corrugated core is calculated based on the monograph of Ventsel and Krauthammer (2001)

$$\tilde{E}_x^{(c-1)} = \frac{x_{b1}}{2(x_{f1} x_{b1} + \tilde{s}_{a1})} x_{01}^3 \quad (3.3)$$

dimensionless shear elastic modulus of the main trapezoidal corrugated core based on the paper of Lewinski *et al.* (2015)

$$\tilde{G}_{xz}^{(c-1)} = \frac{1 - x_{01}}{4(1 - \nu^2) x_{b1} f_u} \left(\frac{x_{01}}{\tilde{s}_{a1}} \right)^3 \quad (3.4)$$

and dimensionless parameters

$$\begin{aligned} x_{01} &= \frac{t_{01}}{t_{c1}} & x_{f1} &= \frac{b_{f1}}{b_{01}} & x_{b1} &= \frac{b_{01}}{t_{c1}} \\ \tilde{s}_{a1} &= \sqrt{(1 - x_{01})^2 + x_{b1}^2 \left(\frac{1}{2} - x_{f1} \right)^2} \end{aligned} \quad (3.5)$$

Substituting expressions (2.4) for strains into expression (3.2) and after integration, the elastic energy of the main corrugated core is obtained in the following form

$$U_{\varepsilon}^{(c-1)} = E_s b t_{c1}^3 \int_0^L \left\{ \frac{1}{24} \tilde{E}_x^{(c-1)} \left[\left(\frac{d^2 w}{dx^2} \right)^2 - 4 \frac{d^2 w}{dx^2} \frac{d\psi}{dx} + 4 \left(\frac{d\psi}{dx} \right)^2 \right] + 2 \tilde{G}_{xz}^{(c-1)} \left(\frac{\psi(x)}{t_{c1}} \right)^2 \right\} dx \quad (3.6)$$

➤ energy of the inner sheets

$$U_{\varepsilon}^{(s-i)} = \frac{1}{2} E_s b t_{c1} \int_0^L \left\{ \int_{-\left(\frac{1}{2}+x_1\right)}^{-\frac{1}{2}} \varepsilon_{x,up}^2 d\zeta + \int_{\frac{1}{2}}^{\frac{1}{2}+x_1} \varepsilon_{x,low}^2 d\zeta \right\} dx \quad (3.7)$$

Substitution of expressions (2.5) for the strains with regard to the upper/lower facings and after integration provides

$$U_{\varepsilon}^{(s-i)} = E_s b t_{c1}^3 \int_0^L \left[\frac{1}{12} x_1 (3 + 6x_1 + 4x_1^2) \left(\frac{d^2 w}{dx^2} \right)^2 - x_1 (1 + x_1) \frac{d^2 w}{dx^2} \frac{d\psi}{dx} + x_1 \left(\frac{d\psi}{dx} \right)^2 \right] dx \quad (3.8)$$

➤ energy of the corrugated cores of the facings

$$U_{\varepsilon}^{(c-2)} = \frac{1}{2} E_s \frac{b}{b_{02}} \int_0^L \left[\int_{A_{TR}^{(c-2)}} \varepsilon_{x,up}^2 dA_{TR}^{(c-2)} + \int_{A_{TR}^{(c-2)}} \varepsilon_{x,low}^2 dA_{TR}^{(c-2)} \right] \quad (3.9)$$

where the area of the trapezoid

$$A_{TR}^{(c-2)} = 2t_{c2}^2 x_{02} (x_{f2} x_{b2} + \tilde{s}_{a2}) \quad (3.10)$$

and dimensionless parameters

$$\begin{aligned} x_{02} &= \frac{t_{02}}{t_{c2}} & x_{f2} &= \frac{b_{f2}}{b_{02}} & x_{b2} &= \frac{b_{02}}{t_{c2}} \\ \tilde{s}_{a2} &= \sqrt{(1 - x_{02})^2 + x_{b2}^2 \left(\frac{1}{2} - x_{f2}\right)^2} \end{aligned} \quad (3.11)$$

Substituting expressions (2.5) for strains into expression (3.9) and after integration, the elastic energy of the corrugated cores of facings is obtained in the following form

$$U_{\varepsilon}^{(c-2)} = E_s b t_{c1}^3 \frac{x_2 x_{02}}{x_{b2}} \int_0^L \left[C_{ww}^{(c-2)} \left(\frac{d^2 w}{dx^2} \right)^2 - C_{w\psi}^{(c-2)} \frac{d^2 w}{dx^2} \frac{d\psi}{dx} + C_{\psi\psi}^{(c-2)} \left(\frac{d\psi}{dx} \right)^2 \right] dx \quad (3.12)$$

where dimensionless parameters are as follows

$$\begin{aligned} C_{ww}^{(c-2)} &= \frac{1}{2} \left[\frac{1}{3} x_2^2 (1 - x_{02})^2 (3x_{f2} x_{b2} + \tilde{s}_{a2}) + (1 + 2x_1 + x_2)^2 (x_{f2} x_{b2} + \tilde{s}_{a2}) \right] \\ C_{w\psi}^{(c-2)} &= 2(1 + 2x_1 + x_2) (x_{f2} x_{b2} + \tilde{s}_{a2}) & C_{\psi\psi}^{(c-2)} &= 2(x_{f2} x_{b2} + \tilde{s}_{a2}) \end{aligned}$$

➤ energy of the outer sheets

$$U_{\varepsilon}^{(s-o)} = \frac{1}{2} E_s b t_{c1} \int_0^L \left\{ \begin{array}{cc} -\left(\frac{1}{2} + x_1 + x_2\right) & \frac{1}{2} + 2x_1 + x_2 \\ \int \varepsilon_{x,up}^2 d\zeta & + \int \varepsilon_{x,low}^2 d\zeta \\ 0 & \frac{1}{2} + x_1 + x_2 \end{array} \right\} dx \quad (3.13)$$

Substitution of expressions (2.5) for the strains with regard to the upper/lower facings and after integration gives

$$U_{\varepsilon}^{(s-o)} = E_s b t_{c1}^3 \int_0^L \left[C_{ww}^{(s-o)} \left(\frac{d^2 w}{dx^2} \right)^2 - x_1 (1 + 3x_1 + 2x_2) \frac{d^2 w}{dx^2} \frac{d\psi}{dx} + x_1 \left(\frac{d\psi}{dx} \right)^2 \right] dx \quad (3.14)$$

where the dimensionless parameter $C_{ww}^{(s-o)} = (1/12)x_1[28x_1^2 + 3(1 + 2x_2)(1 + 6x_1 + 2x_2)]$.

Therefore, the elastic strain energy of the inner and outer sheets is as follows

$$U_{\varepsilon}^{(s)} = U_{\varepsilon}^{(s-i)} + U_{\varepsilon}^{(s-o)} = E_s b t_{c1}^3 \int_0^L \left[C_{ww}^{(s)} \left(\frac{d^2 w}{dx^2} \right)^2 - C_{w\psi}^{(s)} \frac{d^2 w}{dx^2} \frac{d\psi}{dx} + 2x_1 \left(\frac{d\psi}{dx} \right)^2 \right] dx \quad (3.15)$$

where dimensionless parameters

$$C_{ww}^{(s)} = \frac{1}{6} x_1 [16x_1^2 + 6x_1(2 + 3x_2) + 3(1 + 2x_2 + 2x_2^2)] \quad C_{w\psi}^{(s)} = 2x_1(1 + 2x_1 + x_2)$$

Thus, the elastic strain energy of the seven-layer beam (6) is in the following form

$$\begin{aligned} U_{\varepsilon}^{(beam)} &= E_s b t_{c1}^3 \int_0^L \left[\frac{1}{2} C_{ww} \left(\frac{d^2 w}{dx^2} \right)^2 - C_{w\psi} \frac{d^2 w}{dx^2} \frac{d\psi}{dx} + \frac{1}{2} C_{\psi\psi} \left(\frac{d\psi}{dx} \right)^2 \right. \\ &\quad \left. + 2\tilde{G}_{xz}^{(c-1)} \left(\frac{\psi(x)}{t_{c1}} \right)^2 \right] dx \end{aligned} \quad (3.16)$$

where dimensionless parameters

$$\begin{aligned} C_{ww} &= \frac{1}{12} \tilde{E}_x^{(c-1)} + 2 \frac{x_2 x_{02}}{x_{b2}} C_{ww}^{(c-2)} + 2C_{ww}^{(s)} & C_{w\psi} &= \frac{1}{6} \tilde{E}_x^{(c-1)} + \frac{x_2 x_{02}}{x_{b2}} C_{w\psi}^{(c-2)} + C_{w\psi}^{(s)} \\ C_{w\psi} &= \frac{1}{3} \tilde{E}_x^{(c-1)} + 2 \frac{x_2 x_{02}}{x_{b2}} C_{w\psi}^{(c-2)} + 2C_{w\psi}^{(s)} \end{aligned}$$

The work of the load

$$W = \int_0^L \left[qw(x) + \frac{1}{2} F_0 \left(\frac{dw}{dx} \right)^2 \right] dx \quad (3.17)$$

where q is the intensity of the transverse load, F_0 – axial compressive force of the beam.

The system of the equations of equilibrium – two ordinary differential equations derived based on the theorem of minimum potential energy $\delta(U_\varepsilon^{(beam)} - W) = 0$, is in the following form

$$\begin{aligned} C_{ww} \frac{d^4 w}{dx^4} - C_{w\psi} \frac{d^3 \psi}{dx^3} &= \frac{1}{E_s b t_{c1}^3} \left(q - F_0 \frac{d^2 w}{dx^2} \right) \\ C_{w\psi} \frac{d^3 w}{dx^3} - C_{\psi\psi} \frac{d^2 \psi}{dx^2} + 4 \tilde{G}_{xz}^{(c-1)} \frac{\psi(x)}{t_{c1}^2} &= 0 \end{aligned} \quad (3.18)$$

The bending moment of the seven-layer beam

$$M_b(x) = \int_A z \sigma_x dA = -E_s b t_{c1}^3 \left(C_{ww} \frac{d^2 w}{dx^2} - C_{w\psi} \frac{d\psi}{dx} \right) \quad (3.19)$$

Integration is analogical as in the case of the elastic strain energy, from which the following equation is obtained

$$C_{ww} \frac{d^2 w}{dx^2} - C_{w\psi} \frac{d\psi}{dx} = -\frac{M_b(x)}{E_s b t_{c1}^3} \quad (3.20)$$

Equations (3.18)₁ and (3.20) are equivalent, therefore, bending and buckling analysis of the seven-layer beam is based on the system of two differential equations (3.18)₂ and (3.20).

4. Deflection of the seven-layer beam under three-point bending

Three-point bending of the seven-layer beam of length L is shown in Fig. 4.

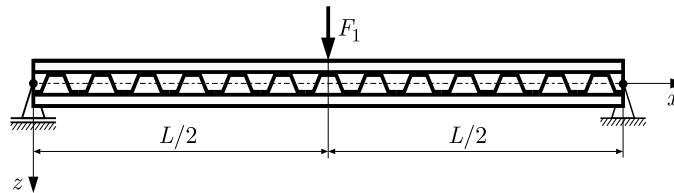


Fig. 4. Scheme of the three-point bending of the beam

The system of two differential equations (3.18)₂ and (3.20) is reduced to one differential equation in the following form

$$\frac{d^2 \psi}{dx^2} - \left(\frac{k}{t_{c1}} \right)^2 \psi(x) = -C_q \frac{Q(x)}{E_s b t_{c1}^3} \quad (4.1)$$

where $Q(x) = dM_b/dx$ is the shear force, k, C_q – dimensionless parameters

$$k = 2\sqrt{\frac{C_{ww}\tilde{G}_{xz}^{(c-1)}}{C_{ww}C_{\psi\psi} - C_{w\psi}^2}} \quad C_q = \frac{C_{w\psi}}{C_{ww}C_{\psi\psi} - C_{w\psi}^2}$$

The general solution to equation (4.1) is in the form

$$\psi(x) = C_1 \sinh\left(k\frac{x}{t_{c1}}\right) + C_2 \cosh\left(k\frac{x}{t_{c1}}\right) + \psi_p(x) \quad (4.2)$$

where C_1, C_2 are integration constants, $\psi_p(x)$ – particular solution.

The shear force in the half beam (Fig. 4) is $Q(x) = F_1/2$, for $0 \leq x \leq L/2$, then the particular solution

$$\psi_p = \frac{C_{w\psi}}{8C_{ww}\tilde{G}_{xz}^{(c-1)}} \frac{F_1}{E_s b t_{c1}^3} \quad (4.3)$$

Taking into account the boundary conditions for the half beam $(d\psi/dx)|_{x=0} = 0$ and $\psi(L/2) = 0$, the integration constants $C_1 = 0$ and $C_2 = -\cosh^{-1}[kL/(2t_{c1})]\psi_0$ are determined, hence, the function of displacement (4.3) is in the following form

$$\psi(x) = \left(1 - \frac{\cosh\frac{kx}{t_{c1}}}{\cosh\frac{kL}{2t_{c1}}}\right)\psi_p \quad (4.4)$$

Substituting this function, and the bending moment $M_b(x) = F_1x/2$, for $0 \leq x \leq L/2$ to equation (3.20), one obtains

$$w(x) = C_4 + C_3x + \frac{C_{w\psi}}{C_{ww}} \left(x - \frac{t_{c1}}{k} \frac{\sinh\frac{kx}{t_{c1}}}{\cosh\frac{kL}{2t_{c1}}}\right)\psi_p - \frac{F_1}{12C_{ww}E_s b t_{c1}^3} x^3 \quad (4.5)$$

Taking into account the boundary conditions for the half beam $w(0) = 0$ and $(dw/dx)|_{x=L/2} = 0$, the integration constants $C_3 = F_1L^2/(16C_{ww}E_s b t_{c1}^3)$ and $C_4 = 0$ are determined. The maximum deflection – the deflection for the middle of the beam is

$$w_{max}^{(7-layer)} = w\left(\frac{L}{2}\right) = \left[1 + 3\left(1 - \frac{2t_{c1}}{kL} \tanh\frac{kL}{2t_{c1}}\right) \frac{C_{w\psi}^2}{C_{ww}\tilde{G}_{xz}^{(c-1)}} \left(\frac{t_{c1}}{L}\right)^2\right] \frac{F_1}{48C_{ww}E_s b} \left(\frac{L}{t_{c1}}\right)^3 \quad (4.6)$$

5. Critical load of the seven-layer beam subjected to axial compression

The axial compression of the simply supported seven-layer beam is shown in Fig. 5.

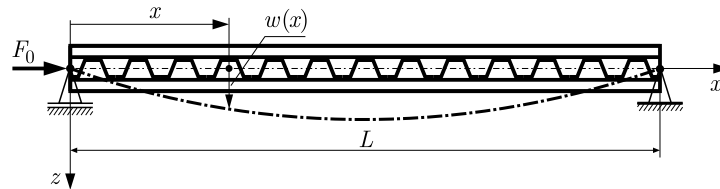


Fig. 5. Scheme of the simply supported seven-layer beam with the axial force F_0

The system of two differential equations (3.18)₂ and (3.20) is reduced to one differential equation in the following form

$$(C_{ww}C_{\psi\psi} - C_{w\psi}^2) \frac{d^4w}{dx^4} - \frac{4}{t_{c1}^2} \tilde{G}_{xz}^{(c-1)} C_{ww} \frac{d^2w}{dx^2} = \left[\frac{4}{t_{c1}^2} \tilde{G}_{xz}^{(c-1)} M_b(x) - C_{\psi\psi} \frac{d^2M_b}{dx^2} \right] \frac{1}{E_s b t_{c1}^3} \quad (5.1)$$

where the bending moment $M_b(x) = F_0w(x)$ (Fig. 5).

Differential equation (5.1) with one unknown function $w(x)$ is approximately solved assuming this function in the form

$$w(x) = w_a \sin \frac{\pi x}{L} \quad (5.2)$$

where w_a is the parameter of the function, L – length of the beam.

Substituting this function into the equation (5.1) the critical force is obtained

$$F_{0,CR}^{(7\text{-lay})} = \left(C_{ww} - \frac{C_{w\psi}^2}{\alpha_1} \right) \frac{\pi^2 E_s b t_{c1}^3}{L^2} \quad (5.3)$$

where

$$\alpha_1 = C_{\psi\psi} + \left(\frac{2L}{\pi t_{c1}} \right)^2 \tilde{G}_{xz}^{(c-1)}$$

6. Equivalent sandwich beam

Comparative analysis is carried out for the classical sandwich beam (Fig. 6) equivalent to the seven-layer beam (Fig. 1). This classical sandwich beam consists of two steel faces of thickness $t_f = t_s$ and the steel foam core of thickness $t_c = t_{c1} + 2(t_s + t_{c2})$. Its sizes and mass are identical to the seven-layer beam.

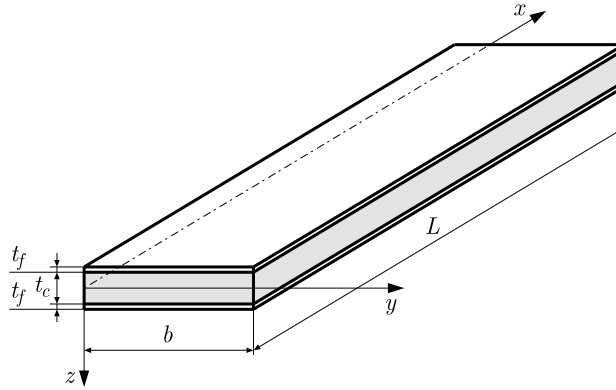


Fig. 6. Scheme of the sandwich (three-layer) beam equivalent to the seven-layer beam

The mass of the metal foam core of this sandwich beam (three-layer beam)

$$m_c^{(3\text{-lay})} = [1 + 2(x_1 + x_2)] t_{c1} b L \rho_c \quad (6.1)$$

where ρ_c is the mass density of the metal foam core.

However, mass of the material (steel with mass density ρ_s) located between the two outer sheets of the seven-layer beam (Fig. 1) is a sum of the mass of particular layers

$$m_c^{(7\text{-lay})} = m_c^{(c-1)} + 2m_c^{(s-i)} + 2m_c^{(c-2)} \quad (6.2)$$

where the mass of the main corrugated core

$$m_c^{(c-1)} = \frac{A_{TR}^{(c-1)}}{b_{01}} b L \rho_s \quad (6.3)$$

Substituting the expression for the area of the trapezoid $A_{TR}^{(c-1)} = 2t_{c1}^2 x_{01} (x_{f1} x_{b1} + \tilde{s}_{a1})$ to the above expression with consideration of the dimensionless parameters (3.5) one obtains

$$m_c^{(c-1)} = 2x_{01} \left(x_{f1} + \frac{\tilde{s}_{a1}}{x_{b1}} \right) t_{c1} b L \rho_s \quad (6.4)$$

and

$$m_c^{(s-i)} = t_s b L \rho_s = x_1 t_{c1} b L \rho_s \quad m_c^{(c-2)} = \frac{A_{TR}^{(c-2)}}{b_{02}} b L \rho_s \quad (6.5)$$

where $m_c^{(s-i)}$ is the mass of the inner sheets, $m_c^{(c-2)}$ – mass of the corrugated cores of the facings.

Substituting the expression for the area of trapezoid (3.10) with dimensionless parameters (3.11), one obtains

$$m_c^{(c-2)} = 2x_2 x_{02} \left(x_{f2} + \frac{\tilde{s}_{a2}}{x_{b2}} \right) t_{c1} b L \rho_s \quad (6.6)$$

Thus, mass (6.2) is in the following form

$$m_c^{(7-lay)} = 2 \left[x_{01} \left(x_{f1} + \frac{\tilde{s}_{a1}}{x_{b1}} \right) + x_1 + x_2 x_{02} \left(x_{f2} + \frac{\tilde{s}_{a2}}{x_{b2}} \right) \right] t_{c1} b L \rho_s \quad (6.7)$$

Then, from the equivalence condition $m_c^{(3-lay)} = m_c^{(7-lay)}$ (Eqs. (6.1) and (6.7)) of these two beams, the proportion of mass densities of the metal foam core to steel is obtained

$$\tilde{\rho}_c = \frac{\rho_c}{\rho_s} = \left[x_{01} \left(x_{f1} + \frac{\tilde{s}_{a1}}{x_{b1}} \right) + x_1 + x_2 x_{02} \left(x_{f2} + \frac{\tilde{s}_{a2}}{x_{b2}} \right) \right] \frac{2}{1 + 2(x_1 + x_2)} \quad (6.8)$$

Taking into account the experimental results related to the mechanical properties of metal foams presented in details by Ashby *et al.* (2000), Smith *et al.* (2012) and Szyniszewski *et al.* (2014), the relationship for Young's moduli and mass densities of the metal foams and the reference material (steel) is as follows

$$\tilde{E}_c = \frac{E_c}{E_s} = \frac{3}{4} \left(\frac{\rho_c}{\rho_s} \right)^2 \quad (6.9)$$

where E_c and E_s are Young's moduli of the metal foam and the steel.

7. Bending and buckling of the equivalent sandwich beam

The hypothesis of deformation of the plane cross-section after bending of the sandwich (three-layer) beam is assumed as the broken line (Fig. 7). The detailed description of this hypothesis and derivation of the equations of equilibrium for the sandwich beam was presented by Magnucka-Blandzi (2012).

The displacements with consideration of this hypothesis are as follows:

— the upper/lower facing for $-(0.5 + x_0) \leq \zeta \leq -0.5$ and $0.5 \leq \zeta \leq 0.5 + x_0$

$$u(x, z) = -t_c \left[\zeta \frac{dw}{dx} \pm \psi_0(x) \right] \quad (7.1)$$

— the metal foam core for $-0.5 \leq \zeta \leq 0.5$

$$u(x, z) = -t_c \zeta \left[\frac{dw}{dx} - 2\psi_0(x) \right] \quad (7.2)$$

where $x_0 = t_f/t_c$ is the dimensionless parameter, $\zeta = z/t_c$ – dimensionless coordinate, $\psi_0(x) = u_f(x)/t_c$ – dimensionless functions of displacements, $u_f(x)$ – displacement in the x direction and $w(x)$ – deflection (Fig. 7).

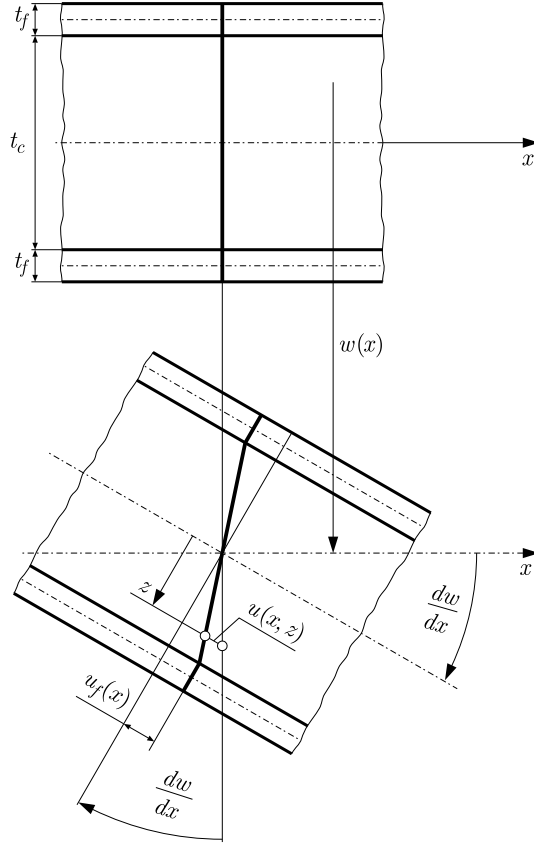


Fig. 7. Scheme of the hypothesis of the sandwich (three-layer) beam

Continuation of the procedure similar to the one applied to the seven-layer beam gives a system of two differential equations of equilibrium for the classical sandwich beam presented by Magnucka (2012) in the following form

$$B_{ww} \frac{d^2 w}{dx^2} - B_{w\psi} \frac{d\psi_0}{dx} = -\frac{M_b(x)}{E_s b t_c^3} \quad B_{w\psi} \frac{d^3 w}{dx^3} - B_{\psi\psi} \frac{d^2 \psi_0}{dx^2} + 4\tilde{G}_c \frac{\psi_0(x)}{t_c^2} = 0 \quad (7.3)$$

where dimensionless parameters

$$B_{ww} = 2C_{2f} + \frac{1}{12}\tilde{E}_c \quad B_{w\psi} = C_{1f} + \frac{1}{6}\tilde{E}_c \quad B_{\psi\psi} = 2x_0 + \frac{1}{3}\tilde{E}_c$$

$$C_{1f} = (1 + x_0)x_0 \quad C_{2f} = \frac{1}{12}(3 + 6x_0 + 4x_0^2)x_0$$

and moduli

$$\tilde{E}_c = \frac{E_c}{E_s} \quad \tilde{G}_c = \frac{\tilde{E}_c}{2(1 + \nu_c)}$$

This system of equations is analogical to the one of the seven-layer beam, (3.20) and (3.18)₂.

Then, the maximum deflection and the critical force of the sandwich equivalent beam are as follows

$$w_{max}^{(3-lay)} = w\left(\frac{L}{2}\right) = \left[1 + 3\left(1 - \frac{2t_c}{k_0 L} \tanh \frac{k_0 L}{2t_c}\right) \frac{B_{w\psi}^2}{B_{ww} \tilde{G}_c} \left(\frac{t_c}{L}\right)^2\right] \frac{F_1}{48B_{ww} E_s b} \left(\frac{L}{t_c}\right)^3 \quad (7.4)$$

and

$$F_{0,CR}^{(3-lay)} = \left(B_{ww} - \frac{B_{w\psi}^2}{\alpha_0}\right) \frac{\pi^2 E_s b t_c^3}{L^2} \quad (7.5)$$

where

$$\alpha_0 = B_{\psi\psi} + \left(\frac{2L}{\pi t_c}\right)^2 \widetilde{G}_c$$

8. Illustrative detailed analysis for selected beams

A detailed analysis for an exemplary steel seven-layer beam and the equivalent sandwich beam is carried out for the following test data: $L = 1620$ mm, $b = 240$ mm, $t_s = 0.8$ mm, $t_{c1} = 32.0$ mm, $t_{01} = 0.8$ mm, $b_{f1} = 10.0$ mm, $b_{01} = [32.4, 36.0, 40.5, 45.0]$ mm, $t_{c2} = 16.0$ mm, $t_{02} = 0.8$ mm, $b_{f2} = 8.0$ mm, $b_{02} = 40.0$ mm and material-steel constants $E_s = 2 \cdot 10^5$ MPa, $\nu = 0.3$, $\rho_s = 7850$ kgm⁻³. Moreover, $t_f = t_s = 0.8$ mm and $t_c = t_{c1} + 2(t_s + t_{c2}) = 65.6$ mm.

The values of maximum deflections (4.6) and critical forces (5.3) of the seven-layer beam are specified in Table 1. The values of maximum deflections (7.4) and critical forces (7.5) of the sandwich (three-layer) beam are specified in Table 2.

Table 1. Maximum deflections and critical forces of the seven-layer beam

	b_{01} [mm]			
	32.4	36.0	40.5	45.0
$w_{max}^{(7-layer)}$ [mm]	3.49	3.18	2.98	2.88
$F_{0,CR}^{(7-layer)}$ [kN]	490.1	535.8	568.5	587.3

Table 2. Maximum deflections and critical forces of the sandwich beam

	b_{01} [mm]			
	32.4	36.0	40.5	45.0
$\widetilde{\rho}_c$ Eq. (6.8)	0.0892374	0.0863605	0.0835631	0.0814007
\widetilde{E}_c Eq. (6.9)	0.005972	0.005594	0.005237	0.004970
$w_{max}^{(3-layer)}$ [mm]	5.13	5.16	5.21	5.24
$F_{0,CR}^{(3-layer)}$ [kN]	328.1	325.6	323.2	321.3

Moreover, the values of maximum deflections and critical forces of the seven-layer beam and the equivalent sandwich beam are presented in Figs. 8 and 9.

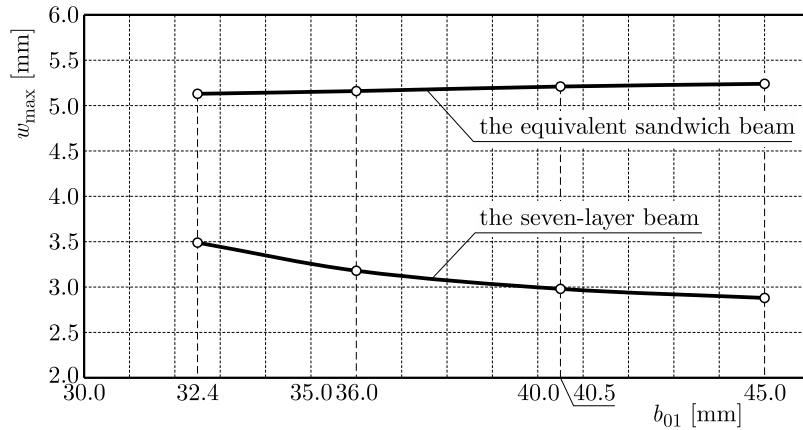


Fig. 8. Maximum deflections of the two beams

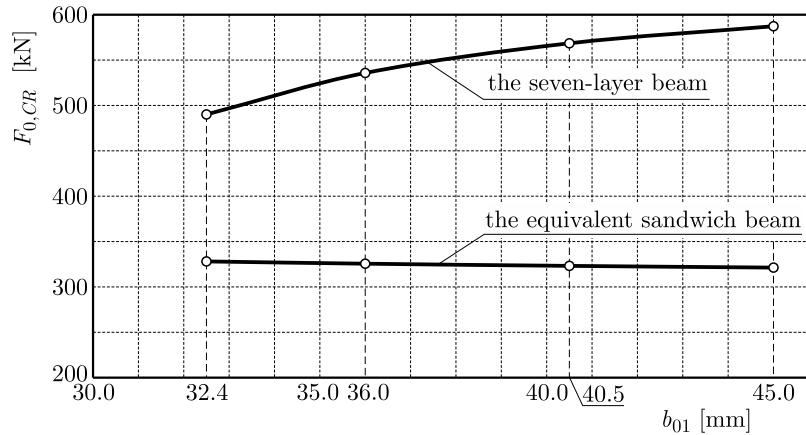


Fig. 9. Critical forces of the two beams

9. Conclusions

The analytical modelling of the seven-layer beam with a lengthwise trapezoidal corrugated main core and two crosswise trapezoidal corrugated cores of faces leads to the conclusions:

- hypotheses of the flat cross-sections deformations of these two beams as the broken line are analogous,
- equations of equilibrium of these two beams are similar,
- proportion of the maximum deflections of these two beams for the studied family of the beams is $w_{max}^{(3-layer)} / w_{max}^{(7-layer)} = 1.47-1.82$,
- proportion of the critical force of these two beams for the studied family of the beams is $F_{0,CR}^{(7-layer)} / F_{0,CR}^{(3-layer)} = 1.49-1.83$,
- stiffness of the seven-layer beam is decidedly greater than that of the equivalent classical sandwich (three-layer) beam.

Acknowledgements

The project was funded by the National Science Centre allocated on the basis of the decision number DEC-2013/09/B/ST8/00170.

References

1. ALLEN H.G., 1969, *Analysis and Design of Structural Sandwich Panels*, Pergamon Press, Oxford, London, Edinburgh, New York, Toronto, Sydney, Paris, Braunschweig
2. ASHBY M.F., EVANS A., FLECK N.A., GIBSON L.J., HUTCHINSON J.W., WADLEY H.N.G., 2000, *Metal Foams, A Design Guide*, Butterworth-Heinemann, An Imprint of Elsevier
3. CARRERA E., 2003, Historical review of Zig-Zag theories for multi-layered plates and shells, *Applied Mechanics Reviews*, **56**, 3, 287-308
4. CARRERA E., BRISCHETTO S., 2009, A survey with numerical assessment of classical and refined theories for the analysis of sandwich plates, *Applied Mechanics Reviews*, **62**, 1, 010803
5. CHEON Y.-J., KIM H.-G., 2015, An equivalent plate model for corrugated-core sandwich panels, *Journal of Mechanical Science and Technology*, **29**, 3, 1217-1223
6. KAZEMAHVAZI S., ZENKERT D., 2009, Corrugated all-composite sandwich structures. Part 1: Modeling, *Composite Science and Technology*, **69**, 7/8, 913-919

7. LEWINSKI J., MAGNUCKA-BLANDZI E., SZYC W., 2015, Determination of shear modulus of elasticity for thin-walled trapezoidal corrugated cores of seven-layer sandwich plates, *Engineering Transactions*, **63**, 4, 421-437
8. MAGNUCKA-BLANDZI E., 2011, Mathematical modelling of a rectangular sandwich plate with a metal foam core, *Journal of Theoretical and Applied Mechanics*, **49**, 2, 439-455
9. MAGNUCKA-BLANDZI E., 2012, Displacement models of sandwich structures (in Polish), [In:] *Strength and Stability Sandwich Beams and Plates with Aluminium Foam Cores*, K. Magnucki, W. Szyk (Eds.), Pub. House of Poznan University of Technology, Poznan, 109-120
10. MAGNUCKA-BLANDZI E., MAGNUCKI K., 2014, Transverse shear modulus of elasticity for thin-walled corrugated cores of sandwich beams, Theoretical study, *Journal of Theoretical and Applied Mechanics*, **52**, 4, 971-980
11. MAGNUCKA-BLANDZI E., MAGNUCKI K., WITTENBECK L., 2015, Mathematical modelling of shearing effect for sandwich beams with sinusoidal corrugated cores, *Applied Mathematical Modelling*, **39**, 2796-2808
12. MAGNUCKI K., MAGNUCKA-BLANDZI E., WITTENBECK L., 2016, Elastic bending and buckling of a steel composite beam with corrugated main core and sandwich faces – Theoretical study, *Applied Mathematical Modelling*, **40**, 1276-1286
13. NOOR A.K., BURTON W.S., BERT C.W., 1996, Computational models for sandwich panels and shells, *Applied Mechanics Reviews*, **49**, 3, 155-199
14. SEONG D.Y., JUNG C.G., YANG D.Y., MOON K.J., AHN D.G., 2010, Quasi-isotropic bending responses of metallic sandwich plates with bi-directionally corrugated cores, *Materials and Design*, **31**, 6, 2804-2812
15. SMITH B.H., SZYNISZEWSKI S., HAJJAR J.F., SCHAFER B.W., ARWADE S.R., 2012, Steel foam for structures: A review of applications, manufacturing and material properties, *Journal of Constructional Steel Research*, **71**, 1-10
16. SZYNISZEWSKI S., SMITH B.H., HAJJAR J.F., SCHAFER B.W., ARWADE S.R., 2014, The mechanical properties and modelling of a sintered hollow sphere steel foam, *Materials and Design*, **54**, 1083-1094
17. VENTSEL E., KRAUTHAMMER T., 2001, *Thin Plates and Shells, Theory, Analysis and Applications*, Marcel Dekker, New York, Basel
18. VINSON JR., 2001, Sandwich structures, *Applied Mechanics Reviews*, **54**, 3, 201-214

Manuscript received February 11, 2016; accepted for print May 5, 2016

CRACK ANALYSIS IN BIMATERIAL INTERFACES USING T-SPLINE BASED XIGA

SADAM HOUCINE HABIB, IDIR BELAIDI

University of M'hamed Bougara, Department of Mechanical Engineering, Boumerdes, Algeria
e-mail: hb_houcine@yahoo.fr; idir.belaidi@gmail.com

Analysis-suitable T-splines are used for the modeling and analyzing of cracks in bimaterial interfaces within the framework of an extended isogeometric analysis (XIGA). The crack tip enrichment functions of bimaterial interface cracks are implemented to reproduce singular fields, and the signed distance functions are used to treat the crack face and the interface in the models. A compatible local refinement algorithm is applied to refine location of the crack and the interface, which helps one to avoid produce excessive propagation of control points. The mixed mode stress intensity factors (SIFs) which are evaluated by the interaction integral (M-integral) are used as analysis parameters. Numerical simulations are performed to analyze the problem and to examine the efficiency of the proposed method. The obtained results are compared with other available results.

Keywords: extended isogeometric analysis, T-splines, bimaterial interface cracks, enrichment functions, local refinement

1. Introduction

As its name indicates, a composite material is made up of two or more different constituents; it has properties that cannot be obtained together by one of the individual constituents, such as high specific strength and stiffness, good durability and good corrosion resistance. Due to their properties, composites have been developed and used in various industrial and engineering applications, like those in aerospace, aircraft, automotive industries, etc. However, these materials are not immune to manufacture defects especially from those which are created as interfacial cracks. This problem greatly influences the behavior of structures and can cause brutal fracture.

The mechanical behavior of composite materials needs more understanding, especially in the presence of strong and weak discontinuities. Many analytical studies were performed based upon the work of Williams (1959) for understanding the problem of bimaterial interface cracks, such as (Erdogan 1963; Rice and Sih, 1965; Sun and Jih, 1987; Hutchinson *et al.*, 1987; Rice, 1988; Evans *et al.*, 1990). However, the complexity of analytical solutions even for simple cases requires the modelling of mechanical behavior of this problem using effective numerical methods. Several investigations have been developed in this domain, via the boundary element method (BEM) (Lee and Choi, 1988; Yuuki and Xu, 1994; Miyazaki *et al.*, 1993), finite element method (FEM) (Ikeda *et al.*, 2006), element free Galerkin method (EFGM) (Pant *et al.*, 2011), extended finite element method (XFEM) (Nagashima *et al.*, 2003; Liu *et al.*, 2004; Belytschko and Gracie, 2007) and other methods (Zhou *et al.*, 2013, 2014; An *et al.*, 2013). Recently, a large field was opened by Hughes *et al.* (2005) offering the possibility of introducing computer aided design (CAD) tools in the analysis methods using the isoparametric concept. The basic idea of this novel alternative method, called isogeometric analysis (IGA), is to exploit the technologies of computational geometry as shape bases to describe the geometry exactly, also for the approximation of unknown fields. Following this discovery, several researches in various

fields have been conducted by this method, including: fluid-structure interaction (Bazilevs *et al.*, 2006), composite materials (Peković *et al.*, 2015), elastic-plastic analysis (Kalali *et al.*, 2016), electromagnetic problems (Buffa *et al.*, 2010), turbulent flow (Bazilevs and Akkerman, 2010), contact problems (Temizer *et al.*, 2011), aero-dynamics (Hsu *et al.*, 2011), heat transfer (Anders *et al.*, 2012) and fluid mechanics (Evan and Hudhes, 2013). For more details about IGA, a recent review has been published, see Nguyen *et al.* (2015). In fracture mechanics problems, IGA has been also applied in different studies (Verhoosel *et al.*, 2011; Borden *et al.*, 2012; Nguyen and Nguen-Xuan, 2013; Nguyen *et al.*, 2014; Peng *et al.*, 2014), however Benson *et al.* (2010) and De Luycker *et al.* (2011) proposed extended isogeometric analysis (XIGA) for modelling cracks. In this method the general principle of the XFEM is used in IGA by including the asymptotic and signed distance enrichment functions. Therefore, this method has the advantages of both XFEM and IGA, which are summarized by the ability to represent complex geometries independently of any discontinuities and without explicit meshing to obtain solutions with higher orders. Some applications in fracture mechanics have been checked by the XIGA, such as in the cases of homogeneous materials (Ghorashi *et al.*, 2012; Bhardwaj and Singh, 2015), functionally graded material (Bhardwaj *et al.*, 2015a,c) and bimaterial interfaces (Bhardwaj *et al.*, 2015b; Jia *et al.*, 2015), where the non-uniform rational B-splines (NURBS) are used. Also, orthotropic media have been studied using T-spline based XIGA (Ghorashi *et al.*, 2015).

There are many CAD basis functions that can be used in IGA, where the Non Uniform Rational B-splines (NURBS) are widely used due to their properties, like continuity, smoothness, variation diminishing, convex hull and possibility of using knot insertion and degree elevation refinements. They have the ability to describe exactly all conic sections but they have difficulties in certain complex geometries which cannot be avoided even by using multiple patches, where NURBS generate a complicated mesh which leads to produce superfluous control points. In order to handle these disadvantages, Sederberg *et al.* (2003) proposed a T-spline as a generalized tool of NURBS, in which the index space (T-mesh) locally refined using T-junctions (Sederberg *et al.*, 2004). Therefore, the major advantages of this technique are the local refinement and the ability to represent complex geometries with a minimal number of control points compared with those used in NURBS.

According to their ability in engineering design, T-splines have been used by analysis to serve as basis functions for IGA in many advanced searches. However T-spline bases are not always valid to be used in analysis for different geometric configurations, because the linear independence and partition unity properties are not always ensured. Li *et al.* (2012) introduced analysis-suitable T-splines, where for any choice of knot vectors the blending functions are linearly independent. Like NURBS bases, analysis-suitable T-spline bases have the properties of the analysis basis functions. Moreover, they provide an efficient algorithm which allows making highly localized refinement (Scott *et al.*, 2012).

In this paper, the interface crack in the case of 2D composites is analyzed using T-spline based XIGA; the accuracy of this approach is first tested in isotropic materials. The analysis-suitable T-spline and its refinement algorithm are highlighted.

2. Analysis-suitable T-splines

An analysis-suitable T-spline is founded when the T-mesh (T-mesh is a mesh of rectangular elements that is defined by the lines corresponding to knot values of the parametric vectors) provides a restricted topology that has no intersecting T-junction extensions. The T-junction extension is defined in each T-junction vertex by an interval which includes two distances. The first distance is between the T-junction and the two next adjoining edges or vertices in the direction of missing edge, while the second distance is between the T-junction and one edge

or vertex in the other direction, as shown in Fig. 1b. The T-mesh that shows all T-junction extensions can be called extended T-mesh. An empty extended T-mesh means there are no intersections between T-junction extensions (see Fig. 1c), which means the T-mesh is analysis-suitable.

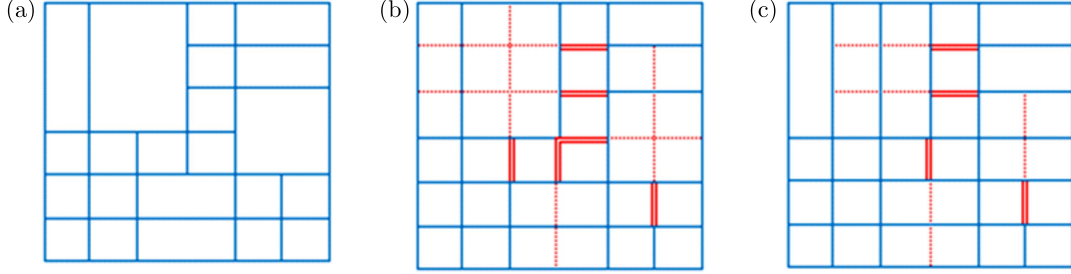


Fig. 1. An example depicts: (a) T-mesh, (b) extended T-mesh and (c) empty extended T-mesh

In order to make local refinement of analysis-suitable T-spline spaces, Scott *et al.* (2012) introduced an algorithm consisting of the following steps:

- create the refined T-mesh T_2 from the original analysis-suitable T-mesh T_{s1} ,
- form the extended T-mesh of T_2 .
- if the extended T-mesh of T_2 has intersecting T-junction extensions, one edge must be inserted into T_2 in such a way that reduces the number of the intersections,
- repeat step 3 until the extended T-mesh has no intersecting T-junction extensions,
- compute the refinement matrix \mathbf{M} .

For more details, see (Scott *et al.*, 2012).

3. Extended isogeometric analysis (XIGA)

XIGA (Benson *et al.*, 2010; De Luycker *et al.*, 2011) uses the same methodology of the extended finite element method (XFEM) for the modelling of discontinuities but with basis functions derived from geometry like in isogeometric analysis (Hughes *et al.*, 2005). For crack problems, XIGA provides the possibility of modelling the crack independently of the mesh and within exactly presented geometry. Uncommonly, in this study, T-splines are adopted in XIGA using analysis-suitable T-splines to approximate the displacement in any point $\zeta = (\xi, \eta)$ as follows

$$\mathbf{u}(\zeta) = \sum_{i=1}^{n_s} \mathbf{R}_i(\zeta) \mathbf{u}_i + \sum_{j=1}^{n_{cf}} \mathbf{R}_j(\zeta) H(\zeta) \mathbf{a}_j + \sum_{k=1}^{n_{ct}} \mathbf{R}_k(\zeta) \left(\sum_{\ell=1}^4 F_\ell(\zeta) \mathbf{b}_k^\ell \right) + \sum_{t=1}^{n_i} \mathbf{R}_t(\zeta) \chi(\zeta) \mathbf{c}_t \quad (3.1)$$

where \mathbf{R} is the T-spline basis function extracted from an empty extended T-mesh, H is the Heaviside function used for the modelling of the crack face, it takes value 1 above the crack and -1 below the crack, F are the crack-tip enrichment functions, \mathbf{u}_i , \mathbf{a}_j , \mathbf{b}_k and \mathbf{c}_t are the displacement vectors corresponding to n_s , n_{cf} , n_{ct} and n_t control points, respectively. The fourth term is used when there is no coincidence between the interface and the finite element mesh for the modelling of weak discontinuity. The enrichment function of Moës *et al.* (2003) χ can be used

$$\chi(\zeta) = \sum \mathbf{R}_I(\zeta) |\phi_I| - \left| \sum \mathbf{R}_I(\zeta) \phi_I \right| \quad (3.2)$$

where ϕ is the signed distance value of the interface control points.

The enrichment functions of bimaterial interface cracks were derived by Sukumar *et al.* (2004) as

$$\begin{aligned} \{F_{\ell}(r, \theta)\}_{\ell=1}^{12} = & \left\{ \sqrt{r} \cos(\varepsilon \log r) e^{-\varepsilon \theta} \sin \frac{\theta}{2}, \sqrt{r} \cos(\varepsilon \log r) e^{-\varepsilon \theta} \cos \frac{\theta}{2}, \sqrt{r} \cos(\varepsilon \log r) e^{\varepsilon \theta} \sin \frac{\theta}{2}, \right. \\ & \sqrt{r} \cos(\varepsilon \log r) e^{\varepsilon \theta} \cos \frac{\theta}{2}, \sqrt{r} \cos(\varepsilon \log r) e^{\varepsilon \theta} \sin \frac{\theta}{2} \sin \theta, \sqrt{r} \cos(\varepsilon \log r) e^{\varepsilon \theta} \cos \frac{\theta}{2} \sin \theta, \\ & \sqrt{r} \sin(\varepsilon \log r) e^{-\varepsilon \theta} \sin \frac{\theta}{2}, \sqrt{r} \sin(\varepsilon \log r) e^{-\varepsilon \theta} \cos \frac{\theta}{2}, \sqrt{r} \sin(\varepsilon \log r) e^{\varepsilon \theta} \sin \frac{\theta}{2}, \\ & \left. \sqrt{r} \sin(\varepsilon \log r) e^{\varepsilon \theta} \cos \frac{\theta}{2}, \sqrt{r} \sin(\varepsilon \log r) e^{\varepsilon \theta} \sin \frac{\theta}{2} \sin \theta, \sqrt{r} \sin(\varepsilon \log r) e^{\varepsilon \theta} \cos \frac{\theta}{2} \sin \theta \right\} \end{aligned} \quad (3.3)$$

4. Numerical simulations

Here, the analysis-suitable T-spline is used in XIGA to simulate the crack in homogeneous isotropic and bimaterial interfaces. Two numerical examples are considered for each material type in plane static problems, where mode I and mode II SIFs are evaluated and compared with other numerical and analytical results. First, the isotropic material is considered in a rectangular plate with an edge crack in order to study the convergence and the domain independence in the computations of SIF, also an isotropic square plate with a center crack is analyzed for different crack angles to verify the accuracy of the proposed approach. Then, numerical applications in the form of parametric studies are considered for edge and center interface cracks in finite rectangular plates.

In all geometric models (NURBS and T-splines) the cubic order is used in both parametric directions, where the weights are taken as unity. In the edge crack problems, the geometry is refined locally once, while for the center crack problems the geometry is refined locally twice. Four types of finite elements are distinguished in these examples according to their positions with respect to the crack, the standard element contains 3×3 Gauss points. The element having tip enriched control points contains 7×7 Gauss points and the sub-triangle technique (Ghorashi *et al.*, 2011) is used for the tip-element by 13 Gauss points in each triangle, however the split element contains 6×6 Gauss points for the horizontal crack problems and the sub-triangle technique is used by 13 Gauss points in each triangle for the inclined crack problems. The SIFs are evaluated using interaction integral (Yau and Wang, 1984), wherein the crack tip element is not considered in the calculation.

4.1. Homogeneous isotropic material

In this case, we simulate a finite rectangular plate containing an edge crack (Fig. 2a) and a square plate containing an inclined central crack (Fig. 2b), subjected to unit uniaxial tension in plane stress state. The convergence of the proposed approach is studied for the edge crack problem with normalized M-integral radius equal to 1 using five different control net configurations (200, 296, 362, 754 and 1800 control points), all shown in Fig. 3. The errors of the normalized SIF values obtained from the proposed approach which are shown in Table. 1 are computed using the following equation

$$\bar{K}_I = \frac{K_I}{\sigma \sqrt{\pi a}} = T_I \left(\frac{a}{L} \right) \quad (4.1)$$

where $T_I(a/L)$ is the analytical formula which corresponds to mode I, it can be computed as (Tada *et al.*, 2000)

$$T_I = 1.122 - 0.231 \frac{a}{L} + 10.55 \left(\frac{a}{L} \right)^2 - 21.71 \left(\frac{a}{L} \right)^3 + 30.382 \left(\frac{a}{L} \right)^4$$

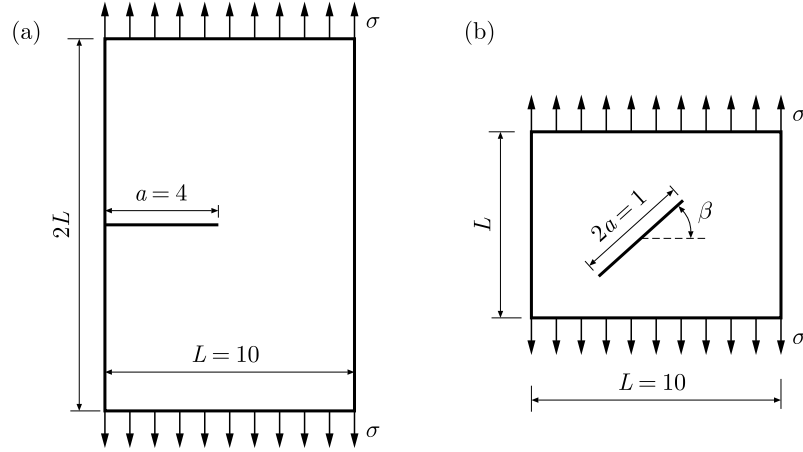


Fig. 2. Geometries and loading of the homogeneous isotropic examples (a) rectangular plate with an edge crack and (b) square plate with a center inclined crack

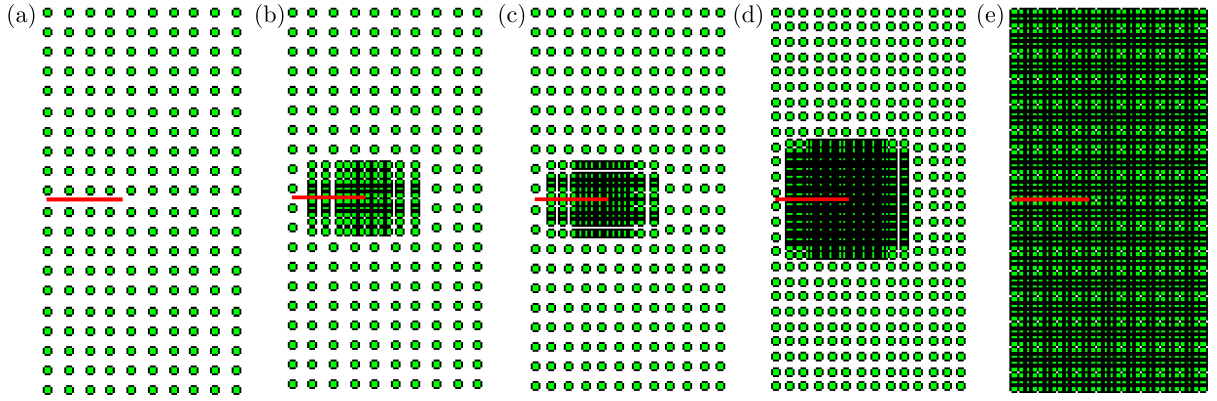


Fig. 3. Different mesh configurations used in the convergence study: (a) 200 points, (b) 296 points, (c) 362 points, (d) 788 points and (e) 1800 points

Table 1. Convergence of the SIF for various control nets

Control points	\bar{K}_I	Error [%]
200	2.1275	1.0257
296	2.1189	0.6173
362	2.1121	0.2944
754	2.1098	0.1852
1800	2.1131	0.3419

The first and the last meshes in Fig. 3 represent a special case of T-splines which is NURBS. According to Table 1, analysis suitable T-splines give us precise results for a different number of control points (meshes 2, 3 and 4), even for the minimal number of control points compared to NURBS (mesh 4 compared to mesh 5) and that attributed to the local refinement property. Table 2 compares the results of the normalized SIF for different radius to study the domain independence in T-spline meshes. We observe that the SIF values are almost not sensitive to the radius of the M-integral. The contour plots of the normal stress component σ_{yy} and the vertical displacement u_y are illustrated in Fig. 4.

For the square plate, we used a mesh consisting of 788 control points and 689 elements (Figs. 5a and 5b) to evaluate the normalized mixed mode SIF for $a = 0.5$ in different inclined angles. The exact SIFs of this problem can be obtained by the following equations

$$K_I = \sigma_0 \sqrt{\pi a} \cos^2 \beta \quad K_{II} = \sigma_0 \sqrt{\pi a} \sin \beta \cos \beta \quad (4.2)$$

Table 2. Domain independence study

Radius	Mesh 2		Mesh 3		Mesh 4	
	$\overline{K_I}$	Error [%]	$\overline{K_I}$	Error [%]	$\overline{K_I}$	Error [%]
0.6	2.1131	0.3419	2.1280	1.0494	2.1245	0.8832
0.7	2.1256	0.9355	2.1202	0.6790	2.1142	0.3941
0.8	2.1256	0.9355	2.1209	0.7123	2.1122	0.2992
0.9	2.1218	0.7550	2.1177	0.5603	2.1122	0.2992
1.0	2.1189	0.6173	2.1121	0.2944	2.1098	0.1852
1.1	2.1146	0.4131	2.1118	0.2802	2.1109	0.2374

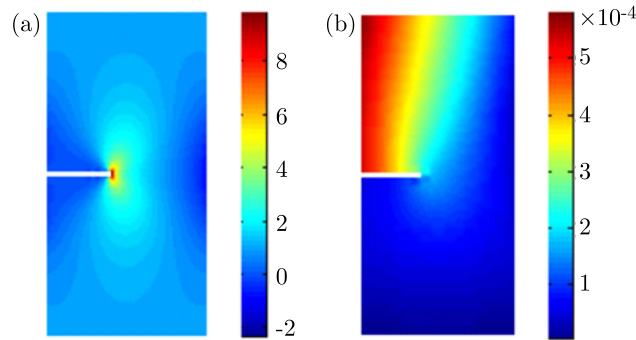


Fig. 4. Graphical visualization: (a) normal stress and (b) vertical displacement

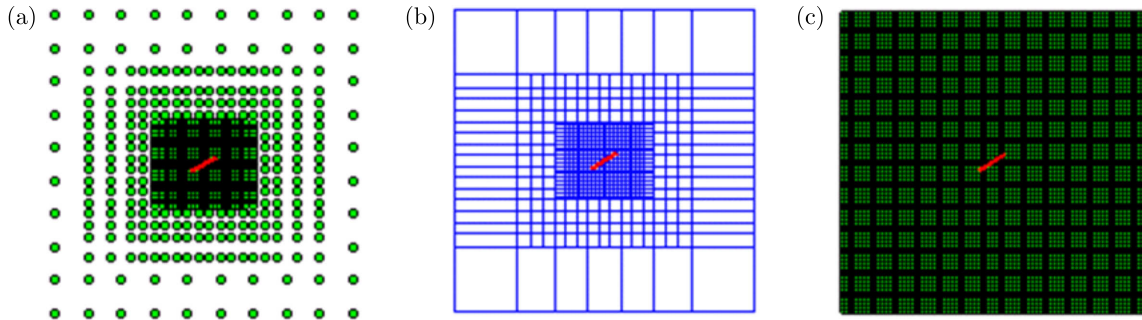


Fig. 5. The meshes used for the isotropic square plate: (a) T-spline control net (788 points), (b) elements corresponding to the T-spline control net (689 elements) and (c) NURBS control net (4625 points)

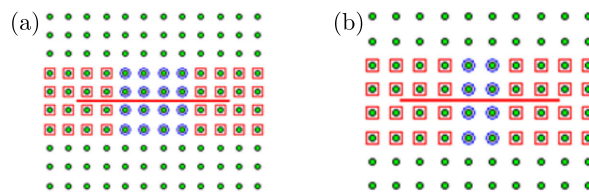
Fig. 6. The crack tip (red squares) and the crack face (blue circles) enriched points of: (a) T-spline control net and (b) NURBS control net, in the case $\beta = 0$

Figure 6a depicts the enriched control points that correspond to the crack face and crack tip elements. Figure 7 shows a comparison between the normalized SIFs calculated by the proposed approach and those derived from the exact solution and NURBS-based XIGA. A uniform NURBS mesh is used Fig. 6c, its enriched control points are presented in Fig. 6b. As seen in both modes, there is a very close agreement between the T-spline results and the other results.

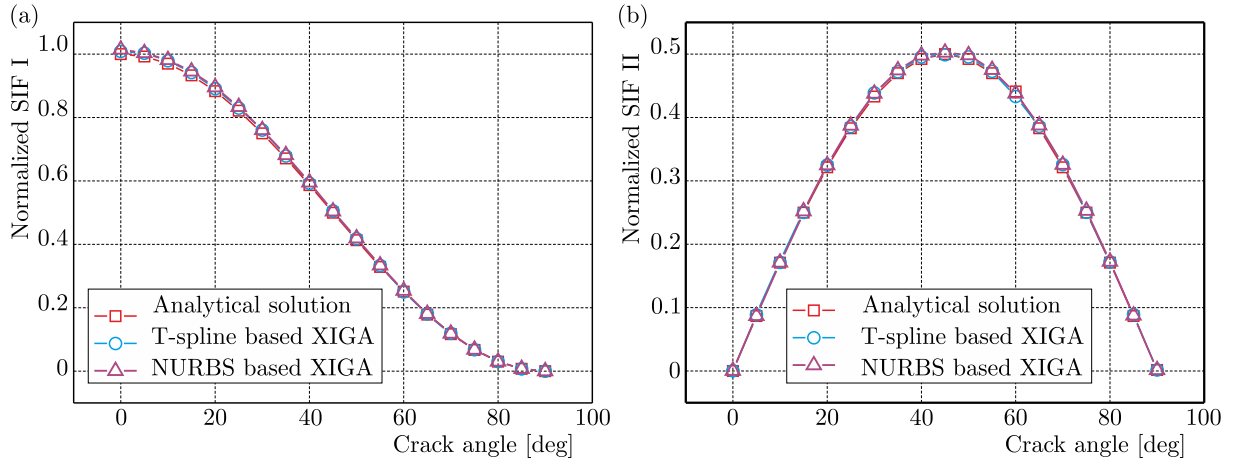


Fig. 7. Variations of normalized mode I and II SIFs with respect to different crack angles using the analysis-suitable T-splines, NURBS and exact solution for the square plate problem

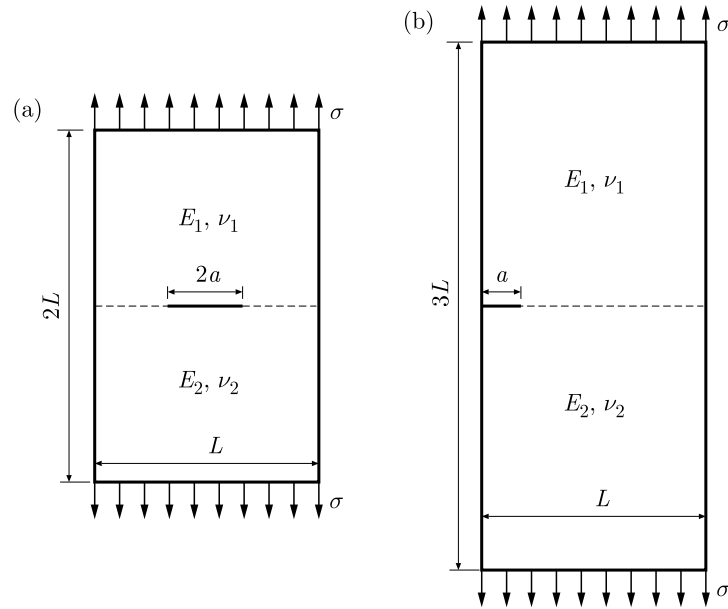


Fig. 8. Geometries and loading of the bimaterial interface examples: (a) interface center crack and (b) interface edge crack

4.2. Bimaterial interface crack

We consider two finite rectangular plates subjected to uniaxial tensions in plane stress conditions, each one constituted of two dissimilar materials and cracked in the interface as shown in Fig. 8. Different ratios of Young's modulus ($E_1/E_2 = 2, 3, 4, 10$ and 100) with fixed Poisson ratios ($\nu_1 = \nu_2 = 0.3$) are taken in the simulation. Similar problems were solved before by Miyazaki *et al.* (1993) utilizing the boundary element method (BEM), Nagashima *et al.* (2003) utilizing an extended finite element method (XFEM), Matsumoto *et al.* (2000) making use of the interaction energy release rates and BEM sensitivity and Liu *et al.* (2004) using XFEM for direct evaluation of the mixed mode SIF. For the center crack problem (Fig. 8a), we use a mesh consisting of 3132 control points and 2925 elements as shown in Figs. 9a and 9b. For the edge crack problem (Fig. 8b), we use a mesh consisting of 1446 control points and 1235 elements as shown in Figs. 9c and 9d. The enriched control points are defined in Fig. 10. In order to verify the accuracy of the obtained results, the normalized SIFs are compared with those obtained by

other methods in Fig. 11 for the center crack problem ($2a/L = 0.4$) and in Fig. 12 for the edge crack problem ($a/L = 0.3$). Figures 13 and 14 illustrate variations of the normalized SIFs in terms of crack lengths for the center and edge crack problems, respectively. For more details, check Table 3 and Table 4.

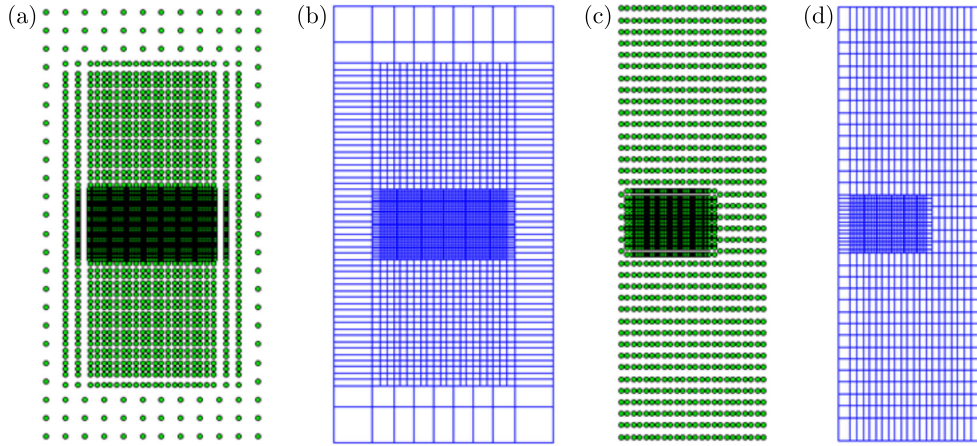


Fig. 9. T-spline meshes used for the bimaterial interface examples: (a) control net for the interface center crack (793 points), (b) mesh for the interface center crack (688 elements), (c) control net for the interface edge crack (566 points) and (d) mesh for the interface edge crack (431 elements)

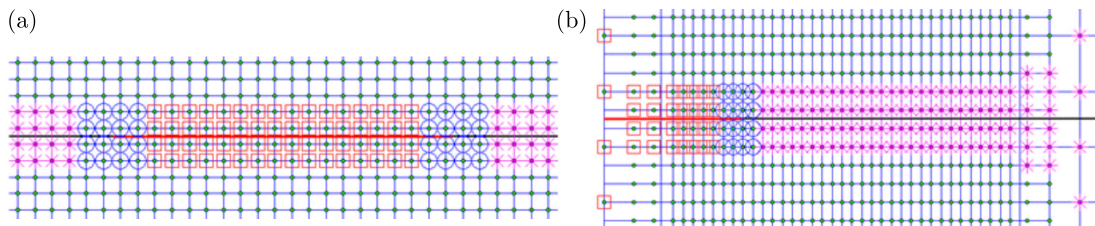


Fig. 10. Crack tip, crack face and interface enriched control points: (a) interface center crack and (b) interface edge crack

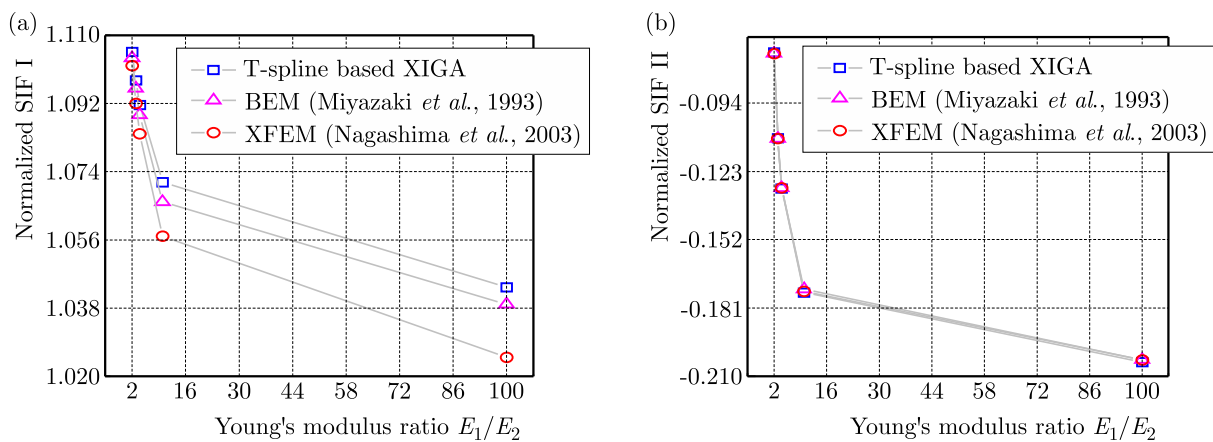


Fig. 11. Variations of normalized mode I and II SIFs with respect to different Young's modulus ratios using T-spline based XIGA, BEM and XFEM for the center interface crack ($2a/L = 0.4$)

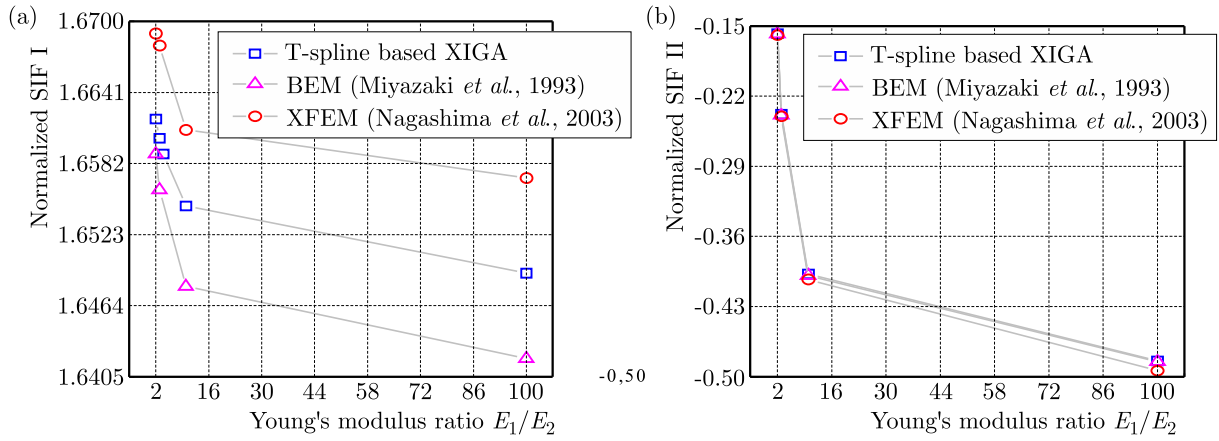


Fig. 12. Variations of normalized mode I and II SIFs with respect to different Young's modulus ratios using T-spline based XIGA, BEM and XFEM for the edge interface crack ($a/L = 0.3$)

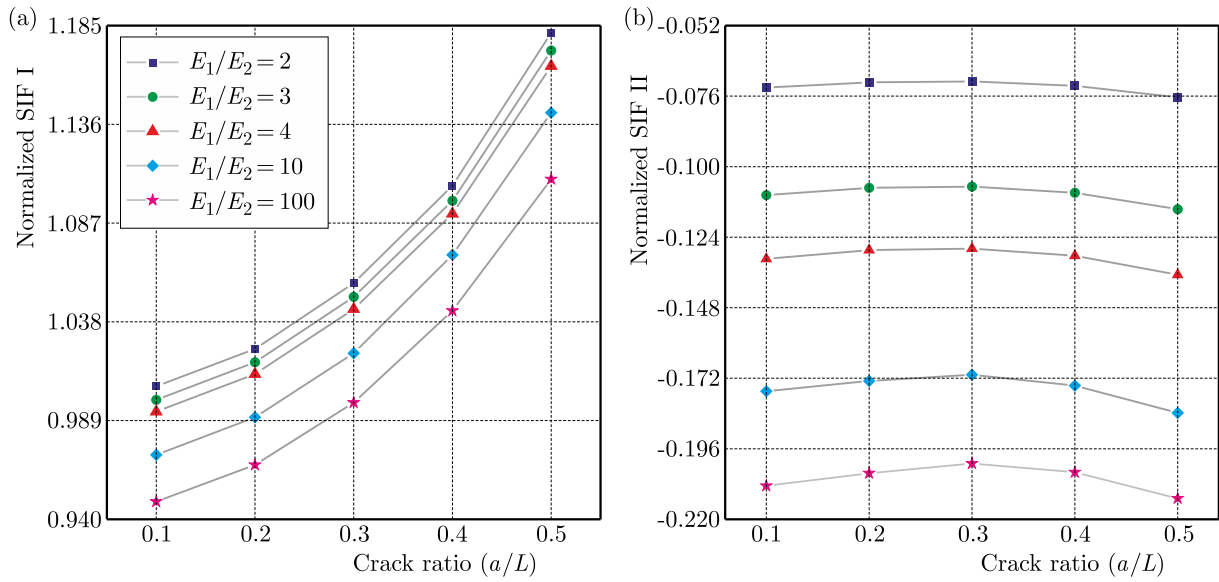


Fig. 13. The effect of Young's modulus ratio on the normalized SIFs for the center interface crack

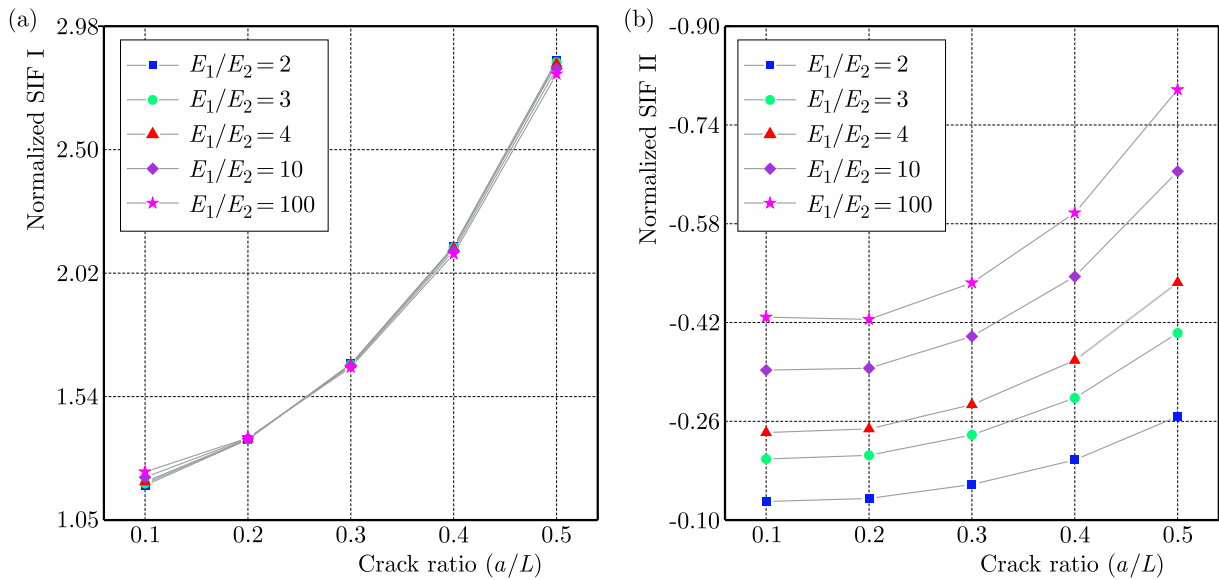


Fig. 14. The effect of Young's modulus ratio on the normalized SIF for the edge interface crack

Table 3. Results of normalized stress intensity factors for the center interface crack

E_1/E_2	$2a/L$	Present study		Matsumto <i>et al.</i> (2000)		Miyazaki <i>et al.</i> (1993)	
		\overline{K}_I	\overline{K}_{II}	\overline{K}_I	\overline{K}_{II}	\overline{K}_I	\overline{K}_{II}
2	0.1	1.006	-0.0731	0.995	-0.072	1.001	-0.072
	0.2	1.0245	-0.0713	1.019	-0.07	1.02	-0.071
	0.3	1.0572	-0.071	1.053	-0.072	1.053	-0.071
	0.4	1.1056	-0.0725	1.104	-0.073	1.104	-0.073
	0.5	1.1814	-0.0764	1.18	-0.077	1.181	-0.077
3	0.1	0.9993	-0.1097	0.987	-0.106	0.993	-0.107
	0.2	1.0179	-0.1072	1.013	-0.105	1.012	-0.106
	0.3	1.0504	-0.1068	1.044	-0.105	1.045	-0.106
	0.4	1.0981	-0.1089	1.095	-0.108	1.096	-0.109
	0.5	1.1726	-0.1145	1.172	-0.115	1.171	-0.115
4	0.1	0.9934	-0.1314	0.981	-0.128	0.987	-0.129
	0.2	1.0121	-0.1284	1.006	-0.126	1.006	-0.127
	0.3	1.0443	-0.1279	1.037	-0.126	1.031	-0.127
	0.4	1.0916	-0.1303	1.088	-0.131	1.089	-0.13
	0.5	1.1649	-0.1368	1.163	-0.136	1.163	-0.137
10	0.1	0.972	-0.1764	0.962	-0.172	0.968	-0.174
	0.2	0.9906	-0.1729	0.987	-0.168	0.986	-0.171
	0.3	1.0224	-0.1708	1.017	-0.171	1.018	-0.17
	0.4	1.0712	-0.1745	1.065	-0.172	1.066	-0.173
	0.5	1.1418	-0.1838	1.135	-0.181	1.136	-0.182
100	0.1	0.9488	-0.2086	0.943	-0.207	0.946	-0.206
	0.2	0.967	-0.2043	0.964	-0.201	0.964	-0.201
	0.3	0.9979	-0.201	0.994	-0.198	0.994	-0.2
	0.4	1.0435	-0.204	1.039	-0.2	1.039	-0.203
	0.5	1.1088	-0.2129	1.104	-0.208	1.104	-0.21

The results of the proposed method are closer to the BEM results than the XFEM results, as shown in Figs. 11 and 12. Young's modulus ratio has a slight effect on the SIFs, as shown in Tables 3 and 4. As it is obvious in the precedent examples, the local refinement property of analysis-suitable T-splines allows increasing the accuracy of the results and using less DOFs. Finally, we note that the evaluation of shape functions in XIGA is slower than some methods such as XFEM.

5. Conclusion

In this study, the analysis-suitable T-spline has been used in XIGA to approximate the solution in cracked bimaterial interfaces in order to construct geometry and to make local refinement around the discontinuities. Furthermore, it helps avoiding the emergence of superfluous control points during the local refinement process. The asymptotic crack-tip enrichment functions and the interaction integral method corresponding to bimaterial interface cracks have been used to evaluate the stress intensity factors. The results obtained by the proposed method have been compared with the results from literature, where a good agreement has been regarded demonstrating the accuracy of the approach.

Table 4. Results of normalized stress intensity factors for the edge interface crack

$\frac{E_1}{E_2}$	$\frac{2a}{L}$	Present study		Matsumoto <i>et al.</i> (2000)		Miyazaki <i>et al.</i> (1993)		Liu <i>et al.</i> (2004)	
		\bar{K}_I	$\bar{K}K_{II}$	\bar{K}_I	\bar{K}_{II}	\bar{K}_I	\bar{K}_{II}	\bar{K}_I	\bar{K}_{II}
2	0.1	1.1899	-0.1299	1.19	-0.127	1.195	-0.129	-	-
	0.2	1.3682	-0.1352	1.367	-0.137	1.368	-0.137	1.374	-0.137
	0.3	1.6619	-0.1576	1.657	-0.156	1.659	-0.158	1.669	-0.159
	0.4	2.1198	-0.1975	2.109	-0.195	2.11	-0.198	2.125	-0.198
	0.5	2.8423	-0.2678	2.819	-0.268	2.882	-0.267	2.844	-0.267
3	0.1	1.1974	-0.1988	1.198	-0.195	1.203	-0.197	-	-
	0.2	1.369	-0.2049	1.368	-0.208	1.368	-0.207	1.375	-0.208
	0.3	1.6603	-0.2379	1.655	-0.235	1.656	-0.239	1.668	-0.240
	0.4	2.116	-0.2977	2.102	-0.298	2.105	-0.298	2.121	-0.299
	0.5	2.8351	-0.403	2.812	-0.402	2.814	-0.402	2.839	-0.402
10	0.1	1.2216	-0.343	1.222	-0.336	1.229	-0.34	-	-
	0.2	1.3719	-0.3461	1.366	-0.348	1.369	-0.349	1.379	-0.354
	0.3	1.6547	-0.3976	1.648	-0.394	1.648	-0.399	1.661	-0.403
	0.4	2.1023	-0.4945	2.09	-0.491	2.09	-0.494	2.109	-0.5
	0.5	2.8103	-0.6649	2.789	-0.661	2.789	-0.663	2.819	-0.668
100	0.1	1.2422	-0.4286	1.251	-0.424	1.251	-0.424	-	-
	0.2	1.3744	-0.4252	1.376	-0.429	1.370	-0.428	1.381	-0.434
	0.3	1.6491	-0.4842	1.647	-0.47	1.642	-0.485	1.657	-0.494
	0.4	2.0895	-0.5975	2.083	-0.569	2.078	-0.597	2.101	-0.608
	0.5	2.7888	-0.7972	2.772	-0.793	2.77	-0.797	2.804	-0.813

References

1. AN X., ZHAO Z., ZHANG H., HE L., 2013, Modeling bimaterial interface cracks using the numerical manifold method, *Engineering Analysis with Boundary Elements*, **37**, 464-474
2. ANDERS D., WEINBERG K., REICHARDT R., 2012, Isogeometric analysis of thermal diffusion in binary blends, *Computational Materials Science*, **52**, 182-188
3. BAZILEVS Y., AKKERMAN I., 2010, Large eddy simulation of turbulent Taylor-Couette flow using isogeometric analysis and the residual-based variational multiscale method, *Journal of Computational Physics*, **229**, 3402-3414
4. BAZILEVS Y., CALO V., ZHANG Y., HUGHES T.J., 2006, Isogeometric fluid-structure interaction analysis with applications to arterial blood flow, *Computational Mechanics*, **38**, 310-322
5. BELYTSCHKO T., GRACIE R., 2007, On XFEM applications to dislocations and interfaces, *International Journal of Plasticity*, **23**, 1721-1738
6. BENSON D., BAZILEVS Y., DE LUYCKER E., HSU M.C., SCOTT M., HUGHES T., BELYTSCHKO, T., 2010, A generalized finite element formulation for arbitrary basis functions: from isogeometric analysis to XFEM, *International Journal for Numerical Methods in Engineering*, **83**, 765-785
7. BHARDWAJ, G., SINGH, I., 2015, Fatigue crack growth analysis of a homogeneous plate in the presence of multiple defects using extended isogeometric analysis, *Journal of the Brazilian Society of Mechanical Sciences and Engineering*, **37**, 1065-1082
8. BHARDWAJ G., SINGH I., MISHRA B., 2015a, Fatigue crack growth in functionally graded material using homogenized XIGA, *Composite Structures*, **134**, 269-284
9. BHARDWAJ G., SINGH I., MISHRA B., 2015b, Stochastic fatigue crack growth simulation of interfacial crack in bi-layered FGMs using XIGA, *Computer Methods in Applied Mechanics and Engineering*, **284**, 186-229

10. BHARDWAJ G., SINGH I., MISHRA B., BUI T., 2015c, Numerical simulation of functionally graded cracked plates using NURBS based XIGA under different loads and boundary conditions, *Composite Structures*, **126**, 347-359
11. BORDEN M.J., VERHOOSSEL C.V., SCOTT M.A., HUGHES T.J., LANDIS C.M., 2012, A phase-field description of dynamic brittle fracture, *Computer Methods in Applied Mechanics and Engineering*, **217**, 77-95
12. BUFFA A., SANGALLI G., VÁZQUEZ R., 2010, Isogeometric analysis in electromagnetics: B-splines approximation, *Computer Methods in Applied Mechanics and Engineering*, **199**, 1143-1152
13. DE LUYCKER, E., BENSON D., BELYTSCHKO T., BAZILEVS Y., HSU M., 2011, X-FEM in isogeometric analysis for linear fracture mechanics, *International Journal for Numerical Methods in Engineering*, **87**, 541-565
14. ERDOGAN F., 1963, Stress distribution in a nonhomogeneous elastic plane with cracks, *Journal of Applied Mechanics*, **30**, 232-236
15. EVANS J.A., HUGHES T.J., 2013, Isogeometric divergence-conforming B-splines for the steady Navier-Stokes equations, *Mathematical Models and Methods in Applied Sciences*, **23**, 1421-1478
16. EVANS A.G., RÜHLE M., DALGLEISH B.J., CHARALAMBIDES P.G., 1990, The fracture energy of bimaterial interfaces, *Metallurgical Transactions A*, **21**, 2419-2429
17. GHORASHI S.S., MOHAMMADI S., SABBAGH-YAZDI, S.-R., 2011, Orthotropic enriched element free Galerkin method for fracture analysis of composites, *Engineering Fracture Mechanics*, **78**, 1906-1927
18. GHORASHI S.S., VALIZADEH N., MOHAMMADI S., 2012, Extended isogeometric analysis for simulation of stationary and propagating cracks, *International Journal for Numerical Methods in Engineering*, **89**, 1069-1101
19. GHORASHI S.S., VALIZADEH N., MOHAMMADI S., RABCZUK T., 2015, T-spline based XIGA for fracture analysis of orthotropic media, *Composite Structures*, **147**, 138-146
20. HSU M.-C., AKKERMAN I., BAZILEVS Y., 2011, High-performance computing of wind turbine aerodynamics using isogeometric analysis, *Computers and Fluids*, **49**, 93-100
21. HUGHES T.J., COTTRELL J.A., BAZILEVS Y., 2005, Isogeometric analysis: CAD, finite elements, NURBS, exact geometry and mesh refinement, *Computer Methods in Applied Mechanics and Engineering*, **194**, 4135-4195
22. HUTCHINSON J.W., MEAR M., RICE J.R., 1987, Crack paralleling an interface between dissimilar materials, *Journal of Applied Mechanics*, **54**, 828-832
23. IKEDA T., NAGAI M., YAMANAGA K., MIYAZAKI N., 2006, Stress intensity factor analyses of interface cracks between dissimilar anisotropic materials using the finite element method, *Engineering Fracture Mechanics*, **73**, 2067-2079
24. JIA Y., ANITESCU C., GHORASHI S.S., RABCZUK T., 2015, Extended isogeometric analysis for material interface problems, *IMA Journal of Applied Mathematics*, **80**, 608-633
25. KALALI A.T., HASSANI B., HADIDI-MOUD S., 2016, Elastic-plastic analysis of pressure vessels and rotating disks made of functionally graded materials using the isogeometric approach, *Journal of Theoretical and Applied Mechanics*, **54**, 113-125
26. LEE K.Y., CHOI H.J., 1988, Boundary element analysis of stress intensity factors for bimaterial interface cracks, *Engineering Fracture Mechanics*, **29**, 461-472
27. LI X., ZHENG J., SEDERBERG T.W., HUGHES T.J., SCOTT M.A., 2012, On linear independence of T-spline blending functions, *Computer Aided Geometric Design*, **29**, 63-76
28. LIU X., XIAO Q.Z., KARIHALOO B., 2004, XFEM for direct evaluation of mixed mode SIFs in homogeneous and bi-materials, *International Journal for Numerical Methods in Engineering*, **59**, 1103-1118

29. MATSUMOTO T., TANAKA M., OBARA R., 2000, Computation of stress intensity factors of interface cracks based on interaction energy release rates and BEM sensitivity analysis, *Engineering Fracture Mechanics*, **65**, 683-702
30. MIYAZAKI N., IKEDA T., SODA T., MUNAKATA T., 1993, Stress intensity factor analysis of interface crack using boundary element method application of contour-integral method, *Engineering Fracture Mechanics*, **45**, 599-610
31. MOËS N., CLOIREC M., CARTRAUD P., REMACLE J.-F., 2003, A computational approach to handle complex microstructure geometries, *Computer Methods in Applied Mechanics and Engineering*, **192**, 3163-3177
32. NAGASHIMA T., OMOTO Y., TANI S., 2003, Stress intensity factor analysis of interface cracks using X-FEM, *International Journal for Numerical Methods in Engineering*, **56**, 1151-1173
33. NGUYEN V.P., ANITESCU C., BORDAS, S.P., RABCZUK T., 2015, Isogeometric analysis: An overview and computer implementation aspects, *Mathematics and Computers in Simulation*, **117**, 89-116
34. NGUYEN V.P., KERFRIDEN P., BORDAS S.P., 2014, Two-and three-dimensional isogeometric cohesive elements for composite delamination analysis, *Composites Part B: Engineering*, **60**, 193-212
35. NGUYEN V.P., NGUYEN-XUAN H., 2013, High-order B-splines based finite elements for delamination analysis of laminated composites, *Composite Structures*, **102**, 261-275
36. PANT M., SINGH I., MISHRA B., 2011, Evaluation of mixed mode stress intensity factors for interface cracks using EFGM, *Applied Mathematical Modelling*, **35**, 3443-3459
37. PEKOVIĆ O., STUPAR S., SIMONOVIĆ A., SVORCAN J., TRIVKOVIĆ S., 2015, Free vibration and buckling analysis of higher order laminated composite plates using the isogeometric approach, *Journal of Theoretical and Applied Mechanics*, **53**, 453-466
38. PENG X., ATROSHCHENKO E., SIMPSON R., KULASEGARAM S., BORDAS S., 2014, Crack growth analysis by a NURBS-based isogeometric boundary element method, *11th World Congress on Computational Mechanics*, Barcelona, Spain
39. RICE J., 1988, Elastic fracture mechanics concepts for interfacial cracks, *Journal of Applied Mechanics*, **55**, 98-103
40. RICE J., SIH G.C., 1965, Plane problems of cracks in dissimilar media, *Journal of Applied Mechanics*, **32**, 418-423
41. SCOTT M., LI X., SEDERBERG T., HUGHES T., 2012, Local refinement of analysis-suitable T-splines, *Computer Methods in Applied Mechanics and Engineering*, **213**, 206-222
42. SEDERBERG T.W., CARDON D.L., FINNIGAN G.T., NORTH N.S., ZHENG J., LYCHE T., 2004, T-spline simplification and local refinement, *ACM Transactions on Graphics (TOG)*, **23**, 276-283
43. SEDERBERG T.W., ZHENG J., BAKENOV A., NASRI A., 2003, T-splines and T-NURCCs, *ACM Transactions on Graphics (TOG)*, **22**, 477-484
44. SUKUMAR N., HUANG Z., PRÉVOST J.H., SUO Z., 2004, Partition of unity enrichment for bimaterial interface cracks, *International Journal for Numerical Methods in Engineering*, **59**, 1075-1102
45. SUN C.T., JIH C., 1987, On strain energy release rates for interfacial cracks in bi-material media, *Engineering Fracture Mechanics*, **28**, 13-20
46. TADA H., PARIS P., IRWIN G., 2000, *The Analysis of Cracks Handbook*, ASME Press 2, 1, New York, USA
47. TEMIZER I., WRIGGERS P., HUGHES T., 2011, Contact treatment in isogeometric analysis with NURBS, *Computer Methods in Applied Mechanics and Engineering*, **200**, 1100-1112
48. VERHOESEL C.V., SCOTT M.A., DE BORST R., HUGHES T.J., 2011, An isogeometric approach to cohesive zone modeling, *International Journal for Numerical Methods in Engineering*, **87**, 336-360

49. WILLIAMS M., 1959, The stresses around a fault or crack in dissimilar media, *Bulletin of the Seismological Society of America*, **49**, 199-204
50. YAU J., WANG S., 1984, An analysis of interface cracks between dissimilar isotropic materials using conservation integrals in elasticity, *Engineering Fracture Mechanics*, **20**, 423-432
51. YUUKI R., XU J.-Q., 1994, Boundary element analysis of dissimilar materials and interface crack, *Computational Mechanics*, **14**, 116-127
52. ZHOU Z., XU X., LEUNG A.Y., HUANG Y., 2013, Stress intensity factors and T-stress for an edge interface crack by symplectic expansion, *Engineering Fracture Mechanics*, **102**, 334-347
53. ZHOU Z.H., LEUNG A.Y.T., XU X.S., 2014, The finite element discretized symplectic method for interface cracks, *Composites Part B: Engineering*, **58**, 335-342

Manuscript received March 7, 2016; accepted for print May 5, 2016

THE CONSTITUENT EQUATIONS OF PIEZOELECTRIC CANTILEVERED THREE-LAYER ACTUATORS WITH VARIOUS EXTERNAL LOADS AND GEOMETRY

GRZEGORZ MIECZKOWSKI

Białystok University of Technology, Białystok, Poland

e-mail: g.mieczkowski@pb.edu.pl

This paper presents test results for deformation conditions of three-layer, piezoelectric cantilever converters subjected to various electrical and mechanical boundary conditions. A general solution has been developed based on implementation of piezoelectric triple segments (*PTS*) to the beam. A working mechanism and conditions for strain of the *PTS* segment have been determined. Basing on the general solution, for the cantilever actuator subjected to an external force (of single and dual *PTS* segments) and a uniform load (of single *PTS* segment), particular solutions have also been developed. Moreover, dimensionless frequencies of the oscillating motion for the analyzed converters have been determined. In the next step, the influence of such factors as length, quantity and position of *PTS* segments, their relative stiffness and unit weight on values of the obtained frequencies of vibration have been defined. The resulting analytical solutions have been compared with the developed FEM solution.

Keywords: piezoelectric bender, constitutive equations, deflection, analytical solutions

1. Introduction

Piezoelectric transducers have been used over the years in many devices. These are exploited as sensors (Ștefănescu, 2011), actuators (Tzou, 1999), energy harvesters (Liu *et al.*, 2014) or dynamic eliminators (Przybyłowicz, 1999). Their working principle is based on the conversion of electric energy to mechanical or other way around (Bush-Vishniac, 1999). The relation between strain and electric field is defined by constitutive equations ((Curie and Curie, 1880; Berlincourt *et al.*, 1964).

A significant aspect influencing the functionality and durability of converters is selection of a proper piezoelectric material. The properties of typical piezoelectric materials are presented in papers by Kawai (1969), Rajabi *et al.* (2015).

Another important factor is a static characteristic of the converter. When designing piezoelectric converters for specific application, it is necessary to define and solve adequate simultaneous equations. These equations bound together geometrical properties, material properties and physical parameters such as force, deflection and electric field. Solving such simultaneous equations is very difficult. Materials and geometrical inhomogeneity of the converter global structure and anisotropy of piezoelectric materials forces the use of some reductions. Smits *et al.* (1991), by using energetic methods, formed and solved constitutive equations for a converter made of two layers of even length (piezoelectric bimorph). In the paper by Wang and Cross (1999) there is an issue of a three-layer converter extended and solved, whereas in (Xiang and Shi, 2008) – a multi-layer one. The static characteristics of two-layer converters with different length of layers are shown in (Park and Moon, 2005; Raeisifard *et al.*, 2014; Mieczkowski, 2016).

Piezoelectric converters as well as other elastic bodies having mass are prone to vibrations. Therefore, it is necessary to define the nature of their oscillating motion. Many authors have

dealt with this issue. Chen *et al.*(1998), Askari Farsangi *et al.* (2013) studied free vibrations of piezoelectric laminated plates presented, whereas Clare *et al.* (1991) analysed a simply supported beam with piezoelectric patches. Also, analyses of dynamic characteristics of transducers where forced vibration occurred are shown in papers by Rouzegar and Abad (2015), Bleustein and Tiersten (1968), Djodjodhardjo *et al.* (2015). Dynamical aspects of converters with the piezoelectric patches, including control strategy, were considered by Tylikowski (1993), Pietrzakowski (2000, 2001), Buchacz and Płaczek (2009).

It is a very rare case that in literature one can find results of tests describing the influence of geometrical and material characteristics, number and location of piezoelectric patches on static deflection and free vibration.

In such cases, in order to determine electromechanical behaviour of the converter, usually the FEM-based analyses are carried out, see (Rahmoune and Osmont, 2010; Mieszczak *et al.*, 2006). However, carrying out this type of analyses is very work-consuming and the solution may be subjected to high error.

Therefore, the main purpose of the present paper is to develop a simple analytical method for determining deflection in function of mechanical and electric loads. By design, the piezoelectric converters have individual components (layers) of different length and the piezoelectric layer can be divided, which is an extension to the researches shown in papers by Smits *et al.* (1991), Wang and Cross (1999), Xiang and Shi (2008), where lengths of the beam element and piezoelectric layers were equal, see Fig. 1.

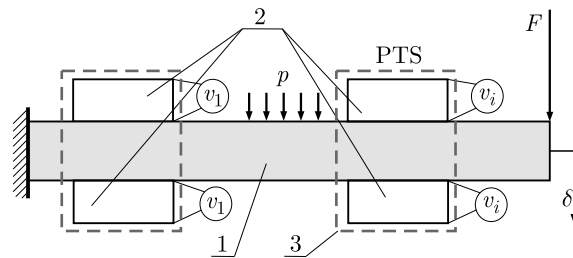


Fig. 1. Three-layer piezoelectric converter, 1 – beam, 2 – piezoelectric elements, 3 – piezoelectric triple segment *PTS*

The proposed method involves the implementation of modules to a homogeneous beam, further referred to as the piezoelectric triple segment (*PTS*). This allows including a local change in stiffness and strain caused by the transverse piezoelectric effect within the analytical description of the beam deflection.

In view of material and geometric discontinuity in the analyzed transducers, natural frequencies of oscillating motion turn out to be different than those in the homogeneous beam. Therefore, the next aim of the paper is analysis of dynamical behavior of such converters. In the present work, examination similar to that carried out by Clare *et al.* (1991) is conducted. It is extended by analysis of the influence of the number, length and location of piezoelectric segments and their material properties on the natural frequency values.

In order to verify the correctness of the solutions, it is required to compare the obtained results with experimental data or results obtained using other methods. Therefore, for converters with the diversified material and geometric structure, FEM simulations have been made and compared with the obtained analytical results.

2. Analytical results

2.1. Basic assumptions

The converters analysed in this work are treated as a homogeneous (one-layer) beam with locally implemented piezoelectric triple segments *PTS* (Fig. 1). The *PTS* is made up of three components – two piezoelectric and one non-piezoelectric element. The non-piezoelectric layer thickness is the same as the beam thickness. The beam and the *PTS* both have the same width. In order to simplify the mathematical model, the following assumptions are made:

- bending of the element takes place according to Euler's hypothesis, and radii of curvatures of the deflected components are identical,
- in the connection plane between components there is no intermediate layer and no sliding occurs,
- in the piezoelectric layer, the transverse piezoelectric effect 1-3 takes place causing clear bending.

2.2. General solution to the piezoelectric converter with implemented *PTS* segment

The task is to consider a section of the piezoelectric converter (Fig. 2) subjected to mechanical bending moment $M(x)$ and electric moment M_e (following the occurrence of the piezoelectric effect).

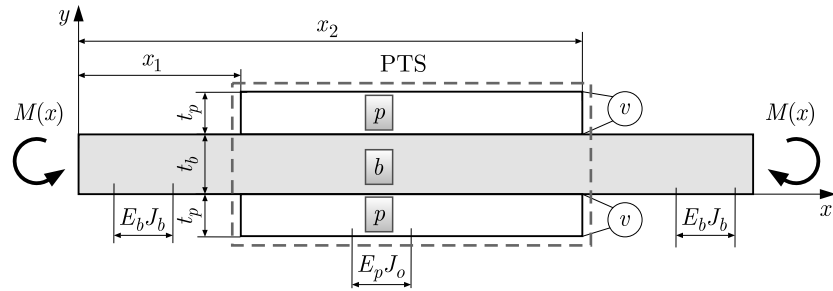


Fig. 2. Section of the piezoelectric converter

In the analysed element subjected to bending, it is possible to determine three characteristic ranges related to a change in load and stiffness. Within the $x_1 < x < x_2$ range, there is a piezoelectric triple segment *PTS* (generating M_e) with flexural stiffness $E_p J_o$. The other two ranges are a homogeneous beam with stiffness $E_b J_b$. Since there are several characteristic ranges on the beam, it is convenient to make use of Heaviside's function. Thus, including the *PTS* presence in the beam, the deflection line can be described using the following dependence

$$\frac{\partial^2 y}{\partial x^2} = \frac{M(x)}{E_b J_b} + M_e \gamma (H[x - x_1] - H[x - x_2]) \quad (2.1)$$

where: $H[x - x_i]$ – Heaviside's function, E_p , E_b – Young's moduli of the piezoelectric and non-piezoelectric element, J_b , J_o – moments of inertia (described in Section 2.3), γ – factor including the change in stiffness with applied formal notation of Heaviside's function

$$\gamma = \frac{E_b J_b [M_e + M(x)] - E_p J_o M(x)}{E_b J_b E_p J_o M_e}$$

As determining the mechanical moment $M(x)$ in general does not pose any problems, determining the electrical load M_e generated by the *PTS* is very burdensome and requires solving the two-dimension problem of the *PTS* bending.

2.3. Piezoelectric triple segment *PTS*

The task is to consider the segment *PTS* (Fig. 3) with constant width b consisting of non-piezoelectric (2) and piezoelectric layers (1) and (3).

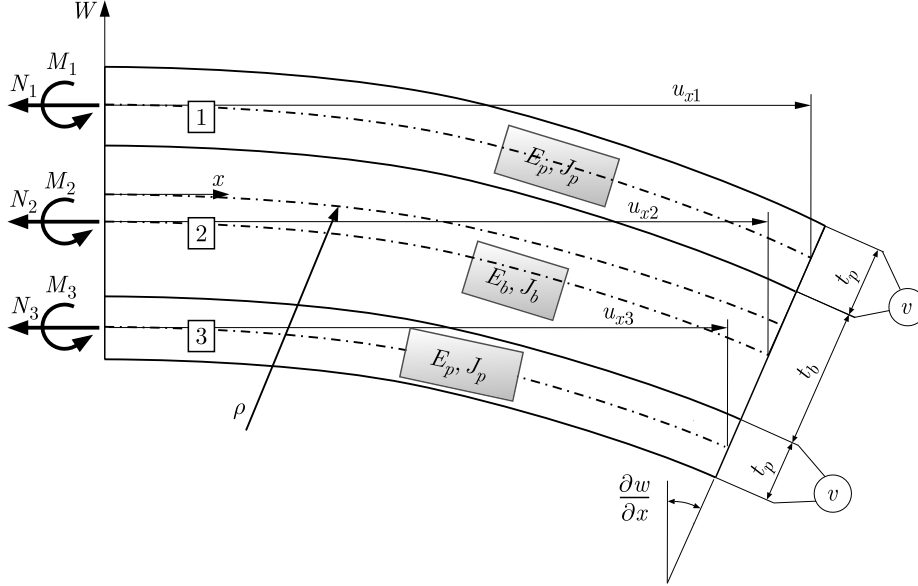


Fig. 3. Distribution of forces and conditions for strain of the piezoelectric triple segment *PTS*

The structure is not subjected to any mechanical load. The longitudinal forces N_i and bending moments M_i occurring in individual layers are a result of the applied voltage v . Basing on the equilibrium equation of forces, the following can be written

$$N_1 + N_2 + N_3 = 0 \quad (2.2)$$

The sum of moments in relation to the upper interface must be zero, therefore

$$M_1 + M_2 + M_3 - \frac{N_2 t_b}{2} - N_3 \left(t_b + \frac{t_p}{2} \right) + \frac{N_1 t_p}{2} = 0 \quad (2.3)$$

According to the adopted Euler hypothesis, bending moments can be described as follows

$$M_1 = \frac{E_p}{J_p} \rho \quad M_2 = \frac{E_b}{J_b} \rho \quad M_3 = \frac{E_p}{J_p} \rho \quad (2.4)$$

Substituting dependences (2.4) to (2.3) and making simple transformations results in the following

$$\frac{1}{\rho} = \frac{(N_2 + 2N_3)t_b + (N_3 - N_1)t_p}{2E_b J_b + 4E_p J_p} \quad (2.5)$$

Including the relation between the radius of curvature ρ and deflection $w(x)$

$$\frac{1}{\rho} = \frac{\partial^2 w}{\partial x^2} \quad (2.6)$$

the differential equation for the converter bending can be found as follows

$$\frac{\partial^2 w}{\partial x^2} = \frac{(N_2 + 2N_3)t_b + (N_3 - N_1)t_p}{2E_b J_b + 4E_p J_p} \quad (2.7)$$

The constitutive equations for all converter layers, including the piezoelectric effect in layer 1 and 3 give the following

$$\frac{\partial u_{x1}}{\partial x} = \frac{N_1}{E_p A_p} - d_{31} \left(\frac{-v}{t_p} \right) \quad \frac{\partial u_{x2}}{\partial x} = \frac{N_2}{E_b A_b} \quad \frac{\partial u_{x3}}{\partial x} = \frac{N_3}{E_p A_p} + d_{31} \left(\frac{-v}{t_p} \right) \quad (2.8)$$

where $A_b = t_b b$, $A_p = t_p b$ are layers cross sectional areas, d_{31} – piezoelectric constant.

Following the relocation continuity condition (Fig. 3), it is found that

$$u_{x1} - u_{x2} - \frac{\partial w}{\partial x} \left(\frac{t_p}{2} + \frac{t_b}{2} \right) = 0 \quad u_{x1} - u_{x3} - \frac{\partial w}{\partial x} \left(\frac{t_p}{2} + \frac{t_b}{2} + t_b \right) = 0 \quad (2.9)$$

Solving differential equations (2.7) and (2.8) with the following boundary conditions

$$\begin{aligned} \frac{\partial w}{\partial x}(0) &= 0 & w(0) &= 0 \\ u_{x1}(0) &= 0 & u_{x2}(0) &= 0 & u_{x3}(0) &= 0 \end{aligned} \quad (2.10)$$

and applying dependence (2.9) and (2.2), the longitudinal force N_i can be determined

$$N_1 = \frac{-b E_p v d_{31} (E_b t_b^3 + 2 E_p t_p^3)}{\alpha} \quad N_2 = 0 \quad N_3 = \frac{b E_p v d_{31} (E_b t_b^3 + 2 E_p t_p^3)}{\alpha} \quad (2.11)$$

where: $\alpha = E_b t_b^3 - 2 E_p t_p (3 t_b^2 + 6 t_b t_p + 2 t_p^2)$.

The differential equation for bending *PTS* in the M_e moment function can be written as follows

$$\frac{\partial^2 w}{\partial x^2} = \frac{-2 M_e}{E_p J_o} \quad (2.12)$$

On the basis of comparing equations (2.7) and (2.12), it is possible to determine the bending moment M_e which results from the piezoelectric effect

$$M_e = \frac{E_p J_o [-(N_2 + 2 N_3) t_b + (N_1 - N_3) t_p]}{4 E_b J_b + 8 E_p J_p} \quad (2.13)$$

where moments of inertia for the individual layers are, respectively

$$J_b = \frac{b t_b^3}{12} \quad J_p = \frac{b t_p^3}{12} \quad (2.14)$$

The averaging value of the moment of inertia J_o can be calculated using the method of transformation of the cross sectional area (Fertis, 1996). Three materials of different stiffness moduli and the same width b (Fig. 4a) are replaced with one material of the section composed of three parts of different widths (Fig. 4b).

The sought moment of inertia, calculated in relation to the neutral layer, is

$$J_o = \frac{b \beta}{12 E_p} \quad (2.15)$$

where: $\beta = E_b t_b^3 + 2 E_p t_p (3 t_b^2 + 6 t_b t_p + 4 t_p^2)$.

Substituting formula (2.13) with (2.11), (2.14) and (2.15) results in the electric bending moment value in function of the applied voltage v

$$M_e = - \frac{b E_p v \beta d_{31} (t_b + t_p)}{2 \alpha} \quad (2.16)$$

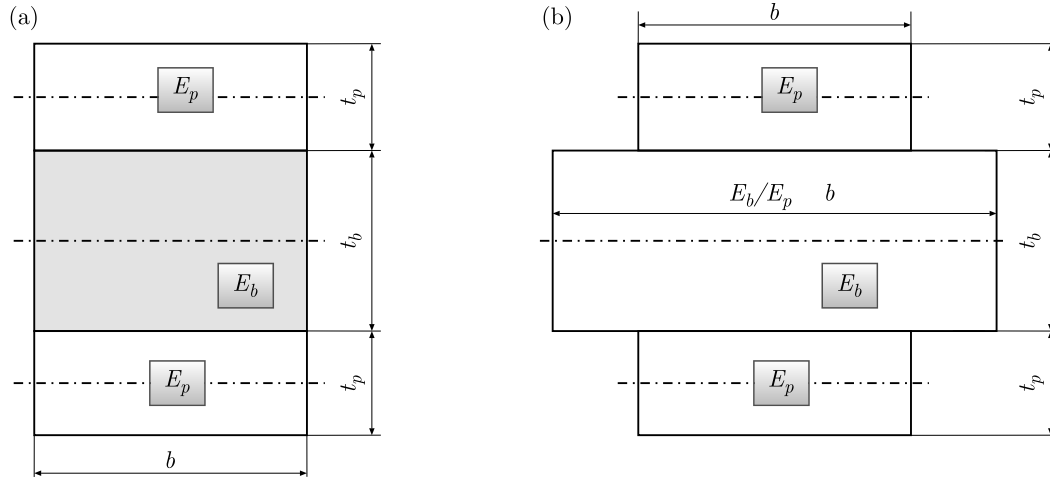


Fig. 4. Original (a) and transformed (b) section in the piezoelectric triple segment *PTS*

2.4. Particular solutions

This part of the work is concerned with the application of the proposed method based on implementing *PTS* segments into the single-layer beam to determine analytical dependences describing bending of the converters of fixed geometry and known boundary conditions. Solutions for the converters of different external loads and the *PTS* number shall be presented.

2.4.1. Cantilever converter subjected to concentrated force F of a single *PTS* segment

In the converter, as shown in Fig. 5, the left end is fixed and the right end can move freely. The load results from the external force F and the electric moment M_e is generated by the applied voltage v . Based on the conditions for equilibrium of forces and moments, the reactions in the mounting are established: $R_y = F$, $R_x = 0$, $M_F = FL$.

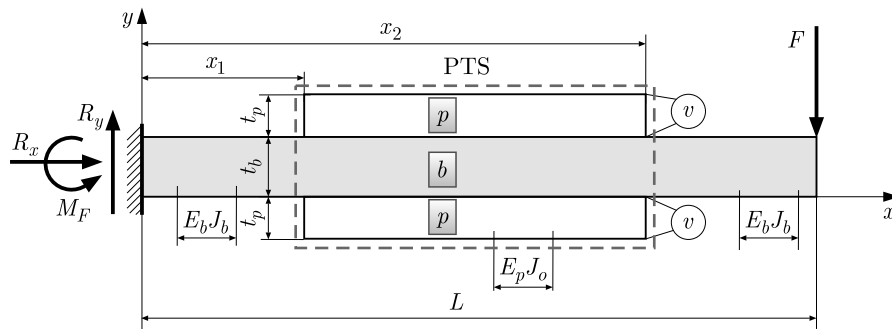


Fig. 5. Cantilever converter of the single *PTS* segment

The mechanical moment $M(x)$ takes the following form

$$M(x) = -M_F + R_y x = -FL + Fx \quad (2.17)$$

Substituting expressions (2.16) and (2.17) to the general solution described with formula (2.1), upon double integration gives a dependence describing the function of bending of the analysed converter

$$y(x) = A_1 v + B_1 F \quad (2.18)$$

where

2.4.3. Cantilever converter subjected to uniform external load p of the single PTS segment

In the actuator shown in Fig. 7, the conditions of mounting are identical as those described in Sections 2.4.1 and 2.4.2. The converter is acted on by a uniform load p . The electrical moment is generated by a single *PTS* located at the left end.

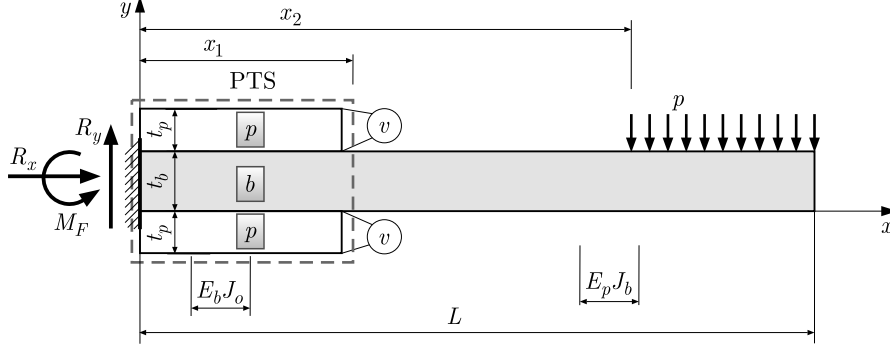


Fig. 7. Cantilever converter of a single *PTS* segment

Based on the conditions for equilibrium of forces and moments, the reactions in the mounting are determined: $R_y = p(L - x_2)$, $M_F = 0.5p(L - x_2)(L + x_2)$. The mechanical moment $M(x)$ takes the following form

$$M(x) = R_y x - M_F - \frac{p(x - x_2)^2}{2} H[x - x_2] \quad (2.23)$$

Solving differential equation (2.1), assuming mechanical (2.23) and electric (2.16) moments gives the equation describing deflection of the analysed converter

$$y(x) = A_3 v + B_3 p \quad (2.24)$$

where

$$\begin{aligned} A_3 &= \frac{-3d_{31}E_p(t_b + t_p)}{\alpha} \left(H[x]x^2 - Hx - x_1^2 \right) \\ B_3 &= \frac{1}{2b\beta E_b t_b^3} \left\{ (\beta - E_b t_b^3) \right. \\ &\quad \cdot \left(H[x - x_1](Hx - x_2^4 + 2(x - x_1)^2(L - x_2)(3L - 2x + 3x_2)) \right. \\ &\quad \left. - H[x](Hx - x_2^4 + 2x^2(L - x_2)(3L - 2x + 3x_2)) \right) \\ &\quad \left. + \beta \left(Hx - x_2^4 + 2x^2(L - x_2)(3L - 2x + 3x_2) \right) \right\} \end{aligned}$$

Integration constants are determined on the basis of the following boundary conditions

$$\frac{\partial y}{\partial x}(0) = 0 \quad y(0) = 0 \quad (2.25)$$

2.5. Dynamical behavior of piezoelectric converters

As mentioned before, piezoelectric transducers similarly to other elastic bodies having mass, are prone to vibrations. In this respect, it is advised to include its oscillating nature of motion in the process of designing and exploitation of piezoelectric structures. Generally, vibrations can be divided into two groups – free and forced. Free vibrations occur when external forces do not influence the body and the system vibrates due to action of inherent forces. In that case, the

system is going to vibrate with one or more natural frequencies. In vibrating systems natural damping occurs caused by forces of the internal friction. Damping is usually slight, thus does not affect the natural frequencies.

In the case when vibrations are caused by external forces, there appear the so called forced vibrations, and the system is going to vibrate with the excitation frequency.

The phenomenon of resonance is greatly dangerous for a structure. It occurs when the excitation frequency coincides with one of the natural frequencies which causes perilously high oscillations that may lead to damaging of the structure. Therefore, it is necessary to determine the natural frequencies and geometrical and material factors affecting their distribution.

Upon elementary theory of bending beams, equation (1) can be presented in the following way

$$\frac{\partial^2}{\partial x^2} \left(E(x)J(x) \frac{\partial^2 y}{\partial x^2} \right) + \rho(x)A(x) \frac{\partial^2 y}{\partial t^2} = \frac{\partial^2 M(x)}{\partial x^2} + M_e(\delta'[x - x_1] - \delta'[x - x_2]) \quad (2.26)$$

where $\delta[x - xi]$, $E(x)$, $J(x)$, $\rho(x)$, $A(x)$ is the derivative of Dirac's function, Young's modulus, moment of inertia, density and cross sectional area of the converter. For free vibration, the exactly same differential equation can be written in the following way

$$\frac{\partial^2}{\partial x^2} \left(E(x)J(x) \frac{\partial^2 y}{\partial x^2} \right) + \rho(x)A(x) \frac{\partial^2 y}{\partial t^2} = 0 \quad (2.27)$$

The solution to equation (2.27) using the method of separation of variables can be written in the following way

$$y(x, t) = W(x)T(t) \quad (2.28)$$

where $W(x)$ is a function of space, and $T(t)$ depends only on time. Substituting (2.28) with (2.27) and performing simple mathematical modifications, the commonly known differential equation describing the beam boundary problem is obtained

$$\frac{\partial^2}{\partial x^2} \left(E(x)J(x) \frac{\partial^2 W}{\partial x^2} \right) - \rho(x)A(x)\omega^2 = 0 \quad (2.29)$$

where ω is the natural frequency of vibration.

Let us consider the piezoelectric transducer shown in Fig. 8.

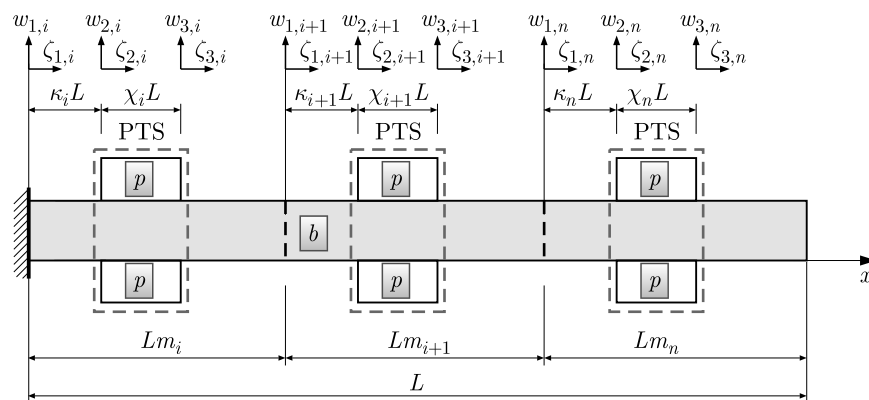


Fig. 8. Cantilever converter of n PTS segment

There can be n fragments distributed on the transducer whose total length is equal to $\sum_{i=1}^n Lm_i = L$. Each and every fragment consists of three elements – a PTS segment and

two beam elements. Applying local frames of reference, using the dimensionless coordinates, differential equation (2.29) is equivalent to

$$\begin{aligned} \frac{\partial^4 W_{1,i}(\zeta_{1,i})}{\partial \zeta_{1,i}^4} - \psi^4 W_{1,i}(\zeta_{1,i}) &= 0 & \text{for } \zeta_{1,i} \in \langle 0, \kappa_i \rangle \\ \frac{\partial^4 W_{2,i}(\zeta_{2,i})}{\partial \zeta_{2,i}^4} - \Lambda^4 \psi^4 W_{2,i}(\zeta_{2,i}) &= 0 & \text{for } \zeta_{2,i} \in \langle 0, \chi_i \rangle \\ \frac{\partial^4 W_{3,i}(\zeta_{3,i})}{\partial \zeta_{3,i}^4} - \psi^4 W_{3,i}(\zeta_{3,i}) &= 0 & \text{for } \zeta_{3,i} \in \langle 0, \frac{Lm_i}{L} - \kappa_i - \chi_i \rangle \end{aligned} \quad (2.30)$$

where

$$\begin{aligned} \psi^4 &= L^4 \omega^2 \frac{\rho_b A_b}{E_b J_b} & \Lambda^4 &= \frac{E_b J_b \rho_b A_b + 2\rho_p A_p}{\rho_b A_b E_p J_o} \\ \zeta_{1,i} &= \frac{x}{L} & \zeta_{2,i} &= \frac{x - \kappa_i L}{L} & \zeta_{3,i} &= \frac{x - \kappa_i L - \chi_i L}{L} \\ \zeta_{1,i+1} &= \frac{x - Lm_i}{L} & & & & i = 1, \dots, n \end{aligned}$$

ω is the natural frequency, ρ_b , ρ_p is density of beam and piezoelectric material, respectively.

Solutions to differential equations (2.30) can be obtained as (Mahmoud and Nassar, 2000)

$$\begin{aligned} W_{1,i}(\zeta_{1,i}) &= A_{1,i} \sin(\psi \zeta_{1,i}) + B_{1,i} \cos(\psi \zeta_{1,i}) + C_{1,i} \cosh(\psi \zeta_{1,i}) + D_{1,i} \sinh(\psi \zeta_{1,i}) \\ W_{2,i}(\zeta_{2,i}) &= A_{2,i} \sin(\Lambda \psi \zeta_{2,i}) + B_{2,i} \cos(\Lambda \psi \zeta_{2,i}) + C_{2,i} \cosh(\Lambda \psi \zeta_{2,i}) + D_{2,i} \sinh(\Lambda \psi \zeta_{2,i}) \\ W_{3,i}(\zeta_{3,i}) &= A_{3,i} \sin(\psi \zeta_{3,i}) + B_{3,i} \cos(\psi \zeta_{3,i}) + C_{3,i} \cosh(\psi \zeta_{3,i}) + D_{3,i} \sinh(\psi \zeta_{3,i}) \end{aligned} \quad (2.31)$$

where $A_{j,i}$, $B_{j,i}$, $C_{j,i}$, $D_{j,i}$, $j = 1, 2, 3$ are constants.

The boundary conditions of mounting of the converter (left end is fix-mounted and the right one freely move) together with continuity conditions at the intermediate ends lead to a set $n \times 12$ linear homogeneous equations.

The continuity conditions adopt the following form

$$\begin{aligned} W_{1,i}(\zeta_{1,i}) \Big|_{\zeta_{1,i}=\kappa_i} &= W_{2,i}(\zeta_{2,i}) \Big|_{\zeta_{2,i}=0} & \frac{\partial W_{1,i}(\zeta_{1,i})}{\partial \zeta_{1,i}} \Big|_{\zeta_{1,i}=\kappa_i} &= \frac{\partial W_{2,i}(\zeta_{2,i})}{\partial \zeta_{1,i}} \Big|_{\zeta_{2,i}=0} \\ \frac{\partial^2 W_{1,i}(\zeta_{1,i})}{\partial \zeta_{1,i}^2} \Big|_{\zeta_{1,i}=\kappa_i} &= \eta \frac{\partial^2 W_{2,i}(\zeta_{2,i})}{\partial \zeta_{2,i}^2} \Big|_{\zeta_{2,i}=0} \\ \frac{\partial^3 W_{1,i}(\zeta_{1,i})}{\partial \zeta_{1,i}^3} \Big|_{\zeta_{1,i}=\kappa_i} &= \eta \frac{\partial^3 W_{2,i}(\zeta_{2,i})}{\partial \zeta_{2,i}^3} \Big|_{\zeta_{2,i}=0} \\ W_{2,i}(\zeta_{2,i}) \Big|_{\zeta_{2,i}=\chi_i} &= W_{3,i}(\zeta_{3,i}) \Big|_{\zeta_{3,i}=0} & \frac{\partial W_{2,i}(\zeta_{2,i})}{\partial \zeta_{2,i}} \Big|_{\zeta_{2,i}=\chi_i} &= \frac{\partial W_{3,i}(\zeta_{3,i})}{\partial \zeta_{3,i}} \Big|_{\zeta_{3,i}=0} \\ \eta \frac{\partial^2 W_{2,i}(\zeta_{2,i})}{\partial \zeta_{2,i}^2} \Big|_{\zeta_{2,i}=\chi_i} &= \frac{\partial^2 W_{3,i}(\zeta_{3,i})}{\partial \zeta_{3,i}^2} \Big|_{\zeta_{3,i}=0} \\ \eta \frac{\partial^3 W_{2,i}(\zeta_{2,i})}{\partial \zeta_{2,i}^3} \Big|_{\zeta_{2,i}=\chi_i} &= \frac{\partial^3 W_{3,i}(\zeta_{3,i})}{\partial \zeta_{3,i}^3} \Big|_{\zeta_{3,i}=0} \end{aligned} \quad (2.32)$$

$$\begin{aligned}
W_{3,i}(\zeta_{3,i}) \Big|_{\zeta_{3,i}=\phi_i} &= W_{1,i+1}(\zeta_{1,i+1}) \Big|_{\zeta_{1,i+1}=0} \\
\frac{\partial W_{3,i}(\zeta_{3,i})}{\partial \zeta_{3,i}} \Big|_{\zeta_{3,i}=\phi_i} &= \frac{\partial W_{1,i+1}(\zeta_{1,i+1})}{\partial \zeta_{1,i+1}} \Big|_{\zeta_{1,i+1}=0} \\
\frac{\partial^2 W_{3,i}(\zeta_{3,i})}{\partial \zeta_{3,i}^2} \Big|_{\zeta_{3,i}=\phi_i} &= \frac{\partial^2 W_{1,i+1}(\zeta_{1,i+1})}{\partial \zeta_{1,i+1}^2} \Big|_{\zeta_{1,i+1}=0} \\
\frac{\partial^3 W_{3,i}(\zeta_{3,i})}{\partial \zeta_{3,i}^3} \Big|_{\zeta_{3,i}=\phi_i} &= \frac{\partial^3 W_{1,i+1}(\zeta_{1,i+1})}{\partial \zeta_{1,i+1}^3} \Big|_{\zeta_{1,i+1}=0}
\end{aligned}$$

where

$$\eta = \frac{E_p J_o}{E_b J_b} \quad \phi_i = \frac{L m_i}{L} - \kappa_i - \chi_i$$

The boundary conditions can be written as follows:

— fixed

$$W_{1,1}(\zeta_{1,1}) = 0 \Big|_{\zeta_{1,1}=0} \quad \frac{\partial W_{1,1}(\zeta_{1,1})}{\partial \zeta_{1,1}} = 0 \Big|_{\zeta_{1,1}=0} \quad (2.33)$$

— free

$$E_b J_b \frac{\partial^2 W_{3,n}(\zeta_{3,n})}{\partial \zeta_{3,n}^2} = 0 \Big|_{\zeta_{3,n}=\frac{L m_n}{L} - \kappa_n - \chi_n} \quad E_b J_b \frac{\partial^3 W_{3,n}(\zeta_{3,n})}{\partial \zeta_{3,n}^3} = 0 \Big|_{\zeta_{3,n}=\frac{L m_n}{L} - \kappa_n - \chi_n} \quad (2.34)$$

Using dependences (2.31)-(2.34), as mentioned before, $n \times 12$ linear homogenous equation can be achieved.

The values of dimensionless frequencies ψ are determined from the characteristic equation representing the zero determinant of the matrix of boundary conditions $\mathbf{M}^{12n \times 12n}$

$$\mathbf{M}^{12n \times 12n} = \begin{bmatrix} \mathbf{M}_i^{12 \times 12} & \mathbf{B}^{12 \times 12} & \dots & \mathbf{0}^{12 \times 12} \\ \mathbf{C}_i^{12 \times 12} & \mathbf{M}_{i+1}^{12 \times 12} & \dots & \mathbf{0}^{12 \times 12} \\ \vdots & \vdots & \ddots & \mathbf{B}^{12 \times 12} \\ \mathbf{0}^{12 \times 12} & \mathbf{0}^{12 \times 12} & \mathbf{C}_{n-1}^{12 \times 12} & \mathbf{M}_n^{12 \times 12} \end{bmatrix} \quad (2.35)$$

where $\mathbf{0}^{12 \times 12}$ is the zero matrix, $\mathbf{M}_i^{12 \times 12} = \begin{bmatrix} \mathbf{M}_{1,i}^{12 \times 4} & \mathbf{M}_{2,i}^{12 \times 4} & \mathbf{M}_{2,i}^{12 \times 4} \end{bmatrix}$, the remaining matrices are shown in Appendix. For the transducer with one segment, matrix (2.35) simplifies to the following form

$$\mathbf{M}^{12 \times 12} = \begin{bmatrix} \mathbf{M}_{1,1}^{12 \times 4} & \mathbf{M}_{2,1}^{12 \times 4} & \mathbf{M}_{2,1}^{12 \times 4} \end{bmatrix} \quad (2.36)$$

An analytical form of the characteristic equation ($|\mathbf{M}^{12n \times 12n}| = 0$) in special cases where $\sum_{i=1}^n \chi_i = 0$ (homogenous beam) and $\sum_{i=1}^n \chi_i = 1$ (*PTS* segment all along) is described from subsequent equations

$$1 + \cos \psi \cosh \psi = 0 \quad 1 + \cos(\Lambda \psi) \cosh(\Lambda \psi) = 0 \quad (2.37)$$

In other cases, in order to determine ψ , the roots of the characteristic equation can be obtained using numerical methods. In Figs. 9 and 10, there are dimensionless frequencies ψ presented in function of length of the piezoelectric layer for different locations and amount of *PTS* segments. The results achieved for the transducer with one *PTS* segment ($L m_1 = L$) are shown in Fig. 9, whereas for the transducer with two *PTS* segments ($L m_1 + L m_2 = L$, $L m_1 = L m_2$) are shown in Fig. 10. Furthermore, three variants of piezoelectric segment locations in the transducer have been examined. Namely:

- *PTS* segment located on the left end ($\kappa_i = 0$),
- transducer with *PTS* segment located in the middle ($\kappa_i + 0.5\chi_i = 0.25$),
- *PTS* segment located on the right end ($\kappa_i + \chi_i = 1$).

Moreover, in the transducer with two piezoelectric segments there are identical geometric and material features adopted for both *PTS* segments.

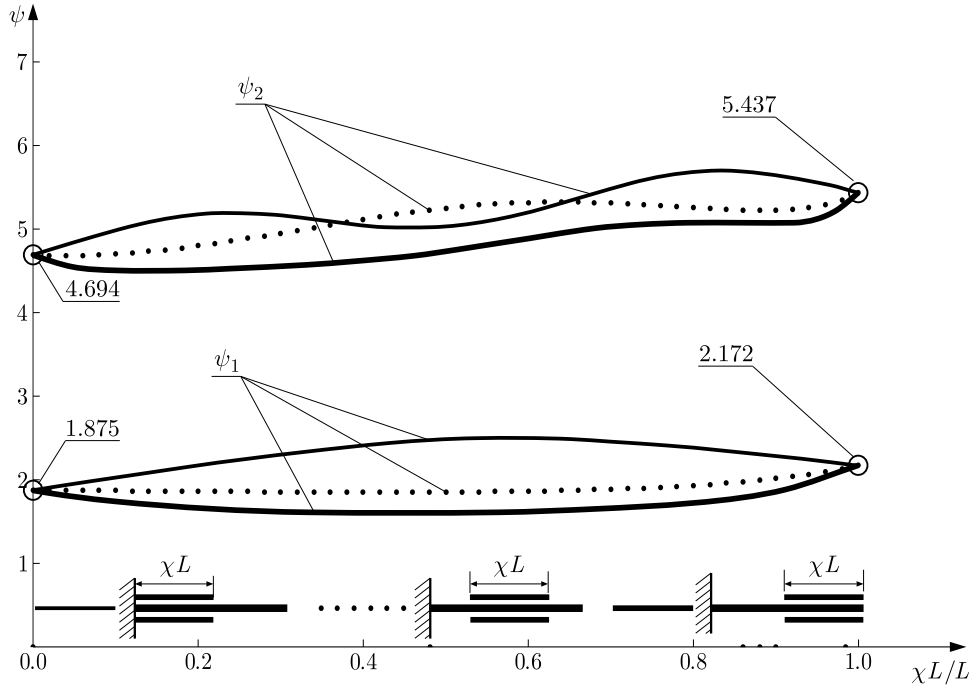


Fig. 9. The dimensionless frequencies ψ for the converter with a single *PTS* segment, ψ_1 – first frequency, ψ_2 – second frequency

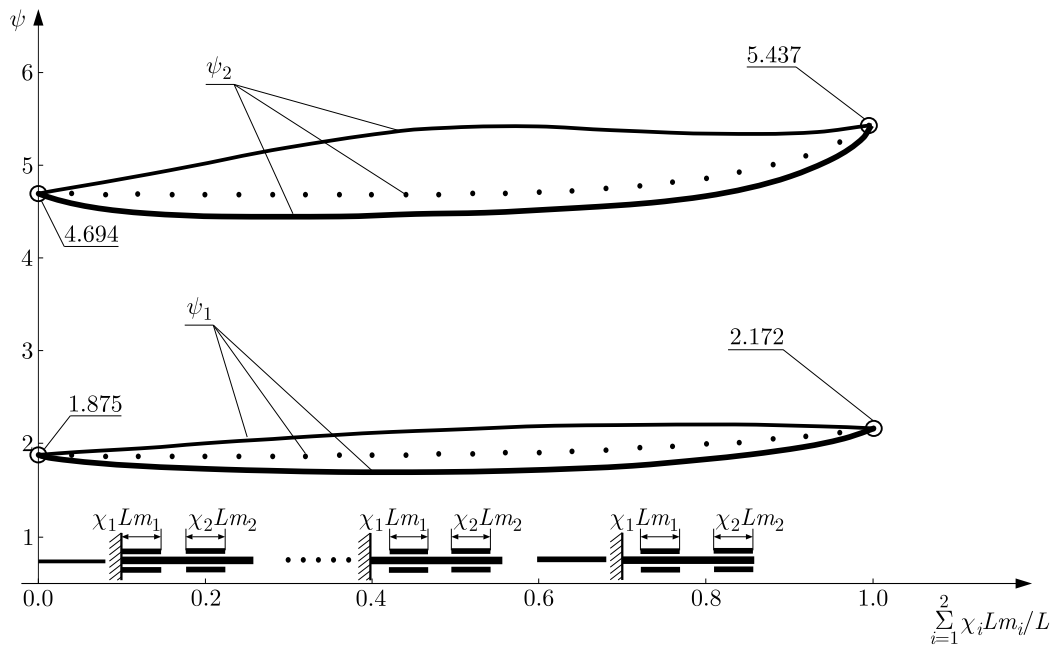


Fig. 10. The dimensionless frequencies ψ for the converter with a double *PTS* segment, ψ_1 – first frequency, ψ_2 – second frequency

Analyzing the obtained results, it can be stated that the highest values of the first dimensionless frequency, independent from *PTS* length, is acquired for the piezoelectric segment placed on the left end (Figs. 9 and 10). Similarly is with the second frequency for the converter with two segments. For the converter with one segment, the second frequency, depending on *PTS* length, takes the highest values for the converter with the segment placed either on the left end, or in the middle.

The dimensionless frequencies ψ depend on the relative stiffness η and the unit weight $\mu = (\rho_b A_b + 2\rho_p A_p)/(\rho_b A_b)$ of the beam and the *PTS* segment. In Figs. 11a and 11b, the influence of η and μ on the ψ value. Upon the received results, it can be stated that the dimensionless frequencies decrease with an increase in the parameters η (Fig. 11a) and μ (Fig. 11b).

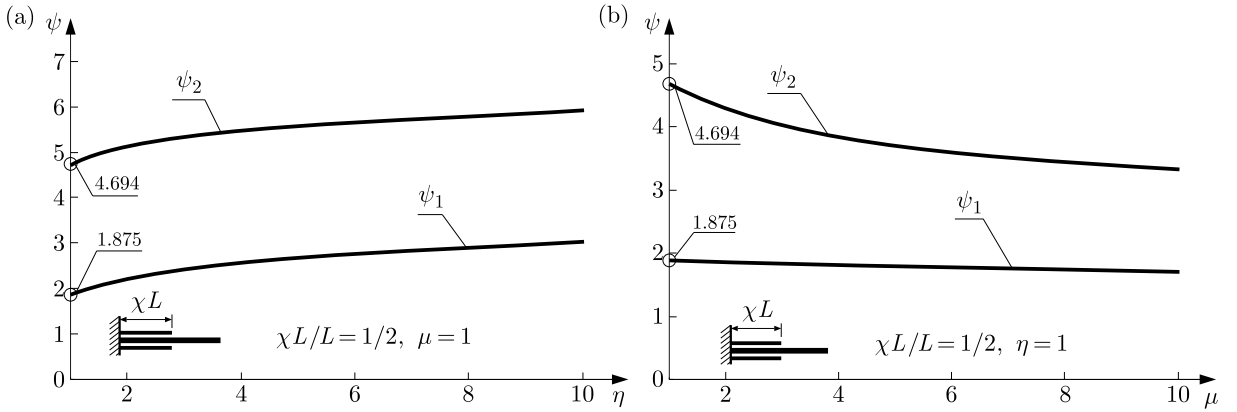


Fig. 11. The impact of relative stiffness (a) and relative unit (b) on the dimensionless frequency ψ for the converter with a single *PTS* segment, ψ_1 – first frequency, ψ_2 – second frequency

The circular frequency ω [Hz] of the transducer can be calculated from formula

$$\omega = \frac{\psi^2}{2\pi} \sqrt{\frac{E_b J_b}{\rho_b A_b L^4}} \quad (2.38)$$

3. Numerical calculations

To confirm the correctness of the obtained analytical solutions (static deflection of the transducer and circular frequencies), it is necessary to perform numerical analyses. FEM simulations have been prepared and compared with the obtained analytical results. Numerical tests aimed at determining the bending line and circular frequencies of the actuators for arbitrarily assumed material constants and geometry. The tested converters, shown in Figs. 5-7, have been modelled using the FEM with the help of ANSYS (Mieszczak *et al.*, 2006; Documentation for ANSYS, 2010). Plane components have been described using a grid of quadrangular, eight-node finite elements, with increased concentration at critical points such as sharp corners, mounting points and places at which the mechanical load was applied. For the piezoelectric component, PLANE223 type elements have been applied, and non-piezoelectric material has been meshed with PLANE183 elements with steel material properties. In view of the fact that the actuators are usually made of piezoelectric ceramics, PZ26 has been used as a material of the piezoelectric component. The size of finite elements was $t_p/4$. The plane issue has been solved for plane strain conditions.

In the calculations, the following geometrical and material data has been assumed: Young's modulus $E_p = 7.7 \cdot 10^{10}$ N/m², $E_b = 2.0 \cdot 10^{11}$ N/m²; Poisson's ratio $\nu_p = 0.3$, $\nu_b = 0.33$; density $\rho_p = 7700$ kg/m³, $\rho_b = 7860$ kg/m³; piezoelectric strain coefficients $d_{31} = -1.28 \cdot 10^{-10}$ m/V,

$d_{33} = 3.28 \cdot 10^{-10} \text{ m/V}$, $d_{15} = 3.27 \cdot 10^{-10} \text{ m/V}$; beam length $L = 60 \text{ mm}$; layers thickness $t_p = 0.5 \text{ mm}$, $t_b = 1 \text{ mm}$. The values of applied load are: electrode voltage $v = 100 \text{ V}$; force $F = 100 \text{ N}$; uniform external load $p = 100 \text{ N/m}$. Coordinates x_i , χ_i (Figs. 5-8), defining the *PTS* and external loads application positions are given in Section 4.

4. Results of tests

In this part of the work, the deflection line of converters for which the resulting special solutions are given in Section 2.4 are graphically presented. The results obtained from the analytical solutions have been compared with FEM solutions. In the analytical equations, the material and geometrical data are identical as the data given in Section 3 was applied.

A comparison of analytical solution (2.18) with FEM for the cantilever converter of the single *PTS* segment (Fig. 5) is shown in Fig. 12.

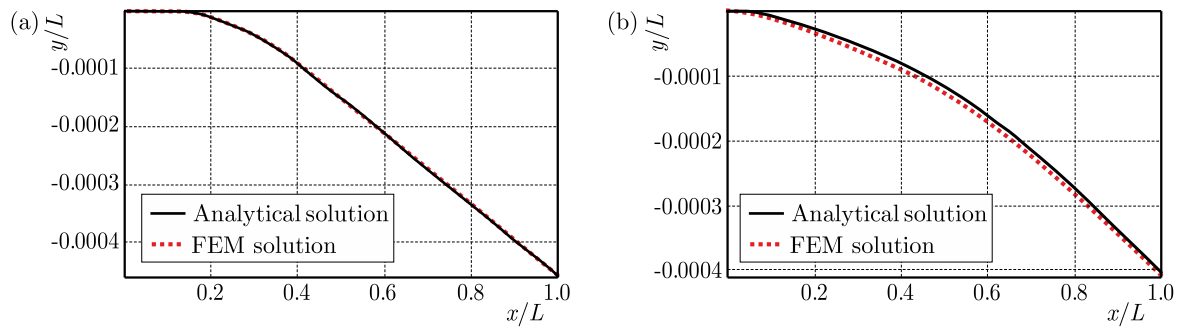


Fig. 12. Deflection of the cantilever converter with a single *PTS* segment for $x_1 = 1/12L$, $x_2 = 5/12L$: (a) subjected only to electrical voltage, $v = 100 \text{ V}$, $F = 0$; (b) subjected only to force, $v = 0 \text{ V}$, $F = 100 \text{ N}$

Figure 13 shows the deflection of the cantilever converter of double *PTS* segments (Fig. 6), for which the analytical solution is described by formula (2.22).

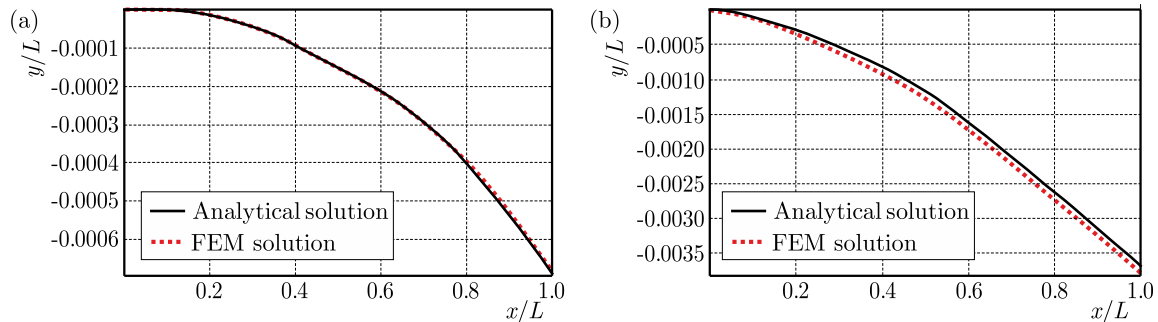


Fig. 13. Deflection of the cantilever converter with double *PTS* segments for $x_1 = 1/12L$, $x_2 = 5/12L$, $x_3 = 7/12L$, $x_4 = 11/12L$: (a) subjected only to electrical voltage, $v_1 = 100 \text{ V}$, $v_2 = 150 \text{ V}$, $F = 0$; (b) subjected only to force, $v_1 = v_2 = 0$, $F = 100 \text{ N}$

Figure 14 shows the strain of the cantilever converter subjected to a uniform external load p of the single *PTS* segment (Fig. 7) for which the analytical solution is described by formula (2.24).

Basing on the obtained results of static deflections of the converters, the qualitative and quantitative compliance of analytical and numerical solutions can be stated. Generally, the difference between the analytical and numerical solutions is approx. 1% for the electrical load, and 2-3% for the mechanical load.

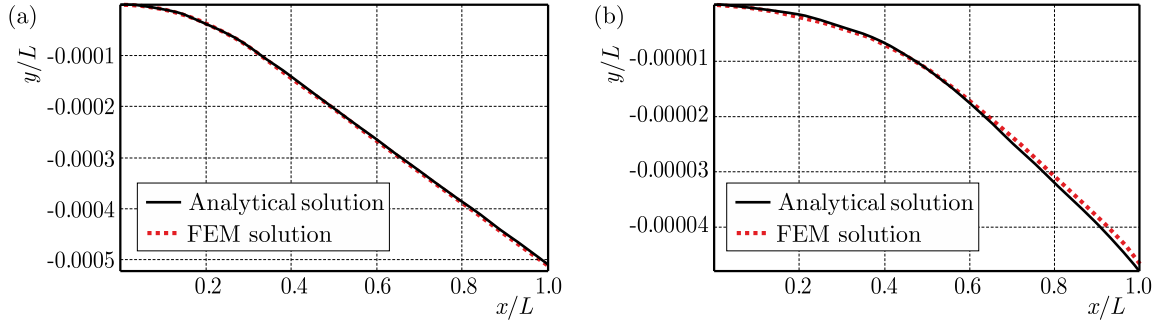


Fig. 14. Deflection of the cantilever converter subjected to a uniform external load p for $x_1 = 1/3L$, $x_2 = 2/3L$: (a) subjected only to electrical voltage, $v = -100$ V, $p = 0$; (b) subjected only to uniform external load, $v = 0$ V, $p = 100$ N/m

By means of FEM, it has been helpful to determine circular frequencies of the transducers with one (Fig. 7) and two (Fig. 6) *PTS* segments. The material and geometric data has been adopted identically as in the above-described static analysis. The obtained results (Table 1) have been compared to the analytical solution (formula (2.38) and Figs. 9 and 10).

Table 1. Comparison of the first two frequencies between the analytical and FEM results

Mode sequence	 $\chi = 1/3$			 $\sum_{i=1}^2 \chi_i = 2/3$		
	ω^* [Hz]	ω^{**} [Hz]	Error [%]	ω^* [Hz]	ω^{**} [Hz]	Error [%]
1	368.5	379.4	2.9	252.1	256.4	1.7
2	1799.8	1837.7	2.1	1575.4	1543.8	2

* – analytical solution, ** – FEM solution

In the dynamical analysis as well as in the static analysis, a satisfactory compatibility of both obtained solutions has been indicated. The disparity in these results ranges less than 3%.

5. Summary and conclusions

The paper deals with the issue of bending of three-layer piezoelectric actuators subjected to electric field and mechanical load. A general solution has been developed, based on the implementation of piezoelectric segments *PTS* to a homogeneous (one-layer) beam. The working mechanism and conditions for strain of the *PTS* segment have been determined. Basing on the general solution, for arbitrarily selected three different types of converters, special solutions have been developed (for the cantilever actuator of single and double *PTS* segments subjected to external force and the converter with a single *PTS* acted on by a uniform external load). Moreover, dynamical analysis of transducers has been performed. Also, a matrix whose determinant enables determination of the characteristic equation for the transducer with any amount of piezoelectric segments has been formulated. On the basis of characteristic equations, for the converter with one and two *PTS*, the natural frequencies and the influence of relative stiffness, size and placing of a segment on their value have been determined. The obtained analytical solutions have been compared with the developed FEM solution.

On the basis of the performed analytical and numerical tests, it is found that:

- the developed method involving the implementation of *PTS* segments into a homogeneous beam allows obtaining solutions for piezoelectric converters:
 - of any either type of the external load,

- of diverse lengths and heights of piezoelectric and non-piezoelectric layers,
 - with any number of piezoelectric components;
- the obtained particular solutions allows determination of the deflection at any point of the converter;
 - the maximum values of the first dimensionless frequency, independently of the length and number of *PTS*, are to be obtained for segments with mountings located closer;
 - for a transducer with two *PTS* segments, the distribution of the second frequency is the same as for the first frequency;
 - for a transducer with one piezoelectric segment, the second frequency depending on *PTS* length holds the highest value for either the converter with the segment located on the left end or for the one with the segment located in the middle;
 - the dimensionless frequencies decrease with an increase in the relative stiffness and unit mass of the piezoelectric segment;
 - the particular solutions of static behaviour confirm with the results obtained from FEM (for the electrical load the maximum difference is approx. 1%, and for the mechanical load – approx. 3%);
 - a similar discrepancy between the analytical solution and FEM (less than 3%) has been obtained while calculating circular frequencies.

Appendix

$$\mathbf{M}_{1,i}^{12 \times 4} = \begin{bmatrix} 0 & 1 & 1 & 0 \\ \psi & 0 & 0 & \psi \\ \sin(\psi\kappa_i) & \cos(\psi\kappa_i) & \cosh(\psi\kappa_i) & \sinh(\psi\kappa_i) \\ \psi \cos(\psi\kappa_i) & -\psi \sin(\psi\kappa_i) & \psi \sinh(\psi\kappa_i) & \psi \cosh(\psi\kappa_i) \\ -\psi^2 \sin(\psi\kappa_i) & -\psi^2 \cos(\psi\kappa_i) & \psi^2 \cosh(\psi\kappa_i) & \psi^2 \sinh(\psi\kappa_i) \\ -\psi^3 \cos(\psi\kappa_i) & \psi^3 \sin(\psi\kappa_i) & \psi^3 \sinh(\psi\kappa_i) & \psi^3 \cosh(\psi\kappa_i) \\ 0 & 0 & 0 & 0 \\ \vdots & \vdots & \vdots & \vdots \\ 0 & 0 & 0 & 0 \end{bmatrix}$$

$$\mathbf{M}_{2,i}^{12 \times 4} = \begin{bmatrix} 0 & 0 & 0 & 0 \\ 0 & 0 & 0 & 0 \\ 0 & -1 & -1 & 0 \\ -\Lambda\psi & 0 & 0 & -\Lambda\psi \\ 0 & \eta\Lambda^2\psi^2 & -\eta\Lambda^2\psi^2 & 0 \\ \eta\Lambda^3\psi^3 & 0 & 0 & -\eta\Lambda^3\psi^3 \\ -\sin(\Lambda\psi\chi_i) & -\cos(\Lambda\psi\chi_i) & -\cosh(\Lambda\psi\chi_i) & -\sinh(\Lambda\psi\chi_i) \\ -\Lambda\psi \cos(\Lambda\psi\chi_i) & \Lambda\psi \sin(\Lambda\psi\chi_i) & -\Lambda\psi \sinh(\Lambda\psi\chi_i) & -\Lambda\psi \cosh(\Lambda\psi\chi_i) \\ \eta\Lambda^2\psi^2 \sin(\Lambda\psi\chi_i) & \eta\Lambda^2\psi^2 \cos(\Lambda\psi\chi_i) & -\eta\Lambda^2\psi^2 \cosh(\Lambda\psi\chi_i) & -\eta\Lambda^2\psi^2 \sinh(\Lambda\psi\chi_i) \\ \eta\Lambda^3\psi^3 \cos(\Lambda\psi\chi_i) & -\eta\Lambda^3\psi^3 \sin(\Lambda\psi\chi_i) & -\eta\Lambda^3\psi^3 \sinh(\Lambda\psi\chi_i) & -\eta\Lambda^3\psi^3 \cosh(\Lambda\psi\chi_i) \\ 0 & 0 & 0 & 0 \\ 0 & 0 & 0 & 0 \end{bmatrix}$$

$$\mathbf{M}_{3,i}^{12 \times 4} = \begin{bmatrix} 0 & 0 & 0 & 0 \\ \vdots & \vdots & \vdots & \vdots \\ 0 & 1 & 1 & 0 \\ \psi & 0 & 0 & \psi \\ 0 & -\psi^2 & \psi^2 & 0 \\ -\psi^3 & 0 & 0 & \psi^3 \\ -\psi^2 \sin(\psi\phi_i) & -\psi^2 \cos(\psi\phi_i) & \psi^2 \cosh(\psi\phi_i) & \psi^2 \sinh(\psi\phi_i) \\ -\psi^3 \cos(\psi\phi_i) & \psi^3 \sin(\psi\phi_i) & \psi^3 \sinh(\psi\phi_i) & \psi^3 \cosh(\psi\phi_i) \end{bmatrix}$$

$$\mathbf{B}^{12 \times 12} = \begin{bmatrix} 0 & 0 & 0 & 0 & 0 & \dots & \dots & 0 \\ \vdots & \vdots & \vdots & \vdots & \vdots & \dots & \dots & \vdots \\ 0 & \psi^2 & -\psi^2 & 0 & 0 & . & . & 0 \\ \psi^3 & 0 & 0 & -\psi^3 & 0 & . & . & 0 \end{bmatrix}$$

$$\mathbf{C}_i^{12 \times 12} = \begin{bmatrix} 0 & \dots & -\sin(\psi\phi_i) & -\cos(\psi\phi_i) & -\cosh(\psi\phi_i) & -\sinh(\psi\phi_i) \\ 0 & \dots & -\psi \cos(\psi\phi_i) & \psi \sin(\psi\phi_i) & -\psi \sinh(\psi\phi_i) & -\psi \cosh(\psi\phi_i) \\ \vdots & \ddots & \vdots & \vdots & \vdots & \vdots \\ 0 & \dots & 0 & 0 & 0 & 0 \end{bmatrix}$$

References

1. ASKARI FARSANGI M.A., SAIDI A.R., BATRA R.C., 2013, Analytical solution for free vibrations of moderately thick hybrid piezoelectric laminated plates, *Journal of Sound and Vibration*, **332**, 5981-5998
2. BERLINCOURT D.A., CURRAN D.R., JAFFE H., MASON W.P., 1964, *Physical Acoustics, Principles and Methods*, Academic Press, New York
3. BLEUSTEIN J.L., TIERSTEN H.F., 1968, Forced thickness-shear vibrations of discontinuously plated piezoelectric plates, *Journal of the Acoustical Society of America*, **43**, 6, 1311
4. BUCHACZ A., PŁACZEK M., 2009, Damping of mechanical vibrations using piezoelements, including influence of connection layer's properties, on the dynamic characteristic, *Solid State Phenomena*, 147/149, 869-875
5. BUSCH-VISHNIAC I.J., 1999, *Electromechanical Sensors and Actuators*, Springer-Verlag
6. CHEN W.Q., XU R.Q., DING H.J., 1998, On free vibration of a piezoelectric composite rectangular plate, *Journal of Sound and Vibration*, **218**, 4, 741-748
7. CLARC R.L., FULLER CH.R., WICKS A., 1991, Characterization of multiple piezoelectric actuators for structural excitation, *Journal of Acoustical Society of America*, **90**, 346-357
8. CURIE P.J., CURIE J., 1880, Crystal physics-development by pressure 0/ polar electricity in hemihedral crystals with inclined faces (in French), *Comptes rendus hebdomadaires des sances de l'Acadmie des sciences*, **294**, pp. 91
9. DJOJODIHARDJO H., JAFARI M., WIRIADIDJAJA S., AHMAD K.A., 2015, Active vibration suppression of an elastic piezoelectric sensor and actuator fitted cantilevered beam configurations as a generic smart composite structure, *Composite Structures*, **132**, 848-863
10. Documentation for ANSYS, 2010, Coupled-Field Analysis Guide
11. FERTIS D.G., 1996, *Advanced Mechanics of Structures*, Marcel Dekker, New York
12. KAWAI H., 1969, The piezoelectricity of poly (vinylidene fluoride), *Japanese Journal of Applied Physics*, **8**, 975
13. LIU X., WANG X., ZHAO H., DU Y., 2014, Myocardial cell pattern on piezoelectric nanofiber mats for energy harvesting, *Journal of Physics: Conference Series*, **557**, 012057

14. MAHMOUD A.A., NASSAR M.A., Free vibration of a stepped beam with two uniform and/or tapered parts, *Mechanics and Mechanical Engineering*, **4**, 2, 165-181
15. MIECZKOWSKI G., 2016, Electromechanical characteristics of piezoelectric converters with freely defined boundary conditions and geometry, *Mechanika*, **22**, 4, 265-272
16. MIESZCZAK Z., KRAWCZUK M., OSTACHOWICZ W., 2006, Interaction of point defects in piezoelectric materials – numerical simulation in the context of electric fatigue, *Journal of Theoretical and Applied Mechanics*, **44**, 4, 650-665
17. PARK J.K., MOON W.K., 2005, Constitutive relations for piezoelectric benders under various boundary conditions, *Sensors and Actuators A*, **117**, 159-167
18. PIETRZAKOWSKI M., 2000, Multiple piezoceramic segments in structural vibration control, *Journal of Theoretical and Applied Mechanics*, **38**, 378-393
19. PIETRZAKOWSKI M., 2001, Active damping of beams by piezoelectric system: effects of bonding layer properties, *International Journal of Solids and Structures*, **38**, 7885-7897
20. PRZYBYŁOWICZ P.M., 1999, Application of piezoelectric elements to semi-adaptive dynamic eliminator of torsional vibration, *Journal of Theoretical and Applied Mechanics*, **37**, 2, 319-334
21. RAEISIFARD H., BAHRAMI M.N., YOUSEFI-KOMA A., FARD H.R., 2014, Static characterization and pull-in voltage of a micro-switch under both electrostatic and piezoelectric excitations, *European Journal of Mechanics A/Solids*, **44**, 116-124
22. RAHMOUNE M., OSMONT D., 2010, Classic finite elements for simulation of piezoelectric smart structures, *Mechanika*, **86**, 6, 50-57
23. RAJABI A.H., JAFFE M., ARINZEH T.J., 2015, Piezoelectric materials for tissue regeneration: A review, Review Article, *Acta Biomaterialia*, **24**, 15, 12-23
24. ROUZEGAR J., ABAD F., 2015, Free vibration analysis of FG plate with piezoelectric layers using four-variable refined plate theory, *Thin-Walled Structures*, **89**, 76-83
25. SMITS J.G., DALKE S.I., COONEY T.K., 1991, The constituent equations of piezoelectric bimorphs, *Sensors and Actuators A*, **28**, 41-61
26. ȘTEFĂNESCU D.M. 2011, Piezoelectric Force Transducers (PZFTs), [In:] *Handbook of Force Transducers*, 109-130
27. TYLIKOWSKI A., 1993, Stabilization of beam parametric vibrations, *Journal of Theoretical and Applied Mechanics*, **31**, 3, 657-670
28. TZOU H.S., 1999, *Piezoelectric Shells: Distributed Sensing and Control of Continua*, Kluwer Academic Publishers, Dordrecht
29. WANG Q., CROSS L.E., 1999, Constitutive equations of symmetrical triple-layer piezoelectric benders, *IEEE Transactions on Ultrasonics, Ferroelectrics, and Frequency Control*, **46**, 1343-1351
30. XIANG H.J., SHI Z.F., 2008, Static analysis for multi-layered piezoelectric cantilevers, *International Journal of Solids and Structures*, **45**, 1, 113-128

Manuscript received October 6, 2015; accepted for print May 6, 2016

QUASI-GREEN'S FUNCTION APPROACH TO FUNDAMENTAL FREQUENCY ANALYSIS OF ELASTICALLY SUPPORTED THIN CIRCULAR AND ANNULAR PLATES WITH ELASTIC CONSTRAINTS

KRZYSZTOF K. ŻUR

Białystok University of Technology, Faculty of Management, Kleosin, Poland

e-mail: k.zur@pb.edu.pl

Free vibration analysis of homogeneous and isotropic thin circular and annular plates with discrete elements such as elastic ring supports is considered. The general form of quasi-Green's function for thin circular and annular plates is obtained. The nonlinear characteristic equations are defined for thin circular and annular plates with different boundary conditions and different combinations of the core and support radius. The continuity conditions at the ring supports are omitted based on the properties of Green's function. The fundamental frequency of axisymmetric vibration has been calculated using the Newton-Raphson method and calculation software. The obtained results are compared with selected results presented in literature. The exact frequencies of vibration presented in a non-dimensional form can serve as benchmark values for researchers to validate their numerical methods when applied for uniform thin circular and annular plate problems.

Keywords: quasi-Green's function, ring supports, movable edges, elastic constraints

1. Introduction

The study of vibration of a thin circular and annular plate is basic in structural mechanics. Components of circular and annular plates are commonly used in the aerospace industry and aviation as well as in marine and civil engineering applications. Circular and annular plates are the most critical structural elements in high speed rotating engineering systems. The natural frequencies of circular and annular plates have been studied extensively for more than a century, because if only the frequency of external load matches the natural frequency of the plate, destruction may occur. Additionally, the influence of elastic or rigid ring supports on dynamic behavior of plates have been studied in a lot of works, because it used to stabilize or to increase the frequency of plates. Knowledge about distribution of ring supports of variable stiffness can allow one to predict dynamic behavior of structural elements such as circular and annular plates.

The free vibration of circular and annular plates with concentric ring supports have been studied in a lot of works. Bodine (1967) studied the influence of rigid supports on the fundamental frequency of circular plates in which radius of the supports was small. Kunukasseril and Swamidas (1974) formulated equations for circular plates with elastic supports, but they solved the free vibration problem for a free circular plate. Singh and Mirza (1976) studied free axisymmetric vibration of circular plates elastically supported along two concentric circles. Azimi (1988) studied natural vibration of circular plates with elastic and rigid supports using the receptance method. Wang and Thevendran (1993) analyzed free vibration of annular plates with concentric supports using by the Rayleigh-Ritz method. Ding (1994) solved the free vibration problem for arbitrarily shaped plates with concentric elastic and rigid ring supports. Liu and Chen (1995) studied axisymmetric vibration of annular and circular plates using simple finite analysis. In works by Vega *et al.* (1999) free vibration analysis was presented for a concentrically

supported annular plate with a free edge using the optimized Rayleigh-Ritz method. Laura *et al.* (1999) analyzed transverse vibration of a circular plate with a free edge and concentric ring supports. Vega *et al.* (2000) analyzed free vibration of concentrically supported annular plates with one edge clamped or simply supported. The fundamental frequency of a free thin circular plate supported on a ring was analyzed by Wang (2001). Influence of the stiffness and location of elastic ring supports on the fundamental frequency of circular plates were analyzed by Wang and Wang (2003). Wang (2006, 2014) studied vibration modes of concentrically supported free circular and annular plates with movable edges. Rao and Rao (2014a) analyzed free vibration of annular plates with both edges elastically restrained and resting on the Winkler foundation. Additionally, Rao and Rao (2014b) analyzed free vibration of a thin circular plate with concentric ring and elastic edge support.

In the works presented above, the analyzed plates were separated into two regions for one ring supports. The number of separated regions increases if the number of considered elastic ring supports increases. In this approach, the solution to boundary value problem is complicated. Additionally, continuity conditions between the support and plate must be used to obtain characteristic equations. Solution to the boundary value problem is very tedious and more complicated based on continuity conditions, because characteristic matrices have a large dimension.

Application of Green's function to the solution to the boundary value problem of free vibration of plates allow one to neglect the continuity condition. In the works of Kukla and Szewczyk (2004, 2005, 2007) Green's function approach to frequency analysis is presented for circular and annular thin plates with elastic supports. The authors calculated nontrivial constants of general solutions to the differential equation to obtain a full form of Green's function for free, simply-supported and clamped plates. The nontrivial constants have a very complicated form, and calculating them is very tedious for different boundary conditions such as sliding supports or elastic constraints.

The novelty of the paper is quasi-Green's function (not full form) approach to obtain characteristic equations of concentrically supported circular and annular plates with clamped, free, simply-supported and sliding (movable) edges or elastic constraints. The quasi-Green function is obtained by the method presented in the previous works (Żur, 2015, 2016a). Nonlinear characteristic equations of plates are obtained without calculating nontrivial constants of the general solution to the differential equation. The numerical results of investigation are compared with selected results presented in literature. The exact fundamental frequencies of axisymmetric vibration are presented in a non-dimensional form for different combinations of the core and support radius as well as selected values of parameters of elastic constraints.

2. Statement of the problem

Consider an isotropic, homogeneous annular (circular) thin plate of constant thickness h in cylindrical coordinates (r, θ, z) with the z -axis along the longitudinal direction. The geometry and coordinate system of the considered plate is shown in Fig. 1. The partial differential equation for free vibration of thin uniform annular (circular) plates has the following form

$$\nabla^4 W(r, t) + \frac{\rho h}{D} \frac{\partial^2 W(r, t)}{\partial t^2} = - \sum_{j=1}^{\chi} K_j W(r, t) \delta(r - r_j) \quad (2.1)$$

where ρ is mass density, $D = Eh^3/[12(1 - \nu^2)]$ is flexural rigidity, E is Young's modulus, ν is Poisson's ratio, $\nabla^2 = (\partial^2/\partial r^2) + (1/r)(\partial/\partial r)$ is Laplacian, K_j is a coefficient of normalized stiffness of the supports, δ is Dirac's delta function, r_j is the position of elastic ring supports, χ is the number of elastic ring supports and $W(r, t)$ is small deflection compared with thickness h of the plate.

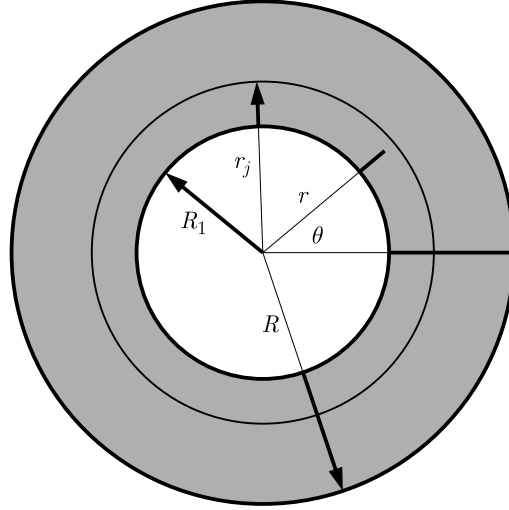


Fig. 1. The geometry and coordinate system of the annular plate with radius of the hole R_1

The axisymmetric deflection of an annular (circular) plate may be expressed as follows

$$W(r, t) = w(r)e^{i\omega t} \quad (2.2)$$

where $w(r)$ is the radial mode function, ω is the natural frequency, and $i^2 = -1$. Substituting Eq. (2.2) into Eq. (2.1) and using the dimensionless coordinates $\xi = r/R$ and $\kappa_j = r_j/R$, the governing differential equation of the annular (circular) plate is obtained

$$L(w) - \lambda^2 w = - \sum_{j=1}^{\chi} K_j w(\kappa_j) \delta(\xi - \kappa_j) \quad (2.3)$$

where

$$L(w) \equiv \frac{d^4 w}{d\xi^4} + \frac{2}{\xi} \frac{d^3 w}{d\xi^3} - \frac{1}{\xi^2} \frac{d^2 w}{d\xi^2} + \frac{1}{\xi^3} \frac{dw}{d\xi} \quad (2.4)$$

is the differential operator and

$$\lambda = \omega R^2 \sqrt{\rho h / D} \quad (2.5)$$

is the dimensionless frequency of vibration.

The boundary conditions at the outer edge ($\xi = 1$) of the annular (circular) plate may be one of the following: clamped, simply supported, free, sliding supports and elastic supports. These conditions may be written in terms of the radial mode function $w(\xi)$ in the following form:

— clamped

$$w(\xi)|_{\xi=1} = 0 \quad \left. \frac{dw}{d\xi} \right|_{\xi=1} = 0 \quad (2.6)$$

— simply supported

$$w(\xi)|_{\xi=1} = 0 \quad M(w)|_{\xi=1} = \left(\frac{d^2 w}{d\xi^2} + \frac{\nu}{\xi} \frac{dw}{d\xi} \right)_{\xi=1} = 0 \quad (2.7)$$

— free

$$M(w)|_{\xi=1} = 0 \quad V(w)|_{\xi=1} = \left(\frac{d^3 w}{d\xi^3} + \frac{1}{\xi} \frac{d^2 w}{d\xi^2} - \frac{1}{\xi^2} \frac{dw}{d\xi} \right)_{\xi=1} = 0 \quad (2.8)$$

— movable edges (sliding)

$$\left. \frac{dw}{d\xi} \right|_{\xi=1} = 0 \quad V(w)|_{\xi=1} = 0 \quad (2.9)$$

— elastic supports

$$\begin{aligned} \Phi(w)|_{\xi=1} &= \left[\left(\frac{d^2 w}{d\xi^2} + \nu \frac{dw}{d\xi} \right) + \phi \frac{dw}{d\xi} \right]_{\xi=1} = 0 \\ \Psi(w)|_{\xi=1} &= \left[\left(\frac{d^3 w}{d\xi^3} + \frac{d^2 w}{d\xi^2} - \frac{dw}{d\xi} \right) - \psi w \right]_{\xi=1} = 0 \end{aligned} \quad (2.10)$$

$M(w)$ and $V(w)$ are the normalized radial bending moment and the normalized effective shear force, respectively. $\phi = K_\phi R/D_R$ and $\psi = K_\psi R^3/D_R$ are the parameters of elastic constraints. K_ϕ and K_ψ are the rotational and translational spring constants, respectively. Similar boundary conditions may be defined at the inner edge ($\xi = R_1/R = \xi_1$), depending on considered annular plates.

3. Finding quasi-Green's function

The general solution to the homogeneous differential equation for thin annular (circular) plates

$$L(w) - \lambda^2 w = 0 \quad (3.1)$$

is a linear combination of the Bessel functions presented in the following form (McLachlan, 1955)

$$w(\xi) = C_1 J_0(\lambda\xi) + C_2 I_0(\lambda\xi) + C_3 Y_0(\lambda\xi) + C_4 K_0(\lambda\xi) \quad (3.2)$$

where $J_0(\lambda\xi)$, $Y_0(\lambda\xi)$ are the Bessel functions of the first and second kind, $I_0(\lambda\xi)$, $K_0(\lambda\xi)$ are the modified Bessel functions of the first and second kind. The quasi-Green function $K(\xi, \alpha)$ is a particular solution to Eq. (3.1) and may be received from the formula presented in the following form (Jaroszewicz and Zoryj, 2005; Żur, 2015)

$$K(\xi, \alpha) = \frac{D(\xi, \alpha)}{W(\alpha)p_0(\alpha)} \quad (3.3)$$

where $p_0(\alpha) = 1$ is a coefficient placed in front of the highest order of derivative of differential equation (3.1), and

$$\begin{aligned} D(\xi, \alpha) &= \begin{vmatrix} \frac{J_0(\lambda\alpha)}{dJ_0(\lambda\alpha)} & \frac{I_0(\lambda\alpha)}{dI_0(\lambda\alpha)} & \frac{Y_0(\lambda\alpha)}{dY_0(\lambda\alpha)} & \frac{K_0(\lambda\alpha)}{dK_0(\lambda\alpha)} \\ \frac{d\alpha}{d^2 J_0(\lambda\alpha)} & \frac{d\alpha}{d^2 I_0(\lambda\alpha)} & \frac{d\alpha}{d^2 Y_0(\lambda\alpha)} & \frac{d\alpha}{d^2 K_0(\lambda\alpha)} \\ \frac{d\alpha^2}{J_0(\lambda\xi)} & \frac{d\alpha^2}{I_0(\lambda\xi)} & \frac{d\alpha^2}{Y_0(\lambda\xi)} & \frac{d\alpha^2}{K_0(\lambda\xi)} \end{vmatrix} \\ W(\alpha) &= \begin{vmatrix} \frac{J_0(\lambda\alpha)}{dJ_0(\lambda\alpha)} & \frac{I_0(\lambda\alpha)}{dI_0(\lambda\alpha)} & \frac{Y_0(\lambda\alpha)}{dY_0(\lambda\alpha)} & \frac{K_0(\lambda\alpha)}{dK_0(\lambda\alpha)} \\ \frac{d\alpha}{d^2 J_0(\lambda\alpha)} & \frac{d\alpha}{d^2 I_0(\lambda\alpha)} & \frac{d\alpha}{d^2 Y_0(\lambda\alpha)} & \frac{d\alpha}{d^2 K_0(\lambda\alpha)} \\ \frac{d\alpha^2}{d^3 J_0(\lambda\alpha)} & \frac{d\alpha^2}{d^3 I_0(\lambda\alpha)} & \frac{d\alpha^2}{d^3 Y_0(\lambda\alpha)} & \frac{d\alpha^2}{d^3 K_0(\lambda\alpha)} \\ \frac{d\alpha^3}{d\alpha^3} & \frac{d\alpha^3}{d\alpha^3} & \frac{d\alpha^3}{d\alpha^3} & \frac{d\alpha^3}{d\alpha^3} \end{vmatrix} \end{aligned} \quad (3.4)$$

The elements of the matrix \mathbf{D} and \mathbf{W} have the following form

$$\begin{aligned} \frac{dJ_0(\lambda\alpha)}{d\alpha} &= -\lambda J_1(\lambda\alpha) & \frac{dI_0(\lambda\alpha)}{d\alpha} &= \lambda I_1(\lambda\alpha) \\ \frac{dY_0(\lambda\alpha)}{d\alpha} &= -\lambda Y_1(\lambda\alpha) & \frac{dK_0(\lambda\alpha)}{d\alpha} &= -\lambda K_1(\lambda\alpha) \end{aligned} \quad (3.5)$$

$$\begin{aligned} \frac{d^2 J_0(\lambda\alpha)}{d\alpha^2} &= \frac{\lambda^2}{2} [J_0(\lambda\alpha) + J_2(\lambda\alpha)] & \frac{d^2 I_0(\lambda\alpha)}{d\alpha^2} &= \frac{\lambda^2}{2} [I_0(\lambda\alpha) + I_2(\lambda\alpha)] \\ \frac{d^2 Y_0(\lambda\alpha)}{d\alpha^2} &= \frac{\lambda^2}{2} [Y_0(\lambda\alpha) + Y_2(\lambda\alpha)] & \frac{d^2 K_0(\lambda\alpha)}{d\alpha^2} &= \frac{\lambda^2}{2} [K_0(\lambda\alpha) + K_2(\lambda\alpha)] \end{aligned} \quad (3.6)$$

$$\begin{aligned} \frac{d^3 J_0(\lambda\alpha)}{d\alpha^3} &= \frac{\lambda^3}{4} [3J_1(\lambda\alpha) + J_3(\lambda\alpha)] & \frac{d^3 I_0(\lambda\alpha)}{d\alpha^3} &= \frac{\lambda^3}{4} [3I_1(\lambda\alpha) + I_3(\lambda\alpha)] \\ \frac{d^3 Y_0(\lambda\alpha)}{d\alpha^3} &= \frac{\lambda^3}{4} [3Y_1(\lambda\alpha) - Y_3(\lambda\alpha)] & \frac{d^3 K_0(\lambda\alpha)}{d\alpha^3} &= -\frac{\lambda^3}{4} [3K_1(\lambda\alpha) + K_3(\lambda\alpha)] \end{aligned} \quad (3.7)$$

After calculations, the function $D(\xi, \alpha)$ has the form

$$D(\xi, \alpha) = \frac{2\lambda^2}{\pi\alpha} [2I_0(\lambda\xi)K_0(\lambda\alpha) - 2I_0(\lambda\alpha)K_0(\lambda\xi) + \pi J_0(\lambda\xi)Y_0(\lambda\alpha) - \pi J_0(\lambda\alpha)Y_0(\lambda\xi)] \quad (3.8)$$

Bessel function (3.2) expresses linear independent solutions, thus the Wronskian must satisfy the condition (Stakgold and Holst, 2011)

$$W(\alpha) = \frac{8\lambda^4}{\pi\alpha^2} \neq 0 \quad (3.9)$$

Condition (3.9) is satisfied for a circular plate ($0 < \alpha \leq 1$) and an annular plate ($0 < \xi_1 \leq \alpha \leq 1$). After calculations, the quasi-Green function has the form

$$K(\xi, \alpha) = \frac{\alpha}{4\lambda^2} [2I_0(\lambda\xi)K_0(\lambda\alpha) - 2I_0(\lambda\alpha)K_0(\lambda\xi) - \pi J_0(\lambda\alpha)Y_0(\lambda\xi) + \pi J_0(\lambda\xi)Y_0(\lambda\alpha)] \quad (3.10)$$

and satisfies the conditions

$$K(a, a) = \frac{\partial K(\xi, \alpha)}{\partial \xi} \Big|_{\xi=a} = \frac{\partial^2 K(\xi, \alpha)}{\partial \xi^2} \Big|_{\xi=a} = 0 \quad \frac{\partial^3 K(\xi, \alpha)}{\partial \xi^3} \Big|_{\xi=a} = 1 \quad (3.11)$$

according to properties of the influence functions (Stakgold and Holst, 2011).

4. Solution of the problem for the circular plate

In the previous paper (Žur, 2016b), the possibility of solving the similar boundary value problem was proposed for non-uniform annular plates without calculations. Based on the paper of Žur (2016b), the limit $\lim_{\xi \rightarrow 0} Y_0(\lambda\xi) = \infty$, $\lim_{\xi \rightarrow 0} K_0(\lambda\xi) = \infty$ of linear independent solutions to Eq. (2.3) for the circular plate can be presented in the following form

$$\begin{aligned} K(\xi, \lambda, \boldsymbol{\kappa}, \mathbf{K})_a &= J_0(\lambda\xi) - \sum_{j=1}^{\chi} K_j J_0(\lambda\kappa_j) G(\xi, \kappa_j) \\ K(\xi, \lambda, \boldsymbol{\kappa}, \mathbf{K})_b &= I_0(\lambda\xi) - \sum_{j=1}^{\chi} K_j I_0(\lambda\kappa_j) G(\xi, \kappa_j) \end{aligned} \quad (4.1)$$

where

$$\begin{aligned} G(\xi, \kappa_j) &= K(\xi, \kappa_j)H(\xi - \kappa_j) \\ K(\xi, \kappa_j) &= \frac{\kappa_j}{4\lambda^2} [2I_0(\lambda\xi)K_0(\lambda\kappa_j) - 2I_0(\lambda\kappa_j)K_0(\lambda\xi) - \pi J_0(\lambda\kappa_j)Y_0(\lambda\xi) + \pi J_0(\lambda\xi)Y_0(\lambda\kappa_j)] \end{aligned} \quad (4.2)$$

and

$$\boldsymbol{\kappa} = [\kappa_1, \dots, \kappa_\chi] \quad \mathbf{K} = [K_1, \dots, K_\chi] \quad (4.3)$$

and $H(\xi - \kappa_j)$ is the Heaviside function.

The characteristic equations $\Delta = 0$ of the circular plate for different boundary conditions and different values of the parameters κ_j and K_j are obtained from well known characteristic determinants given by:

— clamped

$$\Delta(\lambda, \boldsymbol{\kappa}, \mathbf{K}) \equiv \left| \begin{array}{cc} K(\xi, \lambda, \boldsymbol{\kappa}, \mathbf{K})_a & K(\xi, \lambda, \boldsymbol{\kappa}, \mathbf{K})_b \\ \frac{\partial K(\xi, \lambda, \boldsymbol{\kappa}, \mathbf{K})_a}{\partial \xi} & \frac{\partial K(\xi, \lambda, \boldsymbol{\kappa}, \mathbf{K})_b}{\partial \xi} \end{array} \right|_{\xi=1} \quad (4.4)$$

— simply supported

$$\Delta(\lambda, \boldsymbol{\kappa}, \mathbf{K}) \equiv \left| \begin{array}{cc} K(\xi, \lambda, \boldsymbol{\kappa}, \mathbf{K})_a & K(\xi, \lambda, \boldsymbol{\kappa}, \mathbf{K})_b \\ M[K(\xi, \lambda, \boldsymbol{\kappa}, \mathbf{K})_a] & M[K(\xi, \lambda, \boldsymbol{\kappa}, \mathbf{K})_b] \end{array} \right|_{\xi=1} \quad (4.5)$$

— free

$$\Delta(\lambda, \boldsymbol{\kappa}, \mathbf{K}) \equiv \left| \begin{array}{cc} M[K(\xi, \lambda, \boldsymbol{\kappa}, \mathbf{K})_a] & M[K(\xi, \lambda, \boldsymbol{\kappa}, \mathbf{K})_b] \\ V[K(\xi, \lambda, \boldsymbol{\kappa}, \mathbf{K})_a] & V[K(\xi, \lambda, \boldsymbol{\kappa}, \mathbf{K})_b] \end{array} \right|_{\xi=1} \quad (4.6)$$

— sliding

$$\Delta(\lambda, \boldsymbol{\kappa}, \mathbf{K}) \equiv \left| \begin{array}{cc} \frac{\partial K(\xi, \lambda, \boldsymbol{\kappa}, \mathbf{K})_a}{\partial \xi} & \frac{\partial K(\xi, \lambda, \boldsymbol{\kappa}, \mathbf{K})_b}{\partial \xi} \\ V[K(\xi, \lambda, \boldsymbol{\kappa}, \mathbf{K})_a] & V[K(\xi, \lambda, \boldsymbol{\kappa}, \mathbf{K})_b] \end{array} \right|_{\xi=1} \quad (4.7)$$

— elastic supports

$$\Delta(\lambda, \boldsymbol{\kappa}, \mathbf{K}, \phi, \psi) \equiv \left| \begin{array}{cc} \Phi[K(\xi, \lambda, \boldsymbol{\kappa}, \mathbf{K})_a] & \Phi[K(\xi, \lambda, \boldsymbol{\kappa}, \mathbf{K})_b] \\ \Psi[K(\xi, \lambda, \boldsymbol{\kappa}, \mathbf{K})_a] & \Psi[K(\xi, \lambda, \boldsymbol{\kappa}, \mathbf{K})_b] \end{array} \right|_{\xi=1} \quad (4.8)$$

5. Solution of the problem for the annular plate

The linear independent solutions to Eq. (2.3) for the annular plate can be presented in the following form

$$\begin{aligned} \mathcal{B}_a &\equiv K(\xi, \lambda, \boldsymbol{\kappa}, \mathbf{K})_a = J_0(\lambda\xi) - \sum_{j=1}^{\chi} K_j J_0(\lambda\kappa_j) G(\xi, \kappa_j) \\ \mathcal{B}_b &\equiv K(\xi, \lambda, \boldsymbol{\kappa}, \mathbf{K})_b = I_0(\lambda\xi) - \sum_{j=1}^{\chi} K_j I_0(\lambda\kappa_j) G(\xi, \kappa_j) \\ \mathcal{B}_c &\equiv K(\xi, \lambda, \boldsymbol{\kappa}, \mathbf{K})_c = Y_0(\lambda\xi) - \sum_{j=1}^{\chi} K_j Y_0(\lambda\kappa_j) G(\xi, \kappa_j) \\ \mathcal{B}_d &\equiv K(\xi, \lambda, \boldsymbol{\kappa}, \mathbf{K})_d = K_0(\lambda\xi) - \sum_{j=1}^{\chi} K_j K_0(\lambda\kappa_j) G(\xi, \kappa_j) \end{aligned} \quad (5.1)$$

The characteristic equations $\Delta = 0$ of the annular plate for different boundary conditions and different values of the parameters κ_j and K_j are obtained from well known characteristic determinants given by:

— free outer edge and clamped inner edge

$$\Delta(\lambda, \boldsymbol{\kappa}, \mathbf{K}) \equiv \begin{vmatrix} M[\mathcal{B}_a]|_{\xi=1} & M[\mathcal{B}_b]|_{\xi=1} & M[\mathcal{B}_c]|_{\xi=1} & M[\mathcal{B}_d]|_{\xi=1} \\ V[\mathcal{B}_a]|_{\xi=1} & V[\mathcal{B}_b]|_{\xi=1} & V[\mathcal{B}_c]|_{\xi=1} & V[\mathcal{B}_d]|_{\xi=1} \\ \mathcal{B}_a|_{\xi=\xi_1} & \mathcal{B}_b|_{\xi=\xi_1} & \mathcal{B}_c|_{\xi=\xi_1} & \mathcal{B}_d|_{\xi=\xi_1} \\ \frac{\partial \mathcal{B}_a}{\partial \xi}|_{\xi=\xi_1} & \frac{\partial \mathcal{B}_b}{\partial \xi}|_{\xi=\xi_1} & \frac{\partial \mathcal{B}_c}{\partial \xi}|_{\xi=\xi_1} & \frac{\partial \mathcal{B}_d}{\partial \xi}|_{\xi=\xi_1} \end{vmatrix} \quad (5.2)$$

— free outer edge and simply supported inner edge

$$\Delta(\lambda, \boldsymbol{\kappa}, \mathbf{K}) \equiv \begin{vmatrix} M[\mathcal{B}_a]|_{\xi=1} & M[\mathcal{B}_b]|_{\xi=1} & M[\mathcal{B}_c]|_{\xi=1} & M[\mathcal{B}_d]|_{\xi=1} \\ V[\mathcal{B}_a]|_{\xi=1} & V[\mathcal{B}_b]|_{\xi=1} & V[\mathcal{B}_c]|_{\xi=1} & V[\mathcal{B}_d]|_{\xi=1} \\ \mathcal{B}_a|_{\xi=\xi_1} & \mathcal{B}_b|_{\xi=\xi_1} & \mathcal{B}_c|_{\xi=\xi_1} & \mathcal{B}_d|_{\xi=\xi_1} \\ M[\mathcal{B}_a]|_{\xi=\xi_1} & M[\mathcal{B}_b]|_{\xi=\xi_1} & M[\mathcal{B}_c]|_{\xi=\xi_1} & M[\mathcal{B}_d]|_{\xi=\xi_1} \end{vmatrix} \quad (5.3)$$

— free both edges

$$\Delta(\lambda, \boldsymbol{\kappa}, \mathbf{K}) \equiv \begin{vmatrix} M[\mathcal{B}_a]|_{\xi=1} & M[\mathcal{B}_b]|_{\xi=1} & M[\mathcal{B}_c]|_{\xi=1} & M[\mathcal{B}_d]|_{\xi=1} \\ V[\mathcal{B}_a]|_{\xi=1} & V[\mathcal{B}_b]|_{\xi=1} & V[\mathcal{B}_c]|_{\xi=1} & V[\mathcal{B}_d]|_{\xi=1} \\ M[\mathcal{B}_a]|_{\xi=\xi_1} & M[\mathcal{B}_b]|_{\xi=\xi_1} & M[\mathcal{B}_c]|_{\xi=\xi_1} & M[\mathcal{B}_d]|_{\xi=\xi_1} \\ V[\mathcal{B}_a]|_{\xi=\xi_1} & V[\mathcal{B}_b]|_{\xi=\xi_1} & V[\mathcal{B}_c]|_{\xi=\xi_1} & V[\mathcal{B}_d]|_{\xi=\xi_1} \end{vmatrix} \quad (5.4)$$

— free outer edge and sliding inner edge

$$\Delta(\lambda, \boldsymbol{\kappa}, \mathbf{K}) \equiv \begin{vmatrix} M[\mathcal{B}_a]|_{\xi=1} & M[\mathcal{B}_b]|_{\xi=1} & M[\mathcal{B}_c]|_{\xi=1} & M[\mathcal{B}_d]|_{\xi=1} \\ V[\mathcal{B}_a]|_{\xi=1} & V[\mathcal{B}_b]|_{\xi=1} & V[\mathcal{B}_c]|_{\xi=1} & V[\mathcal{B}_d]|_{\xi=1} \\ \frac{\partial \mathcal{B}_a}{\partial \xi}|_{\xi=\xi_1} & \frac{\partial \mathcal{B}_b}{\partial \xi}|_{\xi=\xi_1} & \frac{\partial \mathcal{B}_c}{\partial \xi}|_{\xi=\xi_1} & \frac{\partial \mathcal{B}_d}{\partial \xi}|_{\xi=\xi_1} \\ V[\mathcal{B}_a]|_{\xi=\xi_1} & V[\mathcal{B}_b]|_{\xi=\xi_1} & V[\mathcal{B}_c]|_{\xi=\xi_1} & V[\mathcal{B}_d]|_{\xi=\xi_1} \end{vmatrix} \quad (5.5)$$

— free inner edge and clamped outer edge

$$\Delta(\lambda, \boldsymbol{\kappa}, \mathbf{K}) \equiv \begin{vmatrix} M[\mathcal{B}_a]|_{\xi=\xi_1} & M[\mathcal{B}_b]|_{\xi=\xi_1} & M[\mathcal{B}_c]|_{\xi=\xi_1} & M[\mathcal{B}_d]|_{\xi=\xi_1} \\ V[\mathcal{B}_a]|_{\xi=\xi_1} & V[\mathcal{B}_b]|_{\xi=\xi_1} & V[\mathcal{B}_c]|_{\xi=\xi_1} & V[\mathcal{B}_d]|_{\xi=\xi_1} \\ \mathcal{B}_a|_{\xi=1} & \mathcal{B}_b|_{\xi=1} & \mathcal{B}_c|_{\xi=1} & \mathcal{B}_d|_{\xi=1} \\ \frac{\partial \mathcal{B}_a}{\partial \xi}|_{\xi=1} & \frac{\partial \mathcal{B}_b}{\partial \xi}|_{\xi=1} & \frac{\partial \mathcal{B}_c}{\partial \xi}|_{\xi=1} & \frac{\partial \mathcal{B}_d}{\partial \xi}|_{\xi=1} \end{vmatrix} \quad (5.6)$$

— elastic constraints at the inner edge and free outer edge

$$\Delta(\lambda, \boldsymbol{\kappa}, \mathbf{K}, \phi, \psi) \equiv \begin{vmatrix} M[\mathcal{B}_a]|_{\xi=1} & M[\mathcal{B}_b]|_{\xi=1} & M[\mathcal{B}_c]|_{\xi=1} & M[\mathcal{B}_d]|_{\xi=1} \\ V[\mathcal{B}_a]|_{\xi=1} & V[\mathcal{B}_b]|_{\xi=1} & V[\mathcal{B}_c]|_{\xi=1} & V[\mathcal{B}_d]|_{\xi=1} \\ \Phi[\mathcal{B}_a]|_{\xi=\xi_1} & \Phi[\mathcal{B}_b]|_{\xi=\xi_1} & \Phi[\mathcal{B}_c]|_{\xi=\xi_1} & \Phi[\mathcal{B}_d]|_{\xi=\xi_1} \\ \Psi[\mathcal{B}_a]|_{\xi=\xi_1} & \Psi[\mathcal{B}_b]|_{\xi=\xi_1} & \Psi[\mathcal{B}_c]|_{\xi=\xi_1} & \Psi[\mathcal{B}_d]|_{\xi=\xi_1} \end{vmatrix} \quad (5.7)$$

6. Results and discussion

The numerical results for fundamental frequencies of elastically supported circular plates are presented in Tables 1 and 2 with comparison to the results by Azimi (1988), Ding (1994), Wang and Wang. (2003). The numerical results for fundamental frequencies of free vibration of free circular plates with rigid ring supports are presented in Table 3 with comparison to the results by Wang (2014). The numerical results for fundamental frequencies of free vibration of free elastically supported annular plates with different boundary condition at the inner edge are presented in Tables 4 and 5 for different combinations of the radius of the core and supports. The fundamental frequencies of free vibration of circular plates with elastic constraints and interior ring supports of variable stiffness are presented in Table 6. Additionally, the eigenvalues of circular plates with elastic constraints depending on radius and stiffness of interior ring supports are shown in Figs. 2 and 3.

Table 1. The fundamental frequency λ_0 of free vibration of circular plates with the elastic ring support

K_1	κ_1	Dimensionless frequency λ_0	Boundary conditions			
			Clamped	Simply supported	Free	Sliding
10	0	GF	3.196	2.221	0.211	0.212
	0.1	GF	3.272	2.360	1.115	1.171
	0.2	GF	3.326	2.460	1.357	1.383
		Wang and Wang (2003)	3.325	2.460	–	–
		Azimi (1988)	3.326	2.461	–	–
		Ding (1994)	3.322	–	–	–
	0.3	GF	3.348	2.523	1.497	1.532
	0.4	GF	3.338	2.547	1.620	1.656
		Wang and Wang (2003)	3.338	2.547	–	–
		Azimi (1988)	3.338	2.547	–	–
		Ding (1994)	3.334	–	–	–
	0.5	GF	3.304	2.530	1.736	1.765
	0.6	GF	3.262	2.478	1.844	1.856
		Wang and Wang (2003)	3.262	2.478	–	–
		Azimi (1988)	3.262	2.479	–	–
		Ding (1994)	3.262	–	–	–
	0.7	GF	3.225	2.403	1.928	1.928
	0.8	GF	3.204	2.321	1.960	1.980
		Wang and Wang (2003)	3.204	2.321	1.961	–
		Azimi (1988)	3.199	2.321	–	–
		Ding (1994)	3.204	–	–	–

The fundamental frequencies of free vibration of annular plates with the clamped outer edge and the free inner edge (rigid interior support) are presented in Table 7 with comparison to the results by Vega (2000). The eigenvalues of free annular plates with elastic constraints at the inner edge and interior ring supports are presented in Table 8 for different combinations of the radius of the core and supports.

Table 2. The fundamental frequency λ_0 of free vibration of circular plates with the elastic ring support

K_1	κ_1	Dimensionless frequency λ_0	Boundary conditions			
			Clamped	Simply supported	Free	Sliding
1000	0	GF	3.204	2.223	0.666	0.667
	0.1	GF	4.677	3.805	1.946	2.238
	0.2	GF	5.175	4.202	2.049	2.418
		Wang and Wang (2003)	5.175	4.202	–	–
		Azimi (1988)	5.187	4.210	–	–
	0.3	Ding (1994)	4.929	–	–	–
		GF	5.763	4.682	2.187	2.656
		GF	6.110	5.276	2.374	2.979
	0.4	Wang and Wang (2003)	6.110	5.276	–	–
		Azimi (1988)	6.129	5.282	–	–
		Ding (1994)	6.114	–	–	–
		GF	5.195	5.136	2.619	3.403
	0.5	GF	4.503	4.479	2.891	3.803
		Wang and Wang (2003)	4.503	4.479	–	–
		Azimi (1988)	4.512	4.486	–	–
		Ding (1994)	4.492	–	–	–
		GF	3.967	3.962	2.992	3.707
	0.6	GF	3.539	3.532	2.787	3.438
		Wang and Wang (2003)	3.539	3.532	–	–
		Azimi (1988)	3.547	3.537	–	–
		Ding (1994)	3.547	–	–	–
		GF	3.751	3.752	–	–
	∞	0.1	3.909	3.909	–	–
		0.2	4.275	4.275	–	–
0.3		4.851	4.851	–	–	
0.4		5.706	5.707	–	–	
0.5		6.929	6.929	–	–	
0.6		8.396	8.390	–	–	
0.7		8.960	8.959	–	–	
0.8		7.809	7.809	–	–	
0.9		6.235	6.235	–	–	
1.0		4.935	4.935	–	–	

Table 3. The fundamental frequency λ_0 of free vibration of free circular plates with the rigid ring support

K_1	κ_1	Dimensionless frequency λ_0	
		GF	Wang (2014)
∞	0	3.751	3.752
	0.1	3.909	3.909
	0.2	4.275	4.275
	0.3	4.851	4.851
	0.4	5.706	5.707
	0.5	6.929	6.929
	0.6	8.396	8.390
	0.7	8.960	8.959
	0.8	7.809	7.809
	0.9	6.235	6.235
1.0	4.935	4.935	

Table 4. The fundamental frequency λ_0 of free vibration of free annular plates with different boundary conditions at the inner edge and interior elastic support

K_1	ξ_1	κ_1	Dimensionless frequency	Boundary conditions at the inner edge			
				Clamped	Simply supported	Free	Sliding
10	0.1	0.2	λ_0	2.043	1.826	1.350	1.364
	0.1	0.4		2.050	1.886	1.617	1.624
	0.1	0.6		2.207	2.091	1.848	1.848
	0.1	0.9		2.658	2.537	1.931	1.946
	0.3	0.5		2.569	1.918	1.730	1.778
	0.3	0.7		2.697	2.209	1.975	1.975
	0.3	0.9		3.003	2.587	1.959	2.041
	0.5	0.7		3.616	2.235	2.039	2.068
	0.5	0.9		3.812	2.736	2.086	2.193
	0.7	0.8		6.077	2.634	2.311	2.363
	0.7	0.9		6.119	3.008	2.401	2.436
0.8	0.9	9.197	3.275	2.658	2.658		

Table 5. The fundamental frequency λ_0 of free vibration of free annular plates with different boundary conditions at the inner edge and interior elastic support

K_1	ξ_1	κ_1	Dimensionless frequency	Boundary conditions at the inner edge			
				Clamped	Simply supported	Free	Sliding
1000	0.1	0.2	λ_0	2.087	1.925	1.979	2.091
	0.1	0.4		2.117	1.105	2.331	2.400
	0.1	0.6		9.335	3.843	2.852	2.934
	0.1	0.9		4.685	4.215	2.467	2.545
	0.3	0.5		2.684	7.401	2.352	2.859
	0.3	0.7		12.106	4.769	2.887	3.561
	0.3	0.9		6.175	5.214	2.439	2.987
	0.5	0.7		13.526	13.323	2.859	4.266
	0.5	0.9		9.260	7.249	2.648	4.106
	0.7	0.8		5.526	6.437	3.293	6.321
	0.7	0.9		8.396	8.054	3.432	7.049
0.8	0.9	9.697	7.774	4.294	8.334		

Table 6. The fundamental frequency λ_0 of free vibration of circular plates with elastic constraints and the interior ring support

K_1	κ_1	Dimensionless frequency	Elastic parameters at the outer edge	
			$\phi = 100, \psi = 10$	$\phi = 0.1, \psi = 100$
10	0	λ_0	2.056	2.203
	0.1		2.129	2.337
	0.2		2.190	2.434
	0.3		2.241	2.497
	0.4		2.285	2.524
	0.5		2.320	2.513
	0.6		2.344	2.469
	0.7		2.357	2.400
	0.8		2.361	2.321
100	0	λ_0	2.056	2.203
	0.1		2.441	2.928
	0.2		2.610	3.247
	0.3		2.770	3.486
	0.4		2.960	3.650
	0.5		3.188	3.648
	0.6		3.387	3.445
	0.7		3.318	3.145
	0.8		3.142	2.809
1000	0	λ_0	2.056	3.563
	0.1		2.715	3.600
	0.2		2.850	3.878
	0.3		3.032	4.176
	0.4		3.287	4.490
	0.5		3.629	4.700
	0.6		3.907	4.321
	0.7		3.719	3.786
	0.8		3.429	3.263
∞	0	λ_0	2.714	3.624
	0.1		2.769	3.746
	0.2		2.888	3.973
	0.3		3.068	4.250
	0.4		3.327	4.536
	0.5		3.664	4.700
	0.6		3.908	4.410
	0.7		3.743	3.892
	0.8		3.458	3.354

The Poisson ratio is taken as $\nu = 0.3$ for all considered cases. The numerical results are obtained by using the Newton-Raphson method and Mathematica v10 software. The obtained results are in good agreement with the results obtained by other methods presented in literature and can be used to validate the accuracy of other numerical methods as benchmark values.

Table 8. The fundamental frequency λ_0 of free vibration of free annular plates with elastic constraints at the inner edge and interior ring support

K_1	ξ_1	κ_1	Dimensionless frequency	Elastic parameters at the inner edge	
				$\phi = 100, \psi = 10$	$\phi = 0.1, \psi = 100$
10	0.1	0.2	λ_0	1.146	1.556
	0.1	0.4		1.530	1.740
	0.1	0.6		1.814	2.001
	0.1	0.9		2.031	2.439
	0.3	0.5		1.537	1.956
	0.3	0.7		1.839	2.238
	0.3	0.9		1.974	2.625
	0.5	0.7		1.648	2.296
	0.5	0.9		1.894	2.788
	0.7	0.8		1.510	2.680
	0.7	0.9		1.759	3.050
0.8	0.9	1.603	3.237		
1000	0.1	0.2	λ_0	2.101	1.941
	0.1	0.4		2.460	6.152
	0.1	0.6		3.091	3.663
	0.1	0.9		2.855	4.239
	0.3	0.5		2.906	0.852
	0.3	0.7		3.739	4.951
	0.3	0.9		3.212	6.150
	0.5	0.7		4.332	6.707
	0.5	0.9		4.267	7.911
	0.7	0.8		6.374	7.977
	0.7	0.9		7.185	8.053
0.8	0.9	8.319	8.196		
∞	0.1	0.2	λ_0	3.308	1.296
	0.1	0.4		3.687	1.463
	0.1	0.6		3.972	2.000
	0.1	0.9		3.022	1.351
	0.3	0.5		1.175	1.937
	0.3	0.7		2.071	2.120
	0.3	0.9		3.834	1.271
	0.5	0.7		2.995	2.030
	0.5	0.9		2.644	1.335
	0.7	0.8		1.998	0.999
	0.7	0.9		1.683	1.385
0.8	0.9	1.046	1.293		

7. Conclusions

In this paper, the quasi-Green function has been employed to solve natural vibration of elastically supported thin circular and annular plates with different boundary conditions. The advantage of quasi-Green's function is the obtaining of characteristic equations without calculating nontrivial constants in complicated forms. Additionally, the number of supports of circular and annular

plates does not influence the dimension of characteristic matrices, because the continuity conditions can be neglected. In the presented approach, the solution to the boundary value problem is much simpler. The quasi-Green function approach can be used to the frequency analysis of plates and beams with other discrete elements such as an additional mass or a mass on the spring. The exact frequencies of vibration presented in a non-dimensional form can serve as benchmark values for researchers to validate their numerical methods applied in similar problems presented in the paper.

Acknowledgements

The research was conducted within S/WZ/1/2014 project and was financed by the funds of the Ministry of Science and Higher Education, Poland.

References

1. AZIMI S., 1988, Free vibration of circular plates with elastic or rigid interior support, *Journal of Sound and Vibration*, **120**, 37-53
2. BODINE R.Y., 1967, Vibration of a circular plate supported by a concentric ring of arbitrary radius, *Journal of the Acoustical Society of America*, **41**, 1551
3. DING Z., 1994, Free vibration of arbitrarily shaped plates with concentric ring elastic and rigid supports, *Computers and Structures*, **50**, 685-692
4. JAROSZEWICZ J., ZORYJ L., 2005, *Methods of Free Axisymmetric Vibration Analysis of Circular Plates Using by Influence Functions*, Bialystok University of Technology, Poland
5. KUKLA S., SZEWCZYK M., 2004, The Green's functions for vibration problems of circular plates with elastic ring supports, *Scientific Research of the Institute of Mathematics and Computer Science*, **4**, 1, 79-86
6. KUKLA S., SZEWCZYK M., 2005, Application of Green's function method in frequency analysis of axisymmetric vibration of annular plates with elastic ring supports, *Scientific Research of the Institute of Mathematics and Computer Science*, **3**, 1, 67-72
7. KUKLA S., SZEWCZYK M., 2007, Frequency analysis of annular plates with elastic concentric supports by Green's function method, *Journal of Sound and Vibration*, **300**, 387-393
8. KUNUKKASSERIL V.X., SWAMIDAS A.S.J., 1974, Vibration of continuous circular plates, *International Journal of Solids and Structures*, **10**, 603-619
9. LAURA P.A.A., GUTIERREZ R.H., VERA S.A., VEGA D.A., 1999, Transverse vibrations of circular plate with a free edge and a concentric circular support, *Journal of Sound and Vibration*, **223**, 5, 843-845
10. LIU C.F., CHEN G.T., 1995, A simple finite element analysis of axisymmetric vibration of annular and circular plates, *International Journal of Mechanical Sciences*, **37**, 8, 861-871
11. MCLACHLAN N.W., 1955, *Bessel Functions for Engineers*, Clarendon Press, Oxford
12. RAO L.B., RAO C.K., 2014a, Frequencies of circular plate with concentric ring and elastic edge support, *Frontiers on Mechanical Engineering*, **9**, 2, 168-176
13. RAO L.B., RAO C.K., 2014b, Frequency analysis of annular plates with inner and outer edges elastically restrained and resting on Winkler foundation, *International Journal of Mechanical Sciences*, **81**, 184-194
14. SINGH A.V., MIRZA S., 1976, Free axisymmetric vibration of a circular plate elastically supported along two concentric circles, *Journal of Sound and Vibration*, **48**, 425-429
15. VEGA D.A., VERA S.A., LAURA P.A.A., GUTIERREZ R.H., PRONSATO M.E., 1999, Transverse vibrations of an annular circular plate with free edges and an intermediate concentric circular support, *Journal of Sound and Vibration*, **223**, 493-496

16. VEGA D.A., LAURA P.A.A., VERA S.A., 2000, Vibrations of an annular isotropic plate with one edge clamped or simply supported and an intermediate concentric circular supports, *Journal of Sound and Vibration*, **233**, 1, 171-174
17. WANG C.M., THEVENDRAN V., 1993, Vibration analysis of annular plates with concentric supports using a variant of Rayleigh-Ritz method, *Journal of Sound and Vibration*, **163**, 137-149
18. WANG C.Y., 2001, On the fundamental frequency of a circular plate supported on a ring, *Journal of Sound and Vibration*, **243**, 5, 945-946
19. WANG C.Y., WANG C.M., 2003, Fundamental frequencies of circular plates with internal elastic ring support, *Journal of Sound and Vibration*, **263**, 1071-1078
20. WANG C.Y., 2006, Fundamental frequencies of annular plates with movable edges, *Journal of Sound and Vibration*, **290**, 524-528
21. WANG C.Y., 2014, The vibration modes of concentrically supported free circular plates, *Journal of Sound and Vibration*, **333**, 835-847
22. ŻUR K.K., 2015, Green's function in frequency analysis of circular thin plates of variable thickness, *Journal of Theoretical and Applied Mechanics*, **53**, 4, 873-884
23. ŻUR K.K., 2016a, Green's function approach to frequency analysis of thin circular plates, *Bulletin of the Polish Academy of Sciences – Technical Sciences*, **64**, 1, 181-188
24. ŻUR K.K., 2016b, Green's function for frequency analysis of thin annular plates with nonlinear variable thickness, *Applied Mathematical Modelling*, **40**, 5-6, 3601-3619

Manuscript received November 2, 2015; accepted for print May 6, 2016

THE APPLICATION OF BECK'S METHOD COMBINED WITH FEM AND TREFFTZ FUNCTIONS TO DETERMINE THE HEAT TRANSFER COEFFICIENT IN A MINICHANNEL

BEATA MACIEJEWSKA

Kielce University of Technology, Department of Management and Computer Modelling, Kielce, Poland

e-mail: beatam@tu.kielce.pl

The aim of this study is to determine the heat transfer coefficient between the heated surface and the boiling fluid flowing in a minichannel on the basis of experimental data. The calculation model is based on Beck's method coupled with the FEM and Trefftz functions. The Trefftz functions used in the Hermite interpolation are employed to construct the shape functions in the FEM. The unknown local values of the heat transfer coefficient at the foil-fluid contact surface are calculated from Newton's law. The temperature of the heated foil and the heat flux on the foil surface are determined by solving a two-dimensional inverse heat conduction problem. The study is focused on the identification of the heat transfer coefficients in the subcooled boiling region and the saturated nucleate boiling region. The results are compared with the data obtained through the one-dimensional method. The investigations also reveal how the smoothing of measurement data affects calculation results.

Keywords: Beck's method, FEM, Trefftz functions, heat transfer coefficient, inverse heat conduction problem, flow boiling

1. Introduction

The main goal of this study is to determine the heat transfer coefficient at the interface between the heated minichannel wall and the boiling fluid flowing through the minichannel. To identify this coefficient we need to know the wall temperature, the temperature gradient and the fluid temperature. The two-dimensional calculation model proposed for determining these quantities requires solving an inverse heat conduction problem. Inverse problems are problems in which the causes of a process are estimated by measuring the process results (Beck *et al.*, 1985). Solutions to inverse problems are generally badly conditioned, which means that small changes in the input lead to large changes in the output (Tikhonov and Arsenin, 1977). Because of this property, inverse problems are much more difficult to solve than direct problems.

One of the classical methods used to solve inverse problems is the sensitivity coefficient method, also known as Beck's method or the sequential function specification method (Beck *et al.*, 1985). This approach involves introducing sensitivity coefficients as a derivative of the measured quantity with respect to the identified quantity and transforming an inverse problem into several direct problems. The direct problems can then be solved using the finite difference method (Beck, 1970; Lin *et al.*, 2008; Shi and Wang, 2009), the boundary element method (Kurpisz and Nowak, 1992; Le Niliot and Lefevre, 2004), the finite element method (Duda and Taler, 2009; Tseng *et al.*, 1996), or the Trefftz method (Kruk and Sokała, 1999, 2000; Piasecka and Maciejewska, 2012). Although the sensitivity coefficient method is generally used to solve unsteady state problems, it can also be adapted to solve steady state problems (Kruk and Sokała, 1999; Piasecka and Maciejewska, 2012; Tseng *et al.*, 1995).

The approach proposed by Trefftz (1926) seems particularly useful to deal with inverse problems. It involves approximating the unknown solution of a differential equation by means

of a linear combination of functions strictly satisfying the differential equation. Such functions are known as Trefftz functions. Then, it is necessary to adjust the approximation function to match the boundary conditions and, additionally, the initial conditions in the case of unsteady state problems. Details of the method based on Trefftz functions can be found in (Ciałkowski and Grysa, 2009; Grysa and Maciejewska, 2013; Herrera, 2000; Hożejewska *et al.*, 2009; Kompis *et al.*, 2001; Li *et al.*, 2006; Maciąg, 2011).

The application of Trefftz functions to construct shape functions in the finite element method and the use of this method to identify the boundary conditions in a steady-state problem are discussed in (Ciałkowski and Frąckowiak, 2002; Grysa *et al.*, 2012; Piasecka and Maciejewska, 2013). Inverse unsteady state problems solved by means of the FEM with space-time basis functions are shown in (Ciałkowski, 2002; Maciejewska, 2004).

In this study, Beck's method combined with the FEM and Trefftz-type basis functions is used to solve the inverse heat conduction problem. This method allows us to directly determine the heat flux on the boundary surface; there is no need to differentiate the temperature function. In numerical calculations, differentiation of a function can lead to errors in results. The use of Beck's method connected with the Trefftz method, as proposed by Piasecka and Maciejewska (2012), was reported to be ineffective in a more complicated distribution of heat flux density on the boundary. It is assumed that the calculations should be performed by means of the FEM. The use of the Trefftz functions and the Hermite interpolation to construct the basis functions give satisfactory results. Details of this approach will be described in the next Sections. The Hermite interpolation was shown by Kincaid and Cheney (2002).

2. Experimental research

The calculation of the heat transfer coefficient has been performed using the experimental data obtained from the experimental setup described in detail in (Piasecka, 2014a,c, 2015; Piasecka and Maciejewska, 2015).

The main element of the experimental setup was a cuboidal minichannel $1\text{ mm} \times 40\text{ mm} \times 360\text{ mm}$. FC-72 was used as the working fluid flowing up the minichannel with the velocity $u = 0.17\text{ m/s}$. The average mass flux G was $282\text{ kg}/(\text{m}^2\text{s})$, Reynolds number Re was 950, inlet liquid subcooling defined as the difference between the saturation temperature at the minichannel inlet and the fluid temperature at the minichannel inlet $\Delta T_{sub,in}$ was 36 K. One of the minichannel walls was a heated foil made of Haynes 230 alloy. Because of the electrical properties of the material, it was possible to produce a large heat flux at a relatively small surface area of the foil. On the side in contact with the fluid, the heated foil had evenly distributed microcavities produced by laser machining (Piasecka, 2014b; Piasecka and Maciejewska, 2015).

The heated foil was separated from the surroundings with a glass panel. The surface of the foil in contact with the glass was covered with a thin layer of thermochromic liquid crystals.

During the experiments, the quantities were measured in the steady state. The measurement data included:

- heat flow parameters:
 - local temperature of the heated foil at the surface in contact with the glass panel determined from the distribution of hues on the liquid crystal layer using the method described by Piasecka (2013);
 - fluid temperature at the minichannel inlet $T_{f,in}$ and the fluid temperature at the minichannel outlet $T_{f,out}$, measured with K-type thermocouples linked to the data acquisition station;
 - volumetric flow rate Q_V measured with rotameters;

- pressure at the minichannel inlet p_{in} and pressure at the minichannel outlet p_{out} measured with pressure transducers linked to the data acquisition station;
- electrical parameters:
 - drop in voltage ΔU along the length of the heated foil, measured with a voltmeter;
 - electric current supplied to the heated foil I measured with an ammeter;
- flow structures.

The capacity of the heat source (volumetric heat flux) has been determined from the formula

$$q_V = \frac{I\Delta U}{A_F\delta_F} = \frac{q_w}{\delta_F} \quad (2.1)$$

where I is the current supplied to the heated foil, ΔU – drop in voltage along the length of the heated foil, A_F – surface area of the heated foil in contact with the fluid, δ_F – thickness of the heated foil, q_w – heat flux.

The numerical calculations have been performed using the measurement data presented in Fig. 1 and Table 1. The other quantities used in the analysis are: surface area of the heated foil in contact with the fluid $A_F = 0.0234 \text{ m}^2$, thickness of the heated foil $\delta_F = 0.00016 \text{ m}$, thickness of the glass panel $\delta_G = 0.006 \text{ m}$, length of the glass panel $L = 0.35 \text{ m}$, thermal conductivity coefficient of the foil $\lambda_F = 8.3 \text{ W}/(\text{mK})$ and thermal conductivity coefficient of the glass panel $\lambda_G = 0.71 \text{ W}/(\text{mK})$.

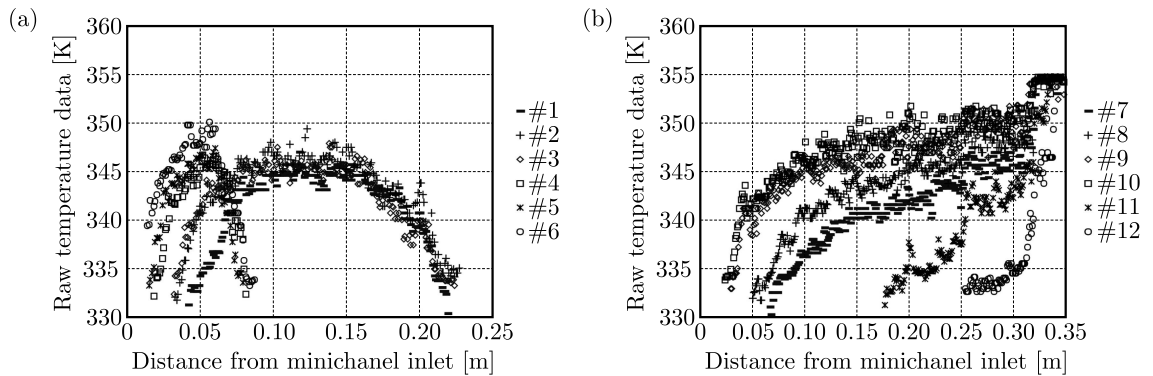


Fig. 1. Raw temperature data obtained from measurements at the foil-glass interface, corresponding to: (a) subcooled boiling region, (b) saturated nucleate boiling region

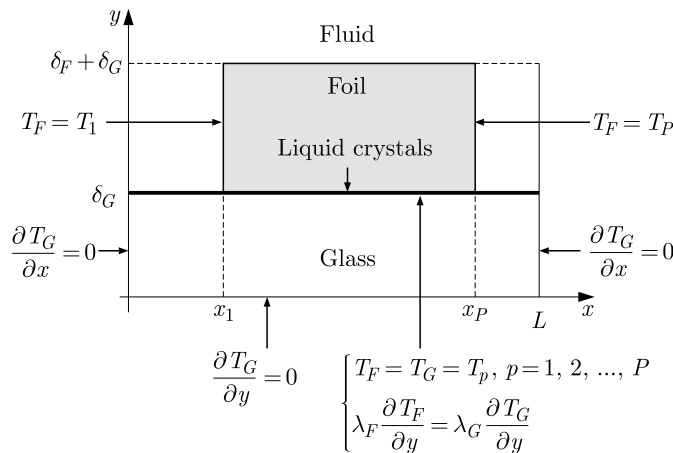


Fig. 2. The boundary conditions (note: figure not to scale)

Table 1. Measurement data used in the calculations: I – current supplied to the heated foil, ΔU – drop in voltage along the length of the heated foil, T_f – fluid temperature, p – pressure; indexes in , out refer to minichannel inlet and outlet

Setting number	I [A]	ΔU [V]	$T_{f,in}$ [K]	$T_{f,out}$ [K]	p_{in} [Pa]	p_{out} [Pa]
#1	39.8	5.93	301.15	310.65	119850	110950
#2	41	6.03	300.95	311.85	119150	113450
#3	42.6	6.14	300.85	312.65	123250	114550
#4	44	6.84	300.85	314.35	124150	113950
#5	45.2	6.47	300.55	314.85	123650	114750
#6	46.60	6.54	300.55	315.65	123950	117450
#7	63.20	8.33	299.95	334.35	132050	124550
#8	64.40	8.53	300.25	335.95	140550	119950
#9	65.40	8.60	300.35	337.85	139650	132350
#10	61.60	8.19	301.25	338.05	140750	133150
#11	51.60	7.05	301.75	330.75	127950	119750
#12	48.20	6.79	300.75	326.05	125650	117050

The numerical calculations have been performed also for the smoothed temperature data (see Fig. 2). The data was smoothed by means of the approximating polynomial based on the Trefftz functions using the least squares method (Grysa *et al.*, 2012).

3. Mathematical model

Two-dimensional stationary heat transfer in the minichannel described in Cartesian coordinates x , y is assumed in the investigations. The x coordinate refers to the fluid flow direction and the y coordinate relates to thickness of the heated foil and the glass panel. In this investigation, variation in temperature along width of the minichannel is neglected.

The local values of the heat transfer coefficient between the heated foil and the boiling fluid flowing in the minichannel are calculated using Newton's law.

$$\alpha_{2D}(x) = \frac{q(x)}{T_F(x, \delta_G + \delta_F) - T_f(x)} \quad (3.1)$$

where q is the heat flux transferred from the heated foil to the fluid, T_F – temperature of the foil, with q and T_F determined by solving the inverse heat conduction problem in the heated foil, δ_G – thickness of the glass panel, δ_F – thickness of the foil, T_f – temperature of the fluid, with $T_f(x) = T_l(x)$ in the subcooled boiling region and $T_f(x) = T_{sat}(x)$ in the saturated nucleate boiling region, T_l – liquid temperature calculated on the assumption of a linear distribution of liquid temperature along the minichannel from the temperature $T_{f,in}$ to the temperature $T_{f,out}$, and T_{sat} – saturation temperature determined on the assumption of a linear distribution of fluid pressure along the minichannel (Piasecka and Maciejewska, 2015; Piasecka *et al.*, 2017).

The mathematical model is based on the model presented by Hozejowska and Piasecka (2014). For the purpose of the FEM, changes in the determinancy domain of the differential equation and in the boundary conditions are taken into account.

The temperature of the heated foil satisfies the Poisson equation

$$\frac{\partial^2 T_F}{\partial x^2} + \frac{\partial^2 T_F}{\partial y^2} = -\frac{q_V}{\lambda_F} \quad (3.2)$$

for $(x, y) \in \Omega_F = \{(x, y) \in R^2 : x_1 < x < x_P, \delta_G < y < \delta_G + \delta_F\}$

and the boundary conditions (see Fig. 2)

$$\begin{aligned} T_F(x, \delta_G) &= T_G(x, \delta_G) & \lambda_F \frac{\partial T_F}{\partial y}(x, \delta_G) &= \lambda_G \frac{\partial T_G}{\partial y}(x, \delta_G) \\ T_F(x_1, y) &= T_1 & T_F(x_P, y) &= T_P \end{aligned} \quad (3.3)$$

and

$$T_F(x_p, \delta_G) = T_p \quad \text{for } p = 1, 2, \dots, P \quad (3.4)$$

where x_1 is the location of the first measurement point at the boundary $y = \delta_G$, x_P – location of the last measurement point, P – number of measurements, T_p – measured temperature, λ_F and λ_G – thermal conductivity coefficients of the foil and glass, respectively, q_V , δ_G , δ_F have the same denotations as in Eqs. (2.1) and (3.1).

The temperature of the glass panel, as in (Hozejowska and Piasecka, 2014), has been determined by solving the direct heat conduction problem

$$\frac{\partial^2 T_G}{\partial x^2} + \frac{\partial^2 T_G}{\partial y^2} = 0 \quad \text{for } (x, y) \in \Omega_G = \{(x, y) \in R^2 : 0 < x < L, 0 < y < \delta_G\} \quad (3.5)$$

and

$$\begin{aligned} \frac{\partial T_G}{\partial y}(x, 0) &= 0 & \frac{\partial T_G}{\partial x}(0, y) &= 0 & \frac{\partial T_G}{\partial x}(L, y) &= 0 \\ T_G(x_p, \delta_G) &= T_p & \text{for } p &= 1, 2, \dots, P \end{aligned} \quad (3.6)$$

where L denotes length of the glass panel, δ_G , x_P , P have the same denotations as in Eqs. (3.2)-(3.4).

The inverse problem, Eqs. (3.2)-(3.4), has been solved using Beck's method combined with the FEM and Trefftz functions. With the Trefftz functions used, the approximate functions exactly satisfy the governing differential equations. The direct problem, Eqs. (3.5) and (3.6), has been solved by means of the Trefftz method described by Hozejowska *et al.* (2015).

4. Beck's method coupled with the FEMT

Beck's method (Beck *et al.*, 1985) involves converting an inverse problem into several direct problems by applying the so-called sensitivity coefficients. Since the heat flux at the boundary is the unknown quantity here, it is essential to determine the sensitivity coefficients as derivatives of temperature with respect to the unknown flux.

The calculations have been performed assuming the heat flux q at the boundary $y = \delta_G + \delta_F$ for $x_1 \leq x \leq x_P$ in the form

$$q = \sum_{m=1}^{L1} [U(x - x_m) - U(x - x_{m+1})] q_m \quad (4.1)$$

where U is the unit step function (the Heaviside function), while q_m for $m = 1, 2, \dots, L1$ take constant values (Kruk and Sokała, 1999). The same partition of the boundary $y = \delta_G + \delta_F$, $x \in \langle x_1, x_P \rangle$ into $L1$ parts will also be used in the FEM.

The temperature T_F dependent on the q_m fluxes for $m = 1, 2, \dots, L1$ at the boundary $y = \delta_G + \delta_F$ for $x_1 \leq x \leq x_P$, like in (Kruk and Sokała, 1999), is expanded into a Taylor series

about a fixed point (q_{01}, \dots, q_{0L1}) . Since higher order derivatives disappear in linear problems, we obtain the formula

$$T_F(x, y, q_1, \dots, q_{L1}) = T_F(x, y, q_{01}, \dots, q_{0L1}) + \sum_{m=1}^{L1} \left. \frac{\partial T_F}{\partial q_m} \right|_{q_m=q_{0m}} (q_m - q_{0m}) \quad (4.2)$$

After introducing the denotations $\Theta_F(x, y) = T_F(x, y, q_{01}, \dots, q_{0L1})$ and $Z_m(x, y) = (\partial T_F / \partial q_m)|_{q_m=q_{0m}}$, expression (4.2) is written as

$$T_F(x, y, q_1, \dots, q_{L1}) = \Theta_F(x, y) + \sum_{m=1}^{L1} Z_m(x, y)(q_m - q_{0m}) \quad (4.3)$$

where $Z_m(x, y)$, for $m = 1, 2, \dots, L1$ are the sensitivity coefficients.

$\Theta_F(x, y)$ and $Z_m(x, y)$ for $m = 1, 2, \dots, L1$ in the domain Ω_F are determined by solving $1+L1$ direct problems that arise after substituting Eq. (4.3) into Eq. (3.2) and boundary conditions Eq. (3.3)

$$\begin{aligned} \frac{\partial^2 \Theta_F}{\partial x^2} + \frac{\partial^2 \Theta_F}{\partial y^2} &= -\frac{qV}{\lambda_F} \quad \text{for } (x, y) \in \Omega_F \\ \Theta_F(x, \delta_G) &= T_G(x, \delta_G) \quad \lambda_F \frac{\partial \Theta_F}{\partial y}(x, \delta_G) = \lambda_G \frac{\partial T_G}{\partial y}(x, \delta_G) \\ \frac{\partial \Theta_F}{\partial y}(x, \delta_G + \delta_F) &= 0 \quad \Theta_F(x_1, y) = T_1 \quad \Theta_F(x_P, y) = T_P \end{aligned} \quad (4.4)$$

and

$$\begin{aligned} \frac{\partial^2 Z_m}{\partial x^2} + \frac{\partial^2 Z_m}{\partial y^2} &= 0 \quad \text{for } m = 1, 2, \dots, L1 \quad \text{and } (x, y) \in \Omega_F \\ Z_m(x_1, y) &= 0 \quad Z_m(x_P, y) = 0 \quad Z_m(x, \delta_G) = 0 \\ \frac{\partial Z_m}{\partial y}(x, \delta_G) &= 0 \quad -\lambda_F \frac{\partial Z_m}{\partial y}(x, \delta_G + \delta_F) = U(x - x_m) - U(x - x_{m+1}) \end{aligned} \quad (4.5)$$

Condition (3.4) will be used in the subsequent calculations.

The functions Θ_F and Z_m for $m = 1, 2, \dots, L1$ have been determined using the finite element method combined with the Trefftz-type basis functions (FEMT), as described in (Piasecka and Maciejewska, 2013). In this paper, the partition of the domain Ω_F into finite elements is closely linked to the partition of the boundary $y = \delta_G + \delta_F$, $x \in \langle x_1, x_P \rangle$ into $L1$ parts, like in Eq. (4.1). The basis functions $f_{jk}(x, y)$, $g_{jk}(x, y)$, $h_{jk}(x, y)$ constructed with the Hermite interpolation (Kincaid and Cheney, 2002), have the following properties in nodes (x_i, y_i)

$$\left. \begin{aligned} f_{jk}(x_i, y_i) &= \delta_{ki} & \frac{\partial f_{jk}}{\partial x}(x_i, y_i) &= 0 & \frac{\partial f_{jk}}{\partial y}(x_i, y_i) &= 0 \\ g_{jk}(x_i, y_i) &= 0 & \frac{\partial g_{jk}}{\partial x}(x_i, y_i) &= \delta_{ki} & \frac{\partial g_{jk}}{\partial y}(x_i, y_i) &= 0 \\ h_{jk}(x_i, y_i) &= 0 & \frac{\partial h_{jk}}{\partial x}(x_i, y_i) &= 0 & \frac{\partial h_{jk}}{\partial y}(x_i, y_i) &= \delta_{ki} \end{aligned} \right\} \quad i = 1, 2, \dots, N \quad (4.6)$$

where j is the element number, k – number of the basis function in the j -th element, N – number of nodes in the j -th element, δ_{ki} – Kronecker delta.

Three nodal parameters are associated with each interpolation node: the value of the function at a node, the value of the partial derivative with respect to x , and the value of the partial derivative with respect to y .

In each element Ω_F^j , the function $\Theta_F(x, y)$ is approximated by means of a linear combination of the basis functions

$$\begin{aligned} \Theta_F^j(x, y) = & u(x, y) + \sum_{k=1}^N \left\{ [a_n - u(x_n, y_n)] f_{jk}(x, y) + [b_n - u'_x(x_n, y_n)] g_{jk}(x, y) \right. \\ & \left. + [c_n - u'_y(x_n, y_n)] h_{jk}(x, y) \right\} \end{aligned} \quad (4.7)$$

where $u(x, y)$ is the particular solution of equation (4.4)₁, n – number of the node in the whole domain Ω_F , a_n – value of the unknown function at the n -th node of the domain Ω_F , b_n – value of the partial derivative of the unknown function with respect to x at the n -th node of the domain Ω_F , c_n – value of the partial derivative of the unknown function with respect to y at the n -th node of the domain Ω_F , $f_{jk}(x, y)$, $g_{jk}(x, y)$ and $h_{jk}(x, y)$ – basis functions, j, k, N have the same denotations as in Eqs. (4.6).

The unknown coefficients a_n, b_n, c_n in linear combination (4.7) have been calculated, like in (Piasecka and Maciejewska, 2013), by minimizing the functional J which describes the mean square error of fit of the approximate function to the boundary conditions and the difference between the values of the approximate function at the common edges of the adjacent elements, and in this calculations has the form

$$\begin{aligned} J = & \sum_{j=1}^{L1} \int_{x_j}^{x_{j+1}} [\Theta_F^j(x, \delta_G) - T_G^j(x, \delta_G)]^2 dx + \sum_{j=1}^{L1} \int_{x_j}^{x_{j+1}} \left[\lambda_F \frac{\partial \Theta_F^j}{\partial y}(x, \delta_G) - \lambda_G \frac{\partial T_G^j}{\partial y}(x, \delta_G) \right]^2 dx \\ & + \sum_{j=1}^{L1} \int_{x_j}^{x_{j+1}} \left[\frac{\partial \Theta_F^j}{\partial y}(x, \delta_G + \delta_F) \right]^2 dx + \sum_{i=0}^{L2-1} \int_{\delta_G + y_{i+1}}^{\delta_G + y_{i+2}} [\Theta_F^{1+iL1}(x_1, y) - T_1]^2 dy \\ & + \sum_{i=0}^{L2-1} \int_{\delta_G + y_{i+1}}^{\delta_G + y_{i+2}} [\Theta_F^{(i+1)L1}(x_P, y) - T_P]^2 dy \\ & + \sum_{i=0}^{L2-1} \sum_{j=1}^{L1-1} \int_{\delta_G + y_{i+1}}^{\delta_G + y_{i+2}} [\Theta_F^{j+iL1}(x_{j+1}, y) - \Theta_F^{j+1+iL1}(x_{j+1}, y)]^2 dy \\ & + \sum_{i=0}^{L2-1} \sum_{j=1}^{L1-1} \int_{\delta_G + y_{i+1}}^{\delta_G + y_{i+2}} \left[\frac{\partial \Theta_F^{j+iL1}}{\partial x}(x_{j+1}, y) - \frac{\partial \Theta_F^{j+1+iL1}}{\partial x}(x_{j+1}, y) \right]^2 dy \\ & + \sum_{i=1}^{L2-1} \sum_{j=1}^{L1} \int_{x_j}^{x_{j+1}} [\Theta_F^{j+(i-1)L1}(x, \delta_G + y_{i+1}) - \Theta_F^{j+iL1}(x, \delta_G + y_{i+1})]^2 dx \\ & + \sum_{i=0}^{L2-1} \sum_{j=1}^{L1} \int_{x_j}^{x_{j+1}} \left[\frac{\partial \Theta_F^{j+(i-1)L1}}{\partial y}(x, \delta_G + y_{i+1}) - \frac{\partial \Theta_F^{j+iL1}}{\partial y}(x, \delta_G + y_{i+1}) \right]^2 dx \end{aligned} \quad (4.8)$$

Similarly, the solutions to the $L1$ direct problems give the sensitivity coefficients Z_m for $m = 1, 2, \dots, L1$.

The values of q_m for $m = 1, 2, \dots, L1$ in expression (4.3) have been calculated by minimizing the functional J_F^P that describes the mean square error between the values of the function $T_F(x, y, q_1, \dots, q_{L1})$ at the measurement points and temperature measurements

$$J_F^P = \sum_{p=1}^P [T_F(x_p, y_p, q_1, \dots, q_{L1}) - T_p]^2 \quad (4.9)$$

5. Calculation results

The values of the heat transfer coefficient have been obtained by solving the inverse heat conduction problem through Beck's method coupled with the finite element method in which the Trefftz functions were used as basis functions. The values of this coefficient were determined in the subcooled boiling region and in the saturated nucleate boiling region.

The calculations were performed using the raw temperature data presented in Fig. 1 as well as the smoothed temperature data. In both approaches, two variants of the partition of the boundary $y = \delta_G + \delta_F$ for $x \in \langle x_1, x_P \rangle$ into subdomains were considered. In variant one, the boundary was partitioned into $L1 = 10$ subdomains, while in variant two, it was partitioned into $L1 = 20$ subdomains. In neither case the domain Ω_F was partitioned in the y -direction. The four Hermite interpolation nodes were placed at the vertices of rectangular elements of the mesh. As three nodal parameters were associated with each interpolation node, the basis functions were constructed using 12 Trefftz functions. The particular solution to Eq. (4.4)₁ was written in the following form $u(x, y) = -0.25q_V \lambda_F^{-1}(y^2 + x^2)$. The calculations were performed using the data from 12 settings shown in Fig. 1 as well as Table 1. The heat transfer coefficients as a function of distance from the minichannel inlet are shown in Figs. 3-5.

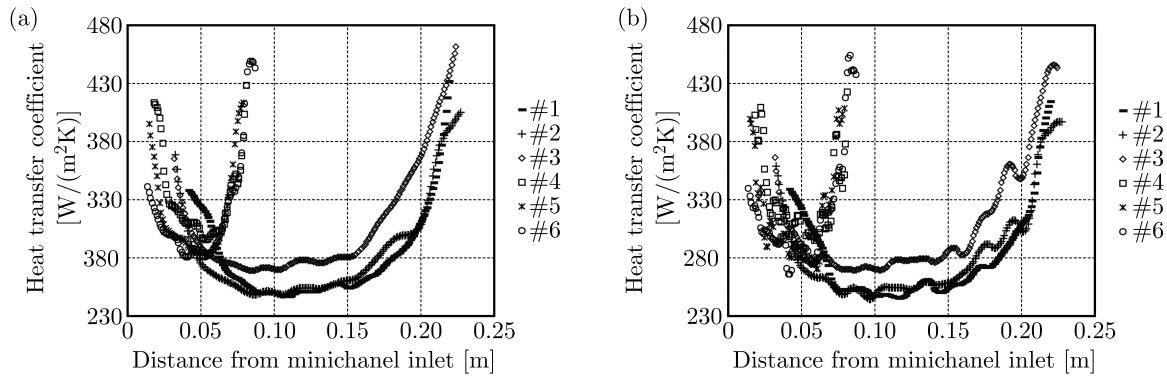


Fig. 3. Heat transfer coefficients in the subcooled boiling region vs. distance from the minichannel inlet obtained on the basis of the raw temperature data with the boundary partitioned into: (a) $L1 = 10$ subdomains, (b) $L1 = 20$ subdomains

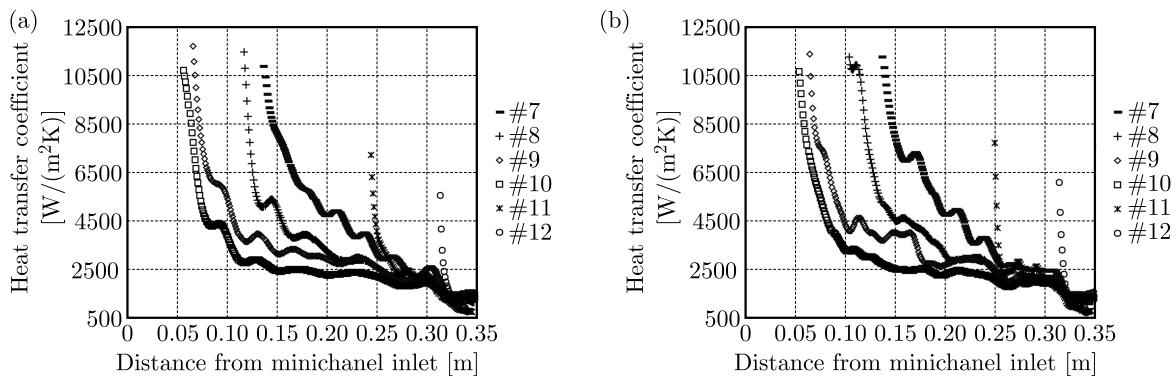


Fig. 4. Heat transfer coefficients in the saturated nucleate boiling region vs. distance from the minichannel inlet obtained on the basis of the raw temperature data with the boundary partitioned into: (a) $L1 = 10$ subdomains, (b) $L1 = 20$ subdomains

The relative differences between the values of the heat transfer coefficients obtained for both variants of the boundary partition into $L1 = 10$ subdomains and $L1 = 20$ subdomains were calculated according to formula (5.1) and shown in Table 2

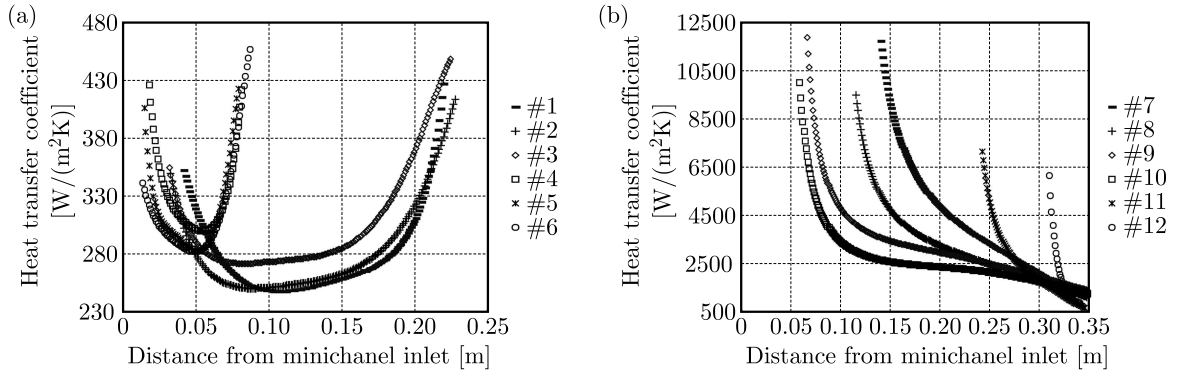


Fig. 5. Heat transfer coefficients vs. distance from the minichannel inlet obtained on the basis of the smoothed temperature data with the boundary partitioned into $L1 = 10$ subdomains: (a) in the saturated nucleate boiling region, (b) in the subcooled boiling region

$$\sigma_i = \frac{1}{P} \sum_{p=1}^P \sqrt{\frac{[\alpha_{2D}^{i,L1=10}(x_p) - \alpha_{2D}^{i,L1=20}(x_p)]^2}{\{\min[\alpha_{2D}^{i,L1=10}(x_p), \alpha_{2D}^{i,L1=20}(x_p)]\}^2}} \quad i = Raw, Smoo \quad (5.1)$$

where P denotes the number of measurements, $\alpha_{2D}^{i,L1=10}$ and $\alpha_{2D}^{i,L1=20}$ are values of the heat transfer coefficients calculated for $L1 = 10$ and $L1 = 20$ subdomains, respectively, indexes $i = Raw$ and $i = Smoo$ refer to the calculations based on the raw measurement data and the smoothed temperature data, respectively. From Table 2, it is evident that the greatest differences between the values of the heat transfer coefficients occurred at setting #11 when the raw measurement data was used. Since there are very small differences between the values of the heat transfer coefficient obtained from the smoothed data for the case when the domain is divided into $L1 = 10$ subdomains and those reported for the division into $L1 = 20$ subdomains, Fig. 5 shows only the results obtained for $L1 = 10$.

Table 2. Relative differences between the values of the heat transfer coefficient obtained for both variants of the boundary partition into $L1 = 10$ subdomains and $L1 = 20$ subdomains using the raw and smoothed temperature data

	Subcooled boiling region						Saturated nucleate boiling region					
	Setting number											
	#1	#2	#3	#4	#5	#6	#7	#8	#9	#10	#11	#12
σ_{Raw} [%]	1.33	1.23	1.2	3.11	2.98	2.07	5.54	5.73	8.55	5.1	12.57	9.32
σ_{Smoo} [%]	0.08	0.12	0.08	0.04	0.05	0.4	1.9	1.57	2.8	2.76	0.17	0.12

The obtained results are in agreement with the data presented in (Grysa *et al.*, 2012; Hozejowska and Piasecka, 2014; Hozejowska *et al.*, 2009; Ozer *et al.*, 2011; Piasecka and Maciejewska, 2012, 2013, 2015; Piasecka *et al.*, 2017), which are provided in Table 3. The values of the heat transfer coefficient are high in the saturated nucleate boiling region (like in Hozejowska and Piasecka, 2014; Piasecka and Maciejewska, 2015, Piasecka *et al.*, 2016); they are much lower in the subcooled boiling region (like in Grysa *et al.*, 2012; Hozejowska *et al.*, 2009; Ozer *et al.*, 2011; Piasecka and Maciejewska, 2012, 2013, 2015). The experimental parameters provided in Section 2 reported for the minichannel in the subcooled boiling region are most similar to the data described by Piasecka and Maciejewska (2012); while in the saturated nucleate boiling region resembled those discussed by Hozejowska and Piasecka (2014). The values of the heat transfer coefficient shown in Figs. 3-5 are not very different from those presented in (Piasecka and Maciejewska, 2012) and (Hozejowska and Piasecka, 2014).

Table 3. Experimental data and heat transfer coefficients presented in (Grysa *et al.*, 2012 [7]; Hozejowska and Piasecka, 2014 [11]; Hozejowska *et al.*, 2009 [12]; Ozer *et al.*, 2011 [23]; Piasecka and Maciejewska, 2012 [29], 2013 [30], 2015 [31]; Piasecka *et al.*, 2017 [32])

	Subcooled boiling region						Saturated nucleate boiling region		
Reference	[7]	[12]	[23]	[29]	[30]	[31]	[11]	[31]	[32]
No. of experim. analysed	1	1	2	3	1	3	1	3	2
Working fluid	R 123	R 123	Novec 649	FC-72	FC-72	FC-72	FC-72	FC-72	FC-72
Minichannel dimensions dept, width, length [mm]	1, 40, 300	1, 40, 360	1, 2, 357	1, 60, 360	1, 40, 360	1, 40, 360	1, 40, 360	1, 40, 360	1.7, 24, 360
Spatial orientation	vert.	vert.	horizontal	Exp. 1: vert. Exp. 2: horiz. Exp. 3: horiz.	vert.	Exp. 1: vert. Exp. 2: horiz. Exp. 3: horiz.	vert.	Exp. 1: vert. Exp. 2: horiz. Exp. 3: horiz.	Exp.1 : vert. Exp. 2: vert. Exp. 3: horiz.
Type of heated surface	smooth	smooth	smooth	smooth	enhanced	enhanced	enhanced	enhanced	enhanced
Heat flux q_w [kW/m ²]	25.4-37.6	14.0, 23.6	Exp. 1: 6.407 Exp. 2: 6.135	Exp. 1: 11.2-16.2 Exp. 2: 9.3-10.1 Exp. 3: 13.8-16.6	9.4-23.1	Exp. 1: 11.7-17.7 Exp. 2: 14.8-18.4 Exp. 3: 7.1-11.6	8.9-27	Exp. 1: 20.2-21.6 Exp. 2: 19.3-22.9 Exp. 3: 13.3-13.9	Exp. 1: 11.6-16.9 Exp. 2: 12.2-17.3
Maximum values of heat transfer coefficient α [kW/(m ² K)]	1.05-1.33	0.36, 0.53	Exp. 1: 0.2 Exp. 2: 0.325	Exp. 1: 0.32-0.5 Exp. 2: 0.202-0.22 Exp. 3: 0.375-500	0.19-0.56	Exp. 1: 0.32-0.55 Exp. 2: 0.4-0.5 Exp. 3: 0.2-0.27	10-80	Exp. 1: 100-175 Exp. 2: 70-130 Exp. 3: 20-33	Exp. 1: 50-70 Exp. 2: 60-65
Pressure at minichannel inlet p_{in} [kPa]	330	190	–	Exp. 1: 136 Exp. 2: 115 Exp. 3: 120-123	130	Exp. 1: 125 Exp. 2: 140 Exp. 3: 120	125	Exp. 1: 125 Exp. 2: 145 Exp. 3: 139	Exp. 1: 140 Exp. 2: 140
Average mass flux G [kg/(m ² s)]	219	412	Exp. 1: 60 Exp. 2: 44	Exp. 1: 160 Exp. 2: 165 Exp. 3: 163	236	Exp. 1: 211 Exp. 2: 207 Exp. 3: 211	285	Exp. 1: 204 Exp. 2: 204 Exp. 3: 208	Exp. 1: 260 Exp. 2: 144
Reynolds number Re	946	–	Exp. 1: 205 Exp. 2: 152	Exp. 1: 552 Exp. 2: 478 Exp. 3: 510	735	Exp. 1: 704 Exp. 2: 720 Exp. 3: 670	880	Exp. 1: 755 Exp. 2: 758 Exp. 3: 714	Exp. 1: 1003 Exp. 2: 968
Inlet liquid subcooling $\Delta T_{sub,in}$ [K]	68	36	Exp. 1: 56.2 Exp. 2: 45	Exp. 1: 54 Exp. 2: 55 Exp. 3: 55	50	Exp. 1: 42 Exp. 2: 43 Exp. 3: 30	42	Exp. 1: 44 Exp. 2: 43 Exp. 3: 42	Exp. 1: 38.5 Exp. 2: 42.5

6. Comparison of the results obtained by Beck's method coupled with the FEMT and those obtained using the one-dimensional method

The one-dimensional method described by Piasecka *et al.* (2017) has been employed to verify the results. This method assumes that the whole heat flux supplied to the heated foil q_V is transferred to the fluid flowing in the minichannel. The temperature measured at the surface $y = \delta_G$ is assumed to be the temperature of the wall $y = \delta_G + \delta_F$. This approach is appropriate only when the foil thickness δ_F is negligible. In the one-dimensional method, the heat transfer coefficients have been calculated from the formula (Piasecka *et al.*, 2017)

$$\alpha_{1D}^i(x_p) = \frac{I\Delta U}{A_F[T_p - T_f(x_p)]} \quad p = 1, 2, \dots, P \quad i = Raw, Smoo \quad (6.1)$$

where I , ΔU , A_F , T_f , T_p , i have the same denotations as in expressions Eqs. (2.1), (3.1), (3.4), (5.1).

The calculations have been performed using the raw and smoothed measurement data.

The relative differences between the values of the heat transfer coefficient determined with the one-dimensional method and those obtained by means of Beck's method coupled with the FEMT have been calculated from the following formula

$$\sigma_i^{L1=j} = \frac{1}{P} \sum_{p=1}^P \sqrt{\frac{[\alpha_{1D}^i(x_p) - \alpha_{2D}^{i,L1=j}(x_p)]^2}{[\alpha_{2D}^{i,L1=j}(x_p)]^2}} \quad \text{for } j = 10, 20; \quad i = Raw, Smoo \quad (6.2)$$

where P , $\alpha_{2D}^{i,L1=10}$, $\alpha_{2D}^{i,L1=20}$, and i have the same denotations as in formula (5.1), α_{1D}^{Raw} and α_{1D}^{Smoo} are values of the heat transfer coefficient obtained by the one-dimensional method using the raw measurement data and the smoothed measurement data, respectively, Eq. (6.1).

The calculation results are presented in Table 4. The greatest differences between the values of the heat transfer coefficient obtained with the one-dimensional method and those reported for Beck's method coupled with the FEMT occurred at setting #11 when the raw measurement data was used and the domain was partitioned into $L1 = 10$ subdomains in the x -direction, see Fig. 6.

Table 4. Relative differences between the values of the heat transfer coefficient obtained with the one-dimensional method and those reported for Beck's method coupled with the FEMT

	Subcooled boiling region					Saturated nucleate boiling region						
	Setting number											
	#1	#2	#3	#4	#5	#6	#7	#8	#9	#10	#11	#12
$\sigma_{Raw}^{L1=10}$ [%]	1.72	1.9	1.85	1.91	1.5	1.4	12.1	9.18	11.34	10.56	13.24	12.33
$\sigma_{Raw}^{L1=20}$ [%]	1.35	1.66	1.57	2.6	2.24	1.49	10.56	8.43	8.79	9.14	8.23	11.96
$\sigma_{Smoo}^{L1=10}$ [%]	0.3	0.33	0.38	0.49	0.6	0.32	6.8	4.87	5.67	4.87	4.0	2.96
$\sigma_{Smoo}^{L1=20}$ [%]	0.31	0.35	0.39	0.49	0.59	0.31	6.48	5.54	5.48	4.48	4.01	2.99

7. Conclusions

This paper discusses the application of Beck's method combined with the FEMT to calculate the local values of the heat transfer coefficients for the heat transfer between the heated foil and the fluid flowing in the minichannel. The sensitivity coefficients are introduced as derivatives

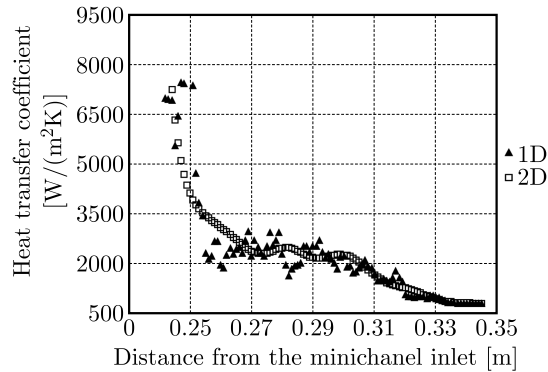


Fig. 6. Heat transfer coefficients at setting #11 vs. distance from the minichannel inlet obtained by means of the one-dimensional method and Beck's method coupled with the FEMT using the raw measurement data for the domain partitioned into $L1 = 10$ subdomains in the x -direction

with respect to the unknown heat flux at the edge in order to directly calculate the values of the heat flux with no need to differentiate the temperature functions.

The calculations have been performed using both the raw and smoothed measurement data. In both cases, the boundary $y = \delta_G + \delta_F$, $x \in \langle x_1, x_P \rangle$ was partitioned into $L1 = 10$ and $L1 = 20$ subdomains.

Partitioning of the domain in the x -direction does not cause considerable changes in the values of the heat transfer coefficient calculated in the subcooled boiling region (the maximum relative difference is approximately 3%, see Table 2 and Fig. 3). However, changes in the values of this coefficient are reported in the saturated nucleate boiling region. Further partitioning in the x -direction has a significant influence on the values of this coefficient when raw data rather than smoothed is used, see Table 2 and Fig. 4.

The local values of the heat transfer coefficients are relatively low in the subcooled boiling region (like in Grysa *et al.*, 2012; Hozejowska *et al.*, 2009; Ozer *et al.*, 2011; Piasecka and Maciejewska, 2012, 2013, 2015; Piasecka and Maciejewska, 2015) and high in the saturated nucleate boiling region (like in Hozejowska and Piasecka, 2014; Piasecka and Maciejewska, 2015; Piasecka *et al.*, 2017), see Figs. 3-5.

The values and distribution of the coefficient obtained by means of the proposed method are similar to those reported for a simple, one-dimensional method, see Fig. 6. The relative differences between the coefficients obtained with the two methods, given in Table 4, does not exceed 2.6% in the subcooled boiling region. In the saturated nucleate boiling region, however, they are greater and reach approximately 13.5%. Further partitioning of the domain, i.e. from $L1 = 10$ into $L1 = 20$ subdomains, contributes to reduction in the differences in the values of the coefficients obtained with both approaches only in the saturated nucleatesboiling region when the raw measurement data is used. The differences are negligible in the subcooled boiling region as well as when the smoothed temperature data is used.

Acknowledgements

The research reported herein was supported by a grant from the National Scientific Center (No. DEC-2013/09/B/ST8/02825).

References

1. BECK J.V., BLACKWELL B., CLAIR C.R.ST., 1985, *Inverse Heat Conduction. Ill-Posed Problems*, Wiley-Interscience Publ., New York

2. BECK J.V., 1970, Nonlinear estimation applied to the nonlinear inverse heat conduction problem, *International Journal of Heat and Mass Transfer*, **13**, 703-716
3. CIAŁKOWSKI M.J., 2002, New type of basic functions of FEM in application to solution of inverse heat conduction problem, *Journal of Thermal Science*, **11**, 163-171
4. CIAŁKOWSKI M.J., GRYSA K., 2010, Trefftz method in solving the inverse problems, *Journal Inverse Ill-Posed Problems*, **18**, 595-616
5. CIAŁKOWSKI M.J., FRĄCKOWIAK A., 2002, Solution of the stationary 2D inverse heat conduction problem by Trefftz method, *Journal of Thermal Science*, **11**, 148-162
6. DUDA P., TALER J., 2009, A new method for identification of thermal boundary conditions in water-wall tubes of boiler furnaces, *International Journal of Heat and Mass Transfer*, **52**, 1517-1524
7. GRYSA K., HOŻEJOWSKA S., MACIEJEWSKA B., 2012, Compensatory calculus and Trefftz functions applied to local heat transfer coefficient determination in a minichannel, *Journal of Theoretical and Applied Mechanics*, **50**, 087-1096
8. GRYSA K., MACIEJEWSKA B., 2013, Trefftz functions for the non-stationary problems, *Journal of Theoretical and Applied Mechanics*, **51**, 251-264
9. HERRERA I., 2000, Trefftz method: a general theory, *Numerical Methods for Partial Differential Equations*, **16**, 561-580
10. HOŻEJOWSKA S., MACIEJEWSKA B., PONIEWSKI M.E., 2015, Numerical analysis of boiling two-phase flow in mini- and microchannels, [In:] *Encyclopedia of Two-Phase Heat Transfer and Flow. I. Fundamentals and Method*, Thome J.R. (Edit.), World Scientific Publishing Co Ltd., New Jersey
11. HOŻEJOWSKA S., PIASECKA M., 2014, Equalizing calculus in Trefftz method for solving two-dimensional temperature field of FC-72 flowing along the minichannel, *Heat and Mass Transfer*, **50**, 1053-1063
12. HOŻEJOWSKA S., PIASECKA M., PONIEWSKI M.E., 2009, Boiling heat transfer in vertical minichannels. Liquid crystal experiments and numerical investigations, *International Journal of Thermal Sciences*, **48**, 1049-1059
13. KINCAID D., CHENEY W., 2002, *Numerical Analysis: Mathematics of Scientific Computing*, 3rd ed., Brooks/Cole Publishing Company, Belmont, California
14. KOMPIS V., KONKOL F., VASKO M., 2001, Trefftz-polynomial reciprocity based FE formulations, *Computer Assisted Mechanics and Engineering Sciences*, **8**, 385-395
15. KRUK B., SOKAŁA M., 1999, Sensitivity coefficients and heat polynomials in the inverse heat conduction problems, *Journal of Applied Mathematics and Mechanics, ZAMM*, **3**, 693-694
16. KRUK B., SOKAŁA M., 2000, Sensitivity coefficients applied to two-dimensional transient inverse heat conduction problems, *Journal of Applied Mathematics and Mechanics, ZAMM*, **81**, 945-946
17. KURPISZ K., NOWAK A.J., 1992, BEM approach to inverse heat conduction problem, *Engineering Analysis with Boundary Elements*, **10**, 291-297
18. LE NILIOT C., LEFEVRE F., 2004, A parameter estimation approach to solve the inverse problem of point heat sources identification, *International Journal of Heat and Mass Transfer*, **47**, 827-841
19. LI Z.-C., LU T.-T., HUANG H.-T., CHENG A.H.-D., 2006, Trefftz, collocation, and other boundary methods – a comparison, *Numerical Methods for Partial Differential Equations*, **23**, 1-52
20. LIN D.T.W., YAN W.-M., LI H.-Y., 2008, Inverse problem of unsteady conjugated forced convection in parallel plate channels, *International Journal of Heat and Mass Transfer*, **51**, 993-1002
21. MACIEJEWSKA B., 2004, Application of the modified method of finite elements for identification of temperature of a body heated with a moving heat source, *Journal of Theoretical and Applied Mechanics*, **42**, 771-787

22. MACIĄG A., 2011, The usage of wave polynomials in solving direct and inverse problems for two-dimensional wave equation, *International Journal for Numerical Methods in Biomedical Engineering*, **27**, 1107-1125
23. OZER B.A., ONCEL A.F., HOLLINGSWORTH D.H., WITTE L.C., 2011, A method of concurrent thermographic-photographic visualization of flow boiling in a minichannel, *Experimental Thermal and Fluid Science*, **35**, 1522-1529
24. PIASECKA M., 2013, Determination of the temperature field using liquid crystal thermography and analysis of two-phase flow structures in research on boiling heat transfer in a minichannel, *Metrology and Measurement Systems*, **XX**, 205-216
25. PIASECKA M., 2014a, Flow boiling heat transfer in a minichannel with enhanced heating surface, *Heat Transfer Engineering*, **35**, 903-912
26. PIASECKA M., 2014b, Laser texturing, spark erosion and sanding of the surfaces and their practical applications in heat exchange devices, *Advanced Material Research*, **874**, 95-100
27. PIASECKA M., 2014c, The use of enhanced surface in flow boiling heat transfer in a rectangular minichannels, *Experimental Heat Transfer*, **27**, 231-255
28. PIASECKA M., 2015, Impact of selected parameters on boiling heat transfer and pressure drop in minichannels, *International Journal of Refrigeration*, **56**, 198-212
29. PIASECKA M., MACIEJEWSKA B., 2012, The study of boiling heat transfer in vertically and horizontally oriented rectangular minichannels and the solution to the inverse heat transfer problem with the use of the Beck method and Trefftz functions, *Experimental Thermal and Fluid Science*, **38**, 19-32
30. PIASECKA M., MACIEJEWSKA B., 2013, Enhanced heating surface application in a minichannel flow and the use of the FEM and Trefftz functions for the solution of inverse heat transfer problem, *Experimental Thermal and Fluid Science*, **44**, 23-33
31. PIASECKA M., MACIEJEWSKA B., 2015, Heat transfer coefficient during flow boiling in a minichannel at variable spatial orientation, *Experimental Thermal and Fluid Science*, **68**, 459-467
32. PIASECKA M., STRĄK K., MACIEJEWSKA B., 2016, Calculations of flow boiling heat transfer in a minichannel using data from LCT and IRT, *Heat Transfer Engineering*, **38**, 3, 332-346, <http://dx.doi.org/10.1080/01457632.2016.1189272>
33. SHI J., WANG J., 2009, Inverse problem of transpiration cooling for estimating wall heat flux by LTNE model and CGM method, *International Journal of Heat and Mass Transfer*, **52**, 2714-2720
34. TIKHONOV A.N., ARSENIN V.Y., 1977, *Solution of Ill-Posed Problems*, Wiley, New York
35. TREFFTZ E., 1926, Ein Gegenstück zum Ritzschen Verfahren, *2 Int. Kongress für Technische Mechanik*, Zürich, 1926, 131-137
36. TSENG A.A., CHEN T.C., ZHAO F.Z., 1995, Direct sensitivity coefficient method for solving two-dimensional inverse heat conduction problems by finite-element scheme, *Numerical Heat Transfer, Part B: Fundamentals*, **27**, 291-307
37. TSENG A.A., CHEN T.C., ZHAO F.Z., 1996, Multidimensional inverse transient heat conduction problems by direct sensitivity coefficient method using a finite-element scheme, *Numerical Heat Transfer, Part B: Fundamentals*, **29**, 365-38

RADIATIVE FALKNER-SKAN FLOW OF WALTER-B FLUID WITH PRESCRIBED SURFACE HEAT FLUX

TASAWAR HAYAT

*Department of Mathematics, Quaid-I-Azam University, Islamabad, Pakistan and
Nonlinear Analysis and Applied Mathematics (NAAM) Research Group, Department of Mathematics,
King Abdulaziz University, Jeddah, Saudi Arabia*

SUMAIRA QAYYUM, MARIA IMTIAZ

Department of Mathematics, Quaid-I-Azam University, Islamabad, Pakistan; e-mail: mi_qau@yahoo.com

AHMED ALSAEDI

*Nonlinear Analysis and Applied Mathematics (NAAM) Research Group, Department of Mathematics,
King Abdulaziz University, Jeddah, Saudi Arabia*

This article addresses the Falkner-Skan flow of an incompressible Walter-B fluid. Fluid flow is caused by a stretching wedge with thermal radiation and prescribed surface heat flux. Appropriate transformations are used to obtain the system of nonlinear ordinary differential equations. Convergent series solutions are obtained by the homotopy analysis method. Influence of pertinent parameters on the velocity, temperature and Nusselt number are investigated. It is observed that by increasing the viscoelastic parameter, the fluid velocity decreases. There is an enhancement of the heat transfer rate for the viscoelastic parameter and power law index. It is also found that the Prandtl number and radiation parameter decrease the heat transfer rate.

Keywords: Walter-B fluid, Falkner-Skan flow, prescribed surface heat flux, thermal radiation

1. Introduction

Non-Newtonian materials in view of its complex constitutive expression yield much more complicated and higher order differential systems when compared with viscous materials. Such complexities in differential systems are due to additional rheological parameters appearing in the constitutive relationships. Even a simpler constitutive equation like for Walter-B gives rise to nonlinear boundary initial value problems which are far from trivial. These boundary value problems have great interest of researchers from different quarters. For example Chang *et al.* (2011) numerically analyzed the free convective heat transfer in viscoelastic flow of Walter-B fluid. Nadeem *et al.* (2015) examined oblique flow of Walter-B fluid in presence of magnetohydrodynamics and nanoparticles. Nandeppanavar *et al.* (2010) explored stretched flow of Walter-B liquid in presence of non-uniform heat source/sink. Hakeem *et al.* (2014) extended such analysis in presence of thermal radiation. Stagnation point flow and Blasius flow for Walter-B liquid were also addressed by Madani *et al.* (2012). Hayat *et al.* (2014a, 2015c) examined heat transfer in flow of Walter-B fluid over a surface with Newtonian heating and convective condition. Talla (2013) studied the flow of Walter-B fluid bounded by an exponentially stretching sheet. Peristalsis of Walter-B fluid in a vertical channel was studied by Ramesh and Devakar (2015).

Falkner-Skan flow is quite popular in fluid mechanics. It is a flow past a wedge placed symmetrically with respect to the flow direction. These types of flows occur frequently to increase

oil recovery and in packed bed reactor geothermal industries. Interest of recent researchers in boundary layer flow over a continuous moving surface with prescribed surface heat flux has increased so much. These type of flows have many applications in industrial and metallurgical processes such as glass fiber, wire drawing, paper production and metallic plate cooling in cooling bath, etc. Falkner and Skan (1931) presented some approximate solutions for the boundary layer equation. Yacob *et al.* (2011) studied the Falkner-Skan problem for a static and moving wedge with prescribed surface heat flux in a nanofluid. Falkner-Skan flow of the Maxwell fluid with mixed convection was analyzed by Hayat *et al.* (2012). Khan and Pop (2013) examined the nanofluid flow past a moving wedge. Abbasbandy *et al.* (2014b) discussed numerical and analytical solutions for MHD Falkner-Skan flow of the Maxwell fluid. Hendi and Hussain (2012) found the solution for MHD Falkner-Skan flow over a permeable sheet. Fang *et al.* (2012) studied the momentum and heat transfer in Falkner-Skan flow with algebraic decay. Su and Zheng (2011) presented the approximate solution of MHD Falkner-Skan flow over a permeable wall. Abbasbandy *et al.* (2014a) worked for Falkner-Skan flow of an Oldroyd-B fluid in presence of the applied magnetic field.

The radiation effect in boundary layer flow has much importance due to its applications in physics, engineering and industrial fields such as glass production, furnace design, polymer processing, gas cooled nuclear reactors and also in space technology like aerodynamics of rockets, missiles, propulsion system, power plants for inter planetary flights and space crafts operating at high temperatures. Heat transfer through radiation takes place in form of electromagnetic waves. Radiation emitted by a body is a consequence of thermal agitation of its composing molecules. Hayat *et al.* (2013c) worked on mixed convection radiative stagnation point flow in presence of convective boundary conditions. Hayat *et al.* (2013b) also discussed the effect of thermal radiation in MHD flow of thixotropic fluid. Pal (2013) analyzed the effects of thermal radiation, Hall current and MHD in flow over an unsteady stretching surface. Bhattacharyya *et al.* (2012) analyzed the flow of micropolar fluid over a porous shrinking sheet with thermal radiation. Hayat *et al.* (2013a) studied the three-dimensional MHD flow of Eyring-Powell fluid with radiative effects. Rashidi *et al.* (2014) discussed the influence of thermal radiation in MHD mixed convective flow of a viscoelastic fluid due to a porous wedge. Bhattacharyya (2013) presented the MHD Casson fluid subject to thermal radiation. Sheikholeslami *et al.* (2015) adopted a two phase model for MHD flow of a nanofluid with thermal radiation.

The aim of present study is to venture further in the region of Falkner-Skan flow of a non-Newtonian fluid. Thus flow formulation here is based upon constitutive relationship of Walters-B fluid. Analysis of heat transfer is carried out in presence of heat flux and thermal radiation. Transformation procedure has been used for the reduction of partial differential systems to ordinary differential systems. The homotopy analysis technique has been implemented for the development of convergent series solutions. Influences of pertinent parameters on the velocity, temperature and Nusselt number are pointed out.

2. Problem formulation

We consider the steady two-dimensional Falkner-Skan flow of an incompressible Walter-B fluid. Heat transfer analysis is carried out in the presence of prescribed surface heat flux and thermal radiation. The fluid flow is induced via stretching a wedge moving with the velocity $U_w = cx^n$ and the fluid flow being confined to $y \geq 0$. Let T_∞ be ambient temperature. The relevant boundary layer equations are (Hakeem *et al.*, 2014)

$$\begin{aligned} \frac{\partial u}{\partial x} + \frac{\partial v}{\partial y} &= 0 \\ u \frac{\partial u}{\partial x} + v \frac{\partial u}{\partial y} &= U_e \frac{dU_e}{dx} + \nu \frac{\partial^2 u}{\partial y^2} - k_0 \left(u \frac{\partial^3 u}{\partial x \partial y^2} + v \frac{\partial^3 u}{\partial y^3} + \frac{\partial u}{\partial x} \frac{\partial^2 u}{\partial y^2} - \frac{\partial u}{\partial y} \frac{\partial^2 u}{\partial y \partial x} \right) \\ u \frac{\partial T}{\partial x} + v \frac{\partial T}{\partial y} &= \frac{k}{\rho c_p} \frac{\partial^2 T}{\partial y^2} - \frac{1}{\rho c_p} \frac{\partial q_r}{\partial y} \end{aligned} \quad (2.1)$$

The corresponding boundary conditions are (Yacob *et al.*, 2011)

$$\begin{aligned} u = U_w = cx^n \quad v = 0 \quad \frac{\partial T}{\partial y} = -\frac{q_w}{k} \quad \text{at } y = 0 \\ u \rightarrow U_e = ax^n \quad T \rightarrow T_\infty \quad \text{as } y \rightarrow \infty \end{aligned} \quad (2.2)$$

where (u, v) are the velocities along (x, y) directions respectively, T is temperature, ν is kinematic viscosity, k_0 is elastic parameter, k is thermal conductivity, ρ is density, c_p is specific heat, c and a are the stretching rates and q_w the wall heat flux. Radiative heat flux by using Rosseland approximation is given by

$$q_r = -\frac{4\sigma^*}{3k^*} \frac{\partial T^4}{\partial y} \quad (2.3)$$

where σ^* is the Stefan-Boltzmann constant and k^* the mean absorption coefficient. Further, we assume that the temperature difference within the flow is such that T^4 may be expanded in a Taylor series. Hence expanding T^4 about T_∞ and neglecting higher order terms, we get

$$T^4 \cong 4T_\infty^3 T - 3T_\infty^4 \quad (2.4)$$

Using Eqs. (2.3) and (2.4) in (2.1)₃, we obtain

$$u \frac{\partial T}{\partial x} + v \frac{\partial T}{\partial y} = \frac{1}{\rho c_p} \left(k + \frac{16\sigma^* T_\infty^3}{3k^*} \right) \frac{\partial^2 T}{\partial y^2} \quad (2.5)$$

Suitable transformations for the present flow are (Yacob *et al.*, 2011)

$$\begin{aligned} \eta = \sqrt{\frac{n+1}{2}} \sqrt{\frac{U_e}{\nu x}} y \quad v = -\sqrt{\frac{n+1}{2}} \sqrt{\frac{\nu U_e}{x}} \left(f(\eta) + \frac{n-1}{n+1} \eta f'(\eta) \right) \\ u = ax f'(\eta) \quad \theta = \frac{k(T - T_\infty)}{q_w} \sqrt{\frac{(n+1)U_e}{2\nu x}} \end{aligned} \quad (2.6)$$

where x is the distance from the leading edge and n the Falkner-Skan power-law parameter. Using Eq. (2.3), the continuity equation is satisfied automatically and Eqs. (2.1)₂-(2.2) take the form

$$\begin{aligned} f''' + f f'' + \frac{2n}{n+1} (1 - f'^2) - k_1 \left((3n-1) f' f''' - \frac{n+1}{2} f f'''' - \frac{3n-1}{2} f''^2 \right) = 0 \\ \frac{1}{\text{Pr}} \left(1 + \frac{4}{3} R \right) \theta'' + f \theta' + \frac{n-1}{n+1} f' \theta = 0 \end{aligned} \quad (2.7)$$

and

$$\begin{aligned} f(0) = 0 \quad f'(\infty) \rightarrow 1 \quad f'(0) = \alpha \\ \theta'(0) = -1 \quad \theta(\infty) \rightarrow 0 \end{aligned} \quad (2.8)$$

where k_1 is the viscoelastic parameter, Pr is the Prandtl number, α is the ratio of stretching rates and R is the radiation parameter. The dimensionless parameters are defined as follows

$$k_1 = \frac{k_0 a x^{n-1}}{\rho \nu} \quad \text{Pr} = \frac{\rho c_p \nu}{k} \quad \alpha = \frac{c}{a} \quad R = \frac{4\sigma^* T_\infty^3}{k k^*} \quad (2.9)$$

The local Nusselt number in the dimensional form is

$$\text{Nu}_x = \frac{xq_w}{k \left[\frac{q_w}{k} \left(\frac{2\nu x}{n+1} \right) U_e(x) \right]} \quad (2.10)$$

with

$$q_w = -k \left. \frac{\partial T}{\partial y} \right|_{y=0} + (q_r)_w \quad (2.11)$$

in which q_r is prescribed as follows

$$(q_r)_w = \frac{-16\sigma^* T_\infty^3}{3k^*} \left. \frac{\partial T}{\partial y} \right|_{y=0} \quad (2.12)$$

The dimensionless form of the Nusselt number is

$$\frac{\text{Nu}_x}{\sqrt{\text{Re}_x}} = -\sqrt{\frac{n+1}{2}} \left(1 + \frac{4R}{3} \right) \theta'(0) \quad (2.13)$$

3. Homotopic solutions

3.1. Zeroth-order deformation equations

Initial approximations and auxiliary linear operators are taken as follows

$$\begin{aligned} f_0(\eta) &= \eta - (1 - \alpha)[1 - \exp(-\eta)] & \theta_0(\eta) &= \exp(-\eta) \\ \mathbf{L}_f &= f''' - f' & \mathbf{L}_\theta &= \theta'' - \theta \end{aligned} \quad (3.1)$$

with

$$\mathbf{L}_f[c_1 + c_2 e^\eta + c_3 e^{-\eta}] = 0 \quad \mathbf{L}_\theta[c_4 e^\eta + c_5 e^{-\eta}] = 0 \quad (3.2)$$

where c_i ($i = 1-5$) are constants.

Denoting $q \in [0, 1]$ as the embedding parameter and \hbar_f and \hbar_θ as the non-zero auxiliary parameters, then the zeroth order deformation problems are

$$\begin{aligned} (1 - q)\mathbf{L}_f[F(\eta, q) - f_0(\eta)] &= q\hbar_f \mathbf{N}_f[F(\eta, q)] \\ (1 - q)\mathbf{L}_\theta[\vartheta(\eta, q) - \theta_0(\eta)] &= q\hbar_\theta \mathbf{N}_\theta[\vartheta(\eta, q), F(\eta, q)] \\ F(0, q) = 0 \quad F'(0, q) = \alpha \quad F'(\infty, q) = 1 \\ \vartheta'(0, q) = -1 \quad \vartheta(\infty, q) = 0 \end{aligned} \quad (3.3)$$

where the nonlinear differential operators \mathbf{N}_f and \mathbf{N}_θ are

$$\begin{aligned} \mathbf{N}_f[F(\eta, q)] &= \frac{\partial^3 F(\eta, q)}{\partial \eta^3} + \frac{2n}{n+1} \left[1 - \left(\frac{\partial F(\eta, q)}{\partial \eta} \right)^2 \right] + F(\eta, q) \frac{\partial^2 F(\eta, q)}{\partial \eta^2} \\ &\quad - k_1 \left[(3n-1) \frac{\partial F(\eta, q)}{\partial \eta} \frac{\partial^3 F(\eta, q)}{\partial \eta^3} - \frac{n+1}{2} F(\eta, q) \frac{\partial^4 F(\eta, q)}{\partial \eta^4} - \frac{3n-1}{2} \left(\frac{\partial^2 F(\eta, q)}{\partial \eta^2} \right)^2 \right] \\ \mathbf{N}_\theta[\vartheta(\eta, q), F(\eta, q)] &= \frac{1}{\text{Pr}} \left(1 + \frac{4}{3} R \right) \frac{\partial^2 \vartheta(\eta, q)}{\partial \eta^2} + \frac{\partial \vartheta(\eta, q)}{\partial \eta} F(\eta, q) \\ &\quad + \frac{n-1}{n+1} \frac{\partial F(\eta, q)}{\partial \eta} \vartheta(\eta, q) \end{aligned} \quad (3.4)$$

3.2. m -th order deformation equations

The m -th order deformation problems are

$$\mathbb{L}_f[f_m(\eta) - \chi_m f_{m-1}(\eta)] = \hbar_f \mathbb{R}_{f,m}(\eta) \quad \mathbb{L}_\theta[\theta_m(\eta) - \chi_m \theta_{m-1}(\eta)] = \hbar_\theta \mathbb{R}_{\theta,m}(\eta) \quad (3.5)$$

and

$$f_m(0) = \frac{\partial f_m(0)}{\partial \eta} = \frac{\partial f_m(\infty)}{\partial \eta} = \theta'(0) = \theta(\infty) = 0 \quad (3.6)$$

where $\mathbb{R}_{f,m}(\eta)$ and $\mathbb{R}_{\theta,m}(\eta)$ have the following forms

$$\begin{aligned} \mathbb{R}_{f,m}(\eta) &= f_{m-1}''' + \frac{2n}{n+1} \left(1 - \sum_{k=0}^{m-1} f'_{m-1-k} f'_k \right) + \sum_{k=0}^{m-1} f_{m-1-k} f''_k \\ &\quad - k_1 \left[(3n-1) f'_{m-1-k} f_k''' - \frac{n+1}{2} \sum_{k=0}^{m-1} f_{m-1-k} f_k'''' - \frac{3n-1}{2} \sum_{k=0}^{m-1} f''_{m-1-k} f''_k \right] \\ \mathbb{R}_{\theta,m}(\eta) &= \frac{1}{\text{Pr}} \left(1 + \frac{4}{3} R \right) \theta_{m-1}'' + \sum_{k=0}^{m-1} f_{m-1-k} \theta'_k + \frac{n-1}{n+1} \sum_{k=0}^{m-1} f'_{m-1-k} \theta_k \end{aligned} \quad (3.7)$$

and

$$\chi_m = \begin{cases} 0 & \text{for } m \leq 1 \\ 1 & \text{for } m > 1 \end{cases} \quad (3.8)$$

The general solutions (f_m, θ_m) comprising the special solutions (f_m^*, θ_m^*) are

$$\begin{aligned} f_m(\eta) &= f_m^*(\eta) + c_1 + c_2 e^\eta + c_3 e^{-\eta} \\ \theta_m(\eta) &= \theta_m^*(\eta) + c_4 e^\eta + c_5 e^{-\eta} \end{aligned} \quad (3.9)$$

where the constants c_i ($i = 1-5$) through boundary conditions (3.6) are

$$\begin{aligned} c_1 &= -c_3 - f_m^*(0) & c_3 &= \frac{\partial f_m^*(0)}{\partial \eta} \\ c_5 &= \frac{\partial \theta_m^*(0)}{\partial \eta} & c_2 &= c_4 = 0 \end{aligned} \quad (3.10)$$

4. Convergence analysis

The homotopy analysis method has great advantage to adjust the convergence region by selecting the appropriate values of \hbar_f and \hbar_θ . For this, we plot the \hbar -curves for the convergence of velocity and temperature profiles (see Fig. 1). Admissible values of auxiliary parameters are $-0.9 \leq \hbar_f \leq 0$ and $-0.6 \leq \hbar_\theta \leq -0.2$. The solution converges in the whole region of η ($0 \leq \eta \leq \infty$) when $k_1 = 0.2$, $n = 0.1$, $R = 1.6$, $\text{Pr} = 1.5$ and $\alpha = 0.9$.

Table 1 shows the convergence of functions $f''(0)$ and $\theta''(0)$ at a different order of approximations. Tabulated values show that the 25-th order of approximations is enough for the convergence of $f''(0)$, and the 22-th order of approximation is appropriate for the convergence of $\theta''(0)$.

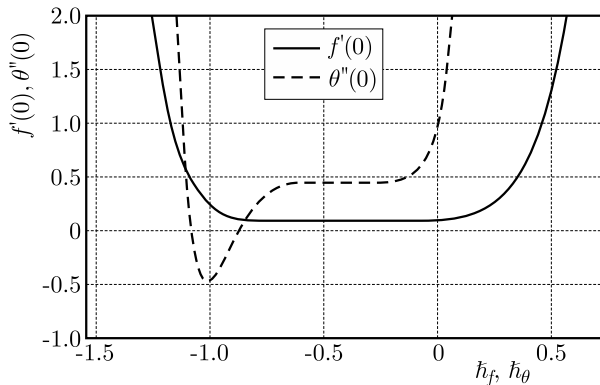


Fig. 1. h -curves for $f''(0)$ and $\theta''(0)$ when $k_1 = 0.2$, $n = 0.1$, $R = 1.6$, $Pr = 1.5$ and $\alpha = 0.9$.

Table 1. Convergence of HAM (homotopy analysis method) solutions when $k_1 = 0.2$, $n = 0.1$, $R = 1.6$, $Pr = 1.5$, $\alpha = 0.9$, $h_f = -0.2 = h_\theta$

Order of approximation	$f''(0)$	$\theta''(0)$
1	0.09734	0.8154
5	0.09262	0.8203
10	0.09262	0.4547
15	0.09171	0.4454
20	0.09168	0.4447
22	0.09169	0.4446
25	0.09170	0.4446
30	0.09170	0.4446
35	0.09170	0.4446
40	0.09170	0.4446
45	0.09170	0.4446

5. Discussion

In this Section, we discussed the influences of different physical parameters on the fluid velocity, temperature and heat transfer rate.

5.1. Dimensionless velocity profile

Figures 2a-2c show the effect of viscoelastic parameter k_1 , power law index n and stretching rates ratio α on the velocity profile. Figure 2a depicts the influence of the viscoelastic parameter on $f'(\eta)$. As k_1 increases, the fluid velocity decreases which corresponds to a thinner momentum boundary layer thickness. The viscoelasticity produces tensile stress which contracts the boundary layer and, consequently, the velocity reduces. Figure 2b represents the impact of α on the velocity profile. Here, the velocity enhances by increasing α . In fact higher values of α correspond to the stronger free stream velocity which enhances the fluid velocity. The effect of Falkner-Skan power law index n is graphed in Fig. 2c. It is observed that velocity is an increasing function of n .

5.2. Dimensionless temperature profile

Figures 3 and 4 show the impact of the Prandtl number Pr , radiation parameter R , viscoelastic parameter k_1 , power law index n and ratio of stretching rates α on the temperature profile.

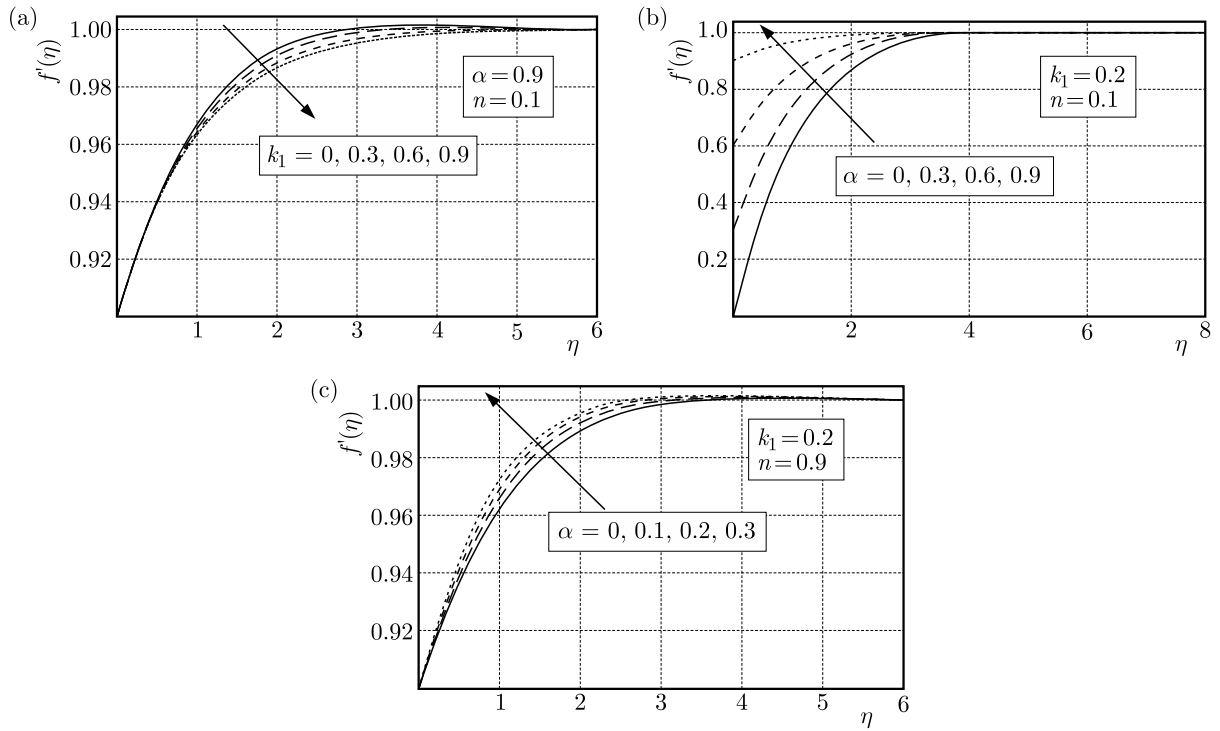


Fig. 2. Impact of: (a) k_1 , (b) α and (c) n on $f'(\eta)$

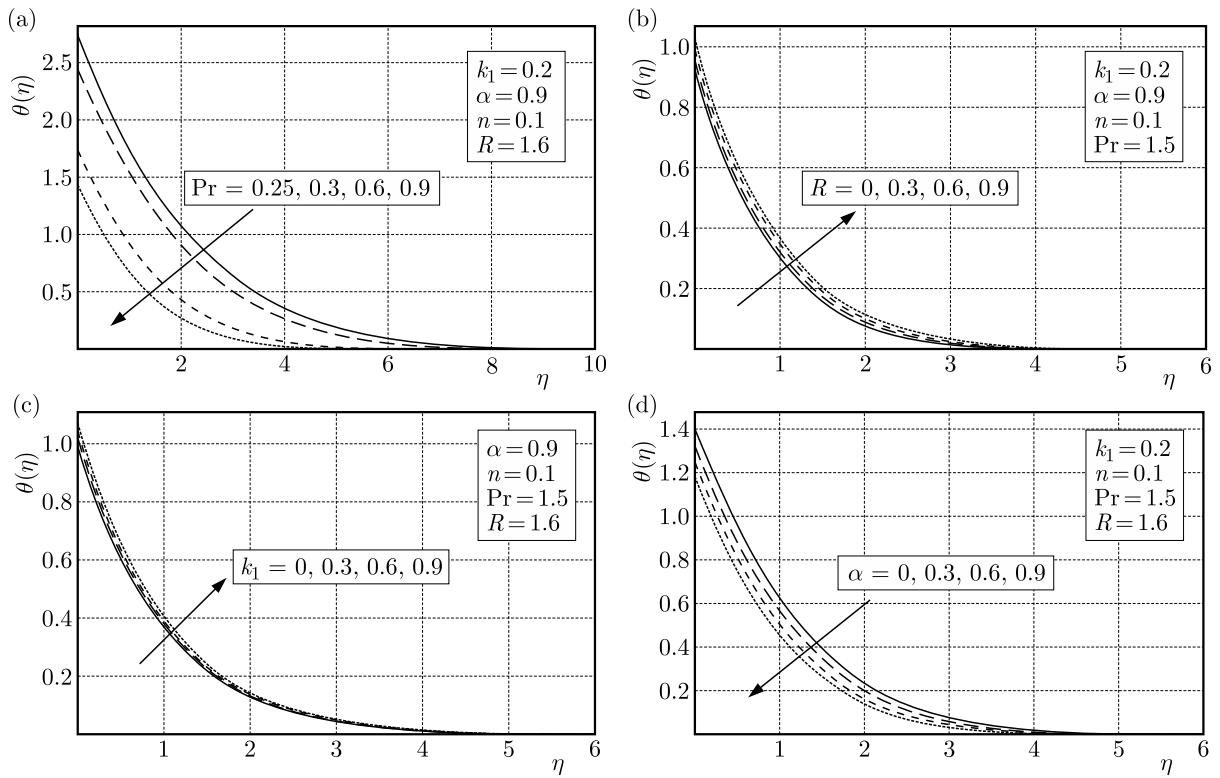


Fig. 3. Impact of (a) Pr , (b) R , (c) k_1 , (d) α

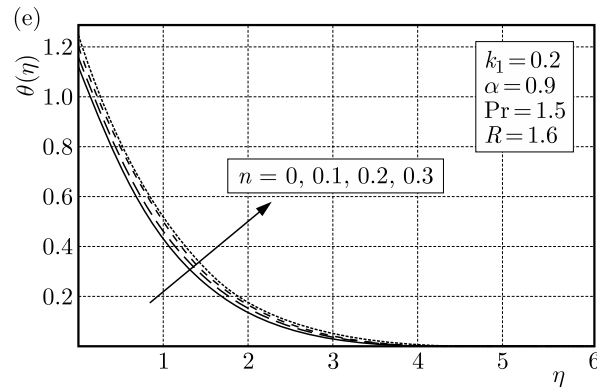


Fig. 4. Impact of n on $\theta(\eta)$

Figure 3a shows the effect of Pr on the temperature profile. For increasing values of the Prandtl number, the temperature decreases. Higher values of Pr correspond to low thermal diffusivity, and the fluid temperature decreases. Figure 3b depicts the behavior of fluid temperature for the radiation parameter R . This figure shows that the temperature profile enhances when radiation effects strengthen. An increase in the radiation parameter corresponds to a decrease in the mean absorption coefficient. Hence the rate of radiative heat transfer to the fluid increases. Figure 3c describes the behavior of temperature for viscoelastic parameter. Fluid temperature enhances for increasing k_1 . Figure 3d presents the effect of stretching ratio rates α on the temperature profile. The temperature profile shows decreasing behavior for increasing values of α . The velocity increases when the ratio of stretching rates enhances. There is less resistance for fluid particles motion and, consequently, the temperature reduces. Figure 4 shows the effect of increasing values of n on fluid temperature. The temperature profile and n have a direct relation with each other.

5.3. Nusselt number

In this Section, we show the effects of different physical parameters on the Nusselt number. Figures 5a-5d depict the influence of the viscoelastic parameter k_1 , Falkner-Skan power law index n , radiation parameter R and Prandtl number Pr . These figures show that by increasing the viscoelastic and power law index parameters, the rate of heat transfer increases whereas the Nusselt number shows decreasing behavior for increasing values of the radiation parameter and the Prandtl number.

6. Conclusions

The Falkner-Skan wedge flow of Walter-B fluid is studied in presence of thermal radiation and prescribed surface heat flux. Key points of the presented analysis are as follows:

- Fluid velocity is a decreasing function of the viscoelastic parameter and increasing function of the ratio of stretching rates.
- The Prandtl number and radiation parameter have opposite impact on the temperature profile.
- For increasing values of the viscoelastic parameter, the temperature enhances.
- The Nusselt number has opposite impact on the power law index and the Prandtl number.

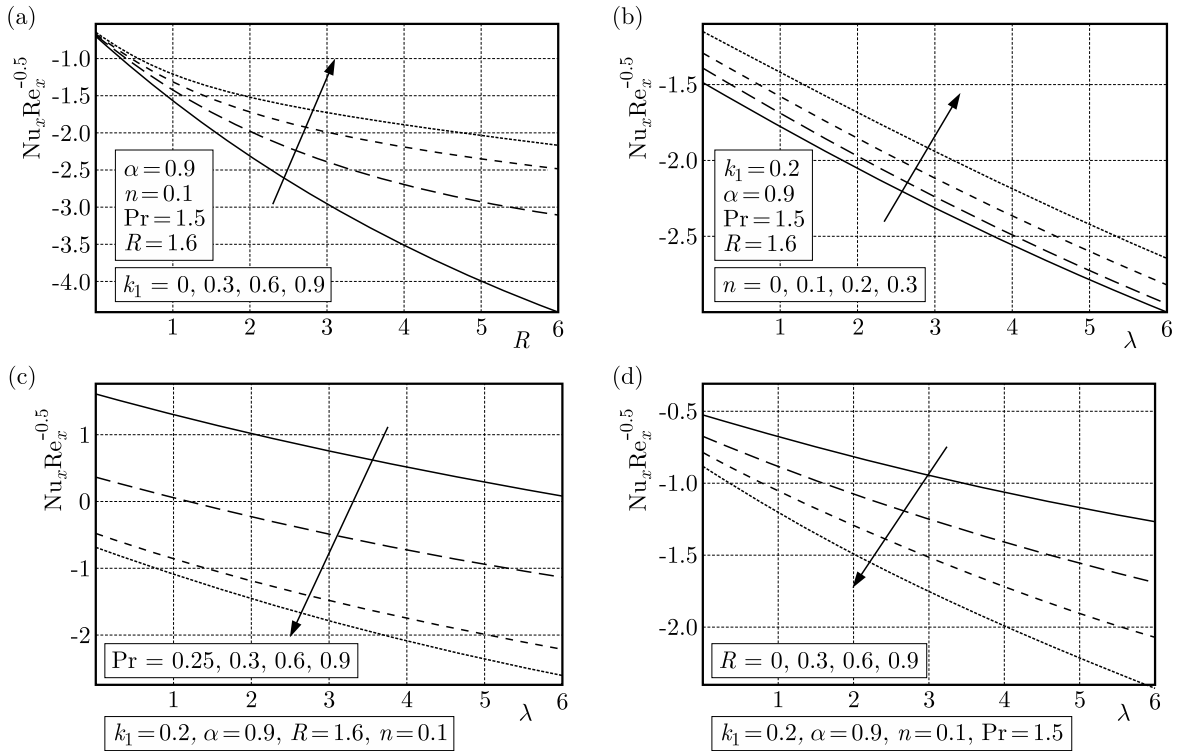


Fig. 5. Impact of (a) k_1 , (b) n , (c) R and (d) Pr on $Nu_x Re_x^{-0.5}$ (see Eq. (2.13))

References

1. ABBASBANDY S., HAYAT T., ALSAEDI A., RASHIDI M. M., 2014a, Numerical and analytical solutions for Falkner-Skan flow of MHD Oldroyd-B fluid, *International Journal of Numerical Methods of Heat and Fluid Flow*, **24**, 390-401
2. ABBASBANDY S., NAZ R., HAYAT T., ALSAEDI A., 2014b, Numerical and analytical solutions for Falkner-Skan flow of MHD Maxwell fluid, *Applied Mathematics and Computation*, **242**, 569-575
3. BHATTACHARYYA K., 2013, MHD stagnation point flow of Casson fluid and heat transfer over a stretching sheet with thermal radiation, *Journal of Thermodynamics*, **2013**, 169674
4. BHATTACHARYYA K., MUKHOPADHYAY S., LAYEK G.C., POP I., 2012, Effects of thermal radiation on micropolar fluid flow and heat transfer over a porous shrinking sheet, *International Journal of Heat and Mass Transfer*, **55**, 2945-2952
5. CHANG T.B., MEHMOOD A., BEG O.A., NARAHARI M., ISLAM M.N., AMEEN F., 2011, Numerical study of transient free convective mass transfer in a Walters-B viscoelastic flow with wall suction, *Communications in Nonlinear Science and Numerical Simulation*, **16**, 216-225
6. FALKNER V.M., SKAN S.W., 1931, Some approximate solutions of the boundary-layer equations, *Philosophical Magazine*, **12**, 865-896
7. FANG T., YAO S., ZHANG J., ZHONG Y., TAO H., 2012, Momentum and heat transfer of the Falkner-Skan flow with algebraic decay, *Communications in Nonlinear Science and Numerical Simulation*, **17**, 2476-2488
8. FAROOQ U., HAYAT T., ALSAEDI A., LIAO S. J., 2014, Heat and mass transfer of two-layer flows of third-grade nano-fluids in a vertical channel, *Applied Mathematics and Computation*, **242**, 528-540
9. HAKEEM A.K.A., GANESH N.V., GANGA B., 2014, Effect of heat radiation in a Walter's liquid B fluid over a stretching sheet with non-uniform heat source/sink and elastic deformation, *Journal of King Saud University - Engineering Sciences*, **26**, 168-175

10. HAYAT T., ASAD S., MUSTAFA M., ALSULAMI H.H., 2014a, Heat transfer analysis in the flow of Walters' B fluid with a convective boundary condition. *Chinese Physics B*, **23**, 084701
11. HAYAT T., AWAIS M., ASGHAR S., 2013a, Radiative effects in a three-dimensional flow of MHD Eyring-Powell fluid, *Journal of Egyptian Mathematical Society*, **21**, 379-384
12. HAYAT T., FAROOQ M., IQBAL Z., ALSAEDI A., 2012, Mixed convection Falkner-Skan flow of a Maxwell fluid, *Journal of Heat Transfer*, **134**, 114504
13. HAYAT T., IMTIAZ M., ALSAEDI A., 2015a, MHD flow of nanofluid with homogeneous-heterogeneous reactions and velocity slip, *Thermal Sciences*, DOI: 10.2298/TSCI140922067H
14. HAYAT T., IMTIAZ M., ALSAEDI A., 2015b, Partial slip effects in flow over nonlinear stretching surface, *Applied Mathematical Mechanics*, **36**, 1513-1526
15. HAYAT T., IMTIAZ M., ALSAEDI A., 2016, Unsteady flow of nanofluid with double stratification and magnetohydrodynamics, *International Journal of Heat and Mass Transfer*, **92**, 100-109
16. HAYAT T., NAZ R., ASGHAR S., ALSAEDI A., 2014b, Soret-Dufour effects on MHD rotating flow of a viscoelastic fluid, *International Journal of Numerical Methods of Heat and Fluid Flow*, **24**, 498-520
17. HAYAT T., SHAFIQ A., MUSTAFA M., ALSAEDI A., 2015c, Boundary-layer flow of Walters' B fluid with Newtonian heating, *Zeitschrift für Naturforschung A*, **70**, 5, 333-341
18. HAYAT T., SHAHZAD S. A., ASGHAR S., 2013b, MHD flow of thixotropic fluid with variable thermal conductivity and thermal radiation, *Walailak Journal of Science and Technology*, **10**, 29-42
19. HAYAT T., WAQAS M., SHEHZAD S. A., ALSAEDI A., 2013c, Mixed convection radiative flow of Maxwell fluid near stagnation point with convective condition, *Journal of Mechanics*, **29**, 403-409
20. HENDI F. A., HUSSAIN M., 2012, Analytic solution for MHD Falkner-Skan flow over a porous surface, *Journal of Applied Mathematics*, **2012**, 123185
21. KHAN W.A., POP I., 2013, Boundary layer flow past a wedge moving in a nano-fluid, *Mathematical Problems in Engineering*, **2013**, 637285
22. LIN Y., ZHENG L., CHENG G., 2015, Unsteady flow and heat transfer of pseudoplasticnanofluid in a finite thin film on a stretching surface with variable thermal conductivity and viscous dissipation, *Powder Technology*, **274**, 324-332
23. MADANI S.A., AKBAR R., KHOEILAR R., 2012, On the study of viscoelastic Walter's B fluid in boundary layer flows, *Mathematical Problems in Engineering*, **2012**, 861508
24. NADEEM S., MEHMOOD R., MOTSA S.S., 2015, Numerical investigation on MHD oblique flow of Walter's B type nanofluid over a convective surface, *International Journal of Thermal Sciences*, **92**, 162-172
25. NANDEPANAVAR M.M., ABEL M.S., TAWADE J.V., 2010, Heat transfer in a Walter's liquid B fluid over an impermeable stretching sheet with non-uniform heat source/sink and elastic deformation, *Communications in Nonlinear Science and Numerical Simulation*, **15**, 1791-1802
26. PAL D., 2013, Hall current and MHD effects on heat transfer over an unsteady stretching permeable surface with thermal radiation, *Computer Mathematical with Applications*, **66**, 1161-1180
27. RAMESH K., DEVAKAR M., 2015, Effect of heat transfer on the peristaltic flow of Walter-B fluid in a vertical channel with external magnetic field, *Journal of Aerospace Engineering*, **10**, 04015050
28. RAMZAN M., FAROOQ M., ALHOTHUALI M.S., MALAIKAH H.M., CUI W., HAYAT T., 2015, Three dimensional flow of an Oldroyd-B fluid with Newtonian heating, *International Journal of Numerical Methods of Heat and Fluid Flow*, **25**, 1, 68-85
29. RASHIDI M.M., ALI M., FREIDONIMEHR N., ROSTAMI B., HOSSAIN M.A., 2014, Mixed convective heat transfer for MHD viscoelastic fluid flow over a porous wedge with thermal radiation, *Advance Mechanical Engineering*, **6**, 735939

30. SHAHZAD S.A., QASIM M., HAYAT T., SAJID M., OBADAT S., 2013, Boundary layer flow of Maxwell fluid with power law heat flux and heat source, *International Journal of Numerical Methods of Heat and Fluid Flow*, **23**, 1225-1241
31. SHEIKHOESLAMI M., GANJI D.D., JAVED M.Y., ELLAHI R., 2015, Effect of thermal radiation on MHD nanofluid flow and heat transfer by means of two phase model, *Journal of Magnetic Magnetism Material*, **374**, 36-43
32. SU X., ZHENG L., 2011, Approximate solutions to MHD Falkner-Skan flow over permeable wall, *Applied Mathematical Mechanics*, **32**, 401-408
33. SUI J., ZHENG L., ZHANG X., CHEN G., 2015, Mixed convection heat transfer in power law fluids over a moving conveyor along an inclined plate, *International Journal of Heat and Mass Transfer*, **85**, 1023-1033
34. TALLA H., 2013, Numerical study of flow of Walter's liquid B over an exponentially stretching sheet, *International Journal of Scientific and Research Publications*, **3**, 2250-3153
35. YACOB N.A., ISHAK A., NAZAR R., POP I., 2011, Falkner-Skan problem for a static and moving wedge with prescribed surface heat flux in nano-fluid, *International Communications in Heat and Mass Transfer*, **38**, 149-153

Manuscript received March 30, 2016; accepted for print May 10, 2016

AN ENERGY-BASED METHOD IN PHENOMENOLOGICAL DESCRIPTION OF MECHANICAL PROPERTIES OF NONLINEAR MATERIALS UNDER PLANE STRESS

TADEUSZ WEGNER, DARIUSZ KURPISZ

Poznan University of Technology, Institute of Applied Mechanics, Poznań, Poland

e-mail: dariusz.kurpisz@put.poznan.pl

A method based on energy is a very useful tool for description of mechanical properties of materials. In the current paper, on the base of geometrical interpretation of a deformation process, the strain energy density function for isotropic nonlinear materials has been constructed. On account of hydrostatic interpretation of the volumetric deformation, the elastic part of energy has been extracted. The initiation of the damage process due to plastic flow of the material under plane stress has been determined and the stability conditions have been formulated by using in the stability analysis the strain energy density function in addition to Sylvester's theorem and assumption of zero volume change during pure plastic deformations. This concept is an original part of the work and continuation of the investigations previously carried out by Wegner and Kurpisz. The theoretical investigations have been illustrated on the example of aluminium.

Keywords: energy-based method, nonlinear material, phenomenological description, strain energy density function, Sylvester's theorem

1. Introduction

The phenomenological description of mechanical properties of nonlinear materials is interesting due to possibility of its application to real engineering structures. The knowledge about mechanisms of deformation under the influence of external loads and the relations between them can be very important in the design process. There is a lot of publications devoted to the modelling of mechanical properties based both on the ground of microstructure relations in the material (multi-scale modelling methods), see for example Silva *et al.* (2007), Terada *et al.* (2008), Speirs *et al.* (2008), or on a phenomenological concept, see for example Wegner (2000, 2005). Because we consider mechanical properties on the base of a real experiment in which the object (material sample) and measured properties are usually in macro-scale, so using the phenomenological method as the way of modelling of the process, which is directly connected with the experiment, is recommended. From this point of view, very interesting are methods based on energy, which were used by Petryk (1985, 1991), Schroder and Neff (2003), Wegner (2000, 2005, 2009) and Dargazany *et al.* (2012). Here, the necessary tool of description of mechanical properties of materials is the strain energy density function. It can be introduced in many different ways, for example as a direct function of invariants of the deformation state, see Wegner (1999, 2009) and Schroder and Neff (2003) or on the base of geometrical interpretation of the deformation process, see Wegner and Kurpisz (2009). Wegner and Kurpisz (2013), using a phenomenological approach and basing on the strain energy density function, investigated the damage process of a metal foam.

Material damage as a dissipative mechanism described in form of free energy per unit volume considered as a thermodynamic potential was taken into account by Cimetiere *et al.* (2005). The

authors, in a major way, split the energy into two parts. The first is an elastic (reversible) part, whereas the second (dissipative) includes, among others, the hardening effect. Because each of these two parts depends on internal variables, so the internal variables influence the damage threshold.

Gajewska and Maciejewska (2005) investigated the influence of internal restrictions (connected with the type of the material, for example isotropic or anisotropic one) in form of limit conditions based on energy of anisotropic materials. Such conditions can be interpreted as different yield conditions. It was shown that as long as the energy scalar product was defined properly in the elastic range, the limit condition having the energy-based interpretation could be found. A much more interesting case takes place when we have nonlinear-elasticity, what implies the necessity of modification of the limit condition.

In the further part of the current paper, on the base of geometrical interpretation, the strain energy density function of a nonlinear material will be introduced and used for formulation of stability conditions due to the damage process, what is an alternative point of view to that presented by Gajewska and Maciejewska (2005).

2. Geometrical interpretation of the deformation state – the basic equation

To introduce a geometrical interpretation of the deformation process, let us take into account the following assumptions:

- The material is isotropic and nonlinear, so the mechanical properties are the same in all directions, but the relations between stress and strain can not be described in form of classic Hook's law (for linear materials).
- The loading process is static, which means that dynamic effects can be neglected.
- The dissipated part of energy includes thermal and plastic deformation energy.
- The material is under plane stress.
- The longitudinal deformation coefficient is a function of the deformation state due to nonlinear properties of the material.
- The principal stress and strain directions are the same due to material isotropy.

Every deformation process can be interpreted as a deformation path C , which is located in space of principal deformation state components. Every point of such path is one deformation state. So a change of deformation due to a change of external loads (change of principal stress components) implies a displacement along the path

$$C : \varepsilon_i = \varepsilon_i^k t \quad \text{for } i = 1, 2, 3 \quad (2.1)$$

where ε_i^k are the final deformation state components, and $t \in T = \langle 0, 1 \rangle$ is a parameter.

The relation between stress and strain in every point of the deformation path takes the form of generalized Hook's law

$$\begin{aligned} \varepsilon_1 &= \frac{\sigma_1(t)}{\tilde{E}(\varepsilon_1)} - \tilde{\nu}(\varepsilon_2) \frac{\sigma_2(t)}{\tilde{E}(\varepsilon_2)} - \tilde{\nu}(\varepsilon_3) \frac{\sigma_3(t)}{\tilde{E}(\varepsilon_3)} \\ \varepsilon_2 &= \frac{\sigma_2(t)}{\tilde{E}(\varepsilon_2)} - \tilde{\nu}(\varepsilon_1) \frac{\sigma_1(t)}{\tilde{E}(\varepsilon_1)} - \tilde{\nu}(\varepsilon_3) \frac{\sigma_3(t)}{\tilde{E}(\varepsilon_3)} \\ \varepsilon_3 &= \frac{\sigma_3(t)}{\tilde{E}(\varepsilon_3)} - \tilde{\nu}(\varepsilon_1) \frac{\sigma_1(t)}{\tilde{E}(\varepsilon_1)} - \tilde{\nu}(\varepsilon_2) \frac{\sigma_2(t)}{\tilde{E}(\varepsilon_2)} \end{aligned} \quad (2.2)$$

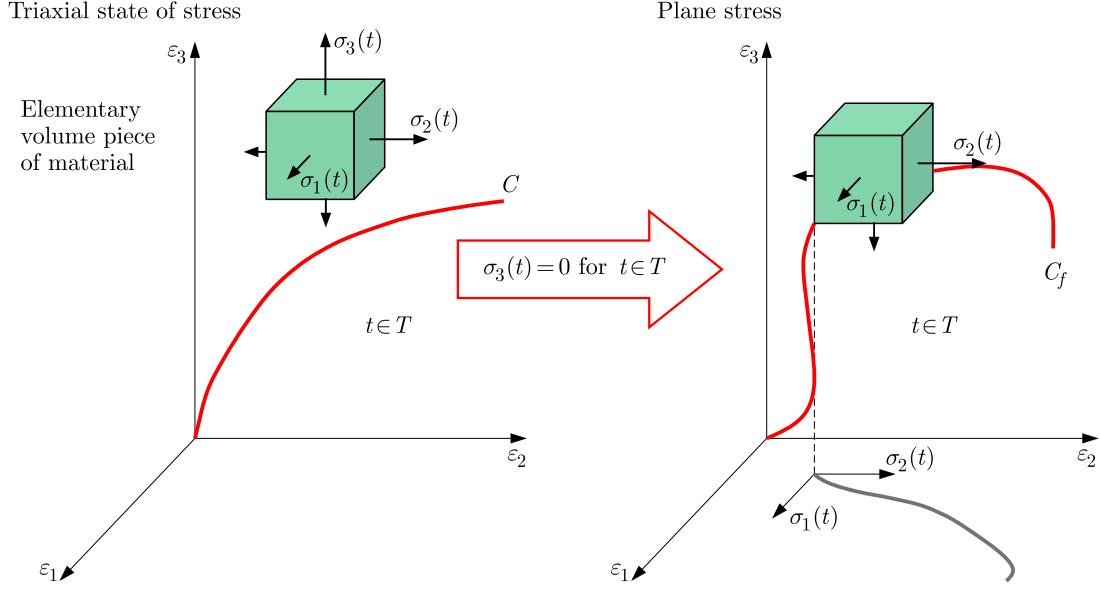


Fig. 1. Deformation paths for a triaxial and plane stress state in a material

where longitudinal and transversal deformation coefficients follow from experimental characteristics $\sigma(\varepsilon)$, $\varepsilon_t(\varepsilon)$ (ε_t is transversal deformation) obtained from a uniaxial tension test and take respectively the form

$$\tilde{E}(\varepsilon) = \frac{\sigma}{\varepsilon} \quad \tilde{v}(\varepsilon) = -\frac{\varepsilon_t}{\varepsilon} \quad (2.3)$$

Because both stress and strain are changeable (along path C_f) in time $t \in \langle 0, 1 \rangle$ of the deformation process, then the density of deformation work from the initial state $\varepsilon_i = 0$ for $t = 0$ to the final state $\varepsilon_i = \varepsilon_i^k$ for $t = 1$ can be expressed as

$$W^C(\varepsilon_1^k, \varepsilon_2^k, \varepsilon_3^k) = \int_{C_f} \sum_{i=1}^3 \sigma_i d\varepsilon_i = \int_0^1 \sum_{i=1}^3 \sigma_i(t) \varepsilon_i'(t) dt \quad (2.4)$$

where on the basis of (2.2) for $i = 1, 2, 3$

$$\sigma_i(t) = \tilde{E}(\varepsilon_i) \frac{\varepsilon_i \prod_{l=1}^3 [1 + \tilde{v}(\varepsilon_l)] + [1 + \tilde{v}(\varepsilon_i)] \sum_{l=1}^3 \tilde{v}(\varepsilon_l) (\varepsilon_l - \varepsilon_i) + \frac{1 + \tilde{v}(\varepsilon_i)}{\tilde{v}(\varepsilon_i)} \prod_{l=1}^3 \tilde{v}(\varepsilon_l) \left(\sum_{l=1}^3 \varepsilon_l - 3\varepsilon_i \right)}{\prod_{l=1}^3 [1 + \tilde{v}(\varepsilon_l)] - [1 + \tilde{v}(\varepsilon_i)]^2 \left(\sum_{l=1}^3 \tilde{v}(\varepsilon_l) - \tilde{v}(\varepsilon_i) + \frac{2}{\tilde{v}(\varepsilon_i)} \prod_{l=1}^3 \tilde{v}(\varepsilon_l) \right)} \quad (2.5)$$

In particular, if we assume the plane stress in plane 102, then the stress components in the third direction are equal zero, and relations (2.4) and (2.5) simplify respectively to

$$W^C(\varepsilon_1^k, \varepsilon_2^k) = \int_{C_f} \sum_{i=1}^2 \sigma_i d\varepsilon_i = \int_0^1 \sum_{i=1}^2 \sigma_i(t) \varepsilon_i'(t) dt \quad (2.6)$$

and

$$\sigma_1(t) = \tilde{E}(\varepsilon_1) \frac{\varepsilon_1 + \varepsilon_2 \tilde{v}(\varepsilon_2)}{1 - \tilde{v}(\varepsilon_1) \tilde{v}(\varepsilon_2)} \quad \sigma_2(t) = \tilde{E}(\varepsilon_2) \frac{\varepsilon_2 + \varepsilon_1 \tilde{v}(\varepsilon_1)}{1 - \tilde{v}(\varepsilon_1) \tilde{v}(\varepsilon_2)} \quad (2.7)$$

The strain component in the passive (third) direction takes the form

$$\varepsilon_3 = -\tilde{v}(\varepsilon_1) \frac{\varepsilon_1 + \varepsilon_2 \tilde{v}(\varepsilon_2)}{1 - \tilde{v}(\varepsilon_1) \tilde{v}(\varepsilon_2)} - \tilde{v}(\varepsilon_2) \frac{\varepsilon_2 + \varepsilon_1 \tilde{v}(\varepsilon_1)}{1 - \tilde{v}(\varepsilon_1) \tilde{v}(\varepsilon_2)} \quad (2.8)$$

In the geometrical interpretation, function (2.6) specifies the values of deformation work density (2.4), which are defined in the space of three-dimensional deformation to present a strain energy density distribution function plot (Fig. 5) along section surface (2.8).

3. Extraction of the volumetric part of energy

Let us consider purely volumetric deformations. Such type of deformations takes place if a material is under influence of hydrostatic pressure. The relation between deformation state components and stress state components according to hydrostatic pressure takes the form

$$\begin{aligned} \varepsilon_1^V &= \frac{ks}{\tilde{E}(\varepsilon_1^V)} - \tilde{v}(\varepsilon_2^V) \frac{ks}{\tilde{E}(\varepsilon_2^V)} - \tilde{v}(\varepsilon_3^V) \frac{ks}{\tilde{E}(\varepsilon_3^V)} \\ \varepsilon_2^V &= \frac{ks}{\tilde{E}(\varepsilon_2^V)} - \tilde{v}(\varepsilon_1^V) \frac{ks}{\tilde{E}(\varepsilon_1^V)} - \tilde{v}(\varepsilon_3^V) \frac{ks}{\tilde{E}(\varepsilon_3^V)} \\ \varepsilon_3^V &= \frac{ks}{\tilde{E}(\varepsilon_3^V)} - \tilde{v}(\varepsilon_1^V) \frac{ks}{\tilde{E}(\varepsilon_1^V)} - \tilde{v}(\varepsilon_2^V) \frac{ks}{\tilde{E}(\varepsilon_2^V)} \end{aligned} \quad (3.1)$$

where $s \in T$ and hence, due to symmetry

$$\varepsilon_1^V = \varepsilon_2^V = \varepsilon_3^V = \varepsilon^V \quad (3.2)$$

where ε^V satisfies the equation

$$\varepsilon^V = \frac{1 - 2\tilde{v}(\varepsilon^V)}{\tilde{E}(\varepsilon^V)} ks = \beta(s) \quad (3.3)$$

and s is a non-dimensional parameter: the ratio of hydrostatic pressure to the basic value k , ks is the current value of hydrostatic pressure.

The above relation does not provide the information about the connection between the current value of deformation (point of path C) and its volumetric part (point of path C^V), see the picture below.

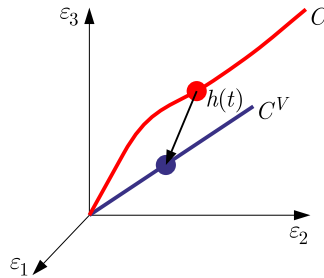


Fig. 2. Relation between the deformation path C and the path due to pure volumetric deformation C^V

To determinate this relation, we have to take into account two analytical descriptions of a volume change in an elementary piece of the material.

The first way

$$\frac{\Delta V}{V_0} = \prod_{i=1}^3 [1 + \varepsilon_i(t)] - 1 \quad (3.4)$$

where $\varepsilon_1(t)$, $\varepsilon_2(t)$ and $\varepsilon_3(t)$ are deformation components of the path C .

The second way explores hydrostatic pressure

$$\Theta = \frac{\Delta V}{V_0} = \prod_{i=1}^3 [1 + \beta(s)] - 1 = [1 + \beta(s)]^3 - 1 \quad (3.5)$$

where Θ is the relative volume change.

After comparison of the right-hand sides of equations (3.4) and (3.5), we receive

$$s = h(t) = \beta^{-1} \left(\sqrt[3]{\prod_{i=1}^3 [1 + \varepsilon_i(t)]} - 1 \right) \quad (3.6)$$

and after substitution into (3.3)

$$\varepsilon^V = \sqrt[3]{\prod_{i=1}^3 [1 + \varepsilon_i(t)]} - 1 \quad (3.7)$$

Hence, we can write that

$$W^{CV} = \int_{C^V} \sigma_1 d\varepsilon_1^V + \int_{C^V} \sigma_2 d\varepsilon_2^V + \int_{C^V} \sigma_3 d\varepsilon_3^V = \sum_{i=1}^3 \int_{C^V} \sigma_i d\varepsilon^V \quad (3.8)$$

where σ_i ($i = 1, 2, 3$) are solutions to the system of equations (2.2) given in form (2.5).

4. Stability conditions for the material under plane stress

The material is in the stable state of equilibrium if every change of the deformation state needs work to be done by external loads. So, in other words, we say about material stability when the strain energy density function is convex. In an analytical form, it can be written as

$$\delta^2 W^C = \sum_{i=1}^3 \sum_{j=1}^3 \frac{\partial^2 W^C}{\partial \varepsilon_i^k \partial \varepsilon_j^k} \delta \varepsilon_i^k \delta \varepsilon_j^k > 0 \quad (4.1)$$

where δ^2 denotes the second order variation of the function W^C .

In the case of plane stress, the deformation work W^C can be interpreted as a function of two deformation state components, however from the other side, the strain energy density depends on three deformation state components and the sign of its second order variation of the strain energy is strictly connected with the three variation increments of deformation state components. Hence, on the base of Sylvester's theorem, we receive

$$\begin{aligned} & \begin{vmatrix} \frac{\partial^2 W^C}{\partial (\varepsilon_1^k)^2} & \frac{\partial^2 W^C}{\partial \varepsilon_1^k \partial \varepsilon_2^k} & \frac{\partial^2 W^C}{\partial \varepsilon_1^k \partial \varepsilon_3^k} \\ \frac{\partial^2 W^C}{\partial \varepsilon_1^k \partial \varepsilon_2^k} & \frac{\partial^2 W^C}{\partial (\varepsilon_2^k)^2} & \frac{\partial^2 W^C}{\partial \varepsilon_2^k \partial \varepsilon_3^k} \\ \frac{\partial^2 W^C}{\partial \varepsilon_1^k \partial \varepsilon_3^k} & \frac{\partial^2 W^C}{\partial \varepsilon_2^k \partial \varepsilon_3^k} & \frac{\partial^2 W^C}{\partial (\varepsilon_3^k)^2} \end{vmatrix} > 0 & \begin{vmatrix} \frac{\partial^2 W^C}{\partial (\varepsilon_1^k)^2} & \frac{\partial^2 W^C}{\partial \varepsilon_1^k \partial \varepsilon_2^k} \\ \frac{\partial^2 W^C}{\partial \varepsilon_1^k \partial \varepsilon_2^k} & \frac{\partial^2 W^C}{\partial (\varepsilon_2^k)^2} \end{vmatrix} > 0 \\ & \begin{vmatrix} \frac{\partial^2 W^C}{\partial (\varepsilon_1^k)^2} & \frac{\partial^2 W^C}{\partial \varepsilon_1^k \partial \varepsilon_3^k} \\ \frac{\partial^2 W^C}{\partial \varepsilon_1^k \partial \varepsilon_3^k} & \frac{\partial^2 W^C}{\partial (\varepsilon_3^k)^2} \end{vmatrix} > 0 & \begin{vmatrix} \frac{\partial^2 W^C}{\partial (\varepsilon_2^k)^2} & \frac{\partial^2 W^C}{\partial \varepsilon_2^k \partial \varepsilon_3^k} \\ \frac{\partial^2 W^C}{\partial \varepsilon_2^k \partial \varepsilon_3^k} & \frac{\partial^2 W^C}{\partial (\varepsilon_3^k)^2} \end{vmatrix} > 0 \\ & \left| \frac{\partial^2 W^C}{\partial (\varepsilon_1^k)^2} \right| > 0 & \left| \frac{\partial^2 W^C}{\partial (\varepsilon_2^k)^2} \right| > 0 & \left| \frac{\partial^2 W^C}{\partial (\varepsilon_3^k)^2} \right| > 0 \end{aligned} \quad (4.2)$$

Inequality (4.1) implicates a system of six nonlinear inequalities (4.2) which allow us to draft the region of material stability. Because the plastic deformation leads to permanent loss of the element shape, so very important is the knowledge about material deformation due to plastic flow. This type of phenomenon takes place if during the deformation process, the volume change of an elementary piece of the material is unchanging.

On the basis of (A.15, see Appendix), the second order variation takes the form

$$\begin{aligned} \delta^2 W^{V=\text{const}} &= \sum_{i=1}^3 \sum_{j=1}^3 \left(\frac{\partial^2 W^C}{\partial \varepsilon_i^k \partial \varepsilon_j^k} - \frac{1}{3} \sum_{k=1}^3 \frac{\sigma_k}{\sqrt[3]{A_1 A_2 A_3}} \frac{\partial A_i}{\partial \varepsilon_j^k} \right) \delta \varepsilon_i^k \delta \varepsilon_j^k \\ &= \sum_{i=1}^3 \sum_{j=1}^3 B_{ij} \delta \varepsilon_i^k \delta \varepsilon_j^k \end{aligned} \quad (4.3)$$

where A_1, A_2, A_3 are given as in Appendix (A.3), and σ_k are expressed by using (2.5).

Hence, stability assumption (4.3) takes respectively the form

$$\begin{aligned} \begin{vmatrix} B_{11} & B_{12} & B_{13} \\ B_{21} & B_{22} & B_{23} \\ B_{31} & B_{32} & B_{33} \end{vmatrix} > 0 & \quad \begin{vmatrix} B_{11} & B_{12} \\ B_{21} & B_{22} \end{vmatrix} > 0 \\ \begin{vmatrix} B_{11} & B_{13} \\ B_{31} & B_{33} \end{vmatrix} > 0 & \quad \begin{vmatrix} B_{22} & B_{23} \\ B_{32} & B_{33} \end{vmatrix} > 0 \\ |B_{11}| > 0 & \quad |B_{22}| > 0 & \quad |B_{33}| > 0 \end{aligned} \quad (4.4)$$

In the case of a plane state of stress, so when $\sigma_3 = 0$, ε_3^k must to be replaced by relation (2.8).

5. Example

As an example of using theoretical investigations, aluminum in plain stress has been taken. The experimental plots of material characteristics are presented in Figs. 3 and 4.

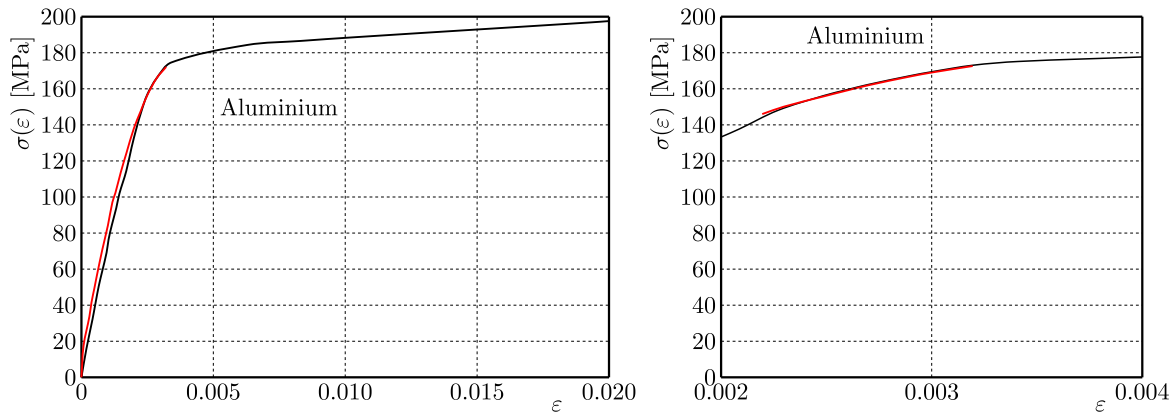


Fig. 3. Experimental relation between stress and strain (in a uniaxial tensile test) and its approximation in the nonlinear range (red line)

However, the precision of approximation of the experimental characteristic between stress and strain is not sufficient for very small (closed to zero) deformations, it is very accurate in the range $\varepsilon \in (0.0023; 0.0033)$, where there exists danger of the appearance of plastic flow. Because in the analytical assessment of the limit surface the second order partial derivatives of the strain

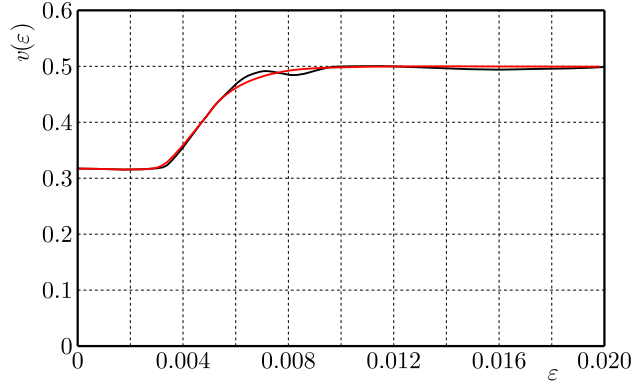


Fig. 4. Experimental plot of transversal deformation coefficient (relation between the ratio of transversal to longitudinal deformation and longitudinal deformation) and its approximation (red line)

energy density function are very important, then much more important is the accuracy of the approximation for $\varepsilon \in \langle 0.0023; 0.0033 \rangle$ than for $\varepsilon \in \langle 0; 0.0023 \rangle$.

Analytical approximations of the above characteristics (σ [MPa], $\tilde{v}(\varepsilon)$ [MPa], $\tilde{E}(\varepsilon)$ [MPa]) can be written respectively as

$$\begin{aligned} \sigma &= -11100000\varepsilon^2 + 86700\varepsilon + 9 && \text{for } \varepsilon \in \langle 0; 0.0033 \rangle \\ \tilde{v}(\varepsilon) &= \begin{cases} 0.317 & \text{for } \varepsilon \in \langle 0; 0.0032 \rangle \\ \frac{0.366}{\pi} \arctan\left(2^{601\varepsilon} \frac{\varepsilon - 0.0032}{0.02 - \varepsilon}\right) + 0.317 & \text{for } \varepsilon > 0.0032 \end{cases} \end{aligned} \quad (5.1)$$

Hence from (2.3)₁ and (5.1), we have

$$\tilde{E}(\varepsilon) = -11100000\varepsilon + 86700 + \frac{9}{\varepsilon} \quad \text{for } \varepsilon \in \langle 0; 0.0033 \rangle \quad (5.2)$$

The strain energy density function (W^C [MJ/m³]) due to (2.5), (5.1) and (5.2) takes the form

$$\begin{aligned} W^C(\varepsilon_1^k, \varepsilon_2^k, \varepsilon_3^k) &= \int_0^1 \sum_{i=1}^3 \sigma_i(t) \varepsilon_i'(t) dt = \int_0^1 \sum_{i=1}^3 \sigma_i(t) \varepsilon_i^k dt \\ &= \frac{a_1(1+c_1) - 3a_1c_1}{3(1+c_1)(1-2c_1)} \sum_{i=1}^3 (\varepsilon_i^k)^3 + \frac{b_1(1+c_1) - 3b_1c_1}{2(1+c_1)(1-2c_1)} \sum_{i=1}^3 (\varepsilon_i^k)^2 \\ &+ \frac{a_1c_1}{3(1+c_1)(1-2c_1)} \sum_{i=1}^3 (\varepsilon_i^k)^2 \sum_{l=1}^3 \varepsilon_l^k + \frac{b_1c_1}{2(1+c_1)(1-2c_1)} \left(\sum_{i=1}^3 \varepsilon_i^k \right)^2 + \frac{1}{1-2c_1} \sum_{i=1}^3 \varepsilon_i^k \end{aligned} \quad (5.3)$$

where $a_1 = -11100000$, $b_1 = 86700$, $c_1 = 0.317$.

If we would like to represent and plot in an easy way the strain energy density function for a plain state of stress, then we have to substitute (on the basis of relation (2.8)) $\varepsilon_3^k = -[c/(1-c)](\varepsilon_1^k + \varepsilon_2^k)$ into relation (5.4). After transformations, we receive

$$\begin{aligned} W^C(\varepsilon_1^k, \varepsilon_2^k) &= -36815920[(\varepsilon_1^k)^3 + (\varepsilon_2^k)^3] + 431343.3[(\varepsilon_1^k)^2 + (\varepsilon_2^k)^2] \\ &+ 117.94(\varepsilon_1^k + \varepsilon_2^k) - 331343284[(\varepsilon_1^k)^2 \varepsilon_2^k + \varepsilon_1^k (\varepsilon_2^k)^2] + 7764179.1 \varepsilon_1^k \varepsilon_2^k \end{aligned} \quad (5.4)$$

for $\varepsilon_1^k \in \langle 0; 0.0033 \rangle$, $\varepsilon_2^k \in \langle 0; 0.0033 \rangle$.

If we apply relation (5.3) to stability assumptions (4.5) then we receive stability regions shown in Fig. 6.

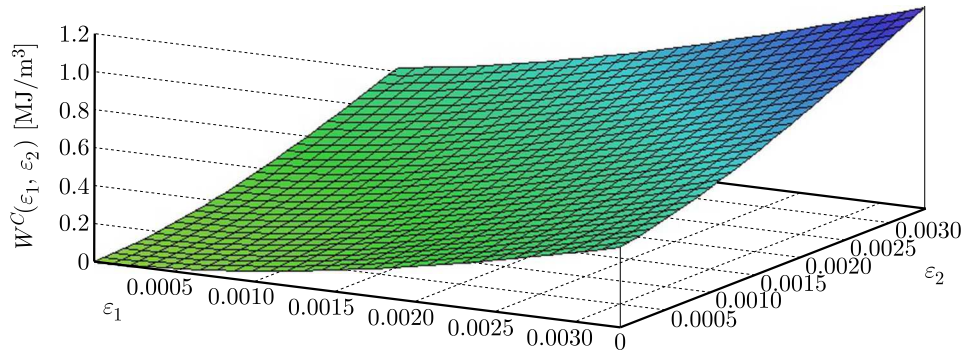


Fig. 5. The strain energy density function

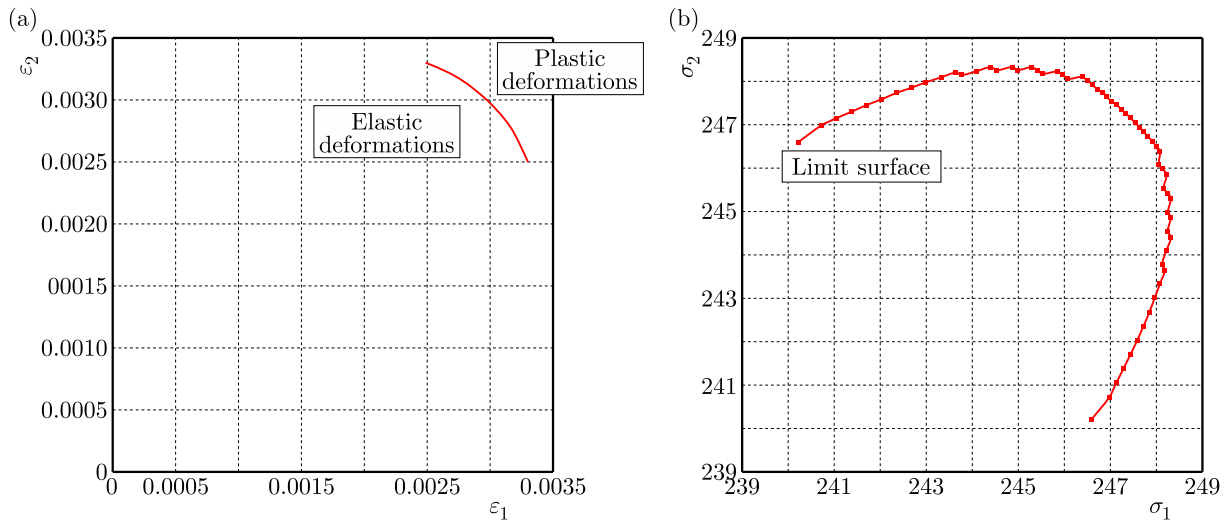


Fig. 6. Region of stability according to assumptions (4.5) in space of the deformation (a) and the stress (b) components

The above plots are obtained from the major form of stability assumptions (formulated for a three-axial state of stress), after substituting the relation $\varepsilon_3^k = -[c(1 - c)](\varepsilon_1^k + \varepsilon_2^k)$, which is true in the case of plain stress.

6. Conclusions

- The strain energy density function is a sufficient tool in the description of mechanical properties of nonlinear material and necessary for stability analysis.
- Extraction of the volumetric part of energy is possible due to hydrostatic interpretation.
- The constant volume assumption plays an important role in formulation of stability conditions due to plastic flow.
- The limit surfaces are convex (see. Figs. 6) and are comparable with the known limit surfaces for linear-elastic materials.

A. Appendix

The material is in the stable state of equilibrium if every change of current deformation state needs a work by external loads. So, if we take into account a very small fluctuation of the current deformation state in three principal directions then relation (4.1) has to be satisfied.

The plastic flow takes place in the case when an increment in volume equals zero, see (Wegner, 2000).

If l_1 , l_2 and l_3 are dimensions of an elementary volume piece of the material in an unloaded state then the ratio of volume change to its virgin state can be written as

$$\theta = \frac{\Delta V}{V_0} = \frac{\prod_{i=1}^3 (l_i + \Delta l_i) - \prod_{i=1}^3 l_i}{\prod_{i=1}^3 l_i} = \prod_{i=1}^3 (1 + \varepsilon_i) - 1 \quad (\text{A.1})$$

and hence

$$\delta\theta = \delta \left[\prod_{i=1}^3 (1 + \varepsilon_i) \right] = \sum_{i=1}^3 A_i \delta\varepsilon_i \quad (\text{A.2})$$

where

$$A_1 = (1 + \varepsilon_2)(1 + \varepsilon_3) \quad A_2 = (1 + \varepsilon_1)(1 + \varepsilon_3) \quad A_3 = (1 + \varepsilon_1)(1 + \varepsilon_2) \quad (\text{A.3})$$

If we take into considerations purely volumetric deformations then $\varepsilon_i = \varepsilon^V$, which by substitution into (A.1) implies

$$\theta = (1 + \varepsilon^V)^3 - 1 \Rightarrow \delta\theta = 3(1 + \varepsilon^V)^2 \delta\varepsilon^V \Rightarrow \delta\varepsilon^V = \frac{\delta\theta}{3(1 + \varepsilon^V)^2} \quad (\text{A.4})$$

The first order variation of the strain energy density function according to plastic flow can be divided as follows

$$\begin{aligned} \delta W^{(V=\text{const})} &= \sigma_1 \delta\varepsilon_1^{(V=\text{const})} + \sigma_2 \delta\varepsilon_2^{(V=\text{const})} + \sigma_3 \delta\varepsilon_3^{(V=\text{const})} \\ \delta\varepsilon_i^{(V=\text{const})} &= \delta\varepsilon_i - \delta\varepsilon^V \end{aligned} \quad (\text{A.5})$$

In the case of the limit surface according to plastic flow, we do not observe a change in the volume, so

$$\delta W^{V=\text{const}} = \delta W^C - \delta W^{CV} = \delta W^s \quad (\text{A.6})$$

where on the basis of (3.8), we have

$$\delta W^{CV} = \sum_{i=1}^3 \sigma_i \delta\varepsilon^V \quad (\text{A.7})$$

Hence, taking into account (A.4)

$$\delta^2 W^{CV} = \frac{1}{3} \sum_{i=1}^3 \sigma_i \left[\frac{\delta^2 \theta}{(1 + \varepsilon^V)^2} - \frac{2\delta\theta \delta\varepsilon^V}{(1 + \varepsilon^V)^3} \right] \quad (\text{A.8})$$

In the absence of volumetric deformations

$$\delta\theta = \delta\varepsilon^V = 0 \quad (\text{A.9})$$

we have

$$\delta^2 W^{CV} = \frac{1}{3} \sum_{i=1}^3 \sigma_i \frac{\delta^2 \theta}{(1 + \varepsilon^V)^2} \quad (\text{A.10})$$

and after using (A.6)

$$\delta^2 W^{V=\text{const}} = \delta^2 W^C - \delta^2 W^{C^V} = \sum_{i=1}^3 \sum_{j=1}^3 \frac{\partial^2 W^C}{\partial \varepsilon_i \partial \varepsilon_j} \delta \varepsilon_i \delta \varepsilon_j - \frac{1}{3} \sum_{i=1}^3 \sigma_i \frac{\delta^2 \theta}{(1 + \varepsilon^V)^2} \quad (\text{A.11})$$

which on the basis of (A.2) gives

$$\delta^2 W^{V=\text{const}} = \sum_{i=1}^3 \sum_{j=1}^3 \left(\frac{\partial^2 W^C}{\partial \varepsilon_i \partial \varepsilon_j} - \frac{1}{3} \sum_{k=1}^3 \frac{\sigma_k}{(1 + \varepsilon^V)^2} \frac{\partial A_i}{\partial \varepsilon_j} \right) \delta \varepsilon_i \delta \varepsilon_j \quad (\text{A.12})$$

On the grounds of (A.4)

$$\begin{aligned} 1 + \theta &= (1 + \varepsilon^V)^3 \Rightarrow 1 + \varepsilon^V = \sqrt[3]{1 + \theta} \Rightarrow 1 + \varepsilon^V = \sqrt[3]{\prod_{i=1}^3 (1 + \varepsilon_i)} \\ &\Rightarrow (1 + \varepsilon^V)^2 = \sqrt[3]{A_1 A_2 A_3} \end{aligned} \quad (\text{A.13})$$

The above relation enables us to write (A.12) in an equivalent form

$$\delta^2 W^{V=\text{const}} = \sum_{i=1}^3 \sum_{j=1}^3 \left(\frac{\partial^2 W^C}{\partial \varepsilon_i \partial \varepsilon_j} - \frac{1}{3} \sum_{k=1}^3 \frac{\sigma_k}{\sqrt[3]{A_1 A_2 A_3}} \frac{\partial A_i}{\partial \varepsilon_j} \right) \delta \varepsilon_i \delta \varepsilon_j \quad (\text{A.14})$$

Acknowledgments

This study was supported by DS: 02/21/DSPB/3452.

References

1. CIMETIERE A., HALM D., MARIGO J.J., MOLINES E., 2005, Damage standard models with a fixed convex, *Archives of Mechanics*, **57**, 4, 265-276
2. DARGAZANY R., KHIEM V.N., NAWRATH U., ISTKOV M., 2012, Network evolution model of anisotropic stress softening in filled rubber-like materials: Parameter identification and finite element implementation, *Journal of Mechanics and Material and Structures*, **7**, 8/9, 861-885
3. GAJEWSKA K., MACIEJEWSKA J., 2005, Energy based limit criteria for anisotropic elastic materials with constraints, *Archives of Mechanics*, **57**, 2/3, 133-155
4. PETRYK H., 1985, On the second-order work in plasticity, *Archives of Mechanics*, **37**, 503-520
5. PETRYK H., 1991, The energy criteria of instability in the time-independent inelastic solids, *Archives of Mechanics*, **43**, 4, 519-545
6. SCHRODER J., NEFF P., 2003, Invariant formulation of hyperelastic transverse isotropy based on polyconvex free energy functions, *International Journal of Solids and Structures*, **40**, 401-445
7. SILVA E., FORST C., LI J., LIN X., ZHU T., YIP S., 2007, Multiscale material modelling: case studies at the atomistic and electronic structure levels, *ESAIM: Mathematical Modelling and Numerical Analysis*, **41**, 2, 427-445
8. SPEIRS D.C.D., DE SOUZA NETO E.A., PERI' C D., 2008, An approach to the mechanical constitutive modelling of arterial wall tissue based on homogenization and optimization, *Journal of Biomechanics*, **41**, 2673-2680
9. TERADA K., INUGAI T., HIRAYAMA N., 2008, A method of numerical material testing in nonlinear multiscale material analyses (in Japanese), *Transactions of the Japan Society of Mechanical Engineering A*, **74**, 1084-1094, 2008

10. WEGNER T., 1999, *Methods Based On Energy in Strength of Materials* (in Polish), Wydawnictwo Politechniki Poznańskiej, Poznań
11. WEGNER T., 2000, Surface of limit state in nonlinear material and its relation with plasticity condition (in Polish), *The Archive of Mechanical Engineering*, **47**, 3, 205-223
12. WEGNER T., 2005, Mathematical modelling of mechanical properties of materials (in Polish), *Biuletyn WAT*, **LIV**, 12, 5-51
13. WEGNER T., 2009, *Modelling Based on Energy in Nonlinear Mechanics of Materials and Structures* (in Polish), Wydawnictwo Politechniki Poznańskiej, Poznań
14. WEGNER T., KURPISZ D., 2009, The conservation energy principle in description of stable and unstable states for aluminium, *Proceedings in Applied Mathematics and Mechanics, PAMM*, **9**, 323-324
15. WEGNER T., KURPISZ D., 2013, Phenomenological modeling of mechanical properties of metal foam, *Journal of Theoretical and Applied Mechanics*, **51**, 203-214

Manuscript received November 21, 2014; accepted for print June 15, 2016

A SEMI-THEORETICAL MODEL FOR TRANSFORMATION PLASTICITY OCCURRED DURING BAINITIC TRANSFORMATION

MAHMOUD YAAKOUBI, FAKHREDDINE DAMMAK

Laboratory of Mechanics, Modeling and Production (LA2MP), ENIS, Sfax, Tunisia
e-mail: mahmoud5yakoubi@gmail.com; fakhreddine.dammak@enis.rn.tn

This study addresses the task of predicting the transformation plasticity induced during phase transformation of the 16MND5 carbon steel from austenite to bainite under low externally applied stress using a semi-theoretical model based on the Greenwood-Johnson mechanism. Both models proposed by Leblond *et al.* (1989) and Taleb and Sidoroff (2003) sufficiently describe the evolution of the TRansformation Induced Plasticity (TRIP) during continuous cooling of the austenitic phase. Nevertheless, TRIP values predicted by these models underestimate measured data through the first half of the transformation and overestimate them through the second half. So, we propose in this paper a method to improve Taleb's model in order to remove discrepancies between theoretical and experimental results throughout the whole transformation and obtain a better description of experimental data.

Keywords: bainitic transformation, transformation induced plasticity (TRIP), traction loading

1. Introduction

In some thermo-mechanical manufacturing processes, especially heat treatment and welding, phase transformations can occur and can affect significantly the mechanical behavior and structural properties of quenched or welded steel parts. Indeed, when metallurgical transformations occur under small external stress lower than the yield stress of the weaker phase (austenite), a supplementary plastic strain is observed (Leblond *et al.*, 1986, 1989; Fischer *et al.*, 1998; Taleb *et al.*, 2001; Taleb and Sidoroff, 2003; Meftah *et al.*, 2007; Hoang *et al.*, 2008; Moumni *et al.*, 2011). This plastic strain increment is called TRansformation Induced Plasticity (TRIP) and has a significant effect on the distribution of the residual stresses, distortions and mechanical properties (Leblond *et al.*, 1986, 1989; Taleb *et al.*, 2004; Dan *et al.*, 2008; Tahimi *et al.*, 2012; Deng and Murakawa, 2013; Song *et al.*, 2014). In the literature, there are two mechanisms proposed to explain the origin of the TRIP: Magee's mechanism which is proposed for displacive transformations and Greenwood-Johnson's mechanism which is well suitable for the diffusional transformations (Meftah *et al.*, 2007; Hoang *et al.*, 2008). According to Magee, TRIP is due to privileged orientation of martensitic plates during transformation in presence of external stress. While Greenwood and Johnson supposed that accommodation between differences in compactness and dilation coefficients of the parent and the product phase leads to apparition of local dislocations in the vicinity of the interface between phases. When deviatoric stress is applied, dislocations are oriented in the direction of the applied stress which induces transformation plasticity at the macroscopic scale. However, it was revealed through experimental analysis that Magee's mechanism was not dominant for low applied stresses; hence, it was admitted that Magee's mechanism might not be considered for carbon steels; however it is normally deemed for shape memory alloys (Moumni *et al.*, 2011). In addition, it was illustrated that only Greenwood-Johnson's mechanism was considered when modeling TRIP for both diffusional and shear transformations (Taleb *et al.*, 2001).

It is well known that much works have been done in the last thirty years for better modeling of the evolution of TRIP during phase transformations of steel alloys under different types of loadings. So this additional strain increment originating from phase transformation is accounted in the development of constitutive behavior of a multiphasic material in order to perfectly simulate the material response in continuum mechanical computation. The approaches describing the evolution of the TRIP during phase transformations can be classified into phenomenological models (Mohr and Jacquemin, 2008), micromechanics-based models (Leblond *et al.*, 1989; Taleb and Sidoroff, 2003; Sun *et al.*, 2009) and discrete dislocation-transformation model (Shi *et al.*, 2010).

In this paper, we focus only on the micromechanics-based model proposed by Leblond *et al.* (1989) and improved later by Taleb and Sidoroff (2003). This theoretical model was established by considering Greenwood-Johnson's mechanism where an elementary volume of austenite having spherical shape in which a spherical core of α -phase was growing. The homogeneity of strain and stress fields in the transforming elementary volume was assumed. So, micromechanical analysis permits establishing the theoretical model describing TRIP during phase transformation.

The purpose of this work is to present a summarization of the hypothesis and theoretical development carried out by the authors to obtain their TRIP models, appraise their simulation results, and improve some assumptions resulting then in a better model which predicts effectually the evolution of the TRIP during phase transformation. Simulations obtained by the new model will be compared with experimental results provided in the literature in order to investigate the efficiency of our modeling.

2. Basic framework

We are interested in the theoretical model developed by Leblond *et al.* (1989) which is one of the most widely used for practical applications and which is implemented in the finite element codes such as SYSWELD and ASTER. This model was improved later by Taleb and Sidoroff (2003).

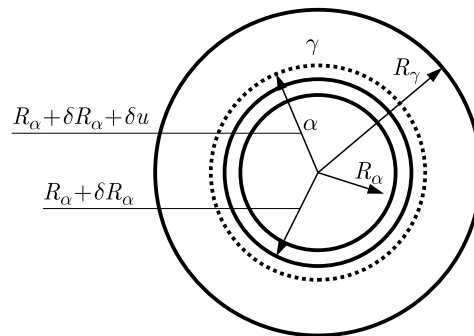


Fig. 1. Geometry considered by Leblond to illustrate phase transformation of austenitic nuclei

Leblond's model is obtained from a micromechanical analysis of stress and strain fields which evolve in an austenitic spherical nuclei occurring during continuous cooling. The growth of a spherical product phase core is carried out in the center of austenitic spherical nuclei as shown in Fig. 1. R_γ and R_α are radii of parent and product phase, respectively. One should note that R_α is nil before the beginning of transformation and it grows progressively during transformation until it reaches R_γ . δR_α is the radius increasing of the spherical phase α during a time increment δt . Because of the positive volume change induced by the transformation, points located originally at $R_\alpha + \delta R_\alpha$ come to a new location $R_\alpha + \delta R_\alpha + \delta u$. As revealed by Leblond, the macroscopic plastic strain rate generated during phase transformation under external loading depends only

on the shape variation of each phase. Indeed, the author assumed through its hypothesis 1 that the effect of local anisotropy due to a small difference between elastic parameters of each phase is negligible with respect to the stresses and deformations due to volume differences between phases α and γ . So, the general expression for the plastic strain rate is given by the following equation

$$\dot{E}^p = (1 - z)\langle \dot{\varepsilon}_\gamma^p \rangle_{V_\gamma} + z\langle \dot{\varepsilon}_\alpha^p \rangle_{V_\alpha} + \dot{z}\langle \Delta \varepsilon_{\gamma \rightarrow \alpha}^p \rangle_F \quad (2.1)$$

where z is the volume fraction of the product phase, $\dot{\varepsilon}_\gamma^p$ and $\dot{\varepsilon}_\alpha^p$ are the microscopic plastic strain rate tensors in phases γ and α , respectively, $\Delta \varepsilon_{\gamma \rightarrow \alpha}^p$ is the deviatoric component of the transformation strain tensor and $\langle \Delta \varepsilon_{\gamma \rightarrow \alpha}^p \rangle_F$ expresses the average value of $\Delta \varepsilon_{\gamma \rightarrow \alpha}^p$ along the transformation front F .

The author assumed that the average of deviatoric transformation strain tensor on the front F is negligible since there is no favorite orientation. Subsequently, the last term in equation (2.1) is omitted. The second hypothesis proposed by the author is that for small or moderately high applied stresses, the austenitic phase is entirely plastic, but the α -phase remains elastic or its plastic strain rate remains always much smaller than that of the γ -phase. Afterward, the second term in the right-hand side of equation (2.1) disappears, and this later is reduced to

$$\dot{E}^p = (1 - z)\langle \dot{\varepsilon}_\gamma^p \rangle_{V_\gamma} \quad (2.2)$$

Given that the plastic strain in the parent phase is the sum of the classical plastic term due to variation of the loading conditions and transformation induced plastic term corresponding to the evolution of new phase fraction z , then

$$\dot{E}^p = \dot{E}^{cp} + \dot{E}^{tp} \quad (2.3)$$

\dot{E}^{cp} is the classical plastic term and the transformation induced plastic term is written as follows

$$\dot{E}^{tp} = (1 - z)\left\langle \frac{\delta \varepsilon_\gamma^p}{\delta z} \right\rangle_{V_\gamma} \dot{z} \quad (2.4)$$

The third hypothesis used by the author is that material obeys the Von Mises criterion and possesses an ideal-plastic flow. By assuming a uniform austenitic yield stress σ_γ^y , equation (2.4) can be transformed into

$$\dot{E}^{tp} = \frac{3(1 - z)}{2\sigma_\gamma^y} \left\langle \frac{\delta \varepsilon_\gamma^{eq}}{\delta z} s_\gamma \right\rangle_{V_\gamma} \dot{z} \quad (2.5)$$

where ε_γ^{eq} is the von Mises equivalent microscopic plastic strain in the parent phase (phase γ), σ_γ^y and s_γ are respectively the yield stress and the deviatoric tensor of the microscopic stress in this phase.

At this stage, Leblond assumed through hypothesis 4 and 5 that correlation between $\delta \varepsilon_\gamma^{eq}/\delta z$ and s_γ can be neglected and the average S_γ of s_γ within the volume V_γ is equal to the overall average S of s in the whole nuclei. Then

$$\dot{E}^{tp} = \frac{3(1 - z)}{2\sigma_\gamma^y} \left\langle \frac{\delta \varepsilon_\gamma^{eq}}{\delta z} \right\rangle_{V_\gamma} S \dot{z} \quad (2.6)$$

Using a spherical coordinate system and considering a purely radial displacement, the solution of the mechanical problem is performed using the dynamic equilibrium equation in the continuous mediums. Finally, it is found that

$$\frac{\delta \varepsilon_\gamma^{eq}}{\delta z} = \frac{2\Delta \varepsilon_{\alpha\gamma} R_\gamma^3}{r^3} \quad (2.7)$$

So

$$\dot{E}^{tp} = -\frac{3\Delta\varepsilon_{\alpha\gamma}}{\sigma_\gamma^y} \ln(z) \dot{z} S \quad (2.8)$$

where $\Delta\varepsilon_{\alpha\gamma}$ is the volume change that corresponds to phase transformation.

Because equation (2.8) includes a singularity at the beginning of the transformation ($z = 0$), the author proposed to cut off the TRIP below $z = 0.03$ leading then to the following model

$$\dot{E}^{tp} = \begin{cases} 0 & \text{if } z \leq 0.03 \\ -\frac{3}{2}k \ln(z) \dot{z} S & \text{if } z > 0.03 \end{cases} \quad (2.9)$$

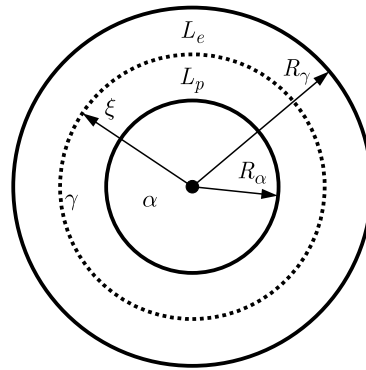


Fig. 2. Geometry considered by Taleb and Sidoroff (2003): γ -phase is composed by an outer elastic layer L_e around an inner plastic layer L_p

Taleb and Sidoroff (2003) developed their model by following the micromechanical scheme assumed by Leblond to formulate its transformation plasticity kinetic model. They extended the Leblond model by keeping all hypotheses except hypothesis 2. Afterwards, the behavior of the austenitic phase has been considered elastoplastic with ideal plasticity. Indeed, according to Taleb and Sidoroff (2003), the product phase remains elastic while the parent phase consists of an outer elastic layer L_e around an inner plastic layer L_p with an elastic-plastic boundary at $r = \xi$ where $R_\alpha \leq \xi \leq R_\gamma$ as shown in Fig. 2. The boundary between these layers increases progressively during transformation until ξ becomes equal to R_γ . At this instant, the remainder of the parent phase turns into completely plastic. By executing the solution of the mechanical problem using the dynamic equilibrium equation in the continuous medium, Taleb and Sidoroff (2003) found that

$$\xi = \sqrt[3]{\frac{2\Delta\varepsilon_{\gamma\alpha}}{\sigma_\gamma^y} \frac{9K\mu}{4\mu + 3K} R_\alpha} \quad (2.10)$$

where K and μ are respectively the bulk and shear elastic moduli.

Finally, Taleb's model assuming elastoplastic parent phase and extending Leblond's one to low values of z ; is the following

$$\dot{E}^{tp} = \begin{cases} -\frac{2\Delta\varepsilon_{\gamma\alpha}}{\sigma_1^y} \ln(z_\ell) \dot{z} \frac{3}{2} S & \text{if } z \leq z_\ell \\ -\frac{2\Delta\varepsilon_{\gamma\alpha}}{\sigma_1^y} \ln(z) \dot{z} \frac{3}{2} S & \text{if } z > z_\ell \end{cases} \quad (2.11)$$

with

$$z_\ell = \frac{\sigma_\gamma^y}{2\Delta\varepsilon_{\alpha\gamma}} \frac{4\mu + 3K}{9K\mu}$$

Experimental tests on bainitic transformation of the 16MND5 steel under small applied stresses were performed and their results were given by Taleb and Sidoroff (2003). These tests allow comparison between simulation and experiment results. Indeed, theoretical and experimental curves are presented in Fig. 3 providing the evolution of the TRIP against the product phase fraction. So, a coincidence between Taleb's and Leblond's models is observed when the threshold of Leblond's model is equal to 0.03. Theoretical prediction given by Taleb's model that agrees with Leblond's forecast (Leblond 0.03) illustrates slow transformation plasticity kinetic during the first half of the transformation with respect to the experimental result while the latter seems overestimated at the end of the transformation. Therefore, the aim of the following Section is to revise some assumptions made by the authors; that lead to formulate enhanced transformation plasticity kinetics ensuring then a better congruence with the experimental curve through all the transformation.

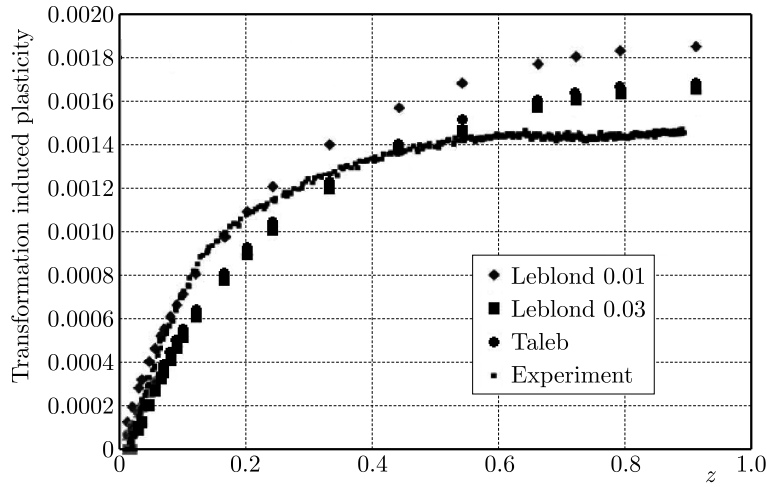


Fig. 3. Transformation plasticity evolution during bainitic transformation in the 16MND5 steel under applied stress (24 MPa) versus volume fraction of the formed bainite

3. Numerical procedure

Our new model will be developed basing on the micromechanical analysis presented above after reviewing some assumptions made by the authors. Indeed, some hypothesis will be more discussed and improved leading thus to a more refined model that better agrees with the experimental results.

Hypothesis 4 suggested by the author which assumes that

$$\left\langle \frac{\delta \varepsilon_{\gamma}^{eq}}{\delta z} s_{\gamma} \right\rangle_{V_{\gamma}} = \left\langle \frac{\delta \varepsilon_{\gamma}^{eq}}{\delta z} \right\rangle_{V_{\gamma}} \langle s_{\gamma} \rangle_{V_{\gamma}}$$

is mathematically inaccurate because the integral of the product of two functions is different to the product of their integrals. So, we suppose that the previous equation can be calibrated by introducing a function $m(z)$ as follows

$$\left\langle \frac{\delta \varepsilon_{\gamma}^{eq}}{\delta z} s_{\gamma} \right\rangle_{V_{\gamma}} = m(z) \left\langle \frac{\delta \varepsilon_{\gamma}^{eq}}{\delta z} \right\rangle_{V_{\gamma}} \langle s_{\gamma} \rangle_{V_{\gamma}} \quad (3.1)$$

In order to have an idea about the evolution of the function $m(z)$, let us consider Fig. 4a which is available in Leblond *et al.* (1989) that points out the simulation of $\langle (\delta \varepsilon_{\gamma}^{eq} / \delta z) s_{\gamma} \rangle_{V_{\gamma}}$ and $\langle \delta \varepsilon_{\gamma}^{eq} / \delta z \rangle_{V_{\gamma}} \langle s_{\gamma} \rangle_{V_{\gamma}}$ versus z . Basing on this result, we remark that disagreement between the two

curves is moderately small; thus we admit that the function $m(z)$ is not varying much in the interval $[0, 1]$; so we can substitute equation (3.1) by

$$\left\langle \frac{\delta \varepsilon_\gamma^{eq}}{\delta z} s_\gamma \right\rangle_{V_\gamma} \approx \langle m(z) \rangle_{[0,1]} \left\langle \frac{\delta \varepsilon_\gamma^{eq}}{\delta z} \right\rangle_{V_\gamma} \langle s_\gamma \rangle_{V_\gamma} \quad (3.2)$$

Then hypothesis 4 is replaced by hypothesis 4', thinking that

$$\left\langle \frac{\delta \varepsilon_\gamma^{eq}}{\delta z} s_\gamma \right\rangle_{V_\gamma} = m \left\langle \frac{\delta \varepsilon_\gamma^{eq}}{\delta z} \right\rangle_{V_\gamma} \langle s_\gamma \rangle_{V_\gamma} \quad (3.3)$$

with m is the average of the function $m(z)$ in the interval $[0, 1]$.

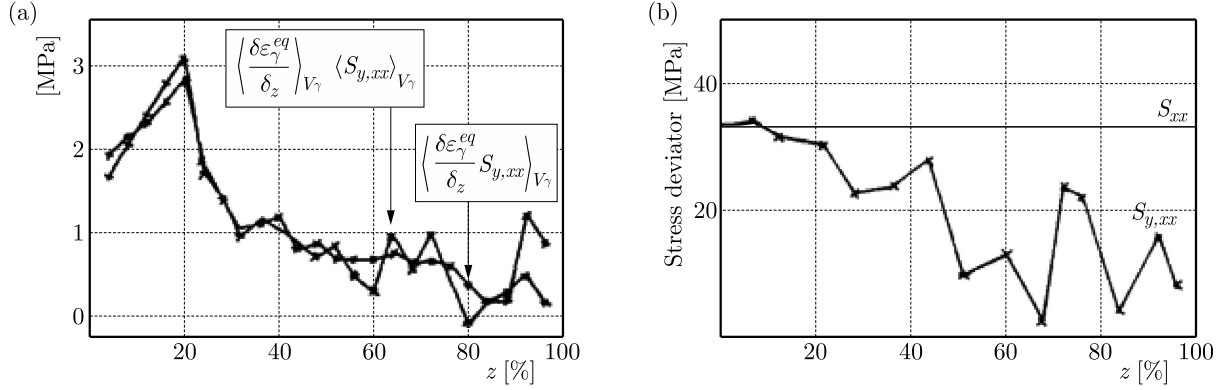


Fig. 4. Verification of: (a) hypothesis 4 and (b) hypothesis 5

Hypothesis 5 assuming that the average stress deviator in the parent phase is almost equal to the overall average stress deviator ($S_\gamma = S$ with $S_\gamma = \langle s_\gamma \rangle_{V_\gamma}$ and $S = \langle s \rangle_V$) is not verified. Indeed, Fig. 4b which is taken from Leblond *et al.* (1989) illustrates the simulation of S_γ and S versus the product phase fraction z in the uniaxial case, and an important discrepancy between them has been shown. More precisely, the curves in this figure prove that S_γ/S is a decreasing function versus z . Afterwards, we propose that the function S_γ/S has a style of $1 - z^n$ defining then hypothesis 5'. The new relationship between S_γ and S is the following

$$S_\gamma = (1 - z^n)S \quad (3.4)$$

with n is a constant.

Replacing hypotheses 4 and 5 by hypotheses 4' and 5' respectively, one can obtain

$$\left\langle \frac{\delta \varepsilon_\gamma^{eq}}{\delta z} s_\gamma \right\rangle_{V_\gamma} = m(1 - z^n) \left\langle \frac{\delta \varepsilon_\gamma^{eq}}{\delta z} \right\rangle_{V_\gamma} S = \chi(z) \left\langle \frac{\delta \varepsilon_\gamma^{eq}}{\delta z} \right\rangle_{V_\gamma} S \quad (3.5)$$

with

$$\chi(z) = m(1 - z^n) \quad (3.6)$$

The function χ depends on two parameters m and n and should accomplish more coincidence between quantities $\langle (\delta \varepsilon_\gamma^{eq} / \delta z) s_\gamma \rangle_{V_\gamma}$ and $\langle \delta \varepsilon_\gamma^{eq} / \delta z \rangle_{V_\gamma} S$. Afterwards, the new model of transformation plasticity evolution is defined as follows

$$\dot{E}^{tp}(z) = \chi(z) \psi(z) \dot{z} \quad (3.7)$$

with

$$\psi(z) = \begin{cases} -\frac{2\Delta\varepsilon_{\alpha\gamma}}{\sigma_\gamma^y} \ln(z_\ell) \frac{3}{2} S & \text{if } z \leq z_\ell \\ -\frac{2\Delta\varepsilon_{\alpha\gamma}}{\sigma_\gamma^y} \ln(z) \frac{3}{2} S & \text{if } z > z_\ell \end{cases} \quad (3.8)$$

with

$$z_\ell = \frac{\sigma_\gamma^y}{2\Delta\varepsilon_{\alpha\gamma}} \frac{4\mu + 3K}{9K\mu}$$

According to the new model, Eq. (3.7), the transformation plasticity increment that corresponds to a product phase increment produced during a time increment is the following

$$\Delta E^{tp}(z_j) = \chi(z_j)\psi(z_j)(\Delta z)_j = \chi(z_j)\Delta TP_T(z_j) \quad (3.9)$$

where z_j is obtained until j -th time increment by accounting from the beginning of bainitic transformation $z_j = \sum_{i=1}^{i=j} (\Delta z)_i$, $(\Delta z)_j$ is the increment of the product phase formed during the j -th time increment. $\Delta TP_T(z_j)$ represents the transformation plasticity increment generated during the j -th time increment according to Taleb's model. Indeed, the function $\chi(z_j)$ is defined as a quotient obtained by dividing $\Delta TP_{Exp}(z_j)$ by $\Delta TP_T(z_j)$ for a non nil value of z_j

$$\chi(z_j) = \frac{\Delta TP_{Exp}(z_j)}{\Delta TP_T(z_j)} \quad z_j \neq 0 \quad (3.10)$$

where $\Delta TP_{Exp}(z_j)$ designates the experimental value of the plasticity transformation increment developed during the j -th time increment. $\Delta TP_{Exp}(z_j)$ and $\Delta TP_T(z_j)$ are determined graphically from curves illustrated in Fig. 3. $\chi(1)$ is directly equal to zero from equation (3.6). Subsequently, the curve characterizing the evolution of function χ against z is illustrated in Fig. 5. One can remark then that the function χ which depends on m and n parameters is

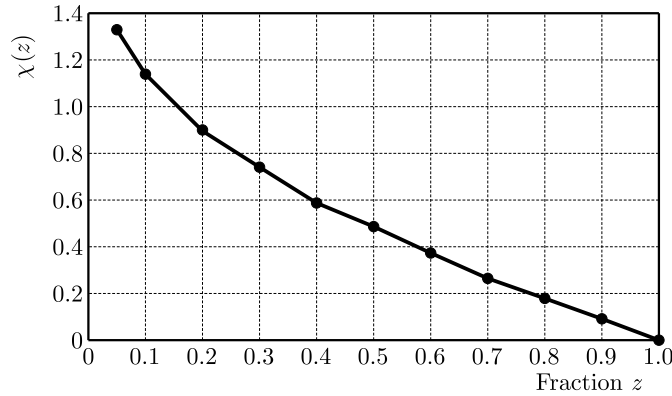


Fig. 5. Evolution of the function χ versus z

decreasing versus z . The parameters m and n can be determined by evaluating the derivative of the function χ for two different values z_1 and z_2 as follows

$$\left. \begin{array}{l} \chi'(z_1) = -mnz_1^{n-1} \\ \chi'(z_2) = -mnz_2^{n-1} \end{array} \right\} \Rightarrow \left\{ \begin{array}{l} n = \frac{\ln \frac{\chi'(z_1)}{\chi'(z_2)}}{\ln \frac{z_1}{z_2}} + 1 \\ m \approx \frac{1}{2} \left(\frac{\chi(z_1)}{1 - z_1^n} + \frac{\chi(z_2)}{1 - z_2^n} \right) \end{array} \right. \quad (3.11)$$

The estimation of the function χ' at a given value z is accomplished by applying the following formulation

$$\chi'(z) = \frac{\chi(z + \hbar) - \chi(z - \hbar)}{2\hbar} \quad (3.12)$$

with \hbar being a parameter of too small value (it is chosen equal to 0.02 in our case). $\chi(z + \hbar)$ and $\chi(z - \hbar)$ are determined graphically from Fig. 5. It is found that $\chi'(0.2) = -1.98$ and $\chi'(0.7) = -0.96$. So

$$n = 0.405 \quad m = 1.93 \quad (3.13)$$

Finally, the function χ is determined

$$\chi(z) = 1.93(1 - z^{0.405}) \quad (3.14)$$

According to equations (3.7) and (3.8), the new model for TRIP kinetics, which is formulated to get an improved agreement with the experimental result, is defined by

$$\dot{E}^{tp} = \begin{cases} -\frac{2\Delta\varepsilon_{\alpha\gamma}}{\sigma_{\gamma}^y} \chi(z) \ln(z_{\ell}) \dot{z} \frac{3}{2} S & \text{if } z \leq z_{\ell} \\ -\frac{2\Delta\varepsilon_{\alpha\gamma}}{\sigma_{\gamma}^y} \chi(z) \ln(z) \dot{z} \frac{3}{2} S & \text{if } z > z_{\ell} \end{cases} \quad (3.15)$$

with

$$\chi(z) = 1.93(1 - z^{0.405}) \quad z_{\ell} = \frac{\sigma_{\gamma}^y}{2\Delta\varepsilon_{\alpha\gamma}} \frac{4\mu + 3K}{9K\mu}$$

Now, the new model will be investigated through comparison between numerical simulations and measured TRIP generated during bainitic transformation of 16MND5 steel specimens.

4. Experimental validation

In this Section, free dilatometry and TRIP tests carried out by Coret *et al.* (2002) are deemed. Specimens were 16MND5 steel tubular cylinders having inner and outer diameters equal to 22.4 mm and 23.4 mm, respectively. The feeble thickness of the specimen enables obtaining low a radial thermal gradient and, subsequently, homogenous stress and strains fields. Specimens were austenitized by induction current at 900°C for 30 s and then cooled by injecting argon inside. The heating and cooling rate were 10°C/s and -3°C/s, respectively. We consider in this paper three experimental results of dilatometric tests provided by Coret *et al.* (2002). The first was the free dilatometric test while the second and the third were the TRIP dilatometric tests under uniaxial traction loading equal to 30 MPa and 60 MPa, respectively. Traction loading was applied during the cooling stage when temperature reached 600°C (somewhat before the beginning of bainitic transformation at 560°C) and released at the end of the test. In this study, dilatation curves obtained by these tests were adjusted in such a way that there was no difference between them before reaching temperature 600°C. In addition, only difference due to elastic strains was considered for temperature between 600°C and 560°C. This procedure takes away experimental uncertainty and allows getting reliable results. Dilatometric curves are plotted together in Fig. 6 for the temperature range 700°C-390°C which includes bainitic transformation during cooling. The difference between TRIP curves and free dilatometric curve is due to elastic strain caused by the external loading and essentially to TRIP generated by phase transformation under external stress.

The total strain occurred during a TRIP test is supposed to be the sum of thermo-metallurgical strain, elastic strain due to external loading and plasticity transformation strain generated through phase transformation (Taleb *et al.*, 2001; Coret *et al.*, 2002; Dutta *et al.*, 2013). Then

$$\varepsilon^{pt}(T) = \varepsilon^{tot}(T) - \varepsilon^{thm}(T) - \varepsilon^e(T) \quad (4.1)$$

with $\varepsilon^{tot}(T)$ being the total strain issued from TRIP curve. $\varepsilon^{thm}(T)$ corresponds to strain obtained from the free dilatometric curve and $\varepsilon^e(T)$ is the elastic strain. It is given by

$$\varepsilon^e(T) = \frac{\sigma}{E(T)} \quad (4.2)$$

where σ is the external applied stress and $E(T)$ is the thermal dependent Young modulus.

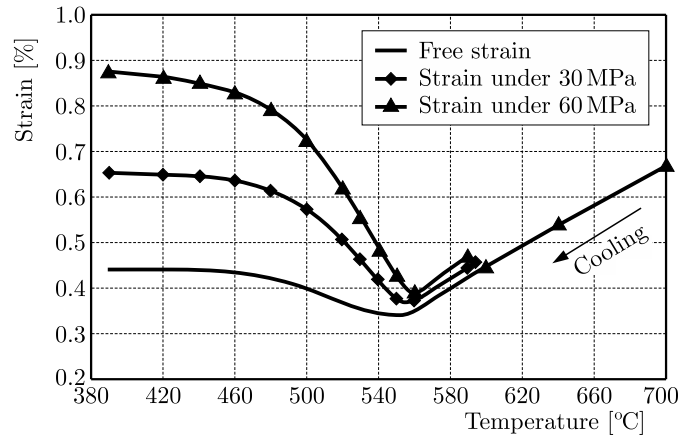


Fig. 6. Dilatometric curves obtained during bainitic transformation under different tension loadings

The evolution of TRIP against the temperature is estimated for two TRIP tests assuming that there is no TRIP evolution before starting of the bainitic transformation. For the 16MND5 steel, when the austenite transforms under cooling rate equal to $-3^{\circ}\text{C}/\text{s}$, the obtained phase proportions are respectively 87% of bainite and 13% of martensite (Moumni *et al.*, 2011). Subsequently, we will not take into account of the TRIP occurred below 390°C when estimating the evolution of TRIP against temperature because we consider in this study only TRIP occurred through bainitic transformation. Experimental results for the evolution of TRIP according to temperature during cooling are illustrated in Table 1. Now, these experimental results will be used to evaluate numerical simulations performed in the following Section.

Table 1. TRIP obtained from dilatometric tests

Temperature [°C]	560	540	520	500	480	460	440	420	390
ε^{tp} [%], $\sigma = 30$ MPa	0	0.052	0.118	0.152	0.169	0.182	0.188	0.192	0.194
ε^{tp} [%], $\sigma = 60$ MPa	0	0.099	0.212	0.290	0.335	0.359	0.378	0.390	0.402

5. Simulations and discussions

The simulation of the quenching process is performed through calculation of temperature evolution in the specimen during treatment. It is coupled with calculation of metallurgical phases distributions followed by the solution of the mechanical problem by the finite element method. The ABAQUS software linked to many subroutines is used to simulate heat treatment phase transformation histories and strain fields as mentioned by Yaakoubi *et al.* (2013b). The thermal cycle recorded by Coret *et al.* (2002) is used as the boundary condition to carry out the simulation (Fig. 7). Phase transformation kinetics is modeled by using the JMAK formalism (Barbe *et al.*, 2008; Yaakoubi *et al.*, 2013a). Thermo-physical properties of the material are available in Moumni *et al.* (2011). The analysis is realized two times for each loading case by using in the first time Taleb's model to predict TRIP evolution and using the new model in the second time. It is found that the maximum value of bainite proportion obtained by simulation is equal to 0.883, which is very close to value (0.87) obtained by Moumni *et al.* (2011).

The comparison between numerical and measured TRIP ($\varepsilon^{tp} = f(T)$) appears in Fig. 8. It is evident that the transformation plasticity predicted by the new model is considerably better than Taleb's predictions for the loading case of 30 MPa. However, for the loading case of 60 MPa, new predictions are not adequate because they show overestimations through the first half of the transformation and underestimations through the second half. We observe that as the tension

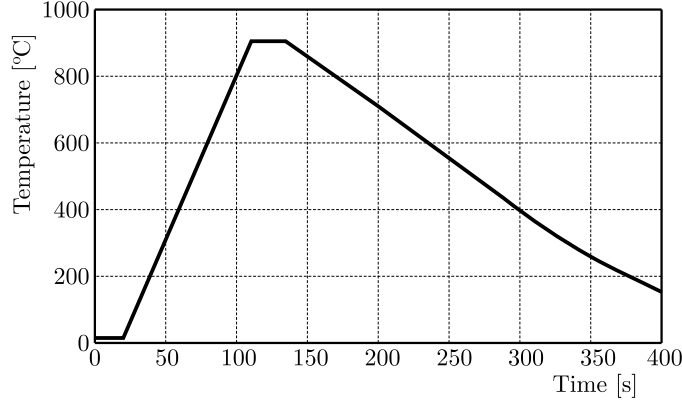


Fig. 7. Thermal cycle used as the boundary condition to carry out the simulation

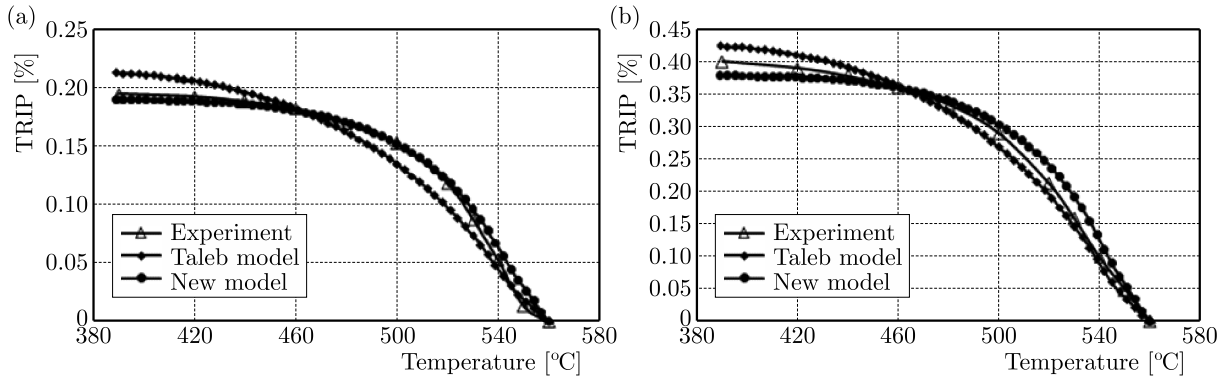


Fig. 8. Transformation plasticity evolution versus temperature during transformation plasticity tests under (a) 30 MPa, (b) 60 MPa. Comparison between experimental results and predictions of Taleb's and the new model

load becomes larger, the discrepancies of the new model become increasingly significant. This fact is explained by that the function χ which appears in the new model is identified for the loading case of 24 MPa. So, we think that this new model can be refined by making parameters m and n (those define the function χ) dependent on the applied stress σ . Indeed, analysis of the function χ shows that the increasing of the parameter m increases the predictions of TRIP at the beginning of transformation, and that the increasing of the parameter n increases them at the end of the transformation and vice versa. The fitting of numerical simulations conducted to define parameters m and n versus σ is as follows

$$m = \frac{10}{\sqrt{\sigma + 3}} \quad n = \frac{\sigma}{60} \quad (5.1)$$

Subsequently, the function χ becomes

$$\chi(z, \sigma) = \frac{10}{\sqrt{\sigma + 3}} (1 - z)^{\frac{\sigma}{60}} \quad (5.2)$$

Then, the final new model that describes the evolution of TRIP during bainitic transformation of the 16MND5 steel under low applied stress is

$$\dot{E}^{tp} = \begin{cases} -\frac{2\Delta\varepsilon_{\alpha\gamma}}{\sigma_{\gamma}^y} \chi(z, \sigma) \ln(z_{\ell}) \dot{z} \frac{3}{2} S & \text{if } z \leq z_{\ell} \\ -\frac{2\Delta\varepsilon_{\alpha\gamma}}{\sigma_{\gamma}^y} \chi(z, \sigma) \ln(z) \dot{z} \frac{3}{2} S & \text{if } z > z_{\ell} \end{cases} \quad (5.3)$$

with

$$\chi(z, \sigma) = \frac{10}{\sqrt{\sigma + 3}}(1 - z)^{\frac{\sigma}{60}} \quad z_\ell = \frac{\sigma_\gamma^y}{2\Delta\varepsilon_{\alpha\gamma}} \frac{4\mu + 3K}{9K\mu}$$

The results of the new refined model and experimental results are illustrated by Fig. 9. It has been found that new predictions achieved by the refined model, Eq. (4.5), are more convenient with experiments than those obtained from the preliminary version of this model for all considerate cases of the applied stress. Indeed, the refined new model is capable to capture not only the fast transformation plasticity observed experimentally at the beginning of the transformation but also the deceleration of this plasticity rate during the second half of the transformation; a profit which cannot be accomplished by the previous models.

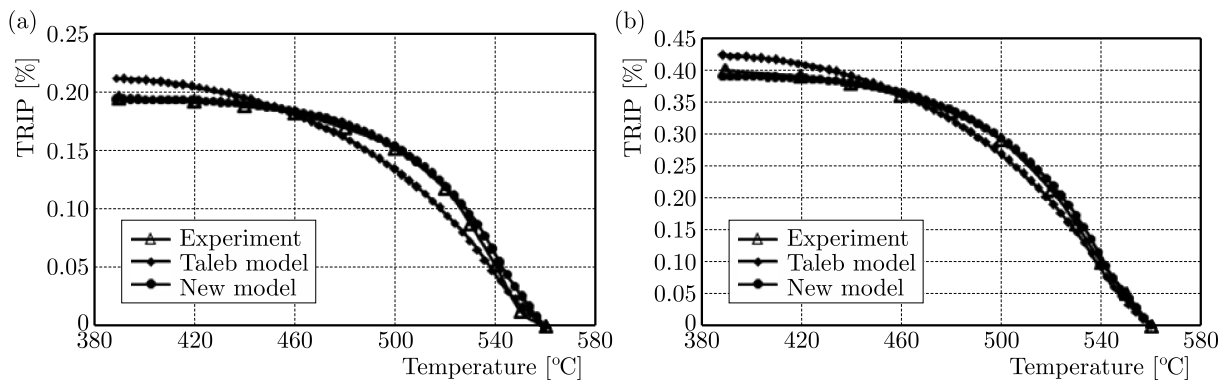


Fig. 9. Transformation plasticity evolution versus temperature during transformation plasticity tests under (a) 30 MPa, (b) 60 MPa. Comparison between experimental results and predictions of Taleb's and new refined models

6. Conclusion

In this study, a new (semi-theoretical) model to predict TRIP induced during bainitic transformation under an external tension loading is developed by upgrading the existing models in the literature. A way to improve these models would be the revising some simplifying assumptions suggested by authors during analysis of the micromechanical approach. Subsequently, new substitute assumptions are reasonably suggested leading then to multiplying Taleb's formula by an appropriate function that is numerically established. The new semi-theoretical model for predicting TRIP produced during bainitic transformation under low tension stress is finally established.

The investigation of the accuracy of the new model is performed in the light of comparison between numerical simulations and experimental results provided in the literature. It has been found that predictions obtained by the refined new model are significantly better than Taleb's forecasts. Furthermore, this new model leads not only to elevate TRIP values at the beginning of the transformation but also to lower them during the second half of the transformation; a result that is experimentally perceived and cannot be described by prior models. Further studies are needed in order to extend this new model for the case of high applied stress and other kinds of transformations.

References

1. BARBE F., QUEY R., TALEB L., EDUARDO S.C., 2008, Numerical modelling of the plasticity induced during diffusive transformation. An ensemble averaging approach for the case of random arrays of nuclei, *European Journal of Mechanics A*, **27**, 1121-1139

2. CORET M., CALLOCH S., COMBESCURE A., 2002, Experimental study of the phase transformation plasticity of 16MND5 low carbon steel under multiaxial loading, *International Journal of Plasticity*, **18**, 1707-1727
3. DAN W.J., LI S.H., ZHANG W.G., LIN Z.Q., 2008, The effect of strain-induced martensitic transformation on mechanical properties of TRIP steel, *Materials and Design*, **29**, 604-612
4. DENG D., MURAKAWA H., 2013, Influence of transformation induced plasticity on simulated results of welding residual stress in low temperature transformation steel, *Computational Materials Science*, **78**, 55-62
5. DUTTA R.K., AMIRTHALINGAM M., HERMANS M.J.M., RICHARDSON I.M., 2013, Kinetics of bainitic transformation and transformation plasticity in a high strength quenched and tempered structural steel, *Material Science Engineering A*, **559**, 86-95
6. FISCHER F.D., OBERAIGNER E.R., TANAKA K., NISHIMURA F., 1998, Transformation induced plasticity revised an updated formulation, *International Journal of Solids and Structure*, **35**, 2209-2227
7. HOANG H., BARBE F., QUEY R., TALEB L., 2008, FE determination of the plasticity induced during diffusive transformation in the case of nucleation at random locations and instants, *Computational Materials Science*, **43**, 101-107
8. LEBLOND J.B., DEVAUX J., DEVAUX J.C., 1989, Mathematical modelling of transformation plasticity in steels. I: Case of ideal-plastic phases, *International Journal of Plasticity*, **5**, 551-572
9. LEBLOND J.B., MOTTET G., DEVAUX J.C., 1986, A theoretical and numerical approach to the plastic behaviour of steels during phase transformations: I – Derivation of general relations, *Journal of the Mechanics and Physic of Solids*, **34**, 395-409
10. MEFTAH S., BARBE F., TALEB L., SIDOROFF F., 2007, Parametric numerical simulations of TRIP and its interaction with classical plasticity in martensitic transformation, *European Journal of Mechanics A*, **26**, 688-700
11. MOHR D., JACQUEMIN J., 2008, Large deformation of anisotropic austenitic stainless steel sheets at room temperature: multi-axial experiments and phenomenological modeling, *Journal of the Mechanics and Physics of Solids*, **56**, 2935-2956
12. MOUMNI Z., ROGER F., TRINH N., 2011, Theoretical and numerical modeling of the thermomechanical and metallurgical behavior of steel, *International Journal of Plasticity*, **27**, 414-439
13. SHI J., TURTELTAUB S., VAN DER GIESSEN E., 2010, Analysis of grain size effects on transformation-induced plasticity based on a discrete dislocation transformation model, *Journal of the Mechanics and Physics of Solids*, **58**, 1863-1878
14. SONG K.J., WEI Y.H., DONG Z.B., MA R., ZHAN X.H., ZHENG W.J., FANG K., 2014, Constitutive model coupled with mechanical effect of volume change and transformation induced plasticity during solid phase transformation for TA15 alloy welding, *Applied Mathematical Modeling*, **39**, 2064-2080
15. SUN C., FANG G., LEI L.P., ZENG P., 2009, Micro-thermomechanical constitutive model of transformation induced plasticity and its application on armour steel, *Materials Science and Engineering A*, **449**, 18-22
16. TAHIMI A., BARBE F., TALEB L., QUEY R., GUILLET A., 2012, Evaluation of microstructure-based transformation plasticity models from experiments on 100C6 steel, *Computational Materials Science*, **52**, 55-60
17. TALEB L., CAVALLO N., WAECKEL F., 2001, Experimental analysis of transformation plasticity, *International Journal of Plasticity*, **17**, 1-20
18. TALEB L., PETIT S., JULIEN J.F., 2004, Prediction of residual stresses in the heat affected zone, *Journal de Physique IV*, **120**, 705-712

19. TALEB L., SIDOROFF F., 2003, A micromechanical modeling of the Greenwood-Johnson mechanism in transformation induced plasticity, *International Journal of Plasticity*, **19**, 1821-1842
20. YAAKOUBI M., KCHAOU M., DAMMAK F., 2013a, Simulation of heat treatment and materials with the use of the Abaqus software, *Metal Science and Heat Treatment*, **55**, 7-8
21. YAAKOUBI M., KCHAOU M., DAMMAK F., 2013b, Simulation of the thermomechanical and metallurgical behavior of steels by using ABAQUS software, *Computational Materials Science*, **68**, 297-306

Manuscript received October 9, 2015; accepted for print June 15, 2016

GENERALIZED THERMOELASTIC FUNCTIONALLY GRADED HALF SPACE UNDER SURFACE ABSORPTION OF LASER RADIATION

MOHAMED N.M. ALLAM

*Mansoura University, Faculty of Science, Department of Mathematics, Mansoura, Egypt
e-mail: mallam@mans.edu.eg*

ISMAIL M. TAYEL

*Majmaah University, College of Education, Department of Mathematics, Saudi Arabia
e-mail: i.tayel@mu.edu.sa*

The subject of this paper is to study the thermoelastic behavior of a functionally graded semi-infinite medium heated uniformly by a laser beam having temporally Gaussian distribution. The surface of the medium is taken as traction free. The general solution is obtained in the Laplace transform domain. The inverse of the Laplace transform is computed numerically using the Riemann-sum approximation method. The numerical results for temperature, displacement and stress are obtained and presented graphically for the generalized theory of thermo-elasticity with one relaxation time.

Keywords: laser pulse, generalized thermoelasticity, non-homogeneous medium, numerical inverse of Laplace transform

1. Introduction

The study of the problem of thermoelasticity has been taken up by several authors. Biot (1956) developed the coupled theory of thermoelasticity to eliminate the paradox inherent in the classical uncoupled theory according to which elastic changes have no effect on temperature. The main drawback of Biot's equations was that they were based on Fourier's law, which predicted an infinite speed of propagation of heat.

Lord and Shulman (1967) derived equations of dynamic thermoelasticity based on modified Fourier's law, and these equations are usually regarded as the basis of generalized thermoelasticity and called the generalized theory of thermoelasticity with one relaxation time. Green and Lindsay (1972) developed another generalized theory of thermoelasticity. This theory modifies both the energy equation and the Duhamel-Neumann relation. It admits two relaxation times. The theory of thermoelasticity without energy dissipation is another generalized theory and was formulated by Green and Naghdi (1993). It includes the thermal displacement gradient among its independent constitutive variables, and differs from the previous theories in that it does not accommodate dissipation of thermal energy. Ozisik and Tzou (1994), and Tzou (1995a,b) developed a new model called the dual phase-lag model for the heat transport mechanism in which Fourier's law is replaced by an approximation to the modification of Fourier's law with two different time translations for the heat flux and the temperature gradient.

A large amount of work has been devoted to solving thermoelasticity problems with consideration of the coupling effect between temperature and strain rate. Stress waves in a half-space induced by variations of surface strain, temperature or stress were studied by Boley and Tolins (1962) and Chandrasekhariaiah and Srinath (1998). Mozina and Dovc (1994) attempted to use the Laplace transform to solve the thermoelastic stress wave induced by volumetric heating.

Due to the difficulty in finding analytical Green's functions, only a solution for locations on the surface was obtained.

Researches have also been examining thermoelastic problems with consideration of the non-Fourier effect, but without considering the coupling effect between temperature and strain rate. Kao (1976) was the first to investigate the non-Fourier effect and the thermoelastic wave in a half-space.

When a solid is illuminated with a laser pulse, absorption of the pulse leads to a localized temperature increase which in turn causes thermal expansion and generates a thermoelastic wave in the solid (Wang and Xu, 2001). McDonald (1990) studied the importance of thermal diffusion on the generation of thermoelastic waves in metals induced by surface Gaussian laser beam heating. Engelhard and Bertrand (1977) studied the influence of optical penetration depth and the laser pulse duration on longitudinal acoustic waves induced by volumetric absorption of a laser beam. Henain *et al.* (2014) studied the thermoelastic interaction caused by heating a homogeneous and isotropic thermoelastic semi-infinite body induced by a Gaussian laser pulse. Allam *et al.* (2014) studied thermoelastic waves induced by pulsed laser in a non-homogeneous microscaler beam.

The purpose of the present work is to study the thermoelastic interaction caused by heating a non-homogeneous and isotropic thermoelastic semi-infinite body induced by a laser pulse by employing the generalized theory of thermoelasticity. The problem is solved by using Laplace transform techniques. The inverse Laplace transform is computed numerically using the Riemann-sum approximation method. Numerical solutions for spatial temperature, displacement and stress are obtained using the generalized theory of thermoelasticity with one relaxation time. At the end of this work, we present the computed results obtained from the theoretical relations applied on a (Cu) target.

2. Mathematical modeling and basic equations

Consider a non-homogeneous anisotropic thermally conducting elastic solid at a uniform temperature T_0 . The governing equations for linear generalized thermoelastic media, in the absence of incremental body forces, and heat source are discussed below:

- The general model of heat conduction equation corresponding to five models of thermoelasticity takes the form (Allam *et al.*, 2014)

$$\left(1 + \lambda_{2k} \frac{\partial}{\partial t}\right) (K_{ij} \theta_j)_{,i} = \left(\lambda_{3k} + \lambda_{4k} \frac{\partial}{\partial t} + \lambda_{5k} \frac{\partial^2}{\partial t^2}\right) \left(\rho C_E \frac{\partial \theta}{\partial t} + T_0 \beta_{ij} \frac{\partial u_{m,m}}{\partial t}\right) \quad (2.1)$$

- The constitutive equations for an anisotropic medium are given by

$$\sigma_{ij} = C_{ijmn} \varepsilon_{mn} - \beta_{ij} \delta_{ij} \left(1 + \lambda_{1k} \frac{\partial}{\partial t}\right) \theta \quad \begin{array}{l} i, j = 1, 2, 3 \\ k = 1, 2, \dots, 5 \end{array} \quad (2.2)$$

The parameters λ_{ik} , are given by

$$\lambda_{ik} = \begin{bmatrix} 0 & 0 & \tau_1 & 0 & 0 \\ 0 & 0 & 0 & 0 & \tau_\theta \\ 1 & 1 & 1 & 0 & 1 \\ 0 & \tau_0 & \tau_0 & 1 & \tau_q \\ 0 & 0 & 0 & 0 & \frac{1}{2} \tau_q^2 \end{bmatrix}$$

which may be called the relaxation time matrix, or given by the relations

$$\begin{array}{lll} \lambda_{1k} = \tau_1 \delta_{3k} & \lambda_{2k} = \tau_\theta \delta_{5k} & \lambda_{3k} = 1 - \delta_{4k} \\ \lambda_{4k} = \delta_{4k} + \tau_0 (\delta_{2k} + \delta_{3k}) + \tau_q \delta_{5k} & \lambda_{5k} = \frac{1}{2} \tau_q^2 \delta_{5k} & \end{array}$$

- The strain-displacement relations are given by Cauchy's relations

$$\varepsilon_{ij} = \frac{1}{2}(u_{i,j} + u_{j,i}) \quad (2.3)$$

- The equations of motion are

$$C_{ijmn}u_{m,jn} - \beta_{ij}\left(1 + \lambda_{1k}\frac{\partial}{\partial t}\right)\theta_{,j} = \rho\ddot{u}_i \quad (2.4)$$

where C_{ijmn} are isothermal elastic constants, u_i are the displacement components, $\theta = T - T_0$ is the temperature increment, and T_0 is the environmental temperature assumed to be such that $|\theta/T_0| \ll 1$.

In the above formulas, K_{ij} is the thermal conductivity tensor, C_E – specific heat at a constant strain, τ_0 , τ_1 are the 1st and 2nd relaxation times, τ_q is the phase-lag of the heat flux, τ_θ is the phase-lag of the temperature gradient $0 \leq \tau_\theta < \tau_q$ and ρ is the mass density. The dummy index implies summation. The dot and comma notations denote differentiation with respect to time and space, respectively.

Equations (2.1)-(2.4) describe the coupled dynamical thermoelasticity theory, generalized thermoelasticity theory proposed by Lord and Shulman, generalized thermo-elasticity theory with two relaxation times developed by Green and Lindsay, Green and Naghdi theory without energy dissipation and dual phase-lag model for different sets of values of the parameters λ_{ik} .

In equations (2.1)-(2.4):

- 1) if we put $k = 1$, then they reduce to equations of the classical theory of thermoelasticity (CTE),
- 2) when $k = 2$, then they reduce to equations of the generalized theory with one relaxation time (LS),
- 3) putting $k = 3$, then they reduce to equations of the generalized theory with two relaxation time (GL),
- 4) when $k = 4$ and $K = K^*$ (K^* is a material constant characteristic of the Green and Naghdi theory), then they reduce to equations of the generalized theory without energy dissipation (GN).
- 5) if $k = 5$, then they reduce to equations of the generalized theory with dual-phase-lags (DPL).

Consider a thermoelastic, non-homogeneous isotropic semi-infinite medium occupying the region ($z \geq 0$) and initially at uniform temperature T_0 . The surface of the target ($z = 0$) is uniformly heated by a pulsed laser beam and assumed to be traction free. The Cartesian coordinates (x, y, z) are considered in the solution with z-axis pointing vertically into the medium.

The generalized equation of heat conduction (2.1) takes the form

$$\left(1 + \lambda_{2k}\frac{\partial}{\partial t}\right)(\nabla K \cdot \nabla\theta + K\nabla^2\theta) = \left(\lambda_{3k} + \lambda_{4k}\frac{\partial}{\partial t} + \lambda_{5k}\frac{\partial^2}{\partial t^2}\right)\frac{\partial}{\partial t}(\rho C_E\theta + \gamma T_0 e) \quad (2.5)$$

where $\gamma = E\alpha_t/(1 - 2\nu)$, E is Young's modulus, α_t is the thermal expansion coefficient, ν is Poisson's ratio, e is the relative volume dilatation and ∇^2 is the Laplace operator.

The equations of motion in the case of body free forces (2.4) reduces to

$$\frac{\partial\sigma_{zz}}{\partial z} = \rho\frac{\partial^2 w(z,t)}{\partial t^2} \quad (2.6)$$

$w(z,t)$ is the only component of the displacement vector.

The strain components (2.3) become

$$e_{zz} = \frac{\partial w}{\partial z} \quad e_{xx} = e_{yy} = e_{xy} = e_{xz} = e_{yz} = 0 \quad (2.7)$$

The volume dilatation e and Laplace operator are thus given by

$$e = e_{xx} + e_{yy} + e_{zz} = \frac{\partial w}{\partial z} \quad \nabla^2 = \frac{\partial^2}{\partial z^2} \quad (2.8)$$

Using (2.7) and (2.2), the stress components are

$$\begin{aligned} \sigma_{zz} &= \frac{E}{1-2\nu} \left[\frac{1-\nu}{1+\nu} \frac{\partial w}{\partial z} - \left(1 + \lambda_{1k} \frac{\partial}{\partial t}\right) \alpha_t \theta \right] \\ \sigma_{xx} = \sigma_{yy} &= \frac{E}{1-2\nu} \left[\frac{\nu}{1+\nu} \frac{\partial w}{\partial z} - \left(1 + \lambda_{1k} \frac{\partial}{\partial t}\right) \alpha_t \theta \right] \end{aligned} \quad (2.9)$$

The boundary conditions at $z = 0$

$$\begin{aligned} - \left(1 + \lambda_{2k} \frac{\partial}{\partial t}\right) K \nabla \theta &= \left(\lambda_{3k} + \lambda_{4k} \frac{\partial}{\partial t} + \lambda_{5k} \frac{\partial^2}{\partial t^2}\right) q \\ \sigma_{zz} &= 0 \end{aligned} \quad (2.10)$$

where q is the laser radiation propagating in the z direction, given by $q = A_0 q_0 f(t)$, with A_0 the coefficient of heat absorption, q_0 intensity of the laser beam and $f(t)$ temporal distribution of the laser radiation.

We use, since the material is considered inhomogeneous

$$\{E(z), K(z), \rho(z)\} = \{E_0, K_0, \rho_0\} F(z)$$

where E_0 , K_0 and ρ_0 are assumed to be constants.

Thus, the stress components are in form

$$\begin{aligned} \sigma_{zz} &= \frac{E_0 F(z)}{1-2\nu} \left[\frac{1-\nu}{1+\nu} \frac{\partial w}{\partial z} - \left(1 + \lambda_{1k} \frac{\partial}{\partial t}\right) \alpha_t \theta \right] \\ \sigma_{xx} = \sigma_{yy} &= \frac{E_0 F(z)}{1-2\nu} \left[\frac{\nu}{1+\nu} \frac{\partial w}{\partial z} - \left(1 + \lambda_{1k} \frac{\partial}{\partial t}\right) \alpha_t \theta \right] \end{aligned} \quad (2.11)$$

3. Non-dimensionalization

The governing equations takes a more convenient form by using the following non-dimensional variables (Allam *et al.*, 2014)

$$\begin{aligned} (z', w') &= \frac{(z, w)}{h} & c_0 &= \sqrt{\frac{E_0}{\rho_0}} & \theta' &= \frac{\theta}{T_0} \\ \sigma'_z &= \frac{\sigma_z}{E_0} & t' &= \frac{c_0}{h} t & \tau'_i &= \frac{c_0}{h} \tau_i \quad i = 0, 1, q, \theta, p \end{aligned}$$

For simplicity, we drop the dashes of all variables and parameters.

The equation of heat conduction (2.5) is in the form

$$\left(1 + \lambda_{2k} \frac{\partial}{\partial t}\right) \left(\frac{\partial^2}{\partial z^2} + \Phi(z) \frac{\partial}{\partial z}\right) \theta = \left(\lambda_{3k} + \lambda_{4k} \frac{\partial}{\partial t} + \lambda_{5k} \frac{\partial^2}{\partial t^2}\right) \frac{\partial}{\partial t} \left(c_1 \theta + c_2 \frac{\partial w}{\partial z}\right) \quad (3.1)$$

Equation of motion (2.6) reduces to

$$c_3 \left(\frac{\partial^2}{\partial z^2} + \Phi(z) \frac{\partial}{\partial z} - \frac{1}{c_3} \frac{\partial^2}{\partial t^2} \right) w - c_4 \left(1 + \lambda_{1k} \frac{\partial}{\partial t} \right) \left(\frac{\partial}{\partial z} + \Phi(z) \right) \theta = 0 \quad (3.2)$$

where

$$\begin{aligned} c_1 &= \frac{h\rho_0 C_E c_0}{K_0} & c_2 &= \frac{\alpha_t h C_E c_0}{K_0(1-2\nu)} & c_3 &= \frac{1-\nu}{(1-2\nu)(1+\nu)} \\ c_4 &= \frac{\alpha_t T_0}{1-2\nu} & \Phi(z) &= \frac{1}{F(z)} \frac{dF(z)}{dz} \end{aligned}$$

z is the dimensionless coordinate.

The structure of the governing equations and the boundary conditions suggests the idea of looking for the solution to the problem in a Laplace transform integral, which was given by (Roberts and Kaufman, 1966)

$$\bar{f}(z, s) = \int_0^\infty f(z, t) e^{-st} dt \quad (3.3)$$

Thus, equations (3.1) and (3.2) assume the form

$$\begin{aligned} \left(\frac{d^2}{dz^2} + \Phi(z) \frac{d}{dz} - \Lambda c_1 \right) \bar{\theta} - \Lambda c_2 \frac{d\bar{w}}{dz} &= 0 \\ c_3 \left(\frac{d^2}{dz^2} + \Phi(z) \frac{d}{dz} - \frac{s^2}{c_3} \right) \bar{w} - c_4 (1 + \lambda_{1k} s) \left(\frac{d}{dz} + \Phi(z) \right) \bar{\theta} &= 0 \end{aligned} \quad (3.4)$$

Eliminating \bar{w} or $\bar{\theta}$ from Eqs. (3.4), we arrive at two differential equations for $\bar{\theta}$ and \bar{w}

$$(D^4 + b_3 D^3 + b_2 D^2 + b_1 D + b_0) \{ \bar{\theta}, \bar{w} \} = 0 \quad (3.5)$$

which may be written in form

$$\left[(D^2 + \Phi(z)D)^2 - a(D^2 + \Phi(z)D) + \frac{s^2 \Lambda c_1}{c_3} - c_5 \frac{d\Phi(z)}{dz} \right] \{ \bar{\theta}, \bar{w} \} = 0 \quad (3.6)$$

where

$$\begin{aligned} c_5 &= \frac{\Lambda c_2 c_4 (1 + \lambda_{1k} s)}{c_3} & D &= \frac{d}{dz} \\ b_0 &= \frac{\Lambda c_1 s^2}{c_3} - c_5 \frac{d\Phi(z)}{dz} & b_1 &= \left(\frac{d^2}{dz^2} + \Phi(z) \frac{d}{dz} - a \right) \Phi(z) \\ b_2 &= \Phi(z)^2 + 2 \frac{d\Phi(z)}{dz} - a & b_3 &= 2\Phi(z) \\ \Lambda &= \frac{s(\lambda_{3k} + \lambda_{4k} s + \lambda_{5k} s^2)}{1 + \lambda_{2k} s} & a &= \Lambda c_1 + c_5 + \frac{s^2}{c_3} \end{aligned}$$

Dimensionless boundary conditions (2.10) after using the Laplace transform are

$$\left. \frac{d\bar{\theta}}{dz} \right|_{z=0} = -\frac{c_1 A_0 q_0 \Lambda}{s} f(s) \quad \left. \bar{\sigma}_{zz} \right|_{z=0} = 0 \quad (3.7)$$

Equations (3.6) and (3.7) are a complete system of ordinary differential equations in \bar{w} and $\bar{\theta}$.

4. Special case

We take $F(z)$ in the form $F(z) = e^{-z}$, then $\Phi(z) = (1/F(z))(dF(z)/dz) = -1$ and then

$$b_0 = \frac{\Lambda c_1 s^2}{c_3} \quad b_1 = a \quad b_2 = 1 - a \quad b_3 = -2 \quad (4.1)$$

In this case, equations (3.6) may be rewritten in form

$$\left[(D^2 - D)^2 - a(D^2 - D) + \frac{s^2 \Lambda c_1}{c_3} \right] \{\bar{\theta}, \bar{w}\} = 0 \quad (4.2)$$

Consider the solution to equations (4.2) in form

$$\bar{\theta} = \sum_{j=1}^2 A_j e^{-m_j z} \quad \bar{w} = \sum_{j=1}^2 B_j e^{-m_j z} \quad (4.3)$$

where m_j ($i = 1, 2$) are the roots of equation

$$(m^2 - m)^2 - a(m^2 - m) + \frac{s^2 \Lambda c_1}{c_3} = 0 \quad (4.4)$$

Substitution of (4.3) into (3.4)₁, yields

$$B_j = -\frac{m_j^2 + m_j - \Lambda c_1}{\Lambda c_2 m_j} A_j \quad j = 1, 2 \quad (4.5)$$

Then, Eqs. (4.3) take the form

$$\bar{\theta} = \sum_{j=1}^2 A_j e^{-m_j z} \quad \bar{w} = \sum_{j=1}^2 -\frac{m_j^2 + m_j - \Lambda c_1}{\Lambda c_2 m_j} A_j e^{-m_j z} \quad (4.6)$$

To evaluate the unknown parameters A_j , we shall use boundary conditions (3.7).

Taking Laplace's transformation of the component of stress σ_{zz} in non-dimensional form, yields

$$\sigma_{zz} = \frac{F(z)}{1 - 2\nu} \left[\frac{1 - \nu}{1 + \nu} \frac{\partial \bar{w}}{\partial z} - (1 + \lambda_{1k} s) \alpha_t T_0 \bar{\theta} \right] \quad (4.7)$$

After applying the boundary conditions, we arrive at the following two equations

$$\sum_{j=1}^2 m_j A_j = -\frac{c_1 A_0 q_0 \Lambda}{s} f(s) \quad \sum_{j=1}^2 f_j(s) A_j = 0 \quad (4.8)$$

where

$$f_i(s) = \frac{1 - \nu}{1 + \nu} \left(\frac{m_j^2 + m_j - \Lambda c_1}{\Lambda c_2} \right) - (1 + \lambda_{1k} s) \alpha_t T_0 \quad i = 1, 2$$

Thus, the solution to system of equations (4.8) is

$$A_1 = \frac{\Lambda A_0 c_1 q_0 f(s) f_2}{s(m_1 f_2 + m_2 f_1)} \quad A_2 = -\frac{\Lambda A_0 c_1 q_0 f(s) f_1}{s(m_1 f_2 + m_2 f_1)} \quad (4.9)$$

5. Inverse Laplace transform

Since the formulas of temperature, displacement and stresses are difficult to invert to the time domain, therefore a numerical inverse will be used. In order to invert the Laplace transform of temperature, displacement and stresses, we apply the Riemann-sum approximation method by using the relation

$$f(t) = \frac{e^{kt}}{t} \left[\frac{1}{2} \bar{f}(k) + \operatorname{Re} \sum_{n=1}^N (-1)^n \bar{f} \left(k + \frac{in\pi}{t} \right) \right]$$

where Re is the real part, $i = \sqrt{-1}$ is the imaginary unit number and N is a sufficiently large integer representing the number of terms. For faster convergence, numerous numerical experiments have shown that the value of k should satisfy the relation $kt = 4.7$, see (Tzou, 1995a,b).

6. Application and computation

Now the generalized theory of thermoelasticity with one relaxation time (LS), where $k = 2$ will be considered in the calculation. Consider the intensity of the laser pulse to be given by a Gaussian distribution $G(t) = \exp[-(t - t_0)^2/(\Delta t)^2]$ that the laser beam incidents uniformly on a (Copper) target. Temperature, displacement and stresses are to be calculated taking the following constants (Henain *et al.*, 2014)

$T_0 = 293 \text{ K}$	$\rho_0 = 8954 \text{ kg/m}^3$	$\tau_0 = 35 \cdot 10^{-15} \text{ s}$
$c_E = 383.1 \text{ J/(kg} \cdot \text{K)}$	$\alpha_t = 1.78 \cdot 10^{-5} \text{ K}^{-1}$	$k_0 = 386 \text{ W/(m} \cdot \text{K)}$
$t_0 = 3 \cdot 10^{-3} \text{ s}$	$\Delta t = 10^{-3} \text{ s}$	$E_0 = 89.6 \text{ GPa}$
$\nu = 0.44$	$h = 1 \text{ m}$	$A_0 = 0.01$

where t_0 is the time at which $G(t)$ is maximum, Δt is the time at which the intensity of the laser beam reduces to $1/e$.

7. Results and discussion

Figure 1 represents in curve (a) the laser pulse with the maximum value at $t = 0.003$. The surface temperature distribution calculated per unit intensity is represented in curve (b). From the figure, it is evident that the maximum of the temperature distribution occurs at a time greater than the maximum of the laser pulse. This behavior can be attributed to the fact that at the beginning of the laser pulse the absorbed power compensates the heat losses due to conductivity. This fact leads to an increase in temperature. This increase lasts up until the absorbed laser power is equal to the heat losses, when the maximum of the temperature occurs. After this point, the absorbed laser radiation can not compensate the losses, and the temperature begins to decrease.

Figure 2 represents the temperature distribution per unit intensity calculated at different times as a function of z . In Fig. 2, it is shown that the temperature decreases as z increases, and that for ($t = 0.002$, $t = 0.004$ and $t = 0.005$) it is smaller than for ($t = 0.0035$). This can be attributed to the temporal profile of the laser radiation which is chosen to be Gaussian having its peak value at (0.003) and a half width (0.003). It is noted that the temperature moves deeper in the target as the time increases and vanishes at large values of z .

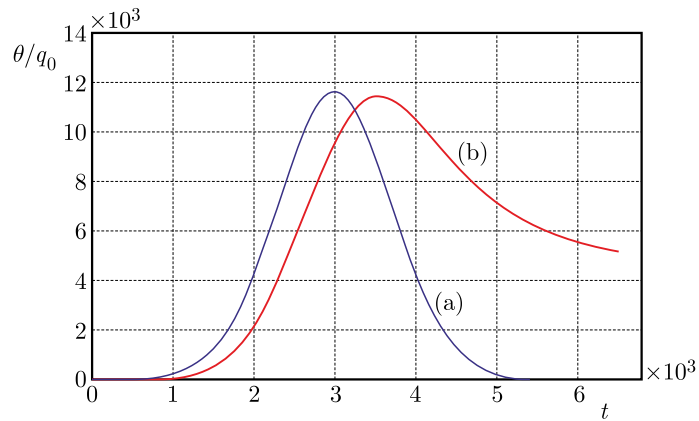


Fig. 1. (a) Temporal behavior of the laser radiation, (b) surface temporal temperature distribution per unit intensity

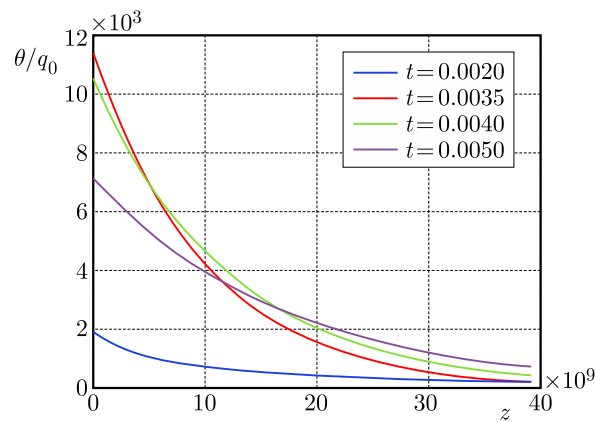


Fig. 2. Temperature distribution per unit intensity as a function of z for different time parameters

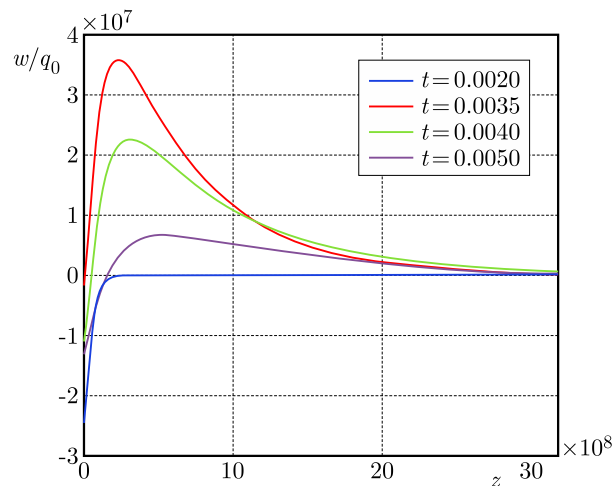


Fig. 3. Displacement distribution per unit intensity as a function of z for different time parameters

Figure 3 represents the displacement w calculated for different z values with time as the parameter. It is found that it is a negative displacement at $z = 0$ and its vicinity, which is due to the heating effect of laser radiation that allowed the particles to move in the upward direction in the free half space corresponding to negative values of z . By increasing z values, Fig. 3 shows a positive displacement representing also movement of the particles downward.

Figure 4 represents the calculated spatial stress σ_{zz} per unit intensity calculated at different z values with time as the parameter. Figure 4 shows a strong negative gradient decrease with an increase in the z values. It takes place after reaching their maximum magnitude when the positive gradient decreases with increasing z values. It is also seen that the behavior of the curve with time is followed by the chosen temporal behavior of the laser radiation.

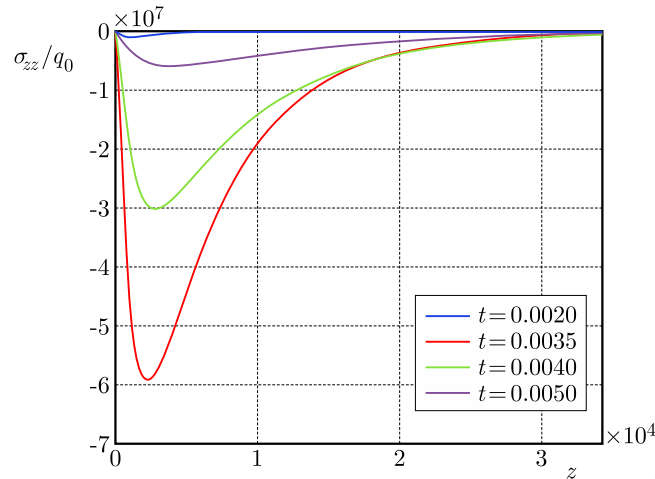


Fig. 4. Stress distribution σ_{zz} per unit intensity as a function of z for different time parameters

Figures 5 represents σ_{xx} per unit intensity as a function of z with time as the parameter. The curves show the same behavior as σ_{zz} .

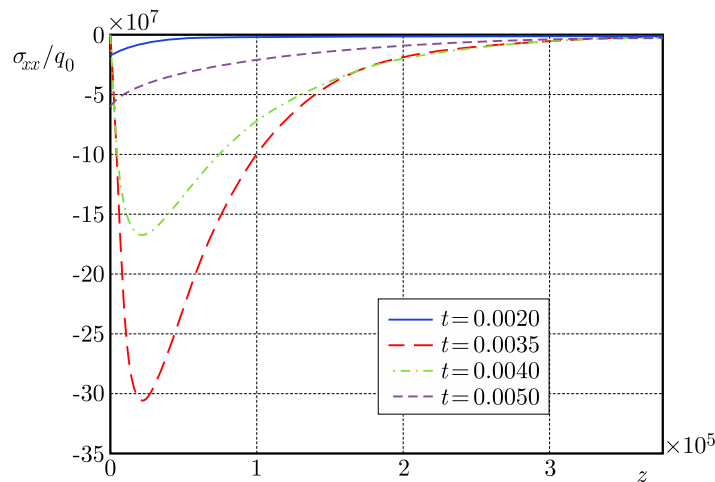


Fig. 5. Stress distribution σ_{xx} per unit intensity as a function of z for different time parameters

Figure 6 represents the temperature distribution θ per unit intensity as a function of z at the time ($t = 0.0035$) with h as the parameter. It is seen that for a fixed time and different values of h , the temperature decreases and enlarges z values as h increases.

Figure 7 represents the displacement distribution w per unit intensity as a function of z at the time ($t = 0.0035$) with h as the parameter. One can observe that for a fixed time and different values of h , the displacement decreases and goes down to small z value as h increases.

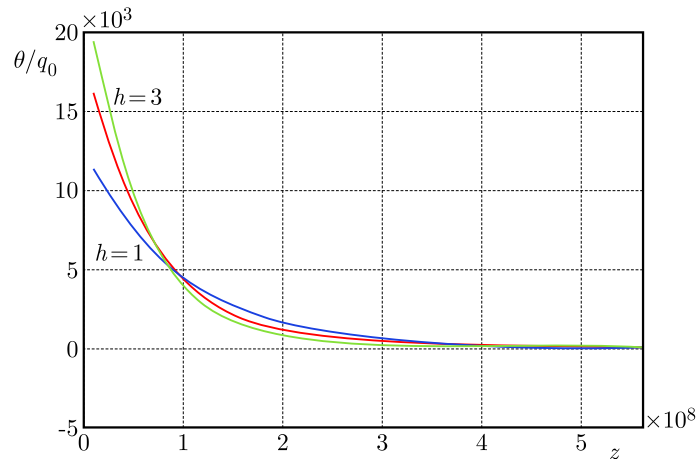


Fig. 6. Temperature distribution θ per unit intensity as a function of z at $t = 0.0035$ with h as the parameter

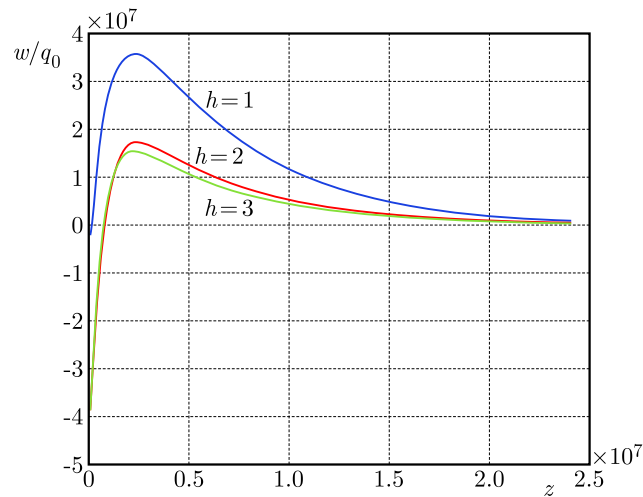


Fig. 7. Displacement distribution w per unit intensity as a function of z at $t = 0.0035$ with h as the parameter

References

1. ALLAM M.N.M., ABOUELREGAL A.E., 2014, The thermoelastic waves induced by pulsed laser and varying heat of inhomogeneous microscale beam resonators, *Journal of Thermal Stresses*, **37**, 4, 455-470
2. BIOT M.A., 1956, Thermoelasticity and irreversible thermodynamics, *Journal of Applied Physics*, **27**, 3, 240-253
3. BOLEY B.A., TOLINS I.S., 1962, Transient coupled thermoelastic boundary value problems in the half-space, *Journal of Applied Mechanics*, **29**, 637-646
4. CHANDRASEKHARAIAH D.S., SRINATH K.S., 1998, Thermoelastic interactions without energy dissipation due to a point heat source, *Journal of Elasticity*, **5**, 97-108
5. ENGUEHARD F., BERTRAND L., 1977, Effects of optical penetration and laser pulse duration on laser generated longitudinal acoustic waves, *Journal of Applied Physics*, **82**, 1532-1538
6. GREEN A.E., LINDSAY K.A., 1972, Thermoelasticity, *Journal of Elasticity*, **2**, 1-7
7. GREEN A.E., NAGHDI P.M., 1993, Thermoelasticity without energy dissipation, *Journal of Elasticity*, **31**, 189-208

8. HENAIN E.F., HASSAN A.F., MEGAHEH F., TAYEL I.M., 2014, Thermoelastic half space under illumination of a laser beam using lord and shulman theory, *Journal of Thermal Stresses*, **37**, 51-72
9. KAO T.T., 1976, On thermally induced non-fourier stress waves in a semi-infinite medium, *AIAA Journal*, **14**, 818-820
10. LORD, H.W. AND SHULMAN, Y., 1967, A Generalized dynamical theory of thermoelasticity, *Journal of the Mechanics and Physics of Solids*, **15**, 299-309
11. McDONALD F.A., 1990, On the precursor in laser-generated ultrasound wave forms in metals, *Journal of Applied Physics Letters*, **56**, 230-232
12. MOZINA J., DOVC M., 1994, One-dimensional model of optically induced thermoelastic waves, *Modern Physics Letters*, **8**, 1791-1801
13. OZISIK M.N., TZOU D.Y., 1994, On the wave theory of heat conduction, *Journal of Heat Transfer (ASME)*, **116**, 526-535
14. ROBERTS G.E., KAUFMAN H., 1966, *Table of Laplace Transform*, W.B. Saunders, Philadelphia
15. TZOU D.Y., 1995a, Experimental support for the lagging behavior in heat propagation, *Journal of Thermophysics and Heat Transfer*, **9**, 686-693
16. TZOU D.Y., 1995b, A unified approach for heat conduction from macro to micro scales, *Journal of Heat Transfer (ASME)*, **117**, 8-16
17. WANG X., XU X., 2001, Thermoelastic wave induced by pulsed laser heating, *Journal of Applied Physics*, **73**, 107-114

Manuscript received February 7, 2016; accepted for print June 18, 2016

MODELING OF THERMAL PROCESSES PROCEEDING IN A 1D DOMAIN OF CRYSTALLINE SOLIDS USING THE LATTICE BOLTZMANN METHOD WITH AN INTERVAL SOURCE FUNCTION

ALICJA PIASECKA-BELKHAYAT, ANNA KORCZAK

Silesian University of Technology, Institute of Computational Mechanics and Engineering, Gliwice, Poland
e-mail: alicja.piasecka@polsl.pl; anna.korczak@polsl.pl

The interval lattice Boltzmann method (ILBM) with an uncertainly defined internal heat source function is used to simulate heat transfer in a thin silicone film. The solution to the interval Boltzmann transport equations has been obtained taking into account the rules of directed interval arithmetics. A similar analysis has been done using the sensitivity model where the Boltzmann transport equations and boundary-initial conditions have been differentiated with respect to the no-interval heat source value. The knowledge of the sensitivity function distribution and the application of the Taylor formula allow one to find the border solutions of the problem analyzed, which (to some extent) correspond to the solution obtained under the assumption of the uncertainly defined source function. In the final part of the paper, numerical computations obtained for both methods are presented.

Keywords: lattice Boltzmann method, directed interval arithmetics, sensitivity analysis

1. Introduction

The problem of heat transfer in nano-layers is frequently encountered in many fields of science and engineering such as mechanical engineering, thermal management of electronic cooling and improvement of performance of heat transfer systems (Escobar *et al.*, 2006; Huang *et al.*, 2005; Joshi and Majumdar, 1993; Mansoor and Yilbas, 2011, 2014). Heat transfer problems are usually solved using equations with deterministic thermophysical parameters (Eshraghi and Felicelli, 2012; Narumanchi *et al.*, 2003). However, in most cases of the engineering practice, values of these parameters cannot be defined with a high precision and, in such cases, it is much more convenient to define these parameters as interval numbers (Piasecka-Belkhat and Korczak, 2014, 2016).

In this paper, an interval version of the lattice Boltzmann method with the uncertainly defined heat source function has been presented with the application of the directed interval arithmetics. The solution obtained corresponds to $\pm 5\%$ perturbations of the heat source function. The results of numerical computations (energy and temperature heating curves at the selected points) have an interval form, of course. Additionally, the sensitivity analysis with respect to the constant heat source function has been done (Chonga *et al.*, 2016; Dems and Rousselet, 1999; Goethals *et al.*, 2011; Hwang *et al.*, 2016). The heat source value has been assumed as the middle value of the heat source interval. The application of the sensitivity function distribution and the Taylor formula with an increment of the source function equal to the half of the width of the heat source interval allows one to find the solution to the boundary-initial problem similar to the solution with some “uncertainties” appearing in the mathematical model. The aim of the paper is comparison of the results obtained using both methods.

2. Directed interval arithmetics

Let us consider a directed interval \bar{a} which can be defined as a set \mathbb{D} of all directed pairs of real numbers defined as follows (Neumaier, 1990; Piasecka-Belkhat, 2011a,b)

$$\bar{a} = [a^-, a^+] \quad \text{for } a^-, a^+ \in \mathbb{R} \quad (2.1)$$

where a^- and a^+ denote the beginning and the end of the interval, respectively.

The left or the right endpoint of the interval \bar{a} can be denoted as a^s , $s \in \{+, -\}$, where s is a binary variable. This variable can be expressed as a product of two binary variables and is defined as

$$\begin{aligned} ++ &= -- = + \\ +- &= -+ = - \end{aligned} \quad (2.2)$$

An interval is called proper if $a^- < a^+$, improper if $a^- > a^+$ and degenerate if $a^- = a^+$. The set of all directed interval numbers can be written as $\mathbb{D} = \mathbb{P} \cup \mathbb{I}$, where \mathbb{P} denotes a set of all directed proper intervals and \mathbb{I} denotes a set of all improper intervals.

Additionally, a subset $\mathbb{Z} = \mathbb{Z}_{\mathbb{P}} \cup \mathbb{Z}_{\mathbb{I}} \subset \mathbb{D}$ should be defined, where

$$\begin{aligned} \mathbb{Z}_{\mathbb{P}} &= \{\bar{a} \in \mathbb{P} \mid a^- \leq 0 \leq a^+\} \\ \mathbb{Z}_{\mathbb{I}} &= \{\bar{a} \in \mathbb{I} \mid a^+ \leq 0 \leq a^-\} \end{aligned} \quad (2.3)$$

For directed interval numbers, two binary variables are defined. The first of them is the direction variable

$$\tau(\bar{a}) = \begin{cases} + & \text{if } a^- \leq a^+ \\ - & \text{if } a^- > a^+ \end{cases} \quad (2.4)$$

and the other is the sign variable

$$\sigma(\bar{a}) = \begin{cases} + & \text{if } a^- > 0, a^+ > 0 \\ - & \text{if } a^- < 0, a^+ < 0 \end{cases} \quad \bar{a} \in \mathbb{D} \setminus \mathbb{Z} \quad (2.5)$$

For the zero argument $\sigma([0, 0]) = \sigma(0) = +$, for all intervals including the zero element $\bar{a} \in \mathbb{Z}$, $\sigma(\bar{a})$ is not defined.

The sum of two directed intervals $\bar{a} = [a^-, a^+]$ and $\bar{b} = [b^-, b^+]$ can be written as

$$\bar{a} + \bar{b} = [a^- + b^-, a^+ + b^+] \quad \bar{a}, \bar{b} \in \mathbb{D} \quad (2.6)$$

The difference is of the form

$$\bar{a} - \bar{b} = [a^- - b^+, a^+ - b^-] \quad \bar{a}, \bar{b} \in \mathbb{D} \quad (2.7)$$

The product of the directed intervals is described by the formula

$$\bar{a}\bar{b} = \begin{cases} [a^{-\sigma(\bar{b})}b^{-\sigma(\bar{a})}, a^{\sigma(\bar{b})}b^{\sigma(\bar{a})}] & \bar{a}, \bar{b} \in \mathbb{D} \setminus \mathbb{Z} \\ [a^{\sigma(\bar{a})\tau(\bar{b})}b^{-\sigma(\bar{a})}, a^{\sigma(\bar{a})\tau(\bar{b})}b^{\sigma(\bar{a})}] & \bar{a} \in \mathbb{D} \setminus \mathbb{Z}, \bar{b} \in \mathbb{Z} \\ [a^{-\sigma(\bar{b})}b^{\sigma(\bar{b})\tau(\bar{a})}, a^{\sigma(\bar{b})}b^{\sigma(\bar{b})\tau(\bar{a})}] & \bar{a} \in \mathbb{Z}, \bar{b} \in \mathbb{D} \setminus \mathbb{Z} \\ [\min(a^-b^+, a^+b^-), \max(a^-b^-, a^+b^+)] & \bar{a}, \bar{b} \in \mathbb{Z}_{\mathbb{P}} \\ [\max(a^-b^-, a^+b^+), \min(a^-b^+, a^+b^-)] & \bar{a}, \bar{b} \in \mathbb{Z}_{\mathbb{I}} \\ 0 & (\bar{a} \in \mathbb{Z}_{\mathbb{P}}, \bar{b} \in \mathbb{Z}_{\mathbb{I}}) \vee (\bar{a} \in \mathbb{Z}_{\mathbb{I}}, \bar{b} \in \mathbb{Z}_{\mathbb{P}}) \end{cases} \quad (2.8)$$

The quotient of two directed intervals can be written as

$$\bar{a}/\bar{b} = \begin{cases} [a^{-\sigma(\bar{b})}/b^{\sigma(\bar{a})}, a^{\sigma(\bar{b})}/b^{-\sigma(\bar{a})}] & \bar{a}, \bar{b} \in \mathbb{D} \setminus \mathbb{Z} \\ [a^{-\sigma(\bar{b})}/b^{-\sigma(\bar{b})\tau(\bar{a})}, a^{\sigma(\bar{b})}/b^{-\sigma(\bar{b})\tau(\bar{a})}] & \bar{a} \in \mathbb{Z}, \bar{b} \in \mathbb{D} \setminus \mathbb{Z} \end{cases} \quad (2.9)$$

In the directed interval arithmetics, two extra operators are defined, the inversion of summation

$$-_{\mathbb{D}}\bar{a} = [-a^-, -a^+] \quad \bar{a} \in \mathbb{D} \quad (2.10)$$

and the inversion of multiplication

$$1/_{\mathbb{D}}\bar{a} = [1/a^-, 1/a^+] \quad \bar{a} \in \mathbb{D} \setminus \mathbb{Z} \quad (2.11)$$

So, two additional mathematical operations can be defined as follows

$$\bar{a} -_{\mathbb{D}} \bar{b} = [a^- - b^-, a^+ - b^+] \quad \bar{a}, \bar{b} \in \mathbb{D} \quad (2.12)$$

and

$$\bar{a}/_{\mathbb{D}}\bar{b} = \begin{cases} [a^{-\sigma(\bar{b})}/b^{-\sigma(\bar{a})}, a^{\sigma(\bar{b})}/b^{\sigma(\bar{a})}] & \bar{a}, \bar{b} \in \mathbb{D} \setminus \mathbb{Z} \\ [a^{-\sigma(\bar{b})}/b^{\sigma(\bar{b})}, a^{\sigma(\bar{b})}/b^{\sigma(\bar{b})}] & \bar{a} \in \mathbb{Z}, \bar{b} \in \mathbb{D} \setminus \mathbb{Z} \end{cases} \quad (2.13)$$

Now, it is possible to obtain the number zero by subtraction of two identical intervals $\bar{a} -_{\mathbb{D}} \bar{a} = \bar{0}$ and the number one as the result of division $\bar{a}/_{\mathbb{D}}\bar{a} = \bar{1}$, which is impossible when applying classical interval arithmetics (Markov, 1995).

3. Boltzmann transport equation

The Boltzmann transport equation (BTE) is one of the fundamental equations of solid state physics and takes the following form (Escobar *et al.*, 2006)

$$\frac{\partial f}{\partial t} + v \nabla f = \frac{f^0 - f}{\tau_r} + g_{ef} \quad (3.1)$$

where f is the phonon distribution function, f^0 is the equilibrium distribution function given by the Bose-Einstein statistics, v is the phonon group velocity, τ_r is the relaxation time and g_{ef} is the phonon generation rate due to electron-phonon scattering.

In order to take advantage of the simplifying assumption of the Debye model, the BTE can be transformed into an equation of the carrier energy density, and for a one-dimensional problem has the following form (Escobar *et al.*, 2006)

$$\frac{\partial e}{\partial t} + v \nabla e = -\frac{e - e^0}{\tau_r} + q_v \quad (3.2)$$

where e is the phonon energy density, e^0 is the equilibrium phonon energy density and q_v is the internal heat source related to a unit of volume. Equation (3.2) must be supplemented by the adequate boundary-initial conditions.

Using the Debye model, the relation between the phonon energy density and lattice temperature is given by the following formula (Escobar *et al.*, 2006)

$$e(T) = \left(\frac{9\eta k_b}{\Theta_{\mathbb{D}}^3} \int_0^{\Theta_{\mathbb{D}}/T} \frac{z^3}{\exp(z) - 1} dz \right) T^4 \quad (3.3)$$

where $\Theta_{\mathbb{D}}$ is the Debye temperature of the solid, k_b is the Boltzmann constant, T is the lattice temperature while η is the number density of phonons, and can be calculated using the formula (Escobar *et al.*, 2006)

$$\eta = \frac{1}{6\pi^2} \left(\frac{k_b \Theta_{\mathbb{D}}}{\hbar \omega} \right)^3 \quad (3.4)$$

where \hbar is the Planck constant divided by 2π and ω is the speed of sound in the analysed material.

4. Interval lattice Boltzmann method

The lattice Boltzmann method (LBM) is a numerical technique for simulation of fluid flows and heat transfer. Here LBM has been successfully applied to simulate heat transfer in nano layers. Unlike the conventional numerical methods based on discretizations of macroscopic continuum equations, the LBM is based on nanoscale models and heat transfer equations.

In this paper, it is shown how the LBM solves a discretized set of the Boltzmann transport equation (BTE) in the case of interval values appearing in the mathematical model. Then the interval Boltzmann transport equation for a one-dimensional problem has the following form (Piasecka-Belkhayat and Korczak, 2014)

$$\frac{\partial \bar{\epsilon}(x, t)}{\partial t} + v \frac{\partial \bar{\epsilon}(x, t)}{\partial x} = -\frac{\bar{\epsilon}(x, t) - \bar{\epsilon}^0(x, t)}{\tau_r} + \bar{q}_v(x, t) \quad (4.1)$$

where $\bar{\epsilon}(x, t)$ is the interval phonon energy density, $\bar{\epsilon}^0(x, t)$ is the interval equilibrium phonon energy density, τ_r is the relaxation time, $v_1 = v$ and $v_2 = -v$ (see Fig. 1) and $\bar{q}_v(x, t)$ is the interval heat source, x is the spatial coordinate and t is the time.

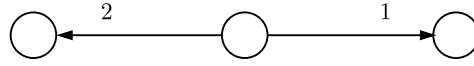


Fig. 1. Directions of the lattice vibrations

The interval total phonon energy density is defined as the sum of phonon energy densities in all directions. In the paper, a one-dimensional model with two directions of the phonon velocities is assumed (Piasecka-Belkhayat and Korczak, 2014, 2016)

$$\bar{\epsilon}(x, t) = \bar{\epsilon}_1(x, t) + \bar{\epsilon}_2(x, t) = \sum_{d=1}^2 \bar{\epsilon}_d(x, t) \quad (4.2)$$

where $\bar{\epsilon}_1(x, t)$ is the phonon energy density in the positive x direction while $\bar{\epsilon}_2(x, t)$ is the phonon energy density in the negative x direction, d means the lattice direction (see Fig. 1).

In the interval lattice Boltzmann method it is needed to solve system of two partial differential equations allowing one to compute phonon energy in different lattice nodes according to the following equations (Piasecka-Belkhayat and Korczak, 2014)

$$\frac{\partial \bar{\epsilon}_d(x, t)}{\partial t} + (-1)^{d-1} v \frac{\partial \bar{\epsilon}_d(x, t)}{\partial x} = -\frac{\bar{\epsilon}_d(x, t) - \bar{\epsilon}_d^0(x, t)}{\tau_r} + \bar{q}_v(x, t) \quad d = 1, 2 \quad (4.3)$$

where $v = \Delta x / \Delta t$ is the component of velocity along the x -axis, Δx is the lattice distance from site to site, $\Delta t = t^{f+1} - t^f$ is the time step needed for a phonon to travel from one lattice site to the neighboring lattice site and

$$\bar{\epsilon}_d^0(x, t) = \bar{\epsilon}(x, t) / d \quad (4.4)$$

The set of equations (4.3) must be supplemented by the boundary-initial conditions (Goethals *et al.*, 2011)

$$\begin{aligned} x = 0 : \quad & e_1(0, t) = e(T_{b1}) \\ x = L : \quad & e_2(L, t) = e(T_{b2}) \\ t = 0 : \quad & e(x, 0) = e(T_0) \end{aligned} \quad (4.5)$$

where T_{b1} and T_{b2} are the boundary temperatures, T_0 is the initial temperature.

The approximate form of equations (4.3) is of the following form

$$\begin{aligned} (\bar{e}_1)_{i+1}^{f+1} &= \left(1 - \frac{\Delta t}{\tau_r}\right) (\bar{e}_1)_i^f + \frac{\Delta t}{\tau_r} (\bar{e}_1^0)_i^f + \Delta t \bar{q}_v \\ (\bar{e}_2)_{i-1}^{f+1} &= \left(1 - \frac{\Delta t}{\tau_r}\right) (\bar{e}_2)_i^f + \frac{\Delta t}{\tau_r} (\bar{e}_2^0)_i^f + \Delta t \bar{q}_v \end{aligned} \quad (4.6)$$

After subsequent computations, the interval lattice temperature is determined according to the rules of directed interval arithmetics using the formula (see Eq. (3.3))

$$\bar{T}^f = \sqrt[4]{\bar{e}^f \Theta_{\mathbb{D}}^3 \left(9\eta k_b \int_0^{\Theta_{\mathbb{D}}/\bar{T}^{f-1}} \frac{z^3}{\exp(z) - 1} dz \right)^{-1}} \quad (4.7)$$

5. Sensitivity analysis

In order to analyze the sensitivity of the phonon energy density field, the governing equations should be differentiated with respect to the chosen parameter (Kleiber, 1997). In the paper, the sensitivity analysis is presented with respect to the value of the internal heat source.

The Boltzmann transport equation for the one-dimensional problem and the constant value of the heat source q_v has the following form (Kałuza *et al.*, 2016; Majchrzak and Mochnicki, 2014; Mochnicki and Majchrzak, 2007; Mohebbi and Sellier, 2016)

$$\frac{\partial e_d(x, t)}{\partial t} + (-1)^{d-1} v \frac{\partial e_d(x, t)}{\partial x} = -\frac{e_d(x, t) - e_d^0(x, t)}{\tau_r} + q_v \quad d = 1, 2 \quad (5.1)$$

with the boundary-initial conditions

$$\begin{aligned} x = 0 : \quad & e_1(0, t) = e(T_{b1}) \\ x = L : \quad & e_2(L, t) = e(T_{b2}) \\ t = 0 : \quad & e(x, 0) = e(T_0) \end{aligned} \quad (5.2)$$

Using the direct approach of sensitivity analysis, equation (5.1) is differentiated with respect to q_v (Jasiński, 2014; Mochnicki and Majchrzak, 2007; Mohebbi and Sellier, 2016)

$$\frac{\partial}{\partial q_v} \left(\frac{\partial e_d(x, t)}{\partial t} \right) + (-1)^{d-1} v \frac{\partial}{\partial q_v} \left(\frac{\partial e_d(x, t)}{\partial x} \right) = -\frac{1}{2\tau_r} \frac{\partial e_d(x, t)}{\partial q_v} + \frac{\partial q_v}{\partial q_v} \quad d = 1, 2 \quad (5.3)$$

Next, differentiation of boundary-initial conditions (5.2) leads to the following formulas

$$\begin{aligned} x = 0 : \quad & \frac{\partial e_1(0, t)}{\partial q_v} = \frac{\partial e(T_{b1})}{\partial q_v} = 0 \\ x = L : \quad & \frac{\partial e_2(L, t)}{\partial q_v} = \frac{\partial e(T_{b2})}{\partial q_v} = 0 \\ t = 0 : \quad & \frac{\partial e(x, 0)}{\partial q_v} = \frac{\partial e(T_0)}{\partial q_v} = 0 \end{aligned} \quad (5.4)$$

To equation (5.3) and boundary-initial conditions (5.4), the sensitivity functions $U_d(x, t, q_v) = \partial e_d(x, t) / \partial q_v$ are introduced

$$\begin{aligned} \frac{\partial U_d(x, t, q_v)}{\partial t} + (-1)^{d-1} v \frac{\partial U_d(x, t, q_v)}{\partial x} &= -\frac{1}{2\tau_r} U_d(x, t, q_v) + 1 & d = 1, 2 \\ x = 0 : \quad U_1(0, t, q_v) &= 0 \\ x = L : \quad U_2(L, t, q_v) &= 0 \\ t = 0 : \quad U(x, 0, q_v) &= 0 \end{aligned} \quad (5.5)$$

Then equations (5.3) are the following

$$\frac{\partial U_d(x, t, q_v)}{\partial t} + (-1)^{d-1} v \frac{\partial U_d(x, t, q_v)}{\partial x} = -\frac{U_d(x, t, q_v) - U_d^0(x, t, q_v)}{\tau_r} + 1 \quad d = 1, 2 \quad (5.6)$$

where

$$U_d^0(x, t, q_v) = \frac{\partial e_d^0(x, t)}{\partial q_v} = \frac{\partial}{\partial q_v} \left(\frac{e(x, t)}{2} \right) = \frac{U(x, t, q_v)}{2} \quad (5.7)$$

while

$$U(x, t, q_v) = \sum_{d=1}^2 U_d(x, t, q_v) \quad (5.8)$$

The phonon energy density function $e(x, t, q_v \pm \Delta q_v)$ is expanded into the Taylor series taking into account the first two components according to the formulas

$$\begin{aligned} e(x, t, q_v + \Delta q_v) &\approx e_b(x, t) + \frac{\partial e(x, t)}{\partial q_v} \Delta q_v \\ e(x, t, q_v - \Delta q_v) &\approx e_b(x, t) - \frac{\partial e(x, t)}{\partial q_v} \Delta q_v \end{aligned} \quad (5.9)$$

where Δq_v is a certain increment of the source function, and the starting point $e_b(x, t)$ corresponds to the basic solution.

Taking into account the sensitivity function $U(x, t, q_v) = \partial e(x, t) / \partial q_v$, one obtains

$$\begin{aligned} e(x, t, q_v + \Delta q_v) &\approx e_b(x, t) + U(x, t, q_v) \Delta q_v \\ e(x, t, q_v - \Delta q_v) &\approx e_b(x, t) - U(x, t, q_v) \Delta q_v \end{aligned} \quad (5.10)$$

and a certain increment of the energy function Δe can be calculated using the formula

$$\Delta e(x, t) \approx 2U(x, t, q_v) \Delta q_v \quad (5.11)$$

6. Numerical example

In the paper, heat transfer in a one-dimensional silicon film of dimension $L = 200$ nm has been analyzed. The following input data have been introduced: relaxation time $\tau_r = 6.53$ ps, Debye temperature $\Theta_D = 640$ K, initial temperature $T_0 = 300$ K, boundary conditions $T_{b1} = T_{b2} = 300$ K, lattice distance $\Delta x = 20$ nm and the time step $\Delta t = 5$ ps.

In the first example, the interval value of the heat source function has been considered $\bar{q}_v = [10^{18} - 0.05 \cdot 10^{18}, 10^{18} + 0.05 \cdot 10^{18}]$ W/m³. Figure 2a illustrates the interval heating curves of the phonon energy at the internal nodes 1 (20 nm), 2 (80 nm) and 3 (140 nm).

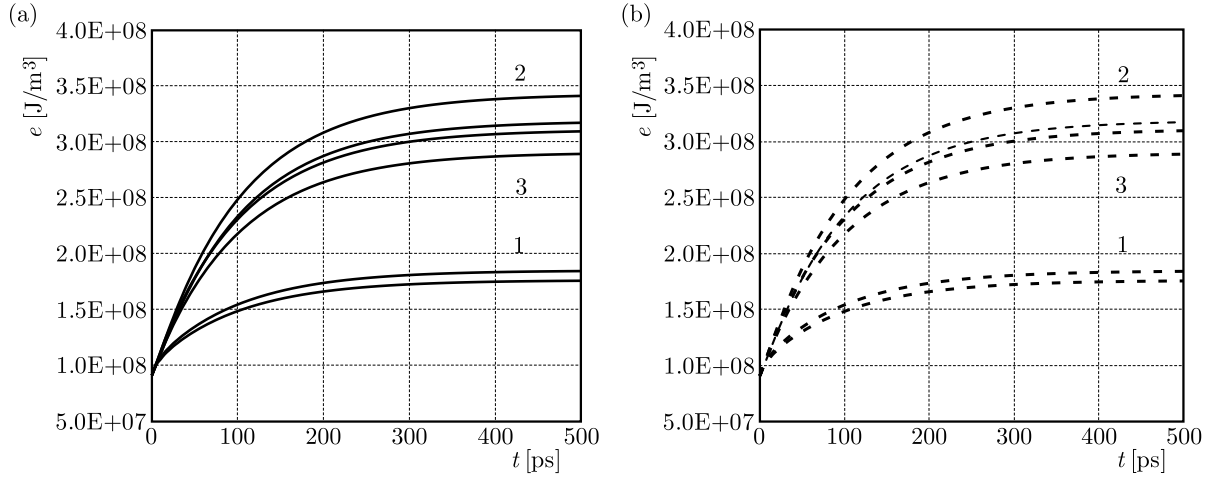


Fig. 2. Energy heating curves: (a) – first method, (b) – second method

In the second example, the no-interval value of the heat source function has been introduced $q_v = 10^{18} \text{ W/m}^3$ and the sensitivity analysis with respect to the heat source parameter has been applied. In this model, an increment of the heat source parameter has been introduced as $\Delta q_v = 0.05 \cdot 10^{18} \text{ W/m}^3$. In Fig. 2b, the courses of heating curves of the phonon energy at the same internal nodes are presented. One can see that the both results are similar.

Figures 3a and 3b present the courses of heating curves taking into account the same internal nodes for the first and second example, respectively.

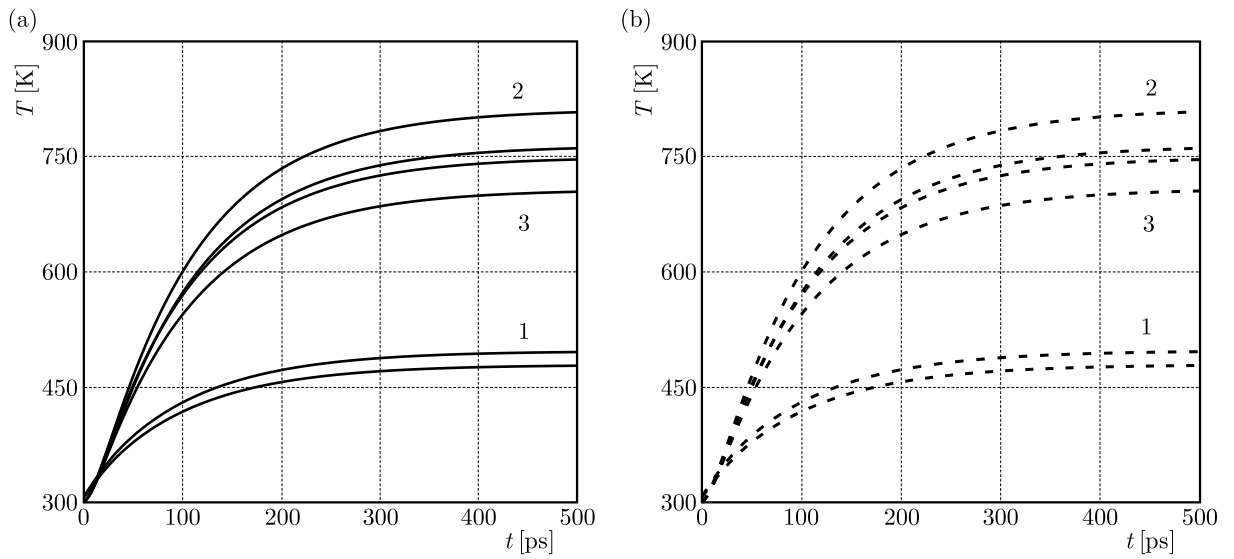


Fig. 3. Temperature heating curves: (a) – first method, (b) – second method

7. Conclusions

In the paper, heat transfer in one-dimensional crystalline solids is considered. The main subject of the paper is the comparison of the results obtained using two methods. In the first method, the interval lattice Boltzmann method with an uncertainly defined internal heat source function is used. The solution to the interval Boltzmann transport equations has been obtained taking into account the rules of directed interval arithmetics. In the second method, the sensitivity

analysis with respect to the internal heat source parameter has been done. The application of the sensitivity functions and the Taylor formula enables one to find a solution similar to the solution received using the interval lattice Boltzmann method.

References

1. CHONGA W.T., AL-MAMOONA A., POHA S.CH., SAWB L.H., SHAMSHIRBANDC S., MOJUMDER J.CH., 2016, Sensitivity analysis of heat transfer rate for smart roof design by adaptive neuro-fuzzy technique, *Energy and Buildings*, **124**, 112-119
2. DEMS K., ROUSSELET B., 1999, Sensitivity analysis for transient heat conduction in a solid body – Part I, *Structural Optimization*, **17**, 36-45
3. ESCOBAR R.A., GHAI S.S., JHON M.S., AMON C.H., 2006, Multi-length and time scale thermal transport using the lattice Boltzmann method with application to electronics cooling, *Journal of Heat and Mass Transfer*, **49**, 97-107
4. ESHRAGHI M., FELICELLI S.D., 2012, An implicit lattice Boltzmann model for heat conduction with phase change, *International Journal of Heat and Mass Transfer*, **55**, 2420-2428
5. GOETHALS K., BREESCHB H., JANSSENS A., 2011, Sensitivity analysis of predicted night cooling performance to internal convective heat transfer modeling, *Energy and Buildings*, **43**, 2429-2441
6. HUANGA S.M., SUN Z., LUK'YANCHUK B.S., HONG M.H., SHI L.P., 2005, Nanobump arrays fabricated by laser irradiation of polystyrene particle layers on silicon, *Applied Physics Letters*, **86**, 161911
7. HWANG S., SON CH., SEO D., RHEE D.H., CHA B., 2016, Comparative study on steady and unsteady conjugate heat transfer analysis of a high pressure turbine blade, *Applied Thermal Engineering*, **99**, 765-775
8. JASIŃSKI M., 2014, Modeling of tissue thermal injury formation process with application of direct sensitivity method, *Journal of Theoretical and Applied Mechanics*, **52**, 4, 947-957
9. JOSHI A.A., MAJUMDAR A., 1993, Transient ballistic and diffusive phonon heat transport in thin films, *Journal of Applied Physics*, **74**, 1, 31-39
10. KAŁUŻA G., MAJCHRZAK E., TURCHAN Ł., 2016, 1D generalized dual-phase lag equation. Sensitivity analysis with respect to the porosity, *Journal of Applied Mathematics and Computational Mechanics*, **15**, 1, 49-58
11. KLEIBER M., 1997, *Parameter Sensitivity in Non-linear Mechanics*, J. Willey & Sons, London
12. MAJCHRZAK E., MOCHNACKI B., 2014, Sensitivity analysis of transient temperature field in microdomains with respect to the dual phase lag model parameters, *International Journal for Multiscale Computational Engineering*, **12**, 1, 65-77
13. MANSOOR S. BIN, YILBAS B.S., 2011, Laser short-pulse heating of silicon-aluminum thin films, *Optical and Quantum Electronics*, **42**, 601-618
14. MANSOOR S. BIN, YILBAS B.S., 2014, Phonon transport in aluminum and silicon film pair: laser short-pulse irradiation at aluminum film surface, *Canadian Journal of Physics*, **92**, 12, 1614-1622
15. MARKOV S.M., 1995, On directed interval arithmetic and its applications, *Journal of Universal Computer Science*, **1**, 514-526
16. MOCHNACKI B., MAJCHRZAK E., 2007, Identification of macro and micro parameters in solidification model, *Bulletin of the Polish Academy of Sciences, Technical Sciences*, **55**, 1, 107-113
17. MOHEBBI F., SELIER M., 2016, Estimation of thermal conductivity, heat transfer coefficient, and heat flux using a three dimensional inverse analysis, *International Journal of Thermal Sciences*, **99**, 258-270

18. NARUMANCHI S., MURTHY J.Y., AMON C.H., 2003, Simulation of unsteady small heat source effects in sub-micron heat conduction, *Journal of Heat Transfer*, **123**, 896-903
19. NEUMAIER A., 1990, *Interval Methods for System of Equations*, Cambridge University Press, Cambridge, New York, Port Chester, Melbourne, Sydney
20. PIASECKA-BELKHAYAT A., 2011, Interval boundary element method for 2D transient diffusion problem using directed interval arithmetic, *Engineering Analysis with Boundary Elements*, **35**, 3, 259-263
21. PIASECKA-BELKHAYAT A., 2011, Interval boundary element method for transient diffusion problem in two-layered domain, *Journal of Theoretical and Applied Mechanics*, **49**, 1, 265-276
22. PIASECKA-BELKHAYAT A., KORCZAK A., 2014, Modelling of transient heat transport in one-dimensional crystalline solids using the interval lattice Boltzmann method, *Recent Advances in Computational Mechanics*, T. Łodygowski, J. Rakowski and P. Litewka (Eds.), Taylor & Francis Group, A Balkema Book, London, 363-368
23. PIASECKA-BELKHAYAT A., KORCZAK A., 2016, Numerical modelling of the transient heat transport in a thin gold film using the fuzzy lattice Boltzmann method with α -cuts, *Journal of Applied Mathematics and Computational Mechanics*, **15**, 1, 123-135

Manuscript received May 16, 2016; accepted for print July 4, 2016

LARGE DEFORMATION AND STABILITY ANALYSIS OF A CYLINDRICAL RUBBER TUBE UNDER INTERNAL PRESSURE

JIANBING SANG, SUFANG XING, HAITAO LIU, XIAOLEI LI, JINGYUAN WANG, YINLAI LV

School of Mechanical Engineering, Hebei University of Technology, Tianjin, China

e-mail: sangjianbing@126.com

Rubber tubes under pressure can undergo large deformations and exhibit a particular non-linear elastic behavior. In order to reveal mechanical properties of rubber tubes subjected to internal pressure, large deformation analysis and stability analysis have been proposed in this paper by utilizing a modified Gent's strain energy function. Based on the nonlinear elastic theory, by establishing the theoretical model of a rubber tube under internal pressure, the relationship between the internal pressure and circumferential principal stretch has been deduced. Meanwhile stability analysis of the rubber tube has also been proposed and the relationship between the internal pressure and the internal volume ratio has been achieved. The effects on the deformation by different parameters and the failure reasons of the rubber tube have been discussed, which provided a reasonable reference for the design of rubber tubes.

Keywords: large deformation analysis, stability analysis, rubber tube, nonlinear elastic theory

1. Introduction

Cylindrical tube structures have been a subject of interest in the recent years due to their applicability in numerous fields. In many engineering applications, cylindrical tubes are subject to internal pressures and as a result undergo large deformations (Bertram, 1982, 1987). In the past, the analysis of this problem was based on small deformations and on the assumption that the material was linear elastic, but this led to prediction results not inaccurate for large deformation. It is well known that rubber-like materials exhibit highly nonlinear behavior character. In the case of nonlinear rubber tube structures undergoing large deformations, the problem is even more acute due to geometric and material nonlinearities (Antman, 1995; Bharatha, 1967; Green and Zerna, 1968; Ogden, 1984), and we can not utilize typical Hooke's law to describe the relationship between stress and strain.

From the point of view of mechanics perspective, the vital problem that should be solved is to select the reasonable and practical strain energy density function that describes the mechanical property of a rubber-like material. It follows from the fundamental representation theory in continuum mechanics that the strain-energy function of an isotropic rubber-like material can be represented in terms of either the principal invariants or principal stretches.

The pioneering work of Mooney, Rivlin and others on the nonlinear theory of elasticity sets up the basis for the analysis of rubber-like materials under large deformations.

In 1948, Rivlin put forward the strain energy function model to isotropic hyper elastic materials (Rivlin, 1948)

$$W = \sum_{i,j=0}^{\infty} C_{ij}(I_1 - 3)^i(I_2 - 3)^j \quad (1.1)$$

in which C_{ij} stands for the material constant; I_1 and I_2 are, respectively, the first and second invariants of the left Cauchy-Green deformation tensor.

Taking the linear combination of the Rivlin model, we can get the Mooney-Rivlin material (Mooney, 1940), the strain energy density function may be written as

$$W = C_1(I_1 - 3) + C_2(I_2 - 3) = C_1[(I_1 - 3) + \alpha(I_2 - 3)] \quad (1.2)$$

in which, C_1 and C_2 are material constants, and $\alpha = C_2/C_1$.

To simplify, the first of the Rivlin model can be used and it is a neo-Hookean material (Treloar, 1976), which can be expressed as follows

$$W(I_1) = \frac{1}{2}nkT(I_1 - 3) \quad (1.3)$$

A generalized neo-Hookean model widely used in the domain of biomechanics is a two-parameter exponential strain-energy named by Fung and Demiray (Fung, 1967)

$$W = \frac{\mu}{2b} \{ \exp[b(I_1 - 3)] - 1 \} \quad (1.4)$$

in which b is a positive dimensionless material parameter which can display the degree of strain-stiffening. In soft tissues, the value of b is in the range $1 \leq b \leq 5.5$.

Another well-known model of this type is the three parameter Knowles power law model (Knowles, 1977) as follows

$$W = \frac{\mu}{2b} \left[\left(1 + \frac{b}{n}(I_1 - 3) \right)^n - 1 \right] \quad (1.5)$$

Gent (1996) proposed a new strain energy function for the non-linear elastic behavior of rubber-like materials. Because of its formal simplicity, this model has been widely applied to large elastic deformations of solids. The energy density function proposed by Gent for incompressible, isotropic, hyper elastic materials is shown as

$$W = -\frac{\mu}{2} J_m \ln \left(1 - \frac{I_1 - 3}{J_m} \right) \quad (1.6)$$

where μ is the shear modulus and J_m is the constant limiting value for $I_1 - 3$. Since W depends on the only first invariant of B , the Gent model belongs to the class of the generalized neo-Hookean materials.

Based on Gent's constitutive model, a modified model by Gent has been proposed to describe the mechanical property of an arterial wall in (Sang *et al.*, 2014), whose modified strain energy function is expressed as

$$W = -\frac{\mu J_m}{2} \ln \left(1 - \frac{I_1^n - 3^n}{J_m} \right) \quad (1.7)$$

where n is the material parameter.

From constitutive model (1.7), we can see that it can be transformed to the Gent model when $n = 1$. If $n = 1$ and $J_m \rightarrow \infty$, constitutive model (1.7) can be transformed to the neo-Hookean model.

The developments of analysis of rubber tubes have continually been accompanied by discussions. Zhu *et al.* (2008, 2010) analyzed the finite axisymmetric deformation of a thick-walled circular cylindrical elastic tube subject to pressure on its external lateral boundaries and zero displacement on its ends. Meanwhile, they considered bifurcation from a circular cylindrical deformed configuration of a thick-walled circular cylindrical tube of an incompressible isotropic elastic material subject to combined axial loading and external pressure. Research on the

physical behavior of compressible nonlinear elastic materials for the problem of inflation of a thin-walled pressurized torus was developed by Papargyri-Pegiou and Stavarakakis (2000). Gent (2005) analyzed a inflating cylindrical rubber tube in terms of simple strain energy functions using Rivlin's theory of large elastic deformations. Mangan and Destrade (2015) used the 3-parameter Mooney and Gent-Gent (GG) phenomenological models to explain the stretch-strain curve of typical inflation. Based on the strain energy function by Gent, a thorough discussion (Feng *et al.*, 2010; Hariharaputhiran and Saravanan, 2016; Horgan, 2015; Horgan and Saccomandi, 2002; Pucci and Saccomandi, 2002; Rickaby and Scott, 2015) was given on molecular models and their relation to deformation of rubber-like materials.

Akyüz and Ertepinar (1999) investigated cylindrical shells of arbitrary wall thickness subjected to uniform radial tensile or compressive dead-load traction. By using the theory of small deformations superposed on large elastic deformations, the stability of the finitely deformed state and small, free, radial vibrations about this state are investigated. Akyüz and Ertepinar (2001) also investigated the stability of homogeneous, isotropic, compressible, hyperelastic, thick spherical shells subjected to external dead-load traction and gave the critical values of stress and deformation for a foam rubber, slightly compressible rubber and a nearly incompressible rubber. Alexander (1971), by using the non-linear analysis, predicted that the axial load had a significant effect on the value of tensile instability pressure. With thin-walled tubes of latex rubber, experiments were performed and the results were according with the results of the non-linear analysis in stable regions where the membrane retained its cylindrical shape. Based on the theory of large elastic deformations, Ertepinar (1977) investigated finite breathing motions of multi-layered, long, circular cylindrical shells of arbitrary wall thickness. And a tube consisting of two layers of neo-Hookean materials was solved both by exact and approximate methods, which was observed as an excellent agreement between the two sets of results. Bifurcation of inflated circular cylinders of elastic materials under axial loading was researched by Haughton and Ogden (1979a,b), who proposed that bifurcation might occur before the inflating pressure reached the maximum. A combination of the two mode interpreted in terms of bending for a tube under axial compression was discussed in terms of the length to radius ratio of the tube. At the same time, prismatic, axisymmetric and asymmetric bifurcations for axial tension and compression combined with internal or external pressure was discussed and presented for a general form of incompressible isotropic elastic strain energy function. Haughton and Ogden (1980) put a research on the deformation of a circular cylindrical elastic tube of finite wall thickness rotating about its axis, and achieved a range of values of the axial extension for which no bifurcation could occur during rotation. Jiang and Ogden (2000) proposed the axial shear deformation of a thick-walled right circular cylindrical tube of the compressible isotropic elastic material and discussed explicit solutions for several forms of the strain-energy function. Jiang and Ogden (2000) also analyzed the plane strain character of the finite azimuthal shear of a circular cylindrical annulus of a compressible isotropic elastic material by utilizing the strain energy as a function of two independent deformation invariants. Merodio and Ogden (2015) proposed a new example of the solution to the finite deformation boundary-value problem for a residually stressed elastic body and combined extension, inflation and torsion of a circular cylindrical tube subject to radial and circumferential residual stresses.

Based on Gent's constitutive model, a modified model has been proposed to describe incompressible rubber-like materials. The inductive material parameter n can reflect the hardening character of rubber-like materials. With the modified model, mechanical properties of rubber tubes subjected to internal pressure has been revealed and large deformation analysis and stability analysis has been proposed by utilizing Gent's modified strain energy function. Based on the nonlinear elastic theory, by establishing the theoretical model of rubber tubes under internal pressure, the relationship between the internal pressure and circumferential principal stretch has been deduced. Meanwhile, stability analysis of rubber tube has also been proposed and the rela-

relationship between the internal pressure and internal volume ratio has been achieved. The results show that the constitutive parameter n has a major impact on mechanical properties of the rubber tube, and when $n \leq 1$, the rubber tube becomes softening. The instability phenomenon in the rubber tube will appear only when n is less than 1.5. For different values of n , the range of the value of J_m which leads to instability also changes.

2. Finite deformation analysis

Based on the elastic finite deformation theory, the left Cauchy–Green tensor can be denoted by $\mathbf{B} = \mathbf{F} \cdot \mathbf{F}^T$, where \mathbf{F} is the gradient of the deformation and $\lambda_1, \lambda_2, \lambda_3$ are the principal stretches, then, for an isotropic material, W is a function of the strain invariants as follows

$$\begin{aligned} I_1 &= \text{tr} \mathbf{B} = \lambda_1^2 + \lambda_2^2 + \lambda_3^2 \\ I_2 &= \frac{1}{2}[(\text{tr} \mathbf{B}^2) - (\text{tr} \mathbf{B})^2] = \lambda_1^2 \lambda_2^2 + \lambda_2^2 \lambda_3^2 + \lambda_3^2 \lambda_1^2 \\ I_3 &= \det \mathbf{B} = \lambda_1^2 \lambda_2^2 \lambda_3^2 \end{aligned} \quad (2.1)$$

By utilizing strain energy function (1.7), the Cauchy stress tensor can be expressed as

$$\boldsymbol{\sigma} = -p\mathbf{I} + \frac{n\mu J_m}{J_m - (I_1^n - 3^n)} I_1^{n-1} \mathbf{B} \quad (2.2)$$

in which I_1 is the first invariant of and p is the undetermined scalar function that justifies the incompressible internal constraint conditions.

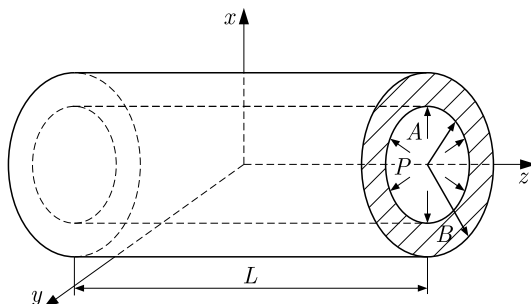


Fig. 1. Rubber tube under pressure

Consider a cylindrical rubber tube under uniform pressure, which is illustrated in Fig. 1. If (R, Θ, Z) and (r, θ, z) are the coordinates of the rubber tube before deformation and after deformation respectively, then the deformation pattern of the rubber tube can be expressed as

$$r = f(R) \quad \theta = \Theta \quad z = \lambda_z Z \quad (2.3)$$

The deformation gradient tensor \mathbf{F} can be expressed as

$$\mathbf{F} = \mathbf{F}^T = \begin{bmatrix} \frac{dr}{dR} & 0 & 0 \\ 0 & \frac{r}{R} & 0 \\ 0 & 0 & \lambda_z \end{bmatrix} = \begin{bmatrix} \lambda_r & 0 & 0 \\ 0 & \lambda_\theta & 0 \\ 0 & 0 & \lambda_z \end{bmatrix} \quad (2.4)$$

in which, $\lambda_r, \lambda_\theta$ and λ_z are the principal stretch in the radial, circumferential and axial direction of the cylinder membrane. It can be expressed as

$$\lambda_r = \frac{dr}{dR} = (\lambda \lambda_z)^{-1} \quad \lambda_\theta = \frac{r}{R} = \lambda \quad \lambda_z = \lambda_z \quad (2.5)$$

The left Cuachy-Green deformation tensor \mathbf{B} can be shown as follows

$$\mathbf{B} = \mathbf{F}\mathbf{F}^T = \begin{bmatrix} \lambda_r^2 & 0 & 0 \\ 0 & \lambda_\theta^2 & 0 \\ 0 & 0 & \lambda_z^2 \end{bmatrix} = \begin{bmatrix} (\lambda\lambda_z)^{-2} & 0 & 0 \\ 0 & \lambda^2 & 0 \\ 0 & 0 & \lambda_z^2 \end{bmatrix} \quad (2.6)$$

And the first invariants of the left Cuachy-Green deformation tensor \mathbf{B} can be expressed as

$$I_1 = \text{tr} \mathbf{B} = (\lambda\lambda_z)^{-2} + \lambda^2 + \lambda_z^2 \quad (2.7)$$

Substituting (2.7) and (2.4) into (2.2), we get

$$\sigma_{rr} = -p + 2(\lambda\lambda_z)^{-2} \frac{\partial W}{\partial I_1} \quad \sigma_{\theta\theta} = -p + 2\lambda^2 \frac{\partial W}{\partial I_1} \quad \sigma_{zz} = -p + 2\lambda_z^2 \frac{\partial W}{\partial I_1} \quad (2.8)$$

in which

$$\frac{\partial W}{\partial I_1} = \frac{\mu}{2} \frac{nJ_m}{J_m - (I_1^n - 3^n)} I_1^{n-1}$$

and p is the Lagrange multiplier associated with hydrostatic pressure.

In the absence of body forces, the equilibrium equation of the axial symmetry in the current configuration can be achieved as

$$\frac{d\sigma_{rr}}{dr} + \frac{1}{r}(\sigma_{rr} - \sigma_{\theta\theta}) = 0 \quad (2.9)$$

For the cylinder rubber tube under internal pressure, it should be satisfied with that the radial stress is zero outside of the rubber tube and the radial stress is equal to the internal pressure, which can be expressed as

$$\sigma_{rr}(a) = -P \quad \sigma_{rr}(b) = 0 \quad (2.10)$$

From (2.9) and (2.10), we can get

$$\int_{-P}^0 d\sigma_{rr} = \int_a^b \frac{1}{r}(\sigma_{\theta\theta} - \sigma_{rr}) dr = \int_a^b \frac{1}{r} \frac{\mu n J_m}{J_m - (I_1^n - 3^n)} I_1^{n-1} [\lambda^2 - (\lambda\lambda_z)^{-2}] dr \quad (2.11)$$

in which, $a = f(A)$, $b = f(B)$, a and b are the internal and external radii of the cylinder rubber tube after deformation. A and B are the internal and external radii of the cylinder rubber tube before deformation.

By utilizing the expression $\lambda = r/R$, we can arrive at the following expression

$$dr = \frac{R}{1 - \lambda^2 \lambda_z} d\lambda \quad (2.12)$$

Substituting (2.12) into (2.11), we get

$$\begin{aligned} P &= \int_{\lambda_a}^{\lambda_b} \frac{1}{\lambda} \frac{\partial W}{\partial I_1} [\lambda^2 - (\lambda\lambda_z)^{-2}] \frac{1}{1 - \lambda^2 \lambda_z} d\lambda \\ &= \int_{\lambda_a}^{\lambda_b} \frac{1}{\lambda} \frac{\mu n J_m}{J_m - (I_1^n - 3^n)} I_1^{n-1} [\lambda^2 - (\lambda\lambda_z)^{-2}] \frac{1}{1 - \lambda^2 \lambda_z} d\lambda \end{aligned} \quad (2.13)$$

in which, $\lambda_a = a/A$, $\lambda_b = b/B$.

Taking into account the incompressibility of rubber-like materials, the following equations can be achieved

$$(r^2 - a^2)\lambda_z = R^2 - A^2 \quad R^2(\lambda^2\lambda_z - 1) = \lambda_z a^2 - A^2 \quad (2.14)$$

Equation (2.14) can be transformed into

$$\lambda_a^2\lambda_z - 1 = (\varepsilon + 1)^2(\lambda_b^2\lambda_z - 1) \quad (2.15)$$

where $\varepsilon = (B - A)/A$. For a thin-walled cylinder rubber tube, wall thickness is far less than the mean radius, so the value of ε is far less than 1. Removing the high-order term of ε , we can get

$$\lambda_a^2\lambda_z - 1 = \lambda_b^2\lambda_z - 1 + 2\varepsilon(\lambda_b^2\lambda_z - 1) \quad (2.16)$$

By utilizing the expressions $\lambda_a + \lambda_b = 2\lambda$, $\lambda_b = \lambda$, Eq. (2.16) can be transformed into

$$\lambda_a - \lambda_b = \frac{\varepsilon}{\lambda\lambda_z}(\lambda^2\lambda_z - 1) \quad (2.17)$$

From (2.17), a simplified equation from (2.13) can be expressed as

$$P = \frac{\mu n J_m}{J_m - (I_1^n - 3^n)} I_1^{n-1} [\lambda^2 - (\lambda\lambda_z)^{-2}] \frac{\varepsilon}{\lambda^2\lambda_z} \quad (2.18)$$

In order to discuss the effect of constitutive parameters J_m and n on the mechanical properties of the rubber tube under pressure, non-dimensional stress is introduced. From Eq. (2.18), we can get

$$P^\# = \frac{n J_m}{J_m - (I_1^n - 3^n)} I_1^{n-1} [\lambda^2 - (\lambda\lambda_z)^{-2}] \frac{1}{\lambda^2\lambda_z} \quad (2.19)$$

where $P^\# = P/(\mu\varepsilon)$.

In order to study the effect on the rubber tube under pressure by the constitutive parameters J_m and n , three circumstances are considered. Firstly, when J_m and λ_z is fixed, the distribution between the internal pressure and circumferential principal stretch with the change of n has been researched. Secondly, when n and λ_z is fixed, the distribution between the internal pressure and circumferential principal stretch with the change of J_m has also been researched. Thirdly, we simultaneously investigate the distribution between the internal pressure and circumferential principal stretch with the change of λ_z when J_m and n is fixed.

Figures 2a-2c show distribution curves between the internal pressure $P^\#$ and circumferential principal stretch λ according to the above three circumstances.

As shown in Fig. 2a, for fixed material parameters $J_m = 2.3$ and $\lambda_z = 1$, when the material parameter n increases, the circumferential principal stretch increases in accordance with the internal pressure. It can also be seen in Fig. 2a that the effect of the constitutive parameter n has a major impact on the mechanical properties of the rubber tube. When the material parameter n takes higher values, the range of the circumferential principal stretch is larger, which means that the rubber tube has strong inflation capability and good elasticity. On the other hand, when the material parameter n takes a lesser value, the range of the circumferential principal stretch is smaller, which means that the rubber inflation capability tube is weak. Especially when $n \leq 1$, the rubber tube starts softening and the material becomes unstable, which means the stability analysis is necessary.

As can be noted in Fig. 2b, the material parameter J_m has also a certain influence on the circumferential principal stretch of the rubber tube. As the value of J_m increases, the circumferential principal stretch increases in accordance with the internal pressure. When the material

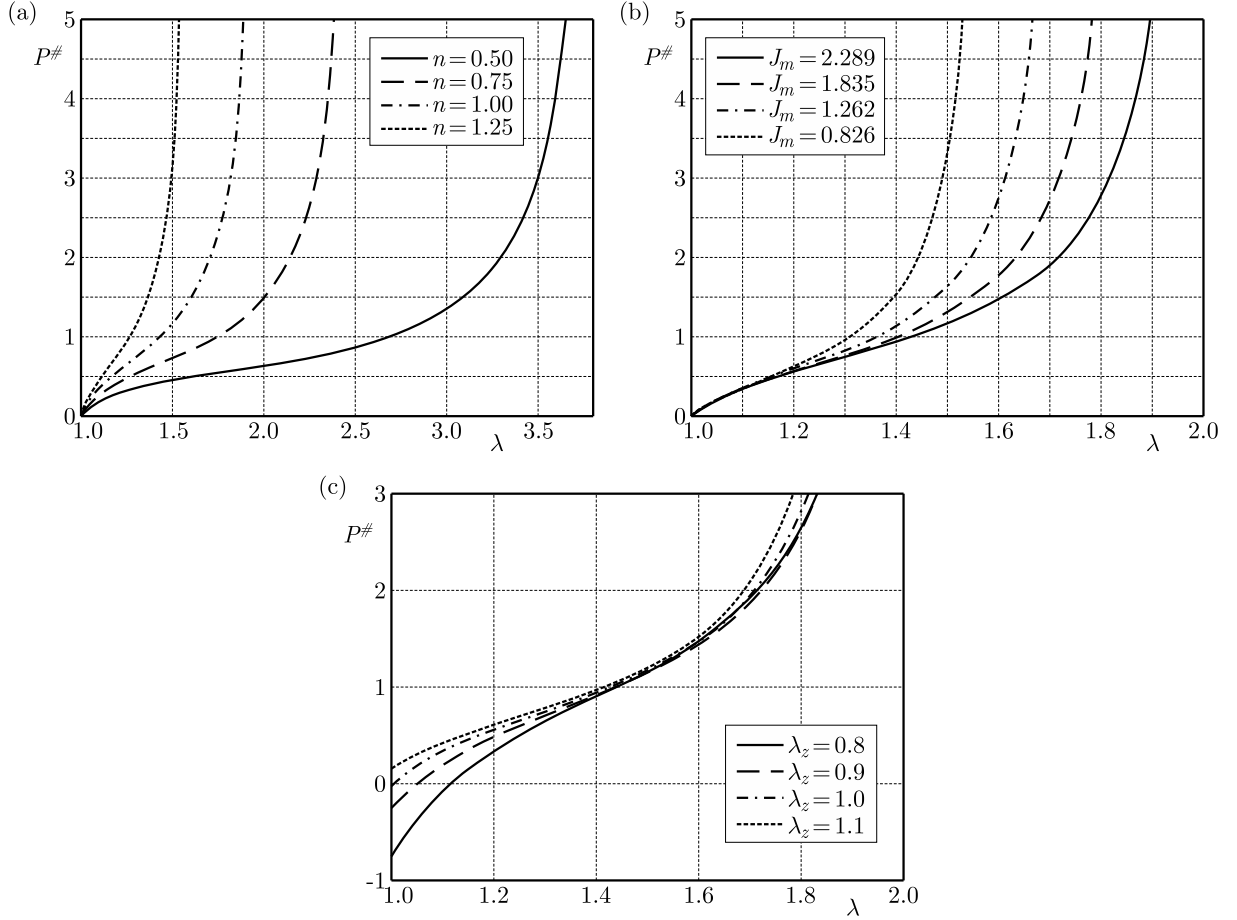


Fig. 2. Distribution curve between $P^\#$ and λ with the effect of the material parameter: (a) n ($J_m = 2.3$, $\lambda_z = 1$), (b) J_m ($n = 1$, $\lambda_z = 1$), (c) λ_z ($n = 1$, $J_m = 2.3$)

parameter J_m takes higher values, the range of the circumferential principal stretch is larger, which means that the rubber tube has strong inflation capability and good elasticity. On the other hand, when the material parameter J_m takes a lesser value, the range of the circumferential principal stretch is smaller, which means that the inflation capability of the tube is weak.

Figure 2c displays the relation between the internal pressure and circumferential principal stretch. From that we can see when the material parameters J_m and n are fixed, the circumferential principal stretch decreases as the axial principal stretch increases, which means that the rubber tube is incompressible. We also can infer that the axial principal stretch has a minor impact on the mechanical properties of the rubber tube.

3. Stability analysis

According with the membrane hypothesis, $\sigma_{rr} = 0$. From (2.8), we can get

$$p = \frac{\mu n J_m}{J_m - (I_1^n - 3^n)} I_1^{n-1} (\lambda \lambda_z)^{-2} \quad (3.1)$$

Substituting (3.1) into (2.8), we get

$$\begin{aligned} \sigma_{\theta\theta} &= 2 \frac{\partial W}{\partial I_1} [\lambda^2 - (\lambda \lambda_z)^{-2}] = \frac{\mu n J_m}{J_m - (I_1^n - 3^n)} I_1^{n-1} [\lambda^2 - (\lambda \lambda_z)^{-2}] \\ \sigma_{zz} &= 2 \frac{\partial W}{\partial I_1} [\lambda_z^2 - (\lambda \lambda_z)^{-2}] = \frac{\mu n J_m}{J_m - (I_1^n - 3^n)} I_1^{n-1} [\lambda_z^2 - (\lambda \lambda_z)^{-2}] \end{aligned} \quad (3.2)$$

For an incompressible rubber tube under pressure, when its two sides are closed, there is no constraint along the length direction, from which the following expression can be achieved

$$\sigma_{\theta\theta} = \frac{Pr_0}{h} \quad \sigma_{zz} = \frac{Pr_0}{2h} \quad (3.3)$$

where P is the internal pressure of the cylinder membrane, r_0 is the mean radius after deformation and h is the thickness of the rubber membrane after deformation.

Considering the incompressibility of the rubber membrane, we can get

$$\sigma_{\theta\theta} = \frac{Pr_0}{h} = \frac{P\lambda^2\lambda_z R_0}{H} \quad \sigma_{zz} = \frac{Pr_0}{2h} = \frac{P\lambda^2\lambda_z R_0}{2H} \quad (3.4)$$

in which, R_0 is the mean radius before deformation and H is the thickness of the rubber membrane before deformation.

From (3.2) and (3.4), the following equation can be formulated

$$\begin{aligned} \frac{P\lambda^2\lambda_z R_0}{H} &= \frac{\mu n J_m}{J_m - (I_1^n - 3^n)} I_1^{n-1} [\lambda^2 - (\lambda\lambda_z)^{-2}] \\ P^\# &= \frac{1}{\lambda^2\lambda_z} [\lambda^2 - (\lambda\lambda_z)^{-2}] \frac{n J_m}{J_m - (I_1^n - 3^n)} I_1^{n-1} \end{aligned} \quad (3.5)$$

where $P^\# = PR_0/H$.

From (3.4), we get

$$\sigma_{\theta\theta} = 2\sigma_{zz} \quad (3.6)$$

Substituting (3.6) into (3.2), the following expression can be found

$$\lambda_z^3 = \frac{(\lambda^2\lambda_z)^2 + 1}{2\lambda^2\lambda_z} \quad (3.7)$$

Substituting (3.7) into (2.5), the principal stretch in the radial and axial direction of the cylinder membrane can be expressed as

$$\lambda = \nu^{\frac{1}{2}} \left(\frac{2\nu}{\nu^2 + 1} \right)^{\frac{1}{6}} \quad \lambda_z = \left(\frac{\nu^2 + 1}{2\nu} \right)^{\frac{1}{3}} \quad (3.8)$$

where $\nu = \lambda^2\lambda_z$, which can reflect the volume expansion ratio, i.e., the ratio of the internal volume of the cylinder membrane in the deformed state to that in the undeformed state.

Substituting (3.8) into (3.5)₂, we get

$$P^\# = \frac{\nu^2 - 1}{\nu^2} \left(\frac{2\nu}{\nu^2 + 1} \right)^{\frac{1}{3}} \frac{n J_m}{J_m - (I_1^n - 3^n)} I_1^{n-1} \quad (3.9)$$

In order to examine stability of the rubber cylinder membrane, the stationary point of $P^\#$ should be determined first.

When $J_m \rightarrow \infty$, Eq. (1.7) can be transformed into the strain energy function proposed by Gao (1990) as follows

$$W = A(I_1^n - 3^n) \quad (3.10)$$

where $A = \mu/2$.

Based on strain energy function (3.10), Eq. (3.9) can be transformed as

$$P_\infty^\# = \frac{\nu^2 - 1}{\nu^2} \left(\frac{2\nu}{\nu^2 + 1} \right)^{\frac{1}{3}} n I_1^{n-1} \quad (3.11)$$

When the material parameter $n = 1$, the neo-Hookean constitutive equation can be achieved from (3.10). Then, we get the following expression from (3.11)

$$P^\# = \frac{\nu^2 - 1}{\nu^2} \left(\frac{2\nu}{\nu^2 + 1} \right)^{\frac{1}{3}} \quad (3.12)$$

4. Discussion

As shown in Fig. 3, when $J_m \rightarrow \infty$ and $n = 1$, we obtain the turning point $\nu^* = 2.930$. For the volume expansion ratio $\nu \leq \nu^*$, the inflation curve is monotonically increasing. But for the volume expansion ratio $\nu \geq \nu^*$, the inflation curve is decreasing.

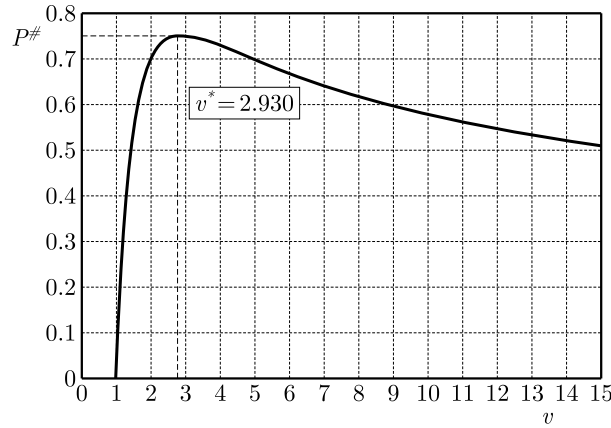


Fig. 3. Distribution curve between $P^\#$ and ν in the rubber tube inflation ($J_m \rightarrow \infty$ and $n = 1$)

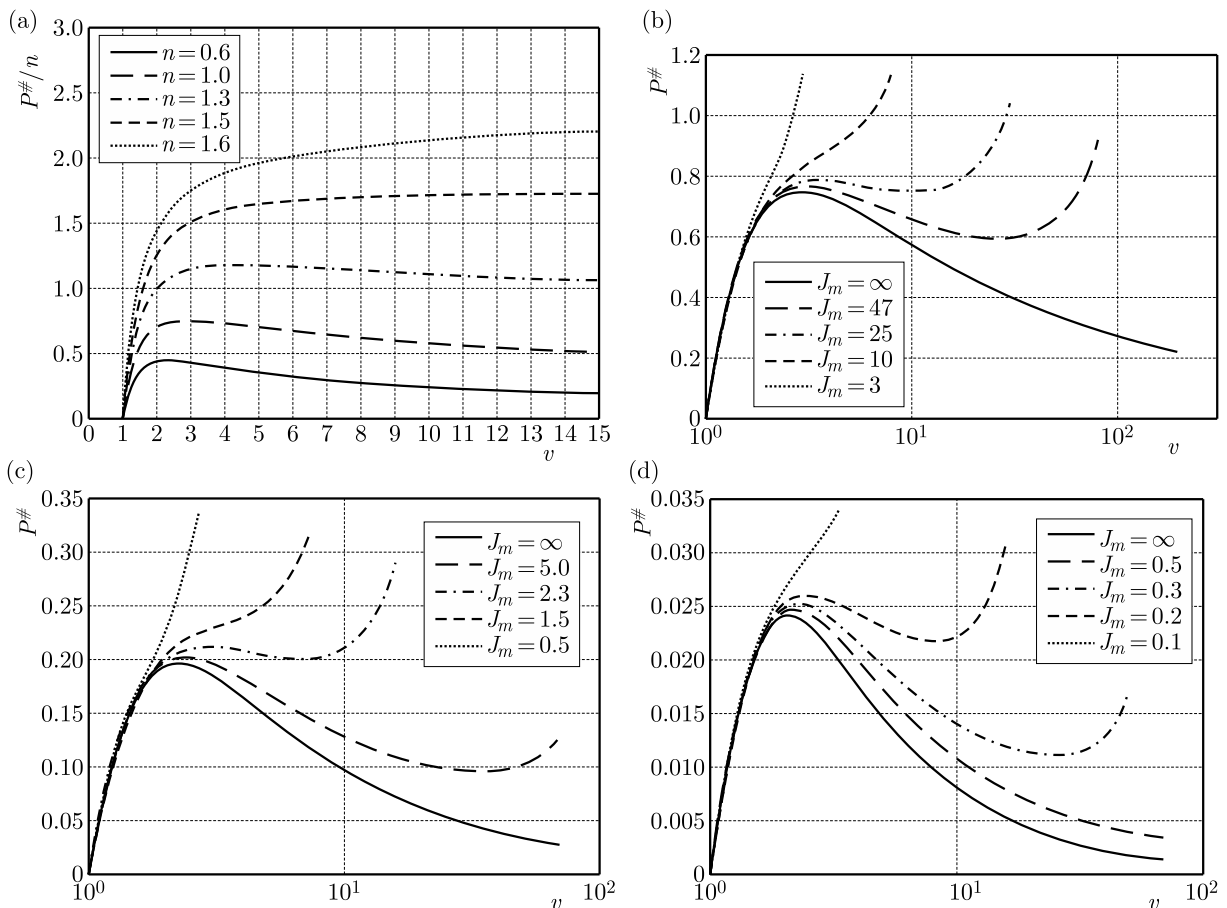


Fig. 4. Distribution curve between $P^\#$ and ν with the effect of: (a) n ($J_m \rightarrow \infty$), (b) J_m ($n = 1$), (c) J_m ($n = 0.5$), (d) J_m ($n = 0.1$)

In order to discuss the effect of the material parameter n on the rubber tube inflation, the distribution between the internal pressure and volume expansion ratio with the change of n has been investigated when $J_m \rightarrow \infty$. Figure 4a displays the relation between the internal pressure

and volume expansion ratio when $n = 0.6, 1.0, 1.3, 1.5$ and 1.6 , respectively. We can see that the inflation curve of the rubber tube has no limit point when $n = 1.6$, which means that there is no instability in the rubber tube. Only if $n \leq 1.5$, instability of the rubber tube under pressure occurs.

As can be seen in Figs. 4b to 4d, the distribution between the internal pressure and volume expansion ratio with the change of J_m when $n = 1, n = 0.5$ and $n = 0.1$, respectively. In Fig. 4b, we can see when $n = 1$, the constitutive parameter J_m has obviously the effect on the stability of the rubber tube. The inflating pressure is seen to pass through a maximum when $J_m \geq 25$, which means that instability of the rubber tube under pressure will occur. The results are consistent with the results by Gent (2005). It can be seen in Fig. 4c that the instability of the rubber tube under pressure occurs when $J_m \geq 2.3$ with the material parameter $n = 0.5$. And we also can see in Fig. 4d that the instability occurs when $J_m \geq 0.5$ with the material parameter $n = 0.1$.

5. Conclusion

A modified Gent's strain energy function has been utilized to examine the large deformation problem and the stability problem of the rubber tube subjected to internal pressure. By establishing the theoretical model of the rubber tube under internal pressure, the relationship between internal pressure and circumferential principal stretch has been deduced with the change of the constitutive parameters J_m and n , from which we can conclude that the constitutive parameter n has a major impact on the mechanical properties of the rubber tube. When $n \leq 1$, the rubber tube becomes softening and the material becomes unstable, which means that the stability analysis is necessary. For a cylinder rubber tube closed at two sides, the relationship between the internal pressure and internal volume ratio has also been deduced and the effect of the two constitutive parameters n and J_m on the stability of the rubber tube has been investigated. Accordingly, the instability phenomenon appears only when n is less than 1.5. For different values of n , the range of the value of J_m leading to the instability also changes.

Acknowledgement

This paper has been supported by Hebei National Nature Science Foundation (Grant No. A2017202076), Scientific Research Key Project of Hebei Province Education Department (Grand No. ZD20131019 and No. ZD2016083) and Scientific Research Project of Hebei Province Education Department (Grand No. QN2014111).

References

1. AKYÜZ U., ERTEPINAR A., 1999, Stability and asymmetric vibrations of pressurized compressible hyperelastic cylindrical shells, *International Journal of Non-Linear Mechanics*, **34**, 391-404
2. AKYÜZ U., A. ERTEPINAR A., 2001, Stability and breathing motions of pressurized compressible hyperelastic spherical shells *Journal of Sound Vibrations*, **247**, 293-304
3. ALEXANDER H., 1971, The tensile instability of an inflated cylindrical membrane as affected by an axial load, *International Journal of Mechanical Sciences*, **13**, 87-95
4. ANTMAN S.S., 1995, *Nonlinear Problems of Elasticity*, Springer-Verlag, NewYork-Budapest
5. BERTRAM C.D., 1982, Two modes of instability in a thick-walled collapsible tube conveying a flow, *Journal of Biomechanics*, **15**, 223-224
6. BERTRAM C.D., 1987, The effects of wall thickness, axial strain and end proximity on the pressure-area relation of collapsible tubes, *Journal of Biomechanics*, **20**, 863-876

7. BHARATHA S., 1967, Cylindrically symmetrical deformations of Mooney materials, *Archiwum Mechaniki Stosowanej (Archives of Mechanics)*, **19**, 6, 857-865
8. ERTEPINAR A., 1977, Large amplitude radial oscillations of layered thick-walled cylindrical shells, *International Journal of Solids and Structure*, **13**, 717-723
9. FENG Z., RENAUDA C., CROS J., ZHANG H., GUAN Z., 2010, A finite element finite-strain formulation for modeling colliding blocks of Gent materials, *International Journal of Solids and Structure*, **47**, 2215-2222
10. FUNG Y.C., 1967, Elasticity of soft tissues in simple elongation, *American Journal of Physiology*, **213**, 1532-1544
11. GAO Y.C., 1990, Elastostatic crack tip behavior for a rubber like material, *Theoretical and Applied Fracture Mechanics*, **14**, 219-231
12. GENT A.N., 1996, A new constitutive relation for rubber, *Rubber Chemistry and Technology*, **69**, 1, 59-61
13. GENT A.N., 2005, Elastic instabilities in rubber, *International Journal of Non-Linear Mechanics*, **40**, 165-175
14. GREEN A.E., ZERNA W., 1968, *Non-linear Elastic Deformations*, Horwood, Chichester
15. HARIHARAPUTHIRAN H., SARAVANAN U., 2016, A new set of biaxial and uniaxial experiments on vulcanized rubber and attempts at modeling it using classical hyperelastic models, *Mechanics of Materials*, **92**, 211-222
16. HAUGHTON D.M., OGDEN R.W., 1979a, Bifurcation of inflated circular cylinders of elastic material under axial loading – I. Membrane theory for thin-walled tubes, *Journal of the Mechanics and Physics of Solids*, **27**, 179-212
17. HAUGHTON D.M., OGDEN R.W., 1979b, Bifurcation of inflated circular cylinders of elastic material under axial loading – II. Exact theory for thick-walled tubes, *Journal of the Mechanics and Physics of Solids*, **27**, 489-512
18. HAUGHTON D.M., OGDEN R.W., 1980, Bifurcation of rotating thick-walled elastic tubes, *Journal of the Mechanics and Physics of Solids*, **28**, 59-74
19. HORGAN C.O., 2015, The remarkable Gent constitutive model for hyperelastic materials, *International Journal of Non-Linear Mechanics*, **68**, 9-16
20. HORGAN C.O., SACCOMANDI G.A., 2002, Molecular-statistical basis for the gent constitutive model of rubber elasticity, *Journal of Elasticity*, **68**, 1, 167-176
21. JIANG X., OGDEN R.W., 2000, Some new solutions for the axial shear of a circular cylindrical tube of compressible elastic material, *International Journal of Non-Linear Mechanics*, **35**, 361-369
22. KNOWLES J.K., 1977, The finite anti-plane field near the tip of a crack of incompressible elastic solids, *International Journal of Fracture*, **13**, 4, 611-639
23. MANGAN R., DESTRADE M., 2015, Gent models for the inflation of spherical balloons, *International Journal of Non-Linear Mechanics*, **68**, 52-58
24. MERODIO J., OGDEN R.W., 2015, Extension, inflation and torsion of a residually stressed circular cylindrical tube, *Continuum Mechanics and Thermodynamics*, **28**, 157-174
25. MOONEY M.A., (1940), A theory of large elastic deformation, *Journal of Applied Physics*, **11**, 582-592
26. OGDEN R.W., 1984, *Non-linear Elastic Deformations*, Ellis Horwood, Chichester
27. PAPARGYRI-PEGIOU S., STAVRAKAKIS E., 2000, Axisymmetric numerical solutions of a thin-walled pressurized torus of incompressible nonlinear elastic materials, *Computers and Structures*, **77**, 747-757
28. PUCCI E., SACCOMANDI G.A., 2002, A note on the Gent model for rubber-like materials, *Rubber Chemistry and Technology*, **75**, 5, 839-851

29. RICKABY S.R., SCOTT N.H., A comparison of limited-stretch models of rubber elasticity, *International Journal of Non-Linear Mechanics*, **68**, 71-86
30. RIVLIN R.S., 1948, Large elastic deformations of isotropic materials: I Fundametal concepts, II. Some uniqueness theories for homogenous deformation, *Philosophical Transactions of the Royal Society A: Mathematical, Physical and Engineering Sciences, London*, **240**, 459-508
31. SANG J.B., SUN L.F., S.F.XING, ET AL., 2014, Mechanical properties of polymer rubber materials based on a new constitutive model, *Polymers and Polymer Composites*, **22**, 8, 693-698
32. TRELOAR L.R.G., 1976, The mechanics of rubber elasticity, *Proceedings of the Royal Society of London. Series A, Mathematical and Physical Sciences*, **351**, 301-330
33. ZHU Y., LUO X.Y., OGDEN R.W., 2008, Asymmetric bifurcations of thick-walled circular cylindrical elastic tubes under axial loading and external pressure, *International Journal of Solids and Structure*, **45**, 3410-3429
34. ZHU Y., LUO X.Y., OGDEN R.W., 2010, Nonlinear axisymmetric deformations of an elastic tube under external pressure, *European Journal of Mechanics – A/Solid*, **29**, 216-229

Manuscript received January 29, 2016; accepted for print July 5, 2016

AN INVESTIGATION OF STRESSES AND DEFORMATION STATES OF CLAMPED ROTATING FUNCTIONALLY GRADED DISKS

AMIT KUMAR THAWAIT, LAKSHMAN SONDHI

Department of Mechanical Engineering, Shri Shankaracharya Technical Campus (SSGI), Bhilai, India

e-mail: amkthawait@gmail.com; lsondhii@gmail.com

SHUBHASHIS SANYAL, SHUBHANKAR BHOWMICK

Department of Mechanical Engineering, National Institute of Technology (NIT), Raipur, India

The present study deals with the linear elastic analysis of variable thickness rotating disks made of functionally graded materials (FGMs) by the finite element method. The disks have radially varying material properties according to an exponential law, which is achieved by the element based grading of the material properties on the meshed domain. The results are reported for three types of thickness profiles, namely, uniform, linearly varying and concave thickness, having their mass constant. The disks are subjected to the clamped boundary condition at the inner surface and the free boundary condition at the outer surface. The obtained results show that in a variable thickness rotating disk, deformation and stresses are less as compared to the uniform thickness disk.

Keywords: functionally graded material (FGM), linear elastic analysis, annular rotating disk, variable thickness rotating disk, finite element method (FEM)

1. Introduction

Functionally graded materials (FGMs) are special composite materials that have continuous and smooth spatial variations of physical and mechanical properties. Functionally graded components, in recent years, are widely used in space vehicles, aircrafts, nuclear power plants and many other engineering applications. Rotating disks, made up of such a FGM are widely used in the field of marine, mechanical and aerospace industry including gas turbines, gears, turbo-machinery, etc. The stresses due to centrifugal load in rotating components have important effects on their strength and safety. Thus, control and optimization of stress and displacement fields can help one to reduce the overall payload in industries. Optimization of the stress to strength ratio is done by varying the material property and thickness of the disk. Disks made up of functionally graded materials and of variable thickness, have significant stress reduction over the disks made up of homogeneous materials and of uniform thickness. Therefore, a higher limit speed and higher pressure is permissible for FGM disks.

A few researchers have reported works on analysis of FGM disks, plates, shells, beams and bars by analytical and finite element methods. Eraslan (2003) obtained analytical solutions for the elastic plastic stress distribution in rotating variable thickness annular disks. Thickness of the disks had parabolic variation and the analysis was based on the Tresca's yield criterion. Bayat *et al.* (2009) reported work on analysis of a variable thickness FGM rotating disk. Material properties varied according to power law and the disk was subjected to both the mechanical and thermal loads. Afsar and Go (2010) analyzed a rotating FGM circular disk subjected to mechanical as well as thermal load by the finite element method. The disk had exponentially varying

material properties in the radial direction. The inner surface was made up of Al_2O_3 having fix boundary condition and the outer surface was made up of Al having free boundary condition. The disk was subjected to a thermal load along with centrifugal load due to non uniform temperature distribution. The axisymmetric problem was formulated in terms of a second order ordinary differential equation and was solved by the finite element method. Callioglu *et al.* (2011a) analyzed functionally a graded rotating annular disk subjected to internal pressure and various temperature distributions such as uniform temperature, linearly increasing and decreasing temperatures in the radial direction. An analytical thermoelasticity solution for a disk made of functionally graded materials (FGMs) was presented by Callioglu (2011). Bayat *et al.* (2011) investigated displacement and stress behavior of a functionally graded rotating disk of variable thickness by a semi analytical method. Radially varying one dimensional FGM was taken and material properties varied according to a power law and the Mori-Tanaka scheme. A disk subjected to centrifugal load was analyzed for the fixed boundary condition at the inner surface and the free boundary condition at the outer surface. The results were reported for both metal-ceramic and ceramic-metal disks and, a comparison was made for uniform and variable thickness disks. Callioglu *et al.* (2011b) analyzed thin FGM disks. Density and modulus of elasticity of them varied according to a power law in an FGM of aluminum ceramic. The effect of the grading parameter on displacement and stresses was investigated. Sharma *et al.* (2012) worked on the analysis of stresses, displacements and strains in a thin circular functionally graded material (FGM) disks by the finite element method. The disk were subjected to mechanical as well as thermal loads. Ali *et al.* (2012) reported a study on the elastic analysis of two sigmoid FGM rotating disks. Metal-ceramic-metal disks were analyzed for both uniform and variable thickness disks and effect of grading index on the displacement and stresses was investigated. Nejad *et al.* (2013) found a closed-form analytical solution for an exponentially varying FGM disk which was subjected to internal and external pressure.

In his recent work, Zafarmand and Hassani (2014) worked on elastic analysis of two-dimensional functionally graded rotating annular and solid disks with variable thickness. Axisymmetric conditions were assumed for the two-dimensional functionally graded disk and the graded finite element method (GFEM) was applied to solve the equations. Rosyid *et al.* (2014) worked on finite element analysis of nonhomogeneous rotating disk with arbitrarily variable thickness. Three types of grading laws, namely, power law, sigmoid and exponential distribution laws were considered for the volume fraction distributions. The work included parametric studies performed by varying volume fraction distributions and boundary conditions. Zafarmand and Kadkhodayan (2015) investigated a nonlinear elasticity solution of functionally graded nanocomposite rotating thick disks with variable thickness reinforced with single-walled carbon nanotubes (SWCNTs). The derived governing nonlinear equations were based on the axisymmetric theory of elasticity with the geometric nonlinearity in axisymmetric complete form and were solved by a nonlinear graded finite element method (NGFEM). The nonlinear graded finite element method (NGFEM) used in that study was based on the Rayleigh–Ritz energy formulation with the Picard iterative scheme. The results were reported for four different thickness profiles, namely, constant, linear, concave and convex.

In the present research work, stress and deformation analysis of annular rotating FGM disks is reported, which is based on the element based grading of material properties. Uniform as well as variable thickness disks, made of exponentially varying FGMs, are analyzed. The disks are subjected to centrifugal body load and have the clamped boundary condition at the inner surface and the free boundary condition at the outer surface. The finite element method based on the principle of stationary total potential is used to analyze disks. Numerical results are evaluated for a uniform, linear varying thickness profile and concave thickness profile disks, and the effect of the thickness parameter on the deformation and stresses is investigated.

2. Geometric modeling

For an annular disk, the governing equation of radially varying thickness is assumed as

$$h(r) = h_0 \left[1 - q \left(\frac{r - a}{b - a} \right)^m \right] \quad (2.1)$$

where a and b are the inner and outer radii, $h(r)$ and h_0 are half of the thickness at the radius r and at the root of the disk, respectively. Symbols m and q are geometric parameters that control the thickness profiles of the disk. For a uniform thickness disk q is taken as zero and for a variable thickness disk, $q > 0$ (Fig. 1b). The value of h_0 is calculated for each thickness profile to get constant mass for all thickness profile disks.

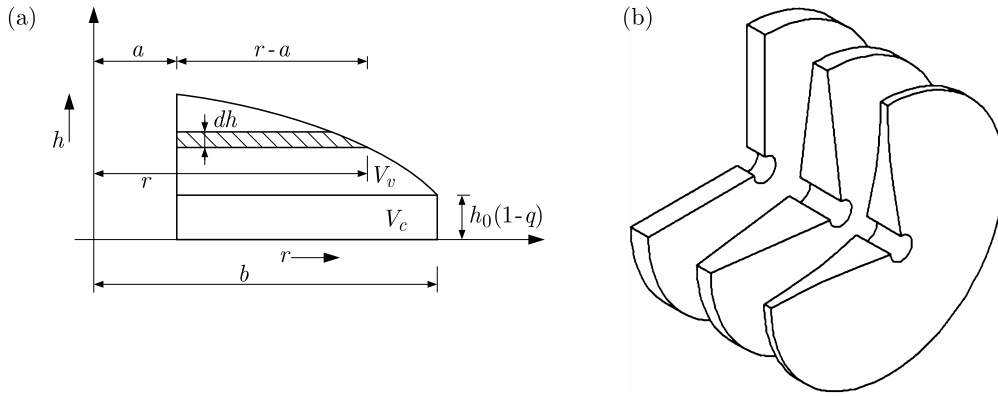


Fig. 1. (a): Geometrical parameters of the variable thickness disk, (b) disks of varying thickness; sectional isometric view

2.1. Calculation of h_0 for the variable thickness profile

Figure 1a shows half of the cross section of the variable thickness disk. The symbol V_c denotes the volume of the disk till height $h_0(1 - q)$ and the symbol V_v is the volume from $h_0(1 - q)$ to height at the inner radius. The symbol V denotes the total volume of the disk

$$V_c = \pi(b^2 - a^2)(1 - q)h_0 \quad V_v = \int_{(1-q)h_0}^{h_0} \pi(r^2 - a^2) dh \quad V = 2(V_c + V_v) \quad (2.2)$$

Since mass of the variable thickness disk equals mass of the uniform thickness disk

$$\rho_1 V = \rho_u V_u \quad (2.3)$$

where ρ_1 and ρ_u are densities of variable thickness and uniform thickness disks, respectively. The symbol V_u is the volume of the uniform thickness disk. Assuming h_0 of the uniform thickness disk as h_u , V_u is obtained as

$$V_u = 2\pi(b^2 - a^2)h_u \quad (2.4)$$

Since density is independent of thickness, it is constant for all thickness profiles, therefore equation (2.3) reduces to

$$V = V_u \quad (2.5)$$

putting the values of V , V_u , V_c , and V_v into equation (2.5)

$$\pi(b^2 - a^2)(1 - q)h_0 + \int_{(1-q)h_0}^{h_0} \pi(r^2 - a^2) dh = \pi(b^2 - a^2)h_u \quad (2.6)$$

Substituting the value of r from equation (2.1) to equation (2.6) and solving the resulting equation for given thickness of the uniform disk and different values of m , we obtain value of h_0 for different thickness profiles.

3. Material modeling

Young's modulus and density of the disk are assumed to vary exponentially along the radial direction as (Afsar and Go, 2010):

$$\begin{aligned} E(r) &= E_0 e^{\beta r} & \rho(r) &= \rho_0 e^{\gamma r} & E_0 &= E_A e^{-\beta a} \\ \rho_0 &= \rho_A e^{-\gamma a} & \gamma &= \frac{1}{a-b} \ln \frac{\rho_A}{\rho_B} & \beta &= \frac{1}{a-b} \ln \frac{E_A}{E_B} \end{aligned} \quad (3.1)$$

where $E(r)$ and $\rho(r)$ are modulus of elasticity and density at the radius r ; E_A , E_B and ρ_A , ρ_B are modulus of elasticity and density at the inner and outer radius, respectively.

4. Finite element modeling

The rotating disk, being thin, is modeled as a plane stress axisymmetric problem. Using quadratic quadrilateral element, the displacement vector \mathbf{u} can be obtained as (Seshu, 2003)

$$\mathbf{u} = \mathbf{N} \boldsymbol{\delta} \quad (4.1)$$

where \mathbf{u} is the element displacement vector, \mathbf{N} is the matrix of quadratic shape functions and $\boldsymbol{\delta}$ is the nodal displacement vector

$$\mathbf{N} = [N_1 \quad N_2 \quad \dots \quad N_8] \quad \boldsymbol{\delta} = \{u_1 \quad u_2 \quad \dots \quad u_8\}^T$$

In natural co-ordinates, the shape functions are given as

$$\begin{aligned} N_1 &= \frac{1}{4}(1 - \xi)(1 - \eta)(-1 - \xi - \eta) & N_2 &= \frac{1}{4}(1 + \xi)(1 - \eta)(-1 + \xi - \eta) \\ N_3 &= \frac{1}{4}(1 + \xi)(1 + \eta)(-1 + \xi + \eta) & N_4 &= \frac{1}{4}(1 - \xi)(1 + \eta)(-1 - \xi + \eta) \\ N_5 &= \frac{1}{2}(1 - \xi^2)(1 - \eta) & N_6 &= \frac{1}{2}(1 + \xi)(1 - \eta^2) \\ N_7 &= \frac{1}{2}(1 - \xi^2)(1 + \eta) & N_8 &= \frac{1}{2}(1 - \xi)(1 - \eta^2) \end{aligned}$$

The strain components are related to elemental displacement components as

$$\begin{aligned} \boldsymbol{\varepsilon} &= \left\{ \varepsilon_r \quad \varepsilon_\theta \right\}^T = \left\{ \frac{\partial u}{\partial r} \quad \frac{u}{r} \right\}^T \\ \left\{ \frac{\partial u}{\partial r} \quad \frac{u}{r} \right\}^T &= \mathbf{B}_1 \left\{ \frac{\partial u}{\partial r} \quad \frac{\partial u}{\partial z} \quad \frac{u}{r} \right\}^T \end{aligned} \quad (4.2)$$

where ε_r and ε_θ are radial and tangential strains, respectively. By transforming the global co-ordinates into natural co-ordinates $(\xi\eta)$, we obtain

$$\begin{aligned} \left\{ \frac{\partial u}{\partial r} \quad \frac{\partial u}{\partial z} \quad \frac{u}{r} \right\}^T &= \mathbf{B}_2 \left\{ \frac{\partial u}{\partial \xi} \quad \frac{\partial u}{\partial \eta} \quad \frac{u}{r} \right\}^T \\ \left\{ \frac{\partial u}{\partial \xi} \quad \frac{\partial u}{\partial \eta} \quad \frac{u}{r} \right\}^T &= \mathbf{B}_3 \left\{ u_1 \quad u_2 \quad \dots \quad u_8 \right\}^T \end{aligned} \quad (4.3)$$

The above elemental strain-displacement relationships can be written as

$$\boldsymbol{\varepsilon} = \mathbf{B}\boldsymbol{\delta}^e \quad (4.4)$$

where \mathbf{B} is the strain-displacement relationship matrix which contains derivatives of the shape functions. For a quadratic quadrilateral element, it is calculated as

$$\mathbf{B} = \mathbf{B}_1\mathbf{B}_2\mathbf{B}_3 \quad (4.5)$$

and

$$\mathbf{B}_1 = \begin{bmatrix} 1 & 0 & 0 \\ 0 & 0 & 1 \end{bmatrix} \quad \mathbf{B}_2 = \begin{bmatrix} \frac{J_{22}}{|\mathbf{J}|} & \frac{-J_{12}}{|\mathbf{J}|} & 0 \\ -\frac{J_{21}}{|\mathbf{J}|} & \frac{J_{11}}{|\mathbf{J}|} & 0 \\ \frac{J_{22}}{|\mathbf{J}|} & \frac{J_{11}}{|\mathbf{J}|} & 1 \end{bmatrix}$$

where \mathbf{J} is the Jacobian matrix used to transform the global co-ordinates into natural co-ordinates. It is given as

$$\mathbf{J} = \begin{bmatrix} \sum_{i=1}^8 \frac{\partial N_i}{\partial \xi} r_i & \sum_{i=1}^8 \frac{\partial N_i}{\partial \xi} z_i \\ \sum_{i=1}^8 \frac{\partial N_i}{\partial \eta} r_i & \sum_{i=1}^8 \frac{\partial N_i}{\partial \eta} z_i \end{bmatrix} \quad \mathbf{B}_3 = \begin{bmatrix} \frac{\partial N_1}{\partial \xi} & \frac{\partial N_2}{\partial \xi} & \dots & \frac{\partial N_8}{\partial \xi} \\ \frac{\partial N_1}{\partial \eta} & \frac{\partial N_2}{\partial \eta} & \dots & \frac{\partial N_8}{\partial \eta} \\ \frac{N_1}{r} & \frac{N_2}{r} & \dots & \frac{N_8}{r} \end{bmatrix} \quad (4.6)$$

From Hooke's law, the components of stresses in the radial and circumferential direction are related to the components of total strain as

$$\varepsilon_r = \frac{1}{E}(\sigma_r - \nu\sigma_\theta) \quad \varepsilon_\theta = \frac{1}{E}(\sigma_\theta - \nu\sigma_r) \quad (4.7)$$

By solving the above equations, the stress-strain relationship can be obtained as follows

$$\sigma_r = \frac{E(r)}{(1-\nu)^2}(\varepsilon_r + \nu\varepsilon_\theta) \quad \sigma_\theta = \frac{E(r)}{(1-\nu)^2}(\varepsilon_\theta + \nu\varepsilon_r) \quad (4.8)$$

In the standard finite element matrix notation, the above stress strain relations can be written as

$$\boldsymbol{\sigma} = \mathbf{D}(r)\boldsymbol{\varepsilon} \quad (4.9)$$

where

$$\boldsymbol{\sigma} = \left\{ \sigma_r \quad \sigma_\theta \right\}^T \quad \mathbf{D}(r) = \frac{E(r)}{(1-\nu)^2} \begin{bmatrix} 1 & \nu \\ \nu & 1 \end{bmatrix} \quad \boldsymbol{\varepsilon} = \left\{ \varepsilon_r \quad \varepsilon_\theta \right\}^T$$

Upon rotation, the disk experiences a body force which under constrained boundary results in deformation and stores internal strain energy U

$$U = \frac{1}{2} \int_V \boldsymbol{\varepsilon}^T \boldsymbol{\sigma} dv \quad (4.10)$$

The work potential due to body force resulting from centrifugal action is given by

$$V = - \int_V \boldsymbol{\delta}^T \mathbf{q}_v dv \quad (4.11)$$

Upon substituting Eq. (4.4) and (4.9) into Eq. (4.10) and Eq. (4.11), the elemental strain energy and work potential are given by

$$U^e = \int_V \pi r h_r \boldsymbol{\delta}^{eT} \mathbf{B}^T \mathbf{D}(r) \mathbf{B} \boldsymbol{\delta}^e dr \quad V^e = -2 \int_V \pi r h_r \boldsymbol{\delta}^{eT} \mathbf{N}^T \mathbf{q}_v dr \quad (4.12)$$

For a disk rotating at ω [rad/s], the body force vector for each element is given by

$$\mathbf{q}_v = \begin{Bmatrix} \rho(r) \omega^2 r \\ 0 \end{Bmatrix} \quad (4.13)$$

The total potential of the element is obtained from Eqs. (4.12)

$$\pi_p^e = \frac{1}{2} \boldsymbol{\delta}^{eT} \mathbf{K}^e \boldsymbol{\delta}^e - \boldsymbol{\delta}^{eT} \mathbf{f}^e \quad (4.14)$$

Here, defining the element stiffness matrix \mathbf{K}^e and the element load vector \mathbf{f}^e as

$$\mathbf{K}^e = 2 \int_V \pi r h_r \mathbf{B}^T \mathbf{D}(r) \mathbf{B} dr \quad \mathbf{f}^e = 2 \int_V \pi r h_r \mathbf{N}^T \mathbf{q}_v dr \quad (4.15)$$

In FEM, the functional grading is popularly carried out by assigning the average material properties over a given geometry followed by adhering the geometries, thus resulting into layered functional grading of material properties. The downside of this approach is that it yields singular field variable values at the boundaries of the glued geometries. To get better results, it is an established practice to divide the total geometry into very fine geometries. However, a better approach is to assign the average material properties to the elements of mesh of the single geometry. This is, in other words, better described as assigning material properties to the finite elements instead of geometry. In Eq. (4.9), the matrix $\mathbf{D}(r)$, being a function of r , is calculated numerically at each node, and this yields continuous material property variation throughout the geometry. The element matrices are then assembled to give the global stiffness matrix and the global load vector, respectively.

The element based grading of the material property yields an appropriate approach of functional grading as the shape functions in the elemental formulations being co-ordinate functions make it easier to implement the same (Kim and Paulino, 2002)

$$\phi^e = \sum_{i=1}^8 \phi_i N_i \quad (4.16)$$

where ϕ_e is the material property of the element, ϕ_i is the material property at the node i , and N_i is the shape function.

Total potential energy of the disk is given by

$$\pi_p = \sum \pi_p^e = \frac{1}{2} \boldsymbol{\delta}^T \mathbf{K} \boldsymbol{\delta} - \boldsymbol{\delta}^T \mathbf{F} \quad (4.17)$$

where \mathbf{K} is global stiffness matrix, \mathbf{F} is global load vector

$$\mathbf{K} = \sum_{n=1}^N \mathbf{K}^e \quad \mathbf{F} = \sum_{n=1}^N \mathbf{f}^e$$

and N is number of elements.

Using the Principle of Stationary Total Potential (PSTP), the total potential is set to be stationary with respect to small variation in the nodal degree of freedom, that is

$$\frac{\partial \pi_p}{\partial \boldsymbol{\delta}^T} = \mathbf{0} \quad (4.18)$$

From above, the system of simultaneous equations is obtained as follows

$$\mathbf{K} \boldsymbol{\delta} = \mathbf{F} \quad (4.19)$$

5. Results and discussion

5.1. Validation

A numerical problem of reference (Bayat *et al.*, 2011) is modeled and analyzed, and the comparison is shown in Fig. 2 for the validation purpose. In the reference rotating disks having uniform and concave thickness, the profiles are analyzed. Gradation of the material properties is done by the Mori-Tanaka scheme and comparison is made for $n = 0$ for ceramic-metal and metal-ceramic disks.

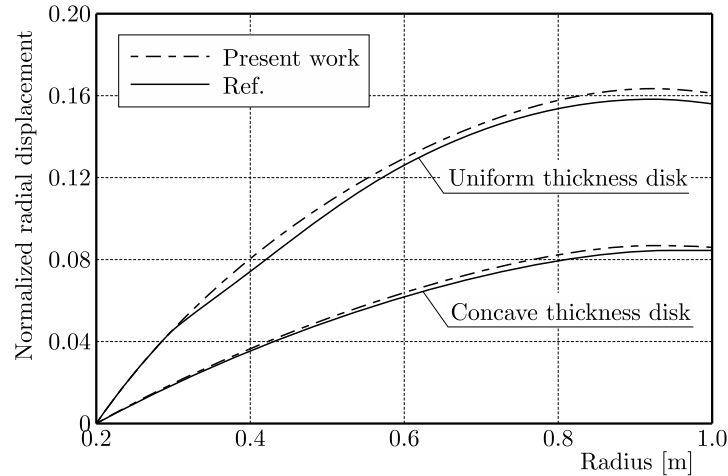


Fig. 2. Comparison of the results of the current work with the reference ones (Bayat *et al.*, 2011)

5.2. Numerical results

Rotating annular disks made of aluminum and alumina ceramic are analyzed, and the distribution of resulting displacement and stresses are presented for different thickness profiles. The material properties are graded according to an exponential law as discussed in Section 3. Figures 3a and 3b show the distribution of Young's modulus and density of the exponential

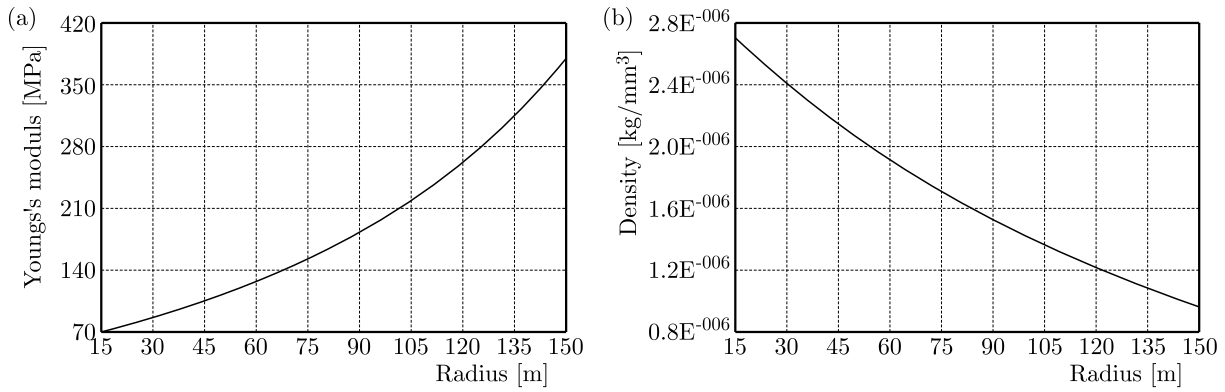


Fig. 3. Radial distribution of Young's modulus (a) and of density (b)

FGM considered here. The properties of aluminum and alumina ceramic are given as (Afsar and Go, 2010): $E_{Al} = 71.0$ MPa, $E_{cer} = 380$ MPa, $\rho_{Al} = 2.7$ g/cm³, $\rho_{cer} = 0.96$ g/cm³ and $\vartheta = 0.3$.

In the present numerical problem, the inner diameter of the disks is taken as 15 mm and outer diameter 150 mm; $q = 0.7$ and h_u is taken as 5 mm, h_0 for linear and concave thickness profiles are obtained as 9.0164 mm and 10.9416 mm from Eq. (2.6) for $m = 1$ and 0.5, respectively. The disks have an angular velocity of 100 rad/s.

Figures 4 and 5 show the distribution of radial displacement, radial stress, tangential stress and von Mises stress, respectively, along the radial direction. It is observed that the uniform thickness disk has highest deformation and stresses as compared to the linear thickness profile and concave thickness profile disk. Stresses and deformations are less near the inner radius and higher near the outer radius for the concave thick disk as compared to the linear disk. This is because of the fact that the concave thick disk has greater thickness near the root as compared to the linear thick disk. The radial displacement is minimum, that is zero at the inner surface and the radial stress is zero at the outer surface for all thickness profiles, which confirms the clamped boundary condition at the inner surface and the free boundary condition at the outer surface applied on the disks. The tangential stress is maximum at the outer radius for all thickness profiles, which corresponds to the complete ceramic material. Since ceramics have low tensile strength, to withstand higher stresses at higher speeds, sufficient thickness at the outer radius should be provided, which means that the value of geometric parameter q in equation (2.1) should be taken smaller at higher speeds. Further it can be seen that the radial stress is higher as compared to the tangential and von Mises stresses for all thickness profiles. Therefore, it is suggested that during designing of rotating disks, the radial stress should be taken as the critical limit stress, and the concave thickness profile should be selected.

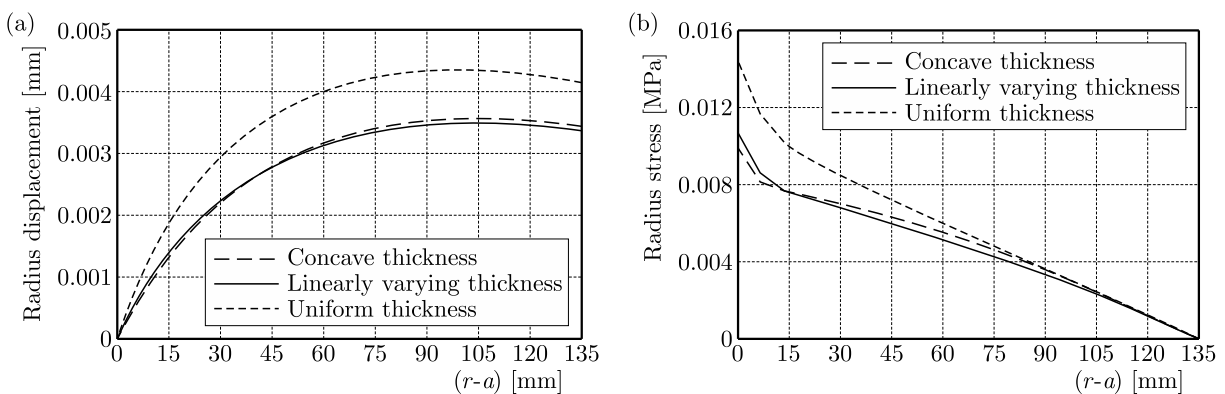


Fig. 4. Distribution of: (a) radial displacements, (b) radial stress

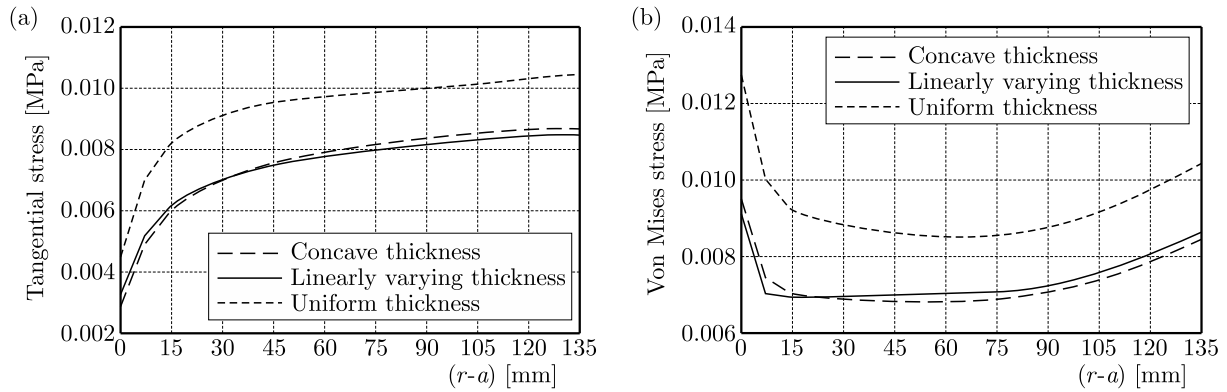


Fig. 5. Distribution of: (a) tangential stress, (b) von Mises stress

6. Conclusion

The present work proposes a study using the element based gradation of a varying material property of rotating disks and reports the stress and deformation behavior of uniform and variable thickness clamped rotating disks of exponentially graded FGMs. The element based grading of the material property yields an appropriate approach of functional grading as the shape functions in elemental formulations being co-ordinate functions make it easier to implement the same. The layered functional grading over a discrete area instead of elements, offers singularities in the field variables at adjoining lines or surfaces. The results obtained are found to be in good agreement with the established reports. Further, it is observed that varying geometry of FGM disks results into lower stress states in the disks and, hence, it can be concluded that variable thickness disks possess better strength than uniform disks of the same mass.

References

1. AFSAR A.M., GO J., 2010, Finite element analysis of thermoelastic field in a rotating FGM circular disk, *Applied Mathematical Modelling*, **34**, 3309-3320
2. ALI A., BAYAT M., SAHARI B.B., SALEEM M., ZAROOG O.S., 2012, The effect of ceramic in combinations of two sigmoid functionally graded rotating disks with variable thickness, *Scientific Research and Essays*, **7**, 25, 2174-2188.
3. BAYAT M., SAHARI B.B., SALEEM M., DEZVAREH E., MOHAZZAB A.H., 2011, Analysis of functionally graded rotating disks with parabolic concave thickness applying an exponential function and the Mori-Tanaka scheme, *IOP Conference Series: Materials Science and Engineering*, **17**, 1-11
4. BAYAT M., SALEEM M., SAHARI B.B., HAMOUDA A.M.S., MAHDI E., 2009, Mechanical and thermal stresses in a functionally graded rotating disk with variable thickness due to radially symmetry loads, *International Journal of Pressure Vessels and Piping*, **86**, 357-372
5. CALLIOGLU H., 2011, Stress analysis in a functionally graded disc under mechanical loads and a steady state temperature distribution, *Sadhana*, **36**, 53-64
6. CALLIOGLU H., BEKTAS N.B., SAYER M., 2011a, Stress analysis of functionally graded rotating discs: analytical and numerical solutions, *Acta Mechanica Sinica*, **27**, 950-955
7. CALLIOGLU H., SAYER M., DEMIR E., 2011b, Stress analysis of functionally graded discs under mechanical and thermal loads, *Indian Journal of Engineering and Material Sciences*, **18**, 111-118
8. ERASLAN A.N., 2003, Elastic-plastic deformations of rotating variable thickness annular disks with free, pressurized and radially constrained boundary conditions, *International Journal of Molecular Sciences*, **45**, 643-667

9. NEJAD A., ABEDI M., HASSAN M., GHANNAD M., 2013, Elastic analysis of exponential FGM disks subjected to internal and external pressure, *Central European Journal of Engineering*, **3**, 459-465
10. ROSYID A., SAHEB M.E., YAHIA F.B., 2014, Stress analysis of nonhomogeneous rotating disc with arbitrarily variable thickness using finite element method, *Research Journal of Applied Sciences, Engineering and Technology*, **7**, 3114-3125
11. SESHU P., 2003, *A Text Book of Finite Element Analysis*, PHI Learning Pvt. Ltd.
12. SHARMA J.N., SHARMA D., KUMAR S., 2012, Stress and strain analysis of rotating FGM Thermoelastic circular disk by using FEM, *International Journal of Pure and Applied Mathematics*, **74**, 3, 339-352
13. ZAFARMAND H., HASSANI B., 2014, Analysis of two-dimensional functionally graded rotating thick disks with variable thickness, *Acta Mechanica*, **225**, 453-464
14. ZAFARMAND H., KADKHODAYAN M., 2015, Nonlinear analysis of functionally graded nanocomposite rotating thick disks with variable thickness reinforced with carbon nanotubes, *Aerospace Science and Technology*, **41**, 47-54
15. KIM J.H., PAULINO G.H., 2002, Isoparametric graded finite elements for nonhomogeneous isotropic and orthotropic materials, *ASME Journal of Applied Mechanics*, **69**, 502-514

Manuscript received June 1, 2016; accepted for print July 5, 2016

ANALYSIS OF STRAIN LOCALIZATION IN POROUS MEDIA WITH TRANSVERSELY ISOTROPIC ELASTICITY UNDER UNDRAINED CONDITIONS

Y.Q. ZHANG, L.Z. WANG, M. PANG, L.F. FAN

College of Civil Engineering and Architecture, Zhejiang University, Hangzhou, China

e-mail: ppmzju@163.com (M. Pang)

The properties of strain localization for elastic-plastic porous media with transversely isotropic elasticity under undrained conditions are investigated. Under non-associated plasticity and tri-axial stress states, the conditions for strain localization of elastic-plastic porous media are derived, in which the effects of deviation from isotropic elasticity and pore fluid compressibility are included. Based on the Mohr-Coulomb yield criterion, the influences of the deviation from isotropic elasticity and pore fluid compressibility on the direction angle of localized band initiation and the corresponding critical hardening modulus for the case of plane strain are discussed. As a result, the properties of strain localization are dependent upon the deviation from isotropic elasticity and pore fluid compressibility. The deviation from isotropic elasticity and pore fluid compressibility has significant impacts on the direction angle of localized band initiation and the corresponding critical hardening modulus.

Keywords: porous medium, strain localization, transverse isotropic elasticity, undrained condition, pore fluid compressibility

1. Introduction

Strain localization of plastic flow into localized deformation bands is a typical feature of geomaterials such as rocks and soils undergoing non-homogeneous deformation. The onset of localized bands is a failure precursor as it signifies the initiation of an emerging localized failure mechanism. Strain localization is mathematically described as the inception of a discontinuous bifurcation in the form of a jump in the velocity gradient field within classical rate independent continuum theory. Analysis of strain localization may provide insight into the failure mechanism of engineering materials. Over the last decades, much attention has been drawn to the field of strain localization (Ottosen and Runesson, 1991; Bigoni and Loret, 1999; Rizzi and Loret, 1999; Zhang and Schrefler, 2001; Zhang *et al.*, 2002; Longere and Dragon, 2007; Alyavuz and Gultop, 2009; Gao and Zhao, 2013). A suitable tool for delineating localization in solid mechanics is on the basis of strain rate discontinuity in continuum theory, and its basic principles were developed by Thomas (1961), Mandel (1962, 1964), and Rice (1976).

For a wide variety of constitutive models, conditions for the onset of strain localization were obtained by Ottosen and Runesson (1991), Neilsen and Schreyer (1993), Runesson *et al.* (1996), Zhang *et al.*, 2002. In these studies, it was assumed that elasticity remained isotropic during the loading process. As a matter of fact, transversely isotropic materials are of primary interest in many engineering applications. Rudnicki (1977) proposed a transversely isotropic constitutive relation and elucidated properties of deformation localization of brittle rocks. Following the associated plastic flow rule, Rizzi and Loret (1997) presented the localization condition for an elastoplastic von Mises material with transversely isotropic elasticity under uniaxial tension.

With associated plasticity and uniaxial tension, further developments concerning both transversely isotropic elasticity and plasticity were given by Loret and Rizzi (1997). Rudnicki (2002) derived the conditions for localized deformation in a transversely isotropic material under axisymmetric compression. For non-associated plasticity, Zhang *et al.* (2003) deduced the general description of properties of strain localization for elastoplastic materials with transversely isotropic elasticity subjected to tri-axial stress states. It is noted that these researches involves only the behaviour of one-phase transversely isotropic materials. As a matter of fact, the localization phenomena are relevant also for porous media with pores filled with a fluid. Based on the specific constitutive model developed by Rudnicki (1977) for transversely isotropic brittle rock, Zhang *et al.* (2005) analysed material instabilities of saturated multiphase porous media.

In this paper, the localization analysis is performed for elastic-plastic saturated porous media with transversely isotropic elasticity under undrained conditions. The general description of the properties of strain localization is deduced for porous media which follow non-associated plasticity and are subjected to tri-axial stress states. The effects of deviation from isotropic elasticity and pore fluid compressibility at plane strain are investigated. The porous body is assumed to undergo small deformations, and thus the nominal time rate is used instead of any objective rate measure.

2. Elastic-plastic constitutive relations under undrained conditions

For saturated porous media (e.g. soils), the deformation and strength under loading is not determined directly by the total stress but the effective stress. With compression being defined as positive, the effective stress can be expressed as

$$\boldsymbol{\sigma}' = \boldsymbol{\sigma} - p\mathbf{I} \quad (2.1)$$

where $\boldsymbol{\sigma}$ is the total stress tensor, $\boldsymbol{\sigma}'$ is the effective stress tensor, p is the pore fluid pressure, and \mathbf{I} is the second-order identity tensor. It is supposed that $\boldsymbol{\sigma}'$ is responsible for deformation in the skeleton of the porous solid, whereas p is responsible for compression of the pore fluid.

Under undrained conditions, it has the form

$$\dot{p} = K^f \mathbf{I} : \dot{\boldsymbol{\epsilon}} \quad (2.2)$$

where $\dot{\boldsymbol{\epsilon}}$ is the strain rate tensor, K^f is the compression modulus of the pore fluid, and the symbol ' $:$ ' is the inner product with double index contraction. It should be pointed out that the effective stress principle defined by Eq. (2.1) is valid when the degree of saturation varies from 0.85 to 1.0. In this case, K^f can be regarded as the bulk modulus of the two-phase mixture comprising liquid/air in the pores, and generally it may be two or three orders of magnitude smaller than that for the case of full saturation (Runesson *et al.*, 1996).

Generally, the relationship between the total stress rate $\dot{\boldsymbol{\sigma}}$ and the strain rate $\dot{\boldsymbol{\epsilon}}$ for plastic loading can be described by the incrementally linear relationship (Runesson *et al.*, 1996)

$$\dot{\boldsymbol{\sigma}} = \mathbf{D}_u : \dot{\boldsymbol{\epsilon}} \quad (2.3)$$

where \mathbf{D}_u is the total tangent stiffness tensor pertinent to the undrained condition, which is given by

$$\mathbf{D}_u = \mathbf{D}' + K^f \mathbf{I} \otimes \mathbf{I} \quad (2.4)$$

where \mathbf{D}' denotes the effective elastic-plastic tangent stiffness tensor, and the symbol \otimes designates the outer product of two tensors. Defining the yield function F and the plastic potential G in the effective stress space, we have

$$\mathbf{D}' = \mathbf{E}' - \frac{1}{A'} (\mathbf{E}' : \mathbf{Q}') \otimes (\mathbf{P}' : \mathbf{E}') \quad (2.5)$$

where \mathbf{P}' and \mathbf{Q}' are the unit outward normals to the yield surface and the plastic potential, respectively, and they are defined as

$$\mathbf{P}' = \frac{\partial F}{\partial \boldsymbol{\sigma}'} / \left\| \frac{\partial F}{\partial \boldsymbol{\sigma}'} \right\| \quad \mathbf{Q}' = \frac{\partial G}{\partial \boldsymbol{\sigma}'} / \left\| \frac{\partial G}{\partial \boldsymbol{\sigma}'} \right\| \quad (2.6)$$

where $\|\cdot\|$ stands for a norm of a tensor. The positive parameter A' is defined as $A' = H' + \mathbf{P}' : \mathbf{E}' : \mathbf{Q}'$, where H' is the generalized plastic modulus and \mathbf{E}' is the effective elastic stiffness tensor.

For a transversely isotropic elastic material, it has the rotational symmetry property with reference to a certain axis. The plane perpendicular to this axis is called the basal plane while planes containing the axis of symmetry will be named the zonal planes. To better express material properties componentwise, the cartesian axes $(\mathbf{e}_1, \mathbf{e}_2, \mathbf{e}_3)$ are adopted, where \mathbf{e}_1 and \mathbf{e}_2 are two arbitrary orthogonal unit vectors of the basal plane, and the unit vector \mathbf{e}_3 denotes the axis of rotational symmetry. Thus, the stiffness \mathbf{E}' can take the form (Rizzi and Loret, 1997)

$$\mathbf{E}' = c_1 \mathbf{I} \otimes \mathbf{I} + c_2 \mathbf{I} \overline{\otimes} \mathbf{I} + c_3 (\mathbf{I} \otimes \mathbf{M} + \mathbf{M} \otimes \mathbf{I}) + c_4 \mathbf{M} \otimes \mathbf{M} + c_5 (\mathbf{I} \overline{\otimes} \mathbf{M} + \mathbf{M} \overline{\otimes} \mathbf{I}) \quad (2.7)$$

where the tensor $\mathbf{M} = \mathbf{e}_3 \otimes \mathbf{e}_3$, c_i ($i \in [1, 5]$) are five material constants, and the symbol $\overline{\otimes}$ denotes a symmetrized outer product, and it has $(\mathbf{M} \overline{\otimes} \mathbf{I})_{ijkl} = (M_{ik}I_{jl} + M_{il}I_{jk})/2$.

3. Localization condition for non-associated plasticity

It is known that the strain rate $\dot{\boldsymbol{\varepsilon}}$ across the localized band is discontinuous. Assuming that $\dot{\boldsymbol{\varepsilon}}^i$ and $\dot{\boldsymbol{\varepsilon}}^o$ denote the strain rates inside and outside the band, respectively, it follows from Eq. (2.3) that

$$\dot{\boldsymbol{\sigma}}^i = \mathbf{D}_u^i : \dot{\boldsymbol{\varepsilon}}^i \quad \dot{\boldsymbol{\sigma}}^o = \mathbf{D}_u^o : \dot{\boldsymbol{\varepsilon}}^o \quad (3.1)$$

where $\dot{\boldsymbol{\sigma}}^i$ and $\dot{\boldsymbol{\sigma}}^o$ are the total stress rate inside and outside the localized band, respectively, and \mathbf{D}_u^i and \mathbf{D}_u^o denote the total tangential stiffness tensors inside and outside the band under undrained conditions, respectively. As mentioned by Zhang *et al.* (2003), the difference between the strain rates inside and outside the band is equal to $(\mathbf{m} \otimes \mathbf{n} + \mathbf{n} \otimes \mathbf{m})/2$ with the vector \mathbf{m} the mode of discontinuity of the strain rate and \mathbf{n} the unit normal vector of the band. The traction rate across the band must be unique, namely $\mathbf{n} \cdot (\dot{\boldsymbol{\sigma}}^i - \dot{\boldsymbol{\sigma}}^o) = 0$ with symbol ' \cdot ' the inner product with single index contraction. Moreover, it can be regarded that $\mathbf{D}_u^o = \mathbf{D}_u^i = \mathbf{D}_u$ at the inception of strain localization. Thus, from Eq. (3.1), we have

$$\mathbf{L} \cdot \mathbf{m} = 0 \quad \text{or} \quad \det(\mathbf{L}) = 0 \quad (3.2)$$

which is the necessary condition for strain localization, and the total acoustic tensor under the undrained condition

$$\mathbf{L} = \mathbf{n} \cdot \mathbf{D}_u \cdot \mathbf{n} = \mathbf{L}' + K^f \mathbf{n} \otimes \mathbf{n} \quad (3.3)$$

where \mathbf{L}' is the effective acoustic tensor, which can be expressed as

$$\mathbf{L}' = \mathbf{n} \cdot \mathbf{D}' \cdot \mathbf{n} = \mathbf{L}'_e - \frac{1}{A'} \mathbf{a} \otimes \mathbf{b} \quad (3.4)$$

where \mathbf{L}'_e denotes the effective elastic acoustic tensor, which is defined as

$$\mathbf{L}'_e = \mathbf{n} \cdot \mathbf{E}' \cdot \mathbf{n} \quad (3.5)$$

Additionally, the vectors \mathbf{a} and \mathbf{b} are formulated by

$$\mathbf{a} = \mathbf{n} \cdot \mathbf{E}' : \mathbf{Q}' \quad \mathbf{b} = \mathbf{P}' : \mathbf{E}' \cdot \mathbf{n} \quad (3.6)$$

Introduction of Eq. (2.7) into Eq. (3.5) yields (Zhang *et al.*, 2003)

$$\mathbf{L}'_e = \alpha_1 \mathbf{I} + \alpha_2 \mathbf{n} \otimes \mathbf{n} + \alpha_3 (\mathbf{e}_3 \otimes \mathbf{n} + \mathbf{n} \otimes \mathbf{e}_3) + \alpha_4 \mathbf{e}_3 \otimes \mathbf{e}_3 \quad (3.7)$$

with

$$\begin{aligned} \alpha_1 &= \frac{c_2}{2} + \frac{c_5}{2} (\mathbf{e}_3 \cdot \mathbf{n})^2 & \alpha_2 &= c_1 + \frac{c_2}{2} \\ \alpha_3 &= \left(c_3 + \frac{c_5}{2} \right) (\mathbf{e}_3 \cdot \mathbf{n}) & \alpha_4 &= \left(\frac{c_5}{2} + c_4 \right) (\mathbf{e}_3 \cdot \mathbf{n})^2 \end{aligned} \quad (3.8)$$

Substitution of Eq. (2.7) into Eq. (3.6) leads to

$$\mathbf{a} = \eta_1 \mathbf{n} + \eta_2 \mathbf{Q}' \cdot \mathbf{n} + \eta_3 \mathbf{e}_3 + \eta_4 \mathbf{Q}' \cdot \mathbf{e}_3 \quad \mathbf{b} = \chi_1 \mathbf{n} + \chi_2 \mathbf{P}' \cdot \mathbf{n} + \chi_3 \mathbf{e}_3 + \chi_4 \mathbf{P}' \cdot \mathbf{e}_3 \quad (3.9)$$

with

$$\begin{aligned} \eta_1 &= c_1 \operatorname{tr} \mathbf{Q}' + c_3 (\mathbf{e}_3 \cdot \mathbf{Q}' \cdot \mathbf{e}_3) & \eta_2 &= c_2 \\ \eta_3 &= [c_3 \operatorname{tr} \mathbf{Q}' + c_4 (\mathbf{e}_3 \cdot \mathbf{Q}' \cdot \mathbf{e}_3)] (\mathbf{e}_3 \cdot \mathbf{n}) + c_5 (\mathbf{n} \cdot \mathbf{Q}' \cdot \mathbf{e}_3) & \eta_4 &= c_5 (\mathbf{e}_3 \cdot \mathbf{n}) \end{aligned} \quad (3.10)$$

and

$$\begin{aligned} \chi_1 &= c_1 \operatorname{tr} \mathbf{P}' + c_3 (\mathbf{e}_3 \cdot \mathbf{P}' \cdot \mathbf{e}_3) & \chi_2 &= c_2 \\ \chi_3 &= [c_3 \operatorname{tr} \mathbf{P}' + c_4 (\mathbf{e}_3 \cdot \mathbf{P}' \cdot \mathbf{e}_3)] (\mathbf{e}_3 \cdot \mathbf{n}) + c_5 (\mathbf{n} \cdot \mathbf{P}' \cdot \mathbf{e}_3) & \chi_4 &= c_5 (\mathbf{e}_3 \cdot \mathbf{n}) \end{aligned} \quad (3.11)$$

where the symbol “tr” denotes the trace operator of tensors.

When the tensor \mathbf{L} is singular, the corresponding hardening modulus can be obtained by

$$H' = \mathbf{a} \cdot \mathbf{R}'_e \cdot \mathbf{b} - \psi \frac{(\mathbf{a} \cdot \mathbf{R}'_e \cdot \mathbf{n})(\mathbf{b} \cdot \mathbf{R}'_e \cdot \mathbf{n})}{\mathbf{n} \cdot \mathbf{R}'_e \cdot \mathbf{n}} - \mathbf{P}' : \mathbf{E}' : \mathbf{Q}' = h_n - h_E \quad (3.12)$$

where $\psi = K^f \mathbf{n} \cdot \mathbf{R}'_e \cdot \mathbf{n} / (1 + K^f \mathbf{n} \cdot \mathbf{R}'_e \cdot \mathbf{n})$, and

$$h_n = \mathbf{a} \cdot \mathbf{R}'_e \cdot \mathbf{b} - \psi \frac{(\mathbf{a} \cdot \mathbf{R}'_e \cdot \mathbf{n})(\mathbf{b} \cdot \mathbf{R}'_e \cdot \mathbf{n})}{\mathbf{n} \cdot \mathbf{R}'_e \cdot \mathbf{n}} \quad h_E = \mathbf{P}' : \mathbf{E}' : \mathbf{Q}' \quad (3.13)$$

where \mathbf{R}'_e is the inverse of the effective elastic acoustic tensor \mathbf{L}'_e , which is expressed as (Zhang *et al.*, 2003)

$$\mathbf{R}'_e = \beta_1 \mathbf{I} + \beta_2 \mathbf{n} \otimes \mathbf{n} + \beta_3 (\mathbf{e}_3 \otimes \mathbf{n} + \mathbf{n} \otimes \mathbf{e}_3) + \beta_4 \mathbf{e}_3 \otimes \mathbf{e}_3 \quad (3.14)$$

where

$$\begin{aligned} \beta_1 &= \frac{1}{\alpha_1} & \beta_2 &= \frac{1}{\alpha_1 \Delta} [-\alpha_2 (\alpha_1 + \alpha_4) + \alpha_3^2] \\ \beta_3 &= \frac{1}{\alpha_1 \Delta} [-\alpha_1 \alpha_3 + (\alpha_2 \alpha_4 - \alpha_3^2) (\mathbf{e}_3 \cdot \mathbf{n})] & \beta_4 &= \frac{1}{\alpha_1 \Delta} [-\alpha_4 (\alpha_1 + \alpha_2) + \alpha_3^2] \end{aligned} \quad (3.15)$$

with

$$\begin{aligned} \Delta &= \frac{1}{2} (c_1 + c_2) (c_2 + c_5) + [(c_3 + c_5) (c_2 - c_3) + c_4 (c_1 + c_2)] (\mathbf{e}_3 \cdot \mathbf{n})^2 \\ &+ \frac{1}{2} [2c_3 (c_3 + 2c_5) - c_4 (2c_1 + c_2) + c_5 (c_4 + 2c_5)] (\mathbf{e}_3 \cdot \mathbf{n})^4 \end{aligned} \quad (3.16)$$

Substituting Eq. (2.7) into Eq. (3.13), we have

$$h_E = c_1(\text{tr } \mathbf{P}')(\text{tr } \mathbf{Q}') + c_2 \mathbf{P}' : \mathbf{Q}' + c_3[(\mathbf{e}_3 \cdot \mathbf{Q}' \cdot \mathbf{e}_3) \text{tr } \mathbf{P}' + (\mathbf{e}_3 \cdot \mathbf{P}' \cdot \mathbf{e}_3) \text{tr } \mathbf{Q}'] \\ + c_4(\mathbf{e}_3 \cdot \mathbf{P}' \cdot \mathbf{e}_3)(\mathbf{e}_3 \cdot \mathbf{Q}' \cdot \mathbf{e}_3) + 2c_5(\mathbf{e}_3 \cdot (\mathbf{P}' \cdot \mathbf{Q}') \cdot \mathbf{e}_3) \quad (3.17)$$

As strain localization may occur along a surface of normal n when the elastoplastic acoustic tensor gets first singular in that direction, the most critical directions \mathbf{n} will be those corresponding to the largest hardening modulus which makes the elastoplastic acoustic tensor singular. Thus, from Eq. (3.12), we have

$$H'_{cr} = \max_{\mathbf{n}, \mathbf{n} \cdot \mathbf{n} = 1} H'(\mathbf{n}) = \max_{\mathbf{n}, \mathbf{n} \cdot \mathbf{n} = 1} (h_{\mathbf{n}}) - h_E \quad (3.18)$$

It is noted from Eq. (2.7) that the material constants c_3 , c_4 , and c_5 can be interpreted as measures of the deviation from isotropic elasticity. When $c_3 = c_4 = c_5 = 0$, Eq. (2.7) reduces to the case of isotropic elasticity. Assuming that λ and μ denote the Lamé coefficients of an isotropic reference elastic material with positive definite elastic stiffness, it has $3\lambda + 2\mu > 0$ and $\mu > 0$ (Zhang *et al.*, 2003). Rizzi and Lorent (1997) carried out numerical simulations on three prototypes of anisotropic materials due to difficulties of theoretical derivations. It was found to include most of the qualitative features common to other simulations for the case of $c_1 = \lambda$, $c_2 = 2\mu$, $c_3 = c_5 = 0$, and $c_4 \neq 0$. As a consequence, the analysis in this study is confined to this case for simplicity in the mathematical derivations. For this case, we have (Zhang *et al.*, 2003)

$$E_L = \frac{\mu(3\lambda + 2\mu) + (\lambda + \mu)c_4}{\lambda + \mu} \quad E_T = \frac{4\mu[\mu(3\lambda + 2\mu) + c_4(\lambda + \mu)]}{4\mu\lambda + \mu + c_4(\lambda + 2\mu)} \\ G_l = G_T = \mu \quad \nu_L = \frac{\lambda}{2(\lambda + \mu)}$$

where E_L and E_T , respectively, denote the longitudinal (or axial) elastic modulus and the transverse (or cross-axial) elastic modulus, G_L and G_T , respectively, denote the longitudinal (or zonal) shear modulus and the transverse (or basal) shear modulus, and ν_L the longitudinal Poisson ratio (representing the contraction in the longitudinal direction due to an imposed traction in the basal plane).

Corresponding to the Loss of Positive Definiteness (LPD) of the elastic stiffness, there is a lower bound for the admissible values of the elastic parameter c_4 , which is herein denoted by c_4^{LPD} and given by

$$c_4 > c_4^{LPD} = -\frac{\mu(3\lambda + 2\mu)}{\lambda + \mu} = -E \quad (3.19)$$

where E is Young's modulus corresponding to the assumed Lamé constants.

In view of the above simplification, it follows from Eq. (3.13) that

$$h_n = U_1 + U_2 - \frac{K^f U_3 U_4}{1 + K^f U_5} \quad (3.20)$$

with

$$U_1 = [2c_1^2 \beta_3 P'_v Q'_v + c_1 c_4 \beta_3 (P'_v Q'_{33} + Q'_v P'_{33})] n_3 + [c_2 c_4 (\beta_1 + \beta_4) (Q'_{33} P'_{3j} n_j + P'_{33} Q'_{3j} n_j) \\ + c_1 c_2 \beta_4 (Q'_v P'_{3j} n_j + P'_v Q'_{3j} n_j)] n_3 + [c_1 c_2 \beta_3 (P'_v + Q'_v) + c_2 c_4 \beta_3 (P'_{33} + Q'_{33})] (n_i Q'_{ij} n_j) n_3 \\ + [c_1^2 \beta_4 P'_v Q'_v + c_1 c_4 (\beta_2 + \beta_4 + \beta_1) (P'_v Q'_{33} + Q'_v P'_{33}) + c_4^2 (\beta_1 + \beta_4) P'_{33} Q'_{33}] n_3^2 \\ + c_2 c_4 \beta_2 (Q'_{33} n_i P'_{ij} n_j + P'_{33} n_i Q'_{ij} n_j) n_3^2 + c_2 c_4 \beta_3 (P'_{33} Q'_{3j} n_j + Q'_{33} P'_{3j} n_j) n_3^2$$

$$\begin{aligned}
U_2 &= c_4^2 \beta_2 Q'_{33} P'_{33} n_3^4 + c_2^2 \beta_4 P'_{3j} n_j Q'_{3k} n_k + c_1 c_2 \beta_3 (Q'_{3j} n_j P'_v + P'_{3j} n_j Q'_v) \\
&\quad + c_2^2 \beta_2 n_i Q'_{ij} n_j n_k P'_{kl} n_l + c_2^2 \beta_1 n_i P'_{ik} Q'_{kj} n_j + c_2^2 \beta_3 (P'_{3j} n_j n_k Q'_{kl} n_l + Q'_{3j} n_j n_k P'_{kl} n_l) \\
&\quad + c_1^2 (\beta_1 + \beta_2) P'_v Q'_v + c_1 c_2 (\beta_1 + \beta_2) (P'_v n_i Q'_{ij} n_j + Q'_v n_i P'_{ij} n_j) \\
&\quad + [c_1 c_4 \beta_3 (Q'_v P'_{33} + P'_v Q'_{33}) + 2c_4^2 \beta_3 Q'_{33} P'_{33}] n_3^3 \\
U_3 &= c_1 Q'_v (\beta_1 + \beta_2 + 2\beta_3 n_3 + \beta_4 n_3^2) + c_2 n_i Q'_{ij} n_j (\beta_1 + \beta_2 + \beta_3 n_3) \\
&\quad + c_2 Q'_{3j} n_j (\beta_3 + \beta_4 n_3) + c_4 Q'_{33} n_3 [\beta_3 + (\beta_1 + \beta_2 + \beta_4) n_3 + \beta_3 n_3^2] \\
U_4 &= c_1 P'_v (\beta_1 + \beta_2 + 2\beta_3 n_3 + \beta_4 n_3^2) + c_2 n_i P'_{ij} n_j (\beta_1 + \beta_2 + \beta_3 n_3) + c_2 P'_{3j} n_j (\beta_3 + \beta_4 n_3) \\
&\quad + c_4 P'_{33} n_3 [\beta_3 + (\beta_1 + \beta_2 + \beta_4) n_3 + \beta_3 n_3^2] \\
U_5 &= \beta_1 + \beta_2 + 2\beta_3 n_3 + \beta_4 n_3^2
\end{aligned}$$

and

$$h_E = c_1 P'_v Q'_v + c_2 P'_{ij} Q'_{ij} + c_4 P'_{33} Q'_{33} \quad (3.21)$$

where the summation convention is adopted for Latin indices, $P'_v = \text{tr } \mathbf{P}'$, and $Q'_v = \text{tr } \mathbf{Q}'$.

When the modulus $K^f = 0$, Eq. (3.20) can be reduced to the solution of the single-phase solid obtained by Zhang *et al.* (2003). When the parameter $c_4 = 0$, Eq. (3.20) can be simplified to the solution given by Runesson *et al.* (1996).

4. Properties of the localized band at plane strain

In the case of plane strain, assuming the stress principal directions are consistent with the symmetrical axes of material and the components n_1 and n_3 are located in the plane of interest, for associated plasticity Eqs. (3.20) and (3.21) can be reduced to

$$h_n = V_1 + V_2 - \frac{K^f (V_3)^2}{1 + K^f V_4} \quad (4.1)$$

with

$$\begin{aligned}
V_1 &= c_1 P'_v (\beta_1 + \beta_2) [c_1 P'_v + 2c_2 (P'_1 n_1^2 + P'_3 n_3^2)] \\
&\quad + c_2^2 (P_1'^2 n_1^2 + P_3'^2 n_3^2) [\beta_1 + \beta_2 (P_1'^2 n_1^2 + P_3'^2 n_3^2)] \\
&\quad + 2\beta_3 [c_1 P'_v + (c_4 + c_2) P'_3] [c_1 P'_v + c_2 (P_1'^2 n_1^2 + P_3'^2 n_3^2)] n_3 \\
V_2 &= [(2c_2 c_4 + c_4^2) (\beta_1 + \beta_4) P_3'^2 + c_1 \beta_4 P'_v (2c_2 P'_3 + c_1 P'_v)] \\
&\quad + 2c_1 c_4 (\beta_1 + \beta_2 + \beta_4) P'_3 P'_v + c_2^2 \beta_4 P_3'^2 n_3^2 + 2c_2 c_4 \beta_2 P'_3 (P_1'^2 n_1^2 + P_3'^2 n_3^2) n_3^2 \\
&\quad + 2c_4 \beta_3 P'_3 (c_2 P'_3 + c_1 P'_v + c_4 P'_3) n_3^3 + c_4^2 \beta_2 P_3'^2 n_3^4 \\
V_3 &= c_1 P'_v (\beta_1 + \beta_2 + 2\beta_3 n_3 + \beta_4 n_3^2) + c_2 (\beta_1 + \beta_2 + \beta_3 n_3) (P_1'^2 n_1^2 + P_3'^2 n_3^2) \\
&\quad + c_2 (\beta_3 + \beta_4 n_3) P'_3 n_3 + c_4 P'_3 n_3 [\beta_3 + (\beta_1 + \beta_2 + \beta_4) n_3 + \beta_3 n_3^2] \\
V_4 &= \beta_1 + \beta_2 + 2\beta_3 n_3 + \beta_4 n_3^2
\end{aligned}$$

and

$$h_E = c_1 P_v'^2 + c_2 (P_1'^2 + P_2'^2 + P_3'^2) + c_4 P_3'^2 \quad (4.2)$$

It should be mentioned that for the present case of plane strain we have

$$n_1^2 + n_3^2 = 1 \quad n_1^2 = 1 - n_3^2 \quad (4.3)$$

Combination of Eqs. (3.8), (3.15), (3.16), (4.1) and (4.3) yields

$$h_{\mathbf{n}} = \frac{1}{u^2 \Delta} \left[u^2 (r_4 n_3^4 + r_2 n_3^2 + r_0) - \frac{K^f (s_5 n_3^5 + s_4 n_3^4 + s_2 n_3^2 + s_0)^2}{\Delta + K^f (u + c_4 n_3^2 - c_4 n_3^4)} \right] \quad (4.4)$$

where

$$\begin{aligned} r_4 &= -P_3'^2 (\lambda + \mu) c_4^2 + [4\mu P_1' P_3' (\lambda + \mu) - 4\mu P_3'^2 (\lambda + \mu) - 4\mu^2 P_1'^2 \\ &\quad - 4\lambda \mu P_1' P_v' - \lambda^2 P_v'^2] c_4 - 4\mu^2 (P_3' - P_1')^2 (\lambda + \mu) \\ r_2 &= (\lambda + 2\mu) P_3'^2 c_4^2 + [4\mu P_3'^2 (\lambda + 2\mu) - 4\mu P_1' P_3' (\lambda + \mu) + 4\mu^2 P_1'^2 \\ &\quad + \lambda^2 P_v'^2 + 4\lambda \mu P_v' P_1' + 2\lambda \mu P_3' P_v'] c_4 + 4\lambda \mu^2 P_v' (P_3' - P_1') \\ &\quad + 4\mu^2 (P_3' - P_1') [(P_3' + P_1') (\lambda + 2\mu) - 2P_1' (\lambda + \mu)] \\ r_0 &= 4\mu^3 P_1'^2 + \lambda^2 \mu P_v'^2 + 4\lambda \mu^2 P_1' P_v' \end{aligned} \quad (4.5)$$

and

$$\begin{aligned} s_5 &= P_3' (\lambda + \mu) c_4^2 & s_4 &= c_4 [P_3' (\lambda + 2\mu) c_4 - \lambda \mu P_v' - 2\mu^2 P_1'] \\ s_2 &= \mu c_4 (\lambda P_v' + 2\mu P_1') + 2\mu^3 (P_3' - P_1') + \mu^2 c_4 P_3' & s_0 &= \mu^2 (\lambda P_v' + 2\mu P_1') \end{aligned} \quad (4.6)$$

Additionally, we have

$$\Delta = \mu (\lambda + 2\mu) + c_4 (\lambda + 2\mu) n_3^2 - c_4 (\lambda + \mu) n_3^4 \quad (4.7)$$

It is seen from Eq. (3.18) that the critical hardening modulus H'_{cr} corresponding to the initiation of strain localization is defined as the constrained maximization of H' over all possible localized band directions \mathbf{n} for a given state. Assuming that the maximum value of H' is reached when $n_3 = n_3^{cr}$, it has $\tan^2 \theta = (n_3^{cr})^2 / [1 - (n_3^{cr})^2]$, where θ denotes the angle in the $\mathbf{e}_1 - \mathbf{e}_3$ plane from the \mathbf{e}_1 -axis to the normal vector (n_1, n_3) as shown in Fig. 1. Then substituting n_3^{cr} into Eq. (4.4) and combining Eq. (4.2), the corresponding maximum value of the hardening modulus H'_{cr} can be obtained.

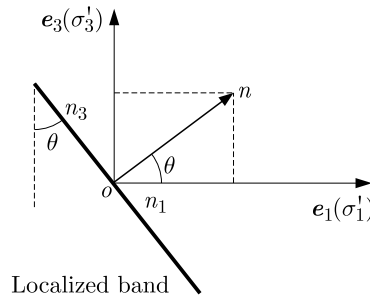


Fig. 1. Geometric relationship among the anisotropy axes, stress principal axes and the localized band direction at plane strain

5. Numerical results and discussions

In this Section, the properties of strain localization at strain plane is investigated based on the Mohr-Coulomb yield criterion. The Mohr-Coulomb yield criterion can be defined by

$$F = \frac{1}{2} (\sigma_I' - \sigma_{III}') + \frac{1}{2} (\sigma_I' + \sigma_{III}') \sin \varphi - c = 0 \quad (5.1)$$

where $\sigma_I' \geq \sigma_{II}' \geq \sigma_{III}'$ are the effective principal stresses (which are taken positive in compression), φ is the angle of internal friction, and c is a cohesion intercept.

As the direction of the effective principal stress σ'_3 is assumed to be consistent with the cartesian axe \mathbf{e}_3 , there exist two situations for the in-plane effective principal stresses, namely $\sigma'_1 \geq \sigma'_3$ and $\sigma'_3 \geq \sigma'_1$. For the situation $\sigma'_1 \geq \sigma'_3$, there are three cases depending on the magnitude of the out-of-plane stress σ'_2 .

Case A

When $\sigma'_1 \geq \sigma'_2 \geq \sigma'_3$, it has $\sigma'_I = \sigma_1$ and $\sigma_{III} = \sigma'_3$, and from Eqs. (2.6) and (5.1), we obtain

$$P'_1 = \frac{\sqrt{2}}{2} \frac{1 + \sin \varphi}{\sqrt{1 + \sin^2 \varphi}} \quad P'_2 = 0 \quad P'_3 = \frac{-\sqrt{2}}{2} \frac{1 - \sin \varphi}{\sqrt{1 + \sin^2 \varphi}} \quad (5.2)$$

and

$$P'_v = \frac{\sqrt{2} \sin \varphi}{\sqrt{1 + \sin^2 \varphi}} \quad (5.3)$$

Substituting Eqs. (5.2) and (5.3) into Eqs. (4.2) and (4.4) and combining Eq. (3.18), the critical hardening modulus and the band direction angle at the onset of strain localization can be determined. Suppose $\lambda/\mu = 1$, we know from Eq. (3.19) that $c_4/\mu > -2.5$. In addition, for soils the magnitude of the ratio $K^f/(2\mu)$ may range from 10^{-1} to 10^3 in practice, which represent extreme states for moduli for partial and full liquid saturation, respectively. Thus, with $\varphi = 10^\circ$, the influences of the parameters c_4 and K^f on the angle θ and the critical hardening modulus H'_{cr} are shown in Figs. 2a and 2b, respectively. As can be seen from Fig. 2a, the angle θ first increases with the increase of the parameter c_4 , and then decreases with its further increase. The influence of the modulus K^f on the angle θ is related to the magnitude of the parameter c_4 . It can be observed from Fig. 2b that at first the critical hardening modulus H'_{cr} becomes larger with the increase of the parameter c_4 , but it becomes smaller with the further increase of the parameter c_4 when $-2.5 < c_4/\mu \leq 0$ or $c_4 \geq 0$. In addition, the critical hardening modulus H'_{cr} generally decreases with the increase of the modulus K^f .

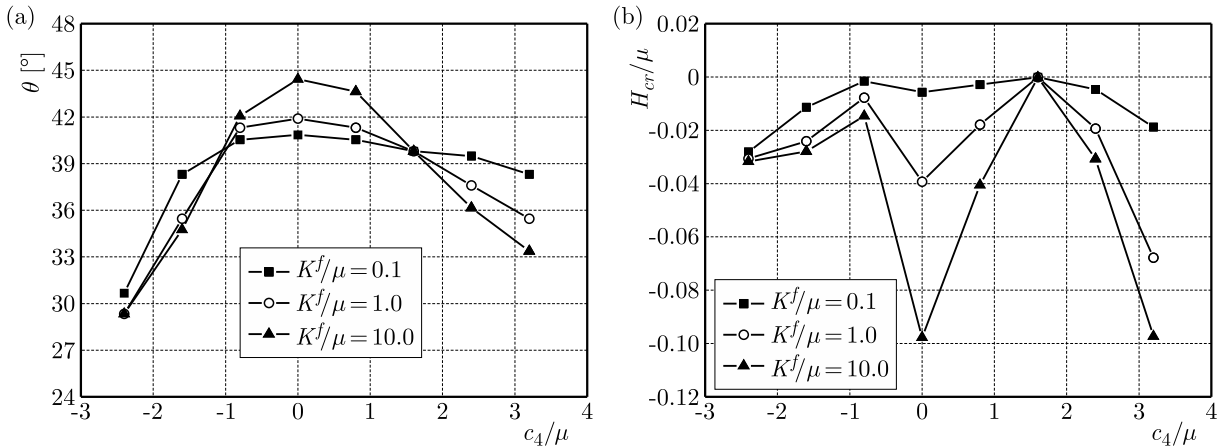


Fig. 2. Variation of the band direction angle θ (a) and the critical hardening modulus H'_{cr} (b) with the parameter c_4 for various K^f in the case $\sigma'_1 \geq \sigma'_2 \geq \sigma'_3$

Case B

When $\sigma'_1 \geq \sigma'_3 \geq \sigma'_2$, it has $\sigma'_I = \sigma'_1$ and $\sigma'_{III} = \sigma'_2$. Then it follows from Eqs. (2.6) and (5.1) that

$$P'_1 = \frac{\sqrt{2}}{2} \frac{1 + \sin \varphi}{\sqrt{1 + \sin^2 \varphi}} \quad P'_2 = \frac{-\sqrt{2}}{2} \frac{1 - \sin \varphi}{\sqrt{1 + \sin^2 \varphi}} \quad P'_3 = 0 \quad (5.4)$$

and

$$P'_v = \frac{\sqrt{2} \sin \varphi}{\sqrt{1 + \sin^2 \varphi}} \quad (5.5)$$

Thus, assuming $\lambda/\mu = 1$ and $\varphi = 10^\circ$, the impacts of the parameters c_4 and K^f on the band angle θ and the critical hardening modulus H'_{cr} are illustrated in Figs. 3a and 3b, respectively. As can be seen, the direction angle of localized band initiation and the corresponding critical hardening modulus are significantly dependent upon the deviation from isotropic elasticity and pore fluid compressibility. For the effect of deviation from isotropic elasticity, it is shown that a larger value of the parameter c_4 leads to smaller values of the band angle θ and the critical hardening modulus H'_{cr} . As for the effect of pore fluid compressibility, it is indicated that a larger value of the modulus K^f results in a larger value of the band angle θ for the vast majority of cases and a smaller value of the critical hardening modulus H'_{cr} .

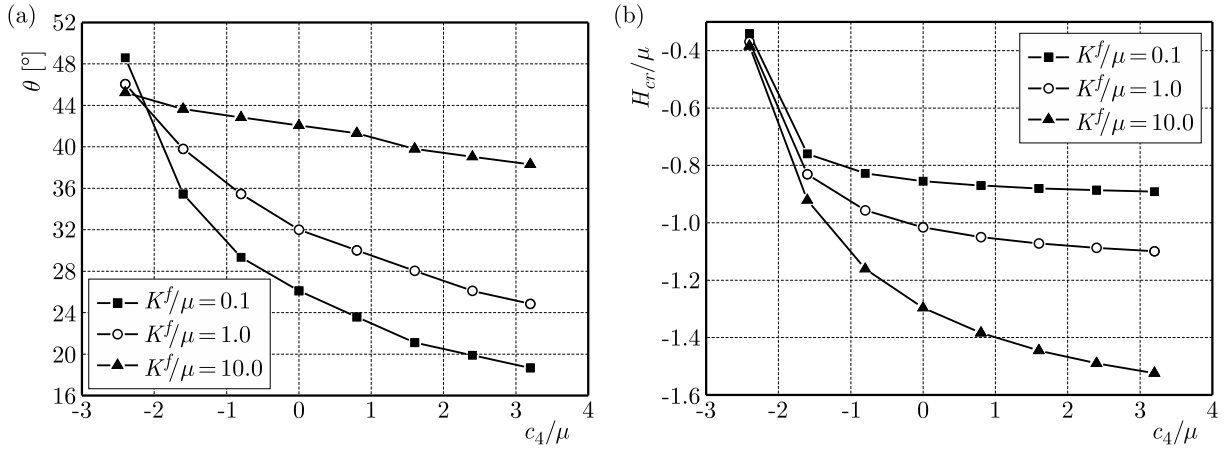


Fig. 3. Variation of the band direction angle θ (a) and the critical hardening modulus H'_{cr} (b) with the parameter c_4 for various K^f in the case $\sigma'_1 \geq \sigma'_3 \geq \sigma'_2$

Case C

When $\sigma'_2 \geq \sigma'_1 \geq \sigma'_3$, it has $\sigma'_I = \sigma'_2$, $\sigma'_{III} = \sigma'_3$. Hence, combination of Eqs. (2.6) and (5.1) yields

$$P'_1 = 0 \quad P'_2 = \frac{\sqrt{2}}{2} \frac{1 + \sin \varphi}{\sqrt{1 + \sin^2 \varphi}} \quad P'_3 = \frac{-\sqrt{2}}{2} \frac{1 - \sin \varphi}{\sqrt{1 + \sin^2 \varphi}} \quad (5.6)$$

and

$$P'_v = \frac{\sqrt{2} \sin \varphi}{\sqrt{1 + \sin^2 \varphi}} \quad (5.7)$$

In this case, with $\lambda/\mu = 1$ and $\varphi = 10^\circ$, the dependences of the band direction angle at the inception of strain localization and the corresponding critical hardening modulus on the deviation from isotropic elasticity and pore fluid compressibility are indicated in Figs. 4a and 4b, respectively. It can be observed that the band direction angle θ and the critical hardening modulus H'_{cr} get smaller with an increase in the value of modulus K^f . However, it should be noted that the influence of pore fluid compressibility on the critical hardening modulus is very limited when c_4/μ ranges between -2.5 and -1 . On the other hand, it is found that the effects of the deviation from isotropic elasticity on the band direction angle and the corresponding critical hardening modulus are obvious. When $c_4 \geq 0$, the band direction angle θ diminishes with an increase in the parameter c_4 . When $c_4 \leq 0$, the band direction angle θ becomes larger with the

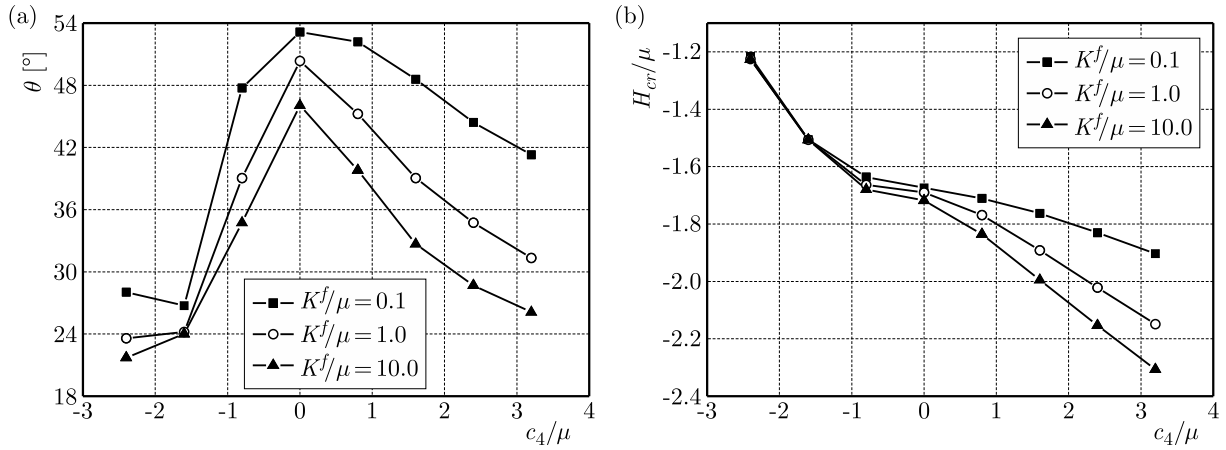


Fig. 4. Variation of the band direction angle θ (a) and the critical hardening modulus H'_{cr} (b) with the parameter c_4 for various K^f in the case $\sigma'_2 \geq \sigma'_1 \geq \sigma'_3$

increasing parameter c_4 in the cases of $K^f/\mu = 1$ and $K^f/\mu = 10$, whereas it first decreases and then increases with the diminishment of the parameter c_4 in the case of $K^f/\mu = 0.1$. Additionally, the critical hardening modulus H'_{cr} becomes smaller with an increase in the parameter c_4 .

For the situation $\sigma'_3 \geq \sigma'_1$, there also exist three cases depending on the magnitude of the out-of-plane stress σ'_2 , which are defined by $\sigma_3 \geq \sigma_2 \geq \sigma_1$, $\sigma_3 \geq \sigma_1 \geq \sigma_2$, and $\sigma_2 \geq \sigma_3 \geq \sigma_1$, respectively. Similar to those cases for the situation $\sigma'_1 \geq \sigma'_3$, with $\lambda/\mu = 1$ and $\varphi = 10^\circ$ the influences of the deviation from isotropic elasticity and pore fluid compressibility on the band direction angle at the initiation of strain localization and the corresponding critical hardening modulus are calculated and shown in Figs. 5-7. Among these figures, Figs. 5a and 5b are for the case $\sigma_3 \geq \sigma_2 \geq \sigma_1$, Figs. 6a and 6b are for the case $\sigma_3 \geq \sigma_1 \geq \sigma_2$, and Figs. 7a and 7b are for the case $\sigma_2 \geq \sigma_3 \geq \sigma_1$. It can be found from Figs. 5-7 that the effects of the deviation from isotropic elasticity and pore fluid compressibility on the band direction angle and the critical hardening modulus are considerable.

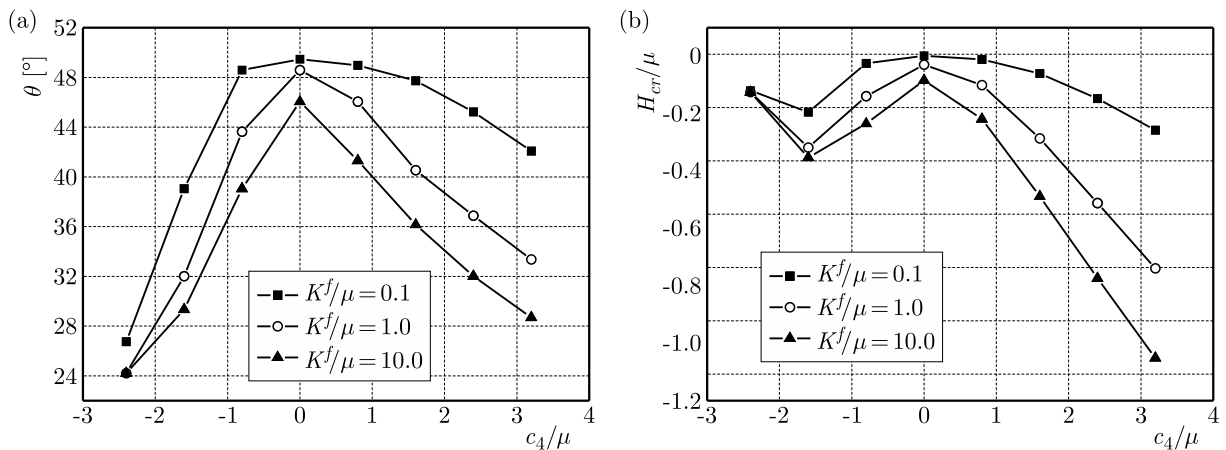


Fig. 5. Relationship between the band direction angle θ (a) and the critical hardening modulus H'_{cr} (b) and parameter c_4 for different K^f for the case $\sigma'_3 \geq \sigma'_2 \geq \sigma'_1$

In addition, for both the situations $\sigma'_1 \geq \sigma'_3$ and $\sigma'_3 \geq \sigma'_1$, it can be concluded from the above discussions that the initiation of strain localization for porous media with transversely isotropic elasticity is delayed with the increase of pore fluid compressibility, which is consistent with the conclusions for isotropic porous media drawn by Han and Vardoulakis (1991) and Runesson *et al.* (1996). For associated plasticity, it is found from the corresponding figures that the values of

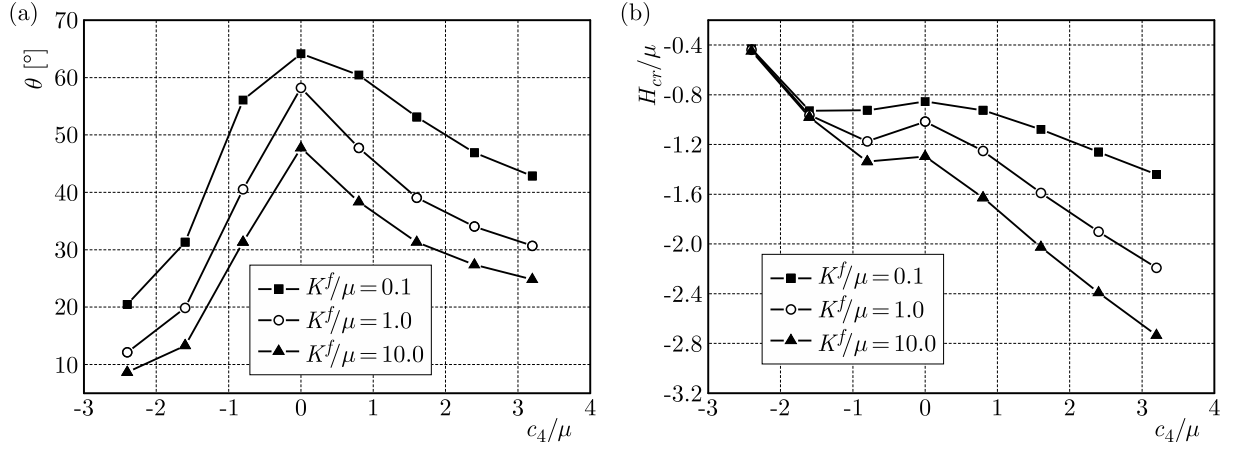


Fig. 6. Relationship between the band direction angle θ (a) and the critical hardening modulus H'_{cr} (b) and parameter c_4 for different K^f for the case $\sigma'_3 \geq \sigma'_1 \geq \sigma'_2$

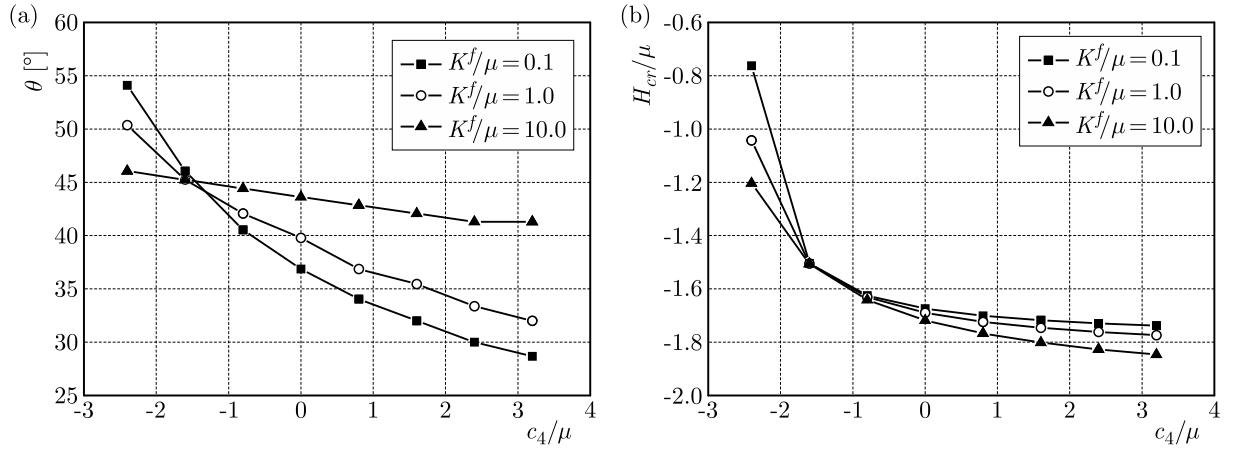


Fig. 7. Relationship between the band direction angle θ (a) and the critical hardening modulus H'_{cr} (b) and parameter c_4 for different K^f for the case $\sigma'_2 \geq \sigma'_3 \geq \sigma'_1$

the critical hardening modulus at the onset of strain localization are non-positive, which is in agreement with the point of view proposed by Ottosen and Runesson (1991).

6. Conclusions

This study conducts an investigation on the properties of strain localization for elastic-plastic porous media with transversely isotropic elasticity under undrained conditions. Under non-associated plasticity and tri-axial stress states, the conditions for localization of deformation into a band in the incremental response of porous media are derived, in which the effects of the deviation from isotropic elasticity and pore fluid compressibility are taken into account. The explicit expression for the hardening modulus at the onset of strain localization are obtained.

With reference to the Mohr-Coulomb yield criterion, the effects of deviation from isotropic elasticity and pore fluid compressibility in the formulation of strain localization for the case of plane strain are discussed. It turns out that the properties of strain localization are dependent upon the deviation from isotropic elasticity and pore fluid compressibility. The deviation from isotropic elasticity and pore fluid compressibility have great impacts on the direction angle of localized band initiation and the corresponding critical hardening modulus. In general, a larger value of the compression modulus of pore fluid leads to a smaller value of the critical hardening

modulus at the initiation of strain localization. In other words, the onset of strain localization for elastic-plastic porous media with transversely isotropic elasticity is delayed with an increase in the pore fluid compressibility. The influence of the pore fluid compressibility on the direction angle of localized band is related to the magnitude of deviation from isotropic elasticity.

Acknowledgments

This work has been supported by National Natural Science Foundation of China (NSFC) (No. 11172265).

References

1. ALYAVUZ B., GULTOP T., 2009, Weak shock waves and shear bands in compressible, inextensible thermoelastic solids, *Archive of Applied Mechanics*, **79**, 1145-1161
2. BIGONI D., LORET B., 1999, Effects of elastic anisotropy on strain localization and flutter instability in plastic solids, *Journal of the Mechanics and Physics of Solids*, **47**, 1409-1436
3. GAO Z.W., ZHAO J.D., 2013, Strain localization and fabric evolution in sand, *International Journal of Solids and Structures*, **50**, 3634-3648
4. HAN C., VARDOULAKIS I., 1991, Plane strain compression experiments on water-saturated fine-grained sand, *Geotechnique*, **16**, 49-78
5. LONGERE P., DRAGON A., 2007, Adiabatic heat evaluation for dynamic plastic localization, *Journal of Theoretical and Applied Mechanics*, **45**, 203-223
6. LORET B., RIZZI E., 1997, Qualitative analysis of strain localization. Part II: Transversely isotropic elasticity and plasticity, *International Journal of Plasticity*, **13**, 501-519
7. MANDEL J., 1962, Ondes plastiques dans un milieu indéfini à trois dimensions, *Journal de Mécanique I*, **1**, 3-30
8. MANDEL J., 1964, Conditions de Stabilité et Postulat de Drucker, [In:] Kravtchenko J., Sirieys P.M. (Eds.), *Rheology and Soil Mechanics*, Springer, Berlin, 58-68
9. NIELSEN K., SCHREYER H.L., 1993, Bifurcations in elastic-plastic materials, *International Journal of Solids and Structures*, **30**, 521-544
10. OTTOSEN N.S., RUNESSON K., 1991, Properties of discontinuous bifurcation solutions in elastoplasticity, *International Journal of Solids and Structures*, **27**, 401-421
11. RICE J.R., 1976, The localization of plastic deformation, [In:] Loiter W.T. (Ed.), *Proceedings of 14th IUTAM Congress*, Delft, Amsterdam: North Holland, 207-220
12. RIZZI E., LORET B., 1997, Qualitative analysis of strain localization. Part I: Transversely isotropic elasticity and isotropic plasticity, *International Journal of Plasticity*, **13**, 461-499
13. RIZZI E., LORET B., 1999, Strain localization in fluid-saturated anisotropic elastic-plastic porous media, *International Journal of Engineering Science*, **37**, 235-251
14. RUDNICKI J.W., 1977, The effect of stress-induced anisotropy on a model of brittle rock failure as localization of deformation, [In:] Wang F.D., Clark G.B. (Eds.), *Energy Resources and Excavation Technology, Proceedings of the 18th US Symposium on Rock Mechanics*, Keystone, Colorado, 1-8
15. RUDNICKI J.W., 2002, Conditions for compaction and shear bands in a transversely isotropic material, *International Journal of Solids and Structures*, **39**, 3741-3756
16. RUNESSON K., PERIC D., STURE S., 1996, Effect of pore fluid compressibility on localization in elastic-plastic porous solids under undrained conditions, *International Journal of Solids and Structures*, **33**, 1501-1518
17. THOMAS T.Y., 1961, *Plastic Flow and Fracture in Solids*, Academic Press, New York

18. ZHANG H.W., SCHREFLER B.A., 2001, Uniqueness and localization analysis of elastic-plastic saturated porous media, *International Journal for Numerical and Analytical Methods Geomechanics*, **25**, 29-48
19. ZHANG H.W., ZHOU L., SCHREFLER B.A., 2005, Material instabilities of anisotropic saturated multiphase porous media, *European Journal of Mechanics A/Solids*, **24**, 713-727
20. ZHANG Y.Q., HAO H., YU M.H., 2002, Effect of porosity on the properties of strain localization in porous media under undrained conditions, *International Journal of Solids and Structures*, **39**, 1817-1831
21. ZHANG Y.Q., LU Y., YU M.H., 2003, Investigation of strain localization in elastoplastic materials with transversely isotropic elasticity, *International Journal of Mechanical Sciences*, **45**, 217-233

Manuscript received September 19, 2015; accepted for print July 5, 2016

MODELING AND ANALYSIS OF COUPLED FLEXURAL-TORSIONAL SPINNING BEAMS WITH UNSYMMETRICAL CROSS SECTIONS

JIE WANG, DONGXU LI, JIANPING JIANG

College of Aerospace Science and Engineering, National University of Defense Technology, Changsha, China
e-mail: wangjie@nudt.edu.cn

The structural modeling and dynamic properties of a spinning beam with an unsymmetrical cross section are studied. Due to the eccentricity and spinning, transverse deflections along the two principal directions and the torsional motion about the longitudinal axis are coupled. The structural model of the beam is established based on the Hamilton principle and by incorporating the torsional inertia. Moreover, because of its significant influence on characteristics for the non-circular cross-sectional beam, the warping effect is considered in the formulation. The proposed model is effectively validated in two cases: the spinning beam with a symmetric cross section and the cantilevered beam with an unsymmetrical cross section. Then the effects of the spinning speed on natural frequencies and mode shapes are investigated. Numerical results reveal that the critical speed is altered with respect to noncoincidence of the centroid and the shear center. For the beams with strong warping rigidities, the warping effect cannot be neglected due to significant influence on natural frequencies.

Keywords: spinning beam, critical speed, warping, coupled flexural-torsional vibration

1. Introduction

Spinning beams are important components of turbine blades, propellers, elastic linkages, satellite booms and are widespread in various branches of structural engineering. Dynamic characteristics such as natural frequencies and mode shapes of these systems are meaningful for analysis of position accuracy, throughput, fatigue and safety. As a consequence, it is essential to accurately establish the dynamic model of spinning beams and predict its vibration characteristics.

For the last decades, there has been a growing interest in the investigation of structural modeling, and excellent work has been done on the dynamic analysis of spinning beams. The fully flexural-torsional coupling model for spinning beams has been successfully established based on the analytical method by Bishop (1959), Dimentberg (1961), Kane (1961), Newland (1972) and Zu and Han (1992). Bishop (1959) utilized Newton's method to derive the characteristic equation of a bent shaft in the Euler-Bernoulli beam model and investigated the stability of the system. Lagrangian approach (Shiau *et al.*, 2006) and Hamilton's principle (Yoon and Kim, 2002) were also utilized to derive the governing equations for the system. Besides, different methods were proposed by researchers in order to solve the governing equations, i.e. assumed-modes method, finite element method, and dynamic stiffness method. Shiau *et al.* (2006) studied the dynamic behavior of a spinning Timoshenko beam with general boundary conditions based on the global assumed mode method. Yoon and Kim (2002) utilized the finite element method to analyze the dynamic stability of an unconstrained spinning beam subjected to a pulsating follower force. Banerjee and Su (2004) developed the dynamic stiffness method and the Wittrick-Williams algorithm was applied to compute natural frequencies and mode shapes. This method was also used in the free vibration analysis of a spinning composite beam (Banerjee and Su, 2006).

Based on the proposed methods, many researchers dealt with problems of spinning beams subjected to different kinds of loads (Ho and Chen, 2006; Lee, 1995; Zu and Han, 1994) under various boundary conditions (Choi *et al.*, 2000; Zu and Melanson, 1998). Sheu and Yang (2005) studied the dynamic response of a spinning Rayleigh beam with rotary inertia and gyroscopic effects in general boundary conditions. The relationship between the critical speed and the hollowness ratio and length-to-radius ratio was investigated by Sheu (2007). Ouyang and Wang (2007) presented a dynamic model for vibration of a rotating Timoshenko beam subjected to a three-directional load moving in the axial direction. Popplewell and Chang (1997) investigated free vibrations of a simply supported but stepped spinning Timoshenko beam with the Galerkin method. Ho and Chen (2006) discussed the vibration problems of a spinning axially loaded pre-twisted Timoshenko beam. Na *et al.* (2006) established the model of a tapered thin-walled composite spinning beam subjected to an axial compressive force. Moreover, dynamic stability of spinning structures around the longitudinal axis such as a shaft or an unconstrained beam has been widely investigated (Lee, 1996; Tylikowski, 2008). Experimental investigations on a cantilevered spinning shaft have been reported. Qian *et al.* (2010) conducted a non-contact dynamic testing of a highly flexible spinning vertical shaft.

In all of these studies, spinning beams had symmetric cross-sections and the shear center and centroid were assumed to superpose each other. In practical applications, the cross-section of the spinning beam can be eccentric due to errors during processing. Moreover, in some circumstances the cross-section is intended to be eccentric to meet the requirement of the engineering. For a beam with an arbitrary uniform cross section, the coupling of bending and torsion may occur when the beam experiences rotating motion. Yoo and Shin (1998) studied the eigenvalue loci veerings and mode shape variations for a rotating cantilever beam with the coupling effect considered. Latalski *et al.* (2014) investigated a rotating composite beam with piezoelectric active elements. An analysis of a rotor with several flexible blades was conducted with the spin softening effects and the centrifugal stiffening effects considered through a pre-stressed potential (Lesaffre *et al.*, 2007). Sinha and Turner (2011) further researched the characteristics of a rotating pre-twisted blade. In these studies, the direction of rotation is vertical to the longitudinal direction. Literature focused on the analysis of a beam rotating about its longitudinal direction is few. Filipich *et al.* (1987) studied the free vibration coupling of bending and torsion of a uniform spinning beam having one axis of symmetry. Then they extended the approach to a beam having no symmetric axis and developed a dynamic model of coupled torsional and bending deformations (Filipich and Rosales, 1990). The model accounted for the dynamic coupling terms due to the rotation and the eccentricity.

This paper further discusses the bending-torsion coupling effects with the warping effect considered. Natural characteristics including natural frequencies and mode shapes with respect to the spinning velocity and the eccentricity are investigated. And the critical spinning speed variation is observed in the presence of coupling effects. The paper is organized as follows. In Section 2, differential equations of the beam are formulated based on the Hamilton principle. The formulations are built on Euler-Bernoulli beam theory with the warping effect and torsional rigidity while neglecting the effect of shear rigidities. In Section 3, we calculate mode shape functions and natural frequencies of the system by applying the assumed mode method. In Section 4, the present model is validated by comparing with literature and numerically simulated with examples. The effects of spinning speed and warping on natural frequencies, mode shapes and critical speed are examined.

2. Governing differential equations

This Section deals with the formulation of differential equations for a spinning beam with an arbitrary cross section based on Hamilton's principle.

2.1. System description

A homogeneous slender beam with a uniform arbitrary cross-section is depicted in Fig. 1a. The left end of the beam is fixed to a base which rotates about the longitudinal axis at a constant angular velocity designated as Ω while the right end is free. When in undeformed configuration, the longitudinal axis of the beam goes through the shear center of the cross section.

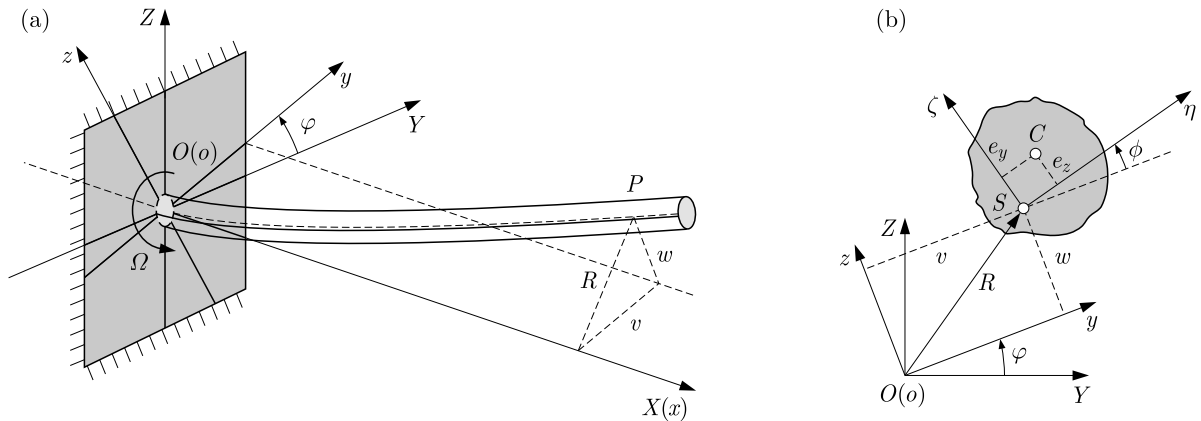


Fig. 1. Deformed configuration of a spinning beam with arbitrary cross section

Three sets of orthogonal right-handed coordinate frames are defined in order to describe the position vector \mathbf{R} of a differential element dM at a generic point P . The rectangular coordinate system XYZ is fixed with the inertial frame and the origin O is placed at the shear center of the cross-section on the clamped end. The frame xyz is a rotating frame whose origin o remains coincident with the point O and the x axis remains parallel to the X axis. When the beam spins, directions of the y and z axes are time-varying. The angle between the y axis and the Y axis is represented by the symbol φ . The third reference frame $\xi\eta\zeta$ is the element coordinate of the differential beam element which is attached to the shear center S of the beam section. C represents the center of mass of the beam section and (e_y, e_z) denote the coordinates of C in the frame $S\eta\zeta$.

The orientations of these frames at a time during free vibration are shown in Fig. 1b. The deformation of a differential beam element located at a distance x from the left end is defined by spatial displacement $v(x, t)$, $w(x, t)$ and rotation $\phi(x, t)$ about x -axis. The $v(x, t)$ and $w(x, t)$ represent lateral displacements in the y and z directions, respectively.

2.2. Equations of motion

The governing equation of the flexible beam is formulated based on the following assumptions: (1) for the elementary case of beam flexure and torsion using the Euler-Bernoulli beam theory with torsional inertia but not shear deformation or axial-force effects, (2) the warping effect is considered due to the fact that the torsion induced warping occurs when the beam section is not circular, (3) the axial displacement of the beam is neglected. Moreover, the deformation of the beam is small and yields to the linear conditions. Physical properties of the material are elastic and constant.

We consider the spinning beam undergoing transverse displacements and torsional motion. Also, it is assumed that the shear center S and the center of mass C of the cross section are not coincident. For such a beam, the position vector of a representative point after beam deformation can be defined as

$$\mathbf{R}(x) = v\mathbf{j} + w\mathbf{k} + e_y\mathbf{j}_1 + e_z\mathbf{k}_1 \quad (2.1)$$

where \mathbf{i} , \mathbf{j} and \mathbf{k} are unit vectors in the x , y and z directions, respectively. And \mathbf{i}_1 , \mathbf{j}_1 and \mathbf{k}_1 are unit vectors in the ξ , η and ζ directions, respectively.

The velocity of the point can be obtained as follows

$$\mathbf{v}(x) = \dot{v}\mathbf{j} + \dot{w}\mathbf{k} + \Omega\mathbf{i} \times (v\mathbf{j} + w\mathbf{k}) + (\Omega + \dot{\phi})\mathbf{i} \times (e_y\mathbf{j}_1 + e_z\mathbf{k}_1) \quad (2.2)$$

The overhead dot denotes partial derivatives with respect to time t .

The kinetic energy can be simplified as

$$\begin{aligned} T = & \frac{1}{2} \int_0^L \rho A (\dot{v}^2 + \dot{w}^2) dx + \frac{1}{2} \rho J_p \int_0^L \dot{\phi}^2 dx + \frac{1}{2} \int_0^L \rho A [\Omega^2 (v^2 + w^2) - 2\Omega\dot{v}w + 2\Omega v\dot{w}] dx \\ & + \frac{1}{2} \int_0^L \rho A [(e_y^2 + e_z^2)\dot{\phi}^2 - 2e_z\dot{v}\dot{\phi} + 2e_y\dot{w}\dot{\phi} + 2e_z\Omega w\dot{\phi} + 2e_y\Omega v\dot{\phi}] dx \\ & + \int_0^L \rho A [(e_y^2 + e_z^2)\Omega\dot{\phi} - e_z\Omega\dot{v} + e_z\Omega^2 w + e_y\Omega\dot{w} + e_y\Omega^2 v] dx \\ & + \int_0^L \rho A [-e_y\Omega\dot{v}\dot{\phi} + e_y\Omega^2 w\dot{\phi} - e_z\Omega\dot{w}\dot{\phi} - e_z\Omega^2 v\dot{\phi}] dx + \frac{1}{2} \int_0^L \rho A (e_y^2 + e_z^2)\Omega^2 dx \end{aligned} \quad (2.3)$$

The symbols ρ , E and A denote density, Young's modulus and cross sectional area. J_p is the polar moment of inertia and is given by

$$J_p = \iint_A r_p^2 d\eta d\zeta \quad (2.4)$$

where r_p represents the distance between a certain point in the section and the center.

The potential strain energy of the beam including the warping effect is considered as below

$$U = \frac{1}{2} \int_0^L E (I_z v''^2 + I_y w''^2) dx + \frac{1}{2} \int_0^L G J_p \phi'^2 dx + \frac{1}{2} \int_0^L E \Gamma \phi''^2 dx \quad (2.5)$$

where G denotes the shear modulus. I_y and I_z show the second moments of area about the z -axis and y -axis, $E\Gamma$ is warping rigidity. Primes denote partial derivatives with respect to x . For uniform beams, A , I_y , I_z , J_p and $E\Gamma$ are constant throughout the span.

Then the Lagrangian function of the beam system can be expressed as

$$\begin{aligned} L = T - U = & \frac{1}{2} \int_0^L \rho A (\dot{v}^2 + \dot{w}^2) dx + \frac{1}{2} \int_0^L \rho A [\Omega^2 (v^2 + w^2) - 2\Omega\dot{v}w + 2\Omega v\dot{w}] dx \\ & + \frac{1}{2} \rho J_p \int_0^L \dot{\phi}^2 dx + \frac{1}{2} \int_0^L \rho A (e^2 \dot{\phi}^2 - 2e_z\dot{v}\dot{\phi} + 2e_y\dot{w}\dot{\phi} + 2e_z\Omega w\dot{\phi} + 2e_y\Omega v\dot{\phi}) dx \\ & + \int_0^L \rho A (e^2 \Omega \dot{\phi} - e_z\Omega\dot{v} + e_z\Omega^2 w + e_y\Omega\dot{w} + e_y\Omega^2 v) dx \\ & + \int_0^L \rho A (-e_y\Omega\dot{v}\dot{\phi} + e_y\Omega^2 w\dot{\phi} - e_z\Omega\dot{w}\dot{\phi} - e_z\Omega^2 v\dot{\phi}) dx + \frac{1}{2} \int_0^L \rho A e^2 \Omega^2 dx \\ & - \frac{1}{2} \int_0^L E (I_z v''^2 + I_y w''^2) dx - \frac{1}{2} \int_0^L G J_p \phi'^2 dx - \frac{1}{2} \int_0^L E \Gamma \phi''^2 dx \end{aligned} \quad (2.6)$$

Using Hamilton's principle, the dynamic model of the system can be obtained

$$\begin{aligned}
 EI_z \frac{\partial^4 v}{\partial x^4} + \rho A (\ddot{v} - \Omega^2 v - 2\Omega \dot{w} - e_z \ddot{\phi} - 2\Omega e_y \dot{\phi} + e_z \Omega^2 \phi) &= \rho A e_x \Omega^2 \\
 EI_y \frac{\partial^4 w}{\partial x^4} + \rho A (\ddot{w} - \Omega^2 w + 2\Omega \dot{v} + e_y \ddot{\phi} - 2\Omega e_z \dot{\phi} - e_y \Omega^2 \phi) &= \rho A e_z \Omega^2 \\
 EI \frac{\partial^4 \phi}{\partial x^4} - GJ_p \frac{\partial^2 \phi}{\partial x^2} + (\rho A e^2 + \rho J_p) \ddot{\phi} + \rho A e_y (2\Omega \dot{v} + \ddot{w} - \Omega^2 w) \\
 + \rho A e_z (-\ddot{v} + \Omega^2 v + 2\Omega \dot{w}) &= 0
 \end{aligned} \tag{2.7}$$

When skipping the eccentricity of the cross section, Eq. (2.7) has the following form

$$\begin{aligned}
 EI_z \frac{\partial^4 v}{\partial x^4} + \rho A (\ddot{v} - \Omega^2 v - 2\Omega \dot{w}) &= 0 & EI_y \frac{\partial^4 w}{\partial x^4} + \rho A (\ddot{w} - \Omega^2 w + 2\Omega \dot{v}) &= 0 \\
 EI \frac{\partial^4 \phi}{\partial x^4} - GJ_p \frac{\partial^2 \phi}{\partial x^2} + \rho J_p \ddot{\phi} &= 0
 \end{aligned} \tag{2.8}$$

The first two equations in Eq. (2.8) are fully consistent with the results by Banerjee and Su (2004). Also, it can be concluded that the eccentricity induces the coupling between transverse deformations and torsional motion.

When skipping the spinning, Eq. (2.7) has the following form, which is consistent with the results by Tanaka and Bercin (1999)

$$\begin{aligned}
 EI_z \frac{\partial^4 v}{\partial x^4} + \rho A (\ddot{v} - e_z \ddot{\phi}) &= 0 & EI_y \frac{\partial^4 w}{\partial x^4} + \rho A (\ddot{w} + e_y \ddot{\phi}) &= 0 \\
 EI \frac{\partial^4 \phi}{\partial x^4} - GJ_p \frac{\partial^2 \phi}{\partial x^2} + (\rho A e^2 + \rho J_p) \ddot{\phi} + \rho A (-e_z \ddot{v} + e_y \ddot{w}) &= 0
 \end{aligned} \tag{2.9}$$

It is obvious that the coupling between v and w takes place due to spinning.

3. Mode shape and frequency equation

For a free homogeneous vibration problem, a sinusoidal oscillation is assumed

$$v(x, t) = V(x)e^{j\omega t} \quad w(x, t) = W(x)e^{j\omega t} \quad \phi(x, t) = \Phi(x)e^{j\omega t} \quad j = \sqrt{-1} \tag{3.1}$$

where ω is the circular frequency of oscillation, V , W and Φ are amplitudes of v , w and ϕ , respectively. Substituting Eq. (3.1) into differential equation (2.7) leads to

$$\begin{aligned}
 \frac{EI_z}{\rho A} V^{(4)} - (\omega^2 + \Omega^2)V - 2j\omega\Omega W + e_z(\omega^2 + \Omega^2)\Phi - 2j\omega\Omega e_y \Phi &= 0 \\
 \frac{EI_y}{\rho A} W^{(4)} - (\omega^2 + \Omega^2)W + 2j\omega\Omega V - e_y(\omega^2 + \Omega^2)\Phi - 2j\omega\Omega e_z \Phi &= 0 \\
 \frac{EI}{\rho A} \Phi^{(4)} - \frac{GJ_p}{\rho A} \Phi'' - \left(e^2 + \frac{J_p}{A}\right)\omega^2 \Phi + (\omega^2 + \Omega^2)(e_z V - e_y W) + 2j\omega\Omega(e_y V + e_z W) &= 0
 \end{aligned} \tag{3.2}$$

For convenience, we consider a beam with a monosymmetric cross-section with the symmetry axis y . The centroid C is on the axis y and the scalar e_z is equal to zero. Then Eq. (3.2) can be simplified as

$$\begin{aligned}
\frac{EI_z}{\rho A} V^{(4)} - (\omega^2 + \Omega^2)V - 2j\omega\Omega W - 2j\omega\Omega e_y \Phi &= 0 \\
\frac{EI_y}{\rho A} W^{(4)} - (\omega^2 + \Omega^2)W + 2j\omega\Omega V - e_y(\omega^2 + \Omega^2)\Phi &= 0 \\
\frac{E\Gamma}{\rho A} \Phi^{(4)} - \frac{GJ_p}{\rho A} \Phi'' - \left(e_y^2 + \frac{J_p}{A}\right)\omega^2 \Phi + 2j\omega\Omega e_y V - e_y(\omega^2 + \Omega^2)W &= 0
\end{aligned} \tag{3.3}$$

Then introducing the differential operator D and subsequent variables as follows

$$\begin{aligned}
D &= \frac{d}{dx} & L_{11} &= \frac{EI_z}{\rho A} D^4 - (\omega^2 + \Omega^2) \\
L_{12} &= -2j\omega\Omega & L_{13} &= -2j\omega\Omega e_y \\
L_{21} &= 2j\omega\Omega & L_{22} &= \frac{EI_y}{\rho A} D^4 - (\omega^2 + \Omega^2) \\
L_{23} &= -e_y(\omega^2 + \Omega^2) & L_{31} &= 2j\omega\Omega e_y \\
L_{32} &= -e_y(\omega^2 + \Omega^2) & L_{33} &= \frac{E\Gamma}{\rho A} D^4 - \frac{GJ_p}{\rho A} D^2 - \left(e_y^2 + \frac{J_p}{A}\right)\omega^2
\end{aligned} \tag{3.4}$$

It can be seen that Y , Z and Ψ satisfy the equation

$$\Delta \begin{bmatrix} V \\ W \\ \Phi \end{bmatrix} = \mathbf{0} \tag{3.5}$$

where

$$\Delta = \begin{bmatrix} L_{11} & L_{12} & L_{13} \\ L_{21} & L_{22} & L_{23} \\ L_{31} & L_{32} & L_{33} \end{bmatrix} \tag{3.6}$$

Introducing

$$\begin{aligned}
\kappa_1 &= \frac{\rho A}{EI_z} & \kappa_2 &= \frac{\rho A}{EI_y} & \kappa_3 &= \frac{\rho A}{E\Gamma} \\
\kappa_4 &= \frac{GJ_p}{E\Gamma} & \kappa_5 &= \left(e_y^2 + \frac{J_p}{A}\right) & \kappa_6 &= \omega^2 + \Omega^2
\end{aligned} \tag{3.7}$$

and setting the determinant of differential operator matrix (3.6) equal to zero leads to the following twelfth order differential equation:

$$\begin{aligned}
(D^4 - \kappa_6\kappa_1)[(D^4 - \kappa_6\kappa_2)(D^4 - \kappa_4D^2 - \kappa_3\kappa_5\omega^2) - e_y^2\kappa_2\kappa_3\kappa_6^2] \\
- 4\omega^2\Omega^2\kappa_1\kappa_2[(D^4 - \kappa_4D^2 - \kappa_3\kappa_5\omega^2) + e_y^2\kappa_3\kappa_6] + 4\omega^2\Omega^2e_y^2\kappa_1\kappa_3D^4 = 0
\end{aligned} \tag{3.8}$$

The solution to the above equation can be expressed in an exponential form

$$R(x) = e^{rx} \tag{3.9}$$

Specifying $s = r^2$, then substituting Eq. (3.9) into (3.8), the following characteristic equation can be obtained

$$\begin{aligned}
s^6 - \kappa_4s^5 - (\kappa_3\kappa_5\omega^2 + \kappa_2\kappa_6 + \kappa_1\kappa_6)s^4 + (\kappa_2\kappa_4\kappa_6 + \kappa_1\kappa_4\kappa_6)s^3 \\
+ (\kappa_1\kappa_2\kappa_6^2 - 4\kappa_1\kappa_2\omega^2\Omega^2 - \kappa_2\kappa_3\kappa_6^2e_y^2 - 4\kappa_1\kappa_3e_y^2\omega^2\Omega^2 + \kappa_1\kappa_3\kappa_5\kappa_6\omega^2 \\
+ \kappa_2\kappa_3\kappa_5\kappa_6\omega^2)s^2 + \kappa_1\kappa_2\kappa_4(4\omega^2\Omega^2 - \kappa_6^2)s - \kappa_1\kappa_2\kappa_3(\kappa_5\kappa_6^2\omega^2 - \kappa_6^3e_y^2 \\
+ 4\kappa_6e_y^2\omega^2\Omega^2 - 4\kappa_5\omega^4\Omega^2) = 0
\end{aligned} \tag{3.10}$$

s_1 - s_6 are solutions to Eq. (3.10). The twelve roots of Eq. (3.8) can be written as

$$\pm r_i \quad r_i = j\sqrt{s_i} \quad i = 1, 2, \dots, 6 \tag{3.11}$$

Then the general solutions of V , W and Φ are expressed as

$$\begin{aligned} V(x) &= A_1 \cosh r_1 x + A_2 \sinh r_1 x + A_3 \cosh r_2 x + A_4 \sinh r_2 x + A_5 \cosh r_3 x + A_6 \sinh r_3 x \\ &\quad + A_7 \cos r_4 x + A_8 \sin r_4 x + A_9 \cos r_5 x + A_{10} \sin r_5 x + A_{11} \cos r_6 x + A_{12} \sin r_6 x \\ W(x) &= B_1 \cosh r_1 x + B_2 \sinh r_1 x + B_3 \cosh r_2 x + B_4 \sinh r_2 x + B_5 \cosh r_3 x + B_6 \sinh r_3 x \\ &\quad + B_7 \cos r_4 x + B_8 \sin r_4 x + B_9 \cos r_5 x + B_{10} \sin r_5 x + B_{11} \cos r_6 x + B_{12} \sin r_6 x \\ \Phi(x) &= C_1 \cosh r_1 x + C_2 \sinh r_1 x + C_3 \cosh r_2 x + C_4 \sinh r_2 x + C_5 \cosh r_3 x + C_6 \sinh r_3 x \\ &\quad + C_7 \cos r_4 x + C_8 \sin r_4 x + C_9 \cos r_5 x + C_{10} \sin r_5 x + C_{11} \cos r_6 x + C_{12} \sin r_6 x \end{aligned} \tag{3.12}$$

where A_i , B_i and C_i ($i = 1$ - 12) are three different sets of constants.

Substituting Eq. (3.12) into Eq. (3.2), relations between A_i , B_i and C_i can be derived

$$\begin{aligned} B_1 &= p_1 A_1 & B_2 &= p_1 A_2 & B_3 &= p_2 A_3 & B_4 &= p_2 A_4 \\ B_5 &= p_3 A_5 & B_6 &= p_3 A_6 & B_7 &= p_4 A_7 & B_8 &= p_4 A_8 \\ B_9 &= p_5 A_9 & B_{10} &= p_5 A_{10} & B_{11} &= p_6 A_{11} & B_{12} &= p_6 A_{12} \\ C_1 &= q_1 A_1 & C_2 &= q_1 A_2 & C_3 &= q_2 A_3 & C_4 &= q_2 A_4 \\ C_5 &= q_3 A_5 & C_6 &= q_3 A_6 & C_7 &= q_4 A_7 & C_8 &= q_4 A_8 \\ C_9 &= q_5 A_9 & C_{10} &= q_5 A_{10} & C_{11} &= q_6 A_{11} & C_{12} &= q_6 A_{12} \end{aligned} \tag{3.13}$$

where

$$\begin{aligned} p_i &= \frac{\kappa_2 \kappa_6}{2j\omega r_i^4 \Omega} \left(\frac{1}{\kappa_1} r_i^4 - \kappa_6 + \frac{4\omega^2 \Omega^2}{\kappa_6} \right) \quad i = 1, 2, \dots, 6 \\ q_i &= \begin{cases} \frac{\kappa_2 \kappa_6^2 e \left(\frac{1}{\kappa_1} r_i^4 - \kappa_6 + \frac{4\omega^2 \Omega^2}{\kappa_6} \right) + 4e_y \omega^2 \Omega^2 r_i^4}{2j\omega r_i^4 \Omega \left(\frac{1}{\kappa_3} r_i^4 - \frac{\kappa_4}{\kappa_3} r_i^2 - \kappa_5 \omega^2 \right)} & i = 1, 2, 3 \\ \frac{\kappa_2 \kappa_6^2 e \left(\frac{1}{\kappa_1} r_i^4 - \kappa_6 + \frac{4\omega^2 \Omega^2}{\kappa_6} \right) + 4e_y \omega^2 \Omega^2 r_i^4}{2j\omega r_i^4 \Omega \left(\frac{1}{\kappa_3} r_i^4 + \frac{\kappa_4}{\kappa_3} r_i^2 - \kappa_5 \omega^2 \right)} & i = 4, 5, 6 \end{cases} \end{aligned} \tag{3.14}$$

The constants A_1 - A_{12} can be determined from the boundary conditions. For a clamped-free beam, the boundaries are as follows

$$\begin{aligned} \text{clamped end } (x = 0) : & \quad V = 0, V' = 0, W = 0, W' = 0, \Phi = 0, \Phi' = 0 \\ \text{free end } (x = L) : & \quad V'' = 0, V''' = 0, W'' = 0, W''' = 0, \kappa_4 \Phi' - \Phi''' = 0, \Phi'' = 0 \end{aligned} \tag{3.15}$$

Using boundary condition (3.15), a set of twelve homogeneous equations in terms of the constants A_1 - A_{12} will be generated. The natural frequencies ω can be numerically solved by setting the determinant of the coefficient matrix of A_1 - A_{12} to be equal to zero.

4. Numerical applications and results

In this Section, firstly some limiting cases are examined to validate the model presented here. Secondly, the dynamic characteristics of the beam with unsymmetrical cross sections are investigated using the proposed method.

4.1. Validation

The example for validating is taken from literature (Banerjee and Su, 2004). The beam has a rectangular cross section and possesses equal flexural rigidities in the two principal directions of the cross section. The properties are given by: $EI_{yy} = 582.996 \text{ Nm}^2$, $EI_{zz} = 582.996 \text{ Nm}^2$, $\rho A = 2.87 \text{ kg/m}$, $L = 1.29 \text{ m}$.

The non-dimensional natural frequency and the spinning speed parameter are defined as in literature (Banerjee and Su, 2004)

$$\omega_i^* = \frac{\omega_i}{\omega_0} \quad \Omega^* = \frac{\Omega}{\omega_0} \quad (4.1)$$

where

$$\omega_0 = \sqrt{\frac{\sqrt{EI_{yy}EI_{zz}}}{\rho AL^4}} \quad (4.2)$$

Comparison of the first three natural frequencies in the current study with those given in published literature is listed in Table 1. Both examples apply to cantilever end conditions, and the effect of warping stiffness is excluded in the analysis. It is concluded that the resulting frequencies are in good agreement with the one given in the previous work. Because EI_{yy} equals EI_{zz} in this example, the natural frequency parameters of the first two modes are equal when the spinning speed parameter is zero.

Table 1. Natural frequencies of the spinning beam: (1) Banerjee and Su (2004), (2) present method

Spinning speed parameter (Ω^*)	Natural frequency parameters (ω_i^*)					
	ω_1^*		ω_2^*		ω_3^*	
	(1)	(2)	(1)	(2)	(1)	(2)
0	3.516	3.516	3.516	3.516	22.034	22.034
2	1.516	1.516	5.516	5.516	24.034	24.034
3.5	0	0	7.016	7.016	25.534	25.534
4	–	–	7.516	7.516	26.034	26.034

Then, to investigate characteristics of the beam with unsymmetrical cross section, two uniform beams with a semi-circular open cross section and with a channel cross section showed in Fig. 2, are considered. Physical properties of the beams for validation are derived from (Bercin and Tanaka, 1997), as shown in Table 2.

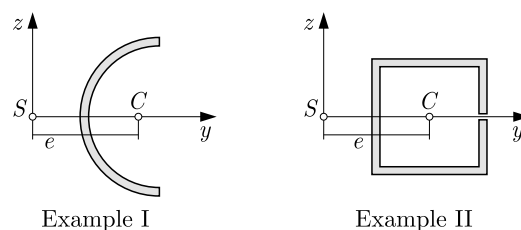


Fig. 2. The cross sections of the two beams studied

The first seven natural frequencies for the beams given in Fig. 2 are obtained by including and excluding the effect of warping stiffness when the spinning speed is zero, and compared with the results by Bercin and Tanaka (1997), as shown in Table 3. It is observed that when the effect of warping is neglected, the errors associated with it become increasingly large as the modal index increases.

Table 2. Physical properties of the beams studied

Parameters	Example I	Example II
EI_y [Nm ²]	6380	$1.436 \cdot 10^5$
EI_z [Nm ²]	2702	$2.367 \cdot 10^5$
GJ [N]	43.46	346.71
EF [Nm ⁴]	0.10473	536.51
ρ [kg/m ³]	2712	2712
A [m ²]	$3.08 \cdot 10^{-4}$	$1.57 \cdot 10^{-3}$
L [m]	0.82	2.7
e [m]	0.0155	0.0735

Table 3. Natural frequencies [Hz] of the beam: (1) Bercin and Tanaka (1997); (2) present approach including warping; (3) present approach excluding warping

Modal index	Example I			Example II		
	(1)	(2)	(3)	(1)	(2)	(3)
1	63.79	63.79	62.65	11.03	11.02	8.332
2	137.7	137.7	130.4	–	18.10	18.10
3	–	149.7	149.7	39.02	39.02	23.92
4	278.4	278.4	261.5	58.19	58.20	36.74
5	484.8	484.8	422.5	–	113.4	47.42
6	663.8	663.8	613.3	152.4	152.4	67.41
7	–	768.4	656.3	209.4	209.4	86.64

4.2. Spinning speed

To examine the effect of the spinning speed on natural frequencies of the beam with an unsymmetrical cross section, various values with the interval $[0, 4]$ for the spinning speed parameter are considered for Example I and Example II, and the corresponding frequencies are presented in Tables 4 and 5.

Table 4. Natural frequencies of Example I versus the spinning speed parameter

Spinning speed parameter (Ω^*)	Natural frequency parameters (ω_i^*)					
	ω_1^*	ω_2^*	ω_3^*	ω_4^*	ω_5^*	ω_6^*
0	2.149	4.639	5.044	9.378	16.333	22.365
1	1.783	4.607	5.453	9.355	16.319	22.340
2	0.760	4.729	6.235	9.287	16.278	22.268
2.25	0	4.783	6.453	9.262	16.264	22.244
3	–	4.988	7.132	9.174	16.212	22.163
4	–	5.327	8.069	9.027	16.122	22.043

It is found that the spinning speed alters the natural frequencies, especially at the lower vibration modes. With an increase of the spinning speed, the coupling between y -axial and z -axial deformations becomes larger, which is demonstrated in Eq. (3.3). Therefore, mode shapes of the system change due to larger coupling and natural frequencies vary correspondingly. Mostly, as the modal index rises, the effect of spinning speed on natural frequencies weakens since the motion amplitudes become smaller with an increasing frequency, which corresponds to an insignificant change in the reference kinetic energy.

Table 5. Natural frequencies of Example II versus the spinning speed parameter

Spinning speed parameter (Ω^*)	Natural frequency parameters (ω_i^*)					
	ω_1^*	ω_2^*	ω_3^*	ω_4^*	ω_5^*	ω_6^*
0	2.426	3.984	8.587	12.809	24.966	33.541
1	1.943	4.461	8.737	12.741	25.038	33.517
2	1.024	5.335	9.166	12.547	25.249	33.448
2.63	0	5.937	9.553	12.372	25.449	33.380
3	–	6.300	9.811	12.255	25.588	33.332
4	–	7.303	10.532	11.971	26.038	33.171

Figures 3a and 3b show variations of the first four non-dimensional natural frequencies with respect to the spinning speed parameter. Because of the large difference between the bending rigidities in the two principal planes, the natural frequencies start off with different values. The fundamental frequencies of both examples decrease with the increasing spinning speed while the others decrease or increase. At a certain spinning speed, which is defined as the critical speed, the first natural frequency becomes negative, resulting in instability. For the spinning beam with circular or rectangular cross-section, the natural frequencies are obtained by subtracting or adding the natural frequencies when $\Omega^* = 0$ to the spinning speed parameter (Banerjee and Su, 2004). So the value of the critical spinning speed when the beam becomes unstable equals to the first frequency of the beam with $\Omega^* = 0$. For the spinning beam with an unsymmetrical cross-section, the noncoincidence of mass center and shear center induces coupled flexural-torsional modes and alters the critical speed. Both values of the critical speed are larger than the first frequencies for the examples studied.

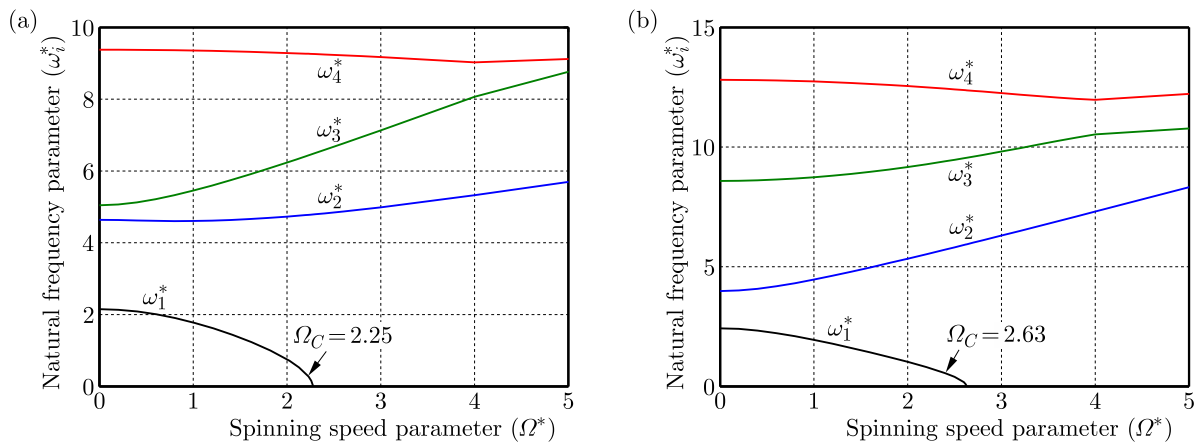


Fig. 3. Natural frequencies versus the spinning speed for (a) Example I, (b) Example II

4.3. Warping effect

The relative errors of natural frequencies due to the warping effect are discussed in this Section. Figures 4a and 4b show changes of natural frequencies with respect to the spinning speed with inclusion and exclusion of the warping for Example I and II, respectively.

It is evident that the inclusion of the warping effect increases the natural frequencies. And when the warping effect is neglected, the errors associated with it become increasingly larger as the modal index increases. Additionally, errors in Example II are more severe than in Example I. This is because the proportion of warping rigidity to bending rigidity in Example II is larger than that in Example I. It is also observed that the exclusion of warping makes the critical speed decrease.

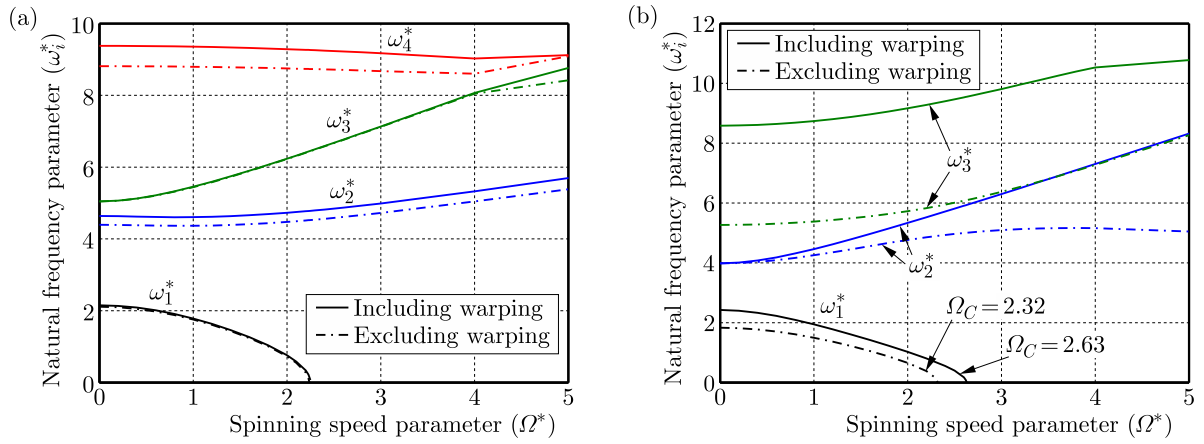


Fig. 4. Natural frequencies versus the spinning speed for (a) Example I, (b) Example II

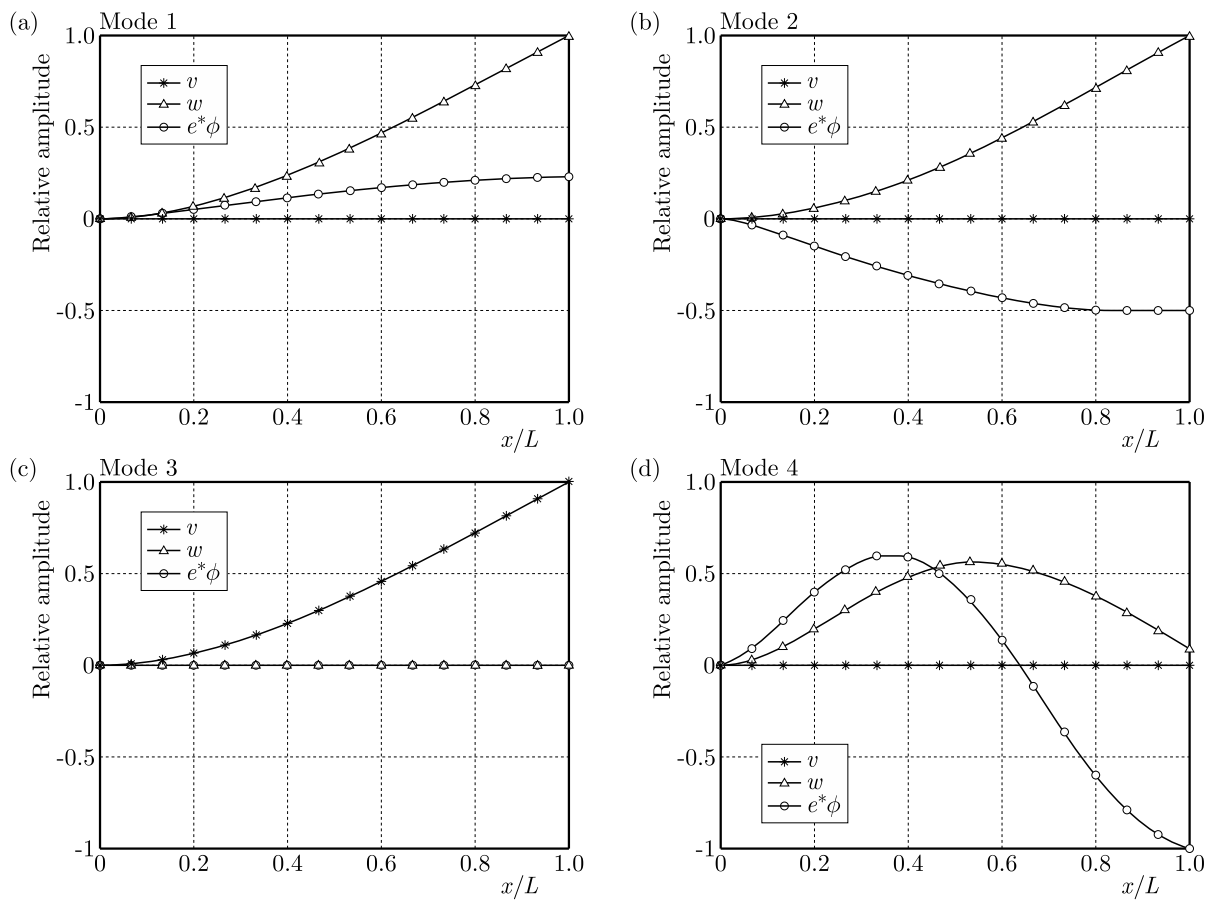


Fig. 5. Mode shapes in Example I with the speed parameter for $\Omega^* = 0$

4.4. Mode shapes

The first four normalized modal shape functions in Example I are illustrated in Figs. 5 and 6. It is concluded that in any case, the transverse deflection along the z -axis and torsional motion about the x -axis are coupled. The first two modes are coupled vibration modes of z -axial bending and x -axial torsion, while the third mode is the y -axial bending mode. When the spinning speed parameter is set to 2.0, all the modes become strongly coupled. Moreover, the speed has caused significant changes to the relative amplitudes between the z -axial displacement and x -axial

torsional angle, especially for lower modes. The beams with unsymmetrical cross-sections show different characteristics compared with symmetric cross-sectional beams, for which the effects of spinning speed on mode shapes are marginal, as declared by Banerjee and Su (2004).

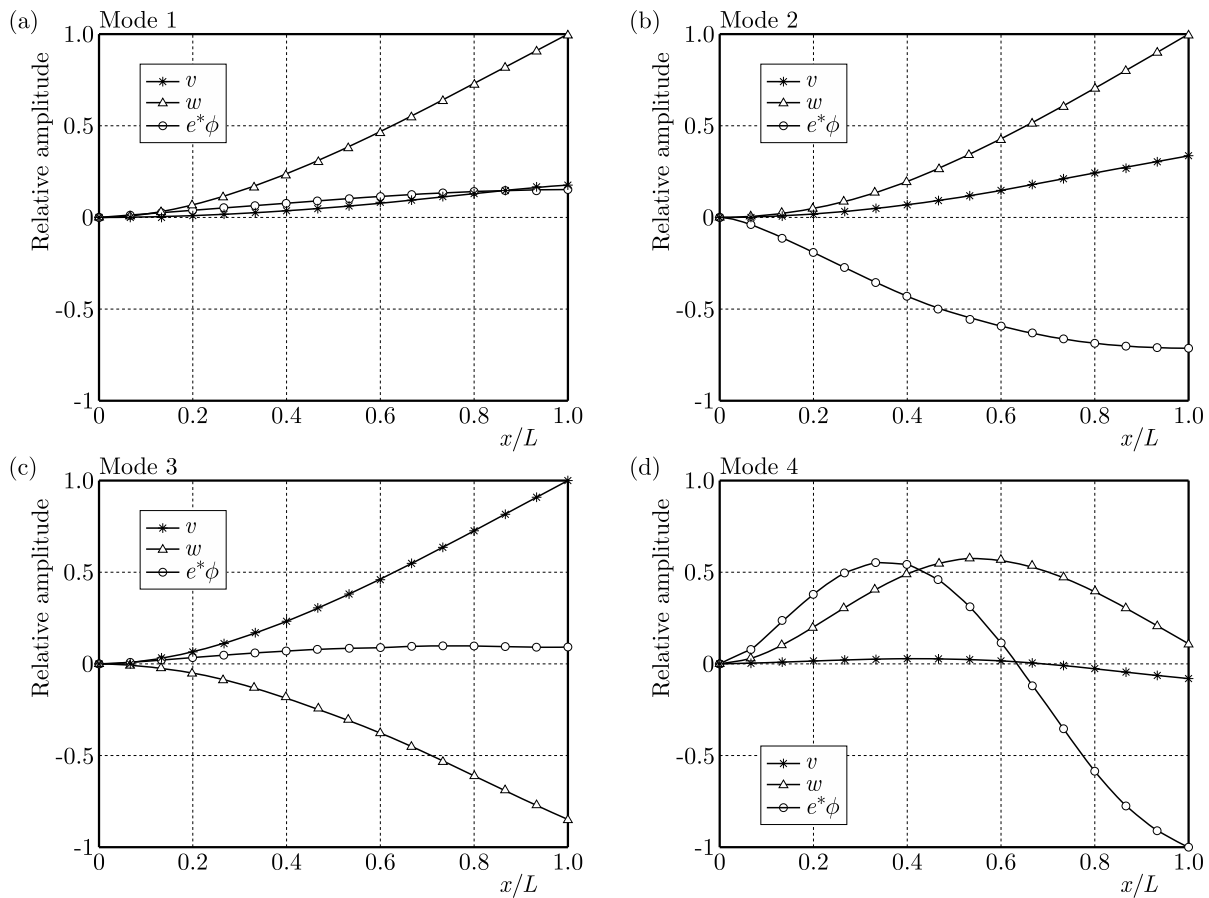


Fig. 6. Mode shapes in Example I with the speed parameter for $\Omega^* = 2$

5. Conclusions

This paper presents dynamic analysis of a spinning beam with an unsymmetrical cross section. The governing equations are formulated based on the Euler-Bernoulli beam theory and the Hamilton principle, and then natural frequencies and mode shapes are derived by the assumed mode method. Effects of the spinning speed and warping on natural frequencies are investigated. Numerical simulations are conducted in order to validate the present method and some main conclusions are derived as follows.

The noncoincidence of centroid and shear center of the unsymmetrical cross section induces the coupling of transverse deflection and torsional motion. The spinning speed induces coupling between transverse deflections along two orthogonal axes. The value of the spinning speed is critical to natural frequencies of the system. The mode shapes are notably changed due to the spinning speed which is different compared to the beam with the symmetric cross section. Also the critical speed increases for the spinning beam with unsymmetrical cross sections. It has also shown that the warping effect has a significant influence on the natural frequencies. Moreover, the effects of warping on the natural frequencies become increasingly large when the proportion of warping rigidity to bending rigidity is notable.

References

1. BANERJEE J., SU H., 2004, Development of a dynamic stiffness matrix for free vibration analysis of spinning beams, *Computers and Structures*, **82**, 23, 2189-2197
2. BANERJEE J.R., SU H., 2006, Dynamic stiffness formulation and free vibration analysis of a spinning composite beam, *Computers and Structures*, **84**, 19/20, 1208-1214
3. BERCIN A., TANAKA M., 1997, Coupled flexural-torsional vibrations of Timoshenko beams, *Journal of Sound and Vibration*, **207**, 1, 47-59
4. BISHOP R., 1959, The vibration of rotating shafts, *Journal of Mechanical Engineering Science*, **1**, 1, 50-65
5. CHOI S.-T., WU J.-D., CHOU Y.-T., 2000, Dynamic analysis of a spinning Timoshenko beam by the differential quadrature method, *AIAA Journal*, **38**, 5, 851-856
6. DIMENTBERG F., 1961, *Flexural Vibrations of Spinning Shafts*, Butterworths press, London
7. FILIPICH C., MAURIZI M., ROSALES M., 1987, Free vibrations of a spinning uniform beam with ends elastically restrained against rotation, *Journal of Sound and Vibration*, **116**, 3, 475-482
8. FILIPICH C., ROSALES M., 1990, Free flexural-torsional vibrations of a uniform spinning beam, *Journal of Sound and Vibration*, **141**, 3, 375-387
9. HO S.H., CHEN C.O.K., 2006, Free transverse vibration of an axially loaded non-uniform spinning twisted Timoshenko beam using differential transform, *International Journal of Mechanical Sciences*, **48**, 11, 1323-1331
10. KANE T., 1961, An addition to the theory of whirling, *Journal of Applied Mechanics*, **28**, 3, 383-386
11. LATALSKI J., BOCHEŃSKI M., WARMIŃSKI J., JARZYNA W., AUGUSTYNIAK M., 2014, Modelling and Simulation of 3 Blade Helicopter's Rotor Model, *Acta Physica Polonica A*, **125**, 6, 1380-1383
12. LEE H., 1995, Dynamic response of a rotating Timoshenko shaft subject to axial forces and moving loads, *Journal of Sound and Vibration*, **181**, 1, 169-177
13. LEE H., 1996, Dynamic stability of spinning beams of unsymmetrical cross-section with distinct end conditions, *Journal of Sound and Vibration*, **189**, 2, 161-171
14. LESAFFRE N., SINOUE J.-J., THOUVEREZ F., 2007, Contact analysis of a flexible bladed-rotor, *European Journal of Mechanics – A/Solids*, **26**, 541-557
15. NA S., YOON H., LIBRESCU L., 2006, Effect of taper ratio on vibration and stability of a composite thin-walled spinning shaft, *Thin-walled Structures*, **44**, 3, 362-371
16. NEWLAND D., 1972, Whirling of a cantilever elastic shaft subjected to external pressure, *Journal of Mechanical Engineering Science*, **14**, 1, 11-18
17. OUYANG H., WANG M., 2007, A dynamic model for a rotating beam subjected to axially moving forces, *Journal of Sound and Vibration*, **308**, 3, 674-682
18. POPPLEWELL N., CHANG D., 1997, Free vibrations of a stepped, spinning Timoshenko beam, *Journal of Sound and Vibration*, **203**, 4, 717-722
19. QIAN X., DU X., PAI P.F., 2010, Experimental nonlinear dynamics of a highly flexible spinning beam using a 3D motion analysis system, *Proceedings of the 51st AIAA Structures, Structural Dynamics and Materials Conference*
20. SHEU G.-J., 2007, On the hollowness ratio effect on the dynamics of a spinning Rayleigh beam, *International Journal of Mechanical Sciences*, **49**, 4, 414-422
21. SHEU G., YANG S.-M., 2005, Dynamic analysis of a spinning Rayleigh beam, *International Journal of Mechanical Sciences*, **47**, 2, 157-169
22. SHIAU T., CHEN E., HUANG K., HSU, W., 2006, Dynamic response of a spinning Timoshenko beam with general boundary conditions under a moving skew force using global assumed mode method, *JSME International Journal Series C*, **49**, 2, 401-410

23. SINHA S.K., TURNER K.E., 2011, Natural frequencies of a pre-twisted blade in a centrifugal force field, *Journal of Sound and Vibration*, **330**, 11, 2655-2681
24. TANAKA M., BERCIN A., 1999, Free vibration solution for uniform beams of nonsymmetrical cross section using Mathematica, *Computers and Structures*, **71**, 1, 1-8
25. TYLIKOWSKI A., 2008, Stability of hybrid rotating shaft with simply supported and/or clamped ends in a weak formulation, *Journal of Theoretical and Applied Mechanics*, **46**, 4, 993-1007
26. YOO H., SHIN S., 1998, Vibration analysis of rotating cantilever beams, *Journal of Sound and Vibration*, **212**, 5, 807-828
27. YOON S.-J., KIM J.-H., 2002, A concentrated mass on the spinning unconstrained beam subjected to a thrust, *Journal of Sound and Vibration*, **254**, 4, 621-634
28. ZU J.-Z., HAN R., 1994, Dynamic response of a spinning Timoshenko beam with general boundary conditions and subjected to a moving load, *Journal of Applied Mechanics*, **61**, 1, 152-160
29. ZU J., MELANSON J., 1998, Natural frequencies and normal modes for externally damped spinning Timoshenko beams with general boundary conditions, *Journal of Applied Mechanics*, **65**, 3, 770-772
30. ZU J.W.-Z., HAN R.P., 1992, Natural frequencies and normal modes of a spinning Timoshenko beam with general boundary conditions, *Journal of Applied Mechanics*, **59**, 2S, S197-S204

Manuscript received September 18, 2015; accepted for print July 14, 2016

SYNCHRONIZATION AND STABILITY OF AN ELASTICALLY COUPLED TRI-ROTOR VIBRATION SYSTEM

YONGJUN HOU, MINGJUN DU, PAN FANG, LIPING ZHANG

School of Mechanical Engineering, Southwest Petroleum University, Chengdu, China

e-mail: ckfangpan@126.com (Pan Fang – corresponding author)

A new mechanism, an elastically coupled tri-rotor system, is proposed to implement synchronization. It is composed of a rigid body, three induction motors, coupling unit and springs. According to the Lagrange equation, the model of the system is established. The average method of small parameters is applied to study the synchronization characteristics of the system, therefore, the balance equation and stability criterion of the system can be obtained. Obviously, many parameters affect the synchronous state of the rotors, especially the spring stiffness, the stiffness of the coupling unit and the installation location of the system. Finally, computer simulations are used to verify the correctness of theoretical analysis.

Keywords: tri-rotor, synchronization characteristics, stability, computer simulations

1. Introduction

The synchronization phenomenon is common in nature. General definitions of synchronization were presented by Blekhman *et al.* (1997, 2002). The synchronization phenomenon is considered as an adjustment of rhythms of oscillating objects due to their internal weak couplings. Dutch scholar Huygens was first to discover the synchronization phenomenon, the synchronous motion of a pendulum hanging on the common base in 1665 (Huygens, 1673). In 1960s, Blekhman proposed the synchronization theory of vibrating machines with two or multiple exciters and successfully solved many engineering problems related to self-synchronization (Blekhman, 1998; Blekhman *et al.*, 1997). Many fields, such as the modeling of nonlinear dynamics, coupling pendulums, mechanical rotors, have attracted attention of researchers. In dynamics of coupled pendulums and rotors, Blekhman proposed the Poincaré method for the synchronization state and stability. Now it is a method widely used in engineering (Jovanovic and Koskhin, 2012). Based on Blekhman's method, many scientists have developed other methods to analyze synchronization of rotors (Blekhman, 1988). Koluda *et al.* (2014a,b) derived synchronization conditions and explained observed types of synchronization for coupled double pendula. They used an energy balance method to show how the energy is transferred between the pendula via an oscillating beam. For synchronization of mechanical rotors, Zhao *et al.* (2010) and Zhang *et al.* (2012) proposed an average method of modified small parameters, which was applied to study of synchronous multiple unbalanced rotors (Zhang *et al.*, 2013). Hou (2007) studied the synchronism theory of three motors using the Hamilton principle. Balthazar (2004) and Balthazar *et al.* (2005) described self-synchronization of two and four non-ideal rotating unbalanced motors via numerical simulations. For synchronization and modeling of nonlinear dynamics, a mechanism of interaction between two non-linear dissipative oscillators was presented by Rui (2014). Two pendulums coupled with a weak spring were proposed by Blekhman (1988). Kumon *et al.* (2002) showed the synchronization phenomenon by designing the controller with applying speed the Gradient Energy method. Fradkov and Andrievsky (2007) focused on the study of phase relations between coupled oscillators.

However, for synchronization of three non-identical coupled exciters, the phase difference of co-rotating motors stabilizes around 120° (Zhang *et al.*, 2013). This results in a weakened amplitude of the center of mass. In order to improve vibration amplitude and screening efficiency of the system, three rotors coupled with a weak spring are proposed in this paper. To explore coupling characteristics of the system, synchronization conditions and the synchronous stability criterion of the system are derived with the Poincaré method. Finally, computer simulations are implemented to verify the results of theoretical analysis. It is demonstrated that the spring stiffness, the coupling spring and the installation location plays a significant role in the vibration system.

This paper is organized as follows. The analysis strategy and considered model are described in Section 2. In Section 3, the synchronization condition and the synchronization stability criterion are obtained. In Section 4, the results of numerical simulations and results of the computer simulations are presented, which validate correctness of the theoretical model of the vibration system. Finally, the results are summarized in Section 5.

2. Model description

2.1. Strategy

The equations of motion for the considered rotation system are as follows (Fang *et al.*, 2015)

$$\begin{aligned} J_s \varphi_s &= \mu \Phi_s(\varphi_s, \ddot{x}) \quad s = 1, \dots, k \\ \ddot{x} + 2\omega_x \xi_x \dot{x} + \omega_x^2 x &= \sum_{j=1}^k F_j(\omega t, \alpha_1, \dots, \alpha_k) + \mu F_{k+1}(\omega t, \alpha_1, \dots, \alpha_k) \end{aligned} \quad (2.1)$$

where $\mu \Phi_s = T_{ms} - T_{fs}$, μ is the small parameter, J_s is the rotational inertia of s -th induction motor, T_{ms} is the driving torque of the induction motors, T_{fs} is the mechanical damping torque of the induction motors, ξ_x and ω_x are the damping coefficient and the natural frequency of the system in the x -direction, ω and φ_s are mechanical velocity and rotation angles of the s -th unbalanced rotor.

In the synchronous state, the velocity of the rotors is assumed as ω . Steady forced vibrations with $T = 2\pi/\omega$ are determined by

$$x = x(\omega t, \alpha_1, \dots, \alpha_k) \quad (2.2)$$

Considering that the rotors are uniformly rotating with an initial phase $\alpha_1, \dots, \alpha_k$, then the phase angle of rotors should satisfy the synchronous solutions from the second formula Eq. (2.2)

$$\varphi_s = \varphi_s^0 = \omega t + \alpha_s \quad (2.3)$$

The above-mentioned basic equation may be satisfied with such values of constants $\alpha_1, \dots, \alpha_k$

$$P_s(\alpha_1, \dots, \alpha_k) = \mu \langle \Phi_s(\varphi_s(\varphi_s, \ddot{x})) \rangle = 0 \quad (2.4)$$

Here, the angle brackets $\langle * \rangle$ show the average value for one period by the variable t , and the symbol $*$ represents a function related to time t

$$\langle * \rangle = \frac{1}{T} \int_0^T * dt \quad (2.5)$$

If a certain set of constants $\alpha_1, \dots, \alpha_k$ is satisfied by Eq. (2.4), all the roots χ of the algebraic equation

$$\begin{vmatrix} \frac{\partial(P_1 - P_k)}{\partial\alpha_1} - \chi & \frac{\partial(P_1 - P_k)}{\partial\alpha_2} & \dots & \frac{\partial(P_1 - P_k)}{\partial\alpha_{k-1}} \\ \frac{\partial(P_2 - P_k)}{\partial\alpha_1} & \frac{\partial(P_2 - P_k)}{\partial\alpha_2} - \chi & \dots & \frac{\partial(P_2 - P_k)}{\partial\alpha_{k-1}} \\ \dots & \dots & \dots & \dots \\ \frac{\partial(P_{k-1} - P_k)}{\partial\alpha_1} & \frac{\partial(P_{k-1} - P_k)}{\partial\alpha_2} & \dots & \frac{\partial(P_{k-1} - P_k)}{\partial\alpha_{k-1}} - \chi \end{vmatrix} = 0 \quad (2.6)$$

would have negative real parts, then unique constant values $\alpha_1, \alpha_2, \dots, \alpha_k$ are determined when the parameter μ is sufficiently small. Meanwhile, there exists an asymptotic periodic solution to Eq. (2.1). Only a single root have a positive real part, and the corresponding solution is unstable. For zero or imaginary roots, additional analysis would further be explored (Blekhman, 1998).

2.2. Kinematic equation of the vibrating system

The model of the vibration system is shown in Fig. 1. The system is mainly composed of three induction motors, coupling unit, crossbeam, screen frame, motor seat. And two motors rotate in the same direction connected with the coupling unit, which consists of a connecting rod, chutes, coupling springs and slide blocks. The chute, linked to the end of the connecting rod by welding, should be mutually parallel. The slide blocks and the coupling springs are installed in the chutes. Besides, the stiffness of the connecting rod is bigger than the coupling springs, and the connecting rod has smaller density. The cross-section area of the connecting rod changes with stiffness of the simplified spring.

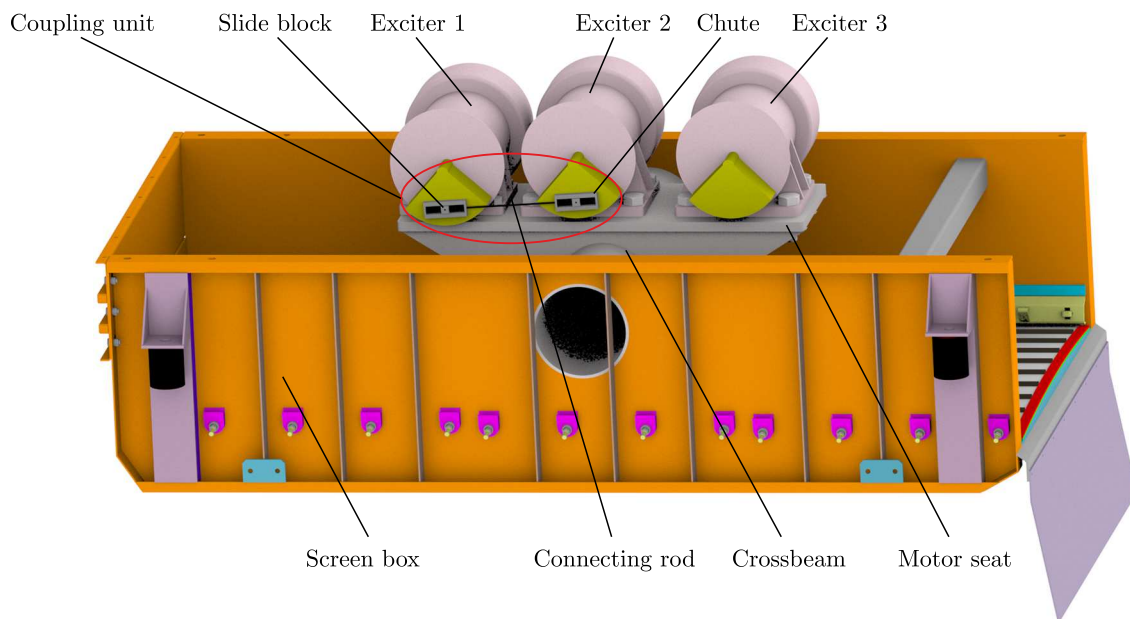


Fig. 1. The model of an elastically coupled tri-rotor system

Figure 2 describes the dynamical model of the considered model. The exciters m_i ($i = 1, 2, 3$) are installed in the screen frame. The rigid vibro-body m_0 is supported on an elastic foundation by some stronger stiffness springs k_x, k_y, k_ψ in x -, y -, ψ -directions. The foundation is characterized by damping constants C_x, C_y, C_ψ . The elastic coupling unit is simplified as a linear spring k , and the distance between the point of connecting of the springs and the motors axles is assumed to be a . As illustrated in Fig. 2b, the mass centers of the rigid vibro-body

is the point o . Three reference coordinate system of the vibration system is designed as follows: the non-rotating moving frame $o'x'y'$ is always parallel to the fixed coordinate frame oxy in the x - and y -directions, and the moving frame $o'x''y''$ swings around the point o' . The exciters also rotate around their own spin axes, which are denoted by φ_i ($i = 1, 2, 3$). M is mass of the system, and the installation angle of the motor is expressed by β_i ($i = 1, 2, 3$). The responses x, y and the angular rotation ψ are considered as independent coordinates.

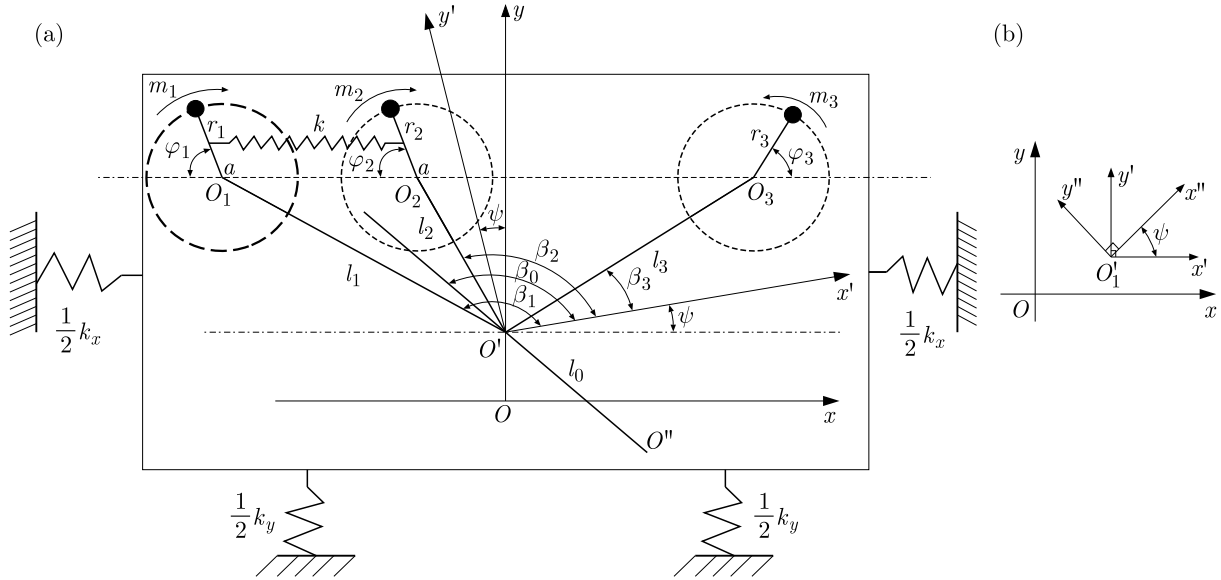


Fig. 2. Simplified model: (a) dynamic model of three rotors coupled with a weak spring, (b) the reference frame system

The expressions for the kinetic energy of the system can be written as follows

$$\begin{aligned}
 T = & \frac{1}{2}m_0 \left\{ [\dot{x} - l_0\dot{\psi} \sin(\beta_0 + \psi + \pi)]^2 + [\dot{y} + l_0\dot{\psi} \cos(\beta_0 + \psi + \pi)]^2 \right\} + \frac{1}{2} \sum_{i=1}^3 J_i \dot{\varphi}_i^2 \\
 & + \frac{1}{2} \sum_{i=1}^2 m_i \left\{ [\dot{x} - l_i\dot{\psi} \sin(\beta_i + \psi) + r_i\dot{\varphi}_i \sin \varphi_i]^2 \right. \\
 & \left. + [\dot{y} + l_i\dot{\psi} \cos(\beta_i + \psi) + r_i\dot{\varphi}_i \cos \varphi_i]^2 \right\} + \frac{1}{2} m_3 \left\{ [\dot{x} - l_3\dot{\psi} \sin(\beta_3 + \psi) - r_3\dot{\varphi}_3 \sin \varphi_3]^2 \right. \\
 & \left. + [\dot{y} + l_3\dot{\psi} \cos(\beta_3 + \psi) + r_3\dot{\varphi}_3 \cos \varphi_3]^2 \right\} + \frac{1}{2} J_0 \dot{\psi}^2
 \end{aligned} \quad (2.7)$$

Moreover, considering that the distance of the co-rotating induction motors is r , and assuming that the ratio $(a/r \ll 1)$ is infinitesimally small, the elongation of the coupled spring can be obtained

$$\Delta l = l - l_0 \approx a(\cos \varphi_1 - \cos \varphi_2) \quad (2.8)$$

And the potential energy of the system can be written as

$$V = \frac{1}{2}k_x x^2 + \frac{1}{2}k_y y^2 + \frac{1}{2}k_\psi \psi^2 + \frac{1}{2}\Delta l^2 \quad (2.9)$$

In addition, the viscous dissipation function of the vibration system can be expressed as

$$D = \frac{1}{2}C_x \dot{x}^2 + \frac{1}{2}C_y \dot{y}^2 + \frac{1}{2}C_\psi \dot{\psi}^2 + \frac{1}{2}C_1 \dot{\varphi}_1^2 + \frac{1}{2}C_2 \dot{\varphi}_2^2 + \frac{1}{2}C_3 \dot{\varphi}_3^2 \quad (2.10)$$

The dynamics equation of the system can be obtained according to Lagrange's equation

$$\frac{d}{dt} \frac{\partial(T - V)}{\partial \dot{q}_i} - \frac{\partial(T - V)}{\partial q_i} + \frac{\partial D}{\partial q_i} = Q_i \quad (2.11)$$

If $q = [x, y, \psi, \varphi_1, \varphi_2, \varphi_3]^T$ is chosen as the generalized coordinates, the generalized forces are $Q_x = Q_y = Q_\psi = 0$, $Q_{\varphi_i} = T_{m_i} - T_{f_i}$. It can be seen that $m_i \ll m_0$ and $\psi \ll 1$ in the system, and the inertia coupling from asymmetry of the system can be neglected. Considering $M = \sum_{i=1}^3 m_i + m_0$, $m_1 = m_2$, $r_1 = r_2$, the kinetic equation of the vibration system is derived as

$$\begin{aligned} M\ddot{x} + C_x\dot{x} + k_x x &= m_3 r_3 (\ddot{\varphi}_3 \sin \varphi_3 + \dot{\varphi}_3^2 \cos \varphi_3) - \sum_{i=1}^2 m_i r_i (\ddot{\varphi}_i \sin \varphi_i + \dot{\varphi}_i^2 \cos \varphi_i) \\ M\ddot{y} + C_y\dot{y} + k_y y &= m_3 r_3 (\dot{\varphi}_3^2 \sin \varphi_3 - \ddot{\varphi}_3 \cos \varphi_3) + \sum_{i=1}^2 m_i r_i (\dot{\varphi}_i^2 \sin \varphi_i - \ddot{\varphi}_i \cos \varphi_i) \\ J\ddot{\psi} + C_\psi\dot{\psi} + k_\psi \psi &= \sum_{i=1}^2 m_i \ell_i r_i [\dot{\varphi}_i^2 \sin(\varphi_i + \beta_i + \psi) - \ddot{\varphi}_i \cos(\varphi_i + \beta_i + \psi)] \\ &\quad + m_3 r_3 \ell_3 [\dot{\varphi}_3^2 \sin(\varphi_3 - \beta_3 - \psi) - \ddot{\varphi}_3 \cos(\varphi_3 - \beta_3 - \psi)] \\ &\quad + C_3(\dot{\varphi}_3 - \dot{\psi}) - C_1(\dot{\varphi}_1 + \dot{\psi}) - C_2(\dot{\varphi}_2 + \dot{\psi}) \\ J_{o1}\ddot{\varphi}_1 &= T_{m1} - T_{f1} - C_1(\dot{\varphi}_1 + \dot{\psi}) - m_1 r_1 [\ddot{x} \sin \varphi_1 + \ddot{y} \cos \varphi_1] \\ &\quad + m_1 r_1 \ell_1 [\dot{\psi}^2 \sin(\varphi_1 + \beta_1 + \psi) - \ddot{\psi} \cos(\varphi_1 + \beta_1 + \psi)] - k a^2 (\cos \varphi_2 - \sin \varphi_1) \sin \varphi_1 \\ J_{o2}\ddot{\varphi}_2 &= T_{m2} - T_{f2} - C_2(\dot{\varphi}_2 + \dot{\psi}) - m_2 r_2 [\ddot{x} \sin \varphi_2 + \ddot{y} \cos \varphi_2] \\ &\quad + m_2 r_2 \ell_2 [\dot{\psi}^2 \sin(\varphi_2 + \beta_2 + \psi) - \ddot{\psi} \cos(\varphi_2 + \beta_2 + \psi)] - k a^2 (\cos \varphi_1 - \sin \varphi_2) \sin \varphi_2 \\ J_{o3}\ddot{\varphi}_3 &= T_{m3} - T_{f3} - C_3(\dot{\varphi}_3 - \dot{\psi}) + m_3 r_3 [\ddot{x} \sin \varphi_3 - \ddot{y} \cos \varphi_3] \\ &\quad + m_3 r_3 \ell_3 [-\dot{\psi}^2 \sin(\varphi_3 - \beta_3 - \psi) - \ddot{\psi} \cos(\varphi_3 - \beta_3 - \psi)] \end{aligned} \quad (2.12)$$

3. Criterion of synchronization and stability of synchronous states

3.1. Method description

According to the Poincaré method (i.e., based on fundamental Eq. (2.1)), introducing the small parameter μ into Eq. (2.12), the influence of the small parameter can be ignored, then a new form of Eq. (2.12) is given

$$\begin{aligned} M\ddot{x} + k_x x &= m_3 r_3 (\dot{\varphi}_3 \sin \varphi_3 + \dot{\varphi}_3^2 \cos \varphi_3) - \sum_{i=1}^2 m_i r_i (\dot{\varphi}_i \sin \varphi_i + \dot{\varphi}_i^2 \cos \varphi_i) \\ M\ddot{y} + k_y y &= m_3 r_3 (\dot{\varphi}_3^2 \sin \varphi_3 - \dot{\varphi}_3 \cos \varphi_3) + \sum_{i=1}^2 m_i r_i (\dot{\varphi}_i^2 \sin \varphi_i - \dot{\varphi}_i \cos \varphi_i) \\ J\ddot{\psi} + k_\psi \psi &= \sum_{i=1}^2 m_i \ell_i r_i [\dot{\varphi}_i^2 \sin(\varphi_i + \beta_i + \psi) - \dot{\varphi}_i \cos(\varphi_i + \beta_i + \psi)] \\ &\quad + m_3 r_3 \ell_3 [\dot{\varphi}_3^2 \sin(\varphi_3 - \beta_3 - \psi) - \dot{\varphi}_3 \cos(\varphi_3 - \beta_3 - \psi)] + C_3 \dot{\varphi}_3 - C_1 \dot{\varphi}_1 - C_2 \dot{\varphi}_2 \\ J_{o1}\ddot{\varphi}_1 &= \mu \phi_1 \quad J_{o2}\ddot{\varphi}_2 = \mu \phi_2 \quad J_{o3}\ddot{\varphi}_3 = \mu \phi_3 \end{aligned} \quad (3.1)$$

where

$$\begin{aligned}
\mu\phi_1 &= T_{m1} - T_{f1} - m_1 r_1 [\ddot{x} \sin \varphi_1 + \ddot{y} \cos \varphi_1] \\
&\quad + m_1 r_1 \ell_1 [\dot{\psi}^2 \sin(\varphi_1 + \beta_1 + \psi) - \ddot{\psi} \cos(\varphi_1 + \beta_1 + \psi)] - k a^2 (\cos \varphi_2 - \sin \varphi_1) \sin \varphi_1 \\
\mu\phi_2 &= T_{m2} - T_{f2} - m_2 r_2 [\ddot{x} \sin \varphi_2 + \ddot{y} \cos \varphi_2] \\
&\quad + m_2 r_2 \ell_2 [\dot{\psi}^2 \sin(\varphi_2 + \beta_2 + \psi) - \ddot{\psi} \cos(\varphi_2 + \beta_2 + \psi)] - k a^2 (\cos \varphi_1 - \sin \varphi_2) \sin \varphi_2 \\
\mu\phi_3 &= T_{m3} - T_{f3} + m_3 r_3 [\ddot{x} \sin \varphi_3 - \ddot{y} \cos \varphi_3] \\
&\quad + m_3 r_3 \ell_3 [-\dot{\psi}^2 \sin(\varphi_3 - \beta_3 - \psi) - \ddot{\psi} \cos(\varphi_3 - \beta_3 - \psi)]
\end{aligned} \tag{3.2}$$

Solving Eq. (3.1), the steady responses in the x -, y - and ψ -directions are obtained

$$\begin{aligned}
x &= a_3 \cos \varphi_3 - a_1 \cos \varphi_1 - a_2 \cos \varphi_2 \\
y &= b_1 \sin \varphi_1 + b_2 \sin \varphi_2 + b_3 \sin \varphi_3 \\
\psi &= c_1 \sin(\varphi_1 + \beta_1) + c_2 \sin(\varphi_2 + \beta_2) + c_3 \sin(\varphi_3 + \beta_3)
\end{aligned} \tag{3.3}$$

where

$$\alpha_i = \frac{m_i r_i \dot{\varphi}_i^2}{k_x - M \dot{\varphi}_i^2} \quad b_i = \frac{m_i r_i \dot{\varphi}_i^2}{k_y - M \dot{\varphi}_i^2} \quad c_i = \frac{m_i r_i \dot{\varphi}_i^2 \ell_i}{k_\psi - J \dot{\varphi}_i^2} \quad i = 1, 2, 3 \tag{3.4}$$

Here, introducing the following dimensionless parameters, the standard mass m is defined, and the natural frequencies are denoted by $\omega_x, \omega_y, \omega_\psi$ in the x -, y -, ψ -direction, respectively.

$$\begin{aligned}
\eta_1 &= \frac{m_1}{m} & \eta_2 &= \frac{m_2}{m} & \eta_3 &= \frac{m_3}{m} & r_m &= \frac{m}{M} & r_e &= \frac{m}{J} \\
\omega_x &= \sqrt{\frac{k_x}{M}} & \omega_y &= \sqrt{\frac{k_y}{M}} & \omega_\psi &= \sqrt{\frac{k_\psi}{J}} & \sigma &= \frac{r_e}{r_m} & \rho &= \frac{r_3}{r_1} \\
\lambda_1 &= \frac{\omega_m^2}{\omega_m^2 - \omega_x^2} & \lambda_2 &= \frac{\omega_m^2}{\omega_m^2 - \omega_y^2} & \lambda_3 &= \frac{\omega_m^2}{\omega_m^2 - \omega_\psi^2}
\end{aligned} \tag{3.5}$$

Consequently, basic Eq. (3.3) will be written as

$$\begin{aligned}
x &= r_m \lambda_1 (\eta_1 r_1 \cos \varphi_1 + \eta_2 r_2 \cos \varphi_2 - \eta_3 r_3 \cos \varphi_3) \\
y &= -r_m \lambda_2 (\eta_1 r_1 \sin \varphi_1 + \eta_2 r_2 \sin \varphi_2 + \eta_3 r_3 \sin \varphi_3) \\
\psi &= -r_e \lambda_3 [\eta_1 r_1 \sin(\varphi_1 + \beta_1) + \eta_2 r_2 \sin(\varphi_2 + \beta_2) + \eta_3 r_3 \sin(\varphi_3 - \beta_3)]
\end{aligned} \tag{3.6}$$

3.2. Synchronization criterion

Theoretical derivation of the synchronization condition is discussed in this Section. Assume that α_i, φ_i are the initial phase and phase angle of the unbalanced rotor i , respectively. The solution mentioned above is corresponding with Eq. (2.3)

$$\varphi_1 = \omega t + \alpha_1 \quad \varphi_2 = \omega t + \alpha_2 \quad \varphi_3 = \omega t + \alpha_3 \tag{3.7}$$

According to Eq. (2.4), substituting Eq. (3.7) into Eq.(3.2), P_i can be calculated

$$\begin{aligned}
P_1 &= \langle \mu \phi_1 \rangle = T_{m1} - T_{f1} - \frac{1}{2} m_1 r_m r_1 \omega^2 [\eta_2 r_2 (\lambda_1 + \lambda_2) \sin(\alpha_2 - \alpha_1) \\
&\quad + \eta_3 r_3 (\lambda_2 - \lambda_1) \sin(\alpha_3 - \alpha_1)] - \frac{1}{2} m_1 r_1 \ell_1 r_e \lambda_3 \omega^2 [\eta_2 r_2 \sin(\alpha_2 - \alpha_1 + \beta_2 - \beta_1) \\
&\quad + \eta_3 r_3 \sin(\alpha_3 - \alpha_1 - \beta_3 - \beta_1)] + \frac{1}{2} k a^2 [\sin(\alpha_2 - \alpha_1) + 1] = 0 \\
P_2 &= \langle \mu \phi_2 \rangle = T_{m2} - T_{f2} - \frac{1}{2} m_2 r_m r_2 \omega^2 [-\eta_1 r_1 (\lambda_1 + \lambda_2) \sin(\alpha_2 - \alpha_1) \\
&\quad + \eta_3 r_3 (\lambda_1 - \lambda_2) \sin(\alpha_2 - \alpha_3)] - \frac{1}{2} m_2 r_2 \ell_2 r_e \lambda_3 \omega^2 [\eta_1 r_1 \sin(\alpha_1 - \alpha_2 + \beta_1 - \beta_2) \\
&\quad + \eta_3 r_3 \sin(\alpha_3 - \alpha_2 - \beta_3 - \beta_2)] + \frac{1}{2} k a^2 [-\sin(\alpha_2 - \alpha_1) + 1] = 0 \\
P_3 &= \langle \mu \phi_3 \rangle = T_{m3} - T_{f3} + \frac{1}{2} m_3 r_m r_3 \omega^2 [\eta_1 r_1 (\lambda_1 - \lambda_2) \sin(\alpha_1 - \alpha_3) \\
&\quad + \eta_2 r_2 (\lambda_1 - \lambda_2) \sin(\alpha_2 - \alpha_3)] \\
&\quad - \frac{1}{2} m_3 r_3 \ell_3 r_e \lambda_3 \omega^2 [\eta_1 r_1 \sin(\alpha_1 - \alpha_3 + \beta_1 + \beta_3) + \eta_2 r_2 \sin(\alpha_2 - \alpha_3 + \beta_2 + \beta_3)] = 0
\end{aligned} \tag{3.8}$$

When the angular velocity of the tri-rotors is near to the synchronous velocity ω_m , the excessive torque $Z_s(\omega)$ of the rotors is equal to zero in the synchronization state

$$Z_i(\omega) = T_{mi} - T_{fi} = 0 \quad i = 1, 2, 3 \tag{3.9}$$

The balance equation of synchronization of the vibrating system can be expressed as

$$\begin{aligned}
&\mu_1 [\sin(\alpha_3 - \alpha_1) + \sin(\alpha_3 - \alpha_2)] + \mu_2 \sin(\alpha_2 - \alpha_1 + \beta_2 - \beta_1) \\
&\quad + \mu_3 \sin(\alpha_3 - \alpha_1 - \beta_3 - \beta_1) + \mu_4 \sin(\alpha_3 - \alpha_2 - \beta_3 - \beta_2) - \mu_7 = 0 \\
&\mu_5 [\sin(\alpha_1 - \alpha_3) + \sin(\alpha_2 - \alpha_3)] + \mu_6 [\sin(\alpha_3 - \alpha_1 - \beta_1 - \beta_3) \\
&\quad + \sin(\alpha_3 - \alpha_2 - \beta_2 - \beta_3)] = 0
\end{aligned} \tag{3.10}$$

where

$$\begin{aligned}
\mu_1 &= \eta_1 \eta_3 \rho (\lambda_2 - \lambda_1) & \mu_2 &= \eta_1 \eta_2 \sigma \lambda_3 (\ell_1 - \ell_2) & \mu_3 &= \eta_1 \eta_3 \ell_1 \sigma \rho \lambda_3 \\
\mu_4 &= \eta_2 \eta_3 \ell_2 \sigma \rho \lambda_3 & \mu_5 &= \lambda_1 - \lambda_2 & \mu_6 &= \ell_3 \sigma \lambda_3 \\
\mu_7 &= \frac{2ka^2}{m_0 r_1^2 r_m \omega^2}
\end{aligned} \tag{3.11}$$

3.3. Stability criterion of synchronization states

Introduce now new parameters A, B, C, D , i.e:

$$A = \frac{\partial(P_1 - P_3)}{\partial \alpha_1} \quad B = \frac{\partial(P_2 - P_3)}{\partial \alpha_2} \quad C = \frac{\partial(P_2 - P_3)}{\partial \alpha_1} \quad D = \frac{\partial(P_2 - P_3)}{\partial \alpha_2} \tag{3.12}$$

According to Eq.(2.6), the stability criterion of synchronization of the system can be expressed as

$$A + B < 0 \tag{3.13}$$

Inserting Eq. (3.8) and Eq. (3.12) into Eq. (3.13), the stability criterion of synchronization states can be simplified as

$$2\mu_8 \cos(\alpha_2 - \alpha_1) + 2\mu_1 [\cos(\alpha_3 - \varphi_1) + \cos(\alpha_2 - \alpha_3)] + \mu_9 \cos(\alpha_2 - \alpha_1 + \beta_2 - \beta_1) + \mu_{10} \cos(\alpha_1 - \alpha_3 + \beta_1 + \beta_3) + \mu_{11} \cos(\alpha_2 - \alpha_3 + \beta_2 + \beta_3) - \mu_7 \cos(\alpha_2 - \alpha_1) < 0 \quad (3.14)$$

where

$$\begin{aligned} \mu_8 &= \eta_1 \eta_2 (\lambda_1 + \lambda_2) & \mu_9 &= \eta_1 \eta_2 (\ell_1 + \ell_2) \sigma \lambda_3 \\ \mu_{10} &= \eta_1 \eta_3 \rho \sigma \lambda_3 (\ell_1 + \ell_3) & \mu_{11} &= \eta_1 \eta_2 \rho \sigma \lambda_3 (\ell_2 + \ell_3) \end{aligned} \quad (3.15)$$

Therefore, only the system parameters satisfy balance equations (3.10) and the stability criterion of synchronization (3.14) can be implemented in the considered case.

4. Numerical verification

In the above Sections, the differential equations, balanced equations and the stability criterion of synchronization have been derived. The theoretical and simulation results are presented in this Section, where the correctness of the theory is to be verified.

4.1. Analysis of numerical results

Some examples are used to prove the correctness of the results of the above theoretical derivation. Based on Eq. (4.1), the stiffness coefficients k_x , k_y and k_φ are separately transformed into frequency ration η_x , η_y , η_φ . Balance equations (3.10) are nonlinear equations related to the system parameters, including the supporting spring stiffness, stiffness of elastic spring k , installation location, etc., which seriously influence the stability of self-synchronization of the system. When the system parameters are simultaneously satisfied, balance equation (3.10), stability criterion (3.14) and the stable phase difference can be estimated by applying a numerical method. In order to simplify calculations, we assume $\eta_x = \eta_y = \eta_\varphi$, i.e.,

$$\eta_x = \frac{\omega}{\omega_x} \quad \eta_y = \frac{\omega}{\omega_y} \quad \eta_\varphi = \frac{\omega}{\omega_\varphi} \quad (4.1)$$

Studying synchronization of the vibration system, the parameters are shown in Table 1, and the dimensionless values are shown in Table 2 according to Eq. (3.5).

Table 1. Parameter values of the system

Unbalanced rotor for $i = 1, 2, 3$	$m_i = 3 \text{ kg}$, $r_i = 0.02 \text{ m}$, $\omega_m = 156 \sim 157 \text{ rad/s}$, $c_i = 0.01 \text{ N}\cdot\text{s/m}$
Vibro-platform	$M = 100 \text{ kg}$ $J = 10 \text{ kg}\cdot\text{m}^2$, $f_x = 1000 \text{ N}/(\text{m/s})$, $f_y = 1000 \text{ N}/(\text{m/s})$, $f_z = 1000 \text{ N}/(\text{m/s})$, $k_x = 1 \cdot 10^4 \sim 3.65 \cdot 10^5 \text{ N/m}$, $k_y = 1 \cdot 10^4 \sim 3.65 \cdot 10^5 \text{ N/m}$, $k_\psi = 1 \cdot 10^3 \sim 3.65 \cdot 10^4 \text{ N/m}$
Other parameters	$l_1 = 0.8 \text{ m}$, $l_2 = 0.73, 0.41 \text{ m}$, $l_3 = 0.8 \text{ m}$, $\beta_1 = 2\pi/3, 5\pi/6$, $\beta_2 = 2\pi/5, 5\pi/12$, $\beta_3 = \pi/3, \pi/6$
The spring	$k = 0 \sim 1.4 \cdot 10^5 \text{ N/m}$, $a = 0.01 \text{ m}$

Equations (3.10) and (3.14) describe the approximate analytical solution for the stable phase difference. Based on the parameters in Table 2, we can acquire an approximate value of $\varphi_1 - \varphi_2$ and $\varphi_1 - \varphi_3$ considering different parameters $k, \eta_x, \eta_y, \eta_\varphi$ when three motors are installed in

Table 2. Parameter values according to dimensionless Eq. (3.5)

$\eta_1 = 1, \eta_2 = 1, \eta_3 = 1, r_m = 0.02, r_e = 0.18, \sigma = 8.82, \rho = 1,$ $n_x = 1 \sim 19, n_y = 1 \sim 19, n_\varphi = 1 \sim 15.7$

different positions. The analytical results are shown in Fig. 3 and Fig. 4. They indicate that the parameters $\eta_x, \eta_y, \eta_\varphi$, have little influence on the value of the phase difference when the above-mentioned balance equation and the stability criterion equation are satisfied. But the parameter k directly affects the phase difference. Figure 3 shows numerical results for positional parameters (i.e, $l_1 = 0.8$ m, $l_2 = 0.73$ m, $l_3 = 0.8$ m, $\beta_1 = 2\pi/3$, $\beta_2 = 2\pi/5$, $\beta_3 = \pi/3$) for different frequency ratios. When $k = 0$ N/m (there is no coupling unit in co-rotating motors), the phase difference $\varphi_1 - \varphi_2$ of the co-rotating motors is stabilized in the vicinity of 3 rad, and the phase difference $\varphi_1 - \varphi_3$ of the counter-rotating motors is near 1 rad. When $k \geq 30000$ N/m, the phase difference of the co-rotating motors is close to 0 rad and the stable difference $\varphi_1 - \varphi_3$ is near 1 rad. Meanwhile, the vibration amplitude improves when the stiffness of the coupling spring k exceeds the maximum value $k_{max} = 140000$ N/m (Fig. 3a), and $k_{max} = 120000$ N/m (Fig. 3b,c,d), which means that the synchronous motion is unstable. The numerical results for $l_1 = 0.8$ m, $l_2 = 0.41$ m, $l_3 = 0.8$ m, $\beta_1 = 5\pi/6$, $\beta_2 = 5\pi/12$, $\beta_3 = \pi/6$ are displayed in Fig. 4. Similar conclusions are also obtained.

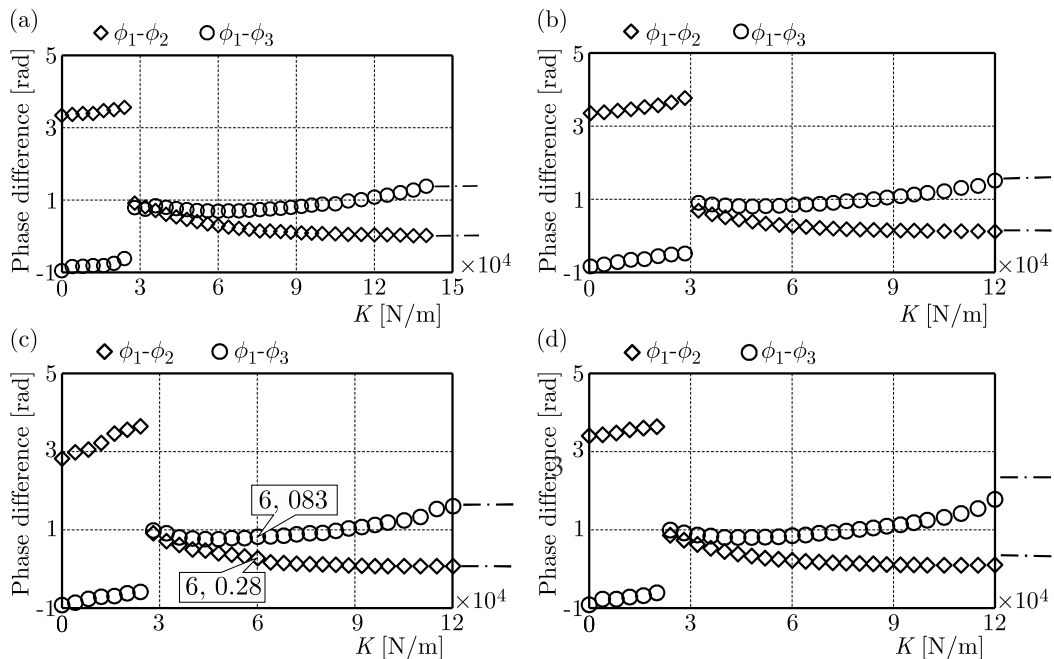


Fig. 3. Stable phase difference with theoretical analysis for $l_1 = 0.8$ m, $l_2 = 0.73$ m, $l_3 = 0.8$ m, $\beta_1 = 2\pi/3$, $\beta_2 = 2\pi/5$, $\beta_3 = \pi/3$; (a) $\eta_x = \eta_y = \eta_\varphi = 1.76$, (b) $\eta_x = \eta_y = \eta_\varphi = 3.51$, (c) $\eta_x = \eta_y = \eta_\varphi = 5.23$, (d) $\eta_x = \eta_y = \eta_\varphi = 7.85$; - · - shows there is no stable phase difference

The above analysis implies that these parameters play an important role in the synchronous state, which mainly include the stiffness coefficient k , frequency ratios and installation location of three induction motors. Besides, the coupled spring connecting the co-rotation rotors is also compliant with the condition and stability of synchronization. By selecting a large value of k , the vibration amplitude and the screening efficiency of the system can be improved.

4.2. Buckling analysis of the connecting rod

The two chutes are connected by the connecting rod. During the process of self-synchronization, the elasticity coupling between the two induction motors can be achieved

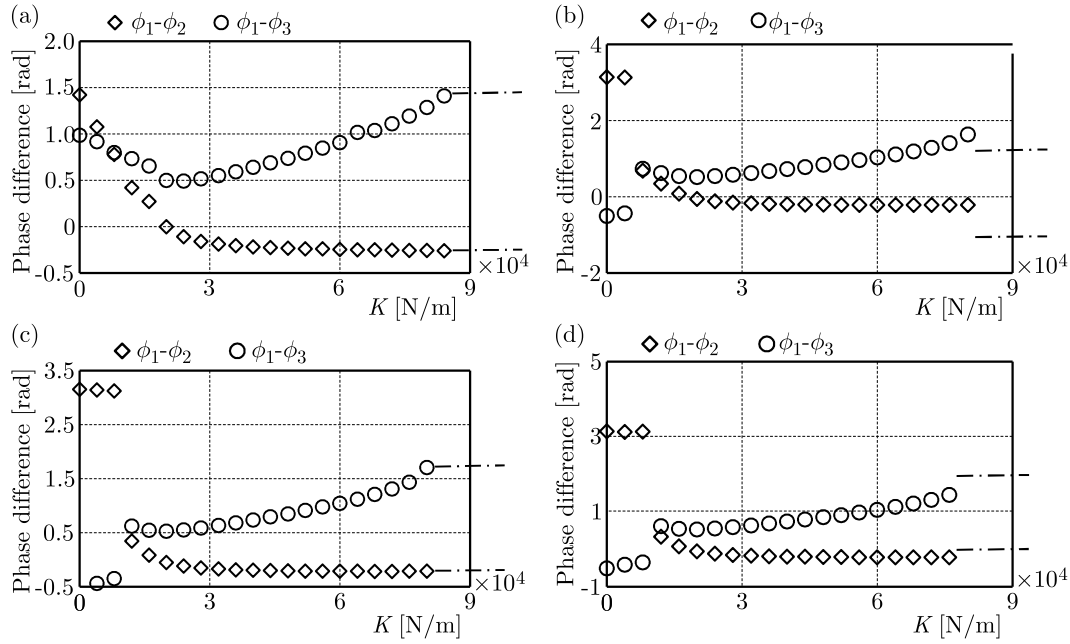


Fig. 4. Stable phase difference with theoretical analysis for $l_1 = 0.8$ m, $l_2 = 0.41$ m, $l_3 = 0.8$ m, $\beta_1 = 5\pi/6$, $\beta_2 = 5\pi/12$, $\beta_3 = \pi/6$; (a) $\eta_x = \eta_y = \eta_\varphi = 2.22$, (b) $\eta_x = \eta_y = \eta_\varphi = 4.96$, (c) $\eta_x = \eta_\varphi = 5.55$, (d) $\eta_x = \eta_y = \eta_\varphi = 7.02$, - - - shows there is no stable phase difference

by the springs in the chutes. Owing to the connecting rod with smaller density and the strong stiffness, the centrifugal inertia force of the rod is small, in which case a deflection of the elastic rod can be ignored. For example, the location parameters of vibration motors are identical with the parameters in Fig. 3. According to theoretical analysis (Fig. 3), the stiffness of the simplified spring has the maximum value $k_{max} = 120000$ N/m. Assume $k = 80000$ N/m in this case.

The phase difference of co-rotating motors is expressed as α , which satisfies

$$\alpha = |\varphi_1 - \varphi_2| \quad (4.2)$$

The range of the phase difference α is obtained as $0 \leq \alpha \leq \pi$. When $\alpha = 0^\circ$, the deformation of the simplified spring is equal to 0; when $\alpha = 180^\circ$, the deformation of the simplified spring has the maximum value, $x_{max} = 2a = 0.02$ m (the simplified spring is in stretched state or under compression), $0 \leq x \leq x_{max}$.

The force in the connecting rod satisfies

$$F = kx \leq F_{max} = kx_{max} = 80000 \frac{\text{N}}{\text{m}} \cdot 0.02 \text{ m} = 1600 \text{ N} \quad (4.3)$$

Assuming that the material of the rod is 2024(LY12), then the yield strength and the density are $[\sigma] = 325$ MPa, $\rho = 2770$ kg·m⁻³, $E = 72$ GPa = $7.2 \cdot 10^4$ N/mm². Then the cross-section area A of the connecting rod can be determined

$$A \geq \frac{F_{max}}{[\sigma]} = 4.92 \text{ mm}^2 \quad (4.4)$$

The model of the connecting rod in buckling analysis is shown in Fig. 5. The applied load is expressed as F ($\mu = 1$). The inertia moment of circular section can be expressed as

$$I = \frac{1}{32} \pi d^4 \quad (4.5)$$

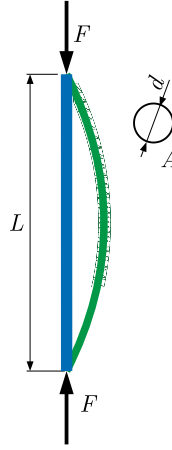


Fig. 5. The model of the connecting rod in buckling analysis

The cross-sectional area A of the connecting rod

$$A = \frac{\pi d^2}{4} \quad (4.6)$$

The critical load of the rod can be computed by Euler's formula

$$F_{cr} = \frac{\pi^2 EI}{(\mu L)^2} \quad (4.7)$$

If the buckling of the rod is not achieved, the statical criterion for elastic stability satisfies

$$F < F_{cr} \quad (4.8)$$

Based on the critical condition $F = F_{max}$, from equation (4.5)-(4.8), A can be calculated

$$A > \sqrt{\frac{2F_{max}(\mu L)^2}{E\pi}} = 35.7 \text{ mm}^2 \quad (4.9)$$

Therefore, the cross-section area the connecting rod A can be obtained

$$A > 35.7 \text{ mm}^2 \quad (4.10)$$

If $A = 36 \text{ mm}^2$, so the mass can be calculated

$$m = \rho LS = 2770 \frac{\text{kg}}{\text{m}^3} \cdot 0.3 \text{ m} \cdot 36 \text{ mm}^2 = 0.03 \text{ kg} \ll M = 100 \text{ kg} \quad (4.11)$$

Therefore, the mass is too small to be neglected.

According to the national design standard, the size of the coupling springs can be finally established.

4.3. Simulation results for $n_x = n_y = n_\varphi = 5.23$, $k = 60000 \text{ N/m}$, $l_1 = 0.8 \text{ m}$, $l_2 = 0.73 \text{ m}$, $l_3 = 0.8 \text{ m}$

Simulation results for the dimensionless parameters in Table 3 are shown in Fig. 6. Here, $k_x = k_y = 9.0 \cdot 10^4 \text{ N/m}$, $k_\psi = 9.0 \cdot 10^3 \text{ N/rad}$, $l_1 = 0.8 \text{ m}$, $l_2 = 0.73 \text{ m}$, $l_3 = 0.8 \text{ m}$, and the other parameters are identical with those in Table 1. From Fig. 6a to Fig. 6f, it can be seen that the self-synchronization of the system is implemented. The three induction motors cannot

Table 3. Dimensionless parameter values

$$\eta_1 = 1, \eta_2 = 1, \eta_3 = 1, r_m = 0.02, r_e = 0.20, \sigma = 8.70, \rho = 1, \\ n_x = 8.54, n_y = 8.54, n_\varphi = 8.54$$

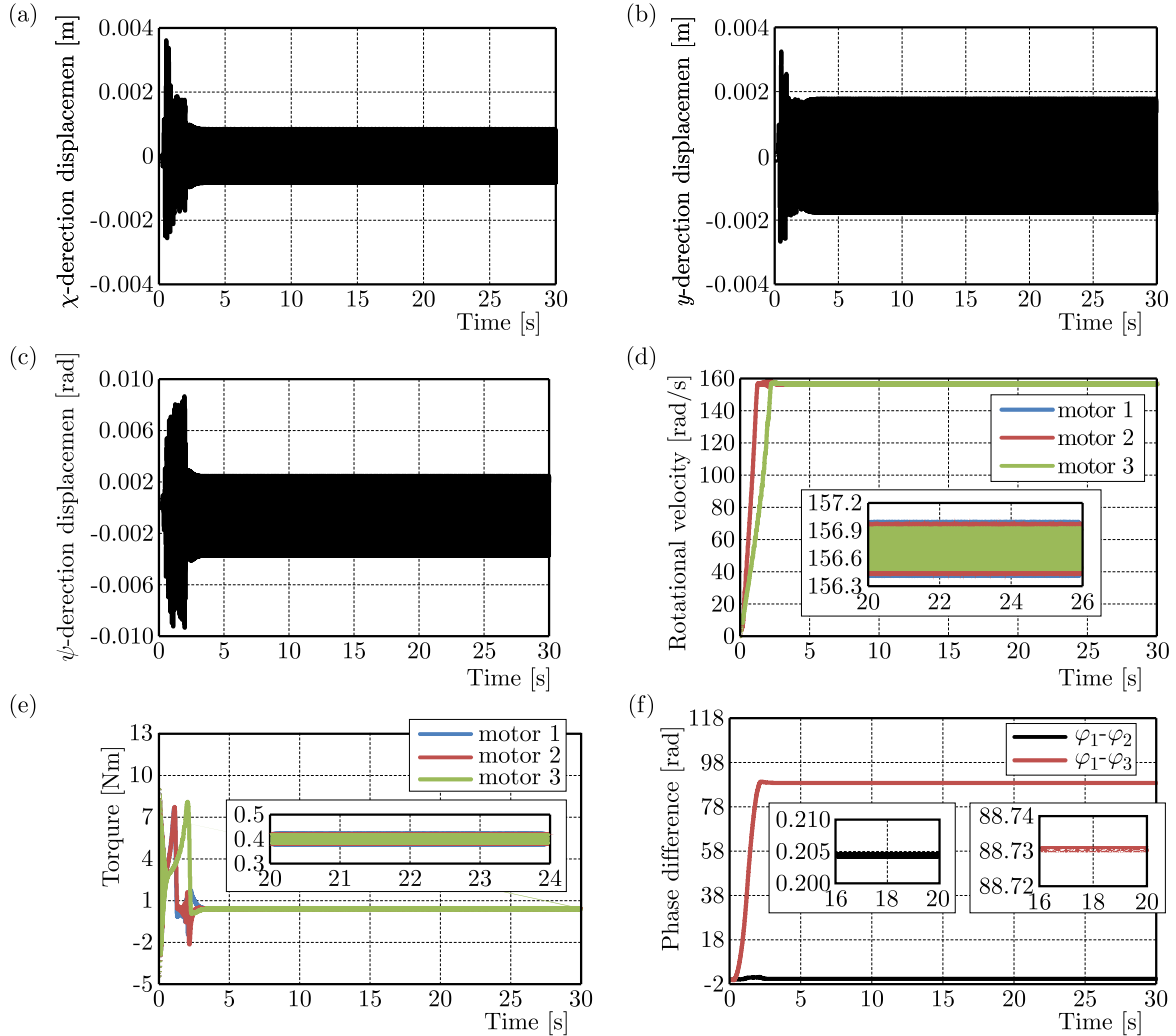


Fig. 6. Results of computer simulations. (a),(b),(c) Displacement responses of the vibrating body in the x -, y -, ψ -directions, respectively; (d) rotational velocities of the vibration system; (e) electromagnetic torques of the tri-rotors; (f) phase difference of unbalanced rotors

simultaneously start at the same angular velocity owing to the difference coupling characteristics when three exciters are switched on at the same time. Eventually, the value of angular velocity is identical, see Fig. 6d. The average angular velocity of the three unbalanced rotors is 155.7 rad/s at about 2 s, which is always defined as the synchronous velocity. In addition, the coupling torques (Fig. 6e), keeping the vibration system working in a steady synchronization state, are approximately 0.4 N/m. The phase difference $\varphi_1 - \varphi_2$ of the co-rotating motors is near 0.205 rad. The phase difference $\varphi_1 - \varphi_3$ of the counter-rotating motors stabilized in the vicinity of 88.73 rad ($88.73 \text{ rad} = (28\pi + 0.77) \text{ rad}$, Fig. 6f), agrees with the approximate theoretical value 0.83 rad. The stable difference $\varphi_1 - \varphi_2$ is equal to 0.28 rad, Fig. 3c. It can be seen that the ideal phase synchronization is achieved by two co-rotation rotors coupled with a weak spring, and the excitation forces of the system are improved. The displacement response of the vibrating body is displayed in the x -, y - and ψ -directions, respectively, Fig. 6a,b,c. The computer simulation results further proved the validity of theoretical analysis.

5. Conclusions

Based on the theoretical research and numerical analysis, the following conclusions are obtained.

In this paper, a new vibration mechanism, an elastically coupled tri-rotor system, is proposed to implement synchronization. The average method of small parameters is used to study synchronization characteristics of the system. The dynamical equations are converted into dimensionless equations, and the synchronized state have been investigated. When the values of the system parameters satisfy the balance equations and the stability criterion of synchronization, the vibration system can operate in a steady state. The study indicates that many factors, such as the spring stiffness, stiffness of the elastic unit and the installation location, influence stability of the system. Finally, computer simulations have been preformed to verify the correctness of the approximate solution from computations for the vibration system. Besides, it can be found that the spring connecting the co-rotation rotors makes the phase difference stabilized in the vicinity of 0 rad, and the vibration amplitude of the system is improved in contrast to the former one. In this case, the screening efficiency of the system can be improved as well. Moreover, when stiffness of the coupling spring exceeds the maximum value, the vibration system locates in an unstable state. In short, a new balanced elliptical vibrating screen is proposed having a bright future in applications.

Acknowledgment

This study has been supported by science and technology support plan of Sichuan province (2016RZ0059) and the National Natural Science Foundation of China (Grant No. 51074132).

References

1. BALTHAZAR J.M., 2004, Short comments on self-synchronization of two non-ideal sources supported by a flexible portal frame structure, *Journal of Vibration and Control*, **10**, 1739-1748
2. BALTHAZAR J.M., FELIX J.L.P., BRASIL R.M., 2005, Some comments on the numerical simulation of self-synchronization of four non-ideal exciters, *Applied Mathematics and Computation*, **164**, 615-625
3. BLEKHMEN I.I., 1988, *Synchronization in Science and Technology*, ASME Press
4. BLEKHMEN I.I., FRADKOV A.L., NIJMEIJER H., POGROMSKY A.Y., 1997, On self-synchronization and controlled synchronization, *Proceedings of European Control Conference*
5. BLEKHMEN I.I., FRADKOV A.L., TOMCHINA O.P., BOGDANOV D.E., 2002, Self-synchronization and controlled synchronization: general definition and example design, *Mathematics and Computers in Simulation*, **58**, 367-384
6. FANG P., HOU Y., NAN Y., YU L., 2015, Study of synchronization for a rotor-pendulum system with Poincare method, *Journal of Vibroengineering*, **17**, 2681-2695
7. FRADKOV A.L., ANDRIEVSKY B., 2007, Synchronization and phase relations in the motion of two-pendulum system, *International Journal of Non-Linear Mechanics*, **42**, 895-901
8. HOU J., 2007, The synchronous theory of three motor self-synchronism exciting elliptical motion shaker, *Journal of Southwest Petroleum University*, **29**, 168-172
9. HUYGENS C., 1673, *Horologium Oscilatorium*, Paris, France
10. JOVANOVIĆ V., KOSHKIN S., 2012, Synchronization of Huygens' clocks and the Poincaré method, *Journal of Sound and Vibration*, **331**, 2887-2900
11. KOLUDA P., PERLIKOWSKI P., CZOLCZYŃSKI K., KAPITANIAK T., 2014, Synchronization configurations of two coupled double pendula, *Communications in Nonlinear Science and Numerical Simulation*, **19**, 977-990

12. KOLUDA P., PERLIKOWSKI P., CZOLCZYNSKI K., KAPITANIAK T., 2014, Synchronization of two self-excited double pendula, *The European Physical Journal Special Topics*, **223**, 613-629
13. KUMON M., WASHIZAKI R., SATO J., KOHZAWA R., MIZUMOTO I., IWAI Z., 2002, Controlled synchronization of two 1-DOF coupled oscillators, *International Journal of Bifurcation and Chaos in Applied Sciences and Engineering*, **15**, 1
14. RUI D., 2014, Anti-phase synchronization and ergodicity in arrays of oscillators coupled by an elastic force, *European Physical Journal Special Topics*, **223**, 665-676
15. ZHANG X.L., WEN B.C., ZHAO C.Y., 2012, Synchronization of three homodromy coupled exciters in a non-resonant vibrating system of plane motion, *Acta Mechanica Sinica*, **28**, 1424-1435
16. ZHANG X.L., WEN B.C., ZHAO C.Y., 2013, Synchronization of three non-identical coupled exciters with the same rotating directions in a far-resonant vibrating system, *Journal of Sound and Vibration*, **332**, 2300-2317
17. ZHAO C.Y., ZHANG Y.M., WEN B.C., 2010, Synchronisation and general dynamic symmetry of a vibrating system with two exciters rotating in opposite directions, *Acta Physica Sinica*, **19**, 14-20

Manuscript received January 16, 2016; accepted for print July 14, 2016

EXPERIMENTAL VALIDATION OF THE USE OF ENERGY TRANSFER RATIO (ETR) FOR DAMAGE DIAGNOSIS OF STEEL-CONCRETE COMPOSITE BEAMS

TOMASZ WRÓBLEWSKI, MAŁGORZATA JAROSIŃSKA, MAŁGORZATA ABRAMOWICZ

West Pomeranian University of Technology, Department of Theory of Structure, Szczecin, Poland

e-mail: wroblewski@zut.edu.pl, jarosinska@zut.edu.pl, mabramowicz@zut.edu.pl

STEFAN BERCZYŃSKI

West Pomeranian University of Technology, Institute of Manufacturing Engineering, Szczecin, Poland

e-mail: Stefan.Berczynski@zut.edu.pl

The paper presents changes of modal parameters such as natural frequencies, damping ratios and energy transfer ratios (ETR) following damage of the connection of a steel-concrete composite beam. Sensitivity analysis of the parameters is conducted both for numerical simulation and experimental results. The energy transfer ratio ETR is determined: i) for the whole beam – as a global parameter which can be used for damage detection, ii) for segments of the beam – as a local parameter which can be used for damage localisation.

Keywords: damage diagnosis, energy transfer ratio (ETR), steel-concrete composite beams

1. Introduction

Steel-concrete composite beams are often used in the bridge engineering as main carrying girders. Safety of bridge structures, both during constructional work and particularly during their use, is of major importance. Therefore, continuous monitoring of the structure condition is an increasingly common practice with a view to damage diagnosis in early stages for substantial reduction of the cost of necessary repairs. Monitoring systems are often based on non-destructive damage detection methods. They enable damage detection in places inaccessible during visual inspection, e.g. in shear connectors of steel-concrete composite bridges (Liu and de Roeck, 2009; Li *et al.*, 2014a,b; Dilena and Morassi, 2004, 2009).

Non-destructive methods are often based on measurements of vibration of the structure. Vibrations that are excited by a changing load are recorded and modal characteristics of the structure are analysed. When damage appears, stiffness, damping and sometimes mass of the structure change, causing changes in frequency response functions. This is reflected in changes of modal parameters, including natural frequencies, mode shapes and damping parameters. Methods based on analysis of such changes can provide an effective tool to damage diagnosis. One of them, which deserves an in-depth analysis, is based on changes of the energy transfer ratio (ETR). Since the method is used for non-proportionally damped structures, it has gained little recognition as most studies assume analysed structures to be proportionally damped.

The energy transfer ratio was defined by Liang and Lee (1991). It defines the ratio of energy which is transferred between different mode shapes. Based on an experimental research conducted on a model of a composite bridge, the authors demonstrated that ETR was much more sensitive to damage than the natural frequency or damping ratio. Their study revealed that modal energy was transferred not only between mode shapes but also between their fragments. It means that ETR can be determined both globally, for the whole construction, and locally, for its segments, which can be used for damage localisation. Similar studies conducted on composite

bridge models were also carried out by Kong *et al.* (1996), Liang *et al.* (1997), Wang and Zong (2002, 2003).

The present paper is a continuation of two earlier studies published by Wróblewski *et al.* (2011, 2013) which demonstrated a method of how ETR changes could be used for damage detection and localisation in steel-concrete composite beams. The results obtained in numerical analysis confirmed that ETR was more sensitive to changes in steel-concrete beam structure than the natural frequency or damping ratio. However, it should be pointed out that the studies were based on numerical damage simulation only. The present paper assesses changes of modal parameters both based on numerical simulation results and experimental data. ETR is discussed and tested as a damage detection tool, i.e. as a global parameter determined for the whole beam and as a local parameter determined for segments of the beam, which can be useful for damage localisation.

2. Experimental research

The analysed composite beam measures 3200 mm in length and consists of IPE 160 made of S235JRG2 steel, connected to a concrete slab made of C30/37 concrete. The connection between the concrete and steel is made using headed steel studs, 10 mm in diameter and 50 mm in height. The studs are placed in pairs every 150 mm. The cross-section of the beam and stud distribution along the beam are shown in Fig. 1.

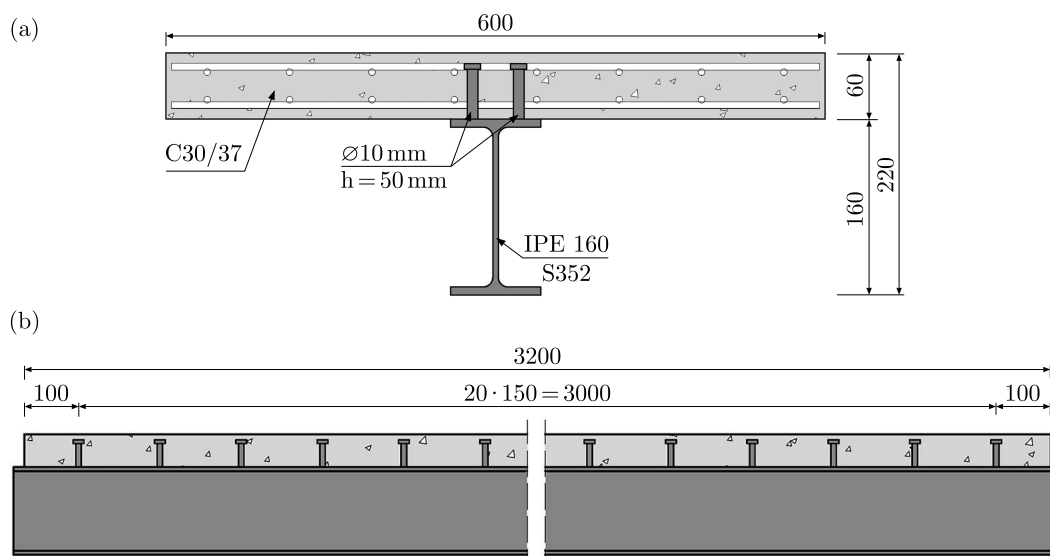


Fig. 1. Composite beam: (a) cross-section, (b) distribution of connectors

Experiments have been conducted for a free-free beam. They were carried out by suspending the tested beam on a steel frame by means of four elastic steel cables. The places where the cables were attached to the concrete slab overlapped with the nodes of the fundamental flexural mode shape of vibration of the beam.

An impulse test with a modal hammer was conducted to excite vibration of the structure. The system response was measured in three orthogonal directions using piezoelectric accelerometers. LMS SCADAS III, a multi-channel analyser, was used to measure the signal. It was connected to a workstation, fitted with LMS Test.Lab software.

A grid of 52 measurement points were defined on the beam. In these points, accelerations were measured. Two additional points, 53 and 54, were situated at one end of the beam. To excite flexural vibration of the beam, force impulse was applied at point 53 perpendicularly to

the slab ($-Y$ direction). To excite axial vibration of the beam, a force impulse was delivered at point 54, on the slab edge ($+X$ direction). A grid of measurement points and the directions of the force impulse are presented in Fig. 2.

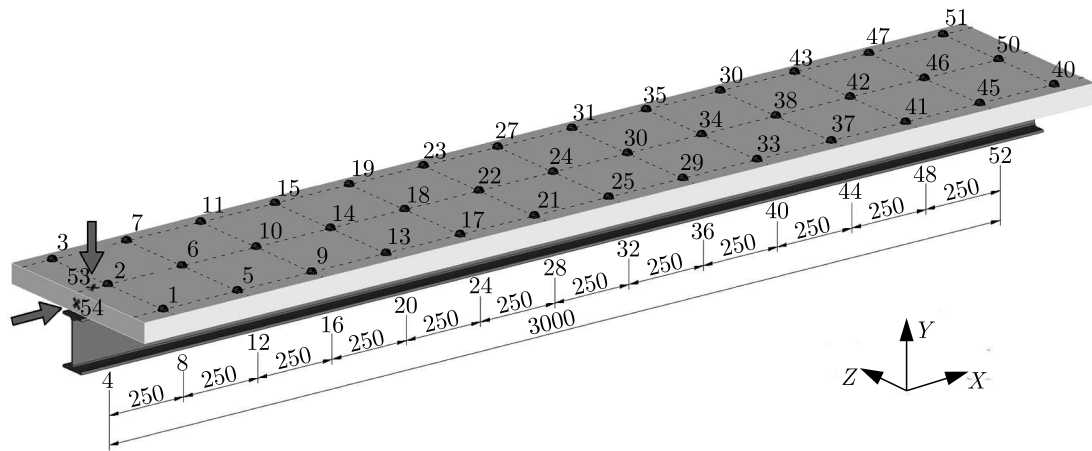


Fig. 2. Measurement point grid, points and directions of the force impulse

The *Polymax* algorithm, available in Test.Lab, was used to determine parameters of the modal beam model. The poles of the system were identified based on the analysis of a stabilisation diagram. Only the measurement points on the beam mid plane (2, 4, 6, 8, . . . , 52) were used in the analysis. This approach substantially made it easier to find flexural vibration modes which were later analysed to detect and locate damage. It also enabled analysis of a two-dimensional beam model.

Natural frequencies $f_{i,exp}$ obtained in experimental research and their corresponding modal damping ratios $\xi_{i,exp}$ for the first five flexural mode shapes are presented in Table 1.

Table 1. Modal parameters obtained during experimental research

$i \rightarrow$	1_{flex}	2_{flex}	3_{flex}	4_{flex}	5_{flex}
$f_{i,exp}$ [Hz]	74.68	172.72	273.01	373.40	472.03
$\xi_{i,exp}$ [%]	0.15	0.30	0.41	0.39	0.34

In the successive stage of the experiment, connection damage was introduced into the beam. The damage was obtained by removing concrete around a pair of studs, which eliminated the interaction between steel and concrete (Fig. 3). Dilena and Morassi (2003) used the same approach to simulate damage.



Fig. 3. Damage of the connection

Two degrees of damage, denoted by UZ1 and UZ2, were introduced into the beam. In damage UZ1 concrete was removed around one pair of studs (Fig. 4a) while in damage UZ2 around two pairs of studs (Fig. 4b).

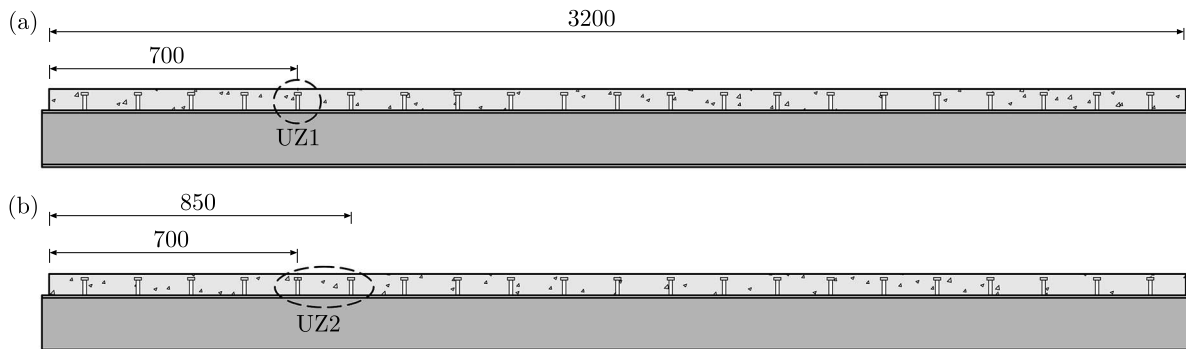


Fig. 4. Damage localisation: (a) damage UZ1, (b) damage UZ2

3. Numerical analysis

The numerical model of the beam has been created using the Rigid Finite Element method (Kruszewski *et al.*, 1975, 1999; Wittbrodt *et al.*, 2006). The central idea of the method is division of a real system into rigid bodies which are called rigid finite elements (RFE), which are then connected by means of spring-damping elements (SDE). For continuous parts of a structure, it is customary to start creating a model with segmentation of a beam into equal or nearly equal segments. This segmentation is also called a primary division, see Fig. 5a. A spring-damping element SDE is placed in the centre of gravity of every segment. This SDE is supposed to concentrate all spring and damping properties of a given segment. In Fig. 5b, SDE elements are shown as \otimes symbols. In the 2D model, each SDE is made up of three (two translational and one rotational) independent spring-damping elements. The next step is to connect SDEs created in the primary division by means of RFE. This is the so-called secondary division, see Fig. 5b.

While creating the model, the steel and concrete parts of the beam are treated separately. Owing to this, the elasticity of the connection can be taken account of the simulations. The connection between adjacent rigid finite elements (RFE) modelling the concrete slab is performed in the classical way, i.e. using one SDE located in the axis of the slab. In the case of the steel beam, another approach is proposed. One SDE is substituted with three separate SDEs placed in the axes of the web and the flanges of the I-section. The SDEs modelling the connection are located in the place where in the real beam a pair of steel studs would be found. Figure 5 presents the composite beam model.

To develop a mathematical model of a composite beam, it is necessary to know parameters characterising the I-section, the concrete slab and the connection. Some parameters, e.g. Young's modulus of the steel, density of the materials, Poisson's ratios, cross-sectional areas, are determined on the basis of measurements and literature data. Other parameters necessary to define the model are determined in two-stage parametric identification.

The first identification stage has been focused on determining the missing stiffness parameters, i.e. Young's modulus of the reinforced concrete slab E_c and stiffness of the connection K_v in the vertical direction (perpendicular to the connection plane) and in the horizontal direction K_h (parallel to the connection plane). The stiffness of the connection is influenced by spring properties of the steel studs, stiffness of concrete surrounding the studs and stiffness of the adjacent section of the steel-concrete interface. The first identification criterion is the best fit of the first five frequencies of flexural vibrations determined numerically to those found experimentally.

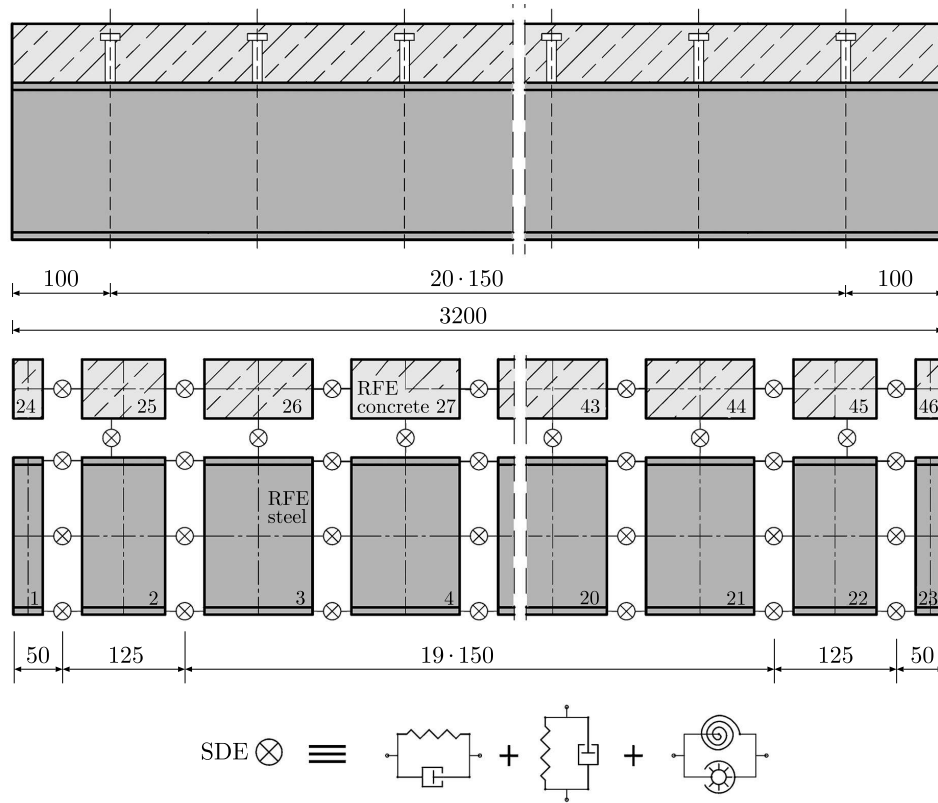


Fig. 5. RFE model of the composite beam: (a) primary division, (b) secondary division

The second identification criterion is defined as the complete fit of the fundamental frequency of axial vibration determined numerically and experimentally (it is due to strong correlation of this frequency with Young's modulus of the concrete slab E_c). Identification process has been conducted with a MATLAB optimization toolbox, using *fmincon* function which finds a minimum of a constrained nonlinear multivariable function. The function can be used to find a minimum with four different algorithms. *Active-set* and *Interior-point* were tested during the analysis. Finally, the second algorithm was selected. The algorithm required determination of the Hessian matrix, a matrix of second-order derivatives. The Hessian was determined using BFGS, a variable metric method. The obtained fit of frequencies and the results of stiffness parameter identification are presented in Table 2.

Table 2. Identification results of stiffness properties of the beam

$i \rightarrow$	1_{flex}	2_{flex}	3_{flex}	4_{flex}	5_{flex}	1_{ax}
$f_{i,exp}$ [Hz]	74.68	172.72	273.01	373.40	472.03	585.94
$f_{i,num}$ [Hz]	74.93	170.91	275.55	375.06	469,05	585.94
Δ_i	0.34%	-1.05%	0.93%	0.44%	-0.63%	0.00%
E_c [N/m ²]	$2.89 \cdot 10^{10}$					
K_h [N/m]	$2.19 \cdot 10^8$					
K_v [N/m]	$1.44 \cdot 10^8$					

At the second identification stage, the values of parameters defining damping properties, loss factors for concrete Q_c^{-1} and connection Q_{con}^{-1} , have been identified. According to Rao (2004), the loss factor for steel is $Q_s^{-1} \in \langle 2 \cdot 10^{-4}, 6 \cdot 10^{-4} \rangle$. Finally, the loss factor for steel was predefined to be equal $Q_s^{-1} = 4 \cdot 10^{-4}$. The identification process was based on fitting the amplitudes

of the frequency response function (FRFs) obtained using RFE model with those obtained during the experiment. For FRFs determined in the vertical direction (axis Y , impulse excitation at point 53 : $-Y$), the frequency range from 50 Hz do 350 Hz was fitted. The range includes frequencies of the first three modes of flexural vibration. For FRFs determined in the horizontal direction (axis X , impulse excitation at point 54 : $+X$), the frequency range including the fundamental longitudinal vibration was considered. The following loss factors were determined in the identification: $Q_c^{-1} = 0.0100$ and $Q_{con}^{-1} = 0.0269$. Figure 6 shows a comparison of illustrative FRFs obtained experimentally with those calculated with the RFE model. The numbers of points from a grid of measurement points used during the experiment and their corresponding rigid finite elements numbers from the numerical model are given in Fig. 6. Location of RFE No. 7 and RFE No. 17 corresponds exactly to the location of point No. 16 and point No. 40 which was placed on the bottom flange of the I-section during experiment (see Fig. 2).

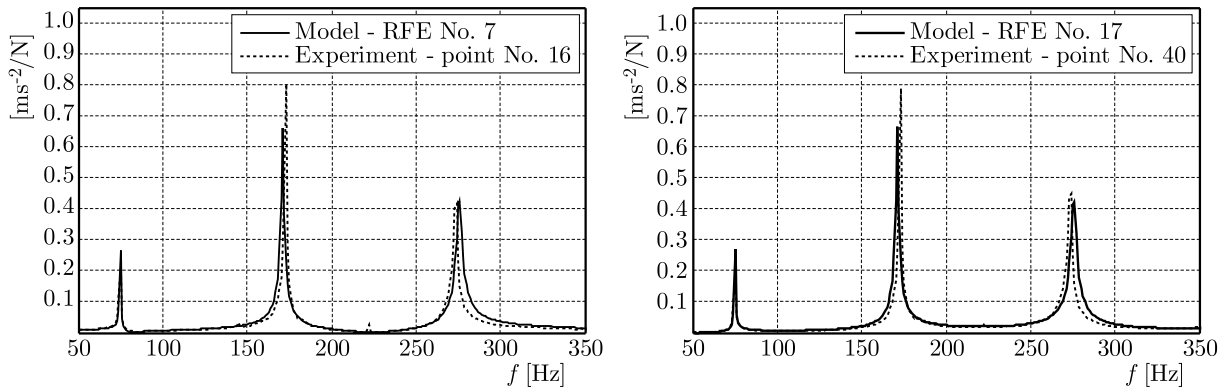


Fig. 6. A comparison of FRFs (Y direction) obtained in the experimental research and those simulated with the RFE model. The excitation force applied at point 53 : $-Y$

The comparison of the experimental and numerical mode shapes of vibration has been determined using the *Modal Assurance Criterion* – MAC (Allemang and Brown, 1982)

$$MAC = \frac{|\mathbf{Q}_{num}^T \mathbf{Q}_{exp}|^2}{(\mathbf{Q}_{num}^T \mathbf{Q}_{num})(\mathbf{Q}_{exp}^T \mathbf{Q}_{exp})} \quad (3.1)$$

where the vectors \mathbf{Q}_{num} and \mathbf{Q}_{exp} denote respectively mode shapes determined numerically and experimentally. The obtained values of MAC are presented in Table 3.

Table 3. Values of the coefficient MAC

$i \rightarrow$	1_{flex}	2_{flex}	3_{flex}	4_{flex}	5_{flex}
MAC_i	0.97	0.92	0.88	0.82	0.72

According to literature reports (Uhl, 1997), the fit of a numerical model and an experiment occurs when the MAC is above 0.8. As can be seen from Table 3, the condition is not satisfied for the fifth mode shape. Therefore, the fifth mode shape is not included in further analysis.

Numerical simulation of damage in the connection, which included damage introduced in experiments into the real beam, has been conducted for the developed model. Damage in the connection was simulated by changing the spring properties of SDEs that modelled the connection: the stiffness coefficients of the respective SDEs were preset to equal zero $K_h = K_v = 0$.

4. Analysis results

The sensitivity analysis of modal parameters following damage introduced into the beam has begun with examination of changes in the fundamental modal parameters, such as natural frequency and damping ratio. Then, the energy transfer ratio (ETR) was analysed. ETR was determined globally, for the whole beam, and locally, for some parts of the beam.

4.1. Vibration frequency and damping ratio

The changes of natural vibrations and damping ratio after damage introduction both for the calculated and experimental data are presented in Tables 4 and 5, respectively.

Table 4. Changes of natural frequencies following beam damage

Beam state →		UZ0	UZ1		UZ2	
$i \downarrow$		$f_{i,num}$ [Hz]	$f_{i,num}$ [Hz]	Δ_i [%]	$f_{i,num}$ [Hz]	Δ_i [%]
Numerical analysis	1_{flex}	74.93	74.53	-0.53	73.96	-1.29
	2_{flex}	170.91	170.23	-0.40	168.89	-1.18
	3_{flex}	275.55	272.87	-0.97	265.71	-3.57
	4_{flex}	375.06	369.74	-1.42	363.58	-3.06
$i \downarrow$		$f_{i,exp}$ [Hz]	$f_{i,exp}$ [Hz]	Δ_i [%]	$f_{i,exp}$ [Hz]	Δ_i [%]
Experiment	1_{flex}	74.68	73.97	-0.95	73.29	-1.86
	2_{flex}	172.72	170.22	-1.45	167.63	-2.95
	3_{flex}	273.01	267.45	-2.04	259.91	-4.80
	4_{flex}	373.40	365.50	-2.12	357.81	-4.18

As can be seen in Table 4, high consistency of natural frequency changes determined experimentally and numerically has been achieved. Somewhat larger changes of the parameter, following damage introduction, were recorded in experimental measurements. In each analysed case, an increase of damage extent caused a decrease in the natural frequency, which was directly associated with a stiffness loss of the beam.

Table 5. Changes of the damping ratio following beam damage

Beam state →		UZ0	UZ1		UZ2	
$i \downarrow$		$\xi_{i,num}$ [%]	$\xi_{i,num}$ [%]	Δ_i [%]	$\xi_{i,num}$ [%]	Δ_i [%]
Numerical analysis	1_{flex}	0.26	0.28	9.62	0.33	27.04
	2_{flex}	0.41	0.42	4.74	0.51	26.47
	3_{flex}	0.51	0.57	12.98	0.86	68.67
	4_{flex}	0.61	0.68	11.47	0.78	27.02
$i \downarrow$		$\xi_{i,exp}$ [%]	$\xi_{i,exp}$ [%]	Δ_i [%]	$\xi_{i,exp}$ [%]	Δ_i [%]
Experiment	1_{flex}	0.15	0.16	4.79	0.16	4.99
	2_{flex}	0.30	0.28	-5.56	0.29	-1.86
	3_{flex}	0.41	0.44	9.28	0.44	8.27
	4_{flex}	0.39	0.44	12.86	0.45	15.66

Changes in the damping ratio determined experimentally and numerically do not show the level of similarity as in the frequency. The ratio is more sensitive than natural frequencies to damage introduction, which is particularly true for numerical simulation results. There is a tendency for the damping ratio to increase as damage extent increases.

4.2. Energy transfer ratio ETR

The sensitivity analysis of the energy transfer ratio ETR for damage introduced into the steel-concrete composite beam has been conducted in two stages. First, the results of numerical simulations of damage produced with the rigid finite element model were analysed. Then, the sensitivity analysis of ETR based on experimental results was conducted.

The equilibrium of a vibrating system with n degrees of freedom, including the effect of damping, can be given by a system of differential equations

$$\mathbf{M}\ddot{\mathbf{X}} + \mathbf{C}\dot{\mathbf{X}} + \mathbf{K}\mathbf{X} = \mathbf{F} \quad (4.1)$$

where: \mathbf{M} , \mathbf{C} , \mathbf{K} – are mass, damping and stiffness matrices, $\ddot{\mathbf{X}}$, $\dot{\mathbf{X}}$, \mathbf{X} – vectors of acceleration, velocity and displacement, \mathbf{F} – the external force vector.

When considering free damped vibrations, the above equation can be written as

$$\dot{\mathbf{Y}} + \overline{\mathbf{C}}\dot{\mathbf{Y}} + \overline{\mathbf{K}}\mathbf{Y} = \mathbf{0} \quad (4.2)$$

where: $\mathbf{Y} = \mathbf{M}^{0.5}\mathbf{X}$, $\overline{\mathbf{C}} = \mathbf{M}^{-0.5}\mathbf{C}\mathbf{M}^{-0.5}$, $\overline{\mathbf{K}} = \mathbf{M}^{-0.5}\mathbf{K}\mathbf{M}^{-0.5}$.

For the system defined with Eq. (4.2), there is a set of modal parameters, i.e. natural frequencies ω_i , modal damping ratios ξ_i and the mode shapes $\overline{\mathbf{P}}_i$, where $i = 1, \dots, n$. For the generalized stiffness matrix $\overline{\mathbf{K}}$, there are eigenvectors $\overline{\mathbf{Q}}_i$, for which in proportionally damped systems it is true that $\overline{\mathbf{Q}}_i = \overline{\mathbf{P}}_i$. In non-proportionally damped systems, for which $\overline{\mathbf{Q}}_i \neq \overline{\mathbf{P}}_i$, it is true that (Liang and Lee, 1991)

$$\zeta_i = \text{Im} \left(\frac{1}{2\omega_i} \frac{\overline{\mathbf{Q}}_i^T \overline{\mathbf{C}} \overline{\mathbf{P}}_i}{\overline{\mathbf{Q}}_i^T \overline{\mathbf{P}}_i} \right) \quad (4.3)$$

where ζ_i denotes the energy transfer ratio ETR. The component $(\overline{\mathbf{Q}}_i^T \overline{\mathbf{C}} \overline{\mathbf{P}}_i) / (\overline{\mathbf{Q}}_i^T \overline{\mathbf{P}}_i)$ is defined as the generalized Rayleigh quotient.

A more comprehensive discussion of ETR can be found in reports by Liang and Lee (1991) and by Wang and Zong (2002).

4.2.1. Numerical analysis

Table 6 presents changes in the global ETR determined in numerical simulation of the beam damage.

Table 6. Changes of global ETR following beam damage

Beam state →		UZ0		UZ1		UZ2	
Numerical analysis	$i \downarrow$	$\zeta_{i,num} \cdot 10^2$ [%]	$\zeta_{i,num} \cdot 10^2$ [%]	Δ_i [%]	$\zeta_{i,num} \cdot 10^2$ [%]	Δ_i [%]	
	1 _{flex}	2.9	3.7	27	5.5	89	
	2 _{flex}	4.3	5.0	16	12.3	187	
	3 _{flex}	4.9	7.6	56	28.9	495	
	4 _{flex}	5.4	7.4	38	12.5	132	

The analysis of the data demonstrates that the value of ETR increases with an increase in the degree of damage in the connection of the beam. ETR can be said to be substantially more sensitive to this type of damage than both the natural frequency and damping ratio. The largest change of ETR occurred in the third mode shape, for UZ2 damage, when it amounted to 495%.

As mentioned above, the local ETR was determined for parts of the beam. It is to be emphasised that the division into parts was conducted individually for each mode shape, so that

each analysed part covered the area of a substantial curvature while at the same time avoiding nodes of the mode shape. The analysis started from the second mode shape.

Figure 7 shows changes of the locally determined ETR following damage introduction. The figure also presents the calculated mode shapes for the undamaged beam – the horizontal axis shows the localisation of damaged stud connectors.

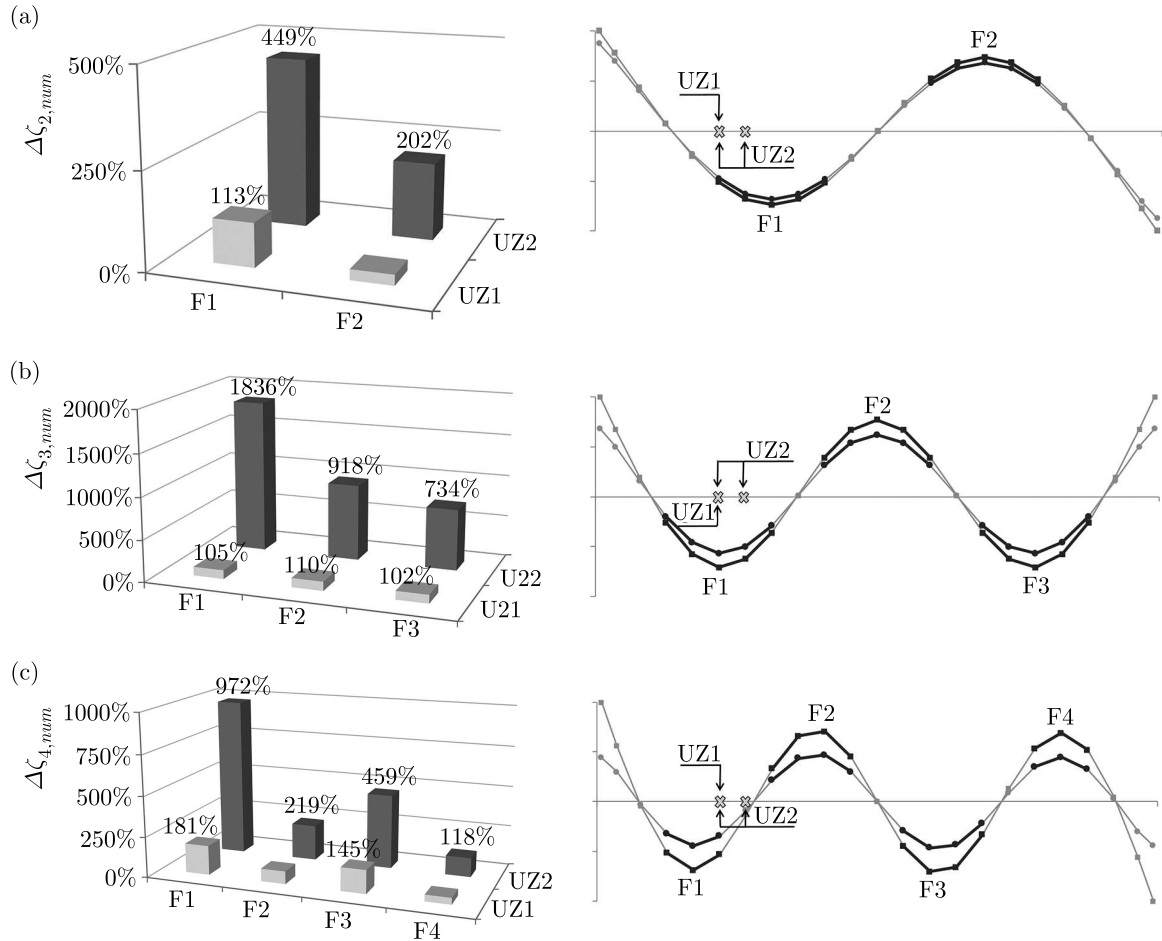


Fig. 7. Changes of local ETR $\zeta_{i,num}$ with mode shapes and damage area: (a) 2nd mode shape, (b) 3rd mode shape, (c) 4th mode shape

The changes of the locally determined ETR distinctly show the area of damage. The minimum sensitivity was observed for UZ1 damage, where the maximum change was 181%. Much larger changes occurred for UZ2 damage, with the order of magnitude ranging from several hundreds to even several thousands percent. The highest sensitivity was observed for the third mode shape when ETR change was 1836%.

4.2.2. Experimental analysis

To determine ETR based on experimental data, it is necessary to know the damping matrix $\bar{\mathbf{C}}$. The matrices determined for the RFE model for successive states of the beam, UZ0, UZ1 and UZ2, were used in the analysis.

Table 7 shows changes of global ETR determined with the experimental data. The results include changes that occurred for the second, third and fourth mode shape, i.e. those which were going to be analysed in damage localisation.

The ETR changes determined with the experimental data occurred in the range of 13%-268%. Compared to numerical analysis results, the changes are smaller. However, it is to be

Table 7. Changes of the global ETR following beam damage

Beam state →		UZ0	UZ1		UZ2	
Experiment	$i \downarrow$	$\zeta_{i,num} \cdot 10^2$ [%]	$\zeta_{i,num} \cdot 10^2$ [%]	Δ_i [%]	$\zeta_{i,num} \cdot 10^2$ [%]	Δ_i [%]
	2_{flex}	20.5	50.8	147	75.4	268
	3_{flex}	26.8	7.2	73	68.6	156
	4_{flex}	30.6	8.0	74	34.5	13

emphasised that the numerical analysis was not affected by distortions which did take place during real measurements. The presence of uncontrolled distortions and measurement noise may affect the results. However, despite this fact, changes of ETR, compared to frequency and damping ratio changes, are much larger. It demonstrates that ETR is more sensitive to the damage introduced into the beam.

Changes of local ETR following the connection damage are presented in a graphical form in Fig. 8. Figure 8 also shows experimentally the determined mode shapes for the undamaged beam – the horizontal axis shows the localisation of damaged stud connectors.

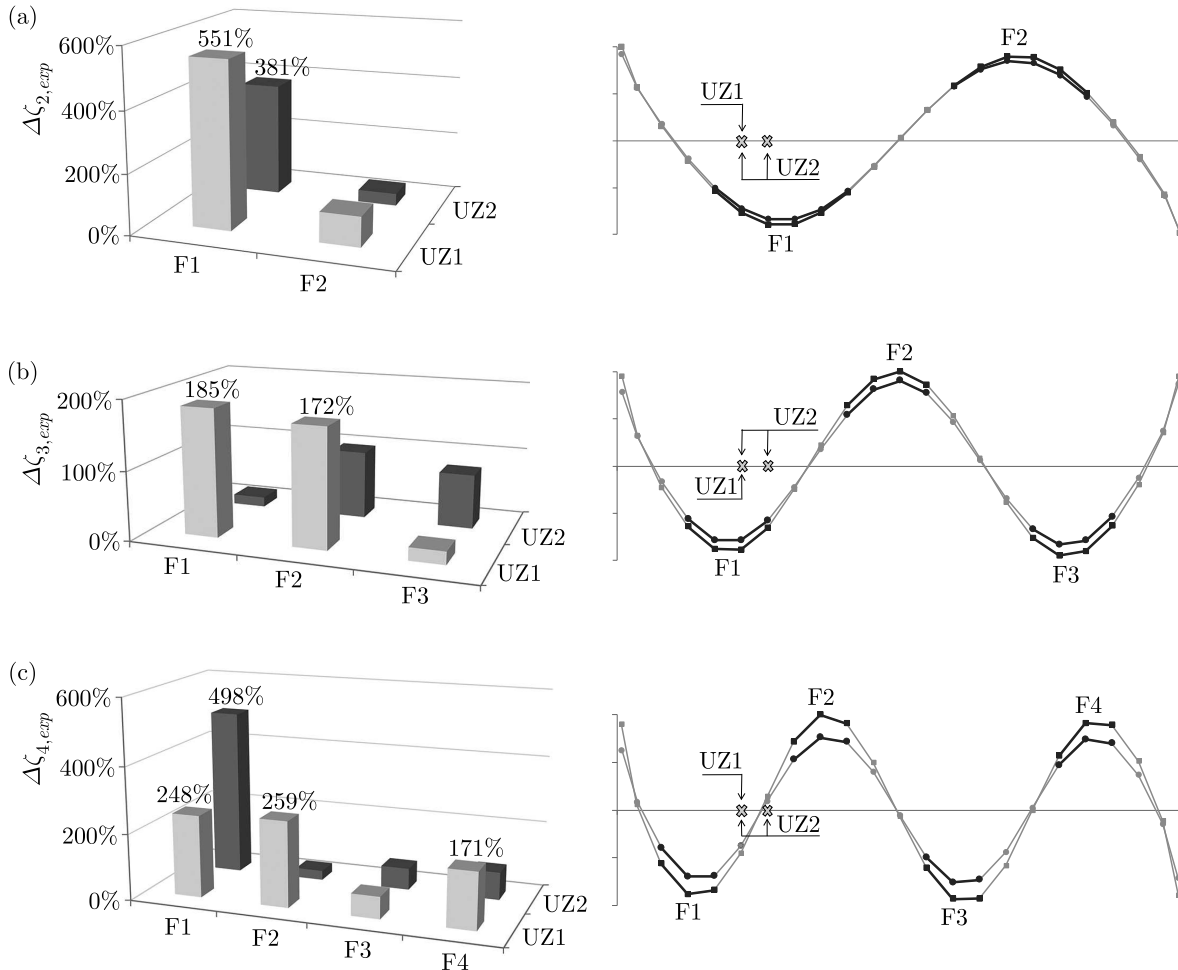


Fig. 8. Changes of local ETR $\zeta_{i,exp}$ with mode shapes and damaged areas: (a) 2nd mode shape, (b) 3rd mode shape, (c) 4th mode shape

The analysis of graphs presented in Fig. 8 can identify locations where damage occurred. Very good results were obtained for the second and fourth mode shapes. A comparison of Figs. 8 and 7 reveals that changes determined with the experimental data are smaller than those obtained in

numerical simulation. As mentioned above, this is due to the influence of external factors and measurement noise.

More comprehensive data on the experimental research, the model and the numerical analysis can be found elsewhere (Jarosińska, 2014).

5. Conclusions

The paper presents results of sensitivity analysis conducted for natural frequencies, damping ratio and energy transfer ratio following damage introduced into the connection of a steel-concrete composite beam. Both numerical analysis results and experimental research confirmed that ETR is more sensitive to the beam damage than the vibration frequency and damping ratio. Interestingly, it is possible to effectively localise the damage introduced into the beam, based on the analysis of changes of the locally determined ETR. It must be stressed, however, that the determination of ETR requires experimental measurements to be conducted with high precision since the method is based on changes in composite mode shapes.

Diagnostics of structures is a multistage process. Firstly, the damage must be detected using modal parameters determined globally for the whole structure: vibration frequency, modal damping coefficient, global ETR, etc. Secondly, the detected damage is localised using locally determined parameters, e.g. PMAC (Heylen and Janter, 1990), CDF (Wahab and de Roeck, 1999) or local ETR which has been used in the paper. Effectiveness of any method may be dependent on external factors and measurement apparatus. The best way to detect and precisely localise the damage is to use several methods at the same time. Evaluation of changes in modal parameters, including global and local ETR, when accompanied by other methods, may be a successful tool for detecting and localising damage in steel-concrete composite structures.

The problem of damage detection and localisation in composite beams is going to be continued in further research. Future investigations will be extended to include other types of damage and localisation techniques.

References

1. ALLEMANG R.J., BROWN D.L., 1982, Correlation coefficient for modal vector analysis, *Proceedings of the 1st International Modal Analysis Conference*, Orlando, Florida, 110-116
2. DILENA M., MORASSI A., 2003a, A damage analysis of steel-concrete composite beams via dynamic methods: Part I. Experimental results, *Journal of Vibration and Control*, **9**, 507-527
3. DILENA M., MORASSI A., 2003b, A damage analysis of steel-concrete composite beams via dynamic methods: Part II. Analytical models and damage detection, *Journal of Vibration and Control*, **9**, 529-565
4. DILENA M., MORASSI A., 2004, Experimental modal analysis of steel concrete composite beams with partially damaged connection, *Journal of Vibration and Control*, **10**, 897-913
5. DILENA M., MORASSI A., 2009, Vibrations of steel-concrete composite beams with partially degraded connection and application to damage detection, *Journal of Sound and Vibration*, **320**, 1/2, 101-124
6. HEYLEN W., JANTER T., 1990, Extensions of the modal assurance criterion, *Journal of Vibration and Acoustics*, **112**, 468-472
7. JAROSIŃSKA M., 2014, Detection of steel-concrete compound beams through modal analysis (in Polish), Doctoral dissertation, Zachodniopomorski Uniwersytet Technologiczny w Szczecinie, Wydział Budownictwa i Architektury, Szczecin

8. KONG F., LIANG Z., LEE G.C., 1996, Bridge damage identification through ambient vibration signature, *Proceedings of the 14th International Modal Analysis Conference*, Dearborn, Michigan, 717-724
9. KRUSZEWSKI J., GAWROŃSKI W., WITTBRODT E., NAJBAR F., GRABOWSKI S., 1975, *Rigid Finite Element Method* (in Polish), Arkady, Warszawa
10. KRUSZEWSKI J., SAWIAK S., WITTBRODT E., 1999, *CAD CAM: Rigid Finite Element Method in Structural Dynamics* (in Polish), Wydawnictwa Naukowo-Techniczne, Warszawa
11. LEE G.C., LIANG Z., 1999, Development of a bridge monitoring system, *Proceedings of the 2nd international Workshop on Structural Health Monitoring*, Stanford University, California, 349-358
12. LI J., HAO H., XIA Y., ZHU H., 2014, Damage detection of shear connectors in bridge structures with transmissibility in frequency domain, *International Journal of Structural Stability and Dynamics*, **14**, 2
13. LI J., HAO H., ZHU H., 2014, Dynamic assessment of shear connectors in composite bridges with ambient vibration measurements, *Advances in Structural Engineering*, **17**, 5, 617-638
14. LIANG Z., LEE G.C., 1991, Damping of structures: Part 1 – Theory of complex damping, National Center for Earthquake Engineering Research, Technical Report NCEER-91-0004, State University of New York at Buffalo, New York
15. LIANG Z., HUANG T.J., LEE G.C., 1997, A study on damage dynamics by using the modal energy transfer, *Proceedings of the 15th International Modal Analysis Conference*, Orlando, Florida, 1339-1345
16. LIU K., DE ROECK G., 2009, Damage detection of shear connectors in composite bridges, *Structural Health Monitoring*, **8**, 5, 345-356
17. RAO S.S., 2004, *Mechanical Vibrations*, Fourth Edition, Pearsons Education International, New Jersey
18. UHL T., 1997, *CAD CAM: Computer Aided identification of Models of Mechanical Structures* (in Polish), Wydawnictwa Naukowo-Techniczne, Warszawa
19. WAHAB M.A., DE ROECK G., 1999, Damage detection in bridges using modal curvatures: Application to a real damage scenario, *Journal of Sound and Vibration*, **226**, 2, 217-235
20. WANG T.L., ZONG Z., 2002, Improvement of evaluation method for existing highway bridges, Technical Report FL/DOT/RMC/6672-818, Florida Department of Transportation, USA
21. WANG T.L., ZONG Z.H., 2003, Structural damage identification by using energy transfer ratio, *Proceedings of the 21st International Modal Analysis Conference: A Conference on Structural Dynamics*, Kissimmee, Florida
22. WITTBRODT E., ADAMIEC-WÓJCIK I., WOJCIECH S., 2006, *Dynamics of Flexible Multibody Systems. Rigid Finite Element Method*, Springer-Verlag, Berlin, Heidelberg, New York
23. WRÓBLEWSKI T., JAROSIŃSKA M., BERCZYŃSKI S., 2011, Application of ETR for diagnosis of damage in steel-concrete composite beams, *Journal of Theoretical and Applied Mechanics*, **49**, 1, 51-70
24. WRÓBLEWSKI T., JAROSIŃSKA M., BERCZYŃSKI S., 2013, Damage location in steel-concrete composite beams using Energy Transfer Ratio (ETR), *Journal of Theoretical and Applied Mechanics*, **51**, 1, 91-103

MODAL ANALYSIS OF GEARBOX TRANSMISSION SYSTEM IN BUCKET WHEEL EXCAVATOR

MAHA KARRAY, NABIH FEKI, MOHAMED T. KHABOU, FAKHER CHAARI, MOHAMED HADDAR
Laboratory of mechanics, Modelling and Production, National school of Engineers of Sfax, Sfax, Tunisia
e-mail: fakher.chaari@gmail.com

Planetary gears are widely used in modern machines as ones of the most effective forms of power transmission. In this paper, a special configuration of a gearbox composed of one stage spiral bevel gear and a two stage helical planetary gear used in a bucket wheel excavator gearbox is presented to investigate its modal properties. A lumped-parameter model is formulated to obtain equations of motion and the eigenvalue problem is solved. The modes are presented in low-frequency and high-frequency bands. Distributions of modal kinetic and strain energies are studied.

Keywords: spiral bevel gear, helical planetary gear, bucket wheel excavator, modal properties

1. Introduction

Gear transmissions such as bevel and planetary gears are widely used in transmissions of wind turbines, agricultural machinery, mining machines such as excavators and transportation such as helicopters. Spiral bevel gears BG coupled in two stages helical planetary gears can be found in gearboxes of bucket wheel excavators. The first step to investigate the dynamic behavior of such systems is the determination of natural frequencies and mode shapes.

Many research works has been done on common parallel axis geared rotor systems dynamics, see e.g. Ozguven and Houser (1988a,b), Blankenship and Singh (1995), Vexel and Maatar (1996) however few research works were dedicated to bevel gears dynamics. The existing models are mostly similar to those of parallel axis gears. Gosselin *et al.* (1995) proposed a general formula and applied it to analyze the load distribution and transmission error in spiral bevel gear pairs and hypoid gear pairs. Karray *et al.* (2013) investigated the dynamic behavior of a single stage bevel gear in the presence of local damage. Choy *et al.* (1991) presented vibration signature analysis for multi-stage gear transmissions which combined gear mesh dynamics and structural modal analysis in the study of transmission vibrations.

For planetary gears, Kahraman (1994b) provided expressions for natural frequencies by using a rotational lumped-parameter model. Lin and Parker (1999a, 2000) showed that two-dimensional, spur planetary gears with equally spaced and diametrically opposed planets possess well-defined modal properties. Wu and Parker (2008) proved the modal properties of spur planetary gears having elastically deformable ring gears. These vibration mode characteristics are crucial in vibration suppression strategies using mesh phasing (Seager, 1975; Lin and Parker, 2004) and eigensensitivity analysis (Lin and Parker, 1999b), Guo and Parker (2010) of planetary gears. Although the vibration modes of two-dimensional planetary gears have been studied, few studies were dedicated to those of helical planetary gears with three-dimensional motion. Habib *et al.* (2005) determined critical frequencies for helical planetary gears and examined their sensitivity to the helix angle. Eritenel and Parker (2009) examined three-dimensional motion of helical gears and shafts.

Researches on modal characteristics of multistage planetary gears are rare. Sun *et al.* (2014) analyzed the natural frequency and coupled mode characteristics in a multi-stage planetary gear and distinguished the dominant vibration stage by a criterion. Hammami *et al.* (2015) discussed the modal properties of a special configuration of two stage planetary gears mounted back-to-back. Zhang *et al.* (2016) attempted to establish a translational-rotational coupled dynamic model of a two-stage closed-form planetary gear set to predict natural frequencies and vibration modes.

This paper discusses the modal properties of a special configuration of a gearbox composed of one stage spiral bevel gear and two stage helical planetary gear used in bucket wheel excavators. A lumped-parameter model is formulated to obtain the equations of motion.

2. Dynamic model

Figure 1 shows a general view of a bucket wheel excavator. The kinematic scheme of its gearbox transmission system is presented in Fig. 2. It is composed of a spiral bevel gear as the input and two stages planetary gear.

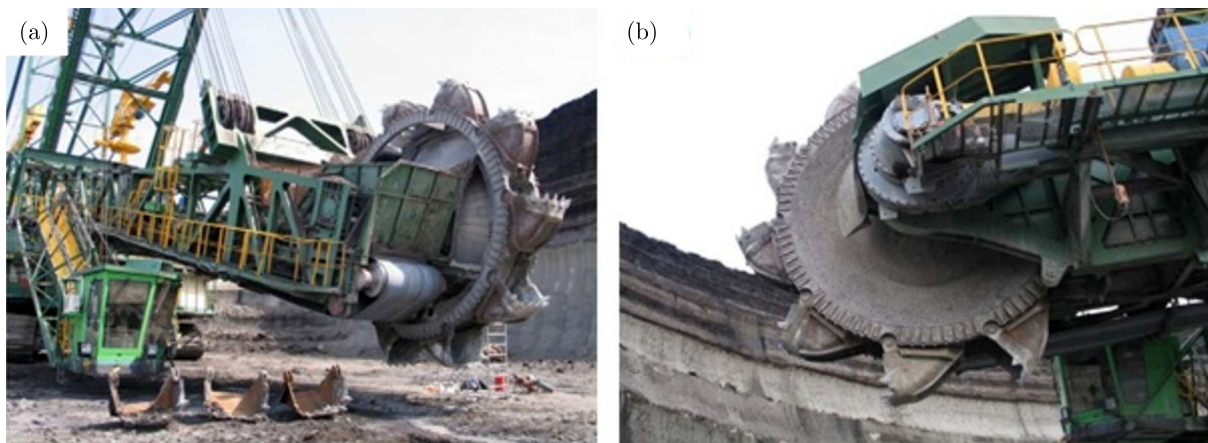


Fig. 1. View of the bucket wheel excavator: (a) from the side of winning-receiving belt and (b) from the side of the transmission system (Rusinski *et al.*, 2010)

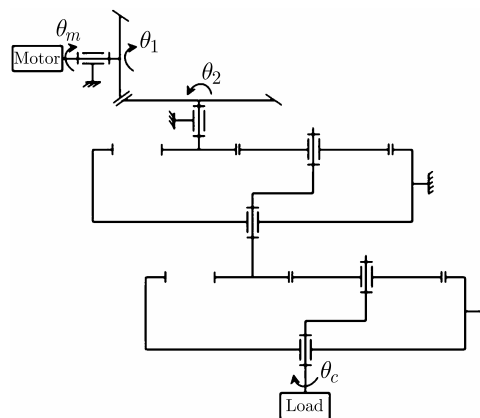


Fig. 2. Kinematic scheme of the gearbox transmission system

3. Model and equation of motion

The model of the transmission is presented in Fig. 3.

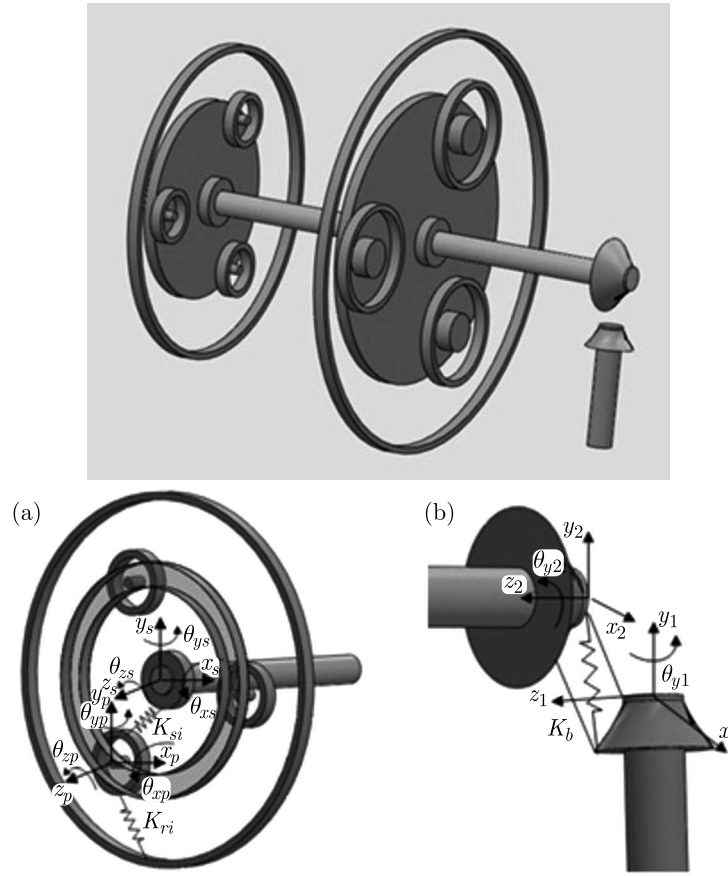


Fig. 3. Lumped parameter model: (a) planetary gear, (b) bevel gear

3.1. Spiral bevel gear model

The spiral BG model is divided into two rigid blocks (pinion with Z_1 teeth and wheel with Z_2 teeth). Each block has four degrees of freedom (three translations x_i, y_i, z_i ($i = 1, 2$), one rotation θ_1 for the pinion, θ_2 for wheel and θ_m for the motor). The shafts are modeled with torsional stiffness. In order to simulate the meshing, linear mesh stiffness acting along the lines of action is considered following the procedure given by Karray *et al.* (2013). The vector defining different degrees of freedom is

$$\mathbf{q}_{BG} = \{x_1, y_1, z_1, \theta_m, \theta_1, x_2, y_2, z_2, \theta_2\}^T \quad (3.1)$$

3.2. Planetary gear model

For both stages of the planetary gear, a three-dimensional model is adopted. Each stage is composed of the sun gear s , ring gear r , which are coupled to each other by 3 planets P mounted on a carrier c . These elements are considered as rigid bodies. Linear springs acting on the lines of action are used to simulate the meshing stiffness (Kahraman, 1994a,c). Bearings are accounted for by linear springs. Each component has six degrees of freedom: three translations u_{ji}, v_{ji} and w_{ji} and three rotations φ_{ji}, ψ_{ji} and θ_{ji} ($j = c, r, s, 1, \dots, n$, $i = 1$ for the first stage and $i = 2$ for the second one). These coordinates are measured with respect to a frame

$(O_i, s_{1i}, t_{1i}, z_{1i})$ fixed to the carrier and rotating with a constant angular speed Ω_{ci} . The rotations φ_{ji} , ψ_{ji} and θ_{ji} are replaced by their corresponding translational gear mesh displacements as

$$\rho_{jix} = Rb_{ji}\varphi_{ji} \quad \rho_{jiy} = Rb_{ji}\psi_{ji} \quad \rho_{jiz} = Rb_{ji}\theta_{ji} \quad \begin{matrix} j = c, r, s, 1, \dots, n \\ i = 1, 2 \end{matrix} \quad (3.2)$$

where Rb_{ji} is the base circle radius for the sun, ring, planet, and the radius of the circle passing through planet centers for the carrier.

The system elasticity is accounted for by $6n + 18$ DOFs for each stage, and the planetary gear displacement vector \mathbf{q}_{jPGi} of each element is defined as

$$\mathbf{q}_{jPGi} = [u_{ji}, v_{ji}, w_{ji}, \rho_{jix}, \rho_{jiy}, \rho_{jiz}]^T \quad j = c, r, s, 1, \dots, n \quad i = 1, 2 \quad (3.3)$$

3.3. Global model

The objective is to obtain a unique differential system combining the BG stage and both stages planetary gear coordinates. The principle of the coupling consists in using an additional torsional stiffness joining the rotational degree of freedom of the bevel gear wheel and the sun gear of the first stage planetary gear and adding a linear spring joining the axial degrees of freedom of the same wheel and sun. The same are used to couple the axial and rotational degree of freedom of the carrier of the first stage and the sun of the second one.

Introducing the following extended state variable vector composed of the bevel and two stages planetary gear displacements

$$\mathbf{q}_G = \{\mathbf{q}_{BG}, \mathbf{q}_{PG1}, \mathbf{q}_{PG2}\} \quad (3.4)$$

Applying Lagrange formulation for each element allows us to obtain the equations of motion of the $9 + 2(18 + 6n)$ degrees of freedom of the global system

$$\mathbf{M}_G \ddot{\mathbf{q}}_G + \mathbf{C}_G \dot{\mathbf{q}}_G + [\mathbf{K}_{pG} + \mathbf{K}_{eG}(t)] \mathbf{q}_G = \mathbf{F}_G(t) \quad (3.5)$$

where \mathbf{q}_G , \mathbf{M}_G , \mathbf{C}_G , \mathbf{K}_{pG} , \mathbf{K}_{eG} , \mathbf{F}_G are respectively the displacement vector, mass, damping, bearing, mesh stiffness matrices and the force vector for the global system.

4. Modal analysis

The characteristics of the bevel gear model are presented in Table 1 while the characteristics of the two stages planetary gear are presented in Table 2. It has a fixed ring and three planets.

Table 1. Characteristics of the spiral bevel gear

Parameters	Pinion	Wheel
Number of teeth Z	27	62
Mass [kg]	300	800
Moment of inertia [kg·m ²]	18	72
Axial stiffness k_{x1}, k_{y2} [N/m]	$1 \cdot 10^9$	$2.3 \cdot 10^9$
Lateral stiffness $k_{y1}, k_{z1}, k_{x2}, k_{z2}$ [N/m]	$8.8 \cdot 10^9$	$1.3 \cdot 10^{10}$
Torsional stiffness $k_{\theta1}, k_{\theta2}$ [Nm/rad]	$1.2 \cdot 10^4$	$7.4 \cdot 10^4$
Pressure angle	$\alpha = 20^\circ$	
Spiral angle	$\beta = 20^\circ$	

Table 2. Characteristics of the planetary gear model

	Sun	Ring	Carrier	Planet
Teeth number	$Z_{s1} = 21$ $Z_{s2} = 27$	$Z_{r1} = 150$ $Z_{r2} = 90$	– –	$Z_{p1} = 64$ $Z_{p2} = 31$
Mass [kg]	$M_{s1} = 270$ $M_{s2} = 446$	$M_{r1} = 4500$ $M_{r2} = 1960$	$M_{c1} = 2600$ $M_{c2} = 1300$	$M_{p1} = 1200$ $M_{p2} = 600$
J/R_{bi}^2	$(J/R_{bi}^2)_1 = 200$ $(J/R_{bi}^2)_2 = 281$	$(J/R_{bi}^2)_1 = 740$ $(J/R_{bi}^2)_2 = 387$	$(J/R_{bi}^2)_1 = 990$ $(J/R_{bi}^2)_2 = 618$	$(J/R_{bi}^2)_1 = 592$ $(J/R_{bi}^2)_2 = 294$
I/R_{bi}^2	$(I/R_{bi}^2)_1 = 100$ $(I/R_{bi}^2)_2 = 140$	$(I/R_{bi}^2)_1 = 370$ $(I/R_{bi}^2)_2 = 193$	$(I/R_{bi}^2)_1 = 495$ $(I/R_{bi}^2)_2 = 310$	$(I/R_{bi}^2)_1 = 296$ $(I/R_{bi}^2)_2 = 147$
Gearmesh stiffness [N/m]	$k_{sp1} = 2.28 \cdot 10^8$, $k_{rp1} = 2.6 \cdot 10^8$ $k_{sp2} = 2.2 \cdot 10^8$, $k_{rp2} = 2.3 \cdot 10^8$			
Bearing stiffness [N/m]	$k_{jx} = k_{jy} = 10^8$, $k_{jz} = 10^9$, $j = c, s$ $k_{rx} = k_{ry} = k_{rz} = 10^{10}$, $k_{xx} = k_{yy} = 10^8$, $k_{zz} = 10^9$			
Torsional stiffness [N/m]	$k_{j\varphi} = k_{j\psi} = 10^9$, $k_{j\theta} = 0$, $j = c, s, 1, \dots, n$ $k_{r\varphi} = k_{r\psi} = k_{r\theta} = 10^{10}$			
Pressure angle	$\alpha = 20^\circ$			
Helix angle	$\beta = 20^\circ$			

Table 3. Eigenfrequencies of the system

Mode type		Multipli- city [m]	Eigenfrequency [Hz]
Bevel gear mode	C	1	$f_{11} = 56$, $f_{17} = 64$
	T		$f_{20} = 67$
	R		$f_{81} = 1237$
First planetary mode	R-A	1	$f_4 = 30$, $f_{35} = 165$, $f_{44} = 212$, $f_{49} = 220$, $f_{50} = 246$, $f_{75} = 649$
	T-T	2	$f_{2,3} = 20$, $f_{8,9} = 38.7$, $f_{12,13} = 58$, $f_{18,19} = 66$, $f_{24,25} = 84.8$, $f_{36,37} = 173$, $f_{41,42} = 204$, $f_{45,46} = 213$, $f_{51,52} = 251$, $f_{56,57} = 313$, $f_{73,74} = 516$, $f_{77,78} = 890$
Second planetary mode	R-A	1	$f_{23} = 84.7$, $f_{59} = 345$, $f_{60} = 361$, $f_{65} = 420$, $f_{68} = 442$, $f_{76} = 838$
	T-T	2	$f_{5,6} = 38.5$, $f_{14,15} = 63$, $f_{27,28} = 100$, $f_{31,32} = 119$, $f_{33,34} = 153$, $f_{47,48} = 216$, $f_{61,62} = 364$, $f_{63,64} = 416$, $f_{66,67} = 434$, $f_{69,70} = 447$, $f_{71,72} = 482$, $f_{79,80} = 1147$
Coupled modes		1	$f_1 = 0$, $f_7 = 38.6$, $f_{10} = 46$, $f_{16} = 63.7$, $f_{21} = 75$, $f_{22} = 79$, $f_{26} = 92$, $f_{29} = 111$, $f_{30} = 117$, $f_{38} = 179$, $f_{39} = 199$, $f_{40} = 203$, $f_{43} = 209$, $f_{53} = 255$, $f_{54} = 275$, $f_{55} = 300$, $f_{58} = 341$

4.1. Natural frequencies and vibration modes

The undamped eigenvalue problem derived from the equation of motion by considering only the mean stiffness matrix $\bar{\mathbf{K}}$ is

$$\left(-\omega_i^2 \mathbf{M}_G + \bar{\mathbf{K}}_G\right) \phi_i = 0 \quad (4.1)$$

where ϕ_i is the eigenvector and ω_i is the corresponding eigenfrequency.

Natural frequencies and vibration modes of the system are given in Table 3. The natural modes are grouped according to the multiplicity of the natural frequencies. Several characteristics are revealed after a thorough comparison on the natural frequencies ω_i and modal vectors ϕ_i .

- The first-order natural frequency is $\omega_1 = 0$, and the corresponding vibration mode is the rigid body mode. It is obvious that the rigid body mode can be eliminated by removing rigid-body motion.
- Bevel gear modes contain only modal deflection of BG components. They include four distinct natural frequencies:
 - two natural frequencies with combined (C) translational and rotational modal deflection. An example of this mode is observed in Fig. 4. The equilibrium positions are represented by a solid black line and the deflected positions are shown by a dashed black line. Similarly, Figs. 5-7 all abide by these rules;
 - one natural frequency in which only rotation (R) is observed;
 - one in which only translation (T) is observed.

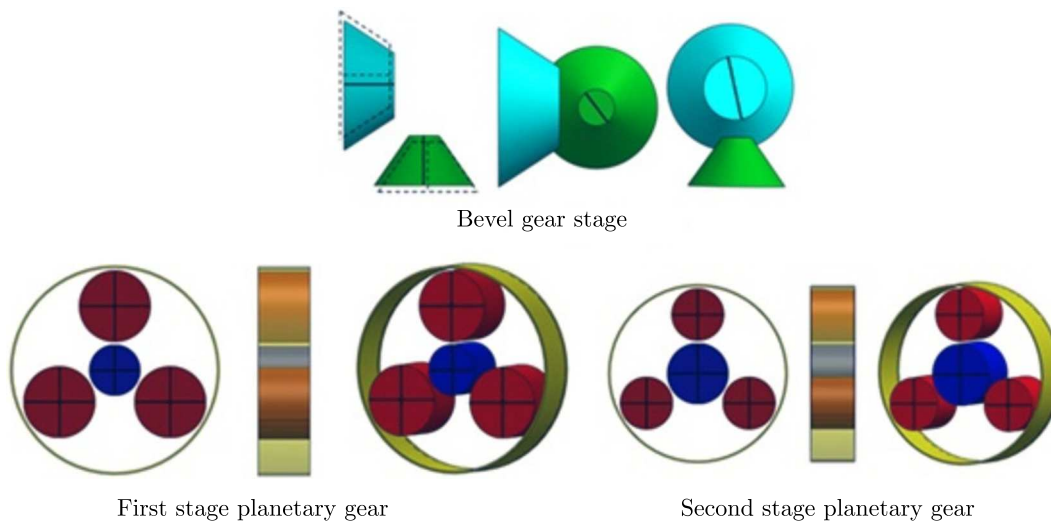


Fig. 4. Combined bevel gear mode at $f_{11} = 56$ Hz

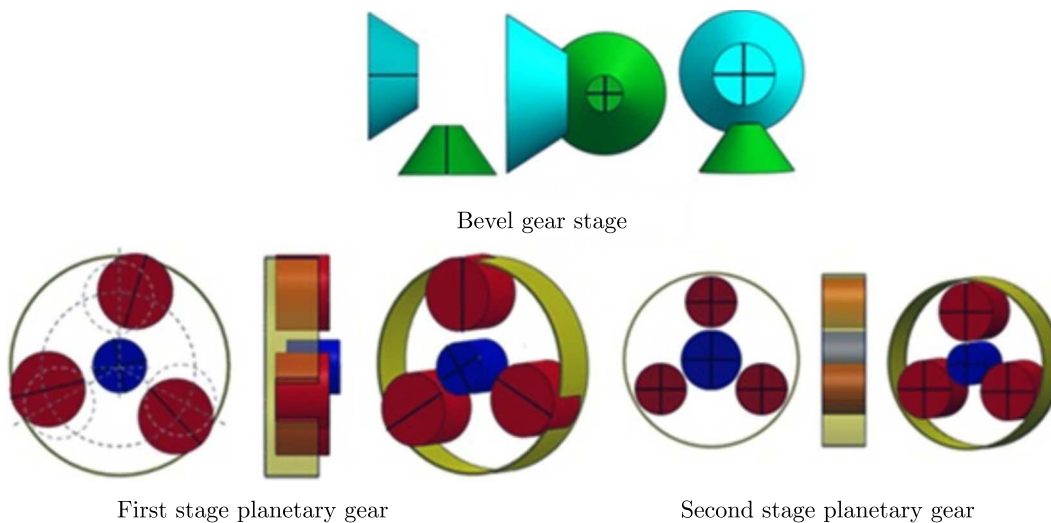


Fig. 5. Rotational-axial mode of the first stage planetary gear at $f_4 = 30$ Hz

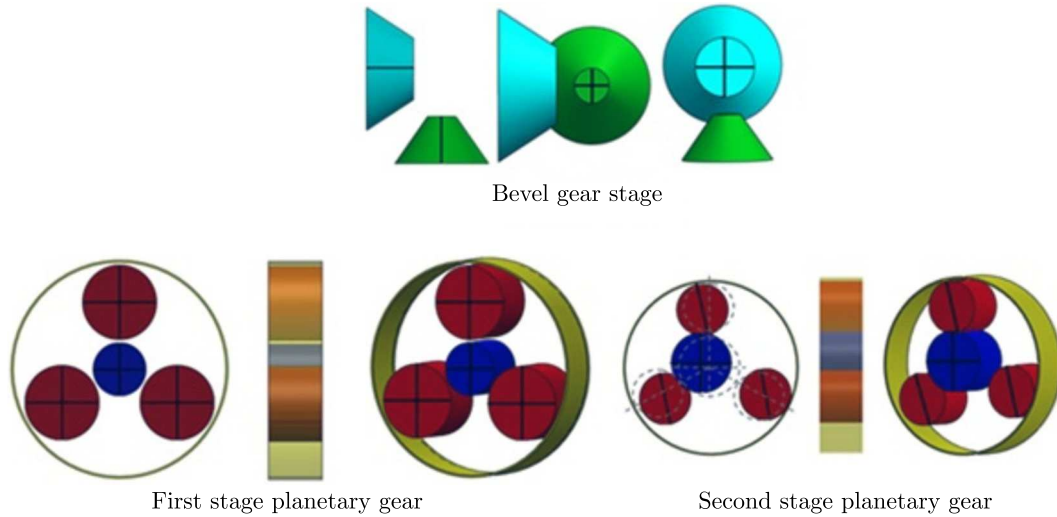


Fig. 6. Translational-tilting mode of the second stage planetary gear at $f_{5,6} = 38.5$ Hz

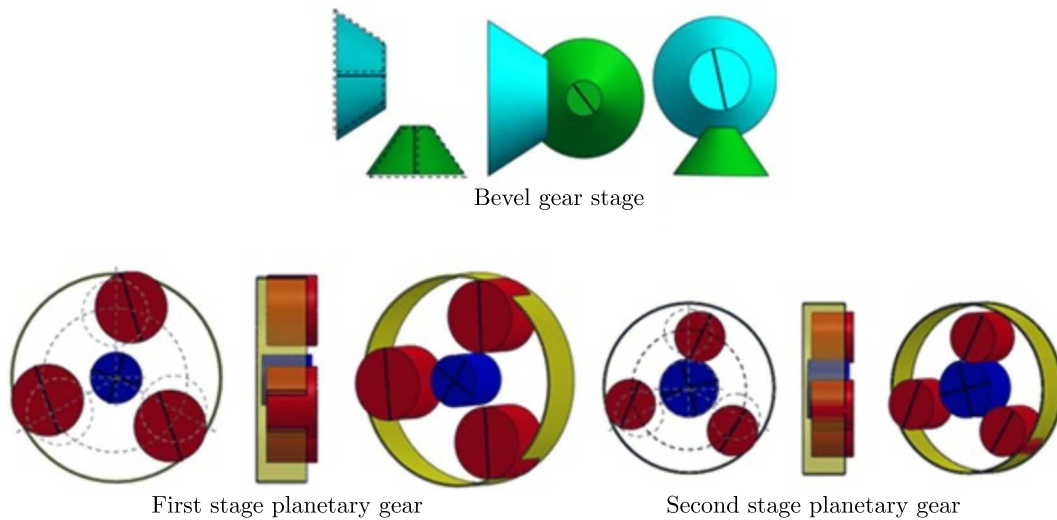


Fig. 7. Coupled mode at $f_7 = 38.6$ Hz

- Planetary gear modes in which there are only modal deflection of the 2 stage planetary gear components include:
 - twelve natural frequencies with the multiplicity $m = 1$. The related vibration modes are rotational-axial (R-A) modes in which the carriers, rings and suns rotate and translate axially, but they do not tilt or translate in-plane. The planets move identically and in phase. Figure 5 shows one rotational mode of the system;
 - twenty four natural frequencies with the multiplicity $m = 2$. The related vibration modes are translational-tilting (T-T) modes in which the carriers, rings and suns only translate in-plane and tilt but do not rotate or translate axially. In addition, the following relations between the deflections are noticed for each double mode: $u_{i1} = v_{i2}$, $v_{i1} = u_{i2}$ and $\varphi_{i1} = \psi_{i2}$, $\psi_{i1} = -\varphi_{i2}$ ($i = c, r, s$), where u_{i1} , v_{i1} , φ_{i1} , ψ_{i1} are modal deflections in the first mode and u_{i2} , v_{i2} , φ_{i2} , ψ_{i2} are modal deflections in the second mode;
 - the planets exhibit sequentially phased motion. Figure 6 shows one rotational mode of the system;

- the planet modes exist only if the number of planet $N > 3$ and have the multiplicity $m = N - 1$. In both stages of the planetary gear, there are only three planets ($N = 3$). So, only the previous classes of modes appear when solving the eigenvalue problem.

- Modal properties of the two-stage planetary gears are analogous to those of simple, single-stage planetary gears. Features of rotational and translational modes are identical.
- The coupled mode which includes seventeen distinct natural frequencies includes movement of the different stages. Figure 7 illustrates the vibration modes of the system.

4.2. Analysis of the distribution of modal kinetic strain energies

Computation of the modal strain energy and the modal kinetic energy distributions gives information on bodies brought to critical speeds (which excite the natural frequencies) in terms of dominant motion and deformation.

The total modal strain energy can be written as the sum of strain energies of rotation and translation from each component of the system

$$Ep_\phi = \frac{1}{2} \phi_i^T \bar{\mathbf{K}} \phi_i = \sum Ep_{\phi k} + \sum Ep_{\phi k\omega} + Ep_{\phi pw} + \sum Ep_{\phi ji} + \sum Ep_{\phi ji\omega} + \sum (Ep_{\phi sin} + Ep_{\phi rin}) \quad (4.2)$$

where $Ep_{\phi k}$ and $Ep_{\phi k\omega}$ are the strain energies of the bearing stiffness in the rotational and translational motion of the pinion and wheel ($k = p, w$), respectively. $Ep_{\phi pw}$ is the strain energy of the pinion-wheel meshing. $Ep_{\phi ji}$ and $Ep_{\phi ji\omega}$ are the strain energies of the bearing stiffness in the rotational and translational motion of the carriers, suns, rings and planets ($j = c, r, s, 1, 2, 3$) in both stages ($i = 1$ for the first stage and $i = 2$ for the second stage). $Ep_{\phi sin}$ and $Ep_{\phi rin}$ are the strain energies of the sun i -planets and ring i -planets meshing in both stages.

The modal kinetic energy can also be written as the sum of the kinetic energies of rotation and translation from each component of the system

$$Ec_\phi = \frac{1}{2} \omega_i^2 \phi_i^T \mathbf{M} \phi_i = \sum Ec_{\phi k} + \sum Ec_{\phi k\omega} + \sum Ec_{\phi ji} + \sum Ec_{\phi ji\omega} \quad (4.3)$$

where $Ec_{\phi k}$ and $Ec_{\phi k\omega}$ are the kinetic energies of the bearing stiffness in the rotational and translational motion of the pinion and wheel ($k = p, w$). $Ec_{\phi ji}$ and $Ec_{\phi ji\omega}$ are the kinetic energies in the rotational and translational motion of the suns, carriers, rings and planets ($j = s, c, r, t, 1, 2, 3$) in the first stage and the second one ($i = 1, 2$).

Figure 8 shows the distribution of modal kinetic energies in low frequencies.

In the X -axis, the contribution of each degree of freedom in the total modal strain energy is represented. Details are given in Table 4.

Figure 9 shows the distribution of modal strain energies in low frequencies, where the X -axis is defined in Table 5.

Table 6 presents a resume of the modal dominant motion and the dominant strain energy in each low-frequency mode.

Figure 10 shows the distribution of modal kinetic and strain energies in high frequencies. The X -axis is defined in Table 4.

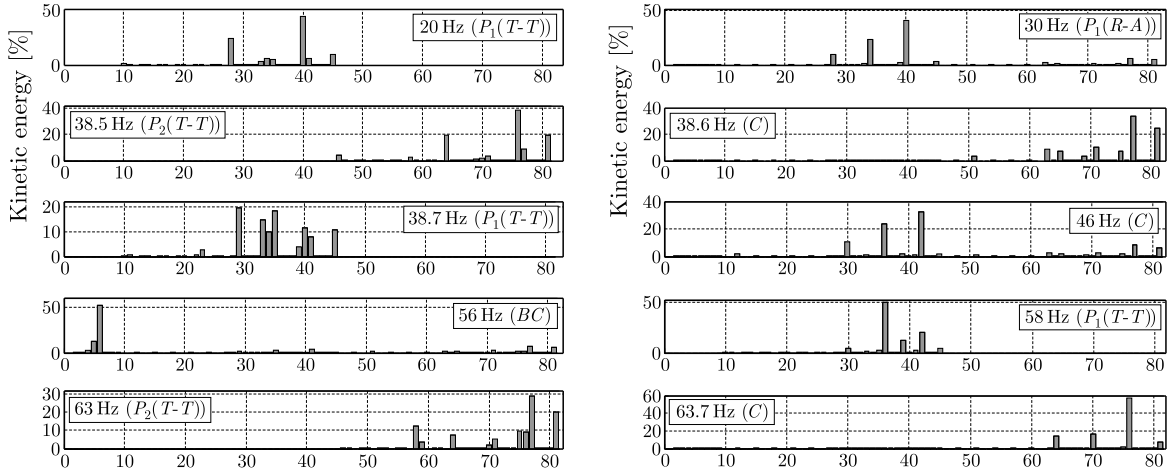


Fig. 8. Modal kinetic energies in low-frequencies

Table 4. The X-axis location of kinetic energies

1-3	Translation of pinion	40-42	Translation of planet 3 of 1st stage
4	Rotation of bearing motor	43-45	Rotation of planet 3 of 1st stage
5	Rotation of pinion	46-48	Translation of carrier of 2nd stage
6-8	Translation of wheel	49-51	Rotation of carrier of 2nd stage
9	Rotation of wheel	52-54	Translation of ring of 2nd stage
10-12	Translation of carrier of 1st stage	55-57	Rotation of ring of 2nd stage
13-15	Rotation of carrier of 1st stage	58-60	Translation of sun of 2nd stage
16-18	Translation of ring of 1st stage	61-63	Rotation of sun of 2nd stage
19-21	Rotation of ring of 1st stage	64-66	Translation of planet 1 of 2nd stage
22-24	Translation of sun of 1st stage	67-69	Rotation of planet 1 of 2nd stage
25-27	Rotation of sun of 1st stage	70-72	Translation of planet 2 of 2nd stage
28-30	Translation of planet 1 of 1st stage	73-75	Rotation of planet 2 of 2nd stage
31-33	Rotation of planet 1 of 1st stage	76-78	Translation of planet 3 of 2nd stage
34-36	Translation of planet 2 of 1st stage	79-81	Rotation of planet 3 of 2nd stage
37-39	Rotation of planet 2 of 1st stage		

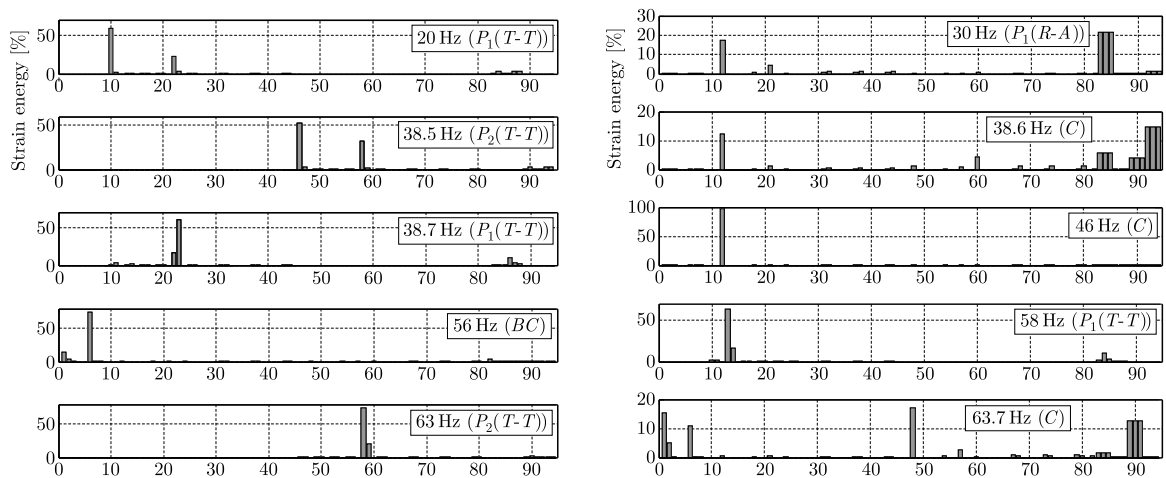


Fig. 9. Strain energy in low-frequencies

Table 5. The X-axis location of strain energies

1-3,5	Bearing of pinion	52-57	Bearing of ring of 2nd stage
4	Bearing of motor	58-63	Bearing of sun of 2nd stage
6-9	Bearing of wheel	64-69	Bearing of planet 1 of 2nd stage
10-15	Bearing of carrier of 1st stage	70-75	Bearing of planet 2 of 2nd stage
16-21	Bearing of ring of 1st stage	76-81	Bearing of planet 3 of 2nd stage
22-27	Bearing of sun of 1st stage	82	Meshing pinion-wheel
28-33	Bearing of planet 1 of 1st stage	83-85	Meshing ring-planets of 1st stage
34-39	Bearing of planet 2 of 1st stage	86-88	Meshing sun-planets of 1st stage
40-45	Bearing of planet 3 of 1st stage	89-91	Meshing ring-planets of 2nd stage
46-51	Bearing of carrier of 2nd stage	92-94	Meshing sun-planets of 2nd stage

Table 6. Dominant motion and dominant strain energy in low-frequencies

No. of mode	Frequencies [Hz]	Modal dominant movement	Dominant strain energy
2,3	20 (T-T)	Transl. of planet 3 of 1st stage	Bearing of carrier of 1st stage
4	30 (R-A)	Transl. of planet 3 of 1st stage	Meshing sun-planets of 1st stage
5,6	38.5 (T-T)	Transl. of planet 3 of 2nd stage	Bearing of carrier of 2nd stage
7	38.6 (C)	Transl. of planet 3 of 2nd stage	Meshing ring-planets of 2nd stage
8,9	38.7 (T-T)	Transl. of all planets of 1st stage	Bearing of sun of 1st stage
10	46 (C)	Transl. of all planets of 1st stage	Bearing of carrier of 1st stage
11	56 (B)	Transl. of wheel	Bearing of wheel
12,13	58 (T-T)	Transl. of planet 2 of 1st stage	Bearing of carrier of 1st stage
14,15	63 (T-T)	Transl. of planet 3 of 2nd stage	Bearing of sun of 2nd stage
16	63.7 (C)	Transl. of planet 3 of 2nd stage	Bearing of carrier of 2nd stage Meshing sun-planets of 2nd stage Bearing of pinion

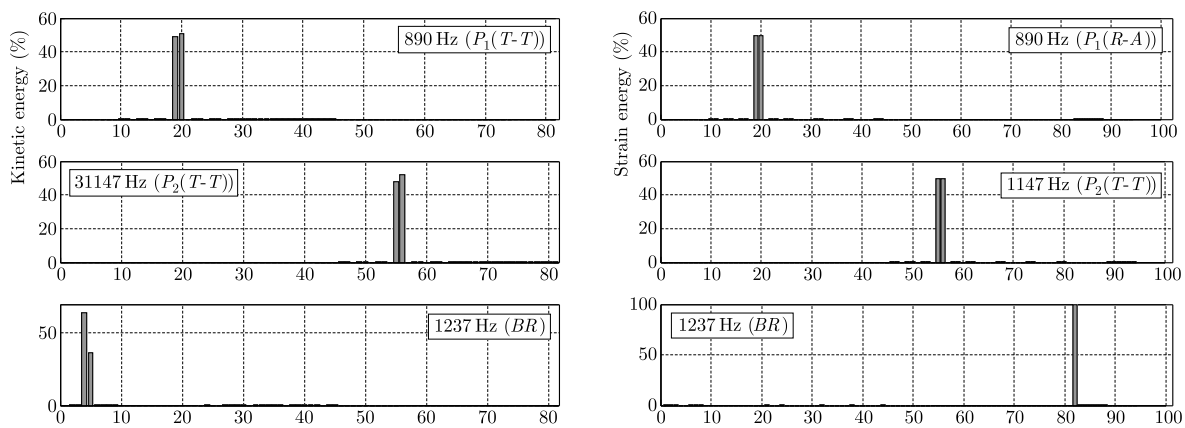


Fig. 10. Kinetic and strain energy in high-frequencies

Table 7 presents a resume of the modal dominant motion and the dominant strain energy in each high-frequency mode.

Table 7. Dominant motion and dominant strain energy in high-frequencies

No. of mode	Frequencies [Hz]	Modal dominant movement	Dominant strain energy
77,78	890 (T-T)	Rotation of ring of 1st stage	Bearing of ring of 1st stage
79,80	1147 (T-T)	Rotation of ring of 2nd stage	Bearing of ring of 2nd stage
81	1237 (B)	Rotation of bearing motor Meshing pinion-wheel	Rotation of pinion

5. Conclusion

This paper investigates modal properties of a special configuration of a gearbox composed of one stage spiral bevel gear coupled in a two stage helical planetary gear. A lumped-parameter model is formulated to obtain the equations of motion. The helical planetary gear system is represented by a three-dimensional lumped-parameter model with six degrees of freedom per gear and the shaft body supported by bearings. Solution of the eigenvalue problem allowed recovering modal characteristics of the transmission. It has been found that natural frequencies can be divided into three main mode classes: coupled modes, bevel gear modes and planetary gear modes. The last class of modes includes two types: the first one is a rotational-axial mode in which the central components rotate and move axially but do not tilt or translate with identical modal deflection of the planets; there are also 12 rotational-axial modes with distinct natural frequencies, the second one is a translational-tilting mode in which the central members tilt and translate in-plane but do not rotate or move axially; there are 12 pairs of degenerate translational-tilting modes with the natural frequency multiplicity two. When looking at the modal kinetic and strain energy distributions, another classification emerges according to the dominant energy in the system for each natural frequency.

References

1. BLANKENSHIP G.W., SINGH R., 1995, A new gear mesh interface dynamic model to predict multidimensional force coupling and excitation, *Mechanism and Machine Theory*, **30**, 1, 43-57
2. CHOY K., TU Y.K., SAVAGE M., TOWNSEND D.P., 1991, Vibration signature and modal analysis of multi-stage gear transmission, *Journal of the Franklin Institute*, **328**, 2/3, 281-298
3. ERITENEL T., PARKER R.G., 2009, Modal properties of three-dimensional helical planetary gears, *Journal of Sound and Vibration*, **325**, 397-420
4. GOSSELIN C., CLOUTIER L., NGUYEN Q.D., 1995, A general formulation for the calculation of the load sharing and transmission error under load of spiral bevel and hypoid gears, *Mechanism and Machine Theory*, **30**, 3, 433-450
5. GUO Y., PARKER R.G., 2010, Sensitivity of general compound planetary gear natural frequencies and vibration modes to modal parameters, *Journal of Vibration and Acoustics*, **132**, 1
6. HABIB R., CHAARI F., FAKHFAKH T., HADDAR M., 2005, Three dimensional model for a helical planetary gear train vibration analysis, *International Journal of Engineering Simulation*, **6**, 3, 32-38
7. HAMMAMI A. DEL RINCON A.F., RUEDA F.V., CHAARI F., HADDAR M., 2015, Modal analysis of back-to-back planetary gear: experiments and correlation against lumped-parameter model, *Journal of Theoretical and Applied Mechanics*, **53**, 1, 125-138
8. KAHRAMAN A., 1994a, Dynamics of a multi-mesh helical gear train, *ASME Journal of Mechanical Design*, **116**, 706-712
9. KAHRAMAN A., 1994b, Natural modes of planetary gear trains, *Journal of Sound and Vibration*, **173**, 125-130

10. KAHRAMAN A., 1994c, Planetary gear train dynamics, *ASME Journal of Mechanical Design*, **116**, 713-720
11. KARRAY M., CHAARI F., VIADERO F., DEL RINCON A.F., HADDAR M., 2013, Dynamic response of single stage bevel gear transmission in presence of local damage, *The 4th European Conference on Mechanism Science, EUCOMES'2012*, Spain, *New Trends in Mechanism and Machine Science, Mechanisms and Machine Science*, **7**, 2013, 337-345
12. LIN J., PARKER R.G., 1999a, Analytical characterization of the unique properties of planetary gear free vibration, *Journal of Vibration and Acoustics*, **121**, 3, 316-321
13. LIN J., PARKER R.G., 1999b, Sensitivity of planetary gear natural frequencies and vibration modes to model parameters, *Journal of Sound and Vibration*, **228**, 1, 109-128
14. LIN J., PARKER R.G., 2000, Structured vibration characteristics of planetary gears with unequally spaced planets, *Journal of Sound and Vibration*, **233**, 5, 921-928
15. LIN J., PARKER R.G., 2004, Mesh phasing relationships in planetary and epicyclic gears, *Journal of Mechanical Design*, **126**, 365-370
16. OZGUVEN H.N., HOUSER D.R., 1988a, Dynamic analysis of high speed gears by using loaded static transmission error, *Journal of Sound and Vibration*, **125**, 71-83
17. OZGUVEN H.N., HOUSER D.R., 1988b, Mathematical models used in gear dynamics – a review, *Journal of Sound and Vibration*, **121**, 383-411
18. RUSINSKI E., HARNATKIEWICZ P., KOWALCZYK M., MOCZKO P., 2010, Examination of the causes of a bucket wheel fracture in a bucket wheel excavator, *Engineering Failure Analysis*, **17**, 1300-1312
19. SEAGER D.L., 1975, Conditions for the neutralization of excitation by the teeth in epicyclic gearing, *Journal of Mechanical Engineering Science*, **17**, 5, 293-298
20. SUN W., DING X., WEI J., HU X., WANG Q., 2014, An analyzing method of coupled modes in multi-stage planetary gear system, *International Journal of Precision Engineering and Manufacturing*, **15**, 11, 2357-2366
21. VELEX P., MAATAR M., 1996, A mathematical model for analyzing the influence of shape deviations and mounting errors on gear dynamic behaviour, *Journal of Sound and Vibration*, **191**, 629-660
22. WU X., PARKER R.G., 2008, Modal properties of planetary gears with an elastic continuum ring gear, *Journal of Applied Mechanics*, **75**, 3, 1-10
23. ZHANG L., WANG Y., WU K., SHENG R., HUANG Q., 2016, Dynamic modeling and vibration characteristics of a two-stage closed-form planetary gear train, *Mechanism and Machine Theory*, **97**, 12-28

Manuscript received March 30, 2016; accepted for print August 12, 2016

DESIGN AND IMPLEMENTATION OF IMPROVED SLIDING MODE CONTROLLER ON 6R MANIPULATOR

MOHARAM H. KORAYEM, SAEED R. NEKOO, ALIREZA KHADEMI, FAEZEH ABDOLLAHI
*Robotic Research Laboratory, Center of Excellence in Experimental Solid Mechanics and Dynamics,
School of Mechanical Engineering, Iran University of Science and Technology (IUST), Tehran, Iran
e-mail: saerafee@yahoo.com*

In this work, we present an improved sliding mode control (ISMC) technique designed and implemented for control of 6R manipulator. Sliding mode control (SMC) is a well-known nonlinear robust method for controlling systems in the presence of uncertainties and disturbances and systems with complex dynamics as in manipulators. Despite this good property, it is difficult to implement this method for the manipulator with a complex structure and more than three degree-of-freedom because of the complicated and massive equation and chattering phenomenon as a property of SMC in control inputs. Here, the chattering phenomenon is eliminated by using an effective algorithm called ISMC and implemented to 6R manipulator by using a low-cost control board based on an ARM microcontroller with high accuracy and memory. The carrying load is considered as the uncertainty for the manipulator, while the dynamic load carrying capacity (DLCC) is considered as a robot performance criterion showing robustness of the controller. The results of simulations and experiments show that the proposed approach has a good performance and is suitable and practical to be applied for manipulators.

Keywords: improved sliding mode control, chattering, DLCC, hardware implementation

1. Introduction

Models of manipulators are complex nonlinear dynamical systems with uncertainties due to differences between mathematical models and real robots. The sliding mode control (SMC) is one of the methods in the category of nonlinear control capable of controlling systems with uncertainties. The SMC technique and the improved SMC (ISMC)-based algorithms have been used frequently in the field of manipulator control. One of the benefits of the SMC is insensitivity to variation of parameters such as load for manipulating. Since the dynamics of manipulators is so complicated, the ISMC method is selected for controlling the system in this work. And yet a lot of work in this field has been applied. Ertugrul *et al.* (2000) presented gain adaptation in SMC of robotic manipulators via MIT rule. The method was implemented on a two-link planar manipulator to validate the proposed algorithm. Vega *et al.* (2003) presented dynamic sliding PID control for trajectory tracking on manipulators. Implementation and comparative experimental study on a two-DOF robot arm were expressed via PD, PID, adaptive and SMC method. Shi *et al.* (2008) expressed robust control of robotic manipulators based on the integral sliding mode. Capisani and Ferrara (2009) used a second-order SMC approach and presented experimental test on COMAU SMART3-S2 rigid industrial manipulator with three joints. Korayem *et al.* (2009) presented the observer-based SMC for determining the dynamic load-carrying capacity of manipulators. Islam and Liu (2011) applied the SMC method for overcoming the problem of large-scale uncertainties in control of manipulators. The parameter uncertainties and external disturbances were considered in the modelling. Foster and Harrison (2011) expressed the experimental investigation of a 5-DOF robot arm with SMC. The method was simulated and verified

with the experimental results. Islam *et al.* (2014) applied SMC and CTC control methods for a multi-DOF articulated robotic arm manipulator and demonstrated superior performance of the SMC by simulation results of a 6-DOF robot manipulator.

The chattering phenomenon is one of the SMC difficulties. This phenomenon occurs because of the existence of switching nature in the sliding mode controller. It is unwanted and leads to an excessive usage of actuator; therefore, the control law may become impractical. Many methods have been proposed for eliminating or reducing the chattering including the boundary layer, continuous approximations and higher order SMC methods. The methods also include synthesized SMC with other techniques such as the fuzzy SMC, adaptive neural network, and optimal SMC (Thangavelusamy and Ponnusamy, 2012; Beyhan *et al.*, 2011; Sefriti *et al.*, 2012; Korayem *et al.*, 2014). Obviation of the chattering phenomenon, in this paper, is the use of ISMC applied to this problem (Ataei *et al.*, 2014).

The model in this paper is a 6R manipulator. The first three links are made as the base of the robot and developed by adding a wrist with three-DOF on that (Jamali *et al.*, 2005; Hamraz *et al.*, 2005). The control system of this manipulator is a digital board with six PIC chips for motors to perform open-loop control. Implementing nonlinear controllers, which are ideal for this manipulator, is not possible. To extend the performance and options of the arm, a new digital board based on ARM LPC1768 CortexM3 microcontroller has been designed and built (Korayem *et al.*, 2013). In the following, we first describe the mathematical model of the manipulator and then design a SMC for it. Then, we briefly describe the control board and, finally, this method is simulated and implemented for the robot.

2. SMC design

SMC is a nonlinear robust control method that is often used in cases that have uncertainty in dynamics and external disturbance. We used this method for its inherent property in robustness and compared to other nonlinear methods. SMC and ISMC are easily implemented.

2.1. SISO system

In order to start the procedure of designing the controller, the dynamical equation should be expressed in the standard form as

$$x^{(n)}(t) = f(\mathbf{x}(t)) + b(\mathbf{x}(t))u(t) \quad (2.1)$$

where the scalar $x(t)$ is the output, the scalar $u(t)$ is the control input and $\mathbf{x}(t) = [x(t), \dot{x}(t), \dots, x^{(n-1)}(t)]^T$ is the state vector. $f(\mathbf{x}(t))$ is an uncertain nonlinear function bounded by a known continuous function of $\mathbf{x}(t)$, and $b(\mathbf{x}(t))$, similarly, is an uncertain nonlinear function that is of known sign and is bounded by the known continuous function of $\mathbf{x}(t)$.

Consider the uncertainty of parameters in the system, which is denoted as follows

$$f(\mathbf{x}(t)) = (1 + \Delta)\hat{f}(\mathbf{x}(t)) \quad b(\mathbf{x}(t)) = (1 + \Delta)\hat{b}(\mathbf{x}(t)) \quad (2.2)$$

Let the subscript $(\hat{\cdot})$ means the system nominal value and symbol Δ means the system uncertainty (small value). The time-varying surface named sliding surface is defined as follows (Slotine and Li, 1991)

$$s(\mathbf{x}(t)) = \left(\frac{d}{dt} + \lambda\right)^{n-1} \tilde{x}(t) \quad (2.3)$$

where λ is a strictly positive constant and $\tilde{x}(t) = x(t) - x_d(t)$ is the tracking error in the variable $x(t)$. For the second-order system, by considering $n = 2$, the sliding surface is obtained as follows

$$s(\mathbf{x}(t)) = \dot{\tilde{x}}(t) + \lambda\tilde{x}(t) \quad (2.4)$$

The control input law in the sliding mode method is considered as

$$u(t) = u_{eq}(t) + u_{corr}(t) \quad (2.5)$$

where $u_{eq}(t)$ is the equivalent control input and $u_{corr}(t)$ is the correction or switching control input for reaching to the sliding surface when distanced from the sliding surface by the effect of uncertainty and disturbance. $u_{eq}(t)$ is defined by solving $\dot{s}(\mathbf{x}(t)) = 0$ and, therefore, we get

$$u_{eq}(t) = \hat{b}^{-1}(\mathbf{x}(t))[-\hat{f}(\mathbf{x}(t)) + \ddot{x}_{desired}(t) - \lambda\dot{\tilde{x}}(t)] \quad (2.6)$$

Hence, $u_{corr}(t)$ is defined as

$$u_{corr}(t) = -\hat{b}^{-1}(\mathbf{x}(t))k(\mathbf{x}(t)) \operatorname{sgn}(s(\mathbf{x}(t))) \quad (2.7)$$

To reach the sliding surface in finite time, the sliding condition that is defined as follows shall be satisfied

$$\frac{1}{2}s(\mathbf{x}(t))\dot{s}(\mathbf{x}(t)) \leq -\eta|s(\mathbf{x}(t))| \quad (2.8)$$

and $\eta > 0$ must be satisfied as well. By assuming

$$\left| \hat{f}(\mathbf{x}(t)) - f(\mathbf{x}(t)) \right| \leq f_b \quad \hat{b}(\mathbf{x}(t)) = \sqrt{b_{max}b_{min}} \quad (2.9)$$

where f_b is the maximum estimation error in the bound of uncertainty of $f(\mathbf{x}(t))$, b_{max} and b_{min} are the maximum and minimum estimation errors, respectively, in the bound of $b(\mathbf{x}(t))$ and considering (Slotine and Li, 1991)

$$k(\mathbf{x}(t)) \geq \beta(f_b + \eta) + (\beta - 1)|u_{eq}(t)| \quad (2.10)$$

where $\beta = \sqrt{b_{max}/b_{min}}$, the sliding condition is satisfied and implies that the system trajectories will asymptotically converge to the sliding surface from any non-zero initial state and guarantees the robust stability of the closed-loop system.

To eliminate the chattering phenomena in the conventional SMC, we use $u_{corr}(t)$ as follows and name it an improved SMC. In this algorithm, for the decreasing rate of variations of $u(t)$ around the sliding surface and in order to increase the convergence rate, the idea of using the following sliding condition is proposed (Ataei *et al.*, 2014)

$$s(\mathbf{x}(t))\dot{s}(\mathbf{x}(t)) \leq -\eta|s(\mathbf{x}(t))| \exp\left(\frac{-\xi}{|s(\mathbf{x}(t))|}\right) - \gamma s^2(\mathbf{x}(t)) \quad (2.11)$$

in which η , γ , and ξ are strictly positive constants. Using the exponential function, makes that whatever the distance of the scalar function $s(\mathbf{x}(t))$ increases from the surface, the fall rate with respect to time is greater and this action develops with an exponential factor. Also, the continuous function $\tanh(s(\mathbf{x}(t))/\varepsilon)$ is used instead of the discontinuous function $\operatorname{sgn}(s(\mathbf{x}(t)))$ for preventing the chattering in which the parameter ε is the boundary layer thickness. By the above-mentioned description, the correction input is defined as follows for the SISO system

$$u_{corr}(t) = -\hat{b}^{-1}(\mathbf{x}(t))w(\mathbf{x}(t)) \quad (2.12)$$

where

$$w(\mathbf{x}(t)) = \left[f_b + \alpha \exp\left(-\frac{\beta}{|s(\mathbf{x}(t))|}\right) \right] \tanh\left(\frac{s(\mathbf{x}(t))}{\varepsilon}\right) + \gamma s(\mathbf{x}(t)) \quad (2.13)$$

$$\alpha > \eta \quad \alpha - \eta < 2f_b \exp\left(-\frac{\beta}{|s(\mathbf{x}(t))|}\right)$$

Therefore, the control input is defined as

$$u(t) = \hat{b}^{-1}(\mathbf{x}(t))[-\hat{f}(\mathbf{x}(t)) + \ddot{x}_{desired}(t) - \lambda\dot{\tilde{x}}(t) - w(\mathbf{x}(t))] \quad (2.14)$$

2.2. MIMO system

In order to extend the method for MIMO systems, a system of second order differential equations is regarded as follows

$$\ddot{\mathbf{q}}(t) = \mathbf{f}(\mathbf{q}(t), \dot{\mathbf{q}}(t)) + \mathbf{B}(\mathbf{q}(t), \dot{\mathbf{q}}(t))\mathbf{u}(t) \quad (2.15)$$

where $\mathbf{q}(t) \in \mathfrak{R}^n$ is the system variable and $\mathbf{u}(t) \in \mathfrak{R}^n$ is the input vector and

$$\begin{aligned} \mathbf{f}(\mathbf{q}(t), \dot{\mathbf{q}}(t)) &: \mathfrak{R}^n \times \mathfrak{R}^n \rightarrow \mathfrak{R}^n \\ \mathbf{B}(\mathbf{q}(t), \dot{\mathbf{q}}(t)) &: \mathfrak{R}^n \times \mathfrak{R}^n \rightarrow \mathfrak{R}^{n \times n} \end{aligned} \quad (2.16)$$

and (2.15) is changed to the state-space form

$$\dot{\mathbf{x}}(t) = \begin{bmatrix} \dot{\mathbf{q}}(t) \\ \mathbf{f}(\mathbf{q}(t), \dot{\mathbf{q}}(t)) \end{bmatrix} + \begin{bmatrix} \mathbf{0}_{n \times n} \\ \mathbf{B}(\mathbf{q}(t), \dot{\mathbf{q}}(t)) \end{bmatrix} \mathbf{u}(t) \quad (2.17)$$

in which the state vector has the shape of $\mathbf{x}(t) = [\mathbf{q}(t), \dot{\mathbf{q}}(t)]^T$. The maximum bound of uncertainties in system (2.2) are modified as

$$\mathbf{f}(\mathbf{x}(t)) = \widehat{\mathbf{f}}(\mathbf{x}(t)) + \overline{\Delta} \widehat{f}(\mathbf{x}(t)) \quad \mathbf{B}(\mathbf{x}(t)) = (\mathbf{I} + \Delta) \widehat{\mathbf{B}}(\mathbf{x}(t)) \quad (2.18)$$

where $\overline{\Delta}$ is the vector of the uncertainty coefficient, Δ is a diagonal matrix of that and \mathbf{I} is the identity matrix. Hence, the maximum bound of $f(\mathbf{x}(t))$ is restricted to

$$\left| \widehat{\mathbf{f}}(\mathbf{x}(t)) - \mathbf{f}(\mathbf{x}(t)) \right| \leq \mathbf{f}_b \quad (2.19)$$

and $\mathbf{B}(\mathbf{x}(t))$ to

$$\widehat{B}_{ij}(\mathbf{x}(t)) = \sqrt{b_{max,ij} b_{min,ij}} \quad (2.20)$$

which leads to an extended form of (2.10)

$$K_i(\mathbf{x}(t)) \geq \beta(f_{b,i} + \eta_i) + (\beta - 1)|u_{eq,i}(t)| \quad (2.21)$$

in which $\beta = b_{max}/b_{min}$, $b_{max} = \max(b_{max,ij})$ and $b_{min} = \min(b_{min,ij})$. $K_i(\mathbf{x}(t))$ is also the i -th diagonal element of the matrix $\mathbf{K}(\mathbf{x}(t))$. The control law of the conventional SMC possesses the shape

$$\mathbf{u}(t) = \widehat{\mathbf{B}}^{-1}(\mathbf{x}(t))[-\widehat{\mathbf{f}}(\mathbf{x}(t)) + \ddot{\mathbf{x}}_{desired}(t) - \lambda \dot{\tilde{\mathbf{x}}}(t)] - \widehat{\mathbf{B}}^{-1}(\mathbf{x}(t))\mathbf{K}(\mathbf{x}(t)) \text{sgn}(\mathbf{s}(\mathbf{x}(t))) \quad (2.22)$$

where $\mathbf{s}(\mathbf{x}(t)) = \dot{\tilde{\mathbf{x}}}(t) + \lambda \tilde{\mathbf{x}}(t)$. The MIMO structure of the control law of ISMC (2.14) is rewritten

$$\mathbf{u}(t) = \mathbf{B}^{-1}(\mathbf{x}(t))[-\widehat{\mathbf{f}}(\mathbf{x}(t)) + \ddot{\mathbf{x}}_{desired}(t) - \lambda \dot{\tilde{\mathbf{x}}}(t) - \mathbf{w}(\mathbf{x}(t))] \quad (2.23)$$

where

$$w_i(\mathbf{x}(t)) = \left[f_{b,i} + \alpha_i \exp\left(-\frac{\beta}{|s_i(\mathbf{x}(t))|}\right) \right] \tanh\left(\frac{s_i(\mathbf{x}(t))}{\varepsilon}\right) + \gamma_i s_i(\mathbf{x}(t)) \quad (2.24)$$

in which $\alpha_i > \eta_i$ and

$$\alpha_i - \eta_i < 2f_{b,i} \exp\left(-\frac{\beta}{|s_i(\mathbf{x}(t))|}\right) \quad (2.25)$$

3. Applied ISMC for the robot manipulator

Let us consider generalized coordinates of an n -link manipulator as $\mathbf{q} = \{q_1, \dots, q_n\}$, where q_i is the generalized coordinate of the i -th joint; either revolute or prismatic. By using Lagrange's approach, the manipulator dynamical equation can be expressed as

$$\mathbf{M}_{n \times n}(\mathbf{q}(t))\ddot{\mathbf{q}}_{n \times 1}(t) + \mathbf{c}_{n \times 1}(\mathbf{q}(t), \dot{\mathbf{q}}(t)) + \mathbf{g}_{n \times 1}(\mathbf{q}(t)) = \mathbf{u}_{n \times 1}(t) \quad (3.1)$$

where $\mathbf{M}_{n \times n}(\mathbf{q}(t))$ is the inertia matrix, $\mathbf{c}_{n \times 1}(\mathbf{q}(t), \dot{\mathbf{q}}(t))$ is a vector consisting of Coriolis and centrifugal forces, $\mathbf{g}_{n \times 1}(\mathbf{q}(t))$ is the gravity force, and $\mathbf{u}_{n \times 1}(t)$ is the input vector of joints. Elements of state-space equation (2.17) are structured as

$$\begin{aligned} \mathbf{f}(\mathbf{q}(t), \dot{\mathbf{q}}(t)) &= -\mathbf{M}^{-1}(\mathbf{q}(t))[\mathbf{c}(\mathbf{q}(t), \dot{\mathbf{q}}(t)) + \mathbf{g}(\mathbf{q}(t))] \\ \mathbf{B}(\mathbf{q}(t), \dot{\mathbf{q}}(t)) &= \mathbf{M}^{-1}(\mathbf{q}(t)) \end{aligned} \quad (3.2)$$

Inserting the proposed ISMC structure into the robot equation of motion changes Eq. (2.23) into

$$\mathbf{u}(t) = \mathbf{M}(\mathbf{q}(t))\left(\mathbf{M}^{-1}(\mathbf{q}(t))[\mathbf{c}(\mathbf{q}(t), \dot{\mathbf{q}}(t)) + \mathbf{g}(\mathbf{q}(t))] + \ddot{\mathbf{q}}_{desired}(t) - \lambda \dot{\mathbf{q}}(t) - \mathbf{w}(s)\right) \quad (3.3)$$

where

$$w_i(s_i) = \left[f_{b,i} + \alpha_i \exp\left(-\frac{\beta}{|s_i(q(t))|}\right) \right] \tanh\left(\frac{s_i(q(t))}{\varepsilon}\right) + \gamma_i s_i(q(t)) \quad (3.4)$$

in which $w_i(s_i)$ is a set as coefficients of tanh function $f_{b,i} + \alpha_i \exp[-\beta/|s_i(q(t))|]$; and $\gamma_i s_i(q(t))$ is added to the first term, $f_{b,i} + \alpha_i \exp[-\beta/|s_i(q(t))|]$ depends on the sign of $s_i(q(t))$. As shown in Fig. 1a, near the origin, $w_i(s_i)$ is equal to zero and then increases exponentially, and far from the origin converges to a constant value. Figures 1b-3b present the effect of parameters on behaviour of $w_i(s_i)$.

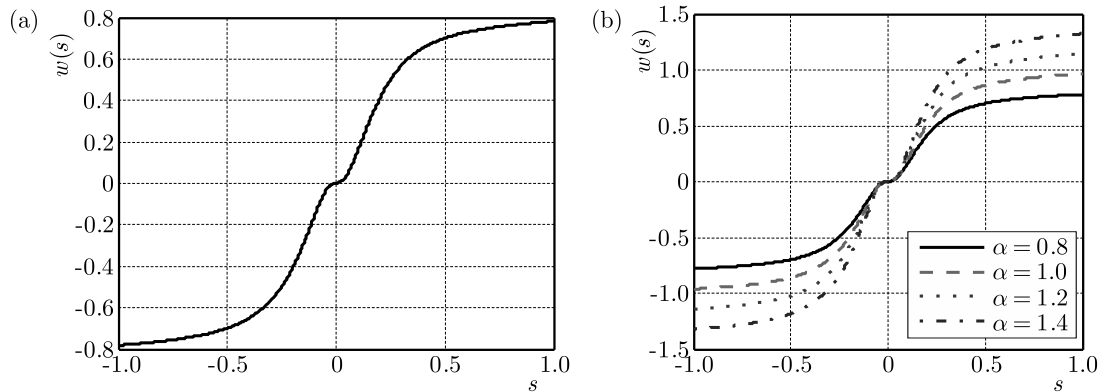


Fig. 1. (a) $w_i(s_i)$ function versus the switching function in the ISMC method; (b) changes of the design parameter α of the ISMC method in function of $w_i(s_i)$

As it is depicted in Fig. 21b, an increase in α_i results in an increase of the ultimate value of $w_i(s_i)$, but around the origin, the effect is less observable. Hence the changes of α_i do not contribute to the chattering. In Fig. 2a, an increase in β makes $w_i(s_i)$ more nonlinear near the origin and does not affect the bounds of $w_i(s_i)$, hence a steady state error might occur. The effects of changes in ε (boundary layer width) are similar to β and do not change the final value of $w_i(s_i)$, though it might lead to the steady state error, presented in Fig. 2b. Figures 3a and 3b show the similarity of f and γ behavior to α as well.

With regard to the try-and-error procedure as well as experimental and simulation study, the mentioned parameters have been designed for the 6R manipulator. The ISMC eliminates the chattering and provides more precision rather than the conventional SMC.

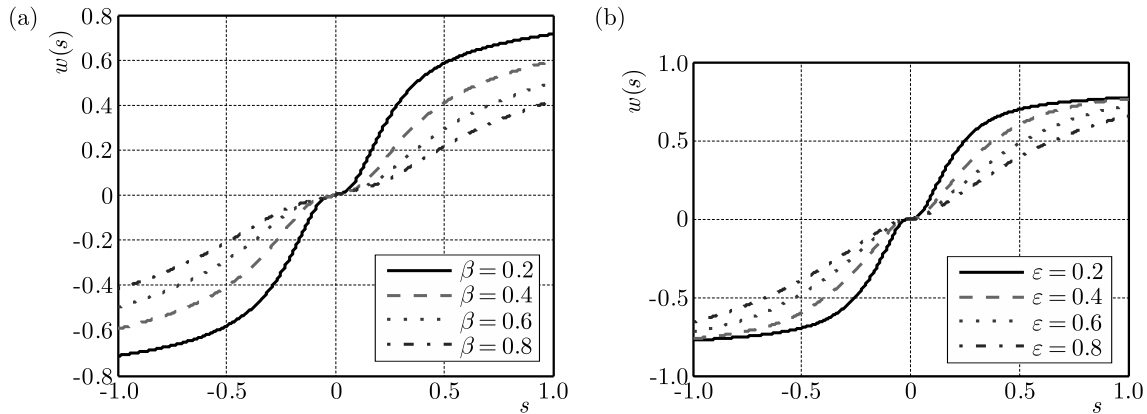


Fig. 2. Changes of the design parameter (a) β and (b) ϵ of the ISMC method in function of $w_i(s_i)$

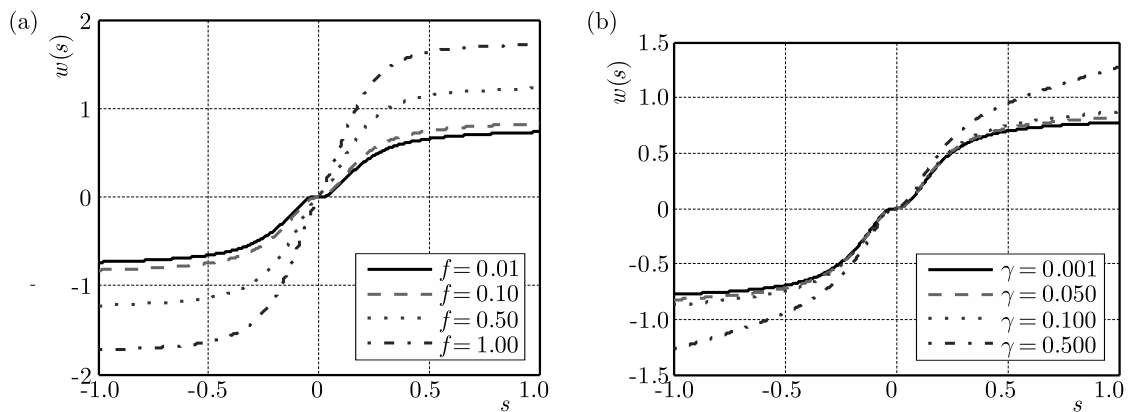


Fig. 3. Changes of the design parameter (a) f and (b) γ of the ISMC method in function of $w_i(s_i)$

4. Dynamic load carrying capacity

The dynamic load carrying capacity (DLCC) is one of the important parameters of robots that should be determined. The DLCC is described as the maximum load that a manipulator can repeatedly lift and carry on the extended configuration in a particular path with an acceptable tracking accuracy. The DLCC is a useful criterion for the assessment of different controllers on the same arm, especially for the estimation of energy consumption and efficiency. The DLCC of a manipulator calculates with respect to the limitation of motors and error of the final point in a finite time. Upper and lower limits of motor torques can be computed from

$$u_{max,i}(t) = u_{s,i} - \frac{u_{s,i}}{\omega_{nl,i}} \dot{q}_i(t) \quad u_{min,i}(t) = -u_{s,i} - \frac{u_{s,i}}{\omega_{nl,i}} \dot{q}_i(t) \quad (4.1)$$

where $u_{s,i}$ is the stall torque of the i -th motor, $\omega_{nl,i}$ is no-load speed of that and $\dot{q}_i(t)$ is actual rotational speed of the motor. In the point-to-point motion, the carrying load increases until the error of the final point in a finite time reaches the allowable bound, while in trajectory tracking, it increases until the torques of motors touch the bounds of limitations. The algorithm of finding the DLCC is shown in Fig. 4.

5. Model of 6R manipulator

5.1. Mechanical structure

The case study of this article is a 6R manipulator with six revolute joints that have massive and complex dynamic and uncertainty in the modelling that shows the capability of the purposed

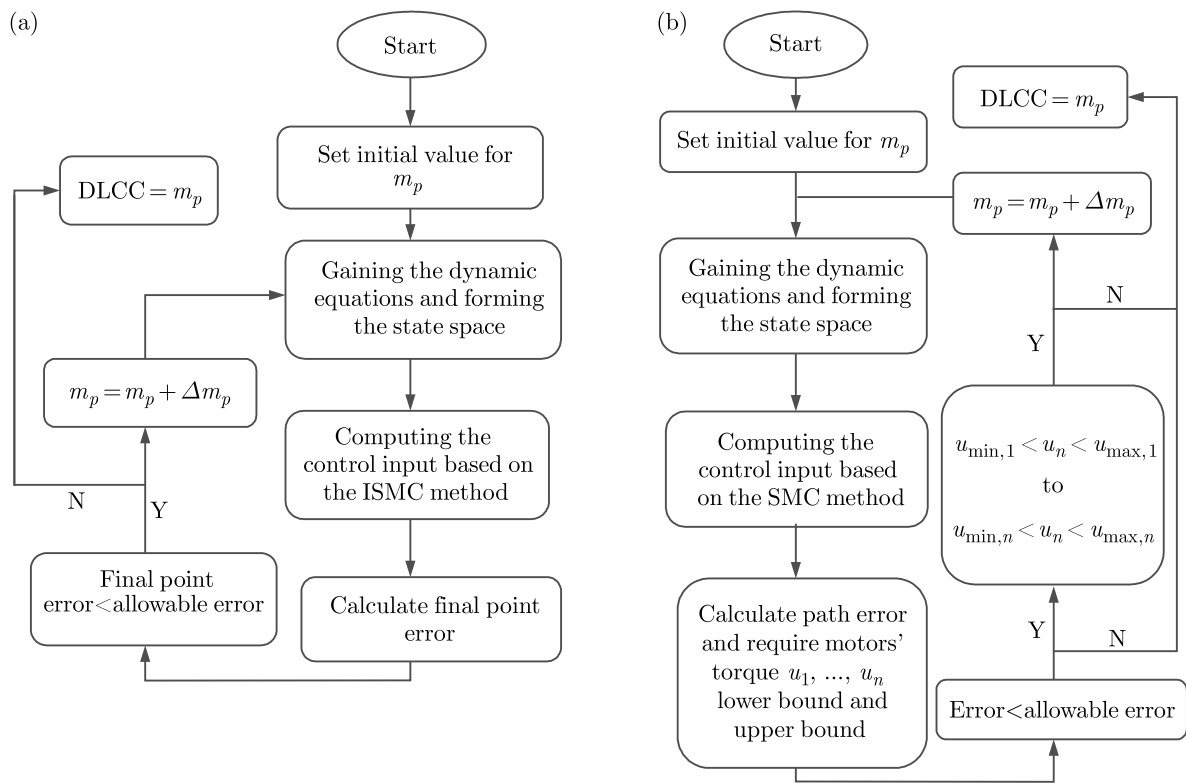


Fig. 4. Algorithms for finding DLCC: (a) point-to-point motion and (b) trajectory tracking

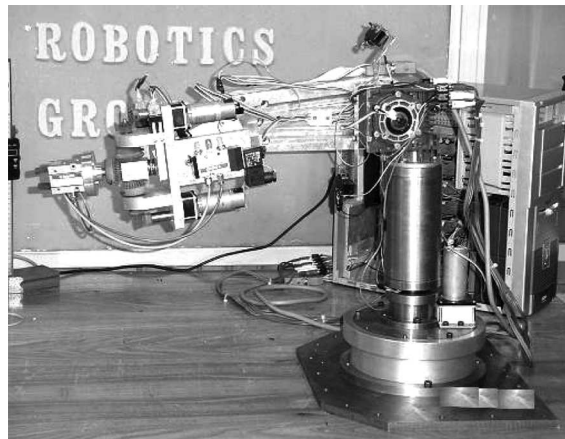


Fig. 5. 6R manipulator (Korayem *et al.*, 2013)

controller. Figure 5 presents the 6R manipulator. Figure 6 shows a schematic of the robot. The Denavit-Hartenberg parameters of the robot are presented in Table 1.

Korayem *et al.* (2013) described the forward kinematics, inverse kinematics, and Jacobian matrix of 6R. The hardware of the previous controller (Korayem *et al.*, 2010) was improved to perform the nonlinear methods better. The new developed digital board of 6R (Korayem *et al.*, 2013) consists of LPC1768 ARM microcontroller. This board is capable of computing massive programs with adequate speed. In the next Subsection, the structure of hardware is explained to a greater extent.

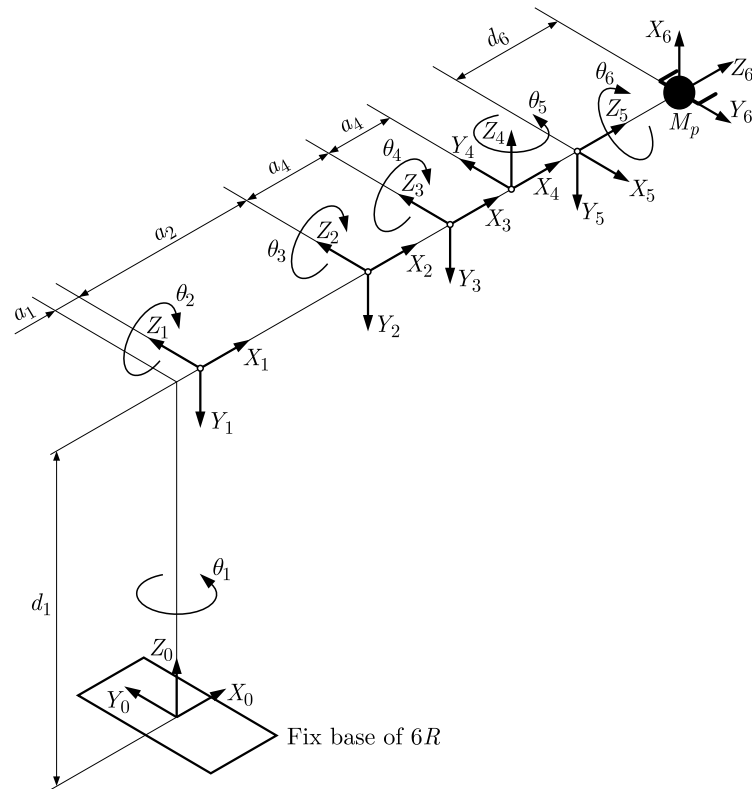


Fig. 6. Schematic of 6R manipulator (Korayem *et al.*, 2013)

Table 1. The Denavit-Hartenberg parameters of 6R arm

Joint i	a_i [mm]	d_i [mm]	α_i [°]
1	0	438	-90
2	251.5	0	0
3	125	0	0
4	92	0	90
5	0	0	-90
6	0	152.8	0

5.2. Hardware of controller

The old system of the controller of 6R was built in a way to perform open loop control (Ahmadi *et al.*, 2009), and it needed an alternative electronic controller unit (ECU) to upgrade the whole system to a closed loop level. The previous ECU was based on PIC microcontrollers; the system used six PIC chips to perform the task. The new 6R robot main board consists of LPC1768 microcontroller, input feedback read, PWM output, and digital communications. LPC1768 is a 32 bit microcontroller based on ARM Cortex M3 processor which operates at up to 100 MHz frequency. This microcontroller has 100 pins, which are allowed to manage driving of six motors easily, and a 12-bit A/D to give feedback on the position of links to the processor. The processor has also six pins for generating different PWMs that enable motors to drive in both directions (Korayem *et al.*, 2013).

The main board duty is to compute and apply the algorithms and for driving the motors, but another board needs to be used. The driver board of motors is an other section of the setup. BTS7810 having H-bridge design is chosen for driving the motors. This driver is capable of providing 40 A and 48 V. Six potentiometers as the feedback are placed on the joints. The

sensitivity and speed of the response are two important items in this part. The voltage of each potentiometer separately passes through a low pass filter and after that an ADC channel converts the voltage to data. The commands are initiated in computers and then are sent to LPC1768. Next, the error is computed by comparing the position of current angles and desired ones. Derivative of the error is computed approximately by division of two consecutive data on the sample time. Then, the control signals are sent to motor drivers to provide the needed power for DC motors.

6. Simulation and experimental result

6.1. Illustrative example

For the assurance of preference of the ISMC method, in this part of article, we compare this method with the conventional SMC and use it for the two-link manipulator as an illustrative example. The schematic of the two-link manipulator is shown in Fig. 7. The parameters of the two-link manipulator are illustrated in Table 2, and the parameters of conventional SMC are considered as $K_1 = K_2 = 10$ and $\lambda_1 = \lambda_2 = 2$; and ISMC coefficients are considered as $f_{b,1} = f_{b,2} = 250$, $\alpha_1 = \alpha_2 = 50$, and $\beta = 500$, $\gamma_1 = \gamma_2 = 10$, $\varepsilon = 0.5$ and $\lambda_1 = \lambda_2 = 2$. Figure 8 shows the end-effector tracking. Figure 9 shows the path error of two methods, and Figs. 10a and 10b show the correction input of the first and second joint of the two methods that caused chattering.

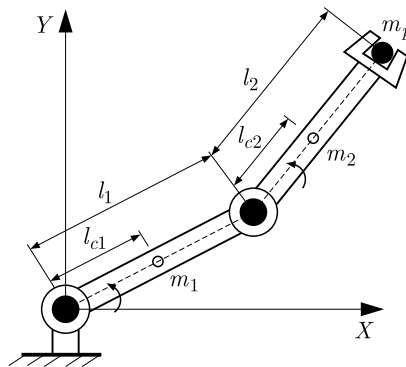


Fig. 7. Schematic of the two-link manipulator

Table 2. Parameters of the two link manipulator

l_1	l_2	l_{c1}	l_{c2}	m_1	m_2	m_p	I_1	I_2
1 m	1 m	0.5 m	0.5 m	2 kg	2 kg	0.5 kg	0.166 kgm ²	0.166 kgm ²

As it is shown in the results, by considering $m_p = 0.1$ kg as the external disturbance, the main distinction between conventional and improved SMC could be directed in chattering reduction topic, which eventually leads to more precision, while less energy is consumed by the actuators.

The point is evident in Figs. 9 and 10; however, to have a clearer view in the matter, Table 3 is arranged for more information in terms of norms of inputs and errors of the system.

6.2. 6R manipulator

In this Section, the results of simulation and experimental tests on the 6R manipulator are presented. For simulation, the dynamical equation of the robot is generated as differential equations and solved with MATLAB software. The motor characteristics are given in Table 4.

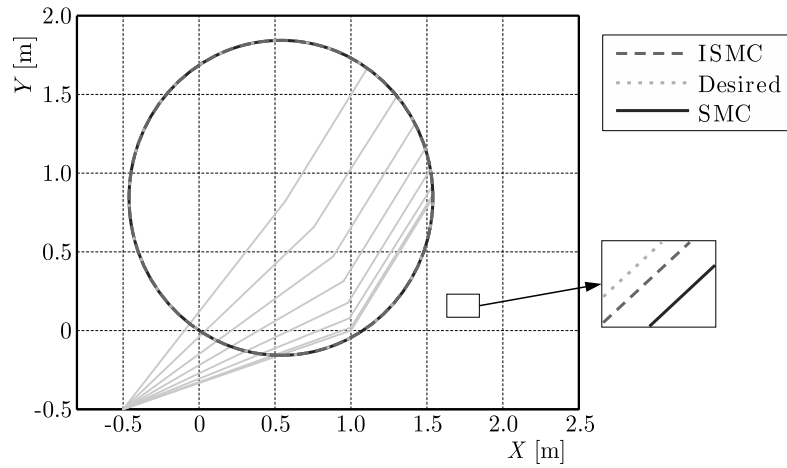


Fig. 8. Trajectories and configuration of the two-link arm

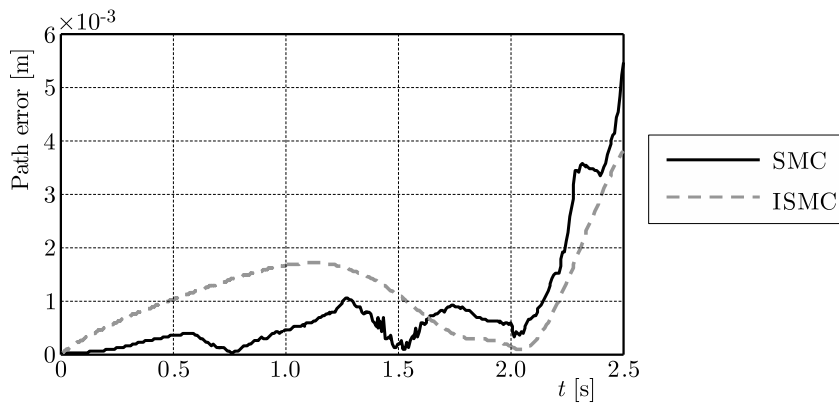


Fig. 9. Error of path tracking of the planar robot

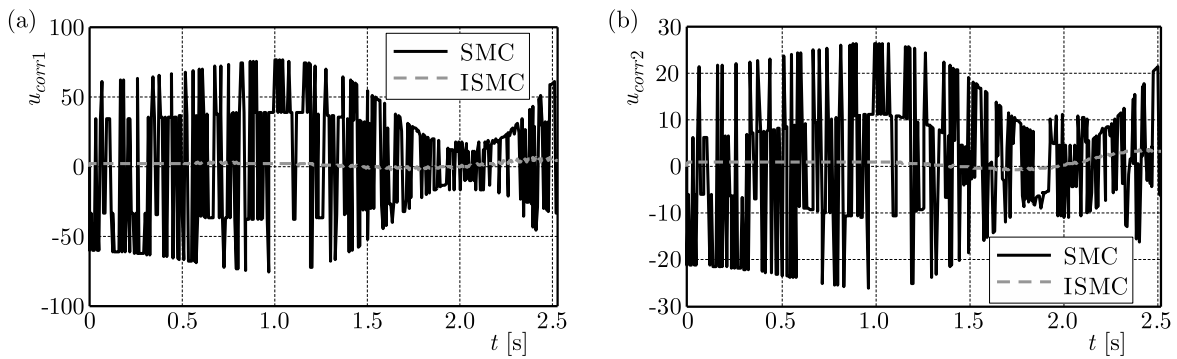


Fig. 10. Correction input of the (a) first link and (b) second link, two-link arm

Table 3. Comparison of errors in inputs and end-effectors between ISMC and SMC of the planar robot

Methods	Max $ u_1 $ [N·m]	Max $ u_2 $ [N·m]	Maximum error [m]
SMC	127.1296	51.5406	0.0054
ISMC	6.8886	3.3870	0.0023

Table 4. Specifications of motors of the 6R robot

Motor	1	2	3	4	5	6
u_s [N·m]	114	98	382.2	40.4	40.4	40.4
ω_{nl} [rad/s]	1.3	1.04	0.73	0.9	0.9	0.9

The torque equation is calculated in a parametric form and programmed in the microcontroller to change to the PWM voltage level. The computed voltages are sent to the motors in real time, and the measured feedback of potentiometers is sent to the main board. This process continues till the error sets in the allowable bound. Then, the values which are obtained from the potentiometers are stored in the main PC.

6.2.1. Point-to-point motion

Point-to-point motion starts from point $A(0.0533, 0.4585, 0.4033)$ and ends with point $B(0.5264, 0.07115, 0.5885)$ during 6 s. The parameters of the SMC controller are given in Table 5 by experiments. Figure 11 shows the end-effector trajectories theoretically and experimentally. In Fig. 12, the variation angles of links are shown. The comparison of simulation results with experiments show sufficient accuracy. The difference between the actual angles and desired ones is due to clearances in the gearbox. Figure 13 shows the chattering reduction and smoothness of ISMC as the main controller for the experimental implementation with respect to the conventional SMC in point-to-point motion.

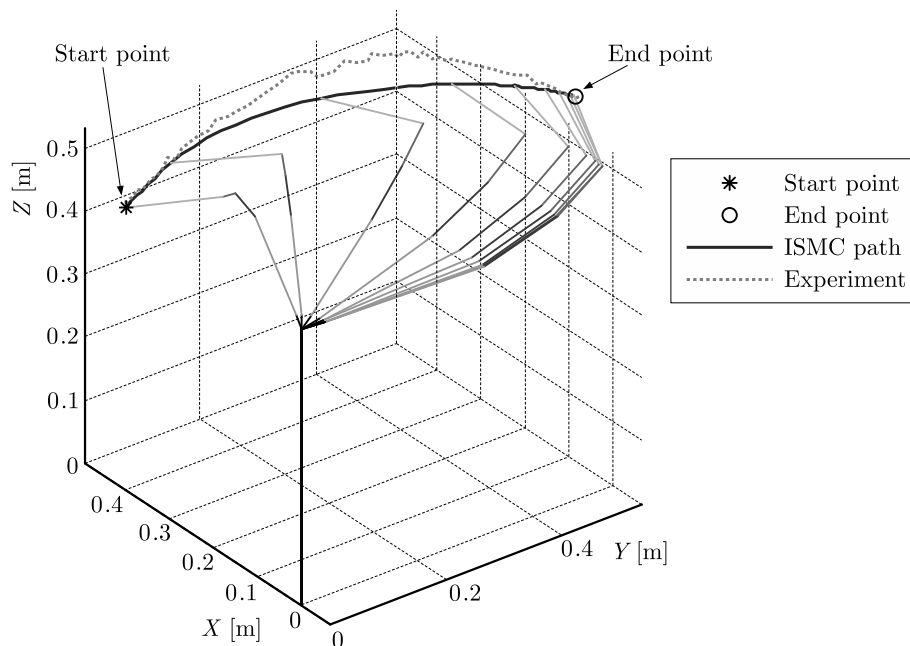


Fig. 11. ISMC point-to-point motion of the 6R robot via simulation and experiment

Regarding the solid structure and heavy links of the 6R manipulator, the conventional SMC has only been implemented theoretically. In experiments, the ISMC method has been applied in the 6R robot to reduce the risk of any defect to motors brought up by probable chattering of SMC. For the error of the end point in a finite time, the allowable bound is given as $\delta = 0.02$. By this constraint, DLCC is obtained to be about 920 g.

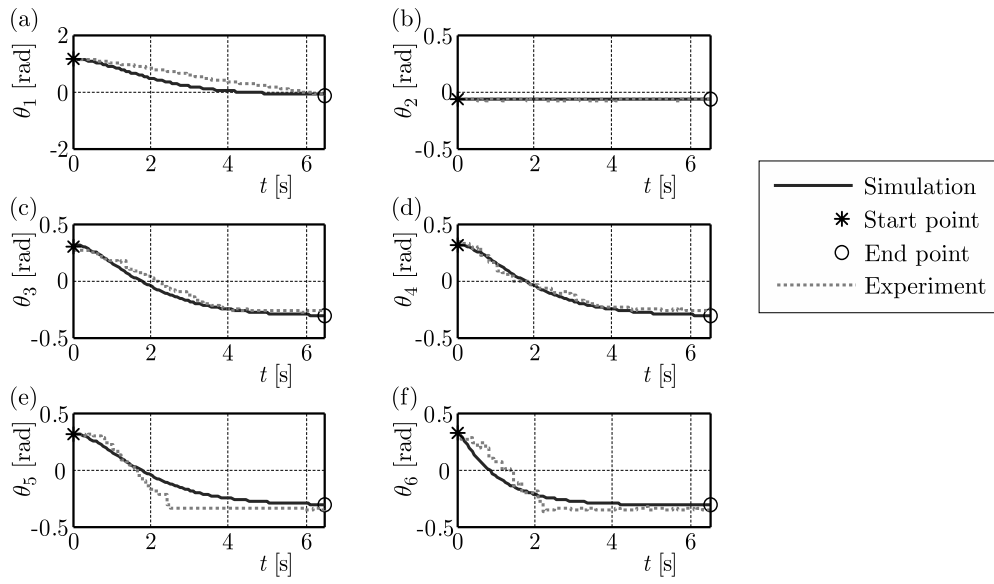


Fig. 12. Angle of links in ISMC point-to-point motion of the 6R robot

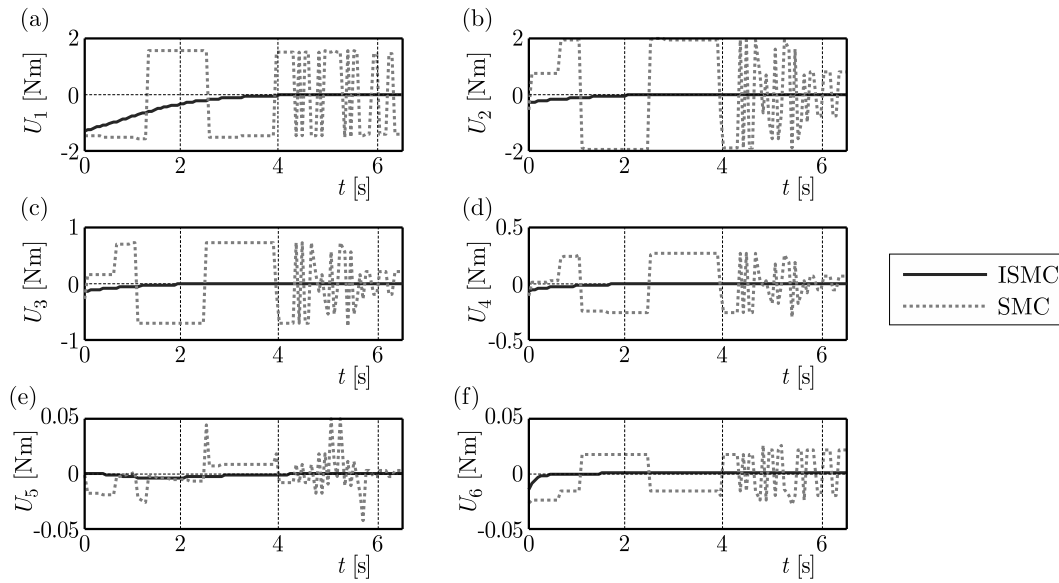


Fig. 13. Theoretical comparison of SMC and ISMC for actuators of the 6R robot

Table 5. Parameters of the ISMC controller for point-to-point motion of the 6R robot

Joint number	λ	f_b	α	β	γ	ε
1	10	10	2	10	0.01	0.5
2	10	10	2	10	0.01	0.5
3	10	10	2	10	0.01	0.5
4	10	10	2	10	0.01	0.5
5	10	50	2	10	0.01	0.5
6	10	50	2	10	0.01	0.5

6.2.2. Trajectory tracking

The trajectory tracking has also been performed in a circular path. Equations of the desired path are given as follows

$$\begin{aligned} x_e(t) &= \frac{7}{9315}t^5 - \frac{1}{1242}t^4 - \frac{5}{621}t^3 + \frac{5}{10} & y_e(t) &= -\frac{14}{9315}t^5 + \frac{1}{621}t^4 + \frac{10}{621}t^3 + \frac{1}{10} \\ z_e(t) &= -\frac{7}{9315}t^5 + \frac{1}{1242}t^4 + \frac{5}{621}t^3 + \frac{6}{10} \end{aligned}$$

The initial conditions are defined as

$$x(0) = \left[-0.1 \quad -0.44 \quad 0.2 \quad 0.65 \quad -1.1 \quad 0 \quad \mathbf{0}_{1 \times 6} \right]^T$$

The best parameters for the SMC controller in this path are given in Table 6 through experiments. Figure 14 shows the end-effector trajectory both theoretically and experimentally. In Fig. 15, the variations of angles of links are shown, and in Fig. 6, angular velocities are shown.

Table 6. Parameters of the ISMC controller for trajectory tracking of the 6R robot

Joint number	λ	f_b	α	β	γ	ε
1	10	100	2	10	0.01	0.5
2	10	100	2	10	0.01	0.5
3	10	100	2	10	0.01	0.5
4	10	100	2	10	0.01	0.5
5	10	150	2	10	0.01	0.5
6	10	150	2	10	0.01	0.5

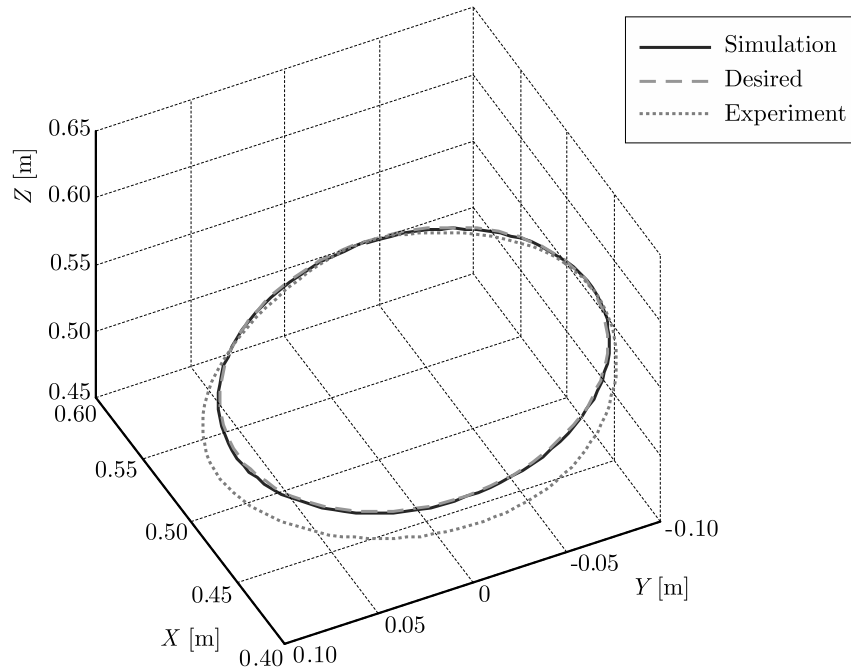


Fig. 14. ISMC trajectory tracking of the 6R robot via simulation and experiment

In the trajectory tracking, DLCC is calculated with respect to the limitation of motors and error path. In Fig. 17, the control inputs are shown. The allowable error is considered 10 mm. As it is shown, the torque of the third motor reaches its lower bound. The DLCC in this trajectory is obtained to be 700 g.

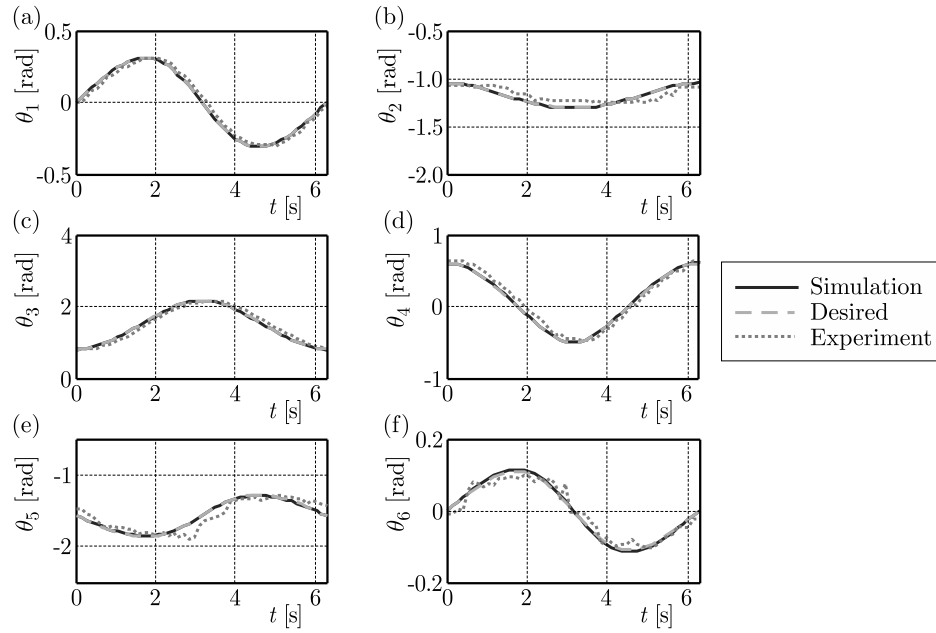


Fig. 15. Angle of links in ISMC trajectory tracking of the 6R robot

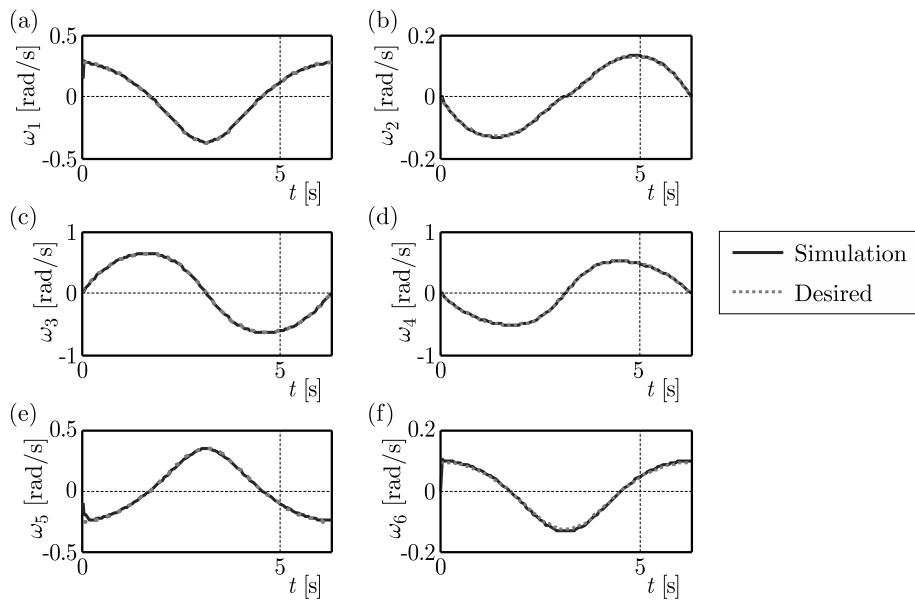


Fig. 16. Angular velocities of links in ISMC trajectory tracking of the 6R robot

7. Conclusions

In this work, we have designed the improved sliding mode control method for manipulators and studied the effect of various parameters on the behaviour of the ISMC controller. First, the ISMC method was simulated for the two-link manipulator for the assurance of good performance and then was implemented to the 6R manipulator as a good case study. The new hardware of robot based on LPC1768 ARM microcontroller allowed performing massive calculation of dynamics and closed loop control of the 6R manipulator. The point-to-point motion and trajectory tracking problems were compared with experimental results. A good performance for manipulator control in the presence of modelling the uncertainty and disturbance was confirmed. The main problem of SMC was the chattering phenomenon, and as a result, the IMSC method provided smooth

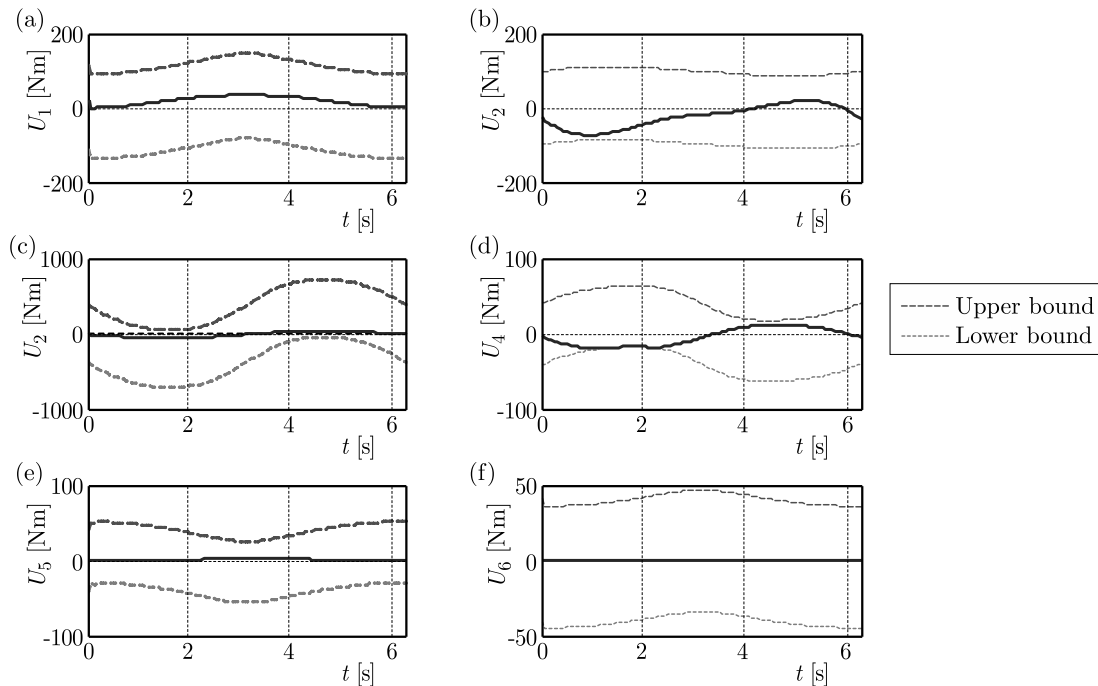


Fig. 17. Control inputs of ISMC trajectory tracking of the 6R robot

input torques for robot motors. Also, the dynamic load carrying capacity for the 6R robot in point-to-point motion and trajectory tracking was increased by considering the robustness of the controller.

References

1. AHMADI R., KORAYEM M.H., JAAFARI N., JAMALI Y., KIOMARSI M., HABIBNEJAD A., 2009, Design, modeling, implementation and experimental analysis of 6R robot, *International Journal of Engineering Science*, **21**, 1, 71-84
2. ATAEI M., HOOSHMAND R.A., SAMANI S.G., 2014, A coordinated MIMO control design for a power plant using improved sliding mode controller, *ISA Transactions*, **53**, 2, 415-422
3. BEYHAN S., LENDEK Z., BABUSKA R., WISSE M., ALCI M., 2011, Adaptive fuzzy and sliding-mode control of a robot manipulator with varying payload, *Proceeding of IEEE Conference on Decision and Control and European Control Conference*, Orlando, FL, USA, 8291-8296
4. CAPISANI L.M., FERRARA A., 2012, Trajectory planning and second-order sliding mode motion/interaction control for robot manipulators in unknown environments, *IEEE Transactions on Industrial Electronics*, **59**, 8, 3189-3198
5. ERTUGRUL M., KAYNAK O., KERESTECIOGLU F., 2000, Gain adaptation in sliding mode control of robotic manipulators, *International Journal of Systems Science*, **31**, 9, 1099-1106
6. FOSTER D., HARRISON A., 2011, Experimental investigation of a 5-DOF robot arm with sliding mode control, *Proceeding of IEEE Conference on Robotics, Automation and Mechatronics*, Qingdao, 125-130
7. HAMRAZ N.J., KORAYEM M.H., JAMALI Y., KIUMARSI M., ASADI M.A., REZAEI S., SOHRABI A., 2005, Design, manufacturing and performance testing of 3r manipulator, *International Congress on Manufacturing Engineering*, Tehran
8. ISLAM S., LIU X.P., 2011, Robust sliding mode control for robot manipulators, *IEEE Transactions on Industrial Electronics*, **58**, 6, 2444-2453

9. ISLAM R.U., IQBAL J., KHAN Q., 2014, Design and comparison of two control strategies for multi-DOF articulated robotic arm manipulator, *Journal of Control Engineering and Applied Informatics*, **16**, 2, 28-39
10. JAMALI Y., KORAYEM M.H., HAMRAZ N.J., SOHRABI A.M., KIOMARSI M., ASADI M.A., REAZAEE S., 2005, Design and manufacturing a robot wrist: performance analysis, *International Congress on Manufacturing Engineering*, Tehran
11. KORAYEM M.H., HAGHIGHI R., NIKOUBIN A., ALAMDARI A., KORAYEM A.H., 2009, Determining maximum load carrying capacity of flexible link manipulators, *Scientia Iranica, Transactions B: Mechanical Engineering*, **16**, 5, 440-450
12. KORAYEM M.H., IRANI M., NEKOO S.R., 2010, Analysis of manipulators using SDRE: A closed loop nonlinear optimal control approach, *Scientia Iranica, Transaction B: Mechanical Engineering*, **17**, 6, 456-467
13. KORAYEM M.H., NEKOO S.R., ABDOLLAHI F., 2013, Hardware implementation of a closed loop controller on 6R robot using ARM microcontroller, *International Research Journal of Applied and Basic Sciences*, **4**, 8, 2147-2158
14. KORAYEM M.H., KHADEMI A., NEKOO S.R., 2014, A comparative study on SMC, OSMC and SDRE for robot control, *IEEE Second RSI/ISM International Conference on Robotics and Mechatronics (ICRoM)*, Tehran, Iran, 013-018
15. SEFRITI S., BOUMHIDI J., NAOUAL R., BOUMHIDI I., 2012, Adaptive neural network sliding mode control for electrically-driven robot manipulators, *Journal of Control Engineering and Applied Informatics*, **14**, 4, 27-32
16. SHI J., LIU H., BAJCINCA N., 2008, Robust control of robotic manipulators based on integral sliding mode, *International Journal of Control*, **81**, 10, 1537-1548
17. SLOTINE J.J.E., LI W., 1991, *Applied Nonlinear Control*, Vol. 60, Englewood Cliffs, NJ: Prentice-Hall
18. THANGAVELUSAMY D., PONNUSAMY L., 2013, Elimination of chattering using fuzzy sliding mode controller for drum boiler turbine System, *Journal of Control Engineering and Applied Informatics*, **15**, 2, 78-85
19. VEGA V.P., ARIMOTO S., LIU Y.H., HIRZINGER G., AKELLA P., 2003, Dynamic sliding PID control for tracking of robot manipulators: theory and experiments, *IEEE Transactions on Robotics and Automation*, **19**, 6, 967-976

DYNAMIC RESPONSE OF LADDER TRACK RESTED ON STOCHASTIC FOUNDATION UNDER OSCILLATING MOVING LOAD

SAEED MOHAMMADZADEH, MOHAMMAD MEHRALI

School of Railway engineering, Iran University of Science and Technology, Tehran, Iran

e-mail: mohammadz@iust.ac.ir; m_mehrali@rail.iust.ac.ir

The ladder track is a new type of an elastically supported vibration-reduction track system that has been applied to several urban railways. This paper is devoted to the investigation of dynamic behavior of a ladder track under an oscillating moving load. The track is represented by an infinite Timoshenko beam supported by a random elastic foundation. In this regard, equations of motion for the ladder track are developed in a moving frame of reference. In continuation, by employing perturbation theory and contour integration, the response of the ladder track is obtained analytically and its results are verified using the stochastic finite element method. Finally, using the verified model, a series of sensitivity analyses are accomplished on effecting parameters including velocity and load frequency.

Keywords: ladder track, moving load, stochastic stiffness, perturbation theory

1. Introduction

In the 1940s to 1960s, weakness caused by resistance to lateral movement of cross-ties prompted studies on longitudinal sleepers laid in parallel pairs under the rails. The aim was to produce a railway track requiring a minimum of maintenance. Ladder sleepers were subsequently developed having parallel longitudinal concrete beams held together by transverse steel pipes (Wakui *et al.*, 1997). Ladder sleepers provide continuous support to the rails assuring train safety, decreasing maintenance and promising an increase in railway efficiency.

In recent years, a floating ladder track (Fig. 1a) has been developed to decrease vibration in a structure and withstand noise. Younesian *et al.* (2006) studied the dynamic performance of a ballasted ladder track. The rail and ladder units were simulated using a Timoshenko beam and the governing equations were solved using the Galerkin method. Figure 1b shows the ballasted ladder track.

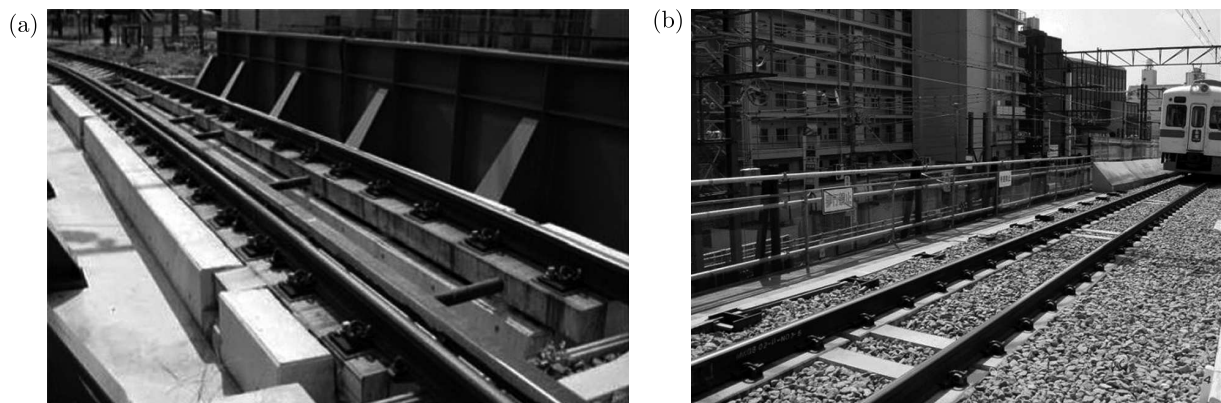


Fig. 1. (a) Floating ladder track; (b) ballasted ladder track

Hosking and Millinazzo (2007) developed a mathematical method for a floating ladder track under a moving oscillating load in which the track was simulated using an Euler-Bernoulli beam on periodic discrete elastic supports. They were able to predict the frequency and critical speed for design purposes. Xia *et al.* (2009) dynamically simulated an elevated bridge with a ladder track under a moving train and measured its dynamic response. Xia *et al.* (2010) carried out a field experiment at the trial section of an elevated bridge on Beijing Metro line where the ladder track was installed and investigated the vibration reduction characteristics of the track.

Yan *et al.* (2014) developed dynamic models of the vehicle and the ladder track to analyze the track vibration behavior. They optimized the mechanical properties of the ladder track to reduce or eliminate the track vibrations at the corrugation frequency and ultimately to reduce the chance of rail corrugation. Ma *et al.* (2016) investigated the effect of ballasted ladder tracks and the vibration reduction effect. The results show that the ballasted ladder track can effectively decrease the peak value in the time domain and has the potential effect to control environmental vibration in low frequencies.

Analysis of beams subjected to moving loads is of substantial practical importance. Many researchers have studied the vibration of beams subjected to various types of moving loads. Since parameters such as loading, rail deflection and nature of the substructure are stochastic, the dynamic response of the track is assumed to be stochastic. Table 1 lists the major studies in this area. Thus far, no study has been carried out on ladder tracks using a stochastic approach.

Table 1. Major research on stochastic approach in railway engineering

Author(s)	Subject	Loading	Year
Fryba <i>et al.</i>	Euler-Bernoulli beam resting on a Winkler random foundation	Harmonic moving load	1993
Anderson and Nielsen	Beam on a random modified Kelvin foundation	Moving vehicle	2003
Kargarnovin <i>et al.</i>	Infinite Timoshenko beams supported by nonlinear foundations	Harmonic moving loads	2005
Younesian <i>et al.</i>	Timoshenko beam on a random foundation under	Harmonic moving load	2005
Younesian and Kargarnovin	Infinite Timoshenko beam supported by a random Pasternak foundation	Harmonic moving loads	2009
Mohammadzadeh and Ghahremani	Risk of derailment using a numerical method	Railway vehicle	2010
Mohammadzadeh <i>et al.</i>	Probability of derailment where irregularity of the track is random	Railway vehicle	2011
Mohammadzadeh <i>et al.</i>	Double Euler-Bernoulli beam resting on a random foundation	Harmonic moving loads	2013
Mehrali <i>et al.</i>	Double Euler-Bernoulli beam resting on a random foundation	Railway vehicle	2014
Mohammadzadeh <i>et al.</i>	Reliability analysis of the rail fastening where load and velocity are random	Moving train	2014
Pouryousef and Mohammadzadeh	Reliability evaluation of design codes applied for railway bridges	Live load (LM71)	2014

Engineering experience has revealed that uncertainties occur in the assessment of loading as well as in the material and geometric properties of engineering systems. The logical behavior of these uncertainties in probability theory and statistics cannot be obtained accurately using the deterministic method. This approach is based on extremes (minimum, maximum) and mean

values of system parameters (Stefanou, 2009). More detail on the random behavior of a structure can be found in Lutes and Sarkani (2004).

The Taylor series expansion of the stochastic finite element matrix of a physical system is known in the literature as the perturbation method. This method is used to solve probabilistic problems (Kleiber and Hein, 1992; Liu *et al.*, 1986). Another method is the Karhunen-Loeve expansion technique (Ghanem and Spanos, 1991a,b). The main initiative of the perturbation method is to formulate an analytical expansion of an input parameter around its mean value using a series representation (Jeulin and Ostoja-Starzewski, 2001; Nayfeh and Mook 1979).

A novel analytical method is presented for the analysis of the governing equations of motion for an infinite Timoshenko ladder track on a viscoelastic foundation with random stiffness under a harmonic moving load. For the stationary analysis of the response of the beam to variations in stiffness in the support, it is useful to describe it in a local moving coordinate system subjected to a harmonic moving load. Furthermore, by applying the perturbation method and complex Fourier transformation, the mean and variance of the response of the beam can be calculated analytically in an integral form. Sensitivity analysis is run using the residue theorem and key parameters are introduced.

2. Theory

Assume a harmonic load moves uniformly along a ladder track at velocity v . The ladder track is modeled using two parallel Timoshenko beams. The connection of the two beams is described using a series of springs and dashpots. In addition, the lower beam rests on a viscoelastic foundation. The vertical stiffness of the support is described by a stochastic variable along the beam with a mean of \bar{k} and a stochastic component of $k_s(x)$ (Mohammadzadeh *et al.*, 2013). Here, $\kappa(x)$ is a random stationary ergodic function with zero mean value and ϕ is a small constant parameter

$$k_B(x) = \bar{k} + \phi\kappa(x) = \bar{k} + k_s(x) \quad (2.1)$$

2.1. Equation of motion

The equations of motion for the rail and ladder units are

$$\begin{aligned} \rho_1 A_1 \frac{\partial^2 w_1}{\partial t^2} + k_1 A_1 G_1 \left(\frac{\partial \psi_1}{\partial x} - \frac{\partial^2 w_1}{\partial x^2} \right) + k_p (w_1 - w_2) + c_p \left(\frac{\partial w_1}{\partial t} - \frac{\partial w_2}{\partial t} \right) \\ = P e^{i\Omega t} \delta(x - vt) \end{aligned} \quad (2.2)$$

$$E I_1 \frac{\partial^2 \psi_1}{\partial x^2} - k_1 A_1 G_1 \left(\psi_1 - \frac{\partial w_1}{\partial x} \right) = \rho_1 I_1 \frac{\partial^2 \psi_1}{\partial t^2}$$

and

$$\begin{aligned} \rho_2 A_2 \frac{\partial^2 w_2}{\partial t^2} + k_2 A_2 G_2 \left(\frac{\partial \psi_2}{\partial x} - \frac{\partial^2 w_2}{\partial x^2} \right) + k_B w_2 - k_p (w_1 - w_2) \\ - c_p \left(\frac{\partial w_1}{\partial t} - \frac{\partial w_2}{\partial t} \right) + c_B \frac{\partial w_2}{\partial t} = 0 \end{aligned} \quad (2.3)$$

$$E I_2 \frac{\partial^2 \psi_2}{\partial x^2} - k_2 A_2 G_2 \left(\psi_2 - \frac{\partial w_2}{\partial x} \right) = \rho_2 I_2 \frac{\partial^2 \psi_2}{\partial t^2}$$

where $w_1(x, t)$ is the upper beam deflection, $w_2(x, t)$ is the lower deflection, $\delta(x)$ is the Dirac delta function, and v and Ω are the speed and frequency of the load, respectively. A , E , G , I , k and ρ are the cross-sectional areas of the beams, modulus of elasticity, shear modulus, second moment of area, sectional shear coefficient, and beam material density, respectively. Figure 2 is a flowchart of the solution of the governing equation for the ladder track.

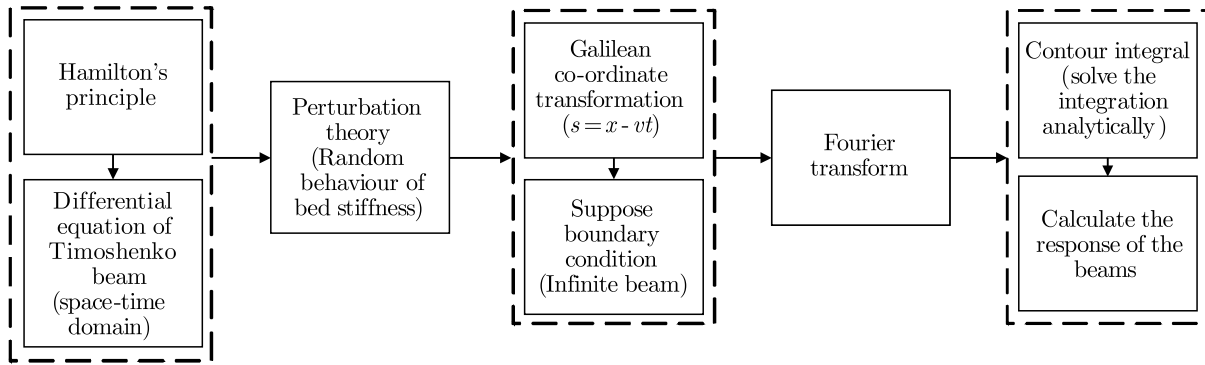


Fig. 2. Solving the governing differential equation

2.2. First-order perturbation approach

The perturbation method is proposed to compute the response of the beams to a harmonic moving load. The responses of the ladder track (rail and ladder unit) are decomposed to zero and first-order terms

$$\begin{aligned} w(x, t) &= w_0^i(x, t) + \phi w_1^i(x, t) \\ \psi(x, t) &= \psi_0^i(x, t) + \phi \psi_1^i(x, t) \end{aligned} \quad i = 1, 2 \quad (2.4)$$

where $i = 1$ for the rail and $i = 2$ for the ladder unit.

2.3. Solution

Equations (2.2) and (2.3) are solved using Eqs. (2.4) and equating terms with the same powers of ϕ . The Galilean coordinate transformation is

$$s = x - vt \quad (2.5)$$

The boundary conditions of deflection, velocity, and acceleration of the beams are assumed to be zero in positive and negative infinity. Using the state variable transformation and applying the complex Fourier transform results in

$$\begin{aligned} w_0^1(q) &= \frac{P(\beta_7 q^2 - \beta_8 q + \beta_9) D_4}{H(q)} & w_1^1(q) &= \frac{D_4 P + D_2 w_0^2}{H(q)} \\ w_0^2(q) &= \frac{P(\beta_7 q^2 - \beta_8 q + \beta_9)(-D\beta_3)}{H(q)} & w_1^2(q) &= \frac{-D_3 P - D\beta_1 w_0^2}{H(q)} \end{aligned} \quad (2.6)$$

D_1 , D_2 , D_3 and D_4 are described in Appendix 1. $H(q)$ is the determinant of the matrix

$$\mathbf{h} = \begin{bmatrix} D_1 & D_2 \\ D_3 & D_4 \end{bmatrix} \quad (2.7)$$

and ψ_0^1 , ψ_0^2 , ψ_1^1 , and ψ_1^2 are equal to

$$\begin{aligned} \psi_0^1(q) &= \frac{-\beta_3 P q D_4}{H(q)} & \psi_1^1(q) &= \frac{-\beta_3 q (P D_4 + D_2 \kappa w_0^2)}{(\beta_7 q^2 - \beta_8 q + \beta_9) H(q)} \\ \psi_0^2(q) &= \frac{\beta_{12} P q (\beta_7 q^2 - \beta_8 q + \beta_9) D_3}{(\beta_{15} q^2 - \beta_{16} q + \beta_{17}) H(q)} & \psi_1^2(q) &= \frac{\beta_{12} q (D_3 P + D_1 \kappa w_0^2)}{(\beta_{15} q^2 - \beta_{16} q + \beta_{17}) H(q)} \end{aligned} \quad (2.8)$$

General definitions for all coefficients are listed in Table 2. The response of the beams can be calculated by applying the inverse Fourier transform and using contour integrals (Mohammadzadeh *et al.*, 2014). The mean values for the beam deflection and bending moment and the covariance of a random function can be calculated as described by Mohammadzadeh *et al.* (2013) and Solnes (1997).

Table 2. Definitions of coefficients

Parameter	Definition	Parameter	Definition
β_1	$k_1 A_1 G_1 - \rho_1 A_1 v^2$	β_{10}	$k_2 A_2 G_2 - \rho_2 A_2 v^2$
β_2	$2\rho_1 A_1 \Omega v$	β_{11}	$2\rho_2 A_2 \Omega v$
β_3	$ik_1 A_1 G_1$	β_{12}	$ik_2 A_2 G_2$
β_4	$ic_p v$	β_{13}	$ic_B v$
β_5	$-\rho_1 A_1 \Omega^2 + k_p - ic_p \Omega$	β_{14}	$-\rho_2 A_2 \Omega^2 + \bar{k} + k_p + ic_p \Omega + ic_B \Omega$
β_6	$k_p + ic_p \Omega$	β_{15}	$\rho_2 I_2 v^2 - EI_2$
β_7	$\rho_1 I_1 v^2 - EI_1$	β_{16}	$2\rho_2 I_2 \Omega v$
β_8	$2\rho_1 I_1 \Omega v$	β_{17}	$\rho_2 I_2 \Omega^2 - k_2 A_2 G_2$
β_9	$\rho_1 I_1 \Omega^2 - k_1 A_1 G_1$	β_{18}	$k_p + ic_p \Omega$

3. Model validation of ladder track

The stochastic simulation of the ladder track foundation has been validated as described below.

3.1. Validation using the stochastic finite element method

The response of a beam resting on a stochastic foundation is obtained using the stochastic finite element method (SFEM) as suggested by Fryba *et al.* (1993). Consider the second beam as a rigid component and evaluate the behavior of the upper beam assuming stochastic behavior for the foundation. Then, the random behavior of the system is calculated and validated using the results of Fryba *et al.* (1993). Figure 3 shows that the results calculated in current study are in good agreement with those reported by Fryba *et al.* (1993).

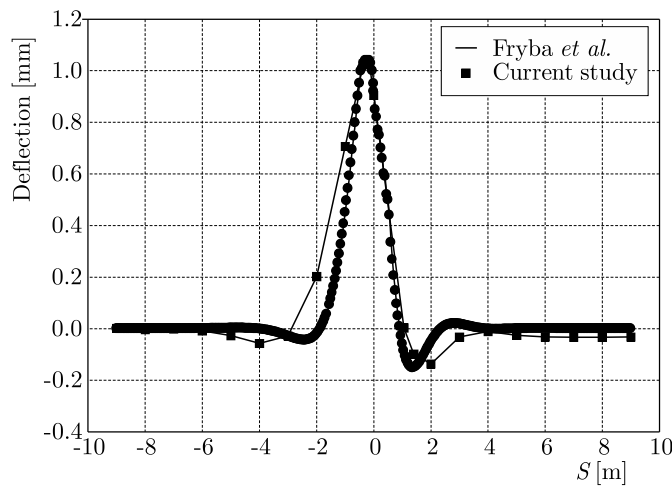


Fig. 3. Comparison between the current modeling and results by Fryba *et al.* (1993)

3.2. Validation by a deterministic model

Next, the deterministic behavior of the ladder track is verified using the results of Younesian *et al.* (2006). They investigated the dynamic behavior of a ladder track of finite length. The ladder track is simulated using a Timoshenko beam and the track is subjected to a moving load. The results of verification are illustrated in Table 3. The results of the current study are in good agreement with those reported by Younesian *et al.* (2006).

Table 3. Comparison of the current study and results by Younesian *et al.* (2006)

S [m]	Current study	Younesian <i>et al.</i>
-8	-4.13E-09	7.86E-05
-6	5.87E-08	-1.7E-05
-4	-3.11E-07	-0.00017
-2	-1.7E-05	-0.00031
0	-0.00083	-0.00037
2	-3E-05	-0.00032
4	1.06E-06	-0.00015
6	-3.24E-08	7.61E-05
8	7.16E-10	0.00018

4. Response of the ladder track

The response of the simulated ladder track is next investigated under a harmonic moving load. The railway substructure should be constructed and confirmed using adequate ground stiffness and standards (Younesian *et al.*, 2005). It is not possible to provide a track bed with absolutely uniform specifications, and there are many factors that influence the subgrade (Phoon, 2008; Griffiths and Fenton, 2007; Fenton and Griffiths, 2008; Baecher and Chrsitian, 2003). The finite distance correlation can be assumed using bed stiffness as a random field. A parametric study was done on the key parameters of solution derived using the track bed stiffness from the field data by Berggren (2009). The physical and geometrical properties of the track are listed in Table 4.

Table 4. Parameters used in the model

Rail		Ladder	
Parameters	Value	Parameters	Value
Young's modulus E_1	210 GPa	Young's modulus E_2	28.2 GPa
Shear modulus G_1	77 GPa	Shear modulus G_2	11.75 GPa
Mass density ρ_1	7850 kg/m ³	Mass density ρ_2	3954.7 kg/m ³
Cross-sectional area A_1	$7.69 \cdot 10^{-3}$ m ²	Cross sectional area A_2	$31 \cdot 10^{-3}$ m ²
Second moment of inertia I_1	$30.55 \cdot 10^{-6}$ m ⁴	Second moment of inertia I_2	$98.3 \cdot 10^{-6}$ m ⁴
Shear coefficient k_1	0.4	Shear coefficient k_2	0.43
Rail pad		Foundation	
Parameters	Value	Parameters	Value
Stiffness k_p	$40 \cdot 10^6$ Nm ⁻²	Mean value of stiffness k_B	$50 \cdot 10^6$ Nm ⁻²
Viscous damping c_p	$6.3 \cdot 10^3$ Nm ⁻²	Variance of stiffness $\sigma_{k_B}^2$	$4.4186 \cdot 10^{13}$ N ² m ⁻⁴
		Viscous damping c_B	$41.8 \cdot 10^3$ Nsm ⁻²

4.1. Load frequency influence

The velocity of the moving load is assumed to be 100 km/h. Figure 4 shows that, by increasing the load frequency, the mean value and standard deviation of the response of the upper beam (rail) initially decreases and then increases. In addition, the distribution widens as the oscillations increase along the rail.

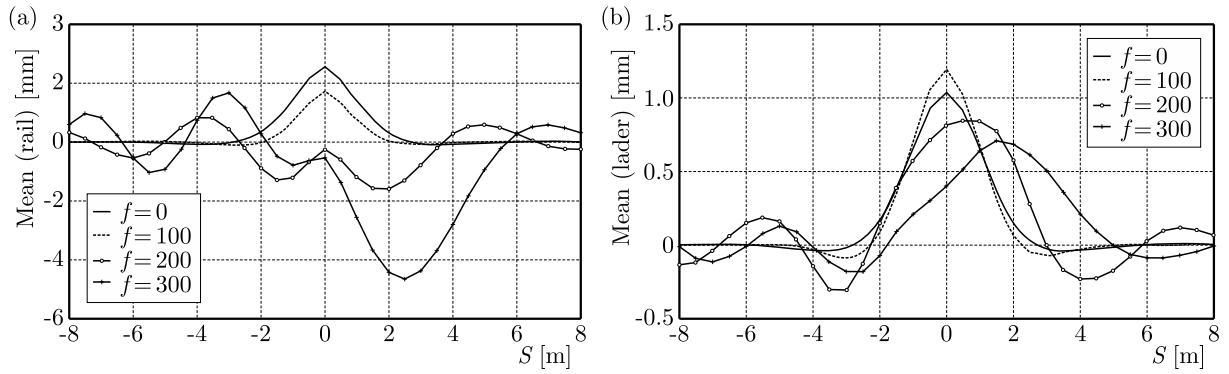


Fig. 4. Effect of load frequency on track deflection (mean value)

An increase in the load frequency decreases the response of the lower beam (ladder unit), indicating that both the mean value and standard deviation of the ladder unit show decreasing trends. Figure 5 shows the wider distribution with the increase in fluctuations along the beam.

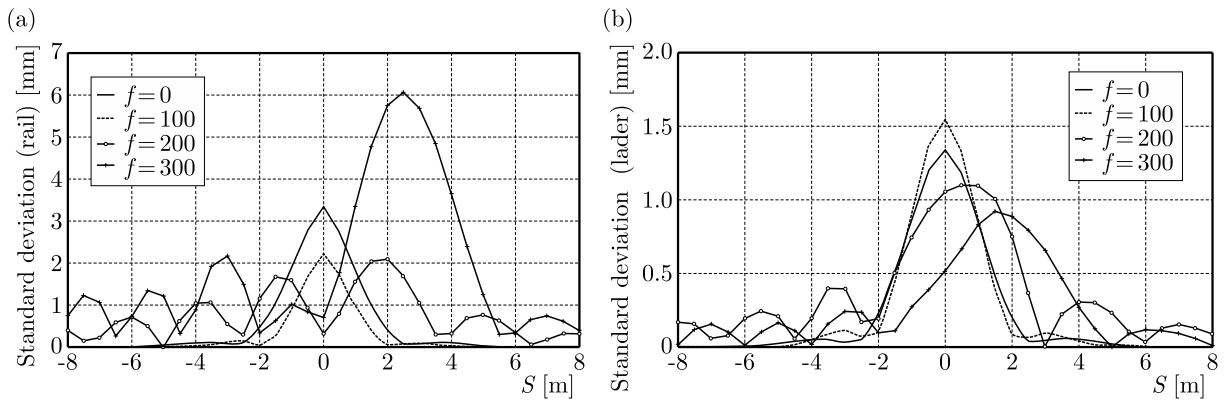


Fig. 5. Effect of load frequency on track deflection (standard deviation)

Figures 6 and 7 show the mean value and standard deviation of the rail and ladder bending moments, respectively. As the load frequency increases, the response of the rail first decreases and then increases. The velocity of the moving load is assumed to be 100 km/h.

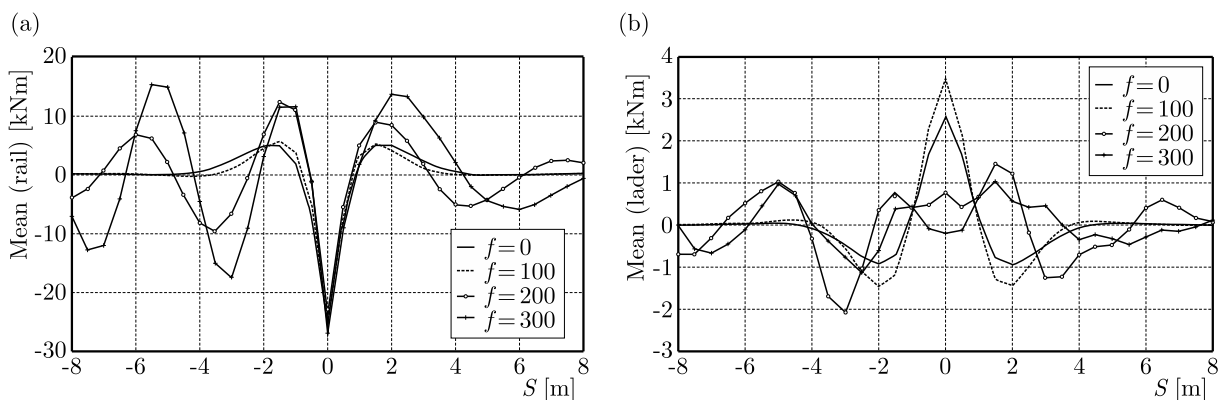


Fig. 6. Effect of load frequency on track bending moment (mean value)

The mean value and standard deviation of the ladder unit decreased as the load frequency increased. As shown, the fluctuation of the ladder first increased and then decreased.

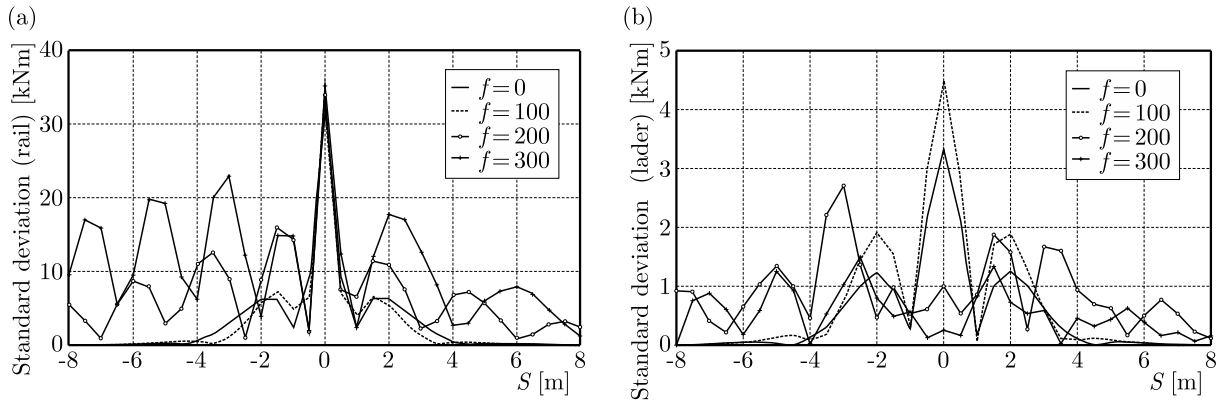


Fig. 7. Effect of load frequency on track bending moment (standard deviation)

4.2. Load velocity influence

The variation in load velocity versus the behavior of the double beam is shown in Figs. 8 and 9 for the response of the ladder track. The figures include the deflection and bending moment of both beams. As shown, the maximum response of the rail versus loading frequency have been attained and employed as design criteria. An increase in the velocity of the moving load decreased the value of this frequency.

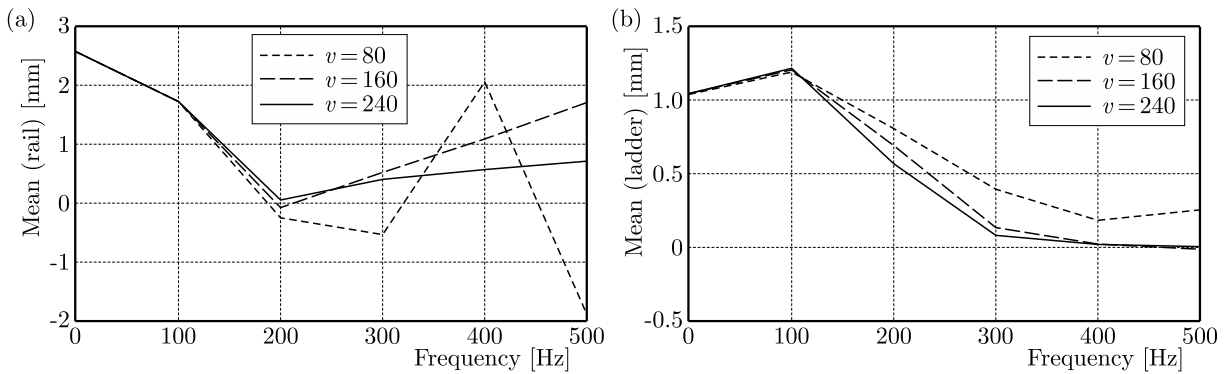


Fig. 8. Effect of velocity on the ladder track (mean value)

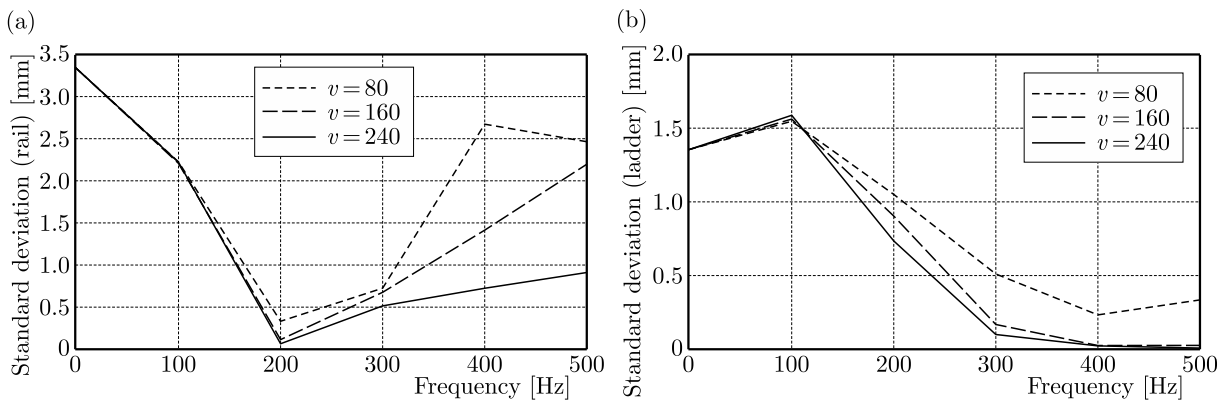


Fig. 9. Effect of velocity on the ladder track (standard deviation)

4.3. Effect of the coefficient of variation of bed stiffness

The coefficient of variation (C_V) of the stiffness of the bed is varied to assess its effect on the track bed (Figs. 10 and 11). It can be observed that increasing the C_V increases the standard deviation of the rail and ladder.

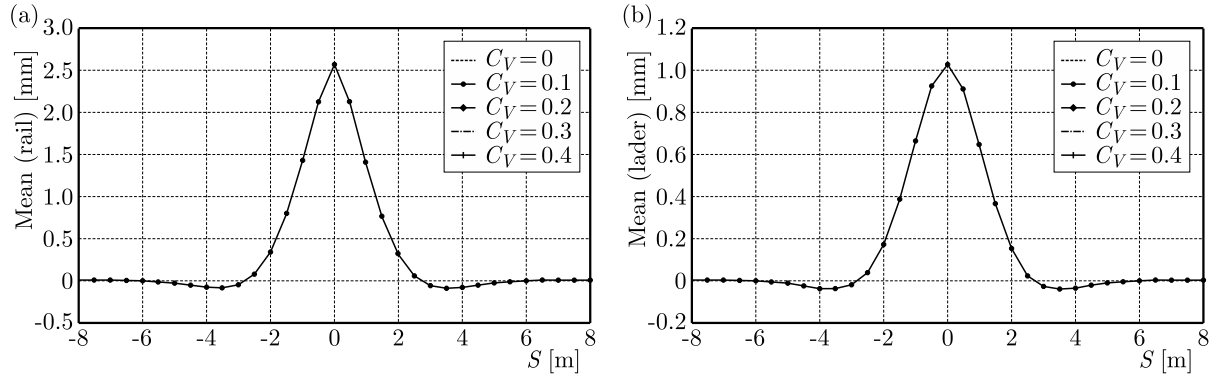


Fig. 10. Effect of C_V on the ladder track (mean value)

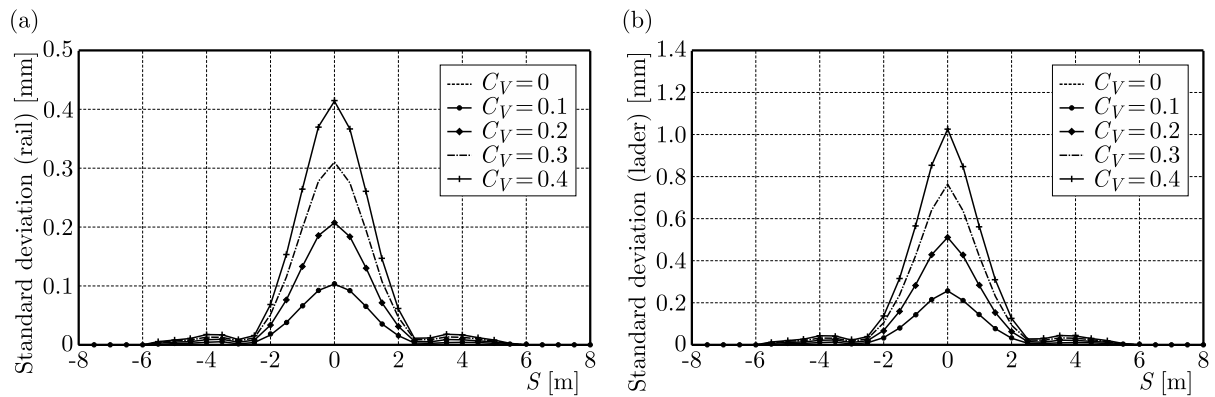


Fig. 11. Effect of C_V on the ladder track (standard deviation)

5. Conclusion

The dynamic behavior of the ladder track has been investigated in the present study. The ladder track has been simulated using an analytical model with a double Timoshenko beam. The upper beam simulated the rail and the lower beam simulated the ladder unit. A series of springs and dashpots represent the rail pad and foundation. The foundation stiffness of the system has been assumed to exhibit stochastic behavior as simulated by field tests. The first-order perturbation method has been applied and the responses, including the deflection and bending moment, are shown in form of the mean value and standard deviation. It has been found that increasing the load frequency decreased and then increased the response of the track. The peak frequency is the point at which all responses are at maximum value. It was found that the peak frequency increases as the velocity of the load velocity increases.

Appendix 1

The parameters in Equations (2.6) and (2.8) are described below

$$D_1 = \beta_1\beta_7q^4 + (-\beta_1\beta_8 + \beta_2\beta_7 - \beta_4\beta_7)q^3 + (\beta_1\beta_9 - \beta_2\beta_8 - \beta_3^2 + \beta_4\beta_8 + \beta_5\beta_7)q^2 + (\beta_2\beta_9 - \beta_4\beta_9 - \beta_5\beta_8)q + \beta_5\beta_9$$

$$\begin{aligned}
D_2 &= \beta_4\beta_7q^3 - (\beta_4\beta_8 + \beta_6\beta_7)q^2 + (\beta_6\beta_8 + \beta_4\beta_9)q - \beta_6\beta_9 \\
D_3 &= \beta_4\beta_{15}q^3 - (\beta_4\beta_{16} + \beta_{15}\beta_{18})q^2 + (\beta_4\beta_{17} + \beta_{16}\beta_{18})q - \beta_{17}\beta_{18} \\
D_4 &= \beta_{10}\beta_{15}q^4 + (-\beta_{10}\beta_{16} + \beta_{11}\beta_{15} - \beta_4\beta_{15} - \beta_{13}\beta_{15})q^3 + (\beta_{10}\beta_{17} - \beta_{11}\beta_{16} - \beta_{12}^2 \\
&\quad + \beta_4\beta_{16} + \beta_{13}\beta_{16} + \beta_{14}\beta_{15})q^2 + (\beta_{11}\beta_{17} - \beta_4\beta_{17} - \beta_{13}\beta_{17} - \beta_{14}\beta_{16})q + \beta_{14}\beta_{17}
\end{aligned}$$

References

1. ANDERSEN L., NIELSEN S.R.K., 2003, Vibrations of a track caused by variation of the foundation stiffness, *Probabilistic Engineering Mechanics*, **18**, 171-184
2. BAECHER G.B., CHRISITIAN J.T., 2003, *Reliability and Statistics in Geotechnical Engineering*, John Wiley & Sons Inc., West Sussex
3. BERGGREN E., 2009, Railway Track Stiffness Dynamic Measurements and Evaluation for Efficient Maintenance, Doctoral Thesis, Royal Institute of Technology (KTH), Aeronautical and Vehicle Engineering, Div. of Rail Vehicles
4. FENTON G.A., GRIFFITHS D.V., 2008, *Risk Assessment in Geotechnical Engineering*, John Wiley & Sons Inc., New Jersey, USA
5. FRYBA L., NAKAGIRI S., YOSHIKAWA N., 1993, Stochastic finite elements for a beam on a random foundation with uncertain damping under a moving force, *Journal of Sound and Vibration*, **163**, 31-45
6. GHANEM R.G., SPANOS P.D., 1991a, Spectral techniques for stochastic finite elements, *Archives of Computer Methods in Engineering*, **4**, 1
7. GHANEM R.G., SPANOS P.D., 1991, *Stochastic Finite Elements: A Spectral Approach*, Springer-Verlag, Berlin
8. GRIFFITHS D.V., FENTON G.A., 2007, *Probabilistic Methods in Geotechnical Engineering*, Spring Wien New York
9. HOSKING R.J., MILINAZZO F., 2007, Floating ladder track response to a steadily moving load, *Mathematical Methods in the Applied Sciences*, **30**, 1823-1841
10. JEULIN D., OSTOJA-STARZEWSKI M. (EDS), 2001, *Mechanics of Random and Multiscale Structures*, CISM Courses and Lectures, Vol. 430, Springer-Verlag, New York, USA
11. KARGARNOVIN M.H., YOUNESIAN D., THOMPSON D.J., JONES C.J.C., 2005, Response of beams on nonlinear viscoelastic foundations to harmonic moving loads, *Computers and Structures*, **83**, 1865-1877
12. KLEIBER M., HIEN T.D., 1992, *The Stochastic Finite Element Method*, John Wiley & Sons, New York, USA
13. LIU W.K., BELYTSCHKO T., MANI A., 1986, Random field finite elements, *International Journal for Numerical Methods in Engineering*, **23**, 1831-1845
14. LUTES L.D., SARKANI S., 2004, *Random Vibrations-Analysis of Structural and Mechanical Systems*, Elsevier Inc, USA
15. MA M., LIU W., LI Y., KIU W., 2016, An experimental study of vibration reduction of a ballasted ladder track, *Journal of Rail and Rapid Transit*, DOI: 10.1177/0954409716642488
16. MEHRALI M., MOHAMMADZADEH S., ESMAEILI M., NOURI M., 2014, Investigating on vehicle-slab track interaction considering random track bed stiffness, *International Journal of Science and Technology, Transaction A, Civil Engineering*, **21**, 1, 82-90
17. MOHAMMADZADEH S., AHADI S., NOURI M., 2014, Stress-based fatigue reliability analysis of the rail fastening spring clip under traffic loads, *Latin American Journal of Solids and Structures*, **11**, 993-1011

18. MOHAMMADZADEH S., ESMAEILI M., MEHRALI M., 2013, Dynamic response of double beam rested on stochastic foundation under harmonic moving load, *International Journal for Numerical and Analytical Methods in Geomechanics*, DOI: 10.1002/nag.2227
19. MOHAMMADZADEH S., GHAREMANI S., 2010, Estimation of train derailment probability using rail profile alterations, *Structure and Infrastructure Engineering*, **8**, 1034-1053
20. MOHAMMADZADEH S., SANGTARASHHA M., MOLATEFI H., 2011, A novel method to estimate derailment probability due to track geometric irregularities using reliability techniques and advanced simulation methods, *Archive of Applied Mechanics*, **81**, 1621-1637
21. NAYFEH A., MOOK H.D., 1979, *Nonlinear Oscillations*, Wiley, New York, USA
22. OKUDA H., ASANUMA K., MATSUMOTO K., WAKUI H., 2003, Environmental performance improvement of railway structural system, In IABSE Symposium Report-Antwerp, Structure for high speed railway transportation, *International Association for Bridge and Structural Engineering*, **87**, 242-243
23. PHOON K.K., 2008, *Reliability-Based Design in Geotechnical Engineering-Computations and Applications*, Taylor & Francis Group, New York
24. POURYOUSEF A., MOHAMMADZADEH S., 2014, A simplified probabilistic method for reliability evaluation of design codes; Applied for railway bridges designed by Euro code, *Advances in Structural Engineering*, **17**, 1, 97-112
25. SOLNES J., 1997, *Stochastic Processes and Random Vibration*, Wiley, New York, USA
26. STEFANOU G., 2009, The stochastic finite element method, past, present and future, *Computer Method in Applied Mechanics and Engineering*, **198**, 1031-1051
27. UIC, 2008, Vertical elasticity of ballastless track, ETF publication
28. WAKUI H., MATSUMOTO N., INOUE H., 1997, Technological innovation in railway structure system with ladder type track system, *Proceedings of WCRR97*, Florence, Italy
29. XIA H., DENG Y., ZOU Y., ROECK G.D., DEGRANDE G., 2009, Dynamic analysis of rail transit elevated bridge with ladder track, *Frontiers of Architecture and Civil Engineering in China*, **3**, 1, 2-8
30. XIA H., CHEN J.G., XIA C.Y., INOUE H., ZENDA Y., QI L., 2010, An experimental study of train-induced structural and environmental vibrations of a rail transit elevated bridge with ladder tracks, *Journal of Rail and Rapid Transit*, **224**, 3, 115-124
31. YAN Z., MARKINE V., GU A., LIANG Q., 2014, Optimisation of the dynamic properties of ladder track to minimise the chance of rail corrugation, *Journal of Rail and Rapid Transit*, **228**, 3, 285-297
32. YOUNESIAN D., KARGARNOVIN M.H., 2009, Response of the beams on random Pasternak foundation subjected to harmonic moving loads, *Journal of Mechanical Science and Technology*, **23**, 3013-3023
33. YOUNESIAN D., KARGARNOVIN M.H., THOMPSON D.J., JONES C.J.C., 2005, Parametrically excited vibration of a timoshenko beam on random viscoelastic foundation subjected to a harmonic moving load, *Journal of Nonlinear Dynamics*, **45**, 75-93
34. YOUNESIAN D., MOHAMMADZADEH S., ESMAILZADEH E., 2006, Dynamic performance, system identification and sensitivity analysis of the ladder track, *7th World Congress on Railway Research*, Montreal, Canada

NUMERICAL LOSS ANALYSIS ON SLOT-TYPE CASING TREATMENT IN A TRANSONIC COMPRESSOR STAGE

MING-MIN ZHU, XIAO-QING QIANG, JIN-FANG TENG

School of Aeronautics and Astronautics, Shanghai Jiao Tong University, Shanghai, China

e-mail: jackzhushen@sjtu.edu.cn

To understand the loss mechanism of slot-type casing treatment, a numerical loss analysis has been carried out in a 1.5 axial transonic compressor stage with various slots. Spanwise and streamwise distribution curves of pitch-averaged entropy have been presented to survey the development of loss generation. Further, detailed entropy distributions at eight axial cuts, which have been taken through the blade row and slots, have been further analyzed to interpret the loss mechanism. The most dramatic loss growth occurred above 95% span, which directly resulted from slots injection flow upstream the leading edge. Loss generations with smooth casing have been primarily ascribed to low-momentum tip leakage flow/vortex and suction surface separation at the leading edge. CU0 slot, the arc-curved slots with 50% rotor tip exposure, has been capable of suppressing the suction surface separation loss. Meanwhile, accelerated tip leakage flow brought about additional loss near the casing and pressure surface. Upstream high entropy flow would be absorbed into the rear portion of slots repeatedly, which resulted in further loss.

Keywords: axial compressor, numerical simulation, slot-type casing treatment, loss mechanism, tip leakage flow

Nomenclature

SC/CT	–	smooth casing/casing treatment
AX, BE, CU	–	axial, bend, arc-curve skewed slot, respectively
$c_{x,tip}$	–	rotor tip axial chord
LE/TE	–	leading edge/trailing edge
G	–	mass flow, [kg/s]
π^*	–	total pressure ratio, [-]
η^*	–	isentropic efficiency, [-]
SCPE	–	peak efficiency point with smooth casing
SCNS	–	near stall point with smooth casing
SM	–	stall margin
Eff	–	isentropic efficiency
SS/PS	–	suction surface/pressure surface
ΔS	–	entropy increase relative to incoming flow, [J/(kg·K)]
$\Delta S_{ref,sc}$	–	the reference entropy value, [J/(kg·K)]
\overline{G}_{slot}	–	normalized mass flow through slot opening surface, [-]

1. Introduction

The axial slot is a preferable configuration of casing treatment with favorable ability of enhancing the compressor operating range. Although the effect of casing treatment has a strong correlation with a specific compressor type and a flow field pattern, a rationally designed slot-type

configuration always achieves higher stall margin improvement than a circumferential groove, ranging from 10% to 20% (Moore *et al.*, 1971; Takata and Tsukuda, 1977). However, slot casing treatment also results in a much higher efficiency loss. According to the research work by Fujita and Takata (1984), a certain amount of loss in efficiency is inevitable in order to obtain desirable stall margin improvement. Particularly superior configuration does not exist.

Increasing performance requirements for aero engine demands less efficiency loss. Improving the stall margin with a serious drop in the efficiency is unacceptable. Researchers continue further investigations on configurations and design parameters of slot-type casing treatment to minimize the loss in efficiency. Arc-curve skewed slot (Yu *et al.*, 2002) and bend skewed slot (Zhu and Chu, 2005) have been proved to achieve favorable stability enhancement with acceptable minor loss in certain circumstances. Some configurations even slightly increase the efficiency in specific cases (Alone *et al.*, 2014; Li *et al.*, 2012; Tuo *et al.*, 2011). Researches working on design parameters presented that the efficiency loss caused by slot treatment is sensitive to slots depth, casing porosity and blade tip axial chord exposure, especially the last one. Lu *et al.* (2006) and Danner *et al.* (2009) both demonstrated that reduction in rotor exposure is conducive to minimizing the efficiency loss.

To design casing treatment with a low level loss, it is urgent to master the loss mechanism of slot treatment. Injection flow from slot casing treatment is the primary source of compressor loss (Fan *et al.*, 2008). This paper is committed to clarifying the influence of injection flow on the compressor efficiency and elaborating the tip loss mechanism. Entropy distributions are utilized to survey the loss generation development by casing treatment along spanwise and streamwise directions. Entropy distributions at several axial cuts are examined in detail to interpret the loss development procedure.

2. Descriptions of the investigated model and numerical method

2.1. Compressor stage and slot-type casing treatment

The 1.5 stage axial transonic compressor consists of variable inlet guide vanes (IGV), rotors (R1) and stators (S1). Figure 1 shows a schematic of the compressor stage. Table 1 provides an overview of the main geometric/operational parameters of this compressor stage. The mean aspect ratio of R1 blades measures 1.4 with a hub-to-tip ratio of 0.7. The solidity at the rotor tip is 1.1 and the clearance size comes to 0.3% span. The stage design total pressure ratio is 1.5. At the design rotating speed, the rotors are characterized by the inlet relative Mach number of 1.2 corresponding to a blade tip velocity of approximately 380 m/s. While at the specified speed discussed in this paper, the maximum Mach number at the rotor tip is just less than 1.0.

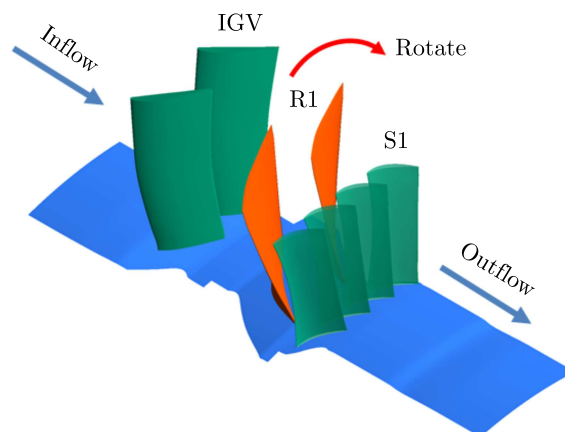
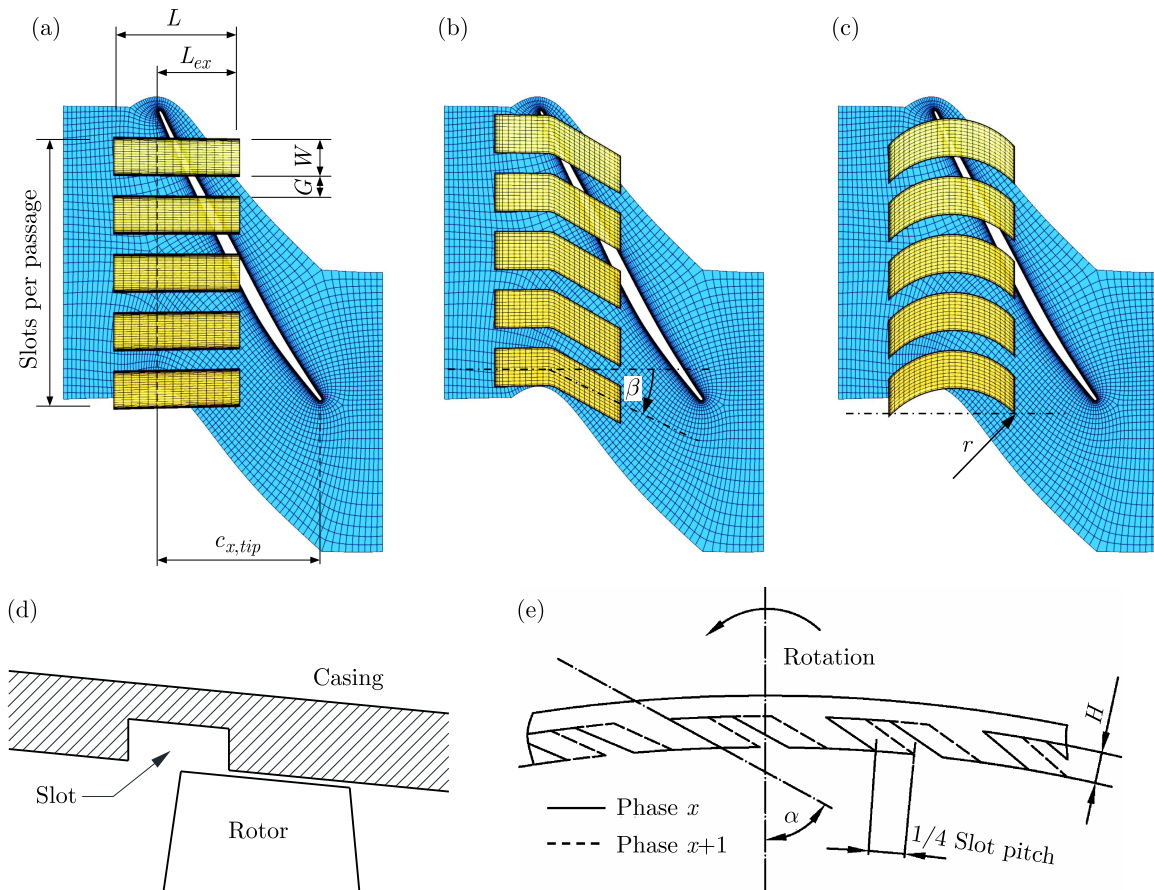


Fig. 1. Schematic of the compressor stage

Table 1. Main geometric/operational parameters of the compressor stage

Parameter [unit]	Value
Mean aspect ratio [-]	1.4
Hub-to-tip ratio [-]	0.7
Rotor solidity at tip [-]	1.1
Relative tip gap [% of blade height]	0.3
Stage design total pressure ratio [-]	1.5
Rotor tip velocity at the design speed [m/s]	380

Three slot-type casing treatments (Notated as CT) have been designed for this compressor stage. They are an axial skewed slot, bend skewed slot and arc-curve skewed slot (notated as AX, BE and CU). BE and CU slot can be treated as variants of AX slot. Three baseline slots with default design parameters are denoted as AX0, BE0 and CU0, respectively, as shown in Fig. 2.


Fig. 2. Schematics of three baseline slots

All slots start from 26% of the tip axial chord $c_{x,tip}$ upstream the leading edge (LE) in the axial direction, and its radial depth H is restricted to 21.5% $c_{x,tip}$. The slots are parallel to the rotation axis of the rotor and are inclined by 60° against a meridional plane in the direction of blade rotation, as shown in Fig. 2d. Baseline slots extend to 50% $c_{x,tip}$ downstream LE, and five slots are evenly distributed along the circumferential direction in one blade passage. Thus, the ratio of W (the slot width) to G (the gap between each slot pitch) is set to 2:1, i.e., the casing porosity Φ (the ratio of slot opening surface area to full annulus area within the slot axial extent) is 66.7%. Fundamental design parameters of the baseline slot are listed in Table 2. Specifically,

for BE slot, the first segment is designed to align with the axial direction, and the bending angle between the axial direction and the second segment β roughly equals to the blade tip stagger angle (Zhu and Chu, 2005). For CU slot, the arc chord is also aligned with the axial direction. The rotor tip exposure L_{ex} and casing porosity Φ are altered to study their influences on the casing treatment effectiveness, via upstream moving of the slot ending position and reducing the number of slots. The slots with L_{ex} of 33.3% and 25% are denoted as CU1 and CU2. On the basis of CU2, the slots with reduced Φ are named as CU3 and CU4. The design parameters of four CU slots are presented in Table 3.

Table 2. Fundamental parameters of baseline slots

Parameter [unit]	Value
Slots/blades ratio [-]	5:1
Axial length of slot L [% $c_{x,tip}$]	79
Rotor tip axial chord exposure L_{ex} [% $c_{x,tip}$]	50
Slot width W [% $c_{x,tip}$]	24
Slot width/slot gap W/G [-]	2:1
Circumferential casing porosity Φ [%]	66.7
Slot radial depth H [% $c_{x,tip}$]	21.5
Radial skewed angle α [°]	60

Table 3. Comparison of CU configurations

Notation	L_{ex} [% $c_{x,tip}$]	Slots/blades ratio [-]	Φ [%]
CU0	50	5:1	66.7
CU1	33.3	5:1	66.7
CU2	20	5:1	66.7
CU3	20	4:1	53.3
CU4	20	3:1	40

2.2. Numerical methods

Commercial CFD solver ANSYS-CFX 14.5 has been employed for 3D steady-state calculations. Three-dimensional RANS equations have been discretized with the finite volume method. The two-equation $k-\omega$ turbulence model has been used. For saving computation resources, single blade passage computation has been conducted. Block-structured grids are generated for blade passages, tip clearance region and casing treatment slots independently. The IGV, R1 and S1 grid consists of about 0.5 million cells per passage, with ATM topology, while the rotor tip clearance geometry is meshed in a simple H-type mesh with 11 cells in the radial direction to simulate tip leakage flow. The casing treatment grid consists of 18081 cells in the H-type mesh for each slot with 41 points in the axial direction and 21 points in both radial and circumferential directions. The grids are clustered at the solid wall to meet the resolution requirement of $y^+ \leq 5$.

One blade passage is calculated with a periodic boundary condition in the circumferential direction. At the IGV inlet, the flow direction is assumed to be axial. A constant total pressure of 101 325 Pa and total temperature of 288.15 K are applied. The static back pressure is imposed at conditions of radial equilibrium to vary the operating point and allow the flow field to develop unimpaird. A mixing-plane scheme is applied on IGV/R1 and R1/S1 interfaces. Since unsteady simulations are time consuming for various slots configurations, a steady frozen rotor model is applied on R1/CT interface.

The grid independence tests and numerical method validations are carried out by NASA Stage 35 (Reid and Moore, 1978), in which the loading and critical flow phenomenon at the rotor tip is similar to the investigated transonic compressor stage. Figure 3 presents the comparison of stage performance at 100% design speed with the grids number of 0.3, 0.5 and 1.0 million cells per passage. All these three predicted results agree well with the experimental data. Note that report by Reid and Moore (1978) gives the stall point of Stage 35 as 18.26 kg/s. As stated by Chima (2009), the rotor is probably in stable rotating stall at this operating point. Therefore, a steady simulation hardly reaches this point.

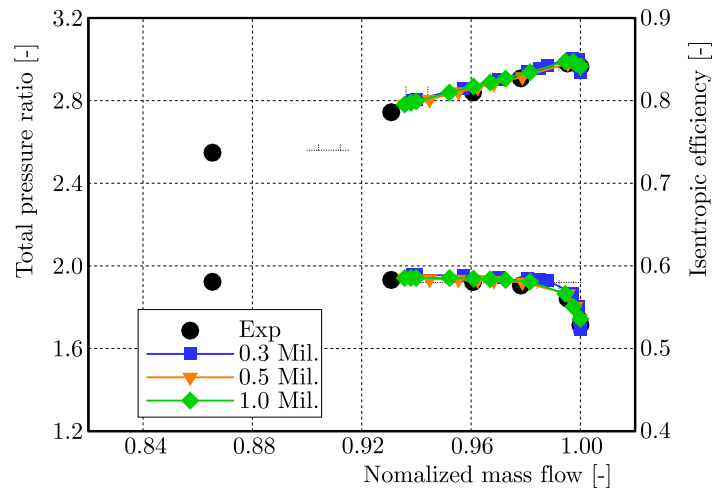


Fig. 3. Compressor maps of NASA Stage 35 (Reid and Moore, 1978) at 100% design speed

Further comparisons of flow parameters are conducted at each peak efficiency point. The total pressure and temperature profiles downstream of rotor are presented in Fig. 4. Simulated profiles of different grid sets are all consistent with the experimental ones in trends. Curves of 0.5 and 1.0 million are rather close. But the total pressure ratio value is over-estimated across the whole span, especially below 40%. While the simulated total temperature ratio profiles agree well with the experimental results. Convergence histories at the peak efficiency point are also presented in Fig. 5. RMS residuals of 0.3 and 0.5 million both descend below 10^{-6} after about 500 iterations, while 1.0 million grid set costs 800 iterations. Since 0.5 million is able to provide grid-independent and reliable solutions with much less computing resources, it is reasonable to use this grid set in this study.

3. Results and discussions

3.1. Compressor characteristics

Compressor speed lines with smooth casing (SC) and seven kinds of casing treatment (CT) are presented in Fig. 6. The total pressure ratio π^* and isentropic efficiency η^* are plotted as a function of mass flow G . π^* and η^* are normalized by each maximum value with SC, while G is normalized by SC near the choked mass flow rate. The stall margin SM is calculated as follow

$$SM = \left(\frac{\pi_{NS}^*/G_{NS}}{\pi_{PE}^*/G_{PE}} - 1 \right) \cdot 100\% \quad (3.1)$$

where subscripts PE and NS represent the peak efficiency and near stall conditions.

According to Equation (3.1), this compressor stage has a SM of 6.67% at the specified rotating speed, which needs to be improved badly. The smooth casing peak efficiency (SCPE) and near

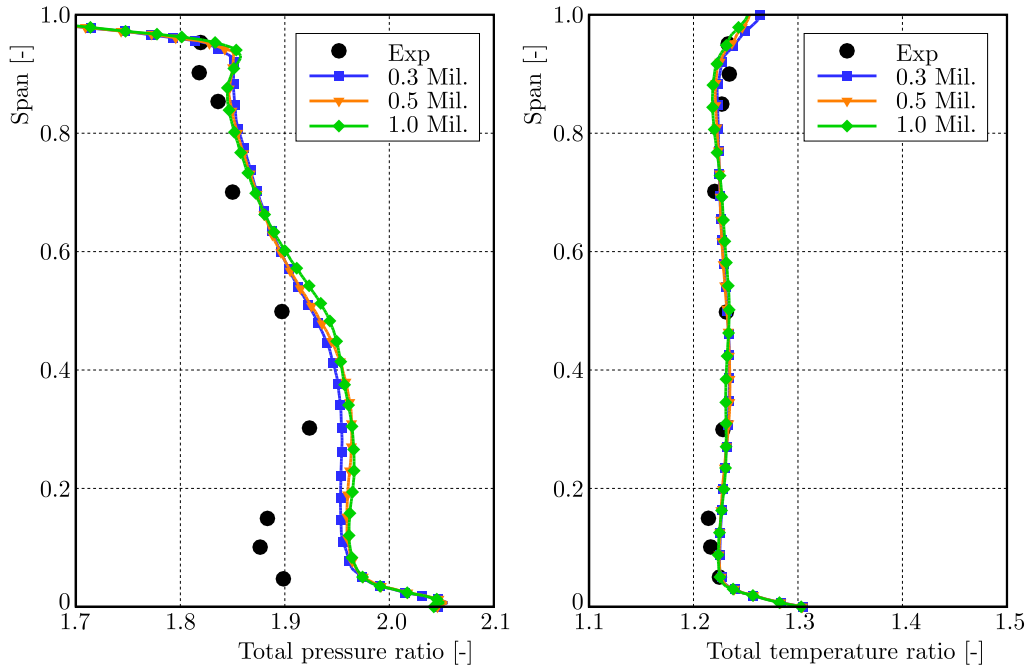


Fig. 4. Total pressure and temperature profiles downstream of Rotor 35 at the peak efficiency point

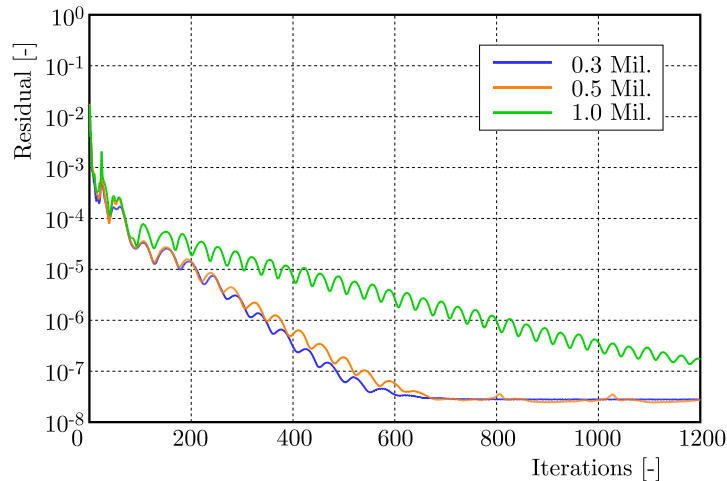


Fig. 5. Convergence histories at the peak efficiency point

stall (SCNS) points are located at 92.5% and 89.5% near the choked mass flow rate. Performance variations with various CTs at both SPCE and SCNS conditions are listed in Table 4. Steady results show that all slots with 50% L_{ex} are capable of extending SM by more than 20%, with more than a 2% peak efficiency decrease. CU0 produces smaller ΔEff compared with AX0 and BE0, along with 23% ΔSM . As L_{ex} is reduced from 50% (CU0) to 33.3% (CU1), both ΔSM and ΔEff drop significantly. Nevertheless, CU2 with 20% L_{ex} is able to provide similar ΔSM and a less efficiency drop compared with CU1. As the slot number decreases from 5 (CU2) to 3 (CU4) per passage, the operating range declines along with smaller ΔEff . Even no efficiency penalty is created by CU4 at SCNS condition.

3.2. Entropy spanwise and streamwise distributions

In this Section, pitch-averaged entropy distributions are analyzed to survey the development of loss generation with CTs. Entropy increase relative to incoming flow (ΔS) is calculated and normalized with the reference value $\Delta S_{ref,sc}$, the entropy value at 100% span with SC at SCPE condition.

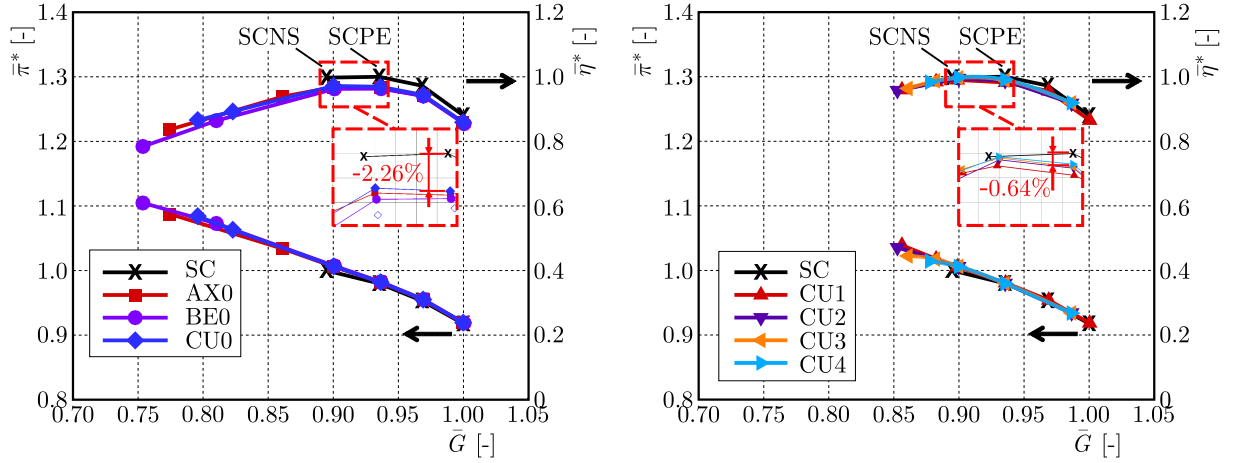


Fig. 6. Compressor maps with SC and three slot configurations

Table 4. Compressor performance variations with various CTs

Notation	ΔSM [%]	ΔEff_{SCPE} [%]	ΔEff_{SCNS} [%]
AX0	27.26	2.50	2.18
BE0	33.05	2.71	2.56
CU0	23.21	2.26	1.89
CU1	9.13	1.31	0.55
CU2	9.23	0.88	0.19
CU3	6.69	0.82	0.07
CU4	3.66	0.64	0.00

Spanwise distributions of ΔS 20% $c_{x,tip}$ downstream the trailing edge (TE) at both conditions are presented in Fig. 7. At SCPE condition, as shown in Fig. 7 (a), ΔS with SC grows gradually from 90% span. While at SCNS condition, ΔS increases from 80% span at a higher growth rate. After the installation of slots, generally, ΔS span is altered only above 80% span. AX0 brought about loss growth from 80% to 95% span at both conditions, but has little impact near the rotor tip. BE0 and CU0 both shift ΔS to a higher level at both conditions, especially at the near tip regions. However, a remarkable entropy increase is merely found below 94% span with BE0/CU0 at SCNS condition, as shown in Fig. 7b. As for CU1 to CU4 slots, intensity and extent of effects on entropy distributions both decrease. It is worth noting that all four CUs are able to reduce entropy generation from 84% to 92% span at SCNS condition.

Since CTs have different influences on entropy spanwise distributions at different spans. The axial distributions of ΔS at two typical spans are presented to interpret the loss streamwise development. The x -coordinate represents the normalized axial position, while the y -coordinate represents $\Delta S/\Delta S_{ref,sc}$. The axial range examined extends from -30% $c_{x,tip}$ upstream LE to 20% $c_{x,tip}$ downstream TE.

Figure 8 presents axial distributions of ΔS at 90% span. As shown in Fig. 8a, ΔS of SC rises gradually downstream LE at SCPE condition. While in Fig. 8b, ΔS curve shows a rapid growth downstream LE at SCNS condition. Slots of $L_{ex} = 50\%$ all raise the entropy value downstream TE at SCPE condition. The largest increase at the outlet is contributed by AX0, followed by BE0. However, a significant growth is not found within the coverage of slots, which indicates that the loss generation at this span does not directly result from the injection flow from slots. CUs with smaller extending length and slots number has little impact on ΔS distribution curves at SCPE condition. At SCNS condition, however, all slots bring down entropy curves within their extending ranges, except AX0. Only entropy value with AX0 is higher than SC case at the rotor outlet. CU0-CU4 even reduce the loss remarkably downstream TE.

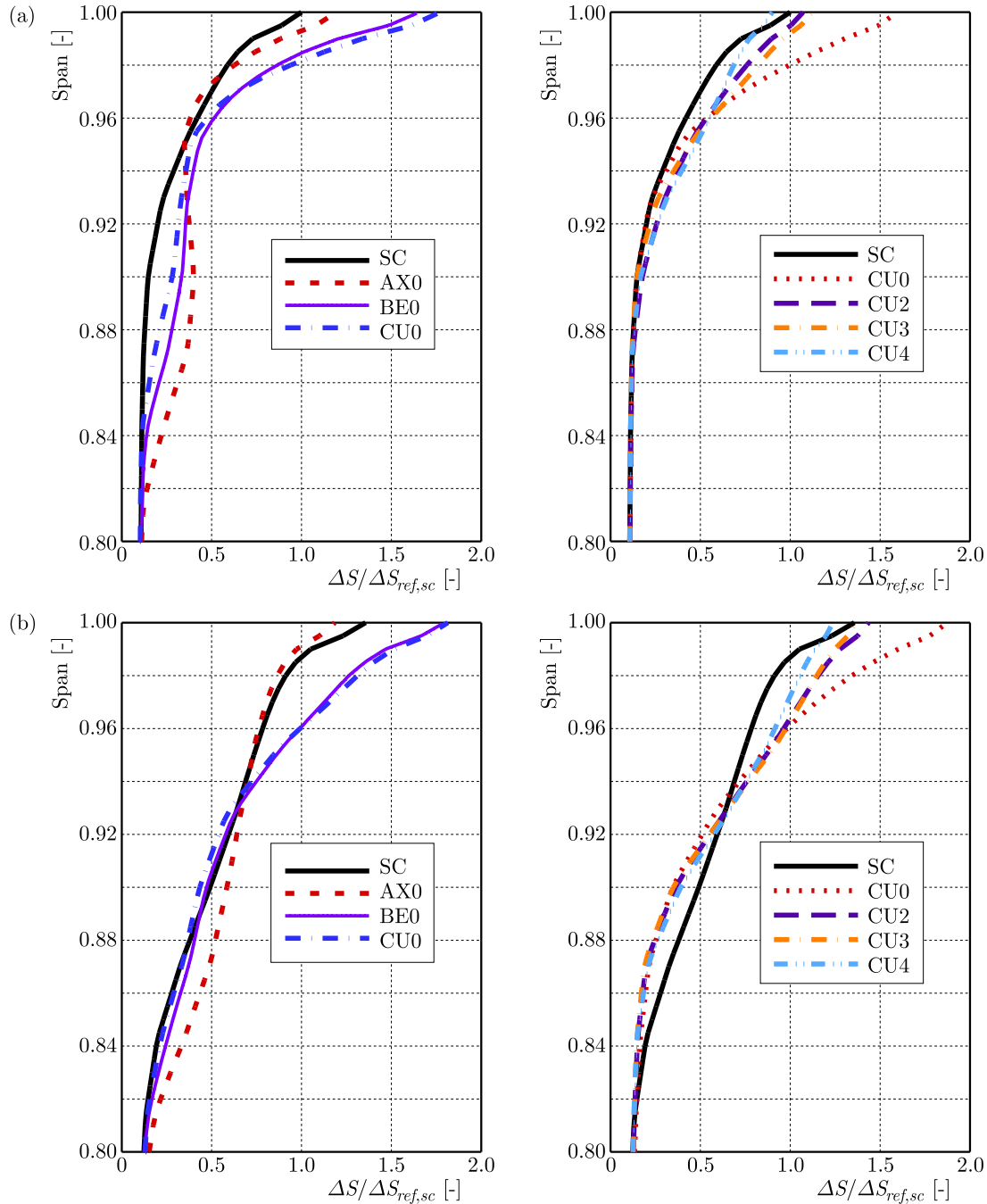


Fig. 7. Entropy distributions along the span at the rotor outlet at both conditions

Entropy streamwise distributions at 99.5% span at SCPE condition are presented in Fig. 9a. ΔS of SC initiates rising gradually from -10% $x/c_{x,tip}$ at SCPE condition. The maximum value is reached at 8% $x/c_{x,tip}$, followed by a tender decrease till 50% $x/c_{x,tip}$. After the installation of CTs, entropy begins to grow ahead of -30% $x/c_{x,tip}$. For all 7 kinds of slots, local entropy increases at the fastest rate within the range from -30% to -20% $x/c_{x,tip}$. It is indicated that the injection procedure becomes the primary source of loss generation at 99.5% span. CU0 reaches the its peak ΔS value at about 15% $x/c_{x,tip}$. Being consistent with thhe spanwise distributions in Fig. 7a, entropy value of CU0 occupies the first place downstream TE; BE0 comes the second.

At SCNS condition, as shown in Fig. 9b, ΔS with SC starts to rise sharply from -15% and reaches the peak value upstream LE. It results from forward motion of the interface between the incoming flow and the tip leakage flow. ΔS distributions with slots of $L_{ex} = 50\%$ vary slightly

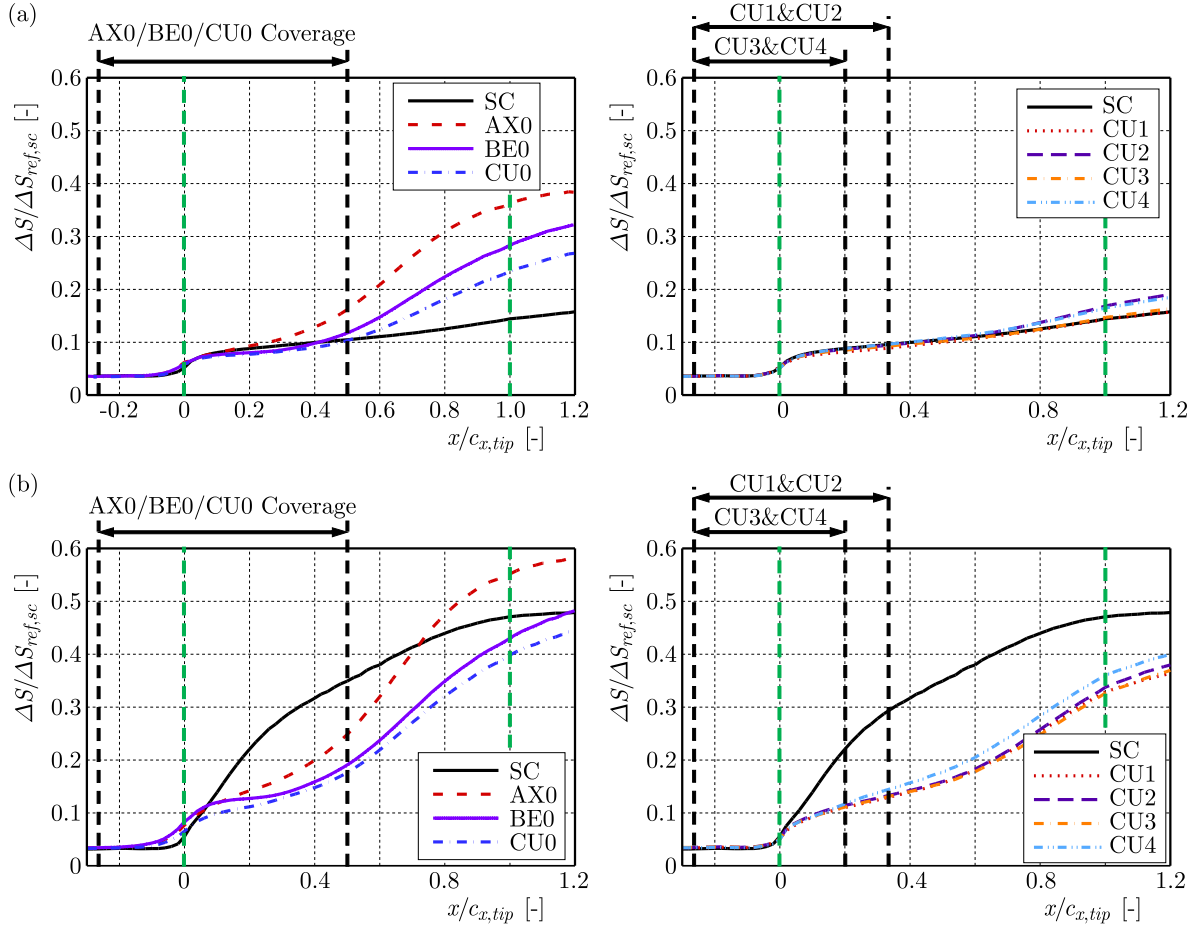


Fig. 8. Pitchwise-averaged entropy distributions along the axial direction at 90% span

compared to SCPE condition, in spite of a significant change in SC curve. But curves of CU1 to CU4 raise obviously compared to SCPE condition. It is indicated that slots with strong effects tend to maintain their influence on the flow field at more critical conditions.

From the above analysis of entropy spanwise and streamwise distributions, it is concluded that the influenced spanwise range of entropy distributions by CTs is above 80% span, and the most dramatic growth generally occurs above 95% span. Primary sources of loss generation are different at lower and higher spans. At higher span high entropy regions are located within the slots axial coverage, which directly results from the injection flow by CTs. At a lower span, the entropy rises gradually along the streamwise direction. It is inferred that entropy variations are indirectly induced by an altered flow field by CTs. The following Section considers the loss development process in the main flow and inside slots, making further efforts to interpret the loss mechanisms with CU slots.

3.3. Detailed Loss analysis with CU0

This Section discusses the loss development process in the main flow and inside slots along the axial direction, making further efforts to interpret the loss mechanisms with CU0. Eight axial cuts are taken through the blade row and slots to show the increase in entropy relative to the inflow. The 8 cuts are plotted with CU0 slots in Fig. 10, with their normalized tip axial locations marked on the right side of the figure. The axial cuts and slots in one passage are numbered by Arabic and Roman numeral respectively, to facilitate the description in the following analysis. On these eight cuts, the normalized entropy distributions above about 80% span with SC at

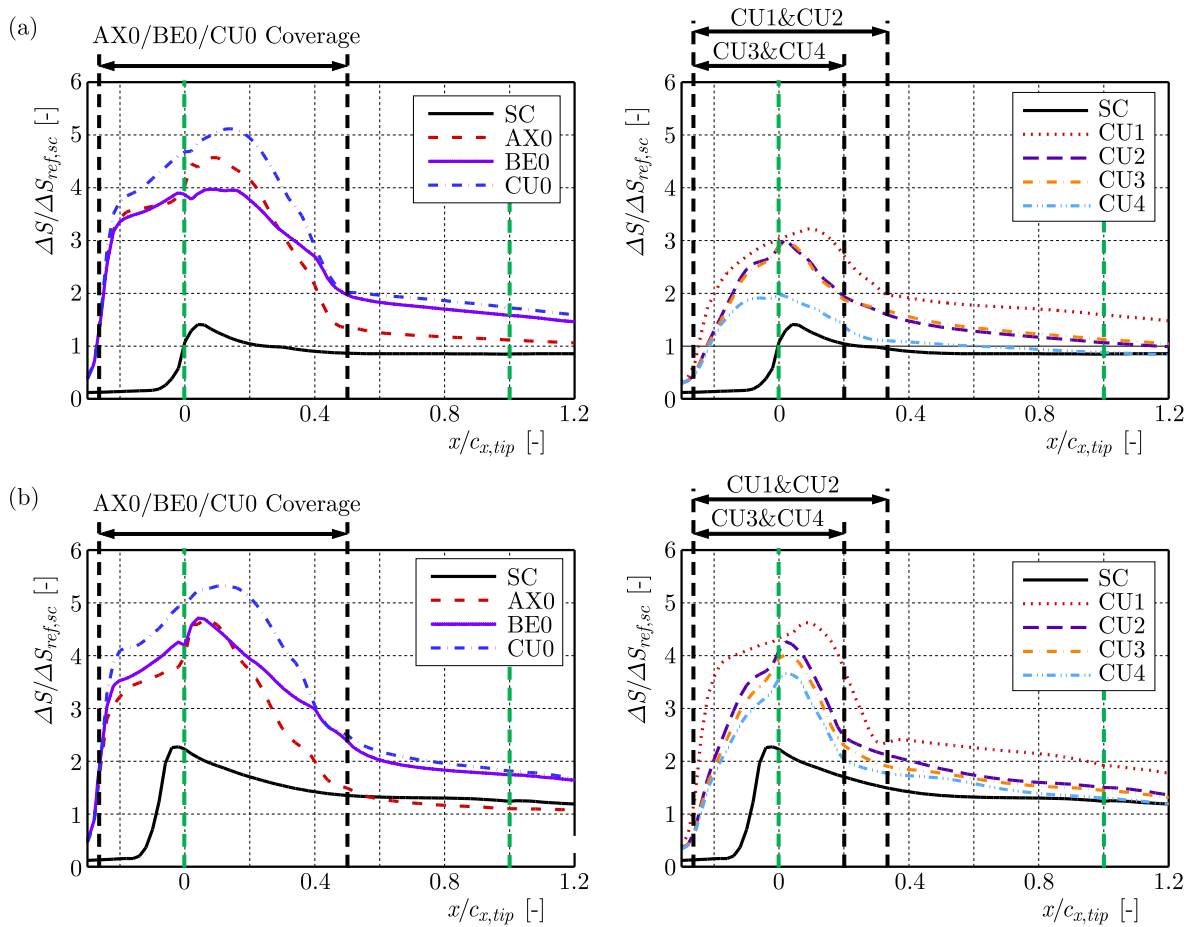


Fig. 9. Pitchwise-averaged entropy distributions along the axial direction at 99.5% span

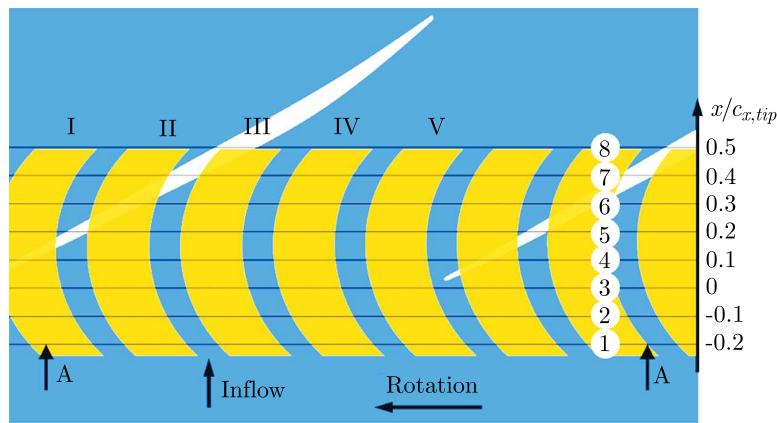


Fig. 10. The locations of eight axial cuts

both conditions are depicted in Fig. 12 (viewing from inlet to outlet). Figure 11 also presents the rotor blade limiting streamlines and 3D streamlines starting above 95% span in Cut 8.

As shown in Fig. 12a, high entropy regions hardly appears in the first two cuts with SC. Then a small piece of a high loss region initiates to emerge near the casing in the 3rd cut, as a result of tip leakage flow spillage at LE. Besides, LE separation also gives rise to a relative high loss at lower span at the suction surface (SS). With the development of separation and tip leakage flow, high entropy regions near SS and casing extend in the main flow passage in following planes. At SCNS condition, the primary losses are still ascribed to the blade separation and tip leakage flow. However, since the tip leakage flow is spilling more upstream at this working condition,

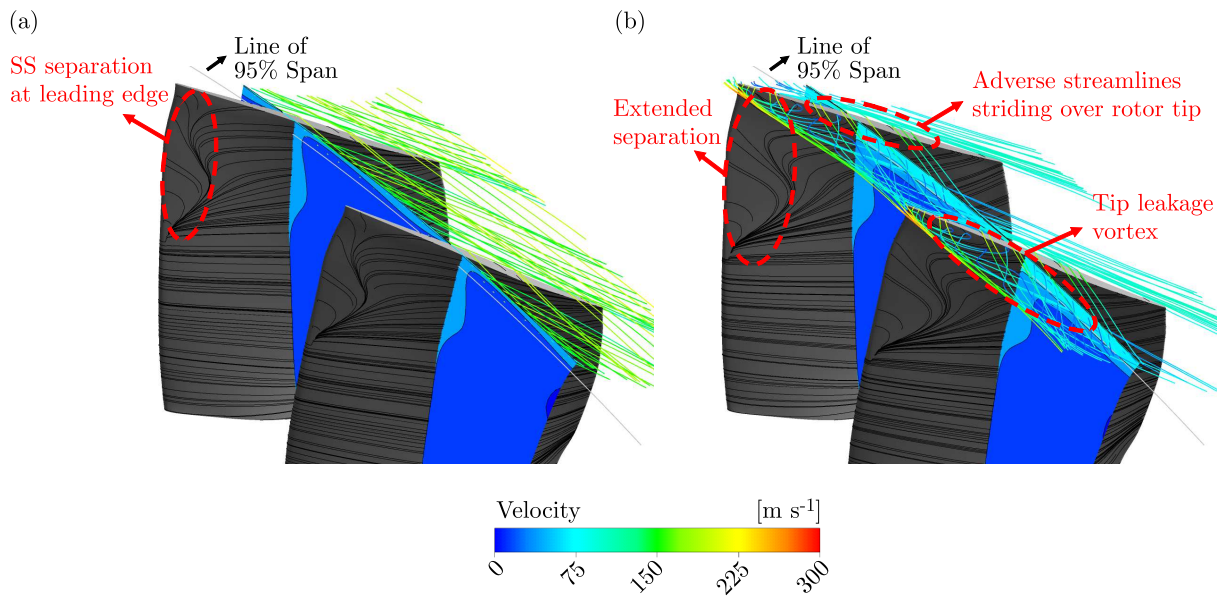


Fig. 11. Blade limiting streamlines and 3D streamlines starting above 95% span in Cut 8

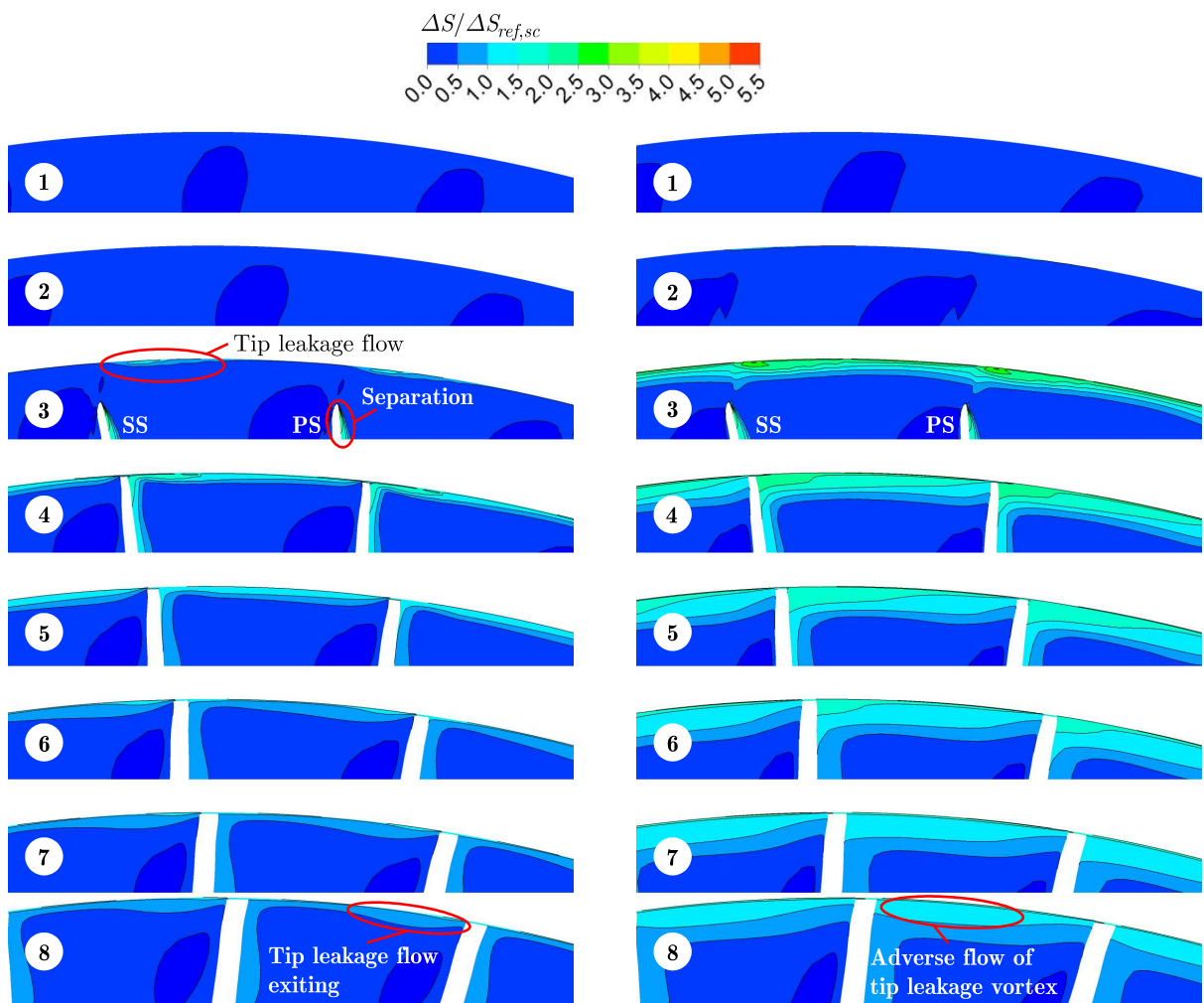


Fig. 12. Entropy distributions on axial cuts with SC (inlet to outlet)

loss of much larger magnitude and extent is generated near the tip region, as shown at Cut 3 to Cut 9 in Fig. 12b. In addition, at SCNS condition, the high entropy region grows larger in the radial extent and moves closer to SS.

As seen in Fig. 11, the limiting streamlines at both two conditions clearly show the suction surface separation at LE. At SCNS condition, the separation region extends in both streamwise and spanwise directions. As shown in Fig. 11a, 3D streamlines just go downstream smoothly at SCPE condition. Streamlines upstream Cut 8 are not observed. At SCNS condition, however, adverse streamlines striding over rotor tip are clearly seen upstream Cut 8 in Fig. 11b as well as a tip leakage vortex. This indicates that the high entropy region above 95% span in Cut 8 is attributed to the adverse flow. Streamlines starting from Cut 8 turn around and flow towards the pressure surface (PS) of the adjacent blade, as a result of a high adverse pressure gradient. Then streamlines strode over rotor tip and continue to propagate in pitchwise and reversed-streamwise directions. Some streamlines roll up and form a tip leakage vortex, consequently giving a rise to a larger area of the high entropy region at Cut 8.

The axial distributions of pitch-averaged mass flow through the slot opening surface \bar{G}_{slot} are depicted in Fig. 13. Values greater than zero represent the flow into the slot, and vice versa. Figure 14 presents the entropy distributions with CU0.

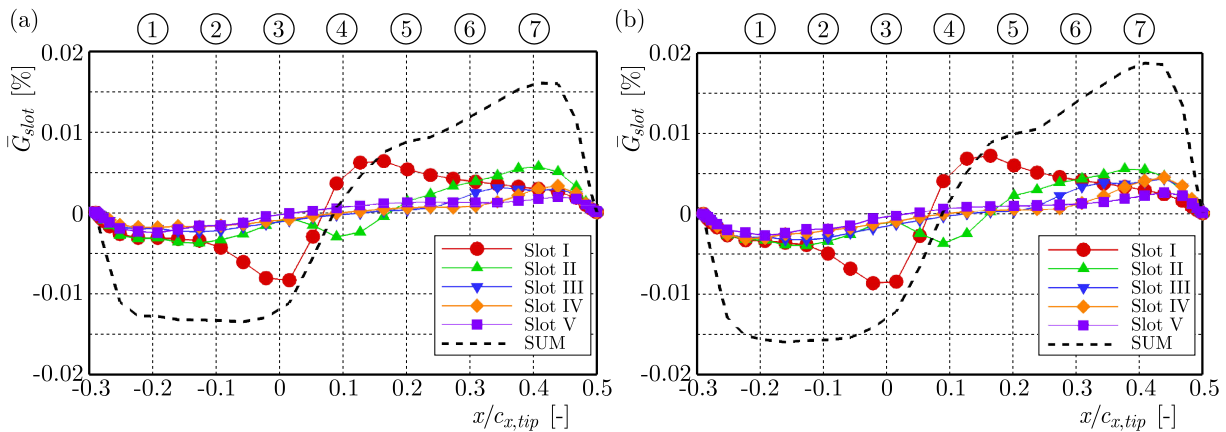


Fig. 13. Axial distributions of pitch-averaged mass flow through each slot opening surface

In Fig. 13, the sum of exchanging mass flow through five slots is also designated by dashed lines. Since the frozen rotor model has been used, the pattern of \bar{G}_{slot} distribution is related to the relative position of R1/CU0. In this case, Slot I just strides over LE as shown in Fig. 10. Thus Slot I reaches its maximum injection mass flow rate at LE. The suction mass flow of Slot II reaches the maximum value at about 40% $x/c_{x,tip}$, where Slot II overlaps with the blade tip. Since Slot III to V do not overlap with the blade tip, their distribution curves are similar. For the SUM curve, 10% $x/c_{x,tip}$ is the dividing location of injection and suction regions. The injection flow rate is relatively large and almost constant from -25% to 0% $x/c_{x,tip}$. The suction flow rate increases downstream 10% $x/c_{x,tip}$ gradually and reaches the peak value at 40% $x/c_{x,tip}$. \bar{G}_{slot} distributions at SCNS condition are similar with SCPE case.

In Fig. 14a, pretty high entropy regions are located on the counter-rotating side of Slot I (on the right side in current view point) at Cut 1-4. It is suggested that mixing of the injection flow and the main flow is the primary cause of the loss. The highest value of entropy appears at Cut 4, i.e. 10% $x/c_{x,tip}$ location, in accordance with the entropy axial distribution in Fig. 9a. Downstream 15% $x/c_{x,tip}$, the injection flow rate is no longer presented in any slot. Accordingly, the entropy value starts to decline as seen in Fig. 9a. At Cut 5-6, the upstream high entropy flow is absorbed into the rear portion of Slot I repeatedly. At Cut 8, SS separation area shrinks slightly. In addition, a noticeable high entropy region rises near casing and PS, which results from the accelerated tip flow by slots. The entropy distribution pattern is similar at SCNS

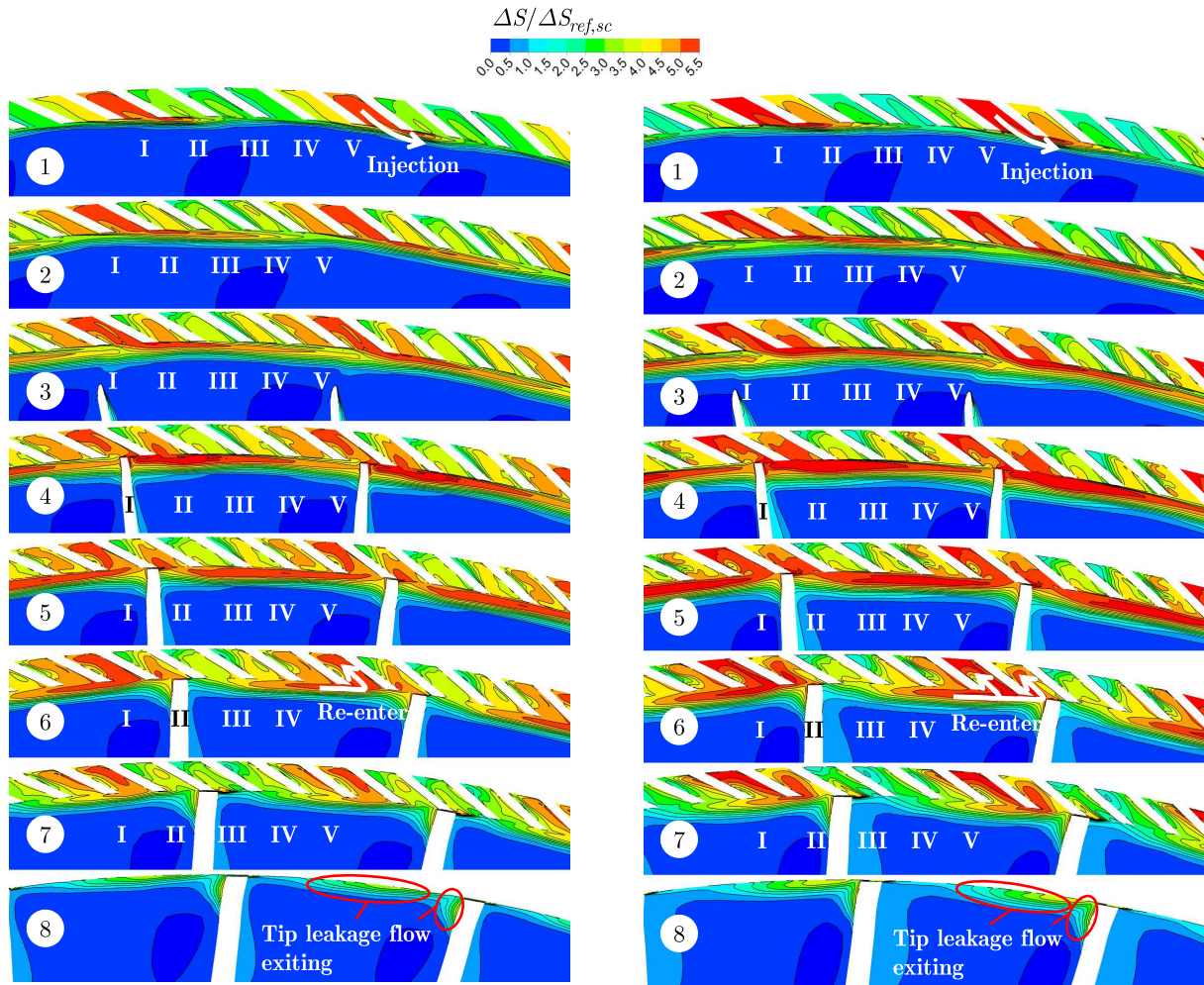


Fig. 14. Entropy distributions on axial cuts with CU0

condition as shown in Fig. 14b, with a slightly higher entropy level inside the slots and rotor passages.

From the above, loss development procedures throughout the passages with SC and CU0 are clarified. Loss generations with SC are primarily ascribed to the tip leakage flow and SS separation at LE. At a more critical condition, the rolled-up tip leakage vortex and consequent adverse flow occupy the major part of the high loss. CU0 is capable of suppressing SS separation loss, meanwhile accelerating the tip leakage flow and, consequently, bringing about an additional loss near the casing and PS. Besides, the upstream high entropy flow would be absorbed into the rear portion of the slot repeatedly, which results in further losses.

4. Conclusions

This paper clarifies the influence of the injection flow on loss distributions and elaborates the loss mechanisms. Several conclusions are drawn below:

- The influenced spanwise range of entropy distributions by slots is above 80% span. The most dramatic growth generally occurs above 95% span, which directly results from the injection flow upstream the leading edge. Entropy generation at a lower span rises gradually along the streamwise direction, which may be indirectly induced by an altered flow field by casing treatment.

- Loss generations with smooth casing are primarily ascribed to the tip leakage flow and suction surface separation at the leading edge. At a more critical condition, the rolled-up tip leakage vortex and the consequent adverse flow occupy the major part of the high loss. CU0 slot is capable of suppressing the suction surface separation loss, meanwhile accelerating the tip leakage flow and, consequently, bringing about an additional loss near the casing and pressure surface. Besides, the upstream high entropy flow would be absorbed into the rear portion of the slot repeatedly, which results in further losses.

Acknowledgements

This work has been supported by the Natural Science Foundation of China (No. 51576124) and the “2011 Aero-Engine Collaborative Innovation Plan”.

References

1. ALONE D.B., KUMAR S.S., THIMMAIAH S.M., MUDIPALLI J.R.R., PRADEEP A.M., RAMAMURTHY S., IYENGAR V.S., 2014, Improvement of moderately loaded transonic axial compressor performance using low porosity bend skewed casing treatment, *International Journal of Rotating Machinery*, **2014**, 1-14
2. CHIMA R.V., 2009, Swift code assessment for two similar transonic compressors, *AIAA*, 2009-1058
3. DANNER F.C.T., KAU H.-P., MÜLLER M.W., SCHIFFER H.-P., BRIGNOLE G.A., 2009, Experimental and numerical analysis of axial skewed slot casing treatments for a transonic compressor stage, *ASME*, GT2009-59647
4. FAN L., NING F., LIU H., 2008, Aerodynamics of compressor casing treatment: part I – experiment and time-accurate numerical simulation, *ASME*, GT2008-51541
5. FUJITA H., TAKATA H., 1984, A study on configurations of casing treatment for axial flow compressors, *Bulletin of JSME*, **27**, 230, 1675-1681
6. LI M., YUAN W., SONG X., LU Y., LI Z., LI Q., 2012, An experimental investigation about the effect of the partial casing treatment on a transonic axial-flow compressor performance under inlet distortion, *ASME*, GT2012-68442
7. LU X., CHU W., ZHU J., WU Y., 2006, Experimental and numerical investigation of a subsonic compressor with bend skewed slot casing treatment, *ASME*, GT2006-90026
8. MOORE R.D., KOVICH G., BLADE R.J., 1971, Effect of casing treatment on overall and blade element performance of a compressor rotor, *NASA TN D-6538*
9. REID L., MOORE D., 1978, Performance of a single-stage axial-flow transonic compressor with rotor and stator aspect ratios of 1.19 and 1.26, respectively, and with design pressure ratio 1.82, *NASA TP-1338*
10. TAKATA H., TSUKUDA Y., 1977, Stall margin improvement by casing treatment – its mechanism and effectiveness, *Journal of Engineering for Power*, **99**, 1, 121-133
11. TUO W., LU Y., YUAN W., ZHOU S., LI Q., 2011, Experimental investigation on the effects of unsteady excitation frequency of casing treatment on transonic compressor performance, *Journal of Turbomachinery*, **133**, 2, 021014-6
12. YU Q., LI Q., LI L., 2002, The experimental researches on improving operating stability of a single stage transonic fan, *ASME*, GT2002-30640
13. ZHU J., CHU W., 2005, The effects of bend skewed groove casing treatment on performance and flow field near endwall of an axial compressor, *AIAA*, 2005-809

PRELIMINARY DESIGN OF AN ADAPTIVE AILERON FOR THE NEXT GENERATION REGIONAL AIRCRAFT

GIANLUCA AMENDOLA, IGNAZIO DIMINO, ANTONIO CONCILIO

Centro Italiano Ricerche Aerospaziali, Department of Smart Structures, Capua, Caserta, Italy
e-mail: g.amendola@cira.it; i.dimino@cira.it; a.concilio@cira.it

FRANCESCO AMOROSO, ROSARIO PECORA

University of Naples "Federico II", Department of Industrial Engineering, Aerospace Division, Naples, Italy
e-mail: f.amoroso@unina.it; rosario.pecora@unina.it

Design of morphing wings at increasing TRL is common to several research programs worldwide. They are focused on the improvement of their performance that can be expressed in several ways, indeed: aerodynamic efficiency optimization, fuel consumption reduction, CO_x and NO_x emission reduction and so on, or targeted to overcome the classical drawbacks related to the introduction of a novel technology such as system complexity increase and management of certification aspects. The Consortium for Research and Innovation in Aerospace in Quebec (CRIAQ) lunched project MD0505 that can be inserted in this crowded frame. The target of this cooperation, involving Canadian and Italian academies and a research centre, is the development of a camber "morphing aileron" integrated on an innovative full scale wing tip of the next generation regional aircraft. This paper focuses on the preliminary design and the numerical modeling of its architecture. The structural layout is, at the beginning, described in detail and furthermore, a finite element (FE) model of the entire aileron architecture is assessed and used to verify the structural integrity under prescribed operational conditions.

Keywords: morphing, actuation system, adaptive wing

1. Introduction

Commercial aircraft wings are typically designed for cruise operations. However, different flight phases are encountered during a standard mission; efficiency is therefore seldom optimal (Barbarino *et al.*, 2011). The realization of lifting surfaces able to "adapt" themselves to variable operative conditions and, therefore, to match the necessity of modifying the reference configuration, may improve the current performance levels. A main feature that can be associated to a morphing structure is then for instance its potentiality to optimize the aircraft L/D ratio all over the flight envelope. Several European projects, such as Clean Sky (2008) and Saristu (2012-2015) were launched in recent years to develop and assess new technologies devoted to add the structural systems with new adaptation capabilities through the use of innovative, integrated devices, demonstrating their real applicability and benefits. Aiming at those same targets, the CRIAQ Project was launched, with a specific focus on the wing trailing edge, specifically in the aileron region, (CRIAQ MDO-505, 2012). In fact, many studies (Monner *et al.*, 1999; Bolonkin and Gilyard, 1999), demonstrated the particular effectiveness of morphing trailing edge devices located in that area. Moreover, the aileron region constitute a very delicate wing zone for several reasons. Mainly, the aileron constitutes a primary safety critical control surface whose failure is catastrophic for the entire aircraft and in addition, it must be demonstrated that no aeroelastic instability (flutter) occurs during operations. Also the reduced available space constitutes an

important aspect which makes the morphing aileron design challenging, because it results are difficult to integrate actuators and kinematic leverage. The present paper describes the design phase of a morphing aileron prototype, ready for installation and tests in a wind tunnel. The adaptive aileron device is integrated with another complementary morphing wing system, described by Kammegne *et al.* (2016). The present aileron is otherwise not aimed at substituting the conventional architecture but adds new functionalities to the classical design. In fact, the aileron can still rotate rigidly around its main hinge axis while it can morph (by modifying its camber). When it is not actuated, the aileron works in the usual manner, preserving the aircraft roll control and stability (the morphing part behaves as a rigid component). In the presented application, the system works in cruise to compensate aircraft weight variations following fuel consumption. During classical manoeuvre, the aileron works classically. The morphing technology can be applied also to give a better solution to the active load control on aircraft with new approaches such as active flow control (Stalewski and Sznajder, 2014), which change the flow conditions on the wing surface and, in turn, the aerodynamic loads. In the current paper, it is described how the modification of wing load distribution could be tailored to achieve wing-root bending moment alleviation as a sudden increase of aerodynamic loads occurs (gust or rapid manoeuvres). The morphing aileron is made of three-segmented ribs assembled into a *finger-like* architecture (Pecora *et al.*, 2014), connected through longitudinal spars to guarantee a suitable torsional rigidity. The actuation system is completely integrated within the structural body. It includes distributed actuators the number of which is fixed according to their load-bearing capability, their force generation possibility, the allowable space and the stiffness requirements. In fact, the complete system must be able to deform while withstanding the external aerodynamic loads. These two requirements may be overcome by the use of load-bearing actuators. The kinematics allow a single degree of freedom per rib that is blocked by the actuator device. It has then the role to absorb the external load and move the system against that load. A mechanical chain converts the actuator torque into a controlled linear displacement in order to amplify the transferred force vs. a limited motion penalty. Linear motion guides are made of two main components: a stainless steel rail and a sliding element directly connected to the leverage, in turn linked to the actuator rotating shaft by means of a fork-shaped crank. The vertical force needed to move the trailing edge results by the contact between the slider and the rail. The complete system is made of commercial elements: actuators, kinematics, linear guides and all the other devices are in fact available on the market. The implemented architecture is a slight modification of the so-called quick-return mechanism (Amendola *et al.*, 2016). In this paper, the aileron structure is sized with respect to the designated load chosen among the most critical operative ones. The working principle of the actuation system is described in detail and preliminary results of a finite element simulation are shown. Static and buckling analyses do not show any particular criticality; in other words, no plasticization arises under the limit loads, herein selected.

2. Morphing aileron: structural layout and evaluation of loads

The morphing aileron consists of segmented adaptive ribs based on finger-like segments enabling aileron camber morphing upon actuation. Each rib (Fig. 1) is assumed to be segmented into three consecutive blocks (B1,B2,B3) connected to each other by means of hinges located on the airfoil camber line (A,B). Block B1 is rigidly connected to the rest of the wing structure through a torsion tube enabling aileron rotation for roll control. Blocks B2 and B3 are free to rotate around the hinges on the camber line, thus physically turning the camber line into an articulated chain of consecutive segments. A linking rod elements (L) hinged on not adjacent blocks forces the camber line segments to rotate according to specific gear ratios.

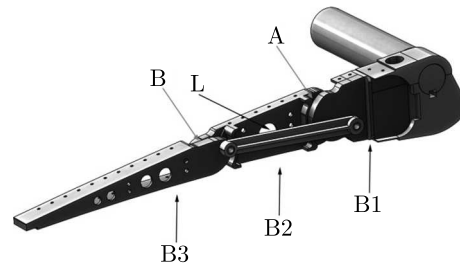


Fig. 1. Morphing rib architecture: (a) blocks and links, (b) hinges

The ribs kinematic is transferred to the overall aileron structure by means of a multi-box arrangement (Fig. 2) where the skin is hidden for clarity.

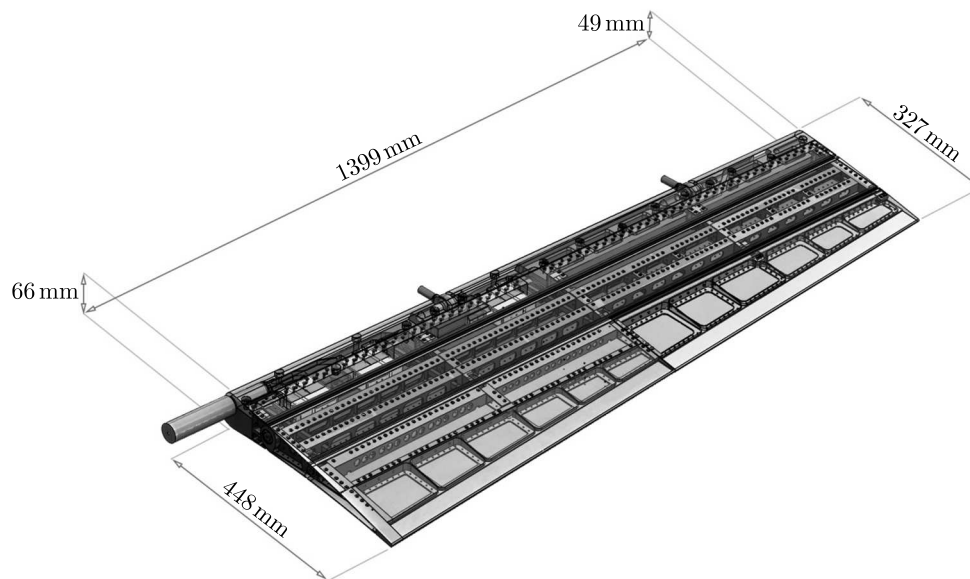


Fig. 2. Morphing aileron structure: multi-box arrangement

Referring to Fig. 3, the internal structural components are depicted, and it is also shown that the aileron is divided into one actuated and one passive segment. The internal kinematic chain actuates the first two bays while the last are considered slaved during the morphing movement.

The reference Cartesian system S_0 (Fig. 4) has been used as the datum for the load evaluation addressed by this paper; the following conceptual definition applies to S_0 :

- Origin (O) at the intersection point between the Test Article (T/A) leading edge and the root rib plane;
- X -axis onto root rib plane, parallel to the chord of the T/A airfoil @ the root section and aft oriented;
- Y -axis normal to the root rib plane and oriented towards the T/A tip;
- Z -axis perpendicular to XOY plane and oriented upwards.

The rotation angle γ of block B2 with respect to block B1 is determined in order to approximate target shapes by means of the articulated one-DOF mechanism described in Fig. 1. The angle γ is represented in Fig. 5.

It is measured respect to the unmorphed chord direction and it corresponds to rigid rotation of the plain control surface comprised between -5° and $+5^\circ$. The VLM method has been adopted to evaluate aerodynamic pressure distribution along the aileron in correspondence to each

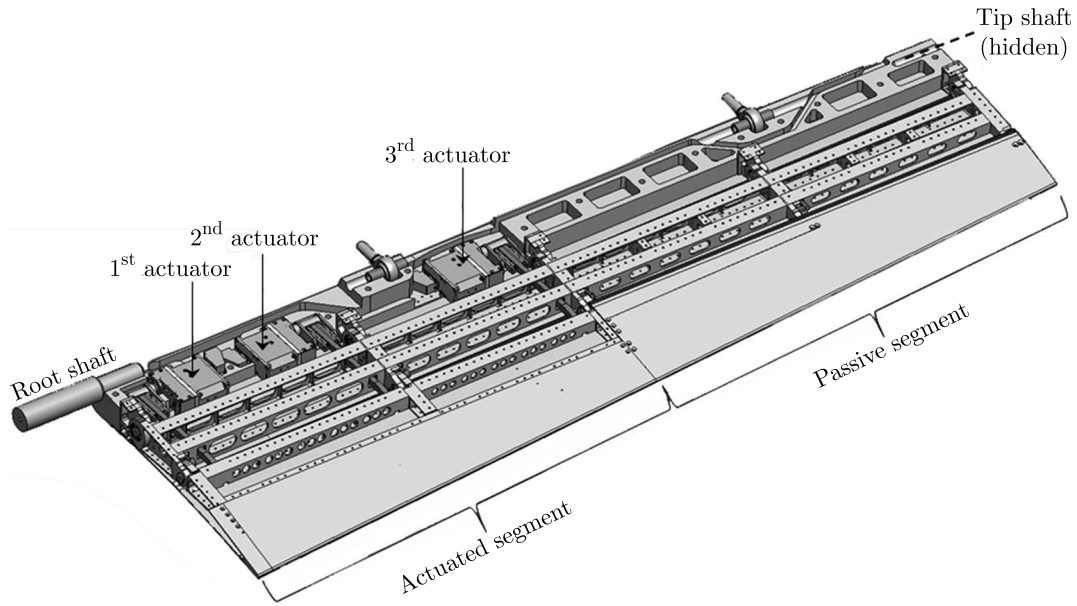


Fig. 3. CAD of the morphing aileron with an internal view to the actuation system

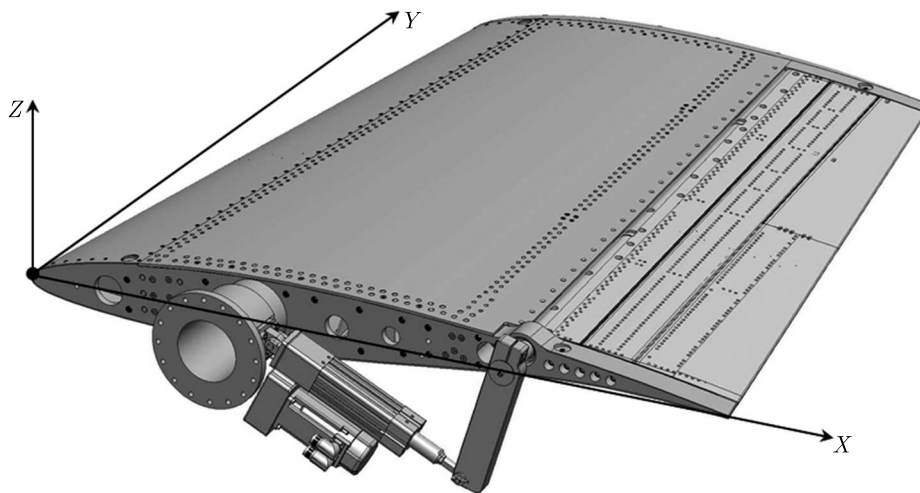


Fig. 4. CAD of the Test Article with the reference system used for aerodynamic loads

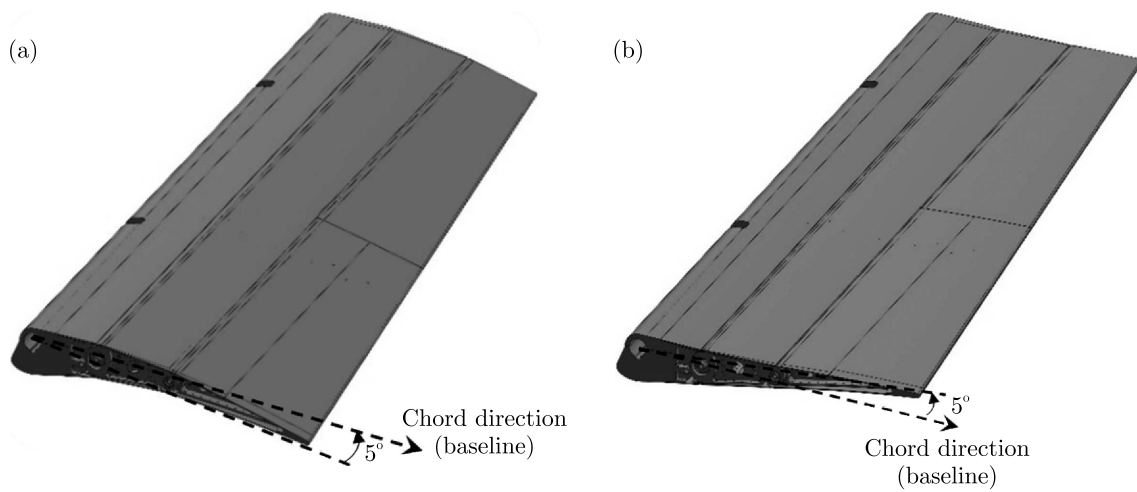


Fig. 5. Morphing aileron deflection angle γ in morphed down and morphed up

considered flight attitude (namely the wing angle of attack, flight altitude and speed) and aileron geometrical configuration. 3D flat-panels mesh is generated in correspondence to the outer wing segment. For each flight attitude and aileron shape, the lifting pressure (P_i) acting along each box (b_i) is calculated according to the following equation

$$P_i = q(P_{0,i} + \alpha P_{\alpha,i} + \gamma P_{\gamma,i}) \quad (2.1)$$

where: $q = 0.5\rho V_\infty^2$ is the dynamic pressure, ρ the air density and V_∞ the airspeed; α is the wing angle of attack; $P_{0,i}$ is the pressure arising on b_i in correspondence to unit dynamic pressure at α , γ equal to zero (airfoil baseline camber effect); $P_{\alpha,i}$ is the pressure on b_i due only to unit α at unit dynamic pressure (incidence effect); $P_{\gamma,i}$ is the pressure on b_i due only to unit γ at unit dynamic pressure (morphing effect).

Thanks to Eq. (2.1), $P_{0,i}$, $P_{\alpha,i}$, $P_{\gamma,i}$ are calculated only one time for all the boxes and then combined according to the flight attitude parameters (α, q) and aileron morphed shape (γ) to be investigated. The combination of α, q, γ leading to the most significant pressure levels along aileron segments is then determined and used as the design operative condition for the structural sizing purpose. The spanwise pressure distributions on the aileron segments at the design point ($\alpha = 2^\circ$, $q = 4425 \text{ N/m}^2$, $\gamma = 7^\circ$) are plotted in Fig. 6.

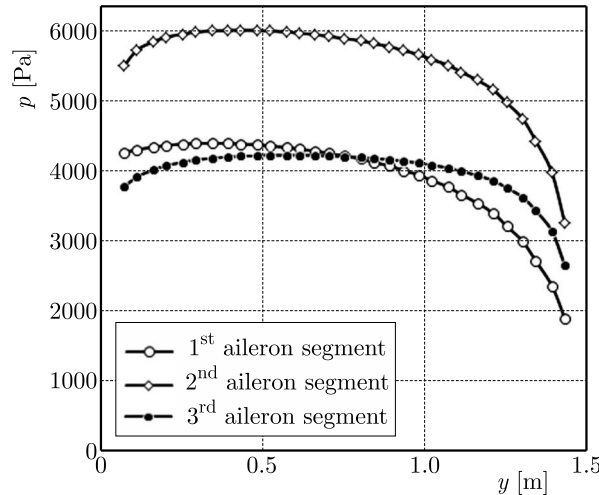


Fig. 6. Pressure distribution along aileron span

The estimated pressure distribution will be considered as the reference load for structural sizing and it will be applied to the aileron finite element model in order to assess the stress analysis. This constitutes the fundamental step to be done before proceeding with the manufacturing process.

3. Actuation system

The main target of the actuation kinematics is to develop a means of transforming the actuator motion to specific rotation of the morphing device. It must be designed to withstand the external aerodynamic loads without undergoing structural damage and at the same time to move the system to the desired morphed shape. It is based on the classical quick-return mechanism, also referred to as oscillating glyph kinematics that (Fig. 7) is widely discussed and was validated by Amendola *et al.* (2016).

Figure 7 shows the main structural components of the glyph kinematic system. It is composed of crank R with an actuator shaft positioned at the point O , leverage beam B_L connected to

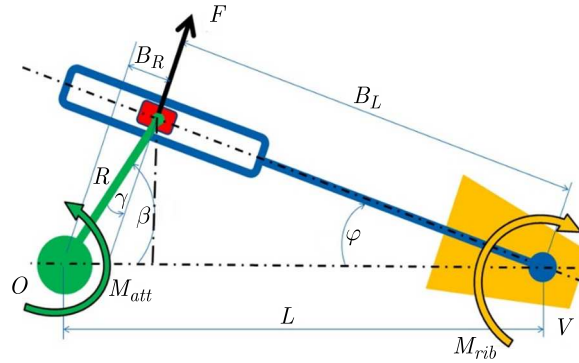


Fig. 7. Oscillating glyph kinematic scheme

aileron B_3 rib segment. The sliding element moves along its rail subjected during operation to the vertical force F . The actuator shaft rotation is transmitted to the structure by means of the crank R and a contact force is generated by the sliding element along the linear guide. Thereby, a moment is produced that equilibrates the aerodynamic hinge moment, so that the system keeps its desired morphed shape. The mechanism is then a SDOF architecture. In the kinematic scheme, the angle β is the actuator shaft rotation while φ is the morphing deflection directly related to the aileron angle γ (Fig. 5). The relation between the achieved angle and the mechanical advantage (MA), expressed as a ratio between the external load and the generated momentum, may be represented as in Fig. 8. The diagram shows that the greater rib morphing angle, the higher MA and, consequently, the actuator torque required to equilibrate the external aerodynamic moment decreases. The aileron design condition (selected as the most severe one) occurs at $\varphi = 7^\circ$ with $MA = 4.2$. This peculiarity may lead to significant benefits in terms of the actuator power and weight.

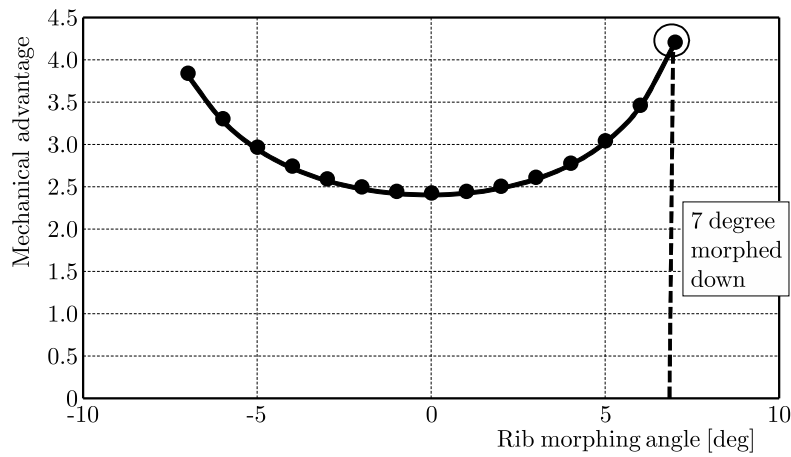


Fig. 8. MA vs. rib morphing angle

The actuator shaft rotation β may be related to the morphing angle φ as described by Eq. (3.1) and represented in Fig. 9

$$\cot \varphi = \frac{L}{R \sin \beta} - \cot \beta \tag{3.1}$$

It is evident that in the design range between $+7^\circ$ of morphed down and -7° of morphed up, the actuator rotation is comprised among $\pm 45^\circ$. The actuation system kinematics with details of the linear guides and its integration on the aileron rib are shown in Fig. 10.

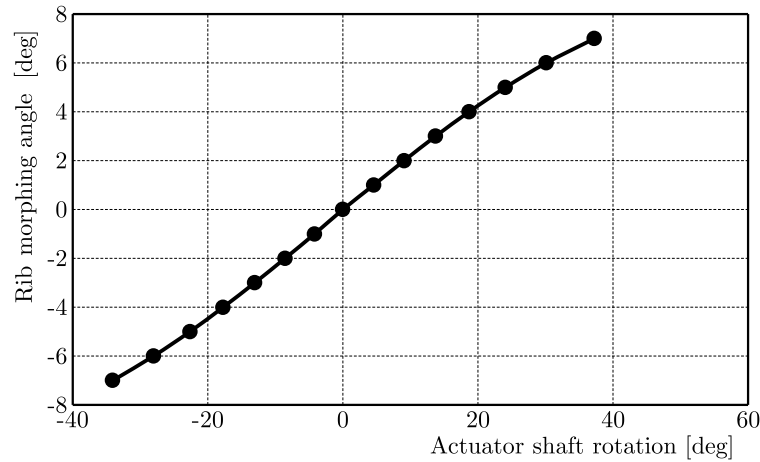


Fig. 9. Rib morphing angle vs. actuator shaft rotation

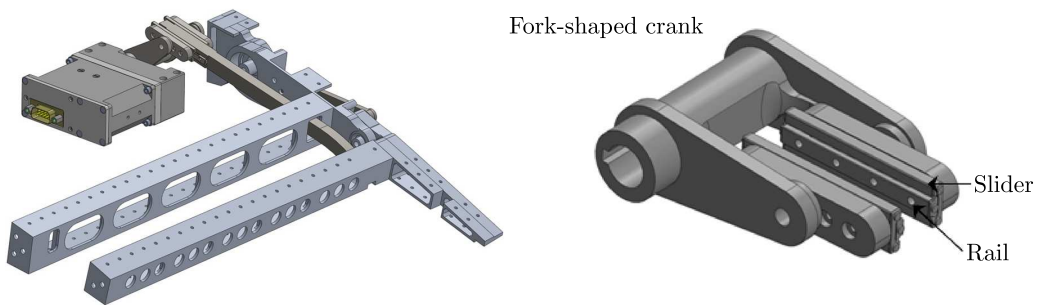


Fig. 10. Integration between the actuation system and rib (left) and details of the linear guide elements (right)

4. FE validation

In order to verify the structural robustness of the conceived morphing architectures as well as to estimate its dynamic behavior, a very refined finite element model (FEM) has been generated (Fig. 11). The model has been realized with solid finite TET10 elements both for structural components (ribs and spars) and actuation system leverages. All the hinges have been modeled by means of two-nodes CBUSH elements. Each node of the CBUSH has been rigidly connected to a representative set of nodes belonging to the structural item by means of RBE2 (Fig. 12) (MSC-Nastran).

The materials adopted for the aileron are described in Table 1 and highlighted in Figs. 13a and 13b. The aluminum components are depicted in grey while the steel components in black.

Table 1. Aileron component materials

Material (isotropic)	E [Gpa]	ρ [kg/m ³]	ν [-]	Items
Harmonic steel	210	7850	0.3	Beam of the actuation system, linear guide features, crank and rib links
Al 2024-T351	70	2768	0.33	All the other items

The aileron model is considered constrained in correspondence to the crank exactly where the actuator shaft is located in order to prevent its rotation (clamped configuration). The following analyses have been carried out:

- Linear static analysis at the limit load
- Buckling analysis at the limit load.

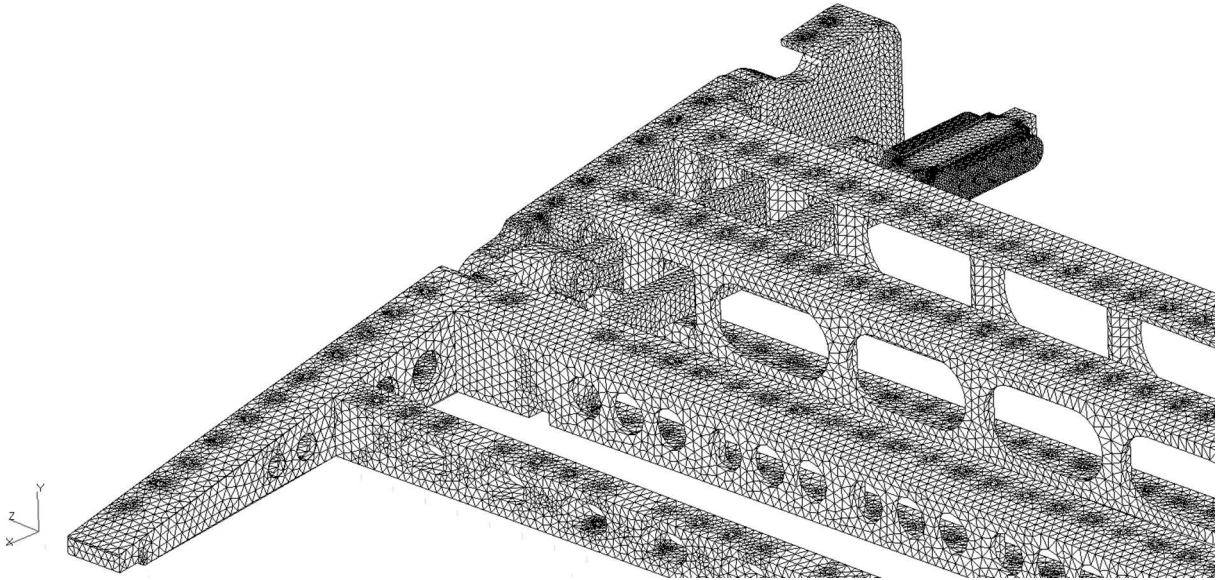


Fig. 11. Details of the aileron structure mesh

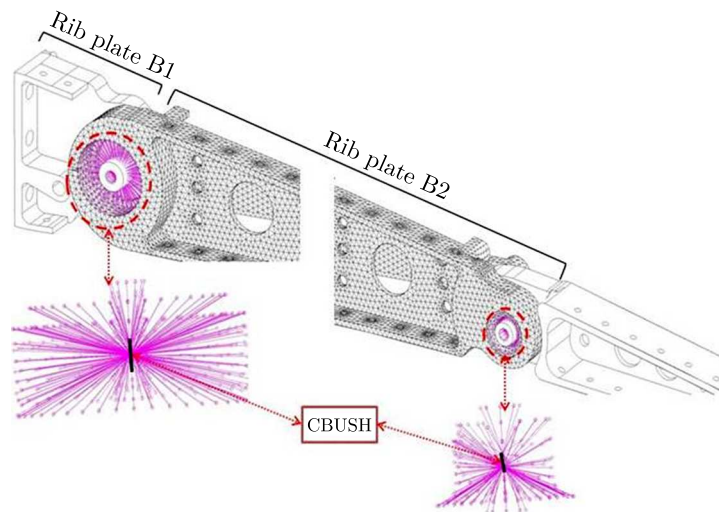


Fig. 12. Morphing aileron finite element model with details of the hinges

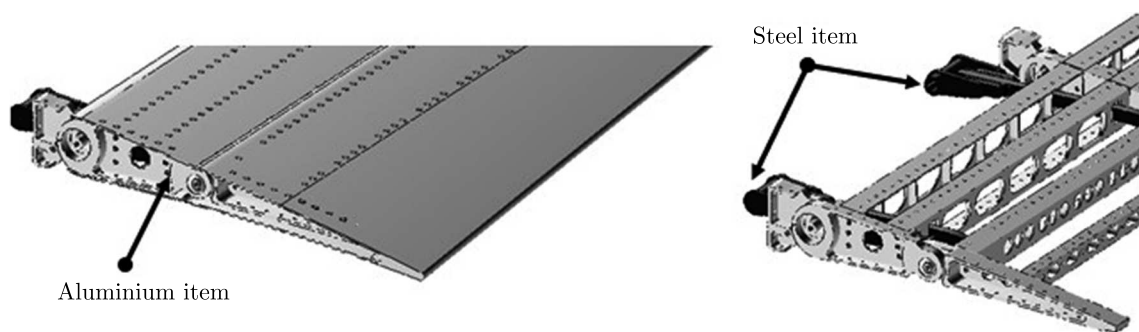


Fig. 13. Aileron materials: complete structure (a), inner structure (b)

The global magnitude of the displacements exhibited by the aileron at the limit load condition is shown. The maximum value (21.8 mm) is located at the trailing edge in proximity of the 1st bay (Fig. 14). The maximum von Mises stresses are detected around the rib links (257 MPa) and around hinges of the second rib (231 MPa) and on the actuation beam (467 MPa), resulting below the yield strength of AL 2024 alloy and steel. The described results are depicted in Figs. 14-16.

The first buckling eigenvalue occurs at -10.391 , which means that the first critical load is more than 10 times of the applied pressure but in the opposite direction. The buckling deformation related to this eigenvalue involves rib connection links as shown in Fig. 16.

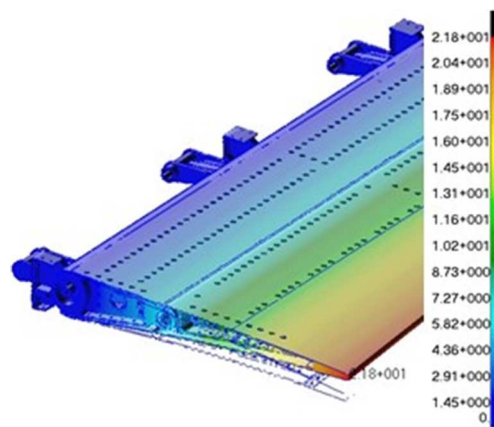


Fig. 14. Global aileron displacement distribution

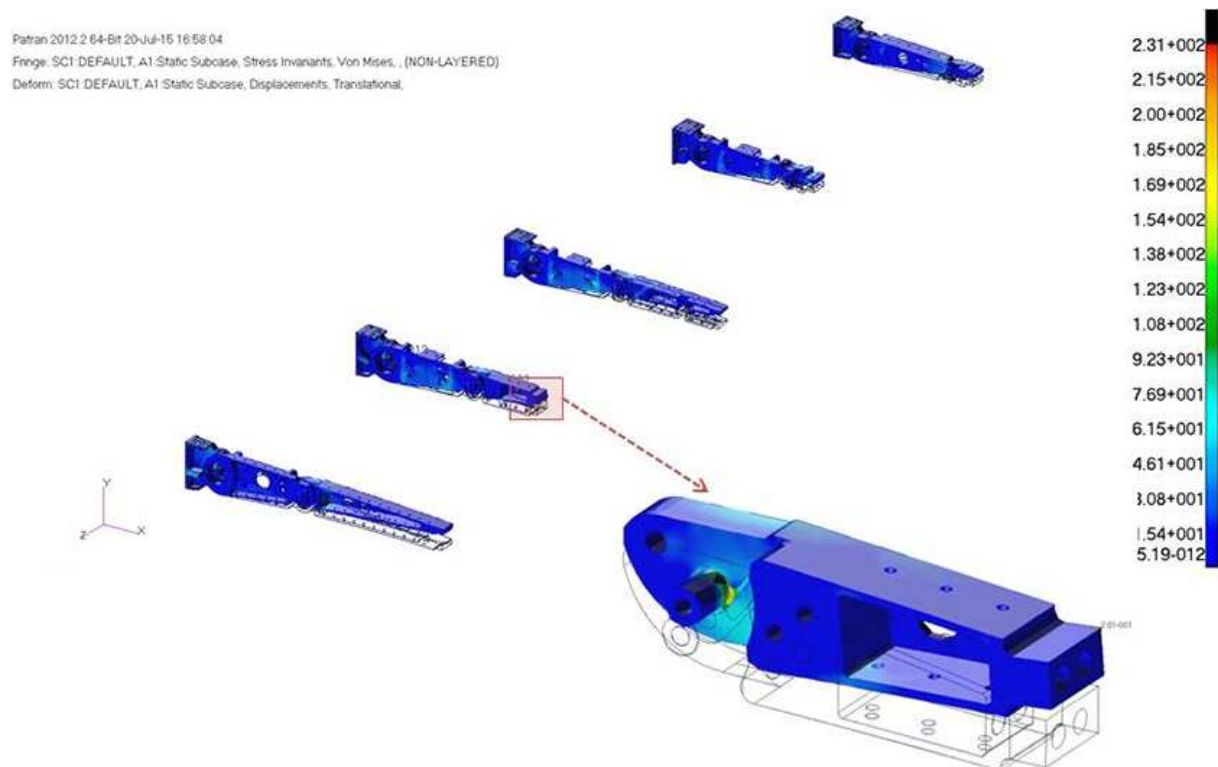


Fig. 15. Global von Mises stress distribution on the ribs

5. Conclusions

In this paper, the working principle of a morphing aileron actuation system is presented. The actuation mechanism is based on an oscillating glyph mechanism, combining characteristics of functionality, robustness and integrability required for adaptive structures. In particular, the study of the smart mechanical system involved functional integration of the kinematic actuation chain into a finger-like adaptive ribs architecture. The static load has been imposed to the structures and the stress results and the buckling eigenvalue have been provided. The results show that all margin of safety are positives and there are no critical points for structural safety

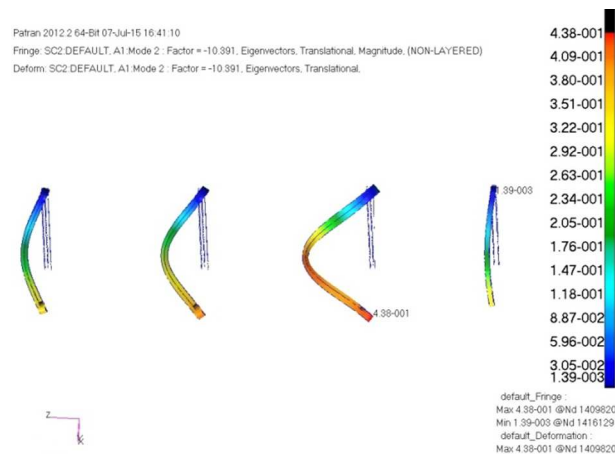


Fig. 16. First buckling deformation mode of the aileron

of the proposed morphing aileron. The next step will involve the manufacture phase where the aileron prototype will be built. Subsequently, the results herein presented will be validated by means of dedicated ground tests campaign where both static and dynamic behavior will be assessed before wind tunnel tests.

References

1. AMENDOLA G., MAGNIFICO M., PECORA R., DIMINO I., 2016, Distribution actuation concepts for a morphing aileron device, *The Aeronautical Journal*, **120**, 1231, 1365-1385, DOI: 10.1017/aer.2016.64
2. BARBARINO S., BILGEN O., AJAJ R.M., FRISWELL M.I., INMAN D.J., 2011, A review of morphing aircraft, *Journal of Intelligent Material System and Structure*, **22**, 9, 823-877
3. BOLONKIN A., GILYARD G.B., 1999, [in:] Estimated benefits of variable-geometry wing camber control for transport aircraft, *NASA Technical Report*
4. CRIAQ MDO-505 (2012) – Morphing Architectures and related technologies for wing efficiency improvement. Available at: <http://en.etsmtl.ca/Unites-de-recherche/LARCASE/Recherche-et-innovation/Projets>
5. KAMMEGNE M.J.T., BOTEZ M.R., MAMOU M., MEBARKI Y., KOREANSCHI A., GABOR O.S., GRIGORIE T.L., 2016, Experimental wind tunnel testing of a new multidisciplinary morphing wing model, *Proceedings of the 18th International Conference on Mathematical Methods, Computational Techniques and Intelligent Systems (MAMECTIS 2016)*
6. MONNER H.P., SACHAU D., BREITBACH E., 1999, Design aspects of the elastic trailing edge for an adaptive wing, *RTO AVT Specialists' Meeting on "Structural Aspects of Flexible Aircraft Control"*, Ottawa, Canada, 18-20 October 1999, published in RTO MP-36
7. MSC-MD/NASTRAN, 2006. Available at: <http://www.mscsoftware.com/>
8. PECORA R., AMOROSO F., AMENDOLA G., CONCILIO A., 2014, Validation of a smart structural concept for wing-flap camber morphing, *Smart Structures and Systems*, **14**, 4, 659-679, DOI: 10.12989/sss.2014.14.4.659
9. STALEWSKI W., SZNAJDER J., 2014, Modification of aerodynamic wing loads by fluidic devices, *Journal of KONES Powertrain and Transport*, **21**, 2, 271-278, DOI: 10.5604/12314005.1133229
10. www.cleansky.eu
11. www.ikont.eu
12. www.saristu.eu

NUMERICAL STUDY OF DROPLET FORMATION IN A Y-JUNCTION MICROCHANNEL

MOUHAMADOU M.L. DIOUF

*ENSIAME – École Nationale Supérieure d'Ingénieurs en Informatique Automatique Mécanique Énergétique
Électronique Engineering School in Valenciennes, France; e-mail: alamine95@yahoo.fr*

OLDRICH J. ROMERO

*Petroleum Engineering Undergraduate Program and Graduate Energy Program, Federal University of Espírito
Santo – UFES, ES, Brazil; e-mail: oldrich.romero@ufes.br*

This study investigates the formation process of droplets in a Y-junction microchannel using two immiscible fluids: water as the continuous fluid and oil as the dispersed phase. We have examined the influence of the capillary number, flow rate ratio and viscosity ratio between the two fluids; parameters which determine the length and generation frequency of the droplets. Numerical simulations have been performed using the software Ansys Fluent with the interface capture method Volume of Fluid (VOF) for solving the governing equations. Three different algorithms have been tested for the pressure-velocity coupling: SIMPLE, SIMPLEC and PISO. The results are quite similar for SIMPLE and SIMPLEC, however it turned out that PISO is a better algorithm to solve the two-phase flow. Additionally, another Y-junction is coupled in the initial geometry to observe a symmetric breakup of the droplets and their formation is explained using the pressure field and the velocity field.

Keywords: microfluidic, Y-junction, two-phase flow, numerical simulation, VOF

1. Introduction

Microfluidics can be defined as science which studies the behaviour of fluids in micro-channels (dimensions varying from $10\ \mu\text{m}$ to $500\ \mu\text{m}$). Micro-channels becomes increasingly used every day due to a microminiaturization of biomedical devices (Micro-electromechanical system – MEMS technologies) (Lih and Miao, 2015). Microfluidics have many applications such as: DNA fabrication, encapsulation of cells, drug delivery and protein crystallization (Dolomite, 2015). For these applications, it is important to control as well as possible the geometry of the generated droplets. There are many ways of making droplets depending on the geometry used, as it was shown and briefly explained by Dolomite (2015).

In this study, we will focus on a segmented flow device. For that, a Y-junction (Fu *et al.*, 2011, 2014; Cong *et al.*, 2014) is used in order to generate periodic droplets. One continuous fluid is injected into the first channel and a dispersed fluid is injected into the secondary channel, both fluids are incompressible and immiscible.

Several parameters such as the viscosity ratio between the two fluids, the flow rate ratio, the capillary number, the aspect ratio of the geometry, the sizing of the meshing between others, can affect considerably droplet generation. This study investigates the influence of those parameters in the formation process by checking for every case the variation in length of generated droplets and the pressure field. To have a better understanding of the phenomena, a comparison between the predicted lengths of droplets by scaling proposed by Garstecki *et al.* (2006) and the numerical ones will be made. Tarchichi *et al.* (2013) showed the influence of the capillary number (Ca). Depending on its value, 3 regimes of droplets can occur: the squeezing regime for low value of Ca,

the dripping regime as Ca increase and the jetting regime at higher value of Ca . The effects of the viscosity ratio on the formation of the droplet are discussed in Tice *et al.* (2004). According to that reference, droplets are formed when the viscosity of the dispersed fluid is significantly higher than that of the continuous fluid.

All numerical simulations have been performed using the software Ansys Fluent 15.0 with the volume-of-fluid (VOF) method. In every case, the continuous phase which is injected in the main channel is water, and the dispersed phase is oil.

2. Problem description

In this study, we are using a Y-geometry (Fig. 1a) which is similar to that of Liu *et al.* (2015). This geometry have two inlets with the same width h . Both extend until they meet in a junction forming channels with two parallel plates whose distances are the same, $4h$. The length of the main channel is taken to be $36h$ for the development of periodic emulsions of oil in water. This geometry is then modified by adding two orthogonal channels at the end of the main channel (Fig. 1b) (Fu *et al.*, 2011, 2014; Cong *et al.*, 2014); channels which have the same width $h/2$ and the same length $10h$. In all the work that follows, $h = 0.1$ mm. Water with a viscosity μ_w of 1 cP (0.001 Pa·s) is injected at inlet 2 and oil with a viscosity μ_o of 10 cP (0.01 Pa·s) in inlet 1; both are moving along their channel until they meet in the junction, named here Y-junction, and moving forward along the main channel. The density of water ρ_w and of oil ρ_o are respectively 1000 kg/m³ and 900 kg/m³. The interfacial tension between water and oil ($\sigma_{w/o}$), which is an important parameter for the formation of droplets, is equal to 0.0003 N/m (30 dyn/cm)

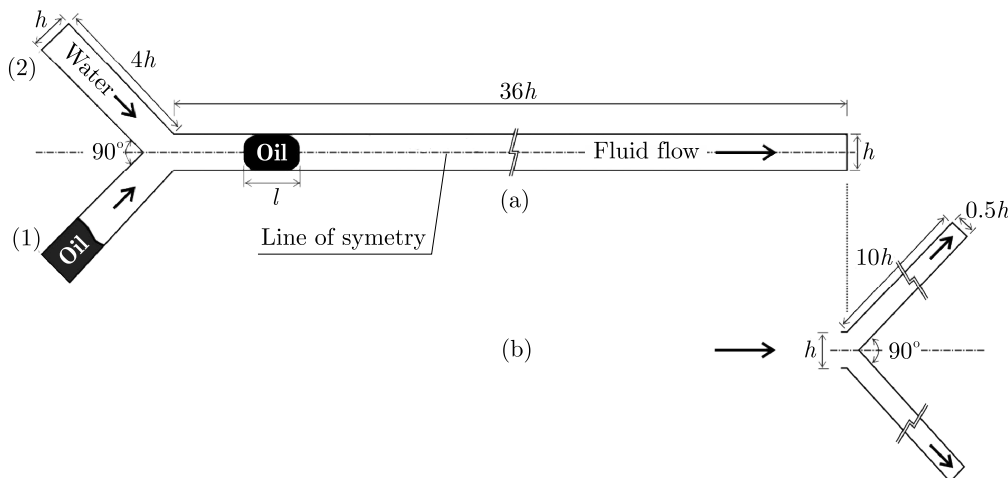


Fig. 1. Schematic view, not in scale, of the Y-junction geometry used in this work

3. Mathematical approach of the liquid-liquid flow problem

The volume fraction of water α_w and oil α_o , both ranging between 0 and 1, determines the interaction between the two fluids in the oil mobilization process, and is obtained using the multiphase model Volume of Fluid – VOF developed by Hirt and Nichols (1981). This model solves mass conservation and momentum equations considering the volume fraction present in every cell from the physical domain of the problem and for different instants. The proposal consists in calculating the volume fraction of the less dense phase, oil in this case

$$\frac{\partial}{\partial t}(\alpha_o \rho_o) + \nabla \cdot (\alpha_o \rho_o \mathbf{v}) = 0 \quad (3.1)$$

Considering the presence of two phases, water w and oil o , the sum of the volume fractions at each point of the domain must be unitary, i.e.

$$\alpha_w + \alpha_o = 1 \quad (3.2)$$

The water volume fraction is obtained directly from Eq. (3.2) as $\alpha_w = 1 - \alpha_o$, since the oil volume fraction is already known from Eq. (3.1).

Density ρ_{wo} and viscosity μ_{wo} in Equation (3.5), are mixture properties which vary within the flow domain and are computed by the volume fraction weighted average as

$$\rho_{wo} = \alpha_w \rho_w + \alpha_o \rho_o \quad \mu_{wo} = \alpha_w \mu_w + \alpha_o \mu_o \quad (3.3)$$

The continuity equation, which describes mass conservation in the whole domain, i.e., in the water and oil region, where the velocity vector is \mathbf{v} , is given by

$$\nabla \cdot \mathbf{v} = 0 \quad (3.4)$$

Similarly, the linear momentum conservation principle is applied in the whole domain

$$\frac{\partial}{\partial t}(\rho_{wo} \mathbf{v}) + \nabla \cdot (\rho_{wo} \mathbf{v} \mathbf{v}) = -\nabla p + \nabla \cdot (2\mu_{wo} \mathbf{D}) + \rho_{wo} \mathbf{g} + \mathbf{f}_{int} \quad (3.5)$$

where ρ_{wo} is the average density, \mathbf{g} represents gravity acceleration and $\mathbf{D} = 0.5[\nabla \mathbf{v} + (\nabla \mathbf{v})^T]$ is the strain rate tensor. The source term \mathbf{f}_{int} in momentum equation, added for modeling water/oil interfacial tension σ_{wo} effects on fluid motion, is described by the Continuum Surface Force (CSF) model proposed by Brackbil *et al.* (1992) and expressed by

$$\mathbf{f}_{int} = \sigma_{wo} \frac{\rho_{wo} \kappa \nabla \alpha_o}{\frac{1}{2}(\rho_w + \rho_o)} \quad (3.6)$$

this term is known in the literature as the Continuum Model Surface Force – CSF, where κ is the curvature of the interface, ρ_w is density of water and ρ_o is density of oil.

The boundary conditions which define the solution domain, are applied as shown in Fig. 2, where:

- (1) In inlet 1, the average velocity of oil V_o is taken to be equal to 0.00009 m/s;
- (2) In inlet 2, water flows with a velocity V_w of 0.000417 m/s;
- (3) In the outlet, the gauge pressure is equal to 0 Pa;
- (4) The interface is applying a force, defined previously by Eq. (3.6); and
- (5) Finally, no-slip and zero diffusive mass flux are specified in the walls.

Also, as an initial condition used in this transient problem, the microchannel is filled with the primary phase, which is in this case water represented by white colour.

In order to deal with the interaction between the two immiscible fluids described in the previous section, some parameter that identifies the shear forces acting on the interface needs to be defined. According to Coelho *et al.* (2016) and Santos *et al.* (2016), the interfacial tension is an important property that contributes to the form adopted by the droplets through the interface. In many cases, the convergence of the solution depends on its value. In addition, several other parameters such as viscosities and velocities of both fluids, channels width, numerical parameters, can influence the droplets formation and convergence of the solution process. Their influence

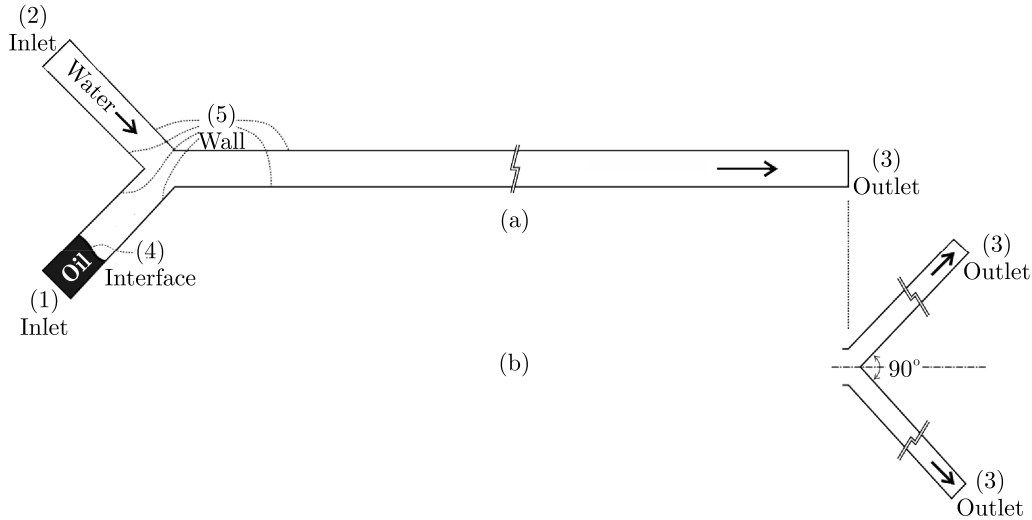


Fig. 2. Boundary conditions at the Y-junction geometry used in this work

in the fluid flow can be better understood using dimensionless numbers, as represented by Eqs. (3.7) to (3.15), the following:

(i) The capillary number Ca reflects the ratio between the viscous forces and the capillary forces. The first term depends on the viscosity of the dispersed fluid, in this case oil μ_o which is injected with an average velocity V_o , and the second term is the interfacial tension between the two fluids σ_{wo}

$$Ca = \frac{\mu_o V_o}{\sigma_{wo}} \quad (3.7)$$

(ii) The comparison between the more viscous fluid, oil μ_o , and less viscous fluid, water μ_w , is represented by the dimensionless viscosity ratio μ_R defined by

$$\mu_R = \frac{\mu_o}{\mu_w} \quad (3.8)$$

(iii) The Reynolds number Re represents the relationship between the inertia forces (represented by the group $\rho_o V_o h$), with the viscous forces of the dispersed fluid, which is oil. The expression is

$$Re = \frac{\rho_o V_o h}{\mu_o} \quad (3.9)$$

where h is the characteristic length chosen to represent the flow, which is in this case the width of the channel through which oil flows. In all simulations performed in this study, the Reynolds number is relatively small ($Re \leq 1$) meaning that the inertial forces are almost insignificant when compared with the viscous forces.

(iv) The way in which droplets are formed throughout the main channel is strongly influenced by the contact angle θ_c of the fluids that are in contact with the walls. Thus, the wettability (or contact angle) indicates which phase is preferably wet to the walls. According to Jamaloei *et al.* (2011), a contact angle equal to zero $\theta_c = 0$ indicates complete wetting of the denser phase (water), $\theta_c = \pi$ rad indicates complete wetting of the less dense phase (oil) and an angle of $\theta_c = \pi/2$ rad indicates that neither of the phases wet preferably than the other. In this study, the contact angle is $\theta_c = 0$ rad.

(v) The flow rates of oil and water are respectively noted q_o and q_w , and the ratio between them is described by

$$q_R = \frac{q_o}{q_w} \quad (3.10)$$

(vi) According to Garstecki *et al.* (2006), the length l of the droplets (Fig. 1a) depends on the flow rate ratio between the two fluids q_R , the width h of the main channel and the constant α depending on the geometry used

$$\frac{l}{h} = 1 + \alpha q_R \quad (3.11)$$

(vii) Based on Coelho *et al.* (2016) and Santos *et al.* (2016), one of the main parameters described in the literature to obtain the convergence of the solution with the explicit approach to time-dependent problems is the Courant number, defined by

$$C_O = \frac{V_m \Delta t}{\Delta x} \quad (3.12)$$

where V_m is the average velocity of the dispersed fluid ($V_m = V_o$), Δx is the size of a representative element of the mesh and Δt is the time-step size. Equation (3.12) which is derived from Eq. (3.12), is known as Courant-Friedrichs-Lewy (CFL)

$$\Delta t_{CFL} = \frac{C_o \Delta x}{V_m} \quad (3.13)$$

the Courant number should be less than 1 ($C_o < 1$) to assure the convergence of iterative solution (Bethke, 2008).

In order to highlight the effects of interfacial tension and viscosities, other equations to determine the time step are presented. One of them is the relation proposed by Brackbill *et al.* (1992) which establishes the time step as a function depending on the mass density of oil and the interfacial tension

$$\Delta t_B = \sqrt{\frac{\rho_o \Delta x^3}{2\pi \sigma_{wo}}} \quad (3.14)$$

another example is the equation proposed by Galusinski and Vigneaux (2008), where the time step Δt_V is depending on the viscosity of oil and the interfacial tension

$$\Delta t_V = \frac{\mu_o \Delta x}{\sigma_{wo}} \quad (3.15)$$

4. Numerical solution of the governing equations

To solve numerically the set of governing equations, Eqs. (3.1), (3.4) and (3.5), it is necessary to discretize it in order to obtain a system of algebraic equations (Patankar, 1980).

4.1. Discretization algorithms

The discrete version of governing equations is solved using the commercial software Ansys Fluent 15.0 with the VOF technique. In this process, one of the key steps is the treatment of the pressure field. In fact, gradients in the pressure appear in the Navier-Stokes equations. However, since we are using an incompressible fluid, the density of each fluid is constant, thus the pressure can not be calculated directly from the equation of state. An alternative way to determine the pressure field is to couple the pressure and the velocity. Three pressure-velocity coupling schemes are available in Fluent: SIMPLE (Semi-Implicit Method for Pressure-Linked Equations); SIMPLEC (SIMPLE Consistent) is an improved version of SIMPLE, and PISO (Pressure Implicit with Splitting of Operators) is using a similar method as SIMPLE and SIMPLEC with a better correction. All three algorithms are used for the pressure-velocity coupling. For more details see

Ferziger and Peric (2002) and Versteeg and Malalasekera (1998). Their effects in the flow field behaviour will be presented and discussed in the results Section.

The PRESTO schemes (Pressure Staggering Option) and Second Order Upwind are used respectively for the interpolation of pressure and velocity. For the evaluation of gradients, the Least Squares Cell based method is used. It is quite accurate and computationally less expensive compared to other methods.

The Geometric Reconstruction (Geo-Reconstruct) method, used for oil and water volumetric fractions, allows good definition of the liquid-liquid interface of the Y-junction since it uses a linear approach to represent the interface between the fluids.

4.2. Mesh test

For the spatial discretization of the domain, three different meshes have been tested, as is shown in Fig. 3 (left) where the maximum size of the rectangular elements is gradually decreased, which means a refined mesh. The first one (Fig. 3a) is the coarsest mesh, containing 1106 rectangular elements and referred as mesh 1. In Fig. 3b, corresponding to the regular mesh contains 4423 rectangular elements. The size of the elements for this mesh is in the range between 0.001 mm and 0.01 mm. Reducing again the size of the rectangular elements leads to the most refined mesh among them (Fig. 3c). This mesh contains 8838 elements. The parameters for each mesh is detailed in Table 1.

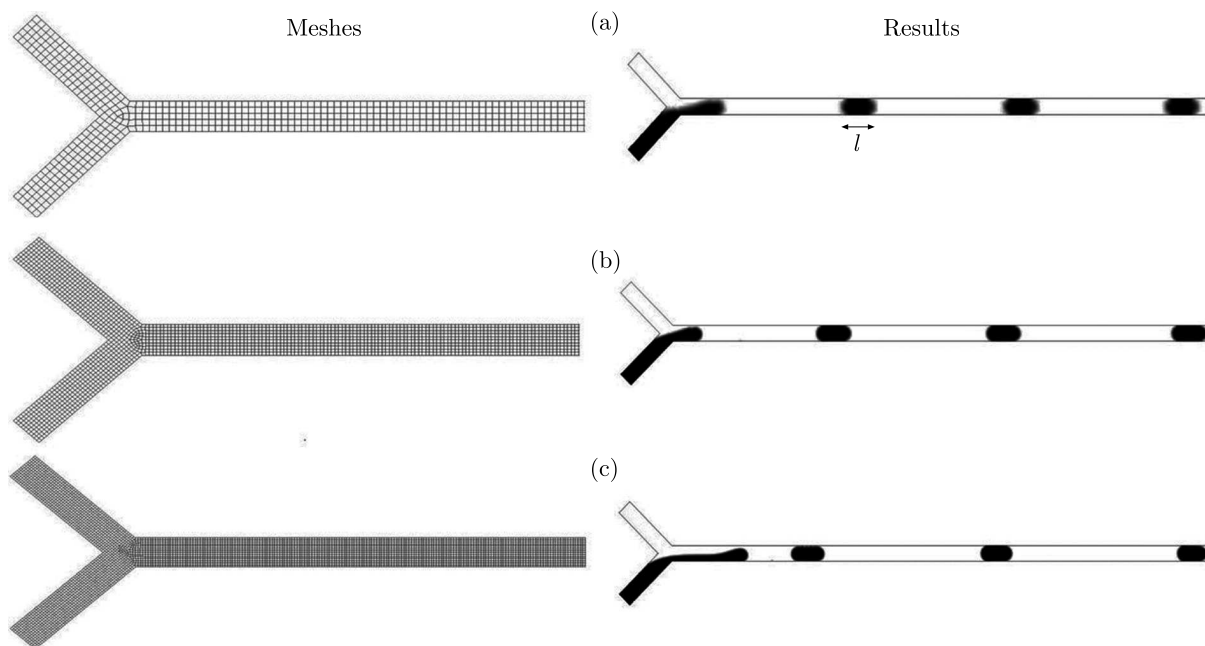


Fig. 3. Mesh (left) and water volume fraction (right) for 3 meshes tested at 13.8 s: (a) coarse mesh, (b) regular mesh, and (c) refined mesh

Table 1. Parameters of the three meshes

Parameters	Mesh 1	Mesh 2	Mesh 3
Number of elements	1106	4423	8838
Minimum size [mm]	0.001	0.001	0.001
Maximum size [mm]	0.02	0.01	0.007

Simulation has been performed for each mesh, with the same boundary conditions. The results are shown in Fig. 3. In the right side of this figure, it can be seen that droplets with similar regularity and shape are obtained for all three meshes. However, the position where the droplet is formed is different from one mesh to another. The way in which droplets are being formed will be explained in the next Section.

In order to choose a better mesh, a comparison between the predicted length of the droplet and the ones obtained for meshes 1 and 2 has been made. For $q_R = 0.2158$ and $h = 0.1$ mm, the length of the droplets obtained from Garstecki equation, Eq. (3.12), with $\alpha = 6.5$ is $l_{Teo} = l = 0.24$ mm. For the three meshes, the length of the droplet obtained numerically l_{Num} is shown in Fig. 4. The relative error is defined as $\varepsilon_R = 100|l_{Num} - l_{Teo}|/l_{Teo}$. After calculations $\varepsilon_{R_{Mesh\ 1}} = 8.33\%$, $\varepsilon_{R_{Mesh\ 2}} = 4.17\%$ and $\varepsilon_{R_{Mesh\ 3}} = 12.50\%$. The relative errors are smaller for Mesh 2. From these results, it is clear that the regular mesh is the most suitable for this geometry, compared to the others. It will be used in the next simulations.

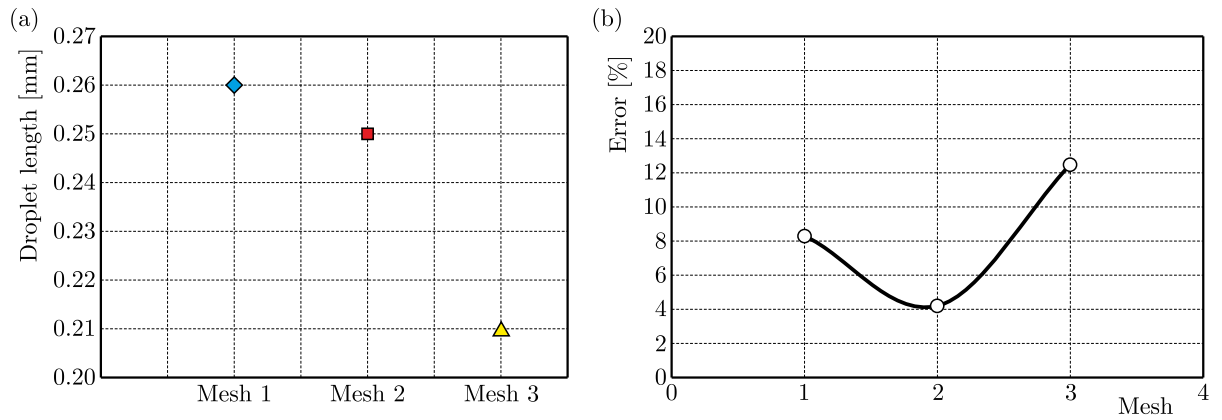


Fig. 4. (a) Length of the generated droplet l_{Num} for each mesh; and (b) comparison between length of the droplet obtained by numerical approach l_{Num} with analytical equation l_{Num}

Although mesh comparisons reported in Fig. 4a is apparently not converging to a constant solution, our main criterion to select the mesh number 2 is the best representation of the analytical equation, Eq. (3.11). The scaling relation proposed by Garstecki *et al.* (2006), obtained by experiments, is commonly applied and used as a reference in the literature. This procedure is adopted because refined mesh were tested, increasing considerable the time computing required to obtain solutions which are not completely converging to a constant droplet length. The comment of Qian and Lawal (2006) “...All these complexities make VOF multiphase flow simulation computationally expensive, and convergence difficult to achieve when compared to its single phase counterpart. In fact, multiphase flow is perhaps the most difficult topic in the CFD simulation...”, it is appropriate at this time.

4.3. Selection of the time-step

In this transient problem, the simulation time t_n is determined from the previous time t_{n-1} by the equation $t_n = t_{n-1} + \Delta t$. The advance in time is repeated until $t_n = t_{final}$, which represents the end of the simulation when $n = N$, where N is the number of time-steps. The choice of the time-step Δt is extremely important for problems with liquid-liquid interfaces. To assure the convergence of the solution, the Courant number should be less than one where fluid particles move from one cell to another within one time step. If it is higher than one, fluid particles move through two or more cells at each time step and this can affect convergence negatively. For $Co = 0.2$, $\Delta x = 10^{-5}$ m, $\sigma_{wo} = 0.0003$ N/m, $V_o = 0.00009$ m/s, $\rho_o = 900$ kg/m³ and $\mu_o = 10$ cP = 0.01 Pa·s, the values for the time step obtained by Eqs. (3.13), (3.14) and (3.15)

are $\Delta t_{CFL} = 0.002$ s, $\Delta t_B = 2.185 \cdot 10^{-5}$ s and $\Delta t_V = 3.33 \cdot 10^{-4}$ s. In simulations performed in this study, it has been used $N = 6900$ time steps of $\Delta t = 0.002$ s, therefore the end of the simulation is at $t_{final} = 13.8$ s.

The nine cases analysed with the values of the dimensionless parameters and the algorithms used are detailed in Table 2. The Reynolds number is $Re = 8.1 \cdot 10^{-4}$ for all the simulated cases.

Table 2. Parameters used in nine simulated cases

Case	Algorithm	Ca Eq. (3.7)	μ_r Eq. (3.8)	qR Eq. (3.10)	Geometry
1	SIMPLE	0.003	10	0.2158	Fig. 1a
2	SIMPLE	0.00474	10	0.2158	Fig. 1a
3	SIMPLE	0.01	10	0.2158	Fig. 1a
4	SIMPLE	0.003	10	0.168	Fig. 1a
5	SIMPLE	0.003	10	0.3	Fig. 1a
6	SIMPLE	0.003	1	0.2158	Fig. 1a
7	SIMPLEC	0.003	10	0.2158	Fig. 1a
8	PISO	0.003	10	0.2158	Fig. 1a
9	SIMPLE	0.003	10	0.2158	Fig. 1b

For a simulation of 13.8 s (6900 time steps), each case takes approximately 56 minutes using a computer ASUS Intel® Core™ i3-4005U CPU@1.7 GHz and 4 GB of RAM.

The convergence criteria is chosen to be 10^{-3} for the residual monitors. For this value, the convergence happens after 9 iterations on average.

5. Results and discussions

The results for all nine cases in Table 2 are explained in the following sections. For Subsections 5.1, 5.2 and 5.3, the physical domain used is defined by Fig. 1a and for Subsections 5.4, the one defined by Fig. 1b is used.

5.1. Microdroplet formation process

Figure 5 shows the time evolution of the droplet formation in the Y-junction for case 1. Initially, all the geometry is filled with water (white colour). From this moment, oil represented by black colour is injected into channel number 1 (according to notations in Fig. 1) with a constant velocity of 0.00009 m/s. In the meantime, water is continuously injected into channel 2 (according to notations in Fig. 1) with a constant velocity of 0.000417 m/s. The formation of droplets can be described as follows. The two immiscible fluids form an interface at the junction (Fig. 5a). The droplet begins to grow due to action of shear stress between the carrier and dispersed phases. Thus the neck width of the droplet becomes smaller until the droplet completely separates from the dispersed phase (Fig. 5b and Fig. 5c) forming two interfaces. At the broken time and due to capillary effects, these two interfaces displace in opposite directions at high velocities. One of the interface, which is always moving forward, forms the downstream meniscus of the droplet recently created. The other interface is moving backward (Fig. 5c) and because the fluid injection is constant, this negative velocity becomes zero and then positive. This process repeats itself periodically and a pattern of a droplet is formed in the main channel (Fig. 5d). The droplets areas equally spaced, have the same length and diameter larger than the main channel. These characteristics depend on the interfacial tension, viscosity ratio and flow rate ratio between the two fluids, besides of the geometry used. In this frame, it is also possible to observe the zero contact angle between the system oil/water/wall.

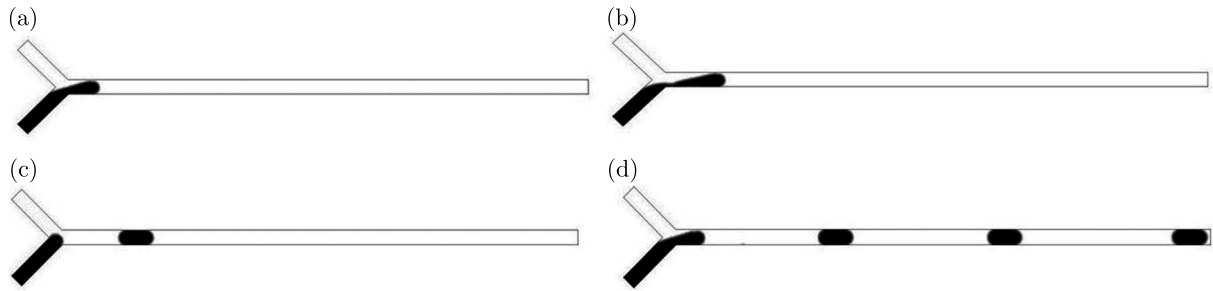


Fig. 5. Time evolution of droplet formation at $Ca = 3 \cdot 10^{-3}$ and $q_R = 0.216$ at different time instants: (a) 6 s, (b) 6.5 s, (c) 7 s, and (d) 12.8 s

The coherence of the previous results can also be explained by variation of pressure through the geometry. The contour of pressure is shown in Fig. 6 for four different time instants: 6 s, 6.5 s, 7 s and 12.8 s which are also the same times used in Fig. 5.

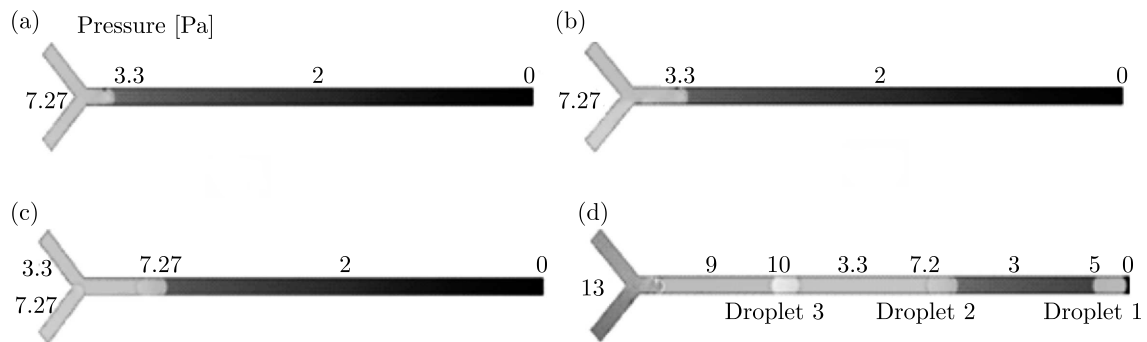


Fig. 6. Contour of pressure (in Pa) for the Y-junction at $Ca = 3 \cdot 10^{-3}$ and $q_R = 0.216$ at different instants: (a) 6 s, (b) 6.5 s, (c) 7 s and (d) 12.8 s

Figure 6a represents the contour of pressure at 6 s after the injection of the fluids, which is when the interface arrives to the junction. Because oil (channel 1) is ten times more viscous than water (channel 2), the pressure necessary to facilitate its movement through the channel is increasing, the pressure in the outlet is almost equal to zero, as set in the boundary conditions. When the dispersed fluid (oil) reaches the junction, the pressure drives a part of that fluid into the main channel and blocks the rest of the dispersed fluid from channel 1, as shown in Fig. 6b. Thus, as the carrier fluid (water) is moving through the secondary channel, a complete droplet is being formed. In Fig. 6c, the upstream pressure decreases once the droplet separates from the junction. This instantaneous drop in pressure happens because the blockage of the dispersed fluid stops and the second droplet starts forming. This formation process repeats periodically as both fluids are continuously injected. Figure 6d represents the contour of pressure when the first droplet reaches the outlet causing a small increase in the outlet pressure.

For this case, the contour of pressure is illustrated by a diagram in Fig. 7. The peaks in this figure represent the positions of droplets in the current instant ($t = 13.8$ s) when they move along the main channel whose length is 0.0036 m ($36h$, with $h = 0.1$ mm). One droplet is situated in a position $x = 0.0015$ m from the junction, almost half length of the channel, and another is at $x = 0.0027$ m, close to the exit plane. The first droplet reaches the outlet, its pressure is equal to zero. In Fig. 7, it can be seen that the pressure in the droplet is as high as the droplet is close to the junction. This is due to the blockage exerted by the pressure, which has been explained previously.

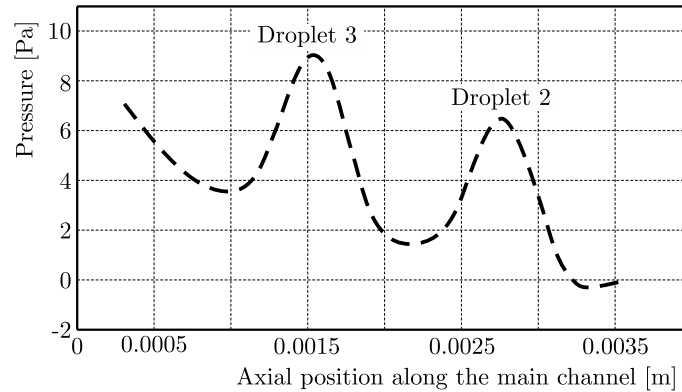


Fig. 7. Evolution of pressure in the main channel at the time instant 13.8 s

5.2. Dimensionless numbers effect

5.2.1. Capillary number

The way in which droplets are formed is highly influenced by the capillary number. Simulations have been performed for three different values of the capillary number: cases 1, 2 and 3 (refer to Table 1).

For case 1, with $Ca = 0.003$ the droplets or droplets generation occurs at the two-phase intersection and they have an elongated shape in the continuous phase microchannel. This regime is called “Squeezing regime” Tarchichi *et al.* (2013) (Fig. 8a). When Ca is increased, the droplets generated do not occupy the entire width of the continuous phase microchannel at the junction and they are smaller than the width of the continuous phase channel (Fig. 8b). This regime of droplet formation is known as “Dripping regime” (Tarchichi *et al.*, 2013). In case 3, where Ca is increased again, the dispersed phase forms a long neck in the main channel (Fig. 8c). In this regime named “Jetting regime” (Tarchichi *et al.*, 2013), the droplet or droplet formation occurs downstream at a some distance from the junction.

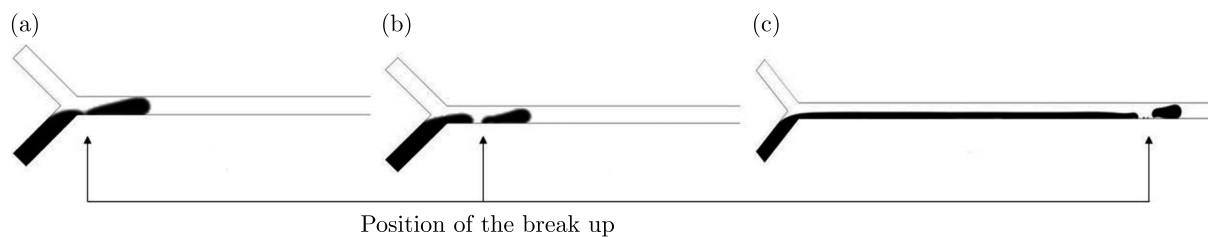


Fig. 8. Position of droplet breakup for three regimes: (a) squeezing at $Ca = 0.003$, (b) dripping at $Ca = 0.00474$ and (c) jetting at $Ca = 0.01$

5.2.2. Flow rate ratio

Here we investigate the influence of the flow rate ratio ($q_R = q_o/q_w$) when the capillary number and the viscosity ratio are constant. Three different flow rate ratios are used: $q_R = 0.168$, $q_R = 0.2158$ and $q_R = 0.3$ corresponding respectively to cases 1, 4 and 5, respectively. Figure 9 shows length of the droplet generated for each flow rate ratio. When q is small (case 4), the droplets are pinched off at the junction. The length of the droplets in this case is $l = 0.23$ mm. However when $q = 0.2158$, the detachment point moves from the corner downstream (Fig. 9b). In this case, the droplets have a size equal to 0.25 mm. When $q = 0.3$, the length of the droplet is $l = 0.26$ mm.

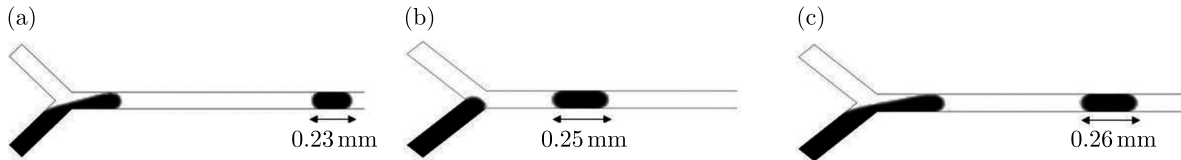


Fig. 9. Droplet length for the three flow rate ratios: (a) $q_R = 0.17$, (b) $q_R = 0.2158$ and (c) $q_R = 0.3$

The results obtained confirm Eq. (3.11) which relates the size of the droplet with the flow rate ratio.

5.2.3. Viscosity ratio

Here we investigate the role of the viscosity ratio ($\mu_R = \mu_o/\mu_w$) defined by Eq. (3.8) in the droplet formation process. The flow rate ratio and the capillary number are kept constant. Figure 10 shows the droplet formation for $\mu_R = 10$ and $\mu_R = 1$, respectively, at the same instant $t = 12.8$ s. With a small viscosity ratio, the droplet formation occurs in the junction, which does not happen with a viscosity ratio equal to 10. Also, it can be seen in Fig. 10 that the decreasing viscosity ratio leads to smaller droplets with higher frequency. At the same instant, three droplets are formed for $\mu_R = 10$, where we have four droplets for $\mu_R = 1$. In fact, the breakup of the droplet is controlled by competition between viscous shear force and capillary force; which means when Ca is constant, the viscosity becomes a key factor in the droplet formation. That is why smaller droplets are obtained when $\mu_R = 1$.

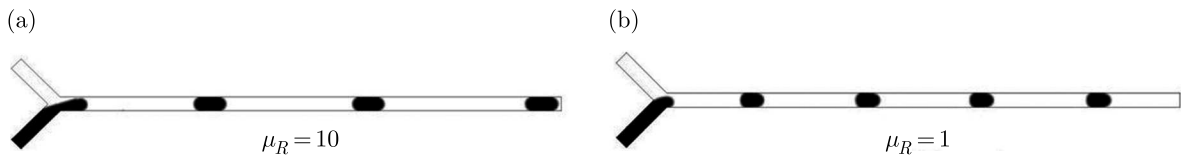


Fig. 10. Water volume fraction for two different viscosity ratios: (a) $\mu_R = 10$ and (b) $\mu_R = 1$

5.3. Influence of discretization algorithms

In this part, we investigate the effect of pressure-velocity schemes. Periodic droplets with a similar shape are obtained for all three algorithms (Fig. 11a, 11b and 11c). In this figure, it can be seen that the position of the droplet is little different from an algorithm to another. In fact,

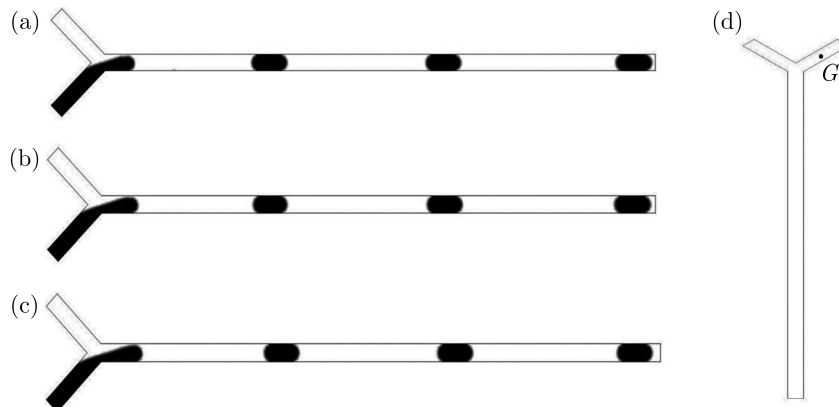


Fig. 11. Oil volume fraction for three algorithms: (a) SIMPLE, (b) SIMPLEC, and (c) PISO at the time instant 12.8 s; (d) position of the center of gravity of the first inlet

the difference between these algorithms lies in the pressure correction and the convergence speed, as has been mentioned in Section “Discretization algorithms”. To have a better understanding of their effects, the time evolution of pressure is compared in each case. The pressure is measured at the same location (point G) which is the centre of gravity of channel 2 (Fig. 11d). This position is chosen because of the results in the contour of pressure shown in Fig. 6 and already commented. Indeed, the pressure in channel 2 varies periodically during the formation of a droplet. Thus, it would be easier to compare the effect of these algorithms in that position.

Figure 12 represents the time evolution of the pressure at the point G for the three algorithms. In this figure, at the beginning, SIMPLE and SIMPLEC are more stable than PISO. However, from the third droplet ($t = 9.5$ s; $N = 4750$ time steps), PISO becomes more stable and accurate compared to the other algorithms, the oscillations amplitude in PISO is smaller than in the others. In fact, PISO is more recommended for simulation with large time steps, as has been mentioned in Section “Discretization algorithms”. The results for SIMPLE and SIMPLEC are quite similar during the simulation. In fact, differences between the methods arise more from the single-phase flow. Also, the number of iterations for each time step is quite smaller in PISO than in the other algorithms. This leads to a faster simulation. All the results confirm that the algorithm PISO is better for a two-phase flow like that considered in our case.

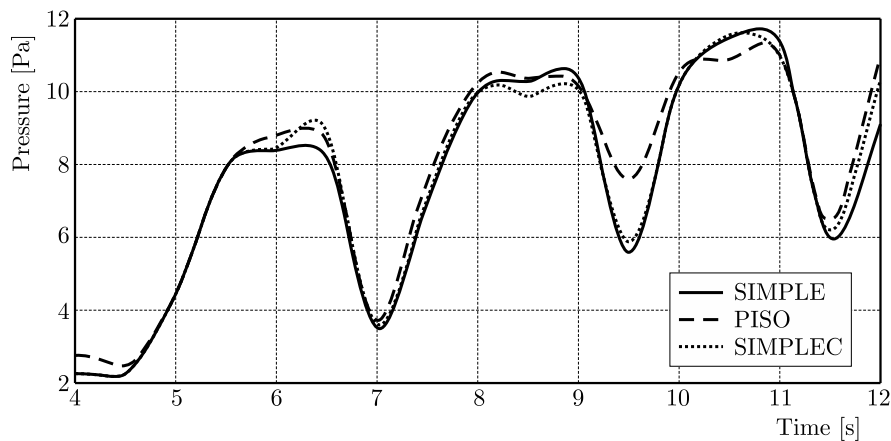


Fig. 12. Time evolution of pressure at the point G (Fig. 11d) for the three algorithms SIMPLE, SIMPLEC and PISO

5.4. Microdroplet breakup process

In this part, the geometry described in Fig. 1a is modified by placing two orthogonal channels at the outlet, thereby forming another Y-junction but with length $10h$ each. A theoretical mathematical point with zero radius of curvature represents the intersection between the two walls of the channels. The objective is to capture the breakup process of droplets formed in the first stage. Figure 13 represents the time evolution of the droplet breakup. When the droplet arrives at the junction, it is deformed symmetrically by the driving fluid (water in this case) in the center of the junction (Fig. 13a). Thus, the actions of the shear force and pressure drive the droplet to each outlet, thereby forming two half-droplets connected by the neck (Fig. 13b). From this moment, the neck becomes smaller until the breakup occurs (Fig. 13c). This process repeats itself when the droplet reaches the junction (Fig. 13d).

Figure 14 shows details of the breakup process with the velocity vectors in the junction. The uniform repartition of the velocity vectors in the two exit branches leads the droplet to form two identical liquid fingers in the upper and lower branch (Fig. 14a and Fig. 14b). When the droplet completely penetrates the branches, the droplet creates restriction to the fluid flow, being necessary a higher pressure to sustain the motion. Thus, a neck is formed at the junction,

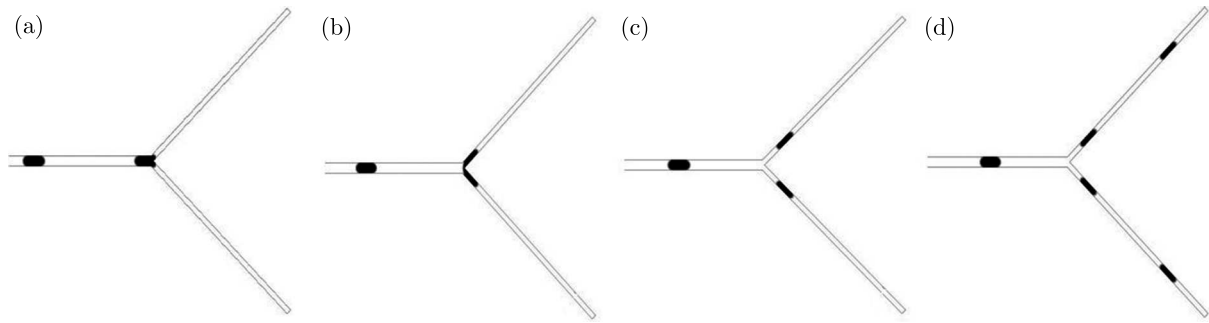


Fig. 13. Droplet breakup in the Y-exit

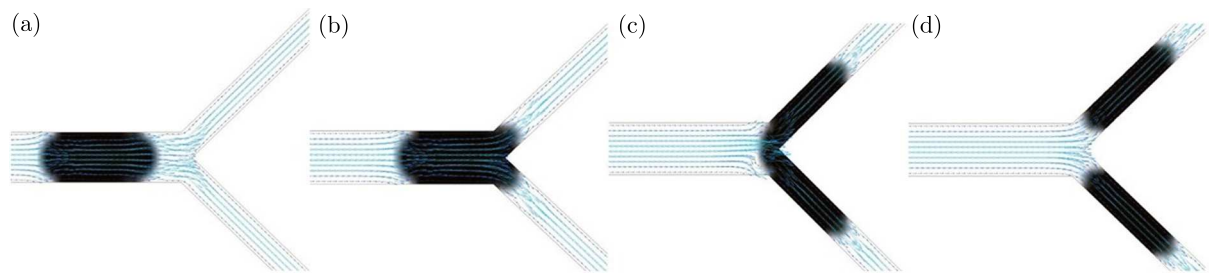


Fig. 14. Velocity fields during the droplet breakup

as it can be seen in Fig. 14c. As the droplet moves through the exit channels, the neck becomes gradually smaller until the droplet breaks into two daughter ones. Once the breakup occurs, the restriction stops, thus the flow restarts normally and the two half-droplets are driven to in the outlets (Fig. 14d).

6. Conclusions

In the study, we investigate the formation process of droplets using geometry called Y-junction. The capillary number, the flow rate ratio and the viscosity ratio are found to be important in droplet formation, and these parameters together control the complex droplet generation process. Our results are in phase with what can be found in the literature. The analysis of pressure field shows that the pressure plays a major role in droplet formations.

The predicted length of droplets, as described by Tarchichi *et al.* (2013) and Garstecki *et al.* (2006) for the squeezing regime, is confirmed through simulations performed in this work, since the analytical and numerical values are almost the same.

The results of the simulations reveal that the algorithm PISO is the most suitable for a two phase flow problem, at least in the range of parameters considered in this work. SIMPLE and SIMPLEC do not show any particular difference in the results, due to the regime of the flows. However, the results for SIMPLE and SIMPLEC are also satisfactory.

The process of breaking the bubbles using a second Y-junction in the end shows a symmetric distribution of the droplets in the two outlet channels. The droplets divide into parts of equal size due to the same conditions in the two outlets (0 Pa). The dimensionless numbers also can affect the breakup process. In fact, a high value of the capillary number can lead to an asymmetric distribution.

Acknowledgement

The authors are thankful to international research program Capes/Brafitec (Coordenação de Aperfeiçoamento de Pessoal de Nível Superior/Brasil France Ingénieur Technologie) for providing the scholarship to carry out this study.

References

1. BETHKE C.M., 2008, *Geochemical and Biogeochemical Reaction Modeling*, Second Edition, Cambridge University Press, p. 297
2. BRACKBILL J.U., KOTHE D.B., ZEMACH C., 1992, A continuum method for modeling surface tension, *Journal of Computational Physics*, **100**, 335-354
3. COELHO J.K., PENA M.D., ROMERO O.J., 2016, Pore-scale modeling of oil mobilization trapped in a square cavity, *IEEE America Latina*, **14**, 4, 1800-1807, DOI: 10.1109/TLA.2016.7483518
4. CONG Z., ZHU C., FU T., MA Y., 2014, Bubble breakup and distribution in asymmetric Y-bifurcating microchannel, *CIESC Journal*, **65**, 1, 93-99
5. Dolomite, 2015, *Droplet microfluidics brochure for biology, food and cosmetics, drug discovery, chemistry*, <http://www.dolomite-microfluidics.com/en/applications>
6. FERZIGER J.H., PERIC M., 2002, *Computational Methods for Fluid Dynamics*, Springer, Berlin
7. FLUENT, 2012, Ansys Inc. Fluent – Theory Guide Documentation
8. FU T., MA Y., FUNFSCHILLING D., LI H.Z., 2011, Dynamics of bubble breakup in a microfluidic T-junction divergence, *Chemical Engineering Science*, **66**, 4184-4195
9. FU T., MA Y., LI H.Z., 2014, Hydrodynamic feedback on bubble breakup at a T-junction within an asymmetric loop, *AIChE Journal*, **60**, 5, 1920-1929
10. GALUSINSKI C., VIGNEAUX P., 2008, On stability condition for bifluid flows with surface tension: Application to microfluidics, *Journal of Computational Physics*, **227**, 6140-6164
11. GARSTECKI P., FUERSTMAN M.J., STONE H.A., WHITESIDES G.M., 2006, Formation of droplets and bubbles in a microfluidic T-junctions: scaling and mechanism of break-up, *Lab on a Chip*, **6**, 437-446
12. HIRT C.W., NICHOLS B.D., 1981, Volume of fluid (VOF) method for the dynamics of free boundaries, *Journal of Computational Physics*, **39**, 201-225
13. JAMALOEI B.Y., KHARRAT R., ASGHARI K., 2011, The influence of pore wettability on the microstructure of residual oil in surfactant-enhanced water flooding in heavy oil reservoirs: Implications for pore-scale flow characterization, *Journal of Petroleum Science and Engineering*, **7**, 1, 121-134
14. LIH F.L., MIAO J.M., 2015, Effect of junction configurations on microdroplet formation in a T-Junction microchannel, *Journal of Applied Mechanics and Technical Physics*, **56**, 2, 220-230
15. LIU Z.M., LIU L.K., FENG S., 2015, Effects of geometric configuration on droplet generation in Y-junctions and anti-Y-junctions microchannels, *Acta Mechanica Sinica*, **31**, 5, 741-749
16. PATANKAR S.V., 1980, *Numerical Heat Transfer and Fluid Flow* (Series in computational methods in mechanics and thermal sciences), Hemisphere Publishing Corporation, Washington-New York-London
17. QIAN D., LAWAL A., 2006, Numerical study on gas and liquid slugs for Taylor flow in a T-junction microchannel, *Chemical Engineering Science*, **61**, 7609-7625, DOI: 10.1016/j.ces.2006.08.073
18. SANTOS K.B., ROMERO O.J., MENEGUELO A.P., RIBEIRO D.C., 2016, A numerical investigation of immiscible water-oil displacement in simplified porous media, *IEEE America Latina*, **14**, 5, 2175-2183, DOI: 10.1109/TLA.2016.7530411
19. TARCHICHI N., CHOLLET F., MANCEAU J., 2013, New regime of droplet generation in a T-Shape microfluidic junction, *Journal of Microfluidics and Nanofluidics*, **14**, 1, 45-51
20. TICE J.D., LYON A.D., ISMAGILOV R.F., 2004, Effects of viscosity on droplet formation and mixing in microfluidic channels, *Analytica Chimica Acta*, **507**, 1, 73-77
21. VERSTEEG, H.K., MALALASEKERA W., 1998, *An Introduction to Computational Fluid Dynamics*, Longman, London
22. WACLAWCZYK T., KORONOWICZ, T., 2008, Comparison of CICSAM and HRIC high-resolution schemes for interface capturing, *Journal of Theoretical and Applied Mechanics*, **46**, 2, 325-345

NUMERICAL CREEP ANALYSIS OF FGM ROTATING DISC WITH GDQ METHOD

HODAIS ZHARFI, HAMID EKHTERAEE TOUSSI

Ferdowsi University of Mashhad, Faculty of Engineering, Mashhad, I.R. Iran

e-mail: ekhteraee@um.ac.ir

Rotating discs are the vital part of many kinds of machineries. Usually, they are operating at relatively high angular velocity and temperature conditions. Accordingly, in practice, the creep analysis is an essential necessity in the study of rotating discs. In this paper, the time dependent creep analysis of a thin Functionally Graded Material (FGM) rotating disc investigated using the Generalized Differential Quadrature (GDQ) method. Creep is described with Sherby's constitutive model. Secondary creep governing equations are derived and solved for a disc with two various boundary conditions and with linear distribution of SiC particles in pure Aluminum matrix. Since the creep rates are a function of stresses, time and temperature, there is not a closed form solution to these equations. Using a solution algorithm and the GDQ method, a solution procedure for these nonlinear equations is presented. Comparison of the results with other existing creep studies in literature reveals the robustness, precision and high efficiency beside rapid convergence of the present approach.

Keywords: creep, FGM, GDQ method, rotating disc, boundary conditions

1. Introduction

A wide area research has assigned to rotating discs because of their numerous utilizations in various industries and rotating machines such as: gas and steam turbines, pumps, turbo generators, compressors, flywheels, ship propellers and automotive braking systems (Gupta *et al.*, 2005; Hojjati and Hassani, 2008; Singh and Ray, 2002). In most of these applications, discs have to operate at high rotational speed leading to large centrifugal forces, and in the presence of high temperatures, the materials strength can be reduced explicitly. These operating conditions lead to a vast continuous time dependent deformations, so the creep phenomenon finds the priority in the research. Creep deformation can affect the performance of systems entirely. As an example, in a turbine rotor there is always a possibility that the heat from the external surface is transmitted to the shaft and then to the bearings, which has adverse effects on the functioning and efficiency of the rotor (Bayat *et al.*, 2008). Under high thermo-mechanical loading, the monolithic materials cannot do well. Augmenting the second strong and stable phase to the based phase causes a significant reduction in creep deformations. In other words, increasing the reinforcements leads to creep strength rising. For this reason and because of more other great benefits of FGM materials, these materials have attracted the interest of many researchers (Loghman *et al.*, 2011; Ghorbani, 2012). In recent years, creep analysis in rotating discs made of functionally graded materials has been addressed by many researchers.

Whal *et al.* (1954) studied steady state creep behavior of a turbine rotating disc using a power function creep law and Huber-Mises-Hencky and Tresca yield criteria. They compared results of their work with the experimental results. Arya and Bhatnagar (1979) investigated creep responses of an orthotropic rotating disc. They illustrated that tangential stress in all over the disc and the radial creep rate at inner radius increased with intensification of material anisotropy. Nieh (1984) demonstrated that a disc with SiC whiskers in Aluminum matrix

has a better creep responses than a disc made of pure Aluminum. Białkiewicz (1986) presented a theoretical finite strain analysis in rotating discs based on creep rupture using Kachanov theory and Norton's creep law. Bhatnagar *et al.* (1986) studied steady state creep behavior in three different discs with anisotropic materials. The discs had constant, linear and hyperbolic decreasing thicknesses. The results illustrated that discs with decreasing thickness in the radial direction had better creep responses. Pandey *et al.* (1992) studied steady state creep behavior of an Al-SiC composite rotating disc in a uniaxial load state and temperature between 623-723 K. They investigated various compositions of particle size (45.9 μm , 14.5 μm , 1.7 μm) with the total volume content of 10%, 20%, and 30%. They observed that the disc with finer particles shows the better creep responses. Gupta *et al.* (2004) investigated the secondary creep response in a rotating disc made of pure Aluminum with SiC particle distribution in the radial direction. The creep law was Sherby's model. Their results showed that the tangential and radial stresses were not affect by governing temperature and particle distributions. Radial and tangential creep rate reduced with particle size reduction, additional of particle volume content and decreased governing temperature. Singh and Ray (2001) studied secondary creep behavior in a thin anisotropic rotating disc made of Aluminum with SiC whickers. The effects of anisotropy and non-homogenous distribution of reinforcements on creep behavior of the rotating disc were investigated.

The Generalized Differential Quadrature method was proposed by Bellman *et al.* (1972) and extended by Shu and coworkers (Shu and Richards, 1992). In this numerical method, function derivatives are approximated in terms of linear summation and weighting coefficients in various grid points. Computation of the weighting coefficient is done using high order polynomial simulation and linear vector space analysis. The weighting coefficient for the first order derivatives is computed by a simple algebraic formulation and higher order coefficients are obtained using a recursive relationship based on the first order weighting coefficient. The major advantage of the GDQ method over the DQ method which was extended by Bellman *et al.* (1972), is its ease in computing the weighting coefficients without any restriction to the grid point selection. The GDQ method has been successfully applied to some fluid flow problems (Shu *et al.*, 1995) and structural vibration analysis (Shu, 1996). In all cases, the method valuable characteristic such as high precision and fast convergence was confirmed.

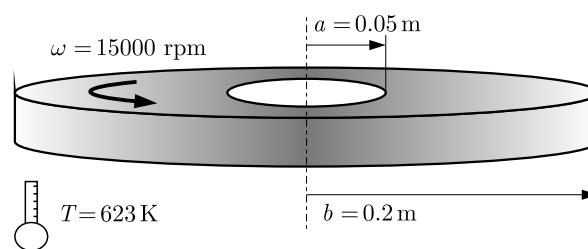


Fig. 1. Studied disc and its parameter

In this paper, the generalized differential quadrature method is used to obtain numerical solution of creep governing equations. For this purpose, the thermo-elastic creep equations of an FGM rotating disc shown in Fig. 1, under free-free and fixed-free boundary conditions is derived. Using a solution algorithm and the GDQ method, creep response of the considered structure is achieved. There is no modeling involved, and the convergence to the final response is very fast. Comparison of the results also illustrates that the method is very efficient and accurate. It avoids simplifications and restrictions which other creep solution methods in the literature are involved, therefore it is a great merit for creep studies of structures.

2. Mathematical formulation

Before starting to develop a closed form solution for the distribution of creep stress and deformation, there are some assumptions that must be asserted. Amongst them presumptions are made that the material of the disc is isotropic and its yield criterion complies with the Huber-Mises-Hencky model. In addition, it is supposed that compared to other dimensions of the disc its thickness is too small so that axial stresses can be ignored and plain stress conditions can be assumed.

The total strain in an FGM rotating disc is an ensemble of elastic, thermal and creep strains in the following form

$$\varepsilon_{total} = \varepsilon_{elastic} + \varepsilon_{thermal} + \varepsilon_{creep} \quad (2.1)$$

For derivation of the primary and secondary creep equation, at first we use a combination of the strain-displacement relation and Eq. (2.1)

$$\begin{aligned} \varepsilon_r &= \frac{du}{dr} = \frac{1}{E}(\sigma_r - \nu\sigma_\theta) + \alpha T + \varepsilon_{r,c} \\ \varepsilon_\theta &= \frac{u}{r} = \frac{1}{E}(\sigma_\theta - \nu\sigma_r) + \alpha T + \varepsilon_{\theta,c} \end{aligned} \quad (2.2)$$

In the above two equations, ε_r and ε_θ are the radial and tangential strains. σ_r and σ_θ are the radial and tangential stresses. u is the radial displacement and E , α and T are the modulus of elasticity, thermal expansion coefficient and governing temperature in Kelvin, respectively. $\varepsilon_{r,c}$ and $\varepsilon_{\theta,c}$ are the radial and tangential creep strains.

The stress relations can be concluded from Eqs. (2.2) as below

$$\begin{aligned} \sigma_r &= \frac{E}{1-\nu^2} \left[\frac{du}{dr} + \nu \frac{u}{r} - (1+\nu)\alpha T - (\varepsilon_{r,c} + \nu\varepsilon_{\theta,c}) \right] \\ \sigma_\theta &= \frac{E}{1-\nu^2} \left[\frac{u}{r} + \nu \frac{du}{dr} - (1+\nu)\alpha T - (\nu\varepsilon_{r,c} + \varepsilon_{\theta,c}) \right] \end{aligned} \quad (2.3)$$

Using the equilibrium condition for an element of the rotating disc in form of Fig. 2, we obtain the equilibrium equation as

$$\frac{d\sigma_r}{dr} + \frac{\sigma_r - \sigma_\theta}{r} + \rho r \omega^2 = 0 \quad (2.4)$$

With replacing the radial and tangential stresses from Eqs. (2.3) into Eq. (2.4), the simplest form of the creep equation is obtained as below

$$A \frac{d^2u}{dr^2} + B \frac{du}{dr} + Cu + D = 0 \quad (2.5)$$

In which the coefficients A , B , C and D in Eq. (2.5) presented in relations given below. It should be noted that all FGM disc parameters are a function of the radius

$$\begin{aligned} A &= \frac{E}{1-\nu^2} \\ B &= \frac{E}{r(1+\nu)} + \frac{1}{1-\nu^2} \frac{dE}{dr} + \frac{2\nu E}{(1-\nu^2)^2} \frac{d\nu}{dr} + \frac{\nu E}{r(1-\nu^2)} \\ C &= \frac{-E}{r^2(1+\nu)} + \frac{\nu}{r(1-\nu^2)} \frac{dE}{dr} + \frac{2E\nu^2}{r(1-\nu^2)^2} \frac{d\nu}{dr} + \frac{E}{r(1-\nu^2)} \frac{d\nu}{dr} - \frac{\nu E}{r^2(1-\nu^2)} \\ D &= \frac{E}{r(1-\nu^2)} [(\nu-1)\varepsilon_{r,c} + (1-\nu)\varepsilon_{\theta,c}] \\ &\quad + \frac{1}{1-\nu^2} \left[(1-\nu^2) \frac{dE}{dr} + 2\nu E \frac{d\nu}{dr} \right] [-(1+\nu)\alpha T - \varepsilon_{r,c} - \nu\varepsilon_{\theta,c}] \\ &\quad + \frac{E}{1-\nu^2} \left[-\frac{d\nu}{dr} \alpha T - (1+\nu) \frac{d\alpha}{dr} T - (1+\nu)\alpha \frac{dT}{dr} - \frac{d\varepsilon_{r,c}}{dr} - \frac{d\nu}{dr} \varepsilon_{\theta,c} - \nu \frac{d\varepsilon_{\theta,c}}{dr} \right] \end{aligned} \quad (2.6)$$

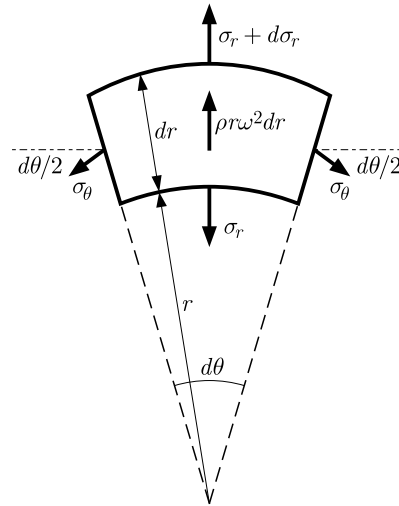


Fig. 2. Schematic of an element of the rotating disc

Creep governing equation for the rotating disc in terms of the displacement rate can be represented as

$$A \frac{d^2 \dot{u}}{dr^2} + B \frac{\dot{u}}{dr} + C \dot{u} = -\dot{D} \quad (2.7)$$

where \dot{u} is the radial displacement rate, A , B and C are presented in Eqs. (2.6)₁₋₃ and \dot{D} is a function of the creep rates as below

$$\begin{aligned} \dot{D} = & \frac{E}{r(1-\nu^2)} [(\nu-1)\dot{\epsilon}_{r,c} + (1-\nu)\dot{\epsilon}_{\theta,c}] + \frac{1}{1-\nu^2} \left[(1-\nu^2) \frac{dE}{dr} + 2\nu E \frac{d\nu}{dr} \right] (-\dot{\epsilon}_{r,c} - \nu\dot{\epsilon}_{\theta,c}) \\ & + \frac{E}{1-\nu^2} \left[-\frac{\dot{\epsilon}_{r,c}}{dr} - \frac{d\nu}{dr} \dot{\epsilon}_{\theta,c} - \nu \frac{\dot{\epsilon}_{\theta,c}}{dr} \right] \end{aligned} \quad (2.8)$$

where $\dot{\epsilon}_{r,c}$ and $\dot{\epsilon}_{\theta,c}$ are the radial and tangential creep rate components, respectively, which can be computed using Sherby's creep law as

$$\dot{\epsilon}_{r,c} = \frac{[M(\sigma_e - \sigma_0)]^n}{2\sigma_e} (2\sigma_r - \sigma_\theta) \quad \dot{\epsilon}_{\theta,c} = \frac{[M(\sigma_e - \sigma_0)]^n}{2\sigma_e} (2\sigma_\theta - \sigma_r) \quad (2.9)$$

where in the above two equations, n is the creep exponent and, in this study, is considered to be 8. σ_e is the effective stress which is obtained from the Huber-Mises-Hencky isotropic yield criterion for the plane stress problem as Eq. (2.10). M and σ_0 are creep parameters and depend on the particle size P which is considered to be $1.7 \mu\text{m}$, particle distribution function $v(r)$, and the level of prevailing temperature T . Based on the experimental creep data reported by Pandey *et al.* (1992) and using a regression technique, Gupta *et al.* (2004) represented M and σ_0 as the following functions Eqs. (2.11)

$$\sigma_e = \sqrt{\sigma_r^2 + \sigma_\theta^2 - \sigma_r \sigma_\theta} \quad (2.10)$$

and

$$\begin{aligned} \ln M = & -35.38 + 0.2077 \ln P + 4.98 \ln T - 0.622 \ln v(r) \\ \sigma_0 = & -2.11916 - 0.03507P + 0.01057T + 1.00536v(r) \end{aligned} \quad (2.11)$$

As it is mentioned above, no exact solution to Eq. (2.7) can be obtained because its right hand side contains the functions of creep rates which all are time, stress and temperature dependent. However, there are numerous numerical methods for solving this problem. In this study, the Generalized Differential Quadrature method is used with a solution technique which is explained in the next section.

3. Solution algorithm

The procedure of creep analysis in an FGM rotating disc is initiated with a GDQ thermo-elastic solution of Eq. (2.5) in which the creep strains are ignored. Afterwards, using this displacement field, the radial and tangential stresses are calculated using Eqs. (2.3). Within this stress field, the distribution of radial and tangential strain rates is obtained using Eqs. (2.9). Then with GDQ analysis of Eq. (2.7), the displacement rate can be computed so the distribution of the radial and tangential stress rates are obtained. Afterwards, by selecting a suitable time interval Δt , the next radial and tangential stress at the next time step are calculated using equations

$$\sigma_{t+1} = \dot{\sigma}_t \Delta t + \sigma_t \quad \varepsilon_{t+1} = \dot{\varepsilon}_t \Delta t + \varepsilon_t \tag{3.1}$$

This procedure is continued until the stress distributions converge and reach the steady state condition.

As mentioned above, for the numerical creep analysis of the FGM rotating disc, a numerical procedure is inevitable. In this study the Generalized differential Quadrature method is used because of high precision and fast convergence of this method. The Differential Quadrature idea was proposed by Bellman *et al.* (1972), and extended by many other researchers later on. In this method, the partial differential of a function with respect to a coordinate direction is expressed as a linear weighted sum of all the functional values at all grid points in that direction (Tornabene *et al.*, 2016). For a smooth function $f(r)$, GDQ discretizes its n -th order derivative with respect to r at the grid point (r_i) as

$$f_r^{(n)}(r_i) = \sum_{k=1}^N a_{ik}^{(n)} f(r_k) \quad n = 1, 2, \dots, N - 1 \quad i = 1, 2, \dots, N \tag{3.2}$$

where N is the number of grid points in the r direction. $a_{ik}^{(n)}$ is the weighting coefficient for the second and higher order derivative which can be completely determined from the first order derivatives as

$$a_{ij}^{(n)} = \begin{cases} n \left(a_{ii}^{(n-1)} a_{ij}^{(1)} - \frac{a_{ij}^{(n-1)}}{r_i - r_j} \right) & j \neq i \\ \sum_{k=1, k \neq i}^N a_{ik}^{(n)} & j = i \end{cases} \tag{3.3}$$

for $i, j = 1, 2, \dots, N, \quad n = 2, 3, \dots, N - 1$

In the above equation $a_{ij}^{(1)}$ is the first weighting coefficient to be obtained using

$$a_{ij}^{(1)} = \begin{cases} \frac{A^{(1)}(r_i)}{(r_i - r_j)A^{(1)}(r_j)} & j \neq i \\ \sum_{k=1, k \neq i}^N a_{ik}^{(1)} & j = i \end{cases} \tag{3.4}$$

for $i, j = 1, 2, \dots, N$

where

$$A^{(1)}(r_i) = \prod_{j=1, j \neq i}^N (r_i - r_j) \tag{3.5}$$

When the coordinates of grid points are known, the weighting coefficient and so the discretized derivative can be easily calculated from Eqs. (3.2)-(3.5) (Shu and Chew, 1999). Various grid point

distributions are investigated in the literature. In this study roots of the Chebyshev polynomial of the first kind are used for grid point generation as (Tornabene *et al.*, 2012)

$$r_i = \frac{g_i - g_1}{g_N - g_1} \quad g_i = \cos\left(\frac{2i - 1}{2N}\pi\right) \quad i = 1, 2, \dots, N \quad (3.6)$$

where N is the total number of grid points along the radial direction. For the problem studied herein, the GDQ method which is presented by the above equations demonstrates its numerical accuracy, high speed and computation amount reduction.

4. Numerical application and discussion

In this Section, the above formulation for creep analysis is applied to a FGM rotating disc with two different boundary conditions. For this purpose, a FGM disc, as can be seen in Fig. 1, with inner radius $a = 0.05$ m and outer radius $b = 0.2$ m is considered. It is subjected to $T = 623$ K temperature and rotates with $\omega = 15000$ rpm. The material of the disc is silicon carbide particles distributed with a linear volume fraction in pure Aluminum matrix

$$v(r) = v_{max} - (v_{max} - v_{min})\frac{r - a}{b - a} \quad (4.1)$$

In the above equation $v_{max} = 0.4$ and $v_{min} = 0.1$ are the maximum and minimum volume fraction of silicon carbide at the inner and outer radius, respectively. The boundary conditions of the disc are established as:

— free-free boundary condition

$$\sigma_r(r = a) = 0 \quad \sigma_r(r = b) = 0 \quad (4.2)$$

— fixed-free boundary condition

$$u_r(r = a) = 0 \quad \sigma_r(r = b) = 0 \quad (4.3)$$

In the distribution patterns of the non-homogeneous disc, the material heterogeneity is mild and the change in thermo-mechanical properties is not very high. Therefore, similarly to the work done by Loghman *et al.* (2011), the disc parameter such as density, Poisson's ratio, thermal expansion coefficient and elasticity modulus can be calculated using a linear mixture rule which is presented by Eq. (4.4). In other words, based on Eq. (4.4), the material and thermal properties depend on the reinforcement particles volume fraction at each point

$$P(r) = P_{Al} + (P_{SiC} - P_{Al})v(r) \quad (4.4)$$

In the above equation, $P(r)$ is the intended property in the composite disc, P_{Al} and P_{SiC} are the value of the same property in pure Aluminum and silicon carbide, respectively. The following data for pure material properties are used in this paper: $E_{Al} = 69$ GPa, $E_{SiC} = 410$ GPa, $\rho_{Al} = 2700$ Kg m^{-3} , $\rho_{SiC} = 3200$ kg m^{-3} , $\alpha_{Al} = 23.1 \cdot 10^{-6}$ K $^{-1}$, $\alpha_{SiC} = 4 \cdot 10^{-6}$ K $^{-1}$.

Based on the creep analysis algorithm and the above specified parameters, a computer code has been developed to find the creep response of the FGM rotating disc. Before providing the results of the FGM rotating disc, to validate the analysis and the developed computer code, the results of tangential strain rate have been computed for a disc which was used by Loghman *et al.* (2011) and Ghorbani (2012). A comparison between the results is shown in Fig. 3. It can be seen that there is a good agreement between the results. However, the time consumed and computation amount by the other method is much higher.

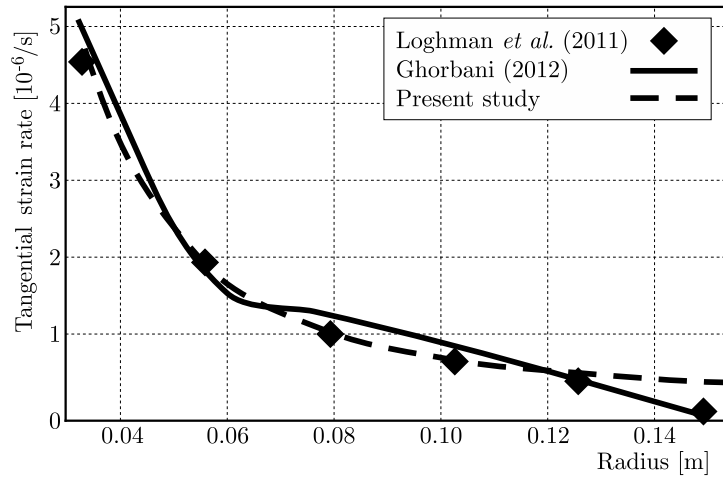


Fig. 3. Results validation

The radial stress distribution versus the radial direction is presented in Fig. 4. Through the free-free boundary condition, the value of radial stress in the inner and the outer radius of the disc becomes zero and the maximum value of radial stress occurs near the middle of the disc. The disc with the fixed-free boundary condition behaves in a different manner. As it can be seen, for this condition the radial stress has its maximum value at the inner radius and then a decreasing trend along the radial direction appears, so the minimum values are observed at the outer radius.

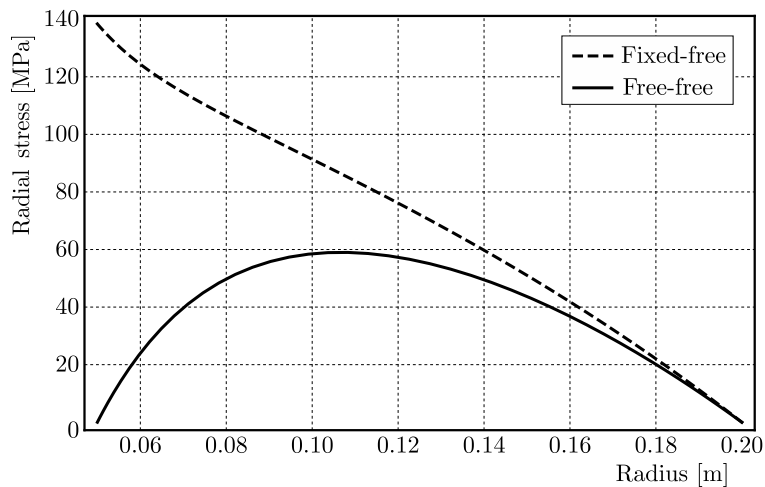


Fig. 4. Radial stress distribution for two various boundary conditions

Figure 5 confirms that the tangential stress for both boundary conditions show a decreasing trend in the radial direction. It means that tangential stress experiences a maximum near the inner radii and gradually decreases to reach a minimum at the outer rim. It seems that the reason for this type of behavior is the existence of a relatively higher content of particles at the inner radius in comparison with other points in the disc. But it is obviously seen that the values of tangential stress in the disc with fixed-free boundary conditions is lower than in the other disc.

The distribution of the radial component of creep strain rate along the disc radius is presented in Fig. 6. As it can be seen, for both boundary conditions the radial creep rate has its maximum value at the inner rim and a decreasing trend along the radial direction. But their behaviour is different, the fixed-free disc has a positive radial creep rate and the free-free disc has a

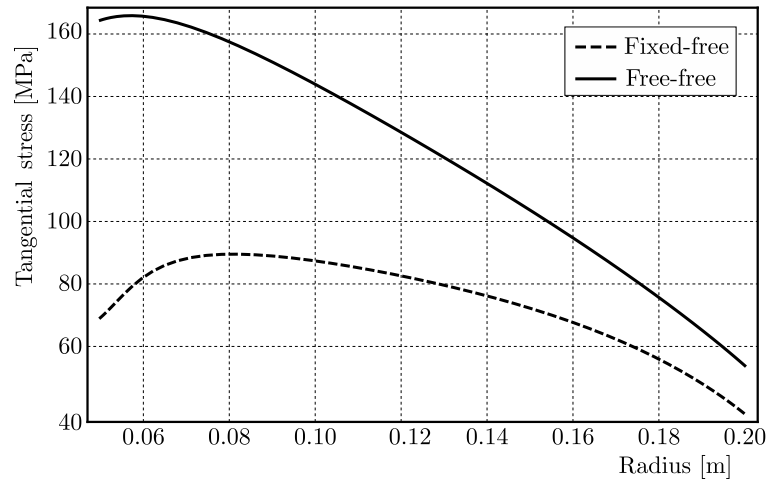


Fig. 5. Tangential stress distribution for two various boundary conditions

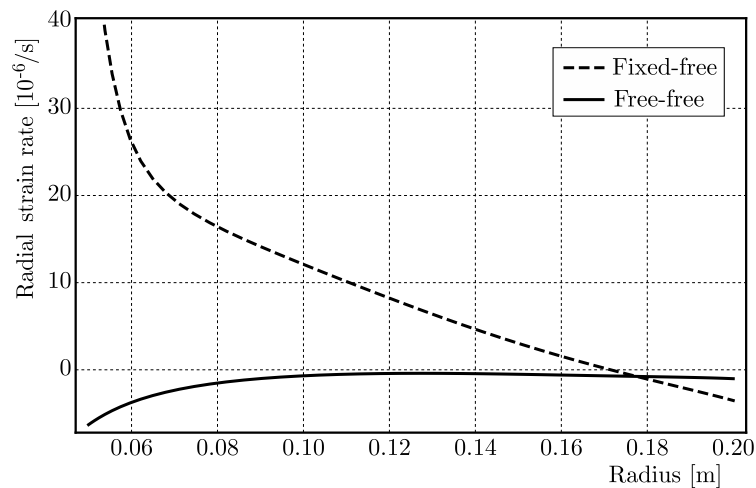


Fig. 6. Radial strain rate distribution for two various boundary conditions

negative one, as well as the absolute value of the radial creep rate in the disc with the fixed-free boundary condition is higher than the disc with the free-free boundary condition. Therefore, it is important to choose appropriate boundary conditions during the disc installation because of high dependency of the FGM disc behavior on boundary conditions. As depicted, the strain rate values in fixed-free boundary conditions are much higher than in the other ones, however this situation is the most practical condition.

Figure 7 shows the disc with the fixed-free boundary condition. It has an increasing-decreasing trend via the radial direction, but in the disc with the free-free boundary condition, the tangential creep rate is maximal at the inner side of the disc and minimal at the outer side. It has a monotonic decreasing behavior at the intermediate radii. It is observed that similarly to the radial creep rate, the maximum rate of the tangential creep rate takes place near the inner radius of discs, also the maximum value of the effective stress occurs at the inner rims, so it is necessary to reinforce the inner side of disc with high strength materials. Therefore, the FGM materials with the higher values of particle reinforcements at the inner radii, in other words, discs with the decreasing type of particle distribution along the radial direction have a better creep responses in comparison with the increasing type ones or homogenous materials.

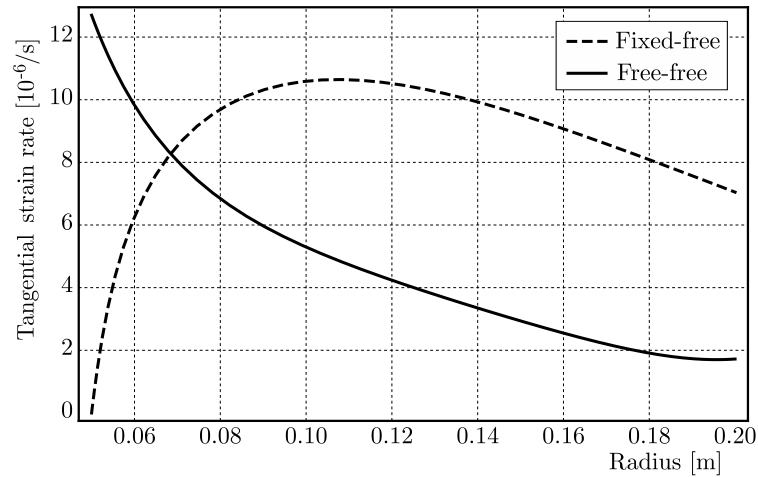


Fig. 7. Tangential strain rate distribution for two various boundary conditions

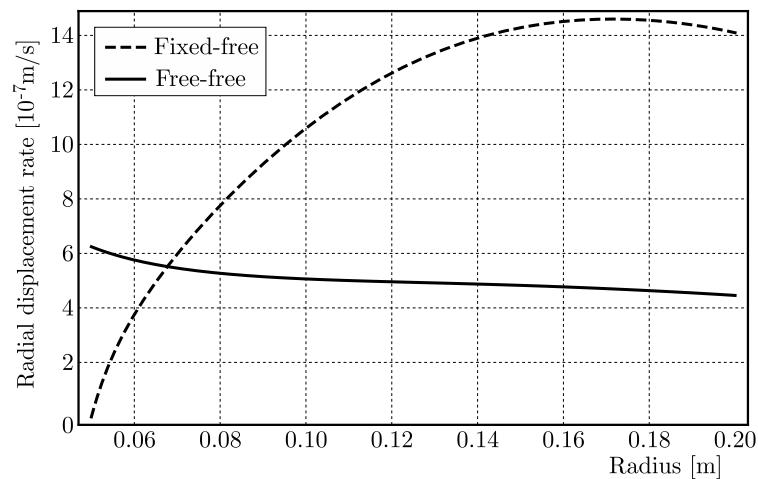


Fig. 8. Radial displacement rate distribution for two various boundary conditions

The variation of the radial displacement rate for two boundary conditions is presented in Fig. 8. As it can be seen, the disc with the free-free boundary condition has a decreasing trend and the disc with the fixed-free boundary condition has an increasing trend along the radial direction, as expected. Obviously, because of the integrated nature of the displacement (compared to the differential nature of strain) this picture does not reveal many details appearing in the previous stress or strain curves.

5. Conclusion

In this paper, the generalized differential quadrature method is used to obtain the time dependent creep responses of an FGM rotating disc. The creep equations are derived for a disc with a linear distribution of the particle content and are solved for two various boundary conditions. It can be demonstrated that the GDQ method is an efficient and accurate method in creep analysis of rotating discs. As it is shown, comparisons of the results with other available approaches show a good agreement. However, the time consumed by the other methods for solving the same problem is much higher. The results also illustrate that the material inhomogeneity has a considerable effect on the creep behavior of FGM rotating discs. Creep rates and stress fields at the inner side of the disc is much greater, so the disc must to be reinforced at this internal

side. Making use of the decreasing type of particle distribution leads to better creep responses as well as higher creep life time.

References

1. ARYA V.K., BHATNAGAR N.S., 1979, Creep analysis of rotating orthotropic discs, *International Journal of Nuclear Engineering and Design*, **55**, 323-330
2. BAYAT M., SLEEM M., SAHARI B.B., HAMOUDA A.M.S., MAHDI E., 2008, Analysis of functionally graded rotating disks with variable thickness, *Mechanics Research Communications*, **35**, 283-309
3. BELLMAN R., KASHEF B.G., CASTI J., 1972, Differential quadrature: a technique for the rapid solution of nonlinear partial differential equations, *Journal of Computational Physics*, **10**, 40-52
4. BHATNAGAR N.S., KULKARNI P.S., ARYA V.K., 1986, Steady state creep of orthotropic rotating discs of variable thickness, *International Journal of Nuclear Engineering and Design*, **91**, 121-141
5. BIAŁKIEWICZ J., 1986, Dynamic creep rupture of a rotating disc of variable thickness, *International Journal of Mechanical Science*, **28**, 671-681
6. GHORBANI M.T., 2012, A semi-analytical solution for time-variant thermoelastic creep analysis of functionally graded rotating disks with variable thickness and properties, *International Journal of Advanced Design and Manufacturing Technology*, **5**, 2, 41-50
7. GUPTA V.K., SINGH S.B., CHANDRAWAT H.N., RAY S., 2004, Steady state creep and material parameters in a rotating disc of Al-SiC composites, *European Journal of Mechanics A Solids*, **23**, 335-344
8. GUPTA V.K., SINGH S.B., CHANDRAWAT H.N., RAY S., 2005, Modeling of creep behavior of a rotating disc in the presence of both composition and thermal gradients, *Journal of Engineering Materials and Technology*, **127**, 97-105
9. HOJJATI M.H., HASSANI A., 2008, Theoretical and numerical analysis of rotating discs of non-uniform thickness and density, *International Journal of Pressure Vessels and Piping*, **85**, 10, 694-700
10. LOGHMAN A., GORBANPOUR ARANI A., SHAJARI A.R., AMIR S., 2011, Time dependent thermoelastic creep analysis of rotating disk made of Al-SiC composite, *Archive of Applied Mechanics*, **81**, 1853-1864
11. NIEH T.G., 1984, Creep rupture of a silicon carbide reinforced aluminum composite, *Metallurgical Transactions*, **15A**, 139-146
12. PANDEY A.B., MISHRA R.S., MAHAJAN Y.R., 1992, Steady state creep behavior of silicon carbide particulate reinforced aluminum composites, *Acta Metallurgica et Materialia*, **40**, 2045-2082
13. SHU C., 1996, Free vibration analysis of composite laminated conical shells by generalized differential quadrature, *Journal of Sound and Vibration*, **194**, 587-604
14. SHU C., CHEW Y.T., 1999, Application of multi-domain GDQ method to analysis of waveguides with rectangular boundaries, *Progress in Electromagnetics Research*, **21**, 1-19
15. SHU C., CHEW Y.T., RICHARDS B.E., 1995, Generalized differential integral quadrature and their application to solve boundary layer equations, *International Journal of Numerical Methods in Fluids*, **21**, 723-733
16. SHU C., RICHARDS B.E., 1992, Application of generalized differential quadrature to solve two-dimensional incompressible Navier-Stokes equations, *International Journal of Numerical Methods in Fluids*, **15**, 791-798
17. SINGH S.B., RAY S., 2001, Steady state creep behavior in an isotropic functionally graded material rotating disc of Al-SiC composite, *Metallurgical and Materials Transactions*, **32A**, 1679-1685
18. SINGH S.B., RAY S., 2002, Modeling the anisotropy and creep in orthotropic aluminum-silicon carbide composite rotating disc, *Mechanics of Materials*, **34**, 363-372

19. TORNABENE F., FANTUZZI N., BACCIOCCHI M., 2016, The GDQ method for the free vibration analysis of arbitrarily shaped laminated composites shells using a NURBS-based isogeometric approach, *Composite Structures*, **153**, 190-218
20. TORNABENE F., LIVERANI A., CALIGIANA G., 2012, Laminated composite rectangular and annular plates: A GDQ solution for static analysis with a posteriori shear and normal stress recovery, *Composite: Part B*, **43**, 1847-1872
21. WHAL A.M., SANKEY G.O., MANJOINE M.J., SHOEMAKER E., 1954, Creep test of rotating discs at elevated temperature and comparisons with theory, *Journal of Applied Mechanics*, **21**, 225-235

Manuscript received May 28, 2016; accepted for print September 12, 2016

A NOVEL APPROACH TO THERMAL AND MECHANICAL STRESSES IN A FGM CYLINDER WITH EXPONENTIALLY-VARYING PROPERTIES

KERIMCAN CELEBI

Adana Science and Technology University, Department of Mechanical Engineering, Adana, Turkey

DURMUS YARIMPABUC

Osmaniye Korkut Ata University, Department of Mathematics, Osmaniye, Turkey
e-mail: durmusyarimpabuc@osmaniye.edu.tr

IBRAHIM KELES

Department of Mechanical Engineering, Ondokuz Mayıs University, Samsun, Turkey

A novel approach is employed to a general solution for one-dimensional steady-state thermal and mechanical stresses in a hollow thick cylinder made of a functionally graded material (FGM). The temperature distribution is assumed to be a function of radius, with general thermal and mechanical boundary conditions on the inside and outside surfaces of the cylinder. The material properties, except Poisson's ratio, are assumed to be exponentially-varying through the thickness. Forcing functions applied to the inner boundary are internal pressures which may be in form of steps. These conditions result in governing differential equations with variable coefficients. Analytical solutions to such equations cannot be obtained except for certain simple grading functions and pressures. Numerical approaches must be adopted to solve the problem in hand. The novelty of the present study lies in the fact that the Complementary Functions Method (CFM) is employed in the analysis. The Complementary Functions method (CFM) will be infused into the analysis to convert the problem into an initial-value problem which can be solved accurately. Benchmark solutions available in the literature are used to validate the results and to observe the convergence of the numerical solutions. The solution procedure is well-structured, simple and efficient and it can be readily applied to cylinders. It is also well suited for problems in which mechanical properties are graded.

Keywords: thermal stresses, functionally-graded materials, thick cylinder, Complementary Functions Method

1. Introduction

Pressure vessel structural members such as cylinders, disks and spheres find broad application fields in the industry, and their vibration analyses are deemed necessary for safe design and operation. Hollow cylinders and thick-walled cylindrical shells are common components in structural applications and device systems involving aerospace and submarine structures, civil engineering structures, machines, pipes, sensors and actuators, etc. These structures are often exposed to temperature environment and thermal stresses are then induced. In many cases, thermal stresses will significantly depress strength and also affect functionality of structures. Thus, the exact analysis of thermal stresses is really important (Ying and Wang, 2010). There have been many studies, such as Timoshenko and Woinowsky-Krieger (1959), Boley and Weiner (1960), Das and Navaratna (1962), Das and Rath (1972), Stavsky (1963) and Thangaratnam *et al.* (1988), which focused on thermal stresses in isotropic homogeneous rectangular plates. Yee and Moon (2002) have been obtained a closed-form analytical solution for the plane thermal stress analysis of a homogeneously orthotropic hollow cylinder subjected to an arbitrary, transient, asymmetric

temperature distribution. They used a stress function approach for obtaining hoop, radial, and shear stresses in a hollow cylinder. Shao (2005) presented, by using a multi-layered approach based on the theory of laminated composites, the solutions of temperature, displacements, and thermal-mechanical stresses in a functionally graded circular hollow cylinder. Shao *et al.* (2008) used complex Fourier series and Laplace transform techniques to investigate transient heat conduction and thermo-mechanical stresses in an FGM hollow cylinder. Jabbari *et al.* (2002, 2003, 2009) derived the exact solution for one-dimensional and two dimensional steady-state thermoelastic problems of functionally graded hollow cylinders where material properties varied with the power product form of the radial coordinate variable. Recently Ruhi *et al.* (2005) studied thermoelastic analysis of thick walled finite length cylinders of functionally graded materials and achieved results for stress, strain and displacement components through the thickness and along the length. The results were presented for uniform internal pressure and thermal loading. Ootao and Tanigawa (2006) analyzed exactly a one-dimensional transient thermoelastic problem of a functionally graded hollow cylinder whose thermal and thermoelastic constants were assumed to vary with the power product form of the radial coordinate variable. The resulting governing differential equation then possessed variable coefficients. General closed-form solutions to such equations are not available. Noda *et al.* (2012) studied the transient thermoelastic analysis for an FGM solid circular disk whose material properties were expressed by a piecewise power law. As it was done in the works cited above, in such situations the solution methods included integral transformations, development of finite element models, and, in some special cases, series solutions were attempted. Assuming that the member was composed of many homogeneous layers of different properties emulating the FGM behavior, there was another way of tackling the problem on hand. All of these approaches required heavy mathematical manipulations and, in the case of having to discretize the domain into many elements, a high amount of computational time.

In the present paper, the governing differential equation is non-homogeneous with variable coefficients which include material properties. A novel approach is attempted to obtain displacements, strains and stresses in a simple and efficient manner. The complementary functions method (CFM), theoretically explained in the literature by Aktaş (1972), Agarwal (1982) and Roberts and Shipman (1979) is infused into analysis to convert the problem to an initial-value problem which can be then easily solved by, for example, the fifth-order Runge-Kutta method (RK5) with great accuracy (Chapra and Canale, 1998). Shell theories or dividing the material into homogeneous subelements of different properties emulating the graded behavior contains the customary approach of modeling FGM structural elements. Finite element analysis, series expansion methods and direct methods are primary solution methods used in the literature. The present paper uses a novel and efficient method which employes CFM. A thick hollow cylinder of FGM under one-dimensional steady-state temperature distribution with general types of thermal and mechanical boundary conditions is analysed. Two material models are used: (a) with a simple power law with constant Poisson's ratio (Jabbari *et al.*, 2002) for which analytical benchmark solutions are available, (b) with exponentially-varying properties. It should be emphasized once again that the solution procedure is not confined to any particular choice of the material model; it is equally suitable for arbitrary functions defining the gradient variation of material properties.

2. Solutions by the Complementary Functions Method

The CFM transforms two-point boundary-value problems to a system of initial-value problems. It reduces to a particularly simple solution scheme when applied to a given class of problems, e.g. for an annular disk of inner radius r_i and outer radius r_o . As it is shown in the proceeding Sections, under axisymmetric conditions, the governing differential equation of the dependent variable $u(r)$ in its most general form is

$$u'' + P(r)u' + Q(r)u = R(r) \tag{2.1}$$

subject to boundary conditions on the inner ($r = r_i$) and outer ($r = r_o$) surfaces. Here $(\cdot)'$ denotes the derivative with respect to r . A general closed-form solution of the above equation cannot be obtained. The complete solution to Eq. (2.1) is

$$u = b_j u_j + u_p \quad j = 1, 2 \tag{2.2}$$

where u_j and u_p are, respectively, homogenous and particular solutions. The coefficients b_j are determined via the boundary conditions. CFM begins by assuming $u_i = Y_1^{(i)}$ and $u'_i = Y_2^{(i)}$, which means

$$(Y_1^{(i)})' = Y_2^{(i)} \tag{2.3}$$

Here, the index $i = 1, 2$ refers to homogeneous solutions and $i = p$ means the particular solution. To determine the homogeneous solutions, the right-hand side of Eq. (2.1) is set equal to zero, and the following is obtained

$$(Y_2^{(i)})' = -P(r)Y_2^{(i)} - Q(r)Y_1^{(i)} \tag{2.4}$$

The system of Eqs. (2.3) and (2.4) can be solved numerically for each homogeneous solution. The Kronecker delta initial conditions given below are used to assure linear independence of the solutions (Roberts and Shipman, 1979)

$$Y_j^{(i)} = \delta_{ji} \quad j, i = 1, 2 \tag{2.5}$$

To obtain the particular solution, Eq. (2.4) is modified as

$$(Y_2^{(p)})' = -P(r)Y_2^{(p)} - Q(r)Y_1^{(p)} + R(r) \tag{2.6}$$

A particular solution needs only to satisfy the differential equation and homogeneous initial conditions

$$Y_j^{(p)} = 0 \quad j = 1, 2 \tag{2.7}$$

be imposed. Equations (2.3), (2.6), (2.7) constitute a system of equations for the particular solution along with the initial conditions. The fifth-order Runge-Kutta method (RK5) is used for all cases considered. Note that by this procedure not only the solution $u(r)$ itself but also its first derivative are readily calculated. Applying the boundary conditions prescribed for the particular problem in hand results in the following system of algebraic equations for the coefficients b_1 and b_2

$$\begin{bmatrix} A_{11} & A_{12} \\ A_{21} & A_{22} \end{bmatrix} \begin{bmatrix} b_1 \\ b_2 \end{bmatrix} = \begin{bmatrix} RHS1 \\ RHS2 \end{bmatrix} \tag{2.8}$$

Here, A_{ij} includes the values of the homogeneous solutions at the boundary points. $RHS1$ and $RHS2$ contain values of the particular solutions. If the cylinder is subjected to internal and external pressures, they will also be included in the right hand-side terms. On the other hand, implementing CFM in the heat conduction problem yields $RHS1$ and $RHS2$ as prescribed temperatures along the boundaries. These points will be illustrated in the following Sections.

3. Heat conduction in the radial direction

The heat conduction equation in the steady-state condition for a one-dimensional problem in polar coordinates and thermal boundary conditions for a FGM hollow cylinder are given, respectively, as

$$\begin{aligned} \frac{1}{r} \left(r k(r) T'(r) \right)' &= 0 & r_i \leq r \leq r_o \\ C_{11} T(r_i) + C_{12} T'(r_i) &= f_1 \\ C_{11} T(r_o) + C_{12} T'(r_o) &= f_2 \end{aligned} \quad (3.1)$$

where $k = k(r)$ is the thermal conduction coefficient, r_i and r_o are the inner and outer radii of the hollow cylinder. C_{ij} are the constant thermal parameters related to the conduction and convection coefficients. The constants f_1 and f_2 are known constants on the inside and outside radii.

It is assumed that the nonhomogeneous thermal conduction coefficient $k(r)$ is an exponential function of r as

$$k(r) = k_o e^{\beta r} \quad (3.2)$$

where k_o is a material constant and β is the inhomogeneity parameter. Using Eq. (3.2), the heat conduction equation becomes

$$\frac{1}{r} \left(r e^{\beta r} T'(r) \right)' = 0 \quad (3.3)$$

Steady-state axisymmetric heat conduction without heat generation is considered. The heat balance equation in the radial direction for a nonuniform disk yields

$$T'' + B(r) T' = 0 \quad (3.4)$$

where $B(r) = (1/r) + \beta$ and it is varying as a function of the radial coordinate r . The boundary conditions are temperatures prescribed on the inner and outer surfaces as

$$T(r_i) = T_i \quad \text{and} \quad T(r_o) = T_o \quad (3.5)$$

The complete solution is the homogeneous solution

$$T = b_j T_j \quad j = 1, 2 \quad (3.6)$$

with

$$T' = b_j T'_j \quad j = 1, 2 \quad (3.7)$$

Following the steps outlined in Section 2, the temperature distribution is obtained at the collocation points. The constants b_j can now be found by imposing the boundary conditions. This process results in a system given by Eq. (2.8) where

$$\begin{aligned} A_{11} &= T_1(r_i) & A_{12} &= T_2(r_i) \\ A_{21} &= T_1(r_o) & A_{22} &= T_2(r_o) \\ RHS1 &= T_i & RHS2 &= T_o \end{aligned} \quad (3.8)$$

4. Governing equation

Consider a thick walled cylinder of the inside radius r_i and the outside radius r_o made of FGM. The material is graded through the r -direction. Let u be the displacement component in the radial direction. Then the strain-displacement relations are

$$\varepsilon_{rr} = \frac{du}{dr} \quad \varepsilon_{\theta\theta} = \frac{u}{r} \tag{4.1}$$

The stress-strain relations are

$$\begin{aligned} \sigma_{rr} &= (\lambda + 2\mu)\varepsilon_{rr} + \lambda\varepsilon_{\theta\theta} - (3\lambda + 2\mu)\alpha T(r) \\ \sigma_{\theta\theta} &= (\lambda + 2\mu)\varepsilon_{\theta\theta} + \lambda\varepsilon_{rr} - (3\lambda + 2\mu)\alpha T(r) \end{aligned} \tag{4.2}$$

where σ_{ij} and ε_{ij} ($i, j = r, \theta$) are stress and strain tensors, $T(r)$ is temperature distribution determined from the heat conduction equation, α is the coefficient of thermal expansion, and λ and μ are the Lamé coefficients related to the modulus of elasticity E and Poisson's ratio ν as

$$\lambda = \frac{\nu E(r)}{(1 + \nu)(1 - 2\nu)} \quad \mu = \frac{E(r)}{2(1 + \nu)} \tag{4.3}$$

The equilibrium equation in the radial direction, disregarding the body force and inertia terms, is

$$\frac{\partial\sigma_{rr}}{\partial r} + \frac{\sigma_{rr} - \sigma_{\theta\theta}}{r} = 0 \tag{4.4}$$

To obtain the equilibrium equation in terms of the displacement component for the FGM cylinder, the functional relationship of the material properties must be known. To ascertain the effect of the inhomogeneity, the properties are considered to vary exponentially across the thickness

$$E(r) = E_o e^{\beta r} \quad \alpha = \alpha_o e^{\beta r} \tag{4.5}$$

where E_o and α_o are the material constants and β is the inhomogeneity parameter. Poisson's ratio varies very little through the thickness in FGM materials. Furthermore, its effects on thermal and mechanical stresses are insignificant. For simplicity, Poisson's ratio is assumed to be constant (Akbari Alashti *et al.*, 2013; Jabbari *et al.*, 2015).

Using relations (4.1)-(4.5), the Navier equation in term of the displacement is

$$u'' + P(r)u' + Q(r)u = R(r) \tag{4.6}$$

where

$$\begin{aligned} P(r) &= (\beta r + 1)\frac{1}{r} & Q(r) &= \left(\frac{\nu\beta r}{1 - \nu} - 1\right)\frac{1}{r^2} \\ R(r) &= \frac{e^{\beta r}\alpha_o(1 + \nu)}{(1 - \nu)}(2\beta T + T') \end{aligned} \tag{4.7}$$

Following the steps outlined in Section 2, the complete displacement is obtained at the collocation points as

$$u = b_1 u_1 + b_2 u_2 + u_p \tag{4.8}$$

with

$$u' = b_1 u'_1 + b_2 u'_2 + u'_p \tag{4.9}$$

The coefficients b_1, b_2 will be determined using the stress free conditions on inner ($\sigma_{rr}(r_i) = -P_i$) and outer ($\sigma_{rr}(r_o) = -P_o$) boundaries. This step is particularly simple since during the solution process the first derivative of the radial displacement has already been calculated.

5. Results and discussions

As an example, consider a thick hollow cylinder of the inner radius a $r_i = 1$ m and the outer radius $r_o = 1.2$ m. Poisson’s ratio is taken to be 0.3, and the modulus of elasticity and the thermal coefficient of expansion at the inner radius are $E_o = 200$ GPa and $\alpha_o = 1.2 \cdot 10^{-6}/^\circ\text{C}$, respectively. The properties are considered to vary exponentially across the thickness. The boundary conditions for temperature are taken as $T(r_i) = 10^\circ\text{C}$ and $T(r_o) = 0^\circ\text{C}$. The hollow cylinder has pressure on its inner surface, so the boundary conditions for stresses are assumed as $\sigma_{rr}(r_i) = -50$ MPa and $\sigma_{rr}(r_o) = 0$ MPa.

The numerical solution in the present study is checked with the results obtained by Jabbari *et al.* (2002) for the validation purpose. Comparison is illustrated in Tables 1-3. It can be observed that the results are in good agreement with the same results by Jabbari *et al.* (2002). The numerical results have been obtained to six-digit accuracy by picking only 11 collocation points.

Table 1. Comparison of CFM with Jabbari *et al.* (2002) for a homogenous cylinder ($m = 0$ and $\beta = 0$)

$\frac{r}{r_i}$	$T/T(r_i)$		u/r_i		σ_{rr}/P_i		$\sigma_{\theta\theta}/P_i$	
	CFM	Jabbari	CFM	Jabbari	CFM	Jabbari	CFM	Jabbari
1	1	1	0.00136642	0.00136642	-1	-1	5.50909	5.50909
1.04	0.784882	0.784882	0.00133799	0.00133799	-0.754183	-0.754183	5.27802	5.27802
1.08	0.577883	0.577883	0.00131239	0.00131239	-0.534644	-0.534644	5.07268	5.07268
1.12	0.378413	0.378413	0.00128932	0.00128932	-0.337716	-0.337716	4.88943	4.88943
1.16	0.185944	0.185944	0.0012685	0.0012685	-0.160351	-0.160351	4.72526	4.72526
1.2	0	0	0.0012497	0.0012497	0	0	4.57766	4.57766

Table 2. Comparison of CFM with Jabbari *et al.* (2002) for FGM cylinders with constant Poisson’s ratio and the elastic modulus obeying a simple power law ($m = -2$ and $\beta = -2$)

$\frac{r}{r_i}$	$T/T(r_i)$		u/r_i		σ_{rr}/P_i		$\sigma_{\theta\theta}/P_i$	
	CFM	Jabbari	CFM	Jabbari	CFM	Jabbari	CFM	Jabbari
1	1	1	0.00161944	0.00161944	-1	-1	6.62127	6.62127
1.04	0.814545	0.814545	0.00158667	0.00158667	-0.722291	-0.722291	5.84288	5.84288
1.08	0.621818	0.621818	0.00155679	0.00155679	-0.491571	-0.491571	5.19022	5.19022
1.12	0.421818	0.421818	0.00152961	0.00152961	-0.29876	-0.29876	4.63928	4.63928
1.16	0.214545	0.214545	0.00150494	0.00150494	-0.136767	-0.136767	4.1713	4.1713
1.2	0	0	0.00148263	0.00148263	0	0	3.77145	3.77145

Table 3. Comparison of CFM with Jabbari *et al.* (2002) for FGM cylinders with constant Poisson’s ratio and the elastic modulus obeying a simple power law ($m = 2$ and $\beta = 2$)

$\frac{r}{r_i}$	$T/T(r_i)$		u/r_i		σ_{rr}/P_i		$\sigma_{\theta\theta}/P_i$	
	CFM	Jabbari	CFM	Jabbari	CFM	Jabbari	CFM	Jabbari
1	1	1	0.00114082	0.00114082	-1	-1	4.51743	4.51743
1.04	0.753093	0.753093	0.00111628	0.00111628	-0.784165	-0.784165	4.70652	4.70652
1.08	0.533109	0.533109	0.00109454	0.00109454	-0.577254	-0.577254	4.89893	4.89893
1.12	0.336271	0.336271	0.00107516	0.00107516	-0.378189	-0.378189	5.09474	5.09474
1.16	0.159442	0.159442	0.00105779	0.00105779	-0.186042	-0.186042	5.29405	5.29405
1.2	0	0	0.00104213	0.00104213	0	0	5.49697	5.49697

Figure 1a shows variations of temperature along the radial direction for different values of the inhomogeneity parameter (β). The figure shows that as the inhomogeneity parameter β increases, the temperature decreases. Figure 1b shows the plot of the radial displacement along the radius. The magnitude of the radial displacement is decreased as the inhomogeneity parameter β is increased. The radial and circumferential stresses are plotted along the radial direction and are shown in Figs. 1c and 1d. The magnitude of the radial stress is increased as β is increased. It is seen that for $\beta < 1$ the hoop stress decreases along the radial direction. For $\beta > 1$, the hoop stress increases as the radius increases, since the modulus of elasticity is an increasing function of the radius, see Eq. (2.6). Physically, this means that the outer layers of the cylinder are biased to maintain the stress due to their higher stiffness. There is a limiting value for β , where the hoop stress remains almost constant along the radius. The curve associated with $\beta = 1$ shows that the variation of hoop stress along the radial direction is minor, and is almost uniform across the radius. To investigate the pattern of stress distribution along the cylinder radius, the effective stress $\sigma^* = \sqrt{2}|\sigma_r - \sigma_\theta|$ is plotted along the radial direction for different values of r_o/r_i and the inhomogeneity parameter β . Figure 2 is plotted for $r_o/r_i = 1.2$. It is interesting to note from Fig. 2 that for $\beta = 1$ the effective stress is almost uniform along the radius of the cylinder.

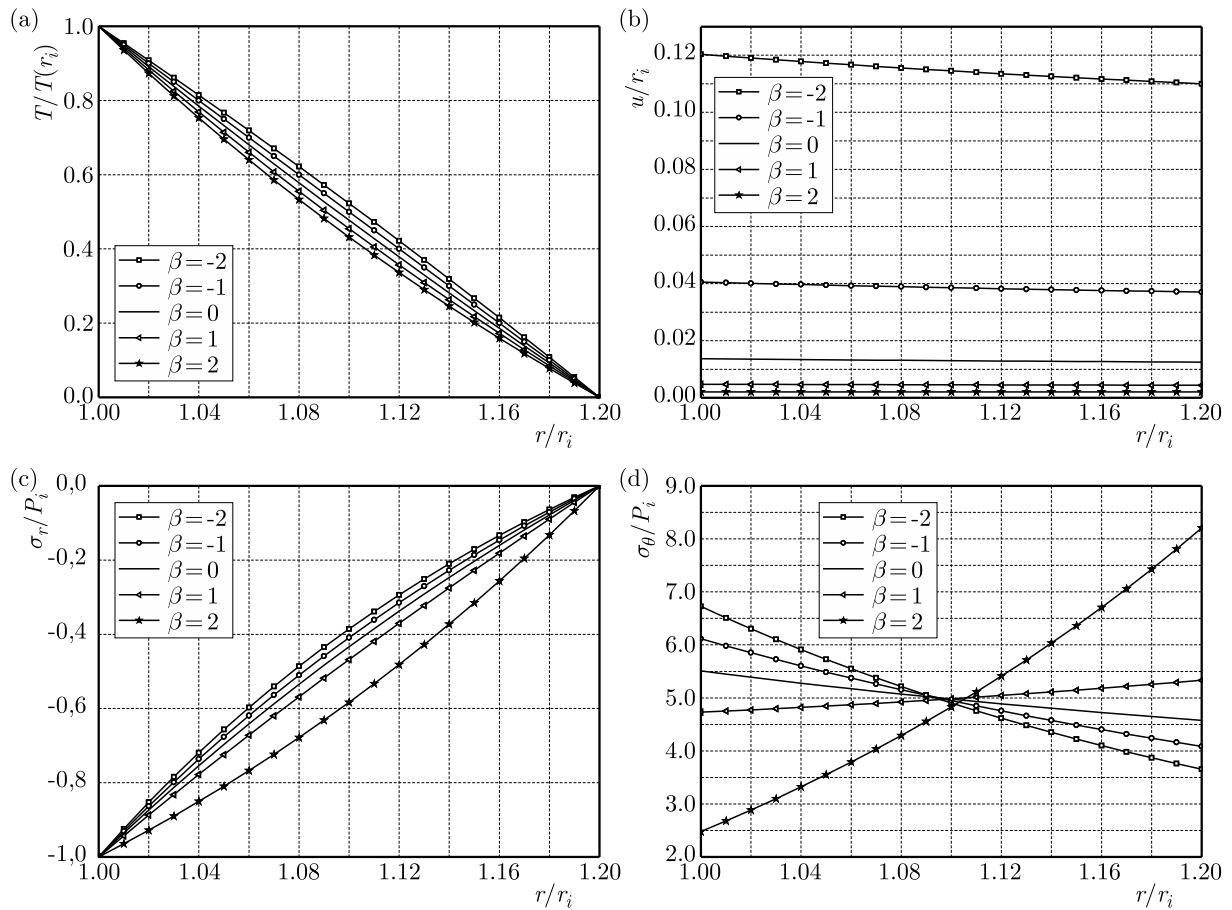


Fig. 1. Radial distribution of: (a) temperature, (b) radial displacement, (c) radial stress and (d) hoop stress for cylinder

It should be pointed out once again that the purpose of the present work is the introduction of CFM to the solution procedure of the class of problems in hand. Converting the two-point boundary value problem to a system of an initial-value problem gives a way to the implementation of well-established numerical schemes. The Runge-Kutta method of fifth-order (RK5) is used to

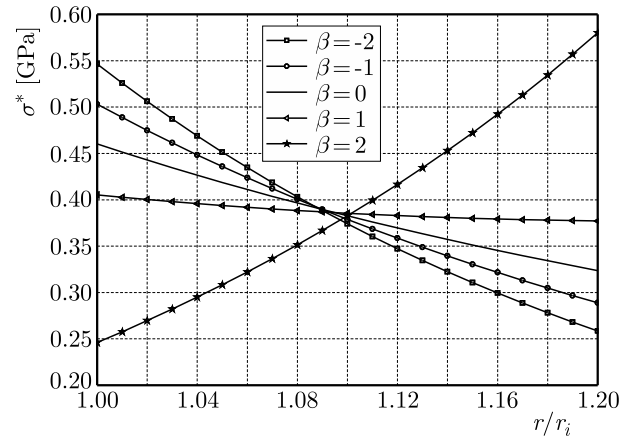


Fig. 2. Effective stress distribution for $r_o/r_i = 1.2$

solve the system of equations. The procedure is simple and efficiently implemented. The numerical results have been obtained exact up to six-digit accuracy by picking only 11 collocation points in RK5.

6. Conclusion

This paper presents a numerical solution for calculation of axisymmetric thermal and mechanical stresses in a thick hollow cylinder made of FGM. The material properties through the graded direction are assumed to be nonlinear with a power law distribution and exponentially-varying properties. The mechanical and thermal stresses are obtained through the CFM of the solution of the Navier equation. The comparisons of temperature distributions and stress distributions are presented in form of tables. The numerical results for all cases are shown to exactly match those reported by Jabbari *et al.* (2002). Finally, we can conclude that:

- With the unified approach presented in the present study, one would not have to compromise on the functional continuity of the material properties. Analysis of any material model in form of an arbitrary function subject to internal pressure has been analyzed efficiently and accurately by employing CFM.
- The unified method used is accurate and more efficient than the conventional methods.
- The method employed in this study allows one to find solutions of continuous functions.
- The CFM of solving the differential equation provides a complete solution, yielding both thermal stresses and temperature distributions.

References

1. AGARWAL R.P., 1982, On the method of complementary functions for nonlinear boundary-value problems, *Journal of Optimization Theory and Applications*, **36**, 1, 139-144
2. AKBARI ALASHTI R., KHORSAND M., TARAHHOMI M.H., 2013, Three-dimensional asymmetric thermo-elastic analysis of a functionally graded rotating cylindrical shell, *Journal of Theoretical and Applied Mechanics*, **51**, 1, 143-158
3. AKTAŞ Z., 1972, *Numerical Solutions of Two-Point Boundary Value Problems*, Ankara Turkey: METU, Dept. of Computer Engineering
4. BOLEY B.A., WEINER J.H., 1960, *Theory of Thermal Stresses*, Wiley Hoboken, New York, 35-45

5. CHAPRA S.C., CANALE R.P., 1998, *Numerical Methods for Engineers*, 2nd ed., McGraw-Hill, New York, 760-766
6. DAS Y.C., NAVARATNA D.R., 1962, Thermal bending of rectangular plates, *Journal of the Aerospace Sciences*, **29**, 11, 1397-1399
7. DAS Y.C., RATH B.K., 1972, Thermal bending of moderately thick rectangular plates, *AIAA Journal*, **10**, 10, 1349-1351
8. JABBARI M., BAHTUI A., ESLAMI M.R., 2009, Axisymmetric mechanical and thermal stresses in thick short length FGM cylinders, *International Journal of Pressure Vessels and Piping*, **86**, 5, 296-306
9. JABBARI M., NEJAD M.Z., GHANNAD M., 2015, Thermo-elastic analysis of axially functionally graded rotating thick cylindrical pressure vessels with variable thickness under mechanical loading, *International Journal of of Engineering Science*, **96**, 1-18
10. JABBARI M., SOHRABPOUR S., ESLAMI M.R., 2002, Mechanical and thermal stresses in a functionally graded hollow cylinder due to radially symmetric loads, *International Journal of Pressure Vessels and Piping*, **79**, 7, 493-497
11. JABBARI M., SOHRABPOUR S., ESLAMI M.R., 2003, General solution for mechanical and thermal stresses in a functionally graded hollow cylinder due to nonaxisymmetric steady-state loads, *ASME Journal of Applied Mechanics*, **70**, 1, 111-118
12. NODA N., OOTAO Y., TANIGAWA Y., 2012, Transient thermoelastic analysis for functionally graded circular disk with piecewise power law, *Journal of Theoretical and Applied Mechanics*, **50**, 3, 831-839
13. OOTAO Y., TANIGAWA Y., 2006, Transient thermoelastic analysis for functionally graded hollow cylinder, *Journal of Thermal Stresses*, **29**, 11, 1031-1046
14. ROBERTS S.M., SHIPMAN J.S., 1979, Fundamental matrix and two-point boundary-value problems, *Journal of Optimization Theory and Applications*, **28**, 1, 77-78
15. RUHI M., ANGOSHTARI A., NAGHDABADI R., 2005, Thermoelastic analysis of thick-walled finite-length cylinders of functionally graded materials, *Journal of Thermal Stresses*, **28**, 4, 391-408
16. SHAO Z.S., 2005, Mechanical and thermal stresses of a functionally graded circular hollow cylinder with finite length, *International Journal of Pressure Vessels and Piping*, **82**, 3, 155-163
17. SHAO Z.S., ANG K.K., REDDY J.N., WANG T.J., 2008, Nonaxisymmetric thermomechanical analysis of functionally graded hollow cylinders, *Journal of Thermal Stresses*, **31**, 6, 515-536
18. STAVSKY Y., 1963, Thermoelasticity of heterogeneous aeolotropic plates, *Journal of the Engineering Mechanics Division*, **89**, 2, 89-105
19. THANGARATNAM R.K., PALANINATHAN, RAMACHANDRAN J., 1988, Thermal stress analysis of laminated composite plates and shells, *Computers and Structures*, **30**, 6, 1403-1411
20. TIMOSHENKO S., WOINOWSKY-KRIEGER S., 1959, *Theory of Plates and Shells*, 2nd ed., McGraw-Hill, New York, 73-132
21. YEE K.C., MOON T.J., 2002, Plane thermal stress analysis of an orthotropic cylinder subjected to an arbitrary, transient, axisymmetric temperature distribution, *ASME Journal of Applied Mechanics*, **69**, 5, 632-640
22. YING J., WANG H.M., 2010, Axisymmetric thermoelastic analysis in a finite hollow cylinder due to nonuniform thermal shock, *International Journal of Pressure Vessels and Piping*, **87**, 12, 714-720

HIGH ORDER SENSITIVITY ANALYSIS OF A MISTUNED BLISK INCLUDING INTENTIONAL MISTUNING

LINUS POHLE, SEBASTIAN TATZKO, LARS PANNING-VON SCHEIDT, JÖRG WALLASCHEK
Leibniz Universität Hannover, Institute of Dynamics and Vibration Research, Hannover, Germany
e-mail: linuspohle@gmx.de

Small deviations between turbine blades exist due to manufacturing tolerances or material inhomogeneities. This effect is called mistuning and usually causes increased vibration amplitudes and also a lower service life expectancy of bladed disks or so called blisks (bladed integrated disk). The major resulting problem is to estimate the maximum amplitude with respect to these deviations. Due to the probability distribution of these deviations, statistical methods are used to predict the maximum amplitude. State of the art is the Monte-Carlo simulation which is based on a high number of randomly re-arranged input parameters. The aim of this paper is to introduce a useful method to calculate the probability distribution of the maximum amplitude of a mistuned blisk with respect to the random input parameters. First, the applied reduction method is presented to initiate the sensitivity analysis. This reduction method enables the calculation of the frequency response function (FRF) of a Finite Element Model (FEM) in a reasonable calculation time. Based on the Taylor series approximation, the sensitivity of the vibration amplitude depending on normally distributed input parameters is calculated and therewith, it is possible to estimate the maximum amplitude. Calculating only a single frequency response function shows a good agreement with the results of over 1000 Monte-Carlo simulations.

Keywords: turbine blades, mistuning, sensitivity analysis

Nomenclature

d_0	– structural damping	σ	– standard deviation
k	– blade index	\mathbf{I}	– identity matrix
u	– modal displacement	\mathbf{K}_b	– stiffness matrix of blades
x	– geometric displacement	\mathbf{K}_d	– stiffness matrix of one disk segment
EO	– engine order	\mathbf{K}_b^A	– stiffness matrix of blades, type A
N	– number of blades	$\tilde{[\cdot]}$	– reduced system matrices
δ_k	– mistuning factors	$\hat{[\cdot]}$	– absolute amplitude
α	– tolerance interval	$[\cdot]^H$	– Hermitian transpose

1. Introduction

A blade integrated disk (blisk), i.e. blades and disk made out of one piece, has a lot of technical benefits like weight reduction or omission of fretting between the blade and disk. This causes lower damping and higher structural coupling between the blades. Due to small deviations between the blade properties, energy localization can occur causing considerably higher vibration amplitudes of a few blades. Whitehead (1966) gave a limit for the maximum vibration amplitude of a mistuned blisk. This theoretical maximum is existent, if all modes have the same eigenfrequency and are in phase at one blade position.

The dynamical behavior of one blade mode can be simulated with a cyclic lumped-mass model (see e.g. Griffin and Hoosac, 1984). The benefits of such a simple model is the simple dynamical behavior and the low calculation time. However, different mode families and multiple mode shapes cannot be described by this model. On the other hand, high computational cost is inevitable to solve a full Finite Element model of a mistuned blisk. Especially for parameter studies, a high number of high-resolution FRF's is necessary. Therefore, a lot of different reduction methods are developed to calculate the FRF of a mistuned blisk with a lower computational effort.

There are two ways that are frequently used to reduce the number of DOF of a mistuned blisk. On the one hand, the model can be described by the system modes (called Subset of Nominal Modes, SNM), which is described in Yang and Griffin (2001), extended to geometric mistuning in Sinha (2009) and compared to the first version of the SNM in Bhartiya and Sinha (2011). The model of the whole blisk is divided into single sectors which could be reduced by a modal transformation using the modes of the segment. Afterwards, the mistuned stiffness matrix can be calculated very efficiently, and a good agreement to the full model can be shown. If there is only one mode describing the blade dominant vibration, this method can be extended to the Fundamental Model of Mistuning (FMM), which was introduced in Feiner and Griffin (2002). The main condition is that the mode shape remains almost unchanged and only small difference occurs between the blades eigenfrequencies. The main benefit is that the knowledge of the system matrices of the Finite Element model is not required. This method is very useful for the identification of mistuning, see Shuai and Jianyao (2010), Feiner and Griffin (2004a,b).

On the other hand, one sector can be divided into a blade and a disk sector. After modal reduction of these components, the matrices are coupled and the dynamical behavior of the whole mistuned blisk can be calculated. This so-called Component Mode Synthesis (see e.g. Bladh *et al.*, 2001a,b) needs more computational effort to regard mistuning, but is much more flexible (see Moyroud *et al.* (2002), for comparison, Castanier and Pierre (2006) for an overview). It is assumed that the disk is cyclic symmetric. Thus it can be described by cyclic boundary conditions (see Thomas (1979) for a description). The DOFs of the blade are reduced by the well-known Craig Bampton method (see Craig and Bampton, 1968; Craig, 2000). This method was extended in Hohl *et al.* (2011) using a reduction of the coupling nodes using Wave-Based Substructuring Čermelj *et al.* (2008) and a secondary modal reduction.

To analyze the influence of mistuning, Monte-Carlo Simulation (MCS) can be used to find an optimal pattern or to find the maximum amplitude of a given probability distribution of the eigenfrequencies, see Hohl *et al.* (2011). In Bladh *et al.* (2001), it is shown that only 50 MCS are necessary to fit the probability density function (PDF) of the maximum vibration amplitude over all frequencies. The PDF is fitted with a Weibull distribution. In Mignolet and Hu (1997), a direct prediction method describes how to find the maximum amplitude for one frequency using the cumulates of the normal distributions. The distribution of a lumped-mass model with one DOF per segment results in a Gaussian distribution.

The presented paper introduces a new method to find the Gaussian distribution of a mistuned blisk. The aim of the paper is to show the benefits of these methods and its possible application. First, the used reduction method is described and the universal validity is given. Thereafter, high order sensitivity analysis is shown and compared to the MCS. The second case study emphasizes its versatile application spectrum based on an intentional mistuned example. Therewith, the dynamical behavior of a mistuned blisk can be analyzed depending on different mistuning factors, engine order, or blade pattern.

2. Reduction method

The first example analyzed is a simplified blisk with $N = 12$ blades (see picture in Fig. 1). This blisk exhibits the typical dynamical behavior of a blisk without spinning effects like spin softening, centrifugal stiffening or Coriolis effects. The blisk is cyclic symmetric with 12 blades ignoring manufacturing tolerances. Thus, cyclic symmetry can be used to analyze the full blisk regarding only one sector.



Fig. 1. Picture of the analyzed blisk

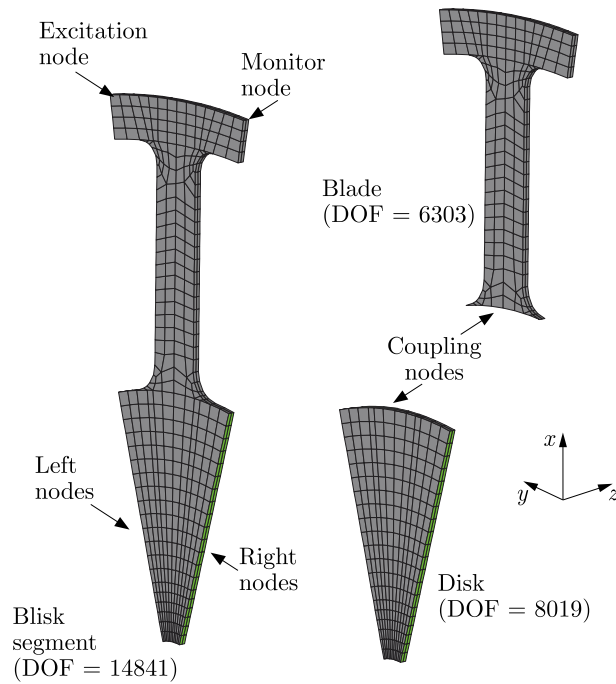


Fig. 2. Finite Element mesh with special nodes of interest

In Fig. 2, the mesh of such a sector is shown. The mesh of the whole system has about 170 000 degrees of freedom (DOF) and a harmonic analysis of the vibration amplitudes cannot

be solved at a common PC in a reasonable time, especially if parameter variations are processed or optimization problems are considered. Regarding cyclic symmetry, the number of DOFs is reduced to 14841 for the calculation. The excitation node and the monitor node are located at the blade tip, and the direction of excitation and monitoring is the z -direction. Of course, the following shown method can be used to analyze a blisk with any arbitrary geometry.

In Fig. 3, the nodal diameter diagram is illustrated for the first four mode families. The first mode family is well separated, and will be used for the analysis in this paper. Nevertheless, the results are verified for other mode families as well. Some chosen mode shapes of the tuned system are depicted in Fig. 3.

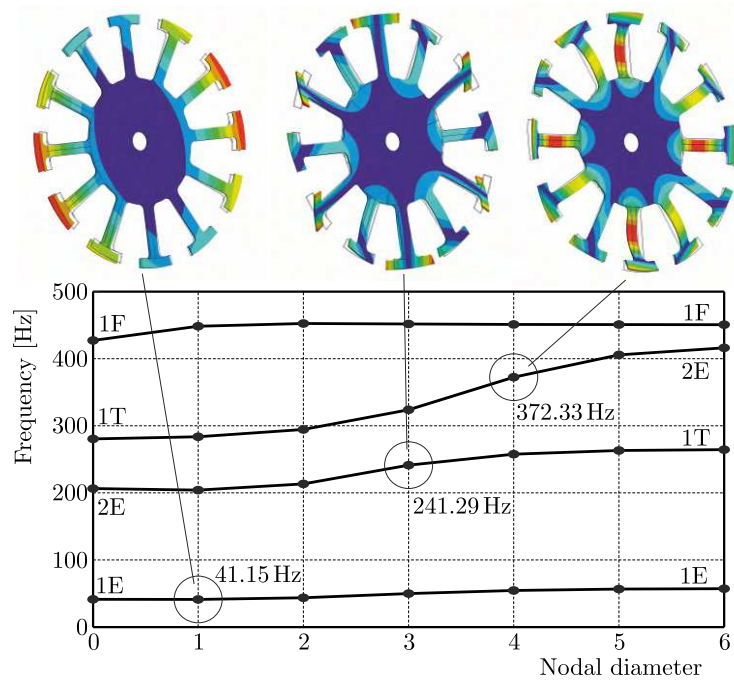


Fig. 3. Nodal diameter diagram

In general, the equation of the dynamical system can be written as

$$\mathbf{M}\ddot{\mathbf{x}}(t) + \mathbf{D}\dot{\mathbf{x}}(t) + \mathbf{K}\mathbf{x}(t) = \mathbf{F}(t) \quad (2.1)$$

with \mathbf{M} , \mathbf{D} , and \mathbf{K} as the mass, damping, and stiffness matrix. The excitation force vector $\mathbf{F}(t)$ is assumed to be harmonic in time with a constant phase shift between the blades depending on the engine order EO

$$\mathbf{F}(t) = \hat{\mathbf{F}}\mathbf{e}^{i\Omega t} = \begin{bmatrix} 1 \\ \vdots \\ e^{-ik\phi} \\ \vdots \\ e^{-i(N-1)\phi} \end{bmatrix} \hat{f}\mathbf{e}^{i\Omega t} \quad (2.2)$$

with the phase shift

$$\phi = \frac{2\pi EO}{N} = \text{const} \quad (2.3)$$

The damping is modeled as structural damping depending on the stiffness matrix

$$\mathbf{D} = \frac{d_0}{\Omega} \mathbf{K} \quad (2.4)$$

Using the modal transformation into the frequency domain with the harmonic approach $\mathbf{x}(t) = \hat{\mathbf{x}} \exp(i\Omega t)$, Eq. (2.1) reads

$$\hat{\mathbf{x}}(\Omega) = [-\mathbf{M}\Omega^2 + (1 + id_0)\mathbf{K}]^{-1}\hat{\mathbf{F}} \quad (2.5)$$

The attentive reader notices that the equation of motion is build up for a linear model. The following process will be described for such a model. Nevertheless, it will be very simple to include rotating effects like centrifugal or Coriolis forces. Therefore, the matrices have to be checked for nonsymmetry and varity over the rotation speed. The following reduction method is limited to linear models, but other reduction methods for nonlinear models can be used.

For a large number of DOFs a lot of computational effort is required to calculate the combined matrix $(-\mathbf{M}\Omega^2 + (1 + id_0)\mathbf{K})^{-1}$.

The chosen reduction method is based on the Component Mode Synthesis (CMS) extended by the Wave-Based Substructuring (WBS) (see Hohl *et al.*, 2011). Firstly, the structural matrices are divided into master nodes (m) and slave nodes (s) as described in Craig and Bampton (1968). The master nodes are the coupling nodes between the blades and the disk (see Fig. 2). The slave nodes are transformed to a small basis of mode shapes. Therefore, the reduced stiffness matrix $\tilde{\mathbf{K}}_b$ of one blade b is obtained by

$$\tilde{\mathbf{K}}_b = \begin{bmatrix} \mathbf{K}_{mm} & \tilde{\mathbf{K}}_{ms} \\ \tilde{\mathbf{K}}_{sm} & \tilde{\mathbf{K}}_{ss} \end{bmatrix} = \begin{bmatrix} \mathbf{I} & \mathbf{0} \\ \Psi & \Phi \end{bmatrix}^H \begin{bmatrix} \mathbf{K}_{mm} & \mathbf{K}_{ms} \\ \mathbf{K}_{sm} & \mathbf{K}_{ss} \end{bmatrix} \begin{bmatrix} \mathbf{I} & \mathbf{0} \\ \Psi & \Phi \end{bmatrix} \quad (2.6)$$

where \mathbf{I} is the identity matrix, $(\cdot)^H$ denotes the Hermitian transformation and

$$\Psi = -\mathbf{K}_{ss}^{-1}\mathbf{K}_{sm} \quad (2.7)$$

and Φ is the modal matrix which contains the eigenvectors of the generalized eigenvalue problem

$$\mathbf{K}_{ss}\Phi = \mathbf{M}_{ss}\Phi\lambda \quad (2.8)$$

Accordingly, the mass matrix is subdivided and reduced. The disk can be reduced using a cyclic symmetric model as shown in Thomas (1979). Thus, all tuned sectors have the same dynamic properties. To couple the segments, it is assumed that the nodes on the right hand side $\mathbf{u}_{k,R}$ have the same motion as the nodes on the left hand side $\mathbf{u}_{k,L}$, except for the phase shift (see Fig. 2). Hence, the displacement of the nodes can be rewritten in cyclic coordinates by

$$\mathbf{u}_k = \begin{bmatrix} \mathbf{u}_{k,L} \\ \mathbf{u}_{k,M} \\ \mathbf{u}_{k,R} \end{bmatrix} = \begin{bmatrix} \mathbf{0} & \exp\left(-i\frac{2\pi k}{N}\right) \\ \mathbf{I} & \mathbf{0} \\ \mathbf{0} & \mathbf{I} \end{bmatrix} \begin{bmatrix} \mathbf{u}_{k,M} \\ \mathbf{u}_{k,R} \end{bmatrix} \quad (2.9)$$

for each nodal diameter k . Due to this transformation, the mass matrix and the stiffness matrix can be formulated for each segment. After the Craig Bampton reduction of all blades, see Eq. (2.6), the reduced matrices can be written in the matrix of the full disk by using a subset of modes and the master nodes

$$\tilde{\mathbf{K}}_d = \begin{bmatrix} \tilde{\mathbf{K}}_{mm}[\text{diag}(\tilde{\mathbf{K}}_{d,ms})] & \\ & [\text{diag}(\tilde{\mathbf{K}}_{d,ss})] \end{bmatrix} \quad (2.10)$$

with

$$[\text{diag}(\tilde{\mathbf{K}}_{d,ss})] = \begin{bmatrix} \tilde{\mathbf{K}}_{d,ss,1} & \cdots & \mathbf{0} \\ \vdots & \ddots & \vdots \\ \mathbf{0} & \cdots & \tilde{\mathbf{K}}_{d,ss,N} \end{bmatrix} \quad (2.11)$$

and just for $[\text{diag}(\tilde{\mathbf{K}}_{d,sm})]$ and $[\text{diag}(\tilde{\mathbf{K}}_{d,ms})]$. The coupling nodes have to be transformed into the full system using the theory of cyclic systems

$$\tilde{\mathbf{K}}_{mm} = \begin{bmatrix} \tilde{\mathbf{K}}_{1,1} & \tilde{\mathbf{K}}_{1,2} & \cdots \\ \tilde{\mathbf{K}}_{2,1} & \tilde{\mathbf{K}}_{2,2} & \cdots \\ \vdots & \vdots & \ddots \end{bmatrix} \quad (2.12)$$

with the submatrices

$$\tilde{\mathbf{K}}_{i,j} = \sum_{h=1}^{N-1} (w^{h(i-1)})^H \tilde{\mathbf{K}}_h w^{h(j-1)} \quad (2.13)$$

where

$$w = e^{-i\frac{2\pi}{N}} \quad (2.14)$$

As a consequence, the size of the structural matrices of the disk is strongly decreased. Nevertheless, the master nodes are in physical notation and can include a lot of DOFs. These coupling nodes are reduced by the single-value decomposition (SVD) of the modal matrix of the whole segment including the disk and the blade

$$\mathbf{K}_{\text{seg}} \Phi_{\text{seg}} = \mathbf{M}_{\text{seg}} \Phi_{\text{seg}} \lambda \quad (2.15)$$

The SVD of a subset of the modal matrix $\Phi_{\text{sub}} = \Phi_{\text{seg}}(\text{cpl}, \cdot)$, including only the coupling DOF, is given by

$$\Phi_{\text{sub}} = \mathbf{U} \Sigma \mathbf{V}^T \quad (2.16)$$

where Σ is a square diagonal matrix with non-negative real numbers on the diagonal. Using the matrix \mathbf{U} to reduce the system with $\mathbf{U}_{\text{red}} = \mathbf{U}(w, \cdot)$, the behavior of the coupled nodes can be projected in an accurate way. w is the number of waves chosen to describe the motion of the coupling nodes. The reduction method is called Wave-Based Substructuring (WBS) which is described in Čermelj *et al.* (2008). In this way, the system matrices for the blades and the disk can be written as

$$\begin{bmatrix} \tilde{\mathbf{K}}_{mm} & \tilde{\mathbf{K}}_{ms} \\ \tilde{\mathbf{K}}_{sm} & \tilde{\mathbf{K}}_{ss} \end{bmatrix} = \overbrace{\begin{bmatrix} \mathbf{I} & \mathbf{0} \\ \Psi & \Phi \end{bmatrix}}^{\text{CMS}} \overbrace{\begin{bmatrix} \mathbf{U}_{\text{red}} & \mathbf{0} \\ \mathbf{0} & \mathbf{I} \end{bmatrix}}^{\text{WBS}} \begin{bmatrix} \mathbf{K}_{mm} & \mathbf{K}_{ms} \\ \mathbf{K}_{sm} & \mathbf{K}_{ss} \end{bmatrix} \begin{bmatrix} \mathbf{U}^* & \mathbf{0} \\ \mathbf{0} & \mathbf{I} \end{bmatrix} \begin{bmatrix} \mathbf{I} & \mathbf{0} \\ \Psi & \Phi \end{bmatrix} \quad (2.17)$$

Thus, the physical DOF are described by

$$\begin{bmatrix} \mathbf{u}_m \\ \mathbf{u}_s \end{bmatrix} = \begin{bmatrix} \mathbf{U}^* & \mathbf{0} \\ \mathbf{0} & \mathbf{I} \end{bmatrix} \begin{bmatrix} \mathbf{I} & \mathbf{0} \\ \Psi & \Phi \end{bmatrix} \begin{bmatrix} \mathbf{x}_m \\ \mathbf{x}_s \end{bmatrix} \quad (2.18)$$

with a significantly smaller number of DOFs than the Finite Element model. After the assembly of the blades and the disks, the system matrices are reduced by the second modal reduction. This reduction is a good possibility to decouple the equation of motion, too. Therewith, equation of motion (2.5) can be written as a scalar function

$$u_i = \frac{\tilde{F}_i}{-\tilde{\mathbf{M}}_{i,i} \Omega^2 + (1 + id_0) \tilde{\mathbf{K}}_{i,i}} \quad (2.19)$$

One possibility to take into account the mistuning is to detune the single blades by a factor of

$$\mathbf{K}_{b,k} = \delta_k \mathbf{K}_{b,0} \Rightarrow \tilde{\mathbf{K}}_{b,k} = \delta_i \tilde{\mathbf{K}}_{b,0} \quad (2.20)$$

This can be a variation of Young's modulus. These factors are randomly built up by a standard deviation σ_0 and a mean value of 1. Afterwards, the full system can be reassembled using the subsystems

$$\tilde{\mathbf{K}}_{sys} = \begin{bmatrix} [\text{diag}(\tilde{\mathbf{K}}_{b,ss})] & [\text{diag}(\tilde{\mathbf{K}}_{b,ms})] & \mathbf{0} \\ [\text{diag}(\tilde{\mathbf{K}}_{b,sm})] & \tilde{\mathbf{K}}_{mm} & \tilde{\mathbf{K}}_{d,ms} \\ \mathbf{0} & \tilde{\mathbf{K}}_{d,sm} & \tilde{\mathbf{K}}_{d,ss} \end{bmatrix} \quad (2.21)$$

where

$$[\text{diag}(\tilde{\mathbf{K}}_{b,ss})] = \begin{bmatrix} \delta_1 \tilde{\mathbf{K}}_{b,ss} & \cdots & \mathbf{0} \\ \vdots & \ddots & \vdots \\ \mathbf{0} & \cdots & \delta_N \tilde{\mathbf{K}}_{b,ss} \end{bmatrix} \quad (2.22)$$

as the reduced diagonal matrix of all slave nodes of the mistuned blades. $\tilde{\mathbf{K}}_{mm}$ is the diagonal matrix of the reduced coupling nodes and $\tilde{\mathbf{K}}_{d,ss}$ is the reduced matrix of the blisk. The mass matrix is assembled in the same way. With the second modal reduction, the system is reduced to a very small number of DOFs and the equations are decoupled.

In Figs. 4a and 4b, a comparison between the reduced order model (ROM) and the FEM is given. The ROM is reduced from overall 170 000 DOF to 84 DOF for the whole system considering mistuning. To prove the capability of the reduced order model as an example a strongly mistuned blisk is used. Young's modulus of one blade is 20% higher than all other. To calculate 131 frequency points, the time needed for the FEM is about 5 minutes on a standard personal computer with a commercial Finite Element code. The calculated points are concentrated around the eigenfrequency to guaranty the absolute amplitude. The calculation of the FRF of the ROM (Eq. (2.19)) with 2000 frequency points requires only 5 seconds with a very good accuracy.

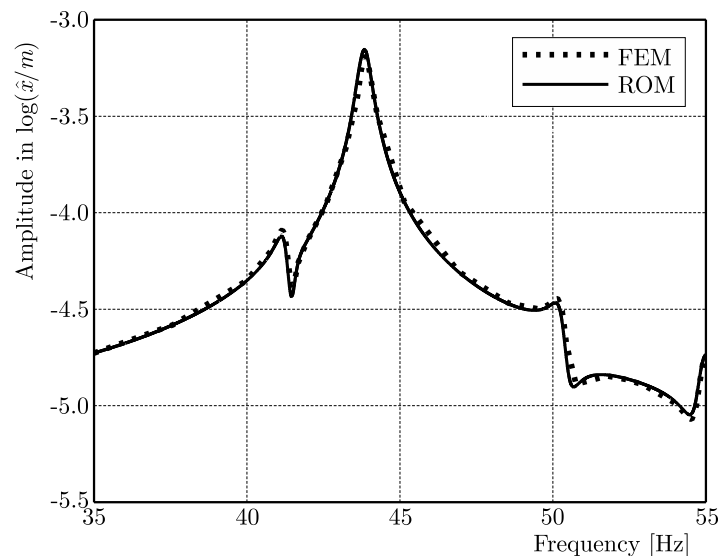


Fig. 4. Comparison between ROM and FEM: frequency response function of (a) 7th blade, (b) 9th blade

3. High order sensitivity analysis

One of the main points of interest is to calculate the maximum amplitude with respect to the standard deviation of the mistuned blades. In this way, the maximum stress can be determined.

Whitehead (1966) described the theoretical possible maximum of the amplitude of a mistuned blisk by

$$\frac{A_{max}}{A_{tuned}} = \frac{1}{2}(1 + \sqrt{N}) \quad (3.1)$$

with N denoting the number of blades. Here it is assumed that all vibration energy of all mode shapes is concentrated in one blade only. However, this case seems to be unreasonable for real bladed disk geometries. The common way to analyze the maximum amplitude of a mistuned bladed disk is the use of Monte-Carlo simulation (see Petrov, 2011; Siewert and Stüer, 2010; Beck *et al.*, 2012). The disadvantages are the very high calculation time and furthermore the lack of reliability of the results, e.g. there is no statement how many MCS are necessary to have convincing results. Using a Weibull estimation, the number of necessary MCS can be defined. Nevertheless, a high number of simulations is needed to obtain a good agreement (50 MCS in Bladh *et al.* (2001) and 500 MCS in Castanier and Pierre (2002)). Due to these problems, another method to calculate the maximum amplitude is given by a sensitivity analysis. This approach is motivated by Sextro *et al.* (2002), who described an extension of the theory of Sinha (1986) and Sinha and Chen (1989). To calculate the maximum amplitude with a given standard deviation of the stiffness of the blades, the sensitivity of the frequency response function is developed. By this means, an estimation of the maximum amplitude is very efficient and a statement of the probability of the amplitudes is given. The amplitude of the single blades can be written as

$$x = x_0 \pm \alpha\sigma \quad (3.2)$$

where x_0 is the average of all blades. Using the reduced DOF u in place of x economizes a lot of calculating time. It should be pointed out again that the equations of motion are decoupled and could be solved using scalar functions. This means that for calculation of the maximum and minimum limit of the tolerance interval of the amplitude, Eq. (3.2) can be written as

$$u = u_0 \pm \alpha\sigma \quad (3.3)$$

considering the transformation finally. Based on the results of Mignolet *et al.* (1999), it is assumed that the maximum amplitudes over all blades distributions at one frequency follow a Gaussian distribution. σ is the standard deviation and α the tolerance interval. $\alpha = 2$ means that 95.45% of all blade amplitudes are within the tolerance interval; for $\alpha = 3$, 99.73% of all blade amplitudes are within the interval. The definition given in Eq. (3.2) specifies the upper and lower limit for a given interval of the vibration amplitudes. In the case of N discrete data points, the standard deviation σ is defined as

$$\sigma = \sqrt{\frac{1}{N-1} \sum_{k=1}^N (u_k - u_0)^2} \quad (3.4)$$

Here, the amplitude of the single blades are used to calculate the standard deviation. It is assumed that the average amplitude of the vibration u_0 is the amplitude of the nominal, tuned system. The amplitude of the blade k is denoted as u_k . The parameters of interest are the mistuning factors δ_k introduced in the previous Section. The function of the amplitude depending on the variation factors can be approximated by a Taylor series

$$u_k(\delta_k) = u_0 + \sum_{h=1}^{\infty} \frac{1}{h!} \left(\frac{\partial u(\delta_k)}{\partial \delta_k} \right)^h \Big|_{\delta_k=1} (\delta_k - 1)^h \quad (3.5)$$

The derivation of the equation of motion in Eq. (2.5) with respect to the mistuning factors reads

$$\frac{\partial u_i(\delta_k)}{\partial \delta_k} = \frac{-(1 + d_0 i) \left(\frac{\partial \tilde{K}_i}{\partial \delta_k} \right) \tilde{F}_i}{[-\tilde{M}_i \Omega^2 + (1 + d_0 i) \tilde{K}_i(\delta_k)]^2} \quad (3.6)$$

where only the stiffness matrix depends on the mistuning factors. \widetilde{K}_i denotes the scalar entry $\widetilde{\mathbf{K}}_{i,i}$ and \widetilde{M}_i the scalar $\widetilde{\mathbf{M}}_{i,i}$. To calculate the higher terms of the Taylor series, the deviation with the higher order is

$$\frac{\partial^h u_i(\delta_k)}{\partial \delta_k^h} = \pm h! \left(\frac{(1 + d_0 i) \left(\frac{\partial \widetilde{K}_i}{\partial \delta_k} \right)}{\underbrace{[-\widetilde{M}_i \Omega^2 + (1 + d_0 i) \widetilde{K}_i(\delta_k)]}_{=S}} \right)^h u_i(\delta_k) \quad (3.7)$$

with “+” for even h and “-” for uneven h . Using the ratio test, it can easily be shown that the Taylor series converges if the supremum of S is less than 1. For this blisk, the maximum is $\delta_k = 10^{-3}$ like the maximum standard deviations of the single blades. As a consequence, the variance of the amplitude results in

$$\sigma_i = \sqrt{\frac{1}{N-1} \sum_{i=1}^N \left(\sum_{h=0}^{\infty} \pm (S)^h u_i(\delta_k) \right)^2} \quad (3.8)$$

In this equation, all variances are known from the system given in Eq. (2.5), except for the deviation of the stiffness matrix from Eq. (2.21) with respect to the mistuning factors

$$\frac{\partial \widetilde{\mathbf{K}}}{\partial \delta_k} = \begin{bmatrix} \left[\text{diag} \left(\frac{\partial \widetilde{\mathbf{K}}_{b,ss}}{\partial \delta_k} \right) \right] & \mathbf{0} & \mathbf{0} \\ \mathbf{0} & \mathbf{0} & \mathbf{0} \\ \mathbf{0} & \mathbf{0} & \mathbf{0} \end{bmatrix} \quad (3.9)$$

with

$$\left[\text{diag} \left(\frac{\partial \widetilde{\mathbf{K}}_{b,ss}}{\partial \delta_1} \right) \right] = \begin{bmatrix} \widetilde{\mathbf{K}}_{b,ss} & & \mathbf{0} \\ & \ddots & \\ \mathbf{0} & & \mathbf{0} \end{bmatrix} \quad (3.10)$$

followed by

$$\left[\text{diag} \left(\text{diag} \frac{\partial \widetilde{\mathbf{K}}_{b,ss}}{\partial \delta_2} \right) \right] = \begin{bmatrix} \mathbf{0} & & \mathbf{0} \\ & \widetilde{\mathbf{K}}_{b,ss} & \\ \mathbf{0} & & \ddots \\ & & & \mathbf{0} \end{bmatrix} \quad (3.11)$$

and so on, until the last one

$$\left[\text{diag} \left(\frac{\partial \widetilde{\mathbf{K}}_{b,ss}}{\partial \delta_N} \right) \right] = \begin{bmatrix} \mathbf{0} & & \mathbf{0} \\ & \ddots & \\ \mathbf{0} & & \widetilde{\mathbf{K}}_{b,ss} \end{bmatrix} \quad (3.12)$$

In Figs. 5a and 5b, the frequency response function is shown for a random mistuning pattern. The variance of the single blades is 10^{-3} , and three terms of the Taylor series are used. In Fig. 5a, the first isolated mode family is shown. Obviously, the FRFs of all blades are between the upper and the lower limit. The tolerance interval is set to $\alpha = 2$, therefore, the amplitude can be higher by 4.55% of the cases. Due to the upper limit, the deviation of the maximum amplitude is given for every frequency with the probability which is needed. In Fig. 5b, the region of nearby eigenfrequencies is shown. The limits show a good agreement with the randomly mistuned blades.

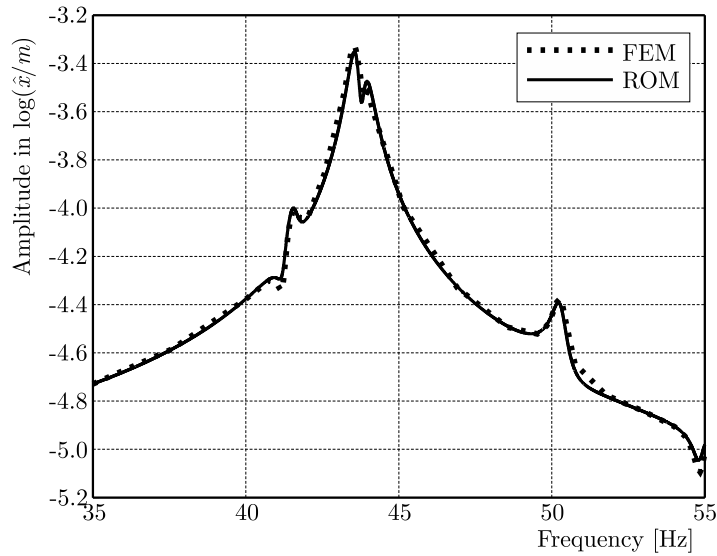


Fig. 5. Upper and lower limit of the FRF compared with a random mistuning for: (a) the first mode with $EO = 1$ and (b) the second and third mode with $EO = 3$

In all studies with the random mistuning, the upper limit fits well. In Fig. 6, a comparison of three sensitivity analyses with different numbers of terms of the Taylor series are given. The amplitudes are very close together but the behavior of the FRF is more detailed than with more terms. Calculating 1000 MCS, the PDF of all amplitudes can be compared with the PDF of the sensitivity analysis. The function of the PDF of the Gaussian distribution is given by

$$p(x) = \frac{1}{\sigma\sqrt{2\pi}} \exp\left[-\frac{1}{2}\left(\frac{x - \mu}{\sigma}\right)^2\right] \tag{3.13}$$

with σ derived from Eq. (3.8) and $\mu = u_0$ as the amplitude of the nominal system. In Figs. 7a and 7b, the probability distributions of the MCS and the Gaussian distribution of the sensitivity analysis using Eq. (3.13) are shown.

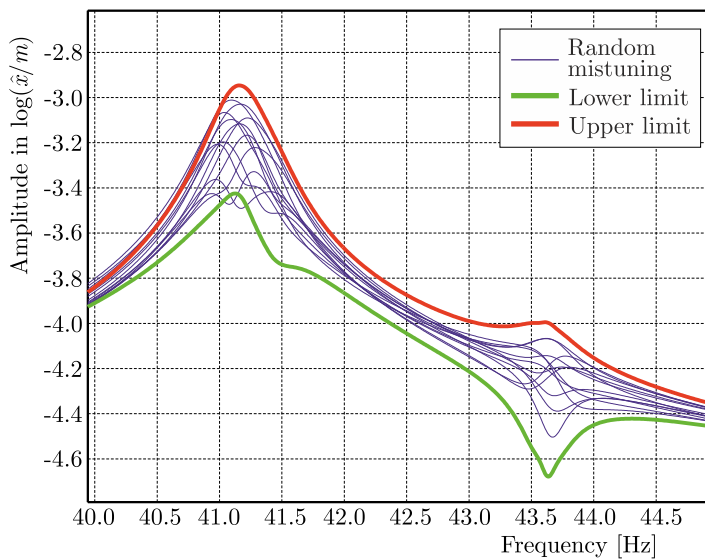


Fig. 6. Comparison of different numbers of terms of the Taylor series (without MCS)

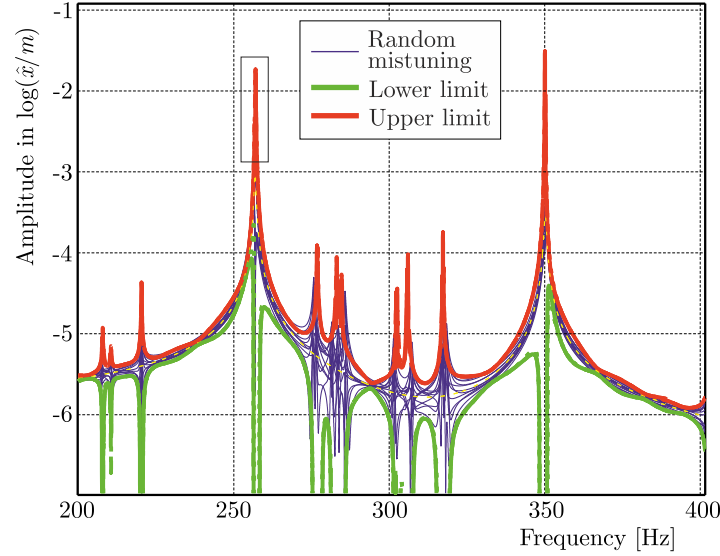


Fig. 7. (a) Comparison between 1000 Monte-Carlo simulations (MCS) and the sensitivity analysis (SA) with σ calculated at the first eigenfrequency at 41.15 Hz for $EO = 1$; (b) comparison between 1000 MCS and the PDF with σ calculated at the third eigenfrequency at 372.33 Hz for $EO = 4$

4. Case study: intentional mistuning

The second model has 30 blades which have an off-axis angle. The first mode is the one of interest. To show the generality of the reduction method, an intentional mistuning is introduced. This case study underlines the possibilities of such a method. A comparison between the reduced order model and the Finite-Element model is given in Hohl *et al.* (2011). With the sensitivity analysis a lot of parameter studies are feasible without consulting the calculating time. One of the most important ways to handle the increase of the amplitude is to use two different types of blades. For this purpose, an alternative pattern is used called AB mistuning. The benefits of this method are shown in Castanier and Pierre (2002), Han and Mignolet (2008), Mignolet *et al.* (2000) and Tatzko *et al.* (2013). An optimal intentional mistuning pattern is found for the frequency response including an additional random mistuning. In this way, costly statistics are used requiring a lot of computation time. With the sensitivity analysis shown here, the intentional mistuning can be classified as a simple method. To calculate the maximum amplitude of the pattern, the upper limit has to be calculated just once. This method is not restricted to just two different blade types or a geometric deviation.

The second blade is slightly thicker at its platform region, see Fig. 9. Therefore, it is necessary to rebuild the finite element mesh. Assuming that the contact nodes are at the same locations like the nodes of the disk, both types of blades are reduced using the Craig-Bampton with the same master nodes, as it is described in Eq. (2.17). With the same mesh at the contact nodes, the waves are the same for all blades. Only the reduced stiffness matrix of the blades is changed to

$$[\text{diag}(\tilde{\mathbf{K}}_{b,ss})] = \begin{bmatrix} \delta_1 \tilde{\mathbf{K}}_{b,ss}^A & \mathbf{0} & \cdots & \mathbf{0} \\ \mathbf{0} & \delta_2 \tilde{\mathbf{K}}_{b,ss}^B & \cdots & \mathbf{0} \\ \vdots & \vdots & \ddots & \vdots \\ \mathbf{0} & \mathbf{0} & \cdots & \delta_N \tilde{\mathbf{K}}_{b,ss}^B \end{bmatrix} \quad (4.1)$$

So, it is very simple to realize the intentional mistuning with geometric differences. The introduced sensitivity analysis is a suitable approach to estimate different patterns of the intentional mistuning using as many different blade types as required. The frequency response function

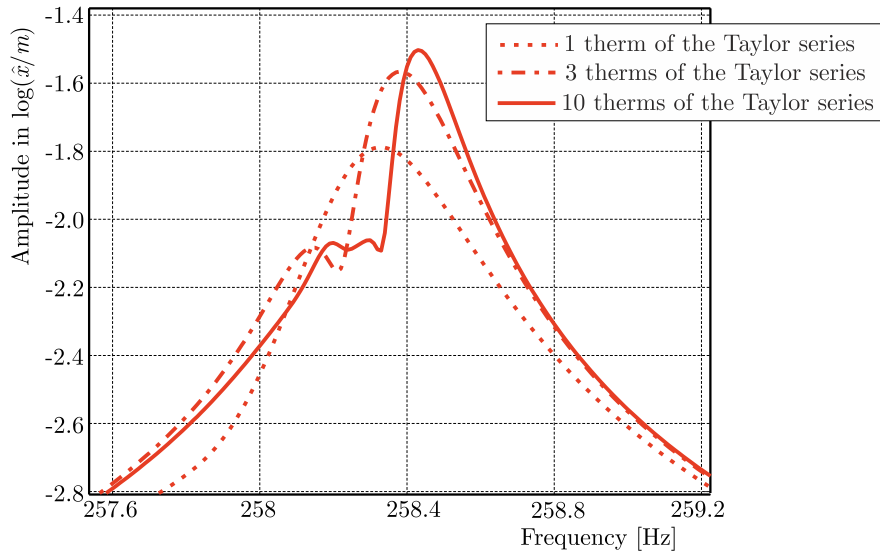


Fig. 8. FEM of the second model blisk

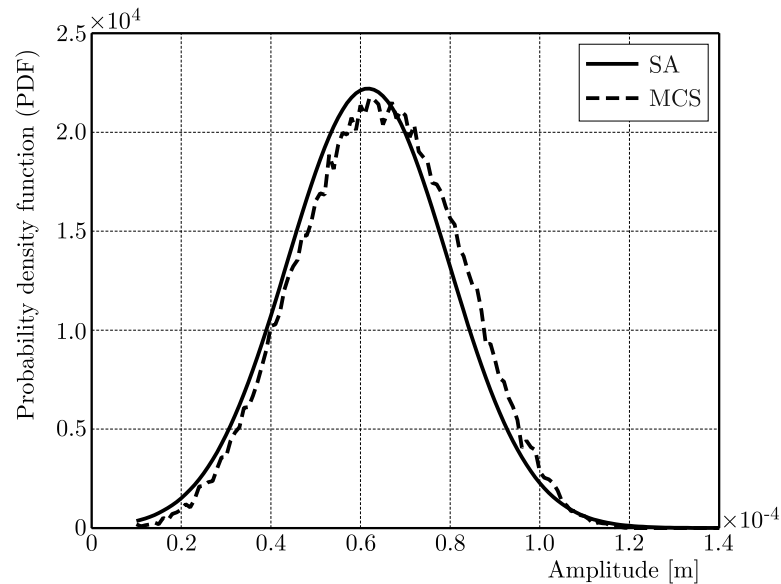


Fig. 9. Two different blade types, including intentional mistuning

has to be calculated only once to have a good estimation for the pattern. In this paper, three different patterns are evaluated. The first version is an AB mistuning, where the blades are set in alternation. In the second version, three blades of the same type are collected and sorted alternately. In the third version, all blades of type A are arranged in a row, followed by all blades of type B arranged in a row (see Fig. 10).

These patterns are examples to show the benefits of the introduced methods. The results are unique for every blade and disk geometry and have to be reproduced for each example.

Regarding the vibration amplitude without aerodynamical coupling, the tuned system with only one blade type has the smallest amplitude. Due to aerodynamical coupling, the intentional mistuning due to flutter or friction damping can be very useful. Nevertheless, the influence of the inevitable random mistuning has to be taken into account. With respect to the standard deviation of random mistuning, the three versions show small differences. With a very small standard deviation between 10^{-8} and 10^{-6} , version 3 is the best one. With a standard deviation higher than 10^{-5} , version 3 is the worst one. The chosen engine order is 2.

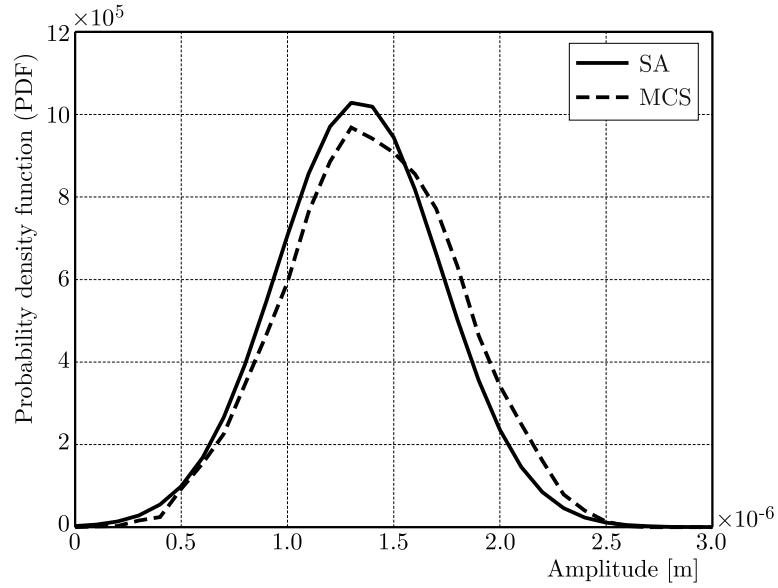


Fig. 10. Three patterns of the two blade types

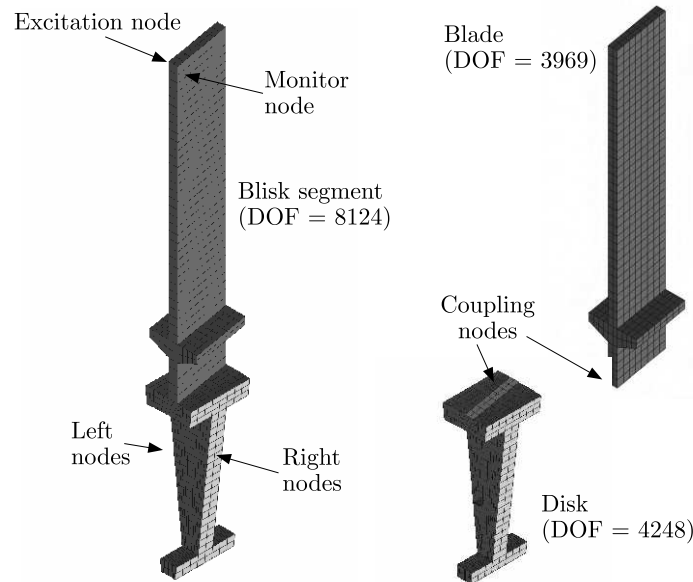


Fig. 11. Maximum amplitude of the three patterns with respect to different standard deviations of the blades at $EO = 2$

Figure 12 shows the normalized amplitude with different engine orders with a standard deviation of 10^{-6} . Versions 1 and 2 are the most sensitive patterns at the first engine order.

5. Conclusions

In this paper, a new analytical method has been introduced to estimate the maximum amplitude of a mistuned bladed disk. Its benefits are proved by a simple model with characteristic dynamic behavior. After a short introduction of the model, the used reduction method has been presented. Therewith, the frequency response function has been calculated in a minimum of time and with good accuracy. Using the sensitivity analysis, the maximum amplitude for a given interval has been estimated. For this purpose, the force response function and the maximum amplitude have

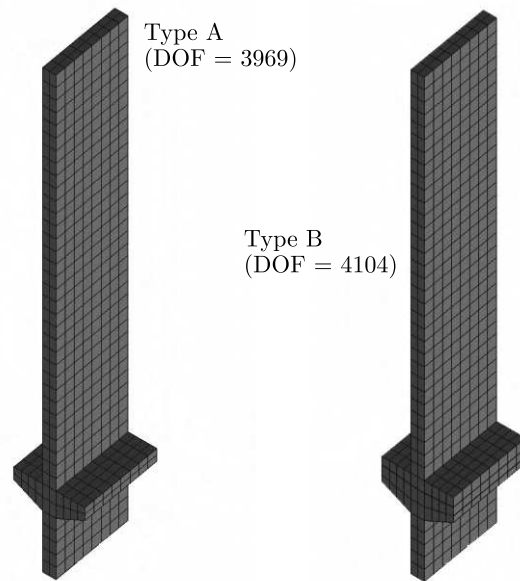


Fig. 12. Normalized amplitude with respect to the EO with a standard deviation of 10^{-6}

to be calculated only once. This saves a significant amount of time for optimization tools or parameter variations. Intentional AB mistuning has been presented as a possible application. Two types of blades have been used to analyze different patterns. The sensitivity analysis is proved to be a good tool for estimating intentional mistuning as well.

Acknowledgment

The authors kindly thank German Research Foundation (DFG) for the financial support of Collaborative Research Center (SFB) 871 “Regeneration of Complex Capital Goods” which provided the opportunity of their collaboration in the research project C3 “Influence of Regeneration-induced Mistuning on the Dynamics of Coupled Structures”.

References

1. BECK J.A., BROWN J.M., CROSS C.J., SLATER J.C., 2012, Probabilistic mistuning assessment using nominal and geometry based mistuning methods, *Proceedings of ASME TURBO EXPO*
2. BHARTIYA Y., SINHA A., 2011, Reduced order model of a bladed rotor with geometric mistuning: comparison between modified modal domain analysis and frequency mistuning approach, *Proceedings of ASME TURBO EXPO*
3. BLADH R., CASTANIER M.P., PIERRE C., 2001a, Component-mode-based reduced order modeling techniques for mistuned bladed disks – part 1: Theoretical models, *Journal of Engineering for Gas Turbines and Power*, **123**, 89-98
4. BLADH R., CASTANIER M.P., PIERRE C., 2001b, Component-mode-based reduced order modeling techniques for mistuned bladed disks – part 2: Application, *Journal of Engineering for Gas Turbines and Power*, **123**, 100-108
5. BLADH R., PIERRE C., CASTANIER M.P., KRUSE M.J., 2001, Dynamic response predictions for a mistuned industrial turbomachinery rotor using reduced-order modeling, *Journal of Engineering for Gas Turbines and Power*, **123**, 100-108
6. CASTANIER M.P., PIERRE C., 2002, Using intentional mistuning in the design of turbomachinery rotors, *AIAA Journal*, **40**, 10, 2077-2086

7. CASTANIER M.P., PIERRE C., 2006, Modeling and analysis of mistuned bladed disk vibration: Status and emerging directions, *Journal of Propulsion and Power*, **22**, 2, 384-396
8. ČERMELJ P., PLUYMERS B., DONDEERS S., DESMET W., BOLTEŽAR M., 2008, Basis functions and their sensitivity in the wave-based substructuring approach, *Proceedings of ISMA*
9. CRAIG R.R., 2000, Coupling of substructures for dynamic analyses: An overview, *American Institute of Aeronautics and Astronautics*, **1573**, 3-14
10. CRAIG R.R., BAMPTON M.C.C., 1968, Coupling of substructures for dynamic analyses, *American Institute of Aeronautics and Astronautics*, **6**, 1313-1317
11. FEINER D.M., GRIFFIN J.H., 2002, A fundamental model of mistuning for a single family of modes, *Journal of Turbomachinery*, **124**, 597-605
12. FEINER D.M., GRIFFIN J.H., 2004a, Mistuning identification of bladed disks using a fundamental mistuning model – part I: Theory, *Journal of Turbomachinery*, **126**, 150-158
13. FEINER D.M., GRIFFIN J.H., 2004b, Mistuning identification of bladed disks using a fundamental mistuning model – part II: Application, *Journal of Turbomachinery*, **126**, 159-165
14. GRIFFIN J.H., HOOSAC T., 1984, Model development and statistical investigation of turbine blade mistuning, *Journal of Vibration, Acoustics, Stress, and Reliability*, **106**, 204-210
15. HAN Y., MIGNOLET M.P., 2008, Optimization of intentional mistuning patterns for the mitigation of the effects of random mistuning, *Proceedings of ASME TURBO EXPO*
16. HOHL A., KRIEGESMANN B., WALLASCHEK J., PANNING L., 2011, The influence of blade properties on the forced response of mistuned bladed disks, *Proceedings of ASME TURBO EXPO*
17. MIGNOLET M.P., HU W., 1997, Direct prediction of the effects of mistuning on the forced response of bladed disks, *International Gas Turbine and Aeroengine Congress and Exhibition*
18. MIGNOLET M.P., HU W., JADIC I., 2000, On the forced response of harmonically and partially mistuned bladed disks. part I: Harmonic mistuning, *International Journal of Rotating Machinery*, **6**, 1, 29-41
19. MIGNOLET M.P., RIVAS-GUERRA A., LABORDE B., 1999, Towards a comprehensive direct prediction strategy of the effects of mistuning on the forced response of turbomachinery blades, *Aircraft Engineering and Aerospace Technology*, **71**, 5, 462-469
20. MOYROUD F., FRANSSON T., JACQUET-RICHARDET G., 2002, A comparison of two finite element reduction techniques for mistuned bladed disks, *Journal of Engineering for Gas Turbines and Power*, **124**, 942-952
21. PETROV E.P., 2011, Reduction of forced response levels for bladed disks by mistuning: Overview of the phenomenon, *Journal of Engineering for Gas Turbines and Power*, **133**, 072501-1-072501-10
22. SEXTRO W., PANNING L., GOETTING F., POPP K., 2002, Fast calculation of the statistics of the forced response of mistuning bladed disk assemblies with friction contracts, *Proceedings of ASME TURBO EXPO*
23. SHUAI W., JIANYAO Y., 2010, Mistuning identification for integrally bladed disks based on the SNM technique, *Proceedings of ASME TURBO EXPO*
24. SIEWERT C., STÜER H., 2010, Forced response analysis of mistuned turbine bladings, *Proceedings of ASME TURBO EXPO*
25. SINHA A., 1986, Calculating the statistics of forced response of a mistuned bladed disk assembly, *AIAA Journal*, **24**, 11
26. SINHA A., 2009, Reduced-order model of a bladed rotor with geometric mistuning, *Journal of Turbomachinery*, **131**, 031007-1-031007-7
27. SINHA A., CHEN S., 1989, A higher order technique to compute the statistics of forced response of a mistuned bladed disk assembly, *Journal of Sound and Vibration*, **130**, 2, 207-221

28. TATZKO S., VON SCHEIDT L.P., WALLASCHEK J., KAYSER A., WALZ G., 2013, Investigation of alternate mistuned turbine blades non-linear coupled by underplatform dampers, *Proceedings of ASME TURBO EXPO*
29. THOMAS D.L., 1979, Dynamics of rotationally periodic structures, *International Journal for Numerical Methods in Engineering*, **14**, 81-102
30. WHITEHEAD D.S., 1966, Effect of mistuning on the vibration of turbomachine blades induced by wakes, *Journal Mechanical Engineering Science*, **8**, 1, 15-21
31. YANG M.-T., GRIFFIN J.H., 2001, A reduced-order model of mistuning using a subset of nominal system modes, *Journal of Engineering for Gas Turbines and Power*, **123**, 893-900

Manuscript received January 29, 2015; accepted for print September 13, 2016

ANATOMICAL PROTOCOL FOR GAIT ANALYSIS: JOINT KINEMATICS MEASUREMENT AND ITS REPEATABILITY

MAGDALENA ŻUK, MARTA TRZECIAK

Wroclaw University of Technology, Department of Biomedical Engineering, Mechatronics and Theory of Mechanisms,
Wroclaw, Poland; e-mail: magdalena.zuk@pwr.edu.pl

International Society of Biomechanics has proposed a general reporting standard for joint kinematics based on anatomical reference frames. Nevertheless, the gait analysis protocols based on this standard are still poorly reported. The purpose of the current study is to propose and preliminarily assess the potential of an anatomically based ISB 6-DOF protocol, which combines the ISB reporting standard together with a marker cluster technique. The proposed technical marker set enables full description of the lower limb kinematics (including three-dimensional ankle-foot complex rotations) according to the current biomechanical recommendation. The marker set provides a clinically acceptable inter-trial repeatability and minimal equipment requirements.

Keywords: joint kinematics, gait analysis protocol, repeatability, anatomical protocol, marker-set, motion capture system

1. Introduction

-Three-dimensional kinematic measures of the human gait provide useful data for clinical practice and biomechanical research (Baker, 2006; Syczewska *et al.*, 2012). Increasingly, quantitative description of the human movement is used as input data in dynamic simulation of the musculoskeletal system (Delp *et al.*, 2007), including joint moment identification using inverse dynamic methods as well as muscle force estimation using optimization based methods (Erdemir *et al.*, 2007; Żuk and Pezowicz, 2016). Furthermore, such data may be helpful in the design of walking machines, exoskeletons (Oliński *et al.*, 2015), limb prosthesis or active orthoses (Dollar and Herr, 2008).

Contemporary quantitative analysis of gait incorporates advanced, still expensive motion capture systems for tracking marker location. The marker set together with the related biomechanical model for mathematical description of lower limb kinematics is called the gait analysis protocol.

The widely used protocol in clinical gait analysis is Conventional Gait Model (Davis *et al.*, 1991; Kadaba *et al.*, 1990) which is better standardised and validated than other models (Baker, 2006); therefore, it seems to be the most appropriate model in clinical practice at the moment. In this protocol, markers are placed both above bony landmarks and wand, therefore, this protocol is not fully anatomical. Simultaneously, the Conventional Gait Model is inconsistent with the ISB reporting standard.

Protocols based on the current ISB recommendation (Wu *et al.*, 2002) are still poorly reported. A recent study evaluated the performance of anatomically based protocols (Manca *et al.*, 2010; Leardini *et al.*, 2007; Ferrati *et al.*, 2008), including those using marker clusters (Collins *et al.*, 2009). However, both those protocols are not fully consistent with the ISB recommendation.

Gait kinematics measured using an anatomically based protocol, which also enables tracking of each segment independently, could increase the accuracy of musculoskeletal modelling and also seems to be more appropriate for consideration of orthoses and exoskeletons design.

The purpose of the current study is to propose and assess the protocol, which fulfils ISB standard, as well as to present reference data for normal subjects obtained using the proposed protocol. The proposed anatomically based protocol combines the general reporting standard recommended by the International Society of Biomechanics (ISB) together with a marker cluster technique. In the previous paper (Żuk and Pezowicz, 2015), the proposed methodology was presented and comparative analysis with a conventional protocol was conducted on the limited group as a preliminary verification of applied methods. In the current study, the reference data for normal subjects have been collected and inter-trial reproducibility has been validated. Furthermore, the applied methodology have been described in greater detail.

2. Methods

Lower limb motion was tracked using a motion capture system (Optotrak Certus, NDI, Canada) with one position sensor, equipped with three embedded infrared cameras (Fig. 1). The system tracked position and orientation of clusters of active markers.

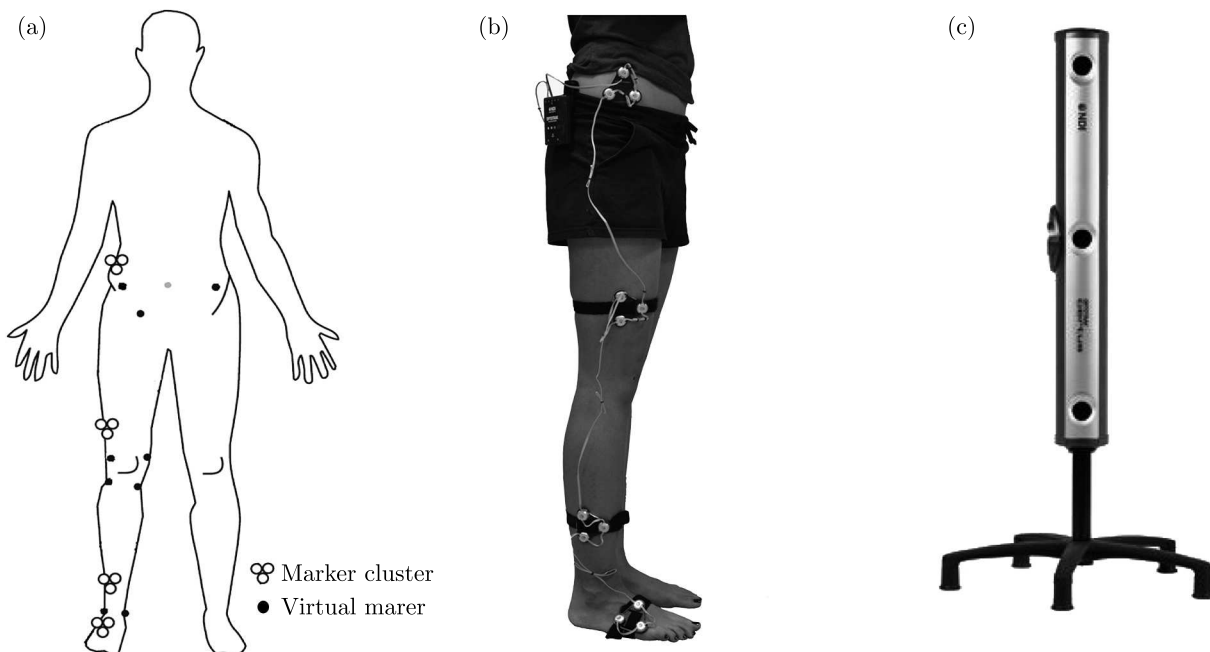


Fig. 1. (a) Marker set including technical markers and virtual markers, (b) marker placement, (c) motion capture system

Four clusters of active markers were located on pelvis and right lower limb segments: thigh, shank, and foot. The clusters were placed laterally on the distal part of each segment. Each cluster, consisting of three active markers (infrared LEDs) attached on a rigid base (Optotrak Smart Marker Rigid Body, NDI, Canada), was mounted with an adhesive tape and a band. The pelvis cluster was mounted using only adhesive tape. Locations of marker clusters and virtual markers are shown in Fig. 1. Furthermore, two additional virtual markers (on the heel and the metatarsal head) were included for foot visualization and gait phase identification. Davis's regression equation was applied to determine the hip joint centre (Davis *et al.*, 1991)

Anatomical landmarks were defined as virtual markers whose positions with respect to the technical markers (cluster) were measured using a tracked pointer during a static trial. The virtual marker set was designed on the basis of the current ISB recommendation (Wu *et al.*, 2002) for anatomical reference frames. Anatomical coordinate systems of each anatomical segment were defined in pursuance of the paper by Wu *et al.* (2002) (Fig. 2).

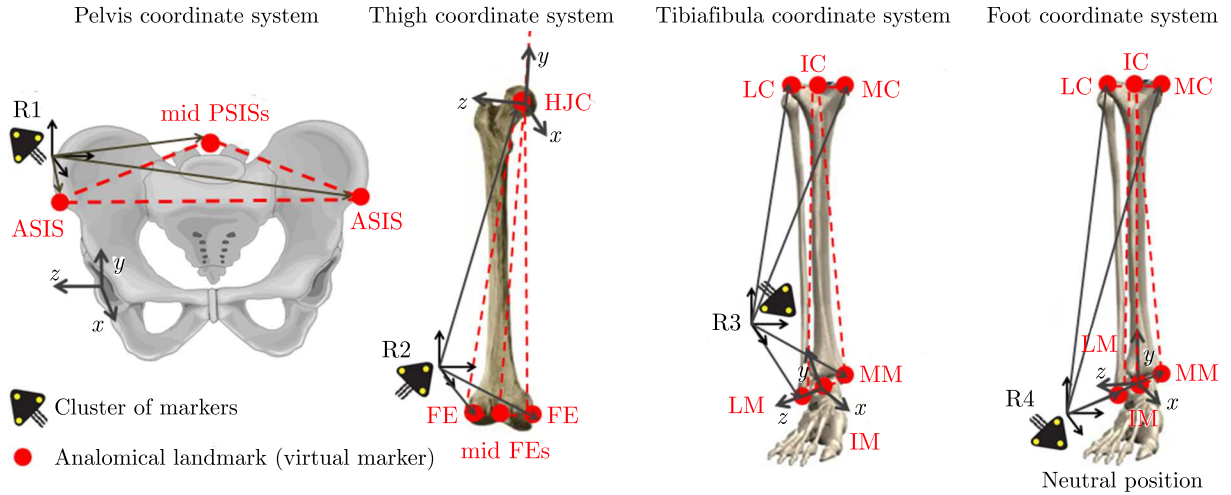


Fig. 2. Anatomical coordinate systems definition according to ISB recommendation (Wu *et al.*, 2002) based on following virtual markeres: ASIS – anterior superior iliac spine, midPSIS – midpoint between posterior superior iliac spines, HJC – hip joint centre, FE – femur epicondyle, midFEs – midpoint between femur epicondyles, LC – the most lateral point on the boarder of the lateral tibial condyle, MC – the most medial point on the border of the medial tibial condyle, IC – the inter-condylar point located modway between the MC and LC, LM – tip of medial malleolus, MM – tip of the medial malleolus

Cardan's angular convention was used to describe relative orientation of adjacent segments (Tupling and Pierrynowski, 1987; Kadaba *et al.*, 1990). In this convention, the joint rotations \mathbf{R} are described as compound rotations

$$\begin{aligned}
 \mathbf{R} &= \begin{bmatrix} r_{11} & r_{12} & r_{13} \\ r_{21} & r_{22} & r_{23} \\ r_{31} & r_{32} & r_{33} \end{bmatrix} = \mathbf{R}_{Z\gamma} \mathbf{R}_{X\alpha} \mathbf{R}_{Y\beta} \\
 &= \begin{bmatrix} \cos \gamma & -\sin \gamma & 0 \\ \sin \gamma & \cos \gamma & 0 \\ 0 & 0 & 1 \end{bmatrix} \begin{bmatrix} 1 & 0 & 0 \\ 0 & \cos \alpha & -\sin \alpha \\ 0 & \sin \alpha & \cos \alpha \end{bmatrix} \begin{bmatrix} \cos \beta & 0 & \sin \beta \\ 0 & 1 & 0 \\ -\sin \beta & 0 & \cos \beta \end{bmatrix} \\
 &= \begin{bmatrix} \cos \gamma \cos \beta - \sin \gamma \sin \alpha \sin \beta & -\sin \gamma \cos \alpha & \cos \gamma \sin \beta + \sin \gamma \sin \alpha \cos \beta \\ \sin \gamma \cos \beta + \cos \gamma \sin \alpha \sin \beta & \cos \gamma \cos \alpha & \sin \gamma \sin \beta - \cos \gamma \sin \alpha \cos \beta \\ -\cos \alpha \sin \beta & \sin \alpha & \cos \alpha \cos \beta \end{bmatrix}
 \end{aligned} \tag{2.1}$$

where $\mathbf{R}_{Z\gamma}$, $\mathbf{R}_{X\alpha}$, $\mathbf{R}_{Y\beta}$ are rotation matrices corresponding to rotations around anatomical axes, respectively: rotation by an angle γ around the frontal axis Z , rotation by an angle α around the sagittal axis X and rotation by an angle β around the longitudinal axis Y ; r_{ij} are rotation matrix elements. Graphical interpretation of the adopted rotation sequence is presented in Fig. 3.

According to the adopted joint angle definition, if $\mathbf{T}_{ALCS1 \rightarrow ALCS2}$ is the matrix of transformation from the proximal segment coordinate system to the distal segment coordinate system, which can be like this

$$\mathbf{T}_{ALCS1 \rightarrow ALCS2} = \begin{bmatrix} r_{11} & r_{12} & r_{13} & T_X \\ r_{21} & r_{22} & r_{23} & T_Y \\ r_{31} & r_{32} & r_{33} & T_Z \\ 0 & 0 & 0 & 1 \end{bmatrix} \tag{2.2}$$

where T_X , T_Y , T_Z refers to translations, then the anatomical joint angles can be calculated as follows

$$\alpha = \arcsin r_{32} \quad \beta = \arcsin \frac{-r_{31}}{\cos \alpha} \quad \gamma = \arcsin \frac{-r_{12}}{\cos \alpha} \tag{2.3}$$

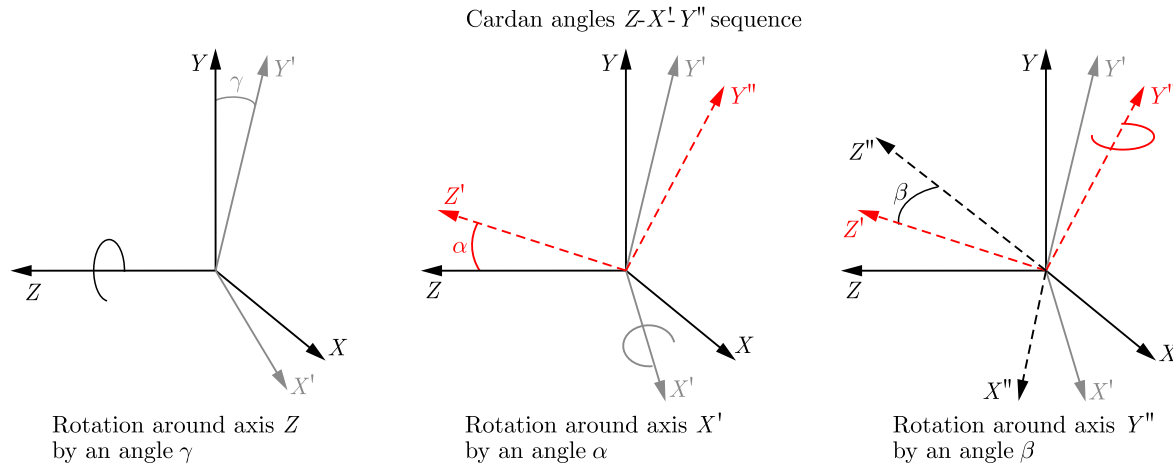


Fig. 3. Graphical representation of Cardan angle convention

where α is abduction/adduction joint angle, β is external/internal rotation angle and γ is flexion/extension joint angle.

Data acquisition and joint angle calculation were performed using custom-made software. Data processing, including gait cycle normalisation and smoothing, was performed using Matlab.

Ten able-bodied subjects without walking disability (five females and five males) were analysed (aged 22 ± 2 years, weight 66 ± 11 kg, height 1.75 ± 0.11 m). In the case of experimental methods or repeatability analysis, it was used to combine females and males while preserving the age range, which was shown in the paper by McGinley *et al.* (2009).

All participants provided written informed consent before participation. The subjects walked barefoot at a preferred pace and three gait cycles were selected.

The mean value and the standard deviation of 12 rotations were calculated over three trials for each sample of the gait cycle in ten subjects. Angle curves were plotted for a single representative subject (mean of three cycles) and for ten subjects (averaged across mean curves of each subject). Inter-trial variability was calculated according to the recommended method (Schwartz *et al.*, 2004; McGinley *et al.*, 2009) and plotted. Average inter-trial variability (AIT) was compared to the corresponding values from recent papers (Manca *et al.*, 2010; Schwartz *et al.*, 2004). Averaged intra-protocol variability was defined as a mean standard deviation over all subjects averaged across the gait cycle.

3. Results

Calculated joint rotations (Fig. 4) are related to corresponding data derived from similar biomechanical models (Benedetti *et al.*, 1998; Leardini *et al.*, 2007; Collins *et al.*, 2009). The lowest consistency of the range of motion (ROM) is observed for the ankle angle, for which the anatomical frame definition and the marker set differ considerably from other models. Average inter-trial variability is low (Table 1) and similar to the corresponding data from other studies (Manca *et al.*, 2010; Schwartz *et al.*, 2004). The most repeatable rotation within the subject is pelvis obliquity (0.9°), while the lowest reproducibility is observed for hip internal/external rotation and pelvis rotation (2.6°). The latter results from slight changes of the gait direction during the study. Inter-trial repeatability clearly depends on the phase of gait (Fig. 5). In particular, for knee flexion/extension and ankle inversion/eversion, inter-trial variability doubles during swing phase. Intra-protocol (Table 1) variability is highest for hip flexion/extension (14.2°) and pelvic tilt (12.7°) while for the other angles it does not exceed 10° .

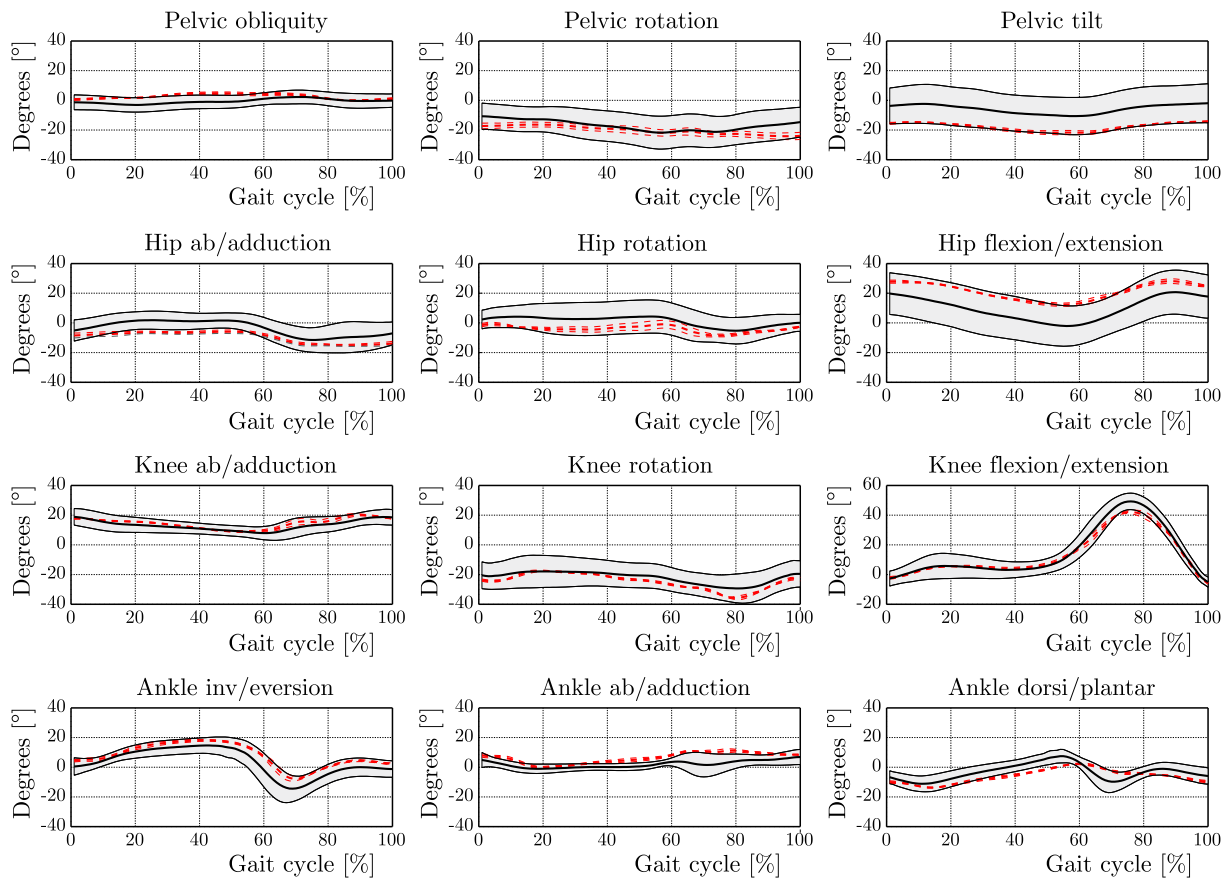


Fig. 4. Kinematic variables as calculated by the ISB 6-DOF of one representative subject (mean across three cycles – gray dashed line, +/- SD – gray dashed thin line) and ten subjects (averaged across mean curves of subjects – black solid line, +/- SD grey band)

Table 1. Average inter-trial and intra-protocol variability over the gait cycle across four subjects. Corresponding values from Manca *et al.* (2010) and Schwartz *et al.*(2004)

Rotations [°]	Inter-trial			Intra-protocol
	Present study	Manca <i>et al.</i>	Schwartz <i>et al.</i>	Present study
Pelvis tilt	1.2	0.9	0.8*	12.7
Pelvis obliquity	0.9	1.4	0.5*	4.6
Pelvis rotation	2.6	1.7	1.0*	10.0
Hip flex/ext	1.6	1.8	1.2*	14.2
Hip abd/add	1.4	1.7	0.5*	7.1
Hip intr/extr	2.6	2.9	1.2*	9.4
Knee flex/ext	1.9	2.2	1.6	6.3
Knee var/valg	1.0	1.6	0.5*	4.8
Knee intr/extr	1.2	4.3	1.2*	9.2
Ankle dor/pla	1.6	2.0	1.3*	4.5
Ankle inv/ev	1.8	2.3	–	6.3
Ankle abd/add	1.1	2.8	1.7	3.7

* data estimated from figures provide

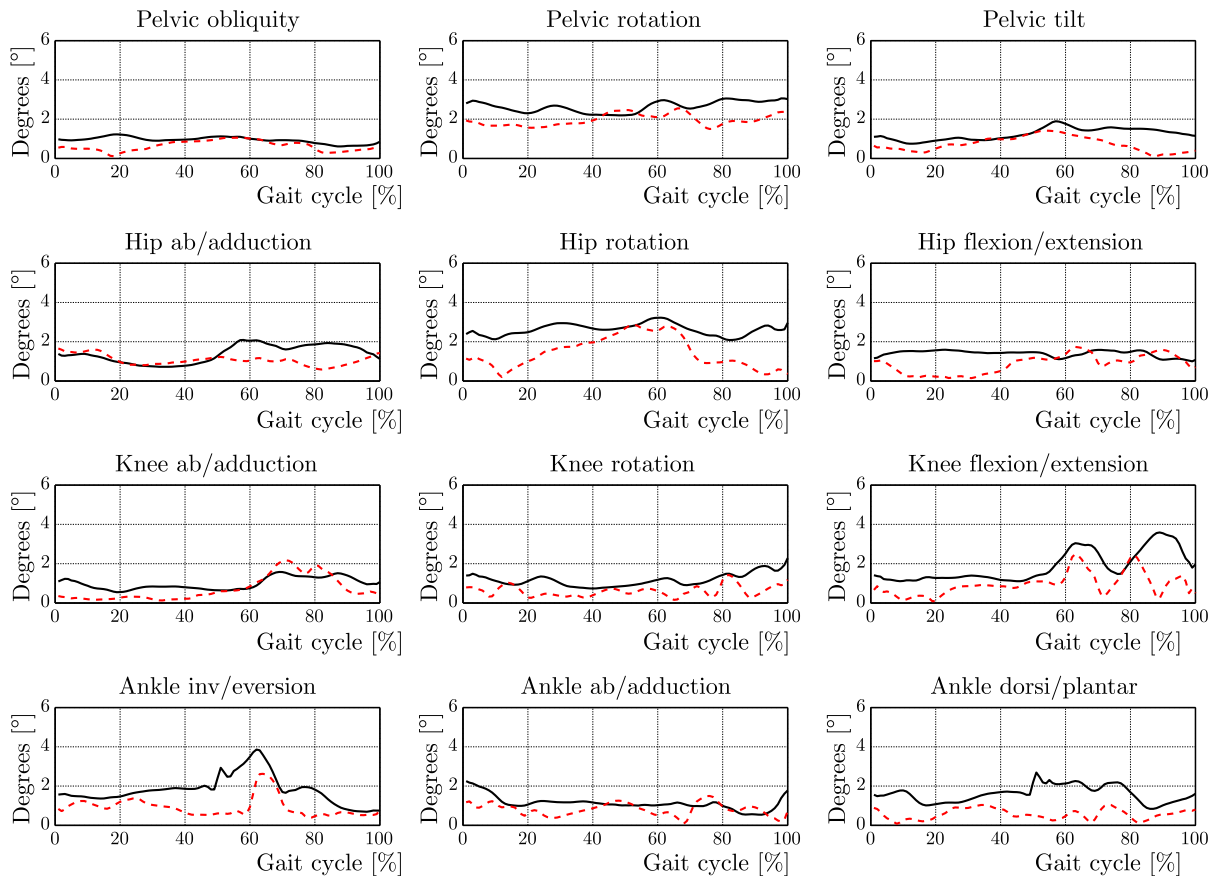


Fig. 5. Patterns of standard deviation across all samples of the gait cycle, one representative subject (gray dashed line) and average for ten subjects (black solid line)

4. Discussion

The proposed technical marker set enables full description of lower limb kinematics, including three-dimensional (3D) ankle-foot complex rotations according to the current biomechanical convention (Wu *et al.*, 2002). Lower limb segments are tracked separately without an assumption being made about joint constraints. Thus, this marker set can be applied to determination the joint centres and axes of rotation using functional methods, which was previously reported by Żuk *et al.* (2014). Besides, marker clusters in combination with an anatomical calibration allow definition of an unlimited number of virtual markers, freely placed within the segment, including those located beyond the “line of sight” of the position sensor. Only one position sensor (consisting of at least two cameras) is needed to track a selected lower limb (clusters located laterally) as well as both limbs (clusters placed frontally). The application of an additional position sensor allows such an arrangement of the clusters, particularly location of the pelvis cluster on the sacrum (Borhani *et al.*, 2013), which could reduce soft tissue artefacts (STA).

Reference data for normal subjects have been collected. Although the obtained selected joint angle curves are in agreement with the literature (Leardini *et al.*, 2007; Collins *et al.*, 2009; Benedetti *et al.*, 1998), caution is recommended when comparing the results among different protocols, especially in the case of non-sagittal planes (Ferrati *et al.*, 2008).

The obtained average inter-trial variability is acceptable in clinical application according to previous papers by Schwartz *et al.* (2004) and McGinley *et al.* (2009). A relatively low inter-trial variability indicates proper mounting of marker clusters, which eliminates sliding during examination. Further evaluation of the ISB 6-DOF protocol should include analysis of inter-

session and inter-assessor repeatability. However, inter-session and inter-assessor repeatability appear to be close to those achieved with other anatomically based protocols (Manca *et al.*, 2010) due to a similar source of variability (palpation of external bony landmarks).

An anatomically based protocol in which virtual markers are placed on bony landmarks without wands, increase reliability of musculoskeletal modelling by more accurate matching of marker trajectories to the scaled model.

The ISB 6-DOF protocol provides a full 3D description of lower limb kinematics according to the current recommendation (Wu *et al.*, 2002) with acceptable inter-trial variability. There are some limitations of the proposed method. The use of only one position sensor is associated with sub-optimal pelvis cluster location, which can affect pelvis and hip rotations. Moreover, at the present time, lack of relevant reference data for patients restricts the use of these methods in clinical practice.

Nevertheless, the proposed marker set can minimize the required equipment and, thereby, can enhance the availability of gait analysis in research and clinical applications.

References

1. BAKER R., 2006, Gait analysis methods in rehabilitation, *Journal of Neuro Engineering and Rehabilitation*, **3**
2. BENEDETTI M.G., CATANI F., LEARDINI A., PIGNOTTI E., GIANNINI G., 1998, Data management in gait analysis for clinical applications, *Clinical Biomechanics*, **13**, 3, 204-215
3. BORHANI M., MCGREGOR A.H., BULL A.M.J., 2013, An alternative technical marker set for the pelvis is more repeatable than standard pelvic marker set, *Gait and Posture*, **38**, 4, 1032-1037
4. COLLINS T.D., GHOUSSAYNI S.N., EWINS D.J., KENT J.A., 2009, A six degrees-of-freedom marker set for gait analysis: Repeatability and comparison with modified Helen Hayes set, *Gait and Posture*, **30**, 173-180
5. DAVIS III R.B., ÖUNPUU S., TYBURSKI D. GAGE J.R., 1991, A gait analysis data collection and reduction technique, *Human Movement Science*, **10**, 5, 575-587
6. DELP S.L., ANDERSON F.C., ARNOLD A.S., LOAN P., HABIB A., JOHN C.T., GUENDELMAN E., THELEN D.G., 2007, OpenSim: open-source software to create and analyze dynamic simulations of movement, *IEEE Transactions on Biomedical Engineering*, **54**, 11, 1940-1950
7. DOLLAR A.M., HERR H., 2008, Lower extremity exoskeletons and active orthoses: challenges and state-of-the-art, *IEEE Transactions on Robotics*, **24**, 1, 144-158
8. ERDEMIR A, MCLEAN S, HERZOG W., VAN DEN BOGERT A.J., 2007, Model-based estimation of muscle forces exerted during movements, *Clinical Biomechanics*, **22**, 131-154
9. FERRATI A., BENEDETTI M.G., PAVAN E., FRIGO C., BETTINELLI D., RABUFFETTI M., CRENNANA P., LEARDINI A., 2008, Quantitative comparison of five current protocols in gait analysis, *Gait and Posture*, **28**, 207-216
10. KADABA M.P., RAMAKRISHNAN H., WOOTTEN M., 1990, Measurement of lower extremity kinematics during level walking, *Journal of Orthopedic Research*, **8**, 383-393
11. LEARDINI A., SAWACHA Z., PAOLINI G., INGROSSO S., NATIVO R., BENEDETTI M.G., 2007, A new anatomically based protocol for gait analysis in children, *Gait and Posture*, **26**, 560-571
12. MANCA M., LEARDINI A., CAVAZZA S., FERRARESI G., MARCHI P., ZANAGA E., BENEDETTI M.G., 2010, Repeatability of new protocol for gait analysis in adult subject, *Gait and Posture*, **32**, 282-284
13. MCGINLEY J.L., BAKER R., WOLFE R., MORRIS M.E., 2009, The reliability of three dimensional kinematic gait measurements: a systematic review, *Gait and Posture*, **29**, 360-369

14. OLIŃSKI M., LEWANDOWSKI B., GRONOWICZ A., 2015, Type synthesis and preliminary design of devices supporting lower limb's rehabilitation, *Acta of Bioengineering and Biomechanics*, **17**, 1, 117-127
15. SCHWARTZ M.H., TROST J.P., WERVEY R.A., 2004, Measurement and management of errors in quantitative gait data, *Gait and Posture*, **20**, 196-203
16. SYCZEWSKA M., GRAFF K., KALINOWSKA M., SZCZERBIK E., DOMANIECKI J., 2012, Influence of the structural deformity of the spine on the gait pathology in scoliotic patients, *Gait and Posture*, **35**, 2, 209-213
17. TUPLING S.J., PIERRYNOWSKI M.R., 1987, Use of cardan angles to locate rigid bodies in three-dimensional space, *Medical and Biological Engineering and Computing*, **25**, 527-532
18. WU G., SIEGLER S., ALLARD P., KIRTLEY C., LEARDINI A., ROSENBAUM D., WHITTLE M., D'LIMA D.D., CRISTOFOLINI L., WITTE H., SCHMID O., STOKES I., 2002, ISB recommendation on definitions of joint coordinate system of various joints for reporting of human joint motion – part I: ankle, hip, and spine, *Journal of Biomechanics*, **35**, 543-548
19. ŻUK M., PEZOWICZ C., 2015, Kinematic analysis of a six-degrees-of-freedom model based on ISB recommendation: a repeatability analysis and comparison with conventional gait model, *Applied Bionics and Biomechanics*, Article ID 503713, 1-9
20. ŻUK M., PEZOWICZ C., 2016, The influence of uncertainty in body segment mass on calculated joint moments and muscle forces, *Information Technologies in Biomedicine*, **5**, 349-359
21. ŻUK M., ŚWIĄTEK-NAJWER E., PEZOWICZ C., 2014, Hip joint centre localization: evaluation of formal methods and effects on joint kinematic, *Information Technologies in Biomedicine*, **4**, 57-67

Manuscript received October 22, 2015; accepted for print October 6, 2016

AUTOMOTIVE VEHICLE ENGINE MOUNT BASED ON AN MR SQUEEZE-MODE DAMPER: MODELING AND SIMULATION

BOGDAN SAPIŃSKI, JACEK SNAMINA

University of Science and Technology, Department of Process Control, Cracow, Poland
e-mail: deep@agh.edu.pl; snamina@agh.edu.pl

The study investigates the performance of a semi-active vehicle engine mount incorporating an MR damper working in the squeeze mode (MRSQD), summarising its design, operating principles and key characteristics. The mathematical model of the mount is formulated based on the newly developed MRSQD. Two control algorithms are proposed for MRSQD control. The first algorithm (ALG1) uses the inverse model of the engine-frame system, the other is the sliding mode algorithm (ALG2). The effectiveness of the engine mount system is demonstrated in computer simulation.

Keywords: engine mount, vibration reduction, MR damper, control, algorithm

1. Introduction

The main source of engine vibrations are unbalanced inertia forces in the assembly of a crankshaft, pistons and connecting rods, as well as forces associated with the combustion process (Jędrzejowski, 1986; Kamiński and Pokorski, 1983). Car body vibrations are mostly attributed to road unevenness. Car body-engine interactions cause the vibrations to be transmitted between these two units. As these sources of vibration cannot be entirely eliminated, minimising the dynamic components of the forces transmitted via engine mounts becomes the major issue.

Elastic vehicle engine mounts were first used in the 1930s, based on rubber components, being small in size and relatively cheap (Yu *et al.*, 2001). In the 1960s, the engine mounts were introduced which used purpose-designed hydraulic elements to stabilise the engine (Flower, 1997; Graf and Shoureshi, 1988). In the years to come, these elements were further modified and upgraded (Singh *et al.*, 1992). They allow control of the mount stiffness and damping parameters in a wide frequency range (Helber *et al.*, 1990). However, parameters that are established at the stage of design have to remain unchanged when the system is in operation.

In the recent years, research efforts have focused on active and semi-active elements to be incorporated in engine mounts (Ivers and Dol, 1991). These elements enable more effective reduction of negative interactions between the engine and the car body. Stiffness and damping parameters can be adapted to the mount operating conditions providing the engine mounts with active or semi-active elements, such as MR dampers (Kim, 2014).

The vehicle engine mount considered in this study is provided with an MR damper operating in the squeeze mode (Sapiński and Krupa, 2013; Sapiński and Gołdasz, 2015; Sapiński, 2015). Its design, operating principles and key characteristics are summarised and the mathematical model is developed incorporating the MRSQD (Snamina and Sapiński, 2014). Two control algorithms are proposed for damper control: the first algorithm (ALG1) uses the inverse model of the engine-frame system, the other is the sliding mode algorithm (ALG2) (Imine *et al.*, 2011). The effectiveness of the ALG1 and ALG2 has been simulated in ideal conditions and during their implementation with a semi-active element.

2. MR squeeze-mode damper

The structure of the former version of the MRSQD was described in the notification of inventive design (Sapiński and Krupa, 2015) and in the works (Sapiński and Gołdasz, 2015; Sapiński, 2015). The present version of the device is characterized by a modified magnetic circuit. The objective of this device improvement was to achieve better characteristics taking into account potential applications of the MRSQD. The structure of the MRSQD with the numeric symbols indicating all key components (1-9) is shown in Fig. 1. The hardware features two concentric

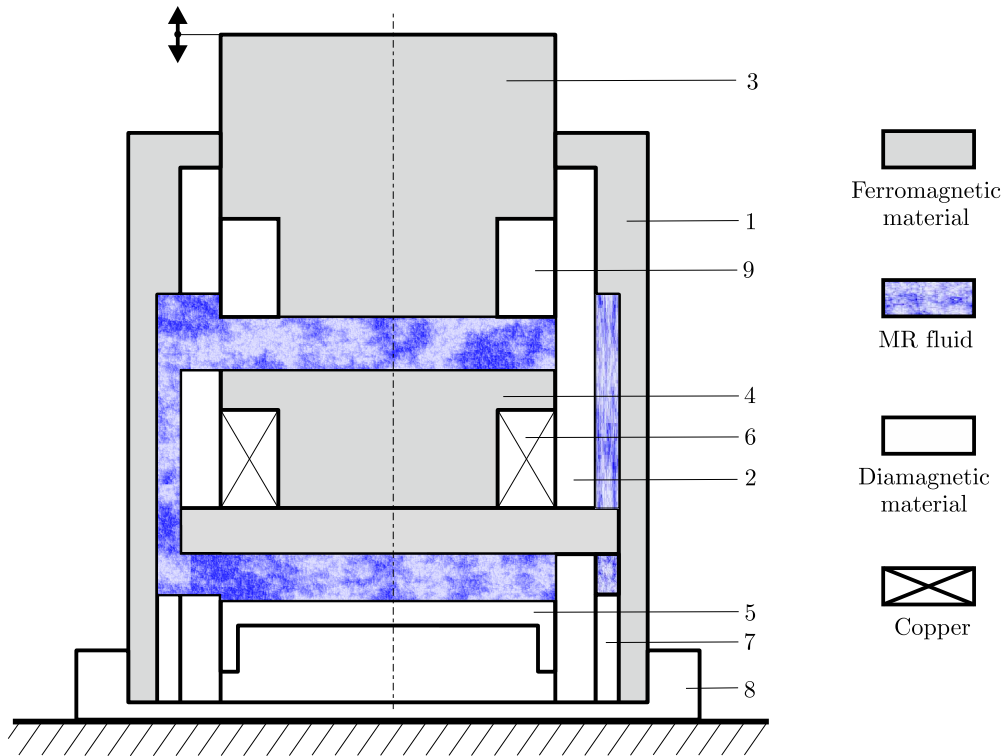


Fig. 1. Structure of the MRSQD

cylinders (1, 2). The inner (non-magnetic) cylinder (2) houses the piston (3) with an integrated non-magnetic ring (9), the core assembly (4), and the floating piston (5). The core assembly incorporates the coil (6). The outer cylinder (1) material is ferromagnetic. The distance between the lower surface of the piston and the upper surface of the core is referred to as the control gap of time-variant height h . The distance between the piston and the core varies according to the prescribed displacement (force) input. The floating piston below the core assembly separates the MR fluid from the coil spring located in the compensating chamber below the floating piston (5). The chamber incorporates a preloaded coil spring (not revealed in the diagram) for fluid volume compensation. The current in the control coil (6) induces a magnetic field. The magnetic flux generated by the current in the control coil travels through the core and into the control gap, the outer cylinder, and back into the core through radially projected arms in the core base. The inner cylinder of sufficient wall thickness is used to reduce the amount of magnetic flux bypassing the working gap, i.e. magnetic short circuit. All of the components ensure an efficient magnetic flux return path. The flux induced in the control gap upon the application of the coil current effectively modifies the yield stress of the MR fluid and its resistance to flow. As the piston moves downward, the distance between the core and the piston decreases. The excess of the MR fluid is squeezed out of the control gap into the fluid volume between the inner cylinder and the outer housing of the damper, and then into the compensating chamber. The additional

MR fluid volume that enters the compensating chamber pushes the floating piston against the coil spring. The structure incorporates a non-magnetic ring (7), whereas the base cap (8) is used for fixing the assembly against the ground.

The control coil of the device is represented by the equivalent circuit (see Fig. 2). The circuit consists of constant resistance $R = 2.8 \Omega$ and inductance $L(i, h)$ that depends on the applied current i and working gap height h . Let us assume that the piston executes sinusoidal motion with a frequency 9 Hz around to the midpoint of the current gap height with the amplitude 0.7 mm and recall the relationship $L(i, h)$ determined in (Sapiński and Krupa, 2013). Then, supplying the coil with the step voltage $u = U \cdot 1(t)$ we obtain plots of the current for $U = 1.4 \text{ V}$ and $U = 2.8 \text{ V}$ and gap height $h = 2.16 \text{ mm}$ as shown in Fig. 3. In the steady-state conditions, the constant component of current in the coil is produced by electric input (voltage u) whilst the variable component is induced by the mechanical input (piston displacement corresponding to the change of the gap height). It can be seen that for the assumed values of U , the steady-state current level is $I = 0.5 \text{ A}$ and $I = 1 \text{ A}$.

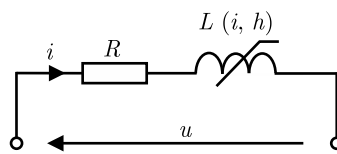


Fig. 2. Equivalent circuit of the control coil

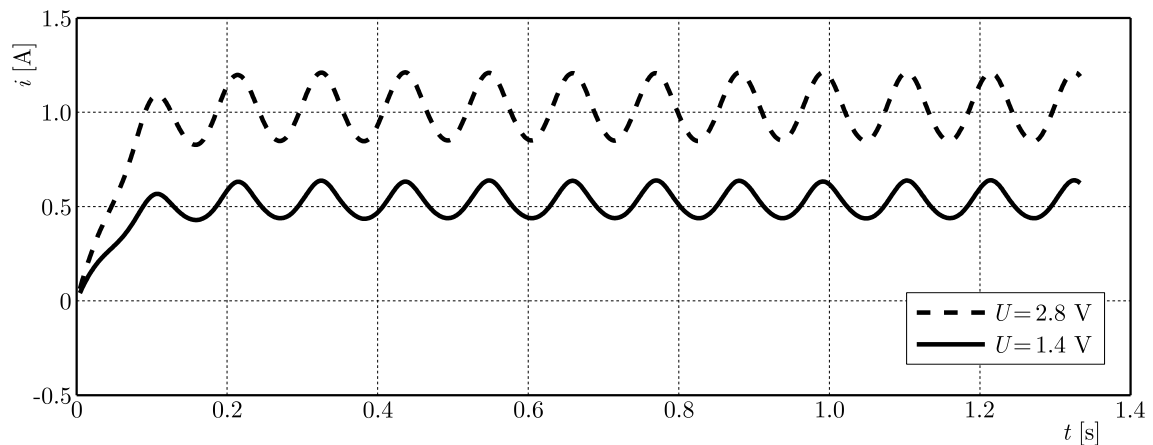


Fig. 3. Current in the control coil at frequency $f = 9 \text{ Hz}$

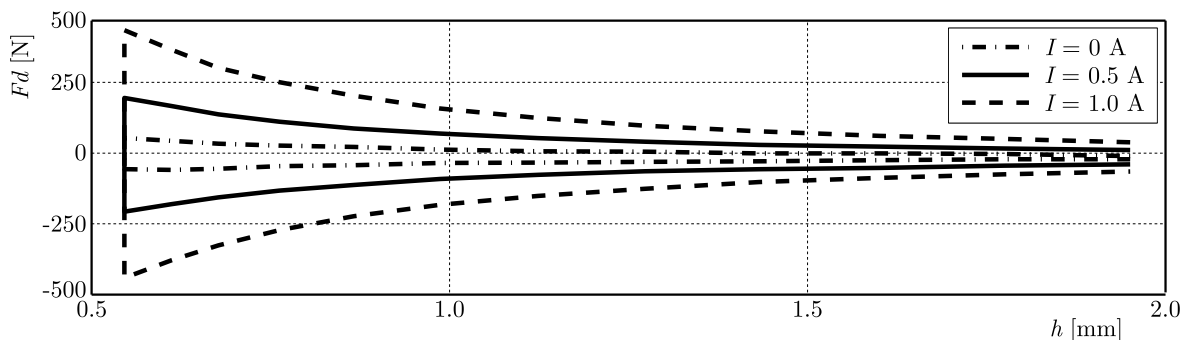


Fig. 4. Force vs. piston displacement for various current levels at frequency $f = 9 \text{ Hz}$

The force F_d produced by the MRSQD has the following components: force associated with fluid viscosity, inertia force of fluid motion and the force associated with yield stress of the fluid (Sapiński, 2015). In Figs. 4 and 5, we present plots between the force F_d and control gap height h and time histories of the force F_d for various piston displacement frequencies and for the control

coil being supplied with no current and the current I : 0.5 A, 1 A. The plots clearly indicate that the applied current in the coil is the major determinant of the damper force whereas for the given current level, the frequency of piston motion (piston velocity) plays a minor role.

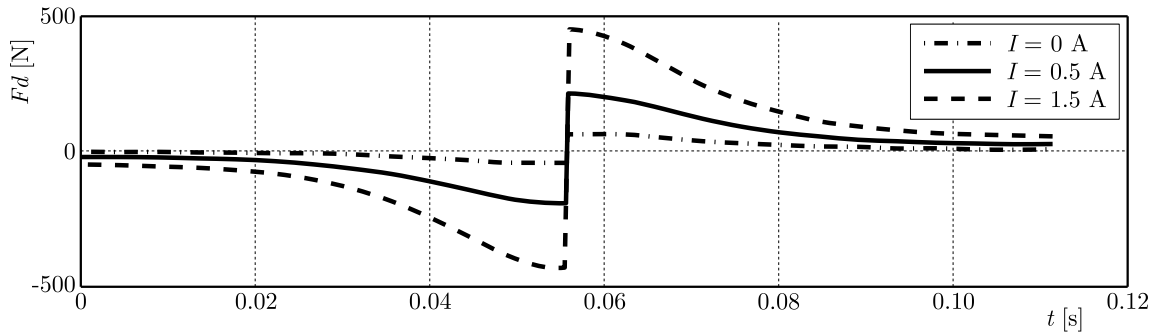


Fig. 5. Time histories of force for various current levels at frequency $f = 9$ Hz

3. Modeling of engine mount based on an MR squeeze-mode damper

Vibrations of the engine and frame linked to the car body are considered as a one process and are investigated using a simplified 2 DOF model schematically shown in Fig. 6. The engine mount system incorporates the MRSQD. The model embraces this part of the car body which includes the engine.

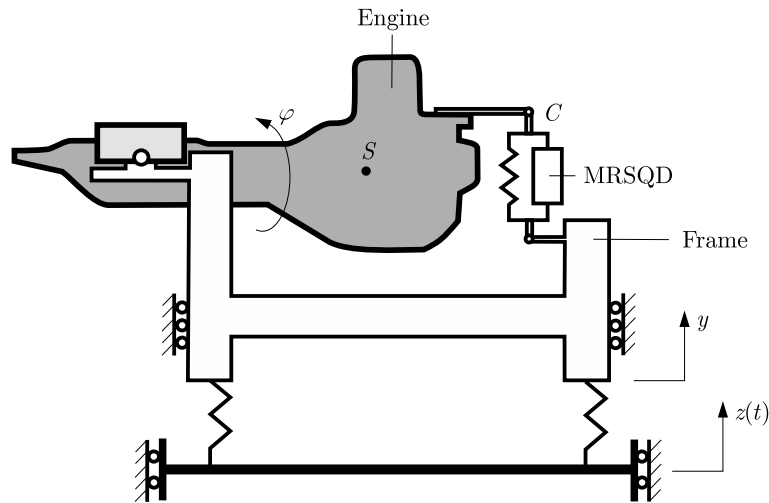


Fig. 6. Schematic diagram of the system

Assuming the kinematic inputs simulating the road unevenness, the following equations are derived

$$\begin{aligned} (M + m)\ddot{y} + ml_S\ddot{\phi} + 2b_p\dot{y} + 2k_p y &= 2k_p z(t) \\ J\ddot{\phi} + ml_S\ddot{y} + kl^2\phi &= -F_d l \end{aligned} \quad (3.1)$$

where M is the frame mass, m – engine mass, J – inertia moment of the engine (incorporating the crankshaft, pistons and rods assembly) with respect to the axis of revolution of the front engine attachment, F_d – MRSQD force acting upon the engine block, l – lever arm of the force F_d with respect to the axis of revolution, k – stiffness coefficient of a spring connected in parallel to the MRSQD, l_S – horizontal distance between the centre of engine mass S and the

axis of rotation, φ – rotation angle of the engine block, y – co-ordinate of the frame position, k_p – stiffness coefficient of each spring in frame guides, b_p – equivalent viscous damping in the frame guides. The co-ordinates φ and y describe motion of the system in relation to the static equilibrium position.

The term on the right-hand side of the first equation in system (3.1) is expressed in the physical unit of the force. Designating $F = 2k_p z(t)$, we are able to obtain the equivalent diagram of the investigated system (see Fig. 7) in which the kinematic input z is replaced by the applied force input F (preferred in the construction of the laboratory stand).

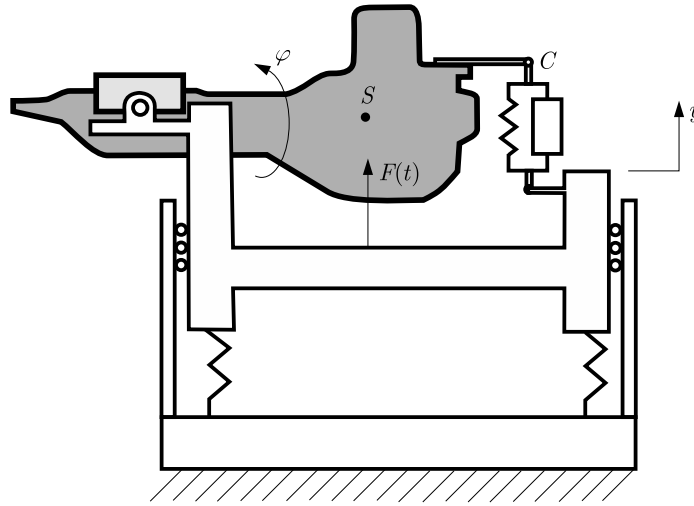


Fig. 7. Modified diagram of the system

The equations governing the system vibrations become

$$\begin{aligned} (M + m)\ddot{y} + ml_S\ddot{\phi} + 2b_p\dot{y} + 2k_p y &= F(t) \\ J\ddot{\phi} + ml_S\ddot{y} + kl^2\phi &= -F_d l \end{aligned} \quad (3.2)$$

The MRSQD force acting upon the vibrating object can be approximated with the formula

$$F_d = \beta_1(\mu, D_p)\frac{1}{h^3}\dot{h} + \beta_2(D_p)\tau_0(i)\frac{1}{h}\operatorname{sgn}(\dot{h}) + \beta_3(\rho, D_p)\frac{1}{h}\ddot{h} - \beta_4(\rho, D_p)\frac{1}{h^2}\dot{h}^2 \quad (3.3)$$

where D_p is the piston diameter in the damper, μ – dynamic viscosity of MR fluid, ρ – density of MR fluid, τ_0 – yield stress of MR fluid, β_1, \dots, β_4 – coefficients whose values are obtained from measurements.

In the static equilibrium position, the height h of the gap equals h_0 . In this piston position, the co-ordinates φ and y are equal to zero. Recalling the MRSQD structure, h_0 – corresponds to the maximum amplitude of piston displacement with respect to the housing, when the piston is on the same level as the upper surface of the core. Components of the force given by Eq. (3.3) have their physical interpretation: the first one is associated with fluid viscosity, the second one with those properties of MR fluids that are associated with magnetic field induction, and the other two terms are due to MR fluid inertia during the flow between the gap and the compensating chamber. Of major importance is the second term associated with magnetic field induction.

4. Control algorithms for the MR squeeze-mode damper

The forces of mount and engine interactions are resultants of static force components compensating for the engine gravity force and dynamic force components associated with the system

motion. These dynamic forces can be treated as those disturbing the state of equilibrium. The MRSQD force ought to minimise the impacts of forces disturbing the system equilibrium.

The active and semi-active vibration reduction systems use usually sky-hook or LQ algorithms as well as algorithms which employ suitable designed filters. This study presents two special algorithms, designated as ALG1 and ALG2 that allow separation of the sub-system from the rest of the system. Algorithm ALG1 bases on the inverse model of the engine-frame system, and algorithm ALG2 is the sliding mode algorithm.

The main objective of the control in the mount system is to minimise the vibration amplitude of a selected point of the engine. In accordance with algorithm ALG1, the MRSQD interaction force is obtained such as to compensate for the dynamic components of the frame-engine interaction force and to eliminate vibration of the point C of the engine. The algorithm is selected such that the vibrations of the point C should be decaying. The damping decrement expressing the effectiveness of control is dependent on actual parameters of the algorithm. The proposed algorithm can be governed by a force as a function of variables φ and y and their derivatives

$$F_d = ky - \left(m\frac{l_S}{l} - \frac{J}{l^2}\right)\ddot{y} - \beta(\dot{y} + l\dot{\varphi}) \quad (4.1)$$

The frame, engine and the control system with the control algorithm are shown in the block diagram (Fig. 8).

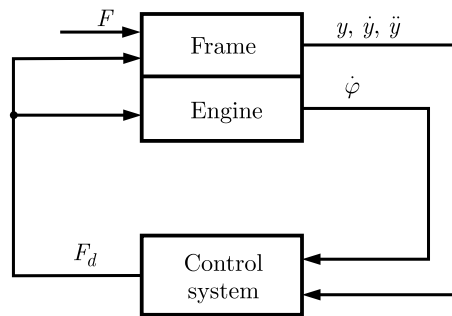


Fig. 8. Block diagram of the investigated system

The coordinates y and φ needed to determine the control signal are designated as output signals from the frame and engine blocks. As the damper interacts not only with the engine but with the frame as well, the force F_d is given as the input signal to the frame and engine blocks. F is an external force acting upon the frame and disturbing the system equilibrium. Taking into account formula (4.1), in the system of equations (3.2) we obtain equations governing the system motion with feedback

$$\begin{aligned} \left[M + m\left(1 - \frac{l_S}{l}\right)\right]\ddot{y} + m\frac{l_S}{l}\ddot{w} + 2b_p\dot{y} + 2k_p y &= F(t) \\ \frac{J}{l^2}\ddot{w} + \beta\dot{w} + kw &= 0 \end{aligned} \quad (4.2)$$

where: $w = y + l\varphi$.

Recalling the inverse model, the force F_d is chosen such that the second equation in system (4.2) is not coupled to the first equation, and that it involves vibration damping. Solution to the second equation determines the solution of the first equation because the force is transmitted onto the frame at the point where the engine is attached.

In accordance with principles of the sliding mode control (Shtessel *et al.*, 2014; Utkin and Chang, 2002), the algorithm contains a sliding variable σ being a linear combination of the position and velocity co-ordinates

$$\sigma = \dot{w} + cw \quad (4.3)$$

When the sliding variable is equal to zero ($\sigma = 0$), Eq. (4.3) implicates a sliding surface in a two-dimensional state space. The measure of the distance between the actual trajectory and the sliding surface can be expressed by a function of the sliding variable σ

$$V = \frac{1}{2}\sigma^2 \quad (4.4)$$

This is a Lyapunov function. The control is determined basing on the inequality which limits the Lyapunov function derivatives with respect to time, along the trajectory of motion. Assuming that the dynamic component of the force of mount and engine interaction is bounded by S_{max} , the Lyapunov function derivative along the trajectory satisfies the following inequality

$$\frac{dV}{dt} < \frac{M + m\left(1 - \frac{l_s}{l}\right)}{(M + m)\frac{J}{I^2} - m^2\left(\frac{l_s}{l}\right)^2} |\sigma| (S_{max} - \chi) < 0 \quad (4.5)$$

which is the basis for determining the control signal

$$F_d = \chi \operatorname{sgn}(\dot{w} + cw) + \frac{(M + m)\frac{J}{I^2} - m^2\left(\frac{l_s}{l}\right)^2}{M + m\left(1 - \frac{l_s}{l}\right)} c\dot{w} \quad (4.6)$$

where the coefficient χ is given by the formula

$$\chi = S_{max} + \frac{(M + m)\frac{J}{I^2} - m^2\left(\frac{l_s}{l}\right)^2}{M + m\left(1 - \frac{l_s}{l}\right)} \frac{\alpha}{\sqrt{2}} \quad (4.7)$$

In order to make the control signal derived from Eqs. (4.6) and (4.7) be implemented, it is required that the parameter S_{max} [N] should be first determined as it imposes a limit on force disturbing the system equilibrium. Besides, the parameters c [1/s] and α [m/s²] should be assumed, expressing the inclination of the sliding surface. The value of the parameter S_{max} can be estimated through investigating the system vibrations or from measurements.

The investigated vibration reduction system incorporating the MRSQD is a semi-active system. In accordance with the fundamental principle of semi-active systems, it is assumed that the system is capable of reproducing the force implicated by the suggested algorithms as long as the power resulting from damper-object interactions should be negative. When this power is positive, the semi-active system interaction force is equal to zero and the power delivered by the semi-active system will be zero, too. This condition can be written as follows

$$F_{d(ef)} = \begin{cases} F_d & \text{if } F_d(\dot{y} - \dot{w}) < 0 \\ 0 & \text{if } F_d(\dot{y} - \dot{w}) \geq 0 \end{cases} \quad (4.8)$$

where F_d is the force implicated by the control algorithm, $F_{d(ef)}$ effective semi-active damper force. The relative velocity is the difference between velocity of the point the damper is attached to the engine (point C , see Fig. 6) and the velocity of the point where the MRSQD is attached to the frame.

5. Simulation of engine mount based on MR squeeze-mode damper

Recalling the mathematical model outlined in Section 4 and using algorithms ALG1 and ALG2, simulations have been performed on the system vibration in the open loop and closed loop

configuration. Parameters in the simulation procedure were: frame mass $M = 60$ kg, engine mass $m = 80$ kg, inertia moment of the engine $J = 40$ kgm², horizontal distance between the engine centre of gravity and the axis of rotation $l_S = 0.5$ m, distance between the damper attachment point and the axis of rotation $l = 0.85$ m, stiffness coefficients $k_p = 6.6 \cdot 10^3$ N/m and $k = 4 \cdot 10^4$ N/m, coefficient of equivalent viscous damping $b_p = 100$ Ns/m. A sinusoidal excitation $F(t) = F_0 \sin(2\pi ft)$; $F_0 = 166$ N, $f = 9$ Hz has been assumed.

In the first stage, simulations were performed to determine the following parameters: displacement w of the point C and displacement y of the frame in the open-loop configuration. Simulation results obtained for the current level $I = 0.5$ A in the MRSQD control coil are shown in Fig. 9.

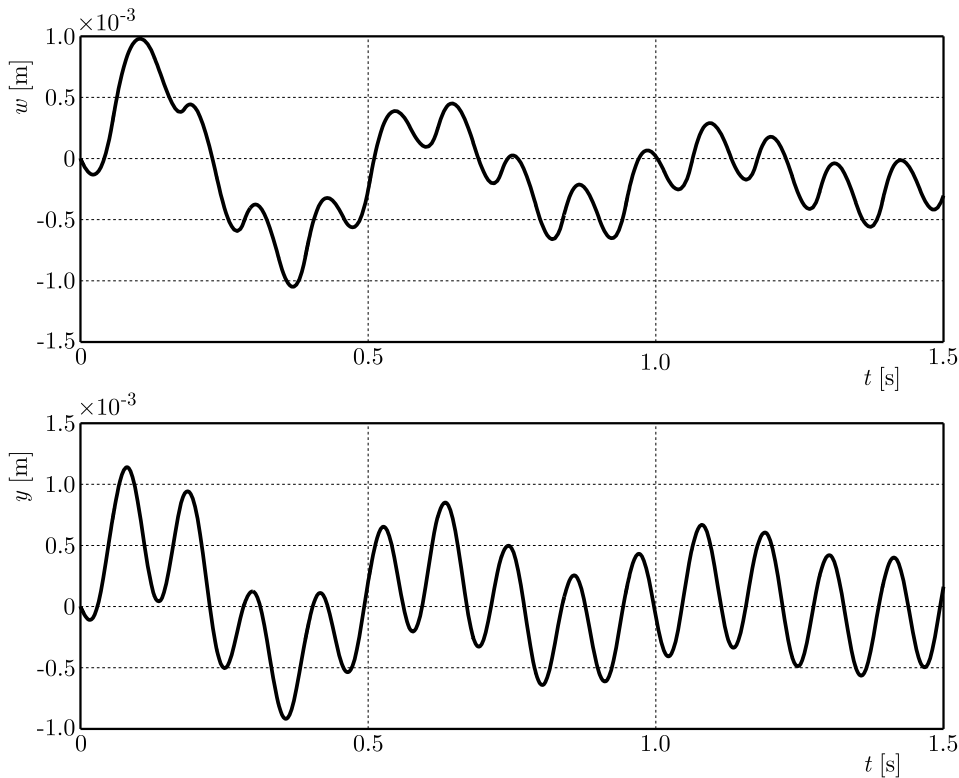


Fig. 9. Time histories of the engine point C and frame displacements (open-loop configuration)

Simulation results obtained using the ideally reproduced control signal in accordance with the algorithm ALG1 are summarized in Fig. 10, the value of the parameter is $\beta = 200$ Ns/m. In accordance with the algorithm ALG1, the vibration amplitude of point C of the engine decreases and its position asymptotically tends to the static equilibrium position. At the same time the amplitude of frame vibration remains almost unchanged.

Simulation results obtained using the ideally reproduced control signal in accordance with the control algorithm ALG2 are summarised in Fig. 11, the value of the parameters $c = 200$ 1/s, $\alpha = 10$ m/s², $S_{max} = 200$ N. When the sliding variable σ and the associated sliding surface are introduced, motion of the point C is now governed by a decreasing exponential function corresponding to the movement along the sliding surface. The position of the point C asymptotically tends to the static equilibrium position whilst the amplitude of frame vibration remains almost unchanged.

The assumption made during the second phase of simulations was that the algorithms ALG1 and ALG2 were to be implemented using a semiactive damper. The simulation procedure uses condition (4.8) which yields the effective force value $F_{d(ef)}$. Simulation data are summarised in

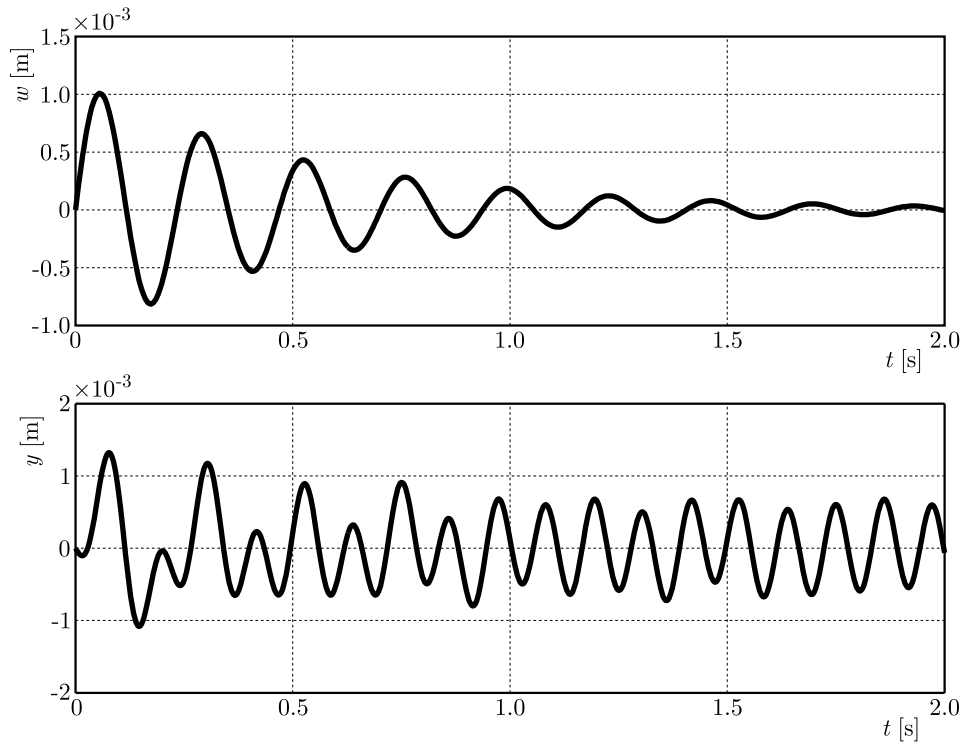


Fig. 10. Time histories of the engine point C and frame displacements (algorithm ALG1)

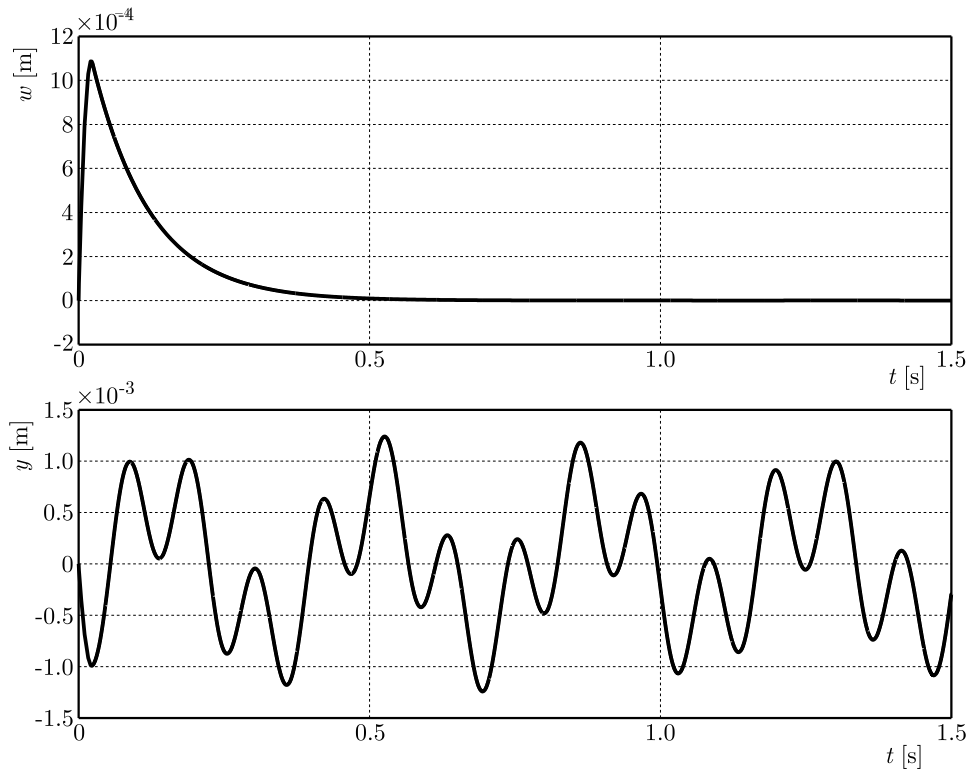


Fig. 11. Time histories of the engine point C and frame displacements (algorithm ALG2)

Figs. 12 and 13, for ALG1 and ALG, respectively. The results show that vibration reduction effectiveness deteriorates in relation to that achievable in the first stage of simulations, particularly in the case of ALG1.

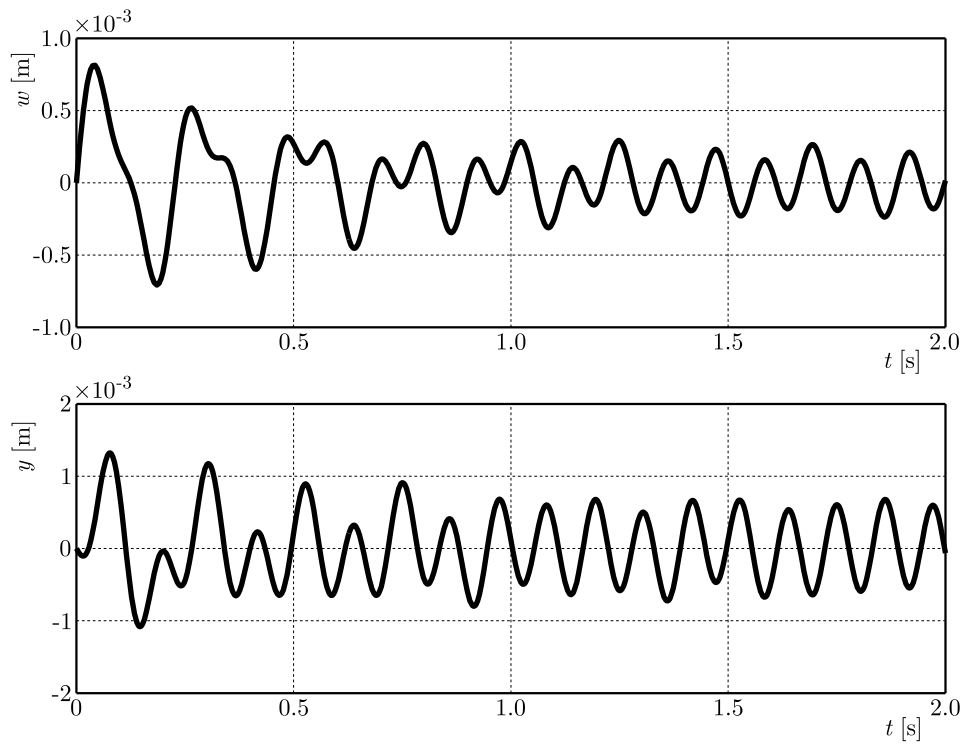


Fig. 12. Time histories of the engine point C and frame displacements (algorithm ALG1, semi-active implementation)

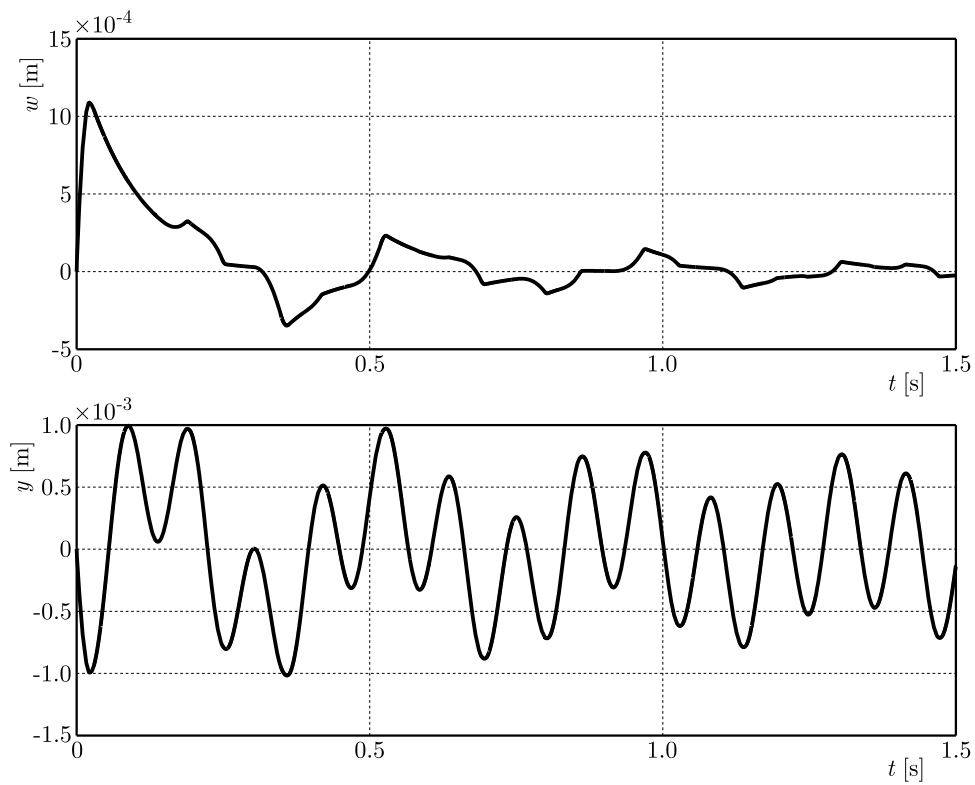


Fig. 13. Time histories of the engine point C and frame displacements (algorithm ALG2, semi-active implementation)

When comparing the simulation results for the proposed algorithms, the quantitative difference in motion of the subsystem to be vibroisolated can be observed. In the case of the ALG1, motion of the vibroisolated subsystem is typical vibration motion with a decreasing amplitude. This is similar to a great deal of such subsystem motion. The ALG2 is more effective and motion of the vibroisolated subsystem is characterized by a combination of both the oscillating and exponential motion.

6. Summary

This study investigates the potential application of a prototype MRSQD in a vehicle engine mount. Two algorithms for MRSQD control are proposed: one based on the inverse model of the engine-frame system (ALG1) and a sliding mode control algorithm (ALG2). In the ideal case, both algorithms ALG1 and ALG2 are effective, and the selected point of the engine can be returned to the position arbitrarily close to the static equilibrium position. In the case of semi-active implementation of ALG1 and ALG2, their effectiveness is significantly reduced. That applies particularly to ALG1, because semi-active actuators have a limited capability of reproducing the predetermined control force patterns. Despite this limitation, algorithms ALG1 and ALG2 can be the base for control of semi-active systems for vibration reduction.

Acknowledgement

This work has been supported by AGH University of Science and Technology under research program No. 11.11.130.958.

References

1. FLOWER W.C., 1997, Understanding hydraulic mounts for improved vehicle noise, vibration and ride qualities, *SAE Paper*, #952666
2. GRAF P.L., SHOURESHI R., 1988, Modeling and implementation of semi-active hydraulic engine mounts, *Journal of Dynamic Systems, Measurement Control*, **110**
3. HELBER R., DONCKER F., BUNG R., 1990, Vibration attenuation by passive stiffness switching mounts, *Journal of Sound and Vibration*, **138**, 1, 47-57
4. IMINE H., FRIDMAN L., SHRAIM H., DJEMAI M., 2011, *Sliding Mode Based Analysis and Identification of Vehicle Dynamics*, Springer Science and Business Media
5. IVERS D.E., DOL K., 1991, Semi-active suspension technology: An evolutionary view, *ASME DE* **40**, *Advanced Automotive Technologies*, Book No. H00719, 1-18
6. JĘDRZEJOWSKI J., 1986, *Mechanics of crank mechanisms used in internal combustion engines* (in Polish), WKŁ, Warszawa
7. KAMIŃSKI E., POKORSKI J., 1983, *Dynamics of vehicle suspensions and car transmission systems* (in Polish), WKŁ, Warszawa
8. KIM J.H., 2014, *Damping Force Control Filled with Magnetorheological Fluids and Engine Mount Having the Same*, US Patent No. US 8,672,105 B2
9. SAPIŃSKI B., 2015, Theoretical analysis of magnetorheological damper characteristics in squeeze mode, *Acta Mechanica et Automatica*, **9**, 2, 89-92
10. SAPIŃSKI B., GOŁDASZ J., 2015, Development and performance evaluation of an MR squeeze-mode damper, *Smart Materials and Structures*, **24**, 115007
11. SAPIŃSKI B., KRUPA S., 2013, Vibration isolator with MR fluid in squeeze mode, *Notification of Inventive Design*, No. P.406179

12. SHTESSEL Y., EDWARDS C., FRIDMAN L., LEVANT A., 2014, *Sliding Mode Control and Observation*, Birkhäuser
13. SINGH R., KIM G., RAVINDRA P.V., 1992, Linear analysis of automotive hydro-mechanical mount with emphasis on decoupler characteristics, *Journal of Sound and Vibration*, **158**, 2, 219-243
14. SNAMINA J., SAPIŃSKI B., 2014, Analysis of an automotive vehicle engine mount based on squeeze-mode MR damper, *Technical Transactions – Mechanics*, **2-M/2014**, 53-63
15. UTKIN V.I., CHANG H.C., 2002 Sliding mode control on electromechanical systems, *Mathematical Problems in Engineering*, **8**, 451-473
16. YU Y., NAGANATHAN N.G., DUKKIPATI R.V., 2001, A literature review of automotive vehicle engine mounting systems, *Mechanism and Machine Theory*, **36**, 123-142

Manuscript received October 28, 2015; accepted for print October 10, 2016

INFORMATION FOR AUTHORS

Journal of Theoretical and Applied Mechanics (JTAM) is devoted to all aspects of solid mechanics, fluid mechanics, thermodynamics and applied problems of structural mechanics, mechatronics, biomechanics and robotics. Both theoretical and experimental papers as well as survey papers can be proposed.

We accept articles in English only. The text of a *JTAM* paper should not exceed **12 pages of standard format A4** (11-point type size, including abstract, figures, tables and references), short communications – **4 pages**.

The material for publication should be sent to the Editorial Office via electronic journal system: <http://www.ptmts.org.pl/jtam/index.php/jtam>

Papers are accepted for publication after the review process. Blind review model is applied, which means that the reviewers' names are kept confidential to the authors. The final decision on paper acceptance belongs to the Editorial Board.

After qualifying your paper for publication we will require L^AT_EX or T_EX or Word document file and figures.

The best preferred form of figures are files obtained by making use of editorial environments employing vector graphics:

- generated in CorelDraw (*.cdr), AutoCad and ArchiCad (*.dwg) and Adobe Illustrator (*.ai). We require original files saved in the standard format of the given program.
- generated by calculation software (e.g. Mathematica) – we need files saved in *.eps or *.pdf formats.
- made in other programs based on vector graphics – we ask for *.eps, *.wmf, *.svg, *.psfiles.

Any figures created without application of vector graphics (scans, photos, bitmaps) are strongly encouraged to be supplied in *.jpg, *.tif, *.png formats with resolution of at least 300 dpi.

Requirements for paper preparation

Contents of the manuscripts should appear in the following order:

- Title of the paper
- Authors' full name, affiliation and e-mail
- Short abstract (**maximum 100 words**) and 3-5 key words (**1 line**)
- Article text (equations should be numbered separately in each section; each reference should be cited in the text by the last name(s) of the author(s) and the publication year)
- References in alphabetical order. See the following:
 1. Achen S.C., 1989, A new boundary integral equation formulation, *Journal of Applied Mechanics*, **56**, 2, 297-303
 2. Boley B.A., Weiner J.H., 1960, *Theory of Thermal Stresses*, Wiley, New York
 3. Canon W., 1955, Vibrations of heated beams, Ph.D. Thesis, Columbia University, New York
 4. Deresiewicz H., 1958, Solution of the equations of thermoelasticity, *Proceedings of Third U.S. National Congress of Applied Mechanics*, 287-305
- Titles of references originally published not in English, should be translated into English and formulated as follows:
 5. Huber M.T., 1904, Specific work of strain as a measure of material effort (in Polish), *Czasopismo Techniczne*, **XXII**, 3, 80-81

All the data should be reported in **SI units**.

Contents

Tengler S., Harlecki A. — Determination of the position of the contact point of a tire model with an uneven road surface for purposes of vehicle dynamical analysis	3
Zhu R., Zhu G., Mao A. — Mechanical analysis of autofrettaged high pressure apparatus	17
Cieplik G., Kopij Ł. — The application of self-oscillation in wire gauges	29
Magnucka-Blandzi E., Rodal M. — Bending and buckling of a metal seven-layer beam with a lengthwise corrugated main core – comparative analysis with the sandwich beam	41
Habib S.H., Belaidi I. — Crack analysis in bimaterial interfaces using T-spline based XIGA	55
Mieczkowski G. — The constituent equations of piezoelectric cantilevered three-layer actuators with various external loads and geometry	69
Żur K.K. — Quasi-Green's function approach to fundamental frequency analysis of elastically supported thin circular and annular plates with elastic constraints	87
Maciejewska B. — The application of Beck's method combined with FEM and Trefftz functions to determine the heat transfer coefficient in a minichannel	103
Hayat T., Qayyum S., Imtiaz M., Alsaedi A. — Radiative Falkner-Skan flow of Walter-B fluid with prescribed surface heat flux	117
Wegner T., Kurpisz D. — An energy-based method in phenomenological description of mechanical properties of nonlinear materials under plane stress	129
Yaakoubi M., Dammak F. — A semi-theoretical model for transformation plasticity occurred during bainitic transformation	141
Allam M.N.M., Tayel I.M. — Generalized thermoelastic functionally graded half space under surface absorption of laser radiation	155
Piasecka-Belkhat A., Korczak A. — Modeling of thermal processes proceeding in a 1D domain of crystalline solids using the lattice Boltzmann method with an interval source function	167
Sang J., Xing S., Liu H., Li X., Wang J., Lv Y. — Large deformation and stability analysis of a cylindrical rubber tube under internal pressure	177
Thawait A.K., Sondhi L., Sanyal S., Bhowmick S. — An investigation of stresses and deformation states of clamped rotating functionally graded disks	189
Zhang Y.Q., Wang L.Z., Pang M., Fan L.F. — Analysis of strain localization in porous media with transversely isotropic elasticity under undrained conditions	199
Wang J., Li D., Jiang J. — Modeling and analysis of coupled flexural-torsional spinning beams with unsymmetrical cross sections	213
Hou Y., Du M., Fang P., Zhang L. — Synchronization and stability of an elastically coupled tri-rotor vibration system	227
Wróblewski T., Jarosińska M., Abramowicz M., Berczyński S. — Experimental validation of the use of energy transfer ratio (ETR) for damage diagnosis of steel-concrete composite beams	241
Karray M., Feki N., Khabou M.T., Chaari F., Haddar M. — Modal analysis of gearbox transmission system in Bucket wheel excavator	253
Korayem M.H., Nekoo S.R., Khademi A., Abdollahi F. — Design and implementation of improved sliding mode controller on 6R manipulator	265
Mohammadzadeh S., Mehrali M. — Dynamic response of ladder track rested on stochastic foundation under oscillating moving load	281
Zhu M.-M., Qiang X.-Q., Teng J.-F. — Numerical loss analysis on slot-type casing treatment in a transonic compressor stage	293
Amendola G., Dimino I., Amoroso F., Pecora R., Concilio A. — Preliminary design of an adaptive aileron for the next generation regional aircraft	307
Diouf M.M.L., Romero O.J. — Numerical study of droplet formation in a Y-junction microchannel	317
Zharfi H., Toussi H.E. — Numerical creep analysis of FGM rotating disc with GDQ method	331
Celebi K., Yarimpabuc D., Keles I. — A novel approach to thermal and mechanical stresses in a FGM cylinder with exponentially-varying properties	343
Pohle L., Tatzko S., Panning-von Scheidt L., Wallaschek Ö. — High order sensitivity analysis of a mistuned blisk including intentional mistuning	353
Żuk M., Trzeciak M. — Anatomical protocol for gait analysis: joint kinematics measurement and its repeatability	369
Sapiński B., Snamina J. — Automotive vehicle engine mount based on an MR squeeze-mode damper: modeling and simulation	377